

UNCLASSIFIED

AD NUMBER
ADB003966
NEW LIMITATION CHANGE
TO Approved for public release, distribution unlimited
FROM Distribution authorized to U.S. Gov't. agencies only; Test and Evaluation; JAN 1975. Other requests shall be referred to Air Force Rocket Propulsion Laboratory, ATTN: STINFO/DOZ, Edwards AFB, CA 93523.
AUTHORITY
AFRPL ltr dtd 13 May 1986

THIS PAGE IS UNCLASSIFIED

✓
AFRPL-TR-75-3

AD B 0 03966

ADVANCED FUELS FOR CHEMICAL LASERS
FINAL REPORT

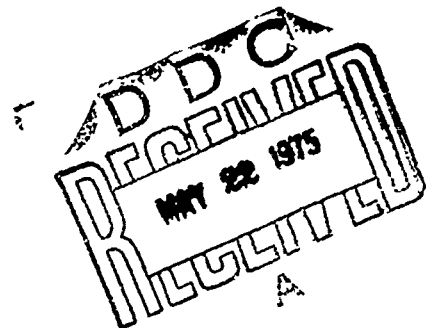
ROCKETDYNE DIVISION
ROCKWELL INTERNATIONAL
6633 CANOGA AVENUE
CANOGA PARK, CALIFORNIA 91304

AUTHORS: L. FORMAN
A. AXWORTHY
J. HON
G. SCHNEIDER

MAY 1975

Distribution limited to U.S. Government Agencies only;
Information covering test and evaluation of military
hardware, January 1975. Other requests for this
document must be referred to AFRPL(STINFO/DOZ),
Edwards, CA., 93523

AIR FORCE ROCKET PROPULSION LABORATORY
DIRECTOR OF SCIENCE AND TECHNOLOGY
AIR FORCE SYSTEMS COMMAND
EDWARDS, CALIFORNIA 93523



NOTICES

When U.S. Government drawings, specifications, or other data are used for any purpose other than a definitely related government procurement operation, the Government thereby incurs no responsibility nor any obligation whatsoever, and the fact that the Government may have formulated, furnished, or in any way supplied the said drawings, specifications or other data, is not to be regarded by implication or otherwise, or in any manner licensing the holder or any other person or corporation, or conveying any rights or permission to manufacture use, or sell any patented invention that may in any way be related thereto.

FOREWORD

This report was submitted by Rocketdyne Division of Rockwell International, 6633 Canoga Avenue, Canoga Park, California 91304, under Contract FO4611-72-C-0094, Job Order No. 573006UC, with the Air Force Rocket Propulsion Laboratory, Edwards, CA 93523.

This technical report is approved for release and distribution in accordance with the distribution statement on the cover and on the DD Form 1473.

CURTIS C. SELPH, GS-13
Project Engineer

B.R. BORNHORST, GS-14, Chief
Gas Dynamics Section

FOR THE COMMANDER

C. E. SIEBER, Colonel, USAF
Chief Liquid Rocket Division

Unclassified

SECURITY CLASSIFICATION OF THIS PAGE (When Data Entered)

REPORT DOCUMENTATION PAGE		READ INSTRUCTIONS BEFORE COMPLETING FORM
1 REPORT NUMBER AFRPL-TR-75-3	2 GOVT ACCESSION NO.	3 RECIPIENT'S CATALOG NUMBER
4 TITLE (and Subtitle) ADVANCED FUELS FOR CHEMICAL LASERS FINAL REPORT		5 TYPE OF REPORT & PERIOD COVERED FINAL 6/26/72-3/20/75
		6 PERFORMING ORG REPORT NUMBER R-9633
7 AUTHOR(s) L. Forman G. Schneider A. Axworthy J. Hon		8 CONTRACT OR GRANT NUMBER(s) F04611-72-C-0094
9 PERFORMING ORGANIZATION NAME AND ADDRESS Rocketdyne Division Rockwell International 6633 Canoga Ave, Canoga Park, CA. 91304		10 PROGRAM ELEMENT PROJECT TASK AREA & WORK UNIT NUMBERS
11 CONTROLLING OFFICE NAME AND ADDRESS Air Force Rocket Propulsion Laboratory Director of Science and Technology - Air Force Systems Command, Edwards, CA. 93523		12 REPORT DATE May 1975
		13 NUMBER OF PAGES 432
14 MONITORING AGENCY NAME & ADDRESS (if different from Controlling Office)		15 SECURITY CLASS (of this report) UNCLASSIFIED
		15a DECLASSIFICATION DOWNGRADING SCHEDULE
16 DISTRIBUTION STATEMENT (of this Report) Distribution limited to U.S. Government Agencies only; Information covering test and evaluation of military hardware, January 1975. Other requests for this document must be referred to AFRPL(STINFO/DOZ), Edwards, CA., 93523		
17 DISTRIBUTION STATEMENT (of the abstract entered in Block 20, if different from Report)		
18 SUPPLEMENTARY NOTES		
19 KEY WORDS (Continue on reverse side if necessary and identify by block number) Chemical Lasers, Fuels and Oxidizers, Hydrogen Fluoride, Chemical Kinetics, Cavity Fuels, Thermochemical Analysis		
20 ABSTRACT (Continue on reverse side if necessary and identify by block number) The report presents the results of a program to evaluate new reactants for the CW HF chemical laser. Reactants considered included the oxidizers F_2 , N_2F_4 , NF_3 , ClF_5 , and ClF_3 ; the precombustor fuels H_2 , N_2H_4 , NH_3 , CS_2 , $(CN)_2$, PF_3 , hydrocarbons, and perfluorohydrocarbons; the diluents He and N_2 ; and the cavity fuels hydrogen halides, hydrocarbons, and partially halogenated hydrocarbons. Also considered as precombustor reactants were nitrogen oxide-oxidizer combinations. Analyses of the precombustor thermochemistry demonstrated that NF_3 and the		

20. Abstract (Continued)

interhalogens have less favorable thermochemical properties than do F_2 and N_2F_4 , but all of the reactant systems considered could generate sufficient F atoms if a large enough fraction of the oxidizer were combusted. The only precombustor products that are expected to be noticeably detrimental in the cavity are HF and DF, and these can be reduced or eliminated by using hydrocarbons or fluorocarbons as the precombustor fuel.

Kinetic analyses of the cavity reactions were carried out (using the premixed approximation) for the cavity fuels H_2 , HCl , C_3H_8 , and HBr . Because of the higher rate of the $F + C_3H_8$ reaction, C_3H_8 gave higher calculated zero-power gains than H_2 . HBr gave lower calculated gains than H_2 on the P1 and P2 lines, but much larger gains on the P3 lines because the pumping reaction is more exothermic with HBr . In all cases, HF-HF V-V processes were found to be the dominant energy-transfer process.

Small-scale laser tests were utilized to evaluate advanced cavity fuels and advanced precombustor oxidizer fuel combinations. Considerable data were obtained on advanced cavity fuels which show that the slower mixing rates attendant with increased molecular weight inhibited the attainment of higher performance promised by faster pumping rates. Also, some of the advanced cavity fuels are faster deactivators than H_2 , further reducing their effectiveness. With the possible exception of HBr , the effective utilization of advanced cavity fuels requires new, innovative nozzle design.

Advanced precombustor reactants were demonstrated. These include NF_3 as an oxidizer and C_4F_8 as a fuel to produce no DF. Tests utilizing N_2 to replace He as a diluent showed performance depression much less than had been anticipated on analytical grounds. Evidence was found that a change in laser gain medium properties, e.g., substantially different deactivation rates, may have a large effect on the optimization of power outcoupling optics.

Global (overall) rates were measured for selected HF "pumping" reactions in a fast-flow reactor in which F atoms were measured by EPR spectroscopy. The rate constants obtained, in units of $(\text{mole/cc})^{-1} \text{sec}^{-1}$, were: 1.0×10^{13} for $F + H_2$, $2.4\text{--}3.1 \times 10^{13}$ for $F + HBr$, 1.0×10^{11} for $F + CF_3H$, 3.2×10^{13} for $F + CH_4$, 5×10^{13} for $F + C_3H_8$, and 1.7×10^{17} for $F + HI$.

SUMMARY

PHASE I: THERMOCHEMICAL AND KINETIC ANALYSIS

To determine which advanced precombustor and cavity reactants warrant experimental study, a theoretical analysis was conducted of the thermochemistry of F-atom generation in combustion and of the kinetics and mechanism of cavity reactions. The thermochemical calculations permitted the final precombustor gas composition and temperature to be predicted, assuming that chemical equilibrium is attained and the reactor is adiabatic. The possible detrimental effects on the cavity reactions of the combustion products of advanced fuels and oxidizers could then be considered. The kinetic analysis gave some indication of which chemical and energy-transfer processes affect the zero-power gain that can be attained when advanced reactants (including cavity fuels) are employed.

Task I-1. Thermochemical Analysis (Precombustor)

The conditions required for the nearly complete dissociation of F_2 to F-atom are calculated. The extent of dissociation increases with temperature and decreases with partial pressure of F-atoms as follows:

Percent F_2 Dissociated	Partial Pressure F-Atoms, psia		
	0.3	3.0	30
95.0	1280 K	1490 K	1800 K
99.0	1430 K	1710 K	2130 K
99.9	1710 K	2130 K	2800 K

At large extents of F_2 dissociation, the percent F_2 undissociated is approximately proportional to the F-atom concentration at a given temperature.

The oxidizers considered are F_2 , N_2F_4 , NF_3 , ClF_5 , and ClF_3 . The fuels are H_2 , N_2H_4 , NH_3 , CS_2 , cyanogen, PF_3 , hydrocarbons, and perfluorohydrocarbons; and the diluents are helium and nitrogen. The following two-component systems are also considered: N_2O-F_2 , N_2O-ClF_5 , N_2O-NF_3 , N_2O-SF_6 , $NO-NF_3$, $NO-ClF_5$ and $NO-SF_6$.

The reactant systems H_2 -He, ClF_5 - NH_3 -He, ClF_5 - C_6H_6 -He, ClF_5 - C_6F_6 -He, and ClF_5 - CS_2 -He are compared. The reactant ratios required to obtain various adiabatic temperatures and F-atom concentrations are calculated and plotted. The equilibrium product distributions are also plotted for these systems as a function of temperature at fixed mole fractions of F-atoms.

Only a limited number of major combustion products are formed. These are HF, CF_4 , ClF , SF_6 , and PF_5 . At higher temperatures, the ClF dissociates to atoms, the SF_6 forms SF_4 , and the CF_4 reacts with O_2 (if present) to form COF_2 . The large amounts of HF that are formed from the fuels H_2 , NH_3 , and N_2H_4 are of the most concern. The use of benzene reduces the amount of HF formed by about a factor of three and, of course, no HF is formed from C_6F_6 and CS_2 .

The theoretical product distributions were calculated also for the helium-free systems: N_2O - F_2 , N_2O - NF_3 , N_2O - ClF_5 , N_2O - SF_6 , NO - NF_3 , NO - ClF_5 , and NO - SF_6 . The nitrogen oxide, which is in large excess, should decompose to N_2 and O_2 (forming the diluent) generating sufficient heat to dissociate the oxidizer. These systems are shown to have satisfactory thermochemical properties. The concern in these systems is whether they will undergo sustained combustion and the possible effects in the cavity of the large amounts of oxygen and nitrogen generated.

Because the systems N_2O - SF_6 and NO - SF_6 may form SOF_4 as a product, estimates and data relating to the heat of formation of SOF_4 are reviewed. It is shown that the heat of formation is probably about -225 kcal/mole rather than -254 kcal/mole as suggested in the literature. Thus, SOF_4 is not predicted to be a major product in these systems but, rather, the sulfur should form mainly SO_2F_2 .

A detailed thermochemical analysis is presented which permits the thermochemical properties of the individual reactants to be investigated. The oxidizers NF_3 , ClF_5 , and ClF_3 are found to burn much colder with any given fuel than do F_2 or N_2F_4 . This requires a larger fraction of the oxidizer to be combusted (rather than dissociated to F-atoms), forming more combustion products such as HF. The thermochemical properties of the fuels have smaller effects on the fraction of the oxidizer combusted (i.e., on the heat of combustion), but the composition of the fuel determines mainly the reaction products.

The less favorable thermochemical properties of the oxidizer NF_3 and ClF_5 and of certain of the fuels do not preclude their use in a chemical laser. In fact, all of the precombustor reactant systems considered are capable, theoretically, of generating sufficient F-atoms when burned and, except for HF and DF, the predicted combustion products are not effective deactivators of HF^* . With some reactant systems, however, a considerable reactant weight penalty may be involved.

Task I-2. Kinetic Analysis (Cavity)

An analysis was made of the effects of advanced reactant systems on the kinetics of cavity reactions. The rates of the many elementary reactions and energy-transfer processes that may occur in the cavity were integrated using the premixed approximation. Estimates were obtained of the expected conditions and zero-power gain as a function of distance from the injector. In addition, the relative importance of the various chemical and energy-transfer processes on the predicted gain was investigated. The kinetic analysis was limited by the unavailability of measured kinetic parameters for many of the important processes.

In the Series I kinetic calculations, HCl was compared with H_2 as the cavity fuel and advanced precombustor reactant systems were compared with the baseline system $\text{F}_2\text{-D}_2\text{-He}$. HCl gave larger calculated gains than H_2 , but the estimated HCl pumping rate used has since been found to be too large by more than an order of magnitude. Deactivation of $\text{HF}(V)$ by DF was found to be the fastest of the V-T process, but the calculated gain was not affected by the presence or absence of DF in the mixture. This is apparently because the HF-HF V-V processes completely dominate with respect to energy transfer. The presence of the other expected precombustor products, ClF, CF_4 , N_2 and O_2 , did not affect the calculated gains although these species do deactivate HF somewhat faster than helium. They do not, however, approach DF in their deactivation efficiencies. H atom was shown to be undesirable because it can undergo exchange reactions HF and DF leading to the formation of $\text{HF}(0)$ both from excited HF and from ground state DF.

In the second series of kinetic calculations, propane was found to produce larger theoretical gains than H_2 , again mainly because of its faster pumping rate (which

has been established experimentally). The benefit obtained by elimination of H atom from the system, by replacing H_2 with C_3H_8 , was compensated for by the greater efficiency of C_3H_8 (and presumably C_3H_7) in deactivating HF compared with H_2 . In the final kinetic calculations, HBr was compared with H_2 as the cavity fuel. Despite its faster pumping rate, HBr gave lower theoretical gains on the P1 and P2 lines. HBr did, however, produce much higher gains on the P3 lines compared to H_2 . These differences result from the larger exothermicity of the $F + HBr$ reaction and the energy distributions of the pumping reactions.

PHASE II: EXPERIMENTAL LASER TESTS

Studies were conducted on the performance of a small CW HF laser using reactants other than the baseline set: $F_2/D_2/He$ in the precombustor and H_2 as the cavity fuel. Alternate cavity fuels (H-atom donors) were evaluated by monitoring laser performance with direct substitution of the alternate cavity fuel for the H_2 baseline cavity fuel. These tests were run in a specially designed test facility utilizing flow and optical diagnostics. The cavity fuels evaluated were: HE , HCl , HCF_2Cl , HCF_3 , $n-C_4H_{10}$, $n-C_3H_8$, $c-C_3H_6$, and CH_3OCH_3 .

Lasing was achieved with HBr, HCl , $n-C_3H_8$, $n-C_4H_{10}$, and $c-C_3H_6$ in order of decreasing performance. Comparison with H_2 was difficult because of substantial differences in molar flowrates. Absolute outcoupled powers obtained were substantially less than H_2 . However, when normalized to molar flowrates, the results compared favorably, suggesting that with appropriate nozzle hardware (not necessarily an easy task), some advanced storable cavity fuels could be used to advantage.

Experimental combustor tests were conducted using C_3F_6 and C_4F_8 fluorocarbons as replacement fuels for deuterium. These experimental tests were conducted using existing small-scale laser hardware to evaluate combustor characteristics and determine the adequacy of this combination (hardware and fuel) to provide the necessary temperatures for the cold reaction to proceed in planned laser experiments. Successful operation of the $C_4F_8/F_2/He$ system was determined in a mixture ratio range of 1.3 to 1.5 at varying diluent ratios.

Small-scale laser tests with this combination and with the combination C_4F_8/NF_3 with He diluent were successful. Semiquantitative analysis of the data indicates that good lasing performance is achievable with advanced reactant precombustors. Furthermore, substitution of N_2 for He as the diluent gave surprisingly good results, indicating that with proper precombustor and nozzle design, N_2 may be effectively utilized in place of He.

PHASE III: KINETIC MEASUREMENTS--GLOBAL PUMPING RATES

Global (overall) rates were measured for selected HF "pumping" reactions in a fast-flow EPR reactor. The following rate constants have been obtained in the apparatus:

<u>Reaction</u>	<u>Global Rate Constant,</u> <u>$(\text{mole/cc})^{-1} \text{ sec}^{-1}$</u>
$F + H_2 = HF + H$	1.0×10^{13}
$F + HBr = HF + Br$	$2.4 \text{ to } 3.1 \times 10^{13}$
$F + CF_3H = HF + CF_3$	1.0×10^{11}
$F + CH_4 = HF + CH_3$	3.2×10^{13}
$F + C_3H_8 = HF + C_3H_7$	5×10^{13}
$F + HI = HF + I$	1.7×10^{13}

The theory required for the determination of accurate rate constants in such a reactor is discussed in detail, including the fluid mechanics involved and the theory associated with the EPR measurement technique. The fast reactions studied required very fast flowrates and low pressures (on the order of a few torr) to spread the reaction zone sufficiently. Low pressure is also necessary for the EPR measurement of F-atom concentrations. These conditions result in axial and radial velocity gradients and radial concentration gradients. In addition, the F-atom concentration is measured within the EPR cavity which has a finite volume. Therefore, calibration of the EPR signal as a function of position within the cavity was required.

A rigorous mathematical description of the fast-flow reactor, including the EPR cavity, was written and a computer program was developed that permitted accurate rate constants to be obtained from the experimental measurements. It is shown that the axial diffusion terms in the mathematical equations are negligible.

Titration experiments indicated that F_2 could be completely dissociated in the microwave discharge but CF_4 could not. The recombination of F-atoms on the reactor wall was negligible. The experimentally measured F-atom decay curves were tested against computer-generated curves to obtain the best rate constant for each reaction.

PREFACE

During the course of this effort, several individuals, in addition to the authors, made substantial contributions. In the effort concerned with thermochemical and kinetic analysis, these include J. Q. Weber and C. Curtis of Rocketdyne and C. C. Selph, the government Project Engineer; during the experimental laser test effort, these include J. Novak, C. Nagai, D. Zwals, and L. Lynds (now with UARL) of Rocketdyne; and during the kinetic measurement phase these include K. Fertig, K. Christe, and L. Lynds of Rocketdyne and I. Goldberg from the Rockwell Science Center.

CONTENTS

Summary	1
Phase I: Thermochemical and Kinetic Analysis	1
Phase II: Experimental Laser Tests	4
Phase III: Kinetic Measurements--Global Pumping Rates	5
Introduction	21
Precombustor Reactants	23
Precombustor Temperature	25
Diluent Concentration	25
HF Concentration	26
Other Precombustor Products	26
Cavity Fuels	28
Program	30
Phase I: Thermochemical and Kinetic Analysis	31
Task I-1. Thermochemical Analysis (Precombustor)	33
Task I-2. Kinetic Analysis (Cavity)	68
Phase II: Small Scale Laser Tests	254
Introduction	254
Experimental Apparatus	257
Cavity Fuel Evaluation	303
Precombustor Fuel Evaluation	329
Phase III: Kinetic Measurements - Global Pumping Rates	377
Theoretical Analysis	378
Experimental	386
Results and Discussion	396
Nomenclature	411
References	414
<u>Appendix A</u>	
Rocketdyne Thermochemical Computer Code	417
<u>Appendix B</u>	
Laser Kinetics Computer Code - VIREL	421
<u>Appendix C</u>	
Numerical Solution of Fast Flow Reactor Equations	424
<u>Appendix D</u>	
Distribution List	430

ILLUSTRATIONS

1. Properties of Chlorine-Fluorine Flames	34
2. Extent of Fluorine Dissociation at Chemical Equilibrium as a Function of Temperature and Total Pressure of F atoms and F ₂ Molecules	36
3. F ₂ (g) - H ₂ (g) - He(g) System	129
4. ClF ₅ (l) - NH ₃ (l) - He(g) System	130
5. ClF ₅ (l) - C ₆ H ₆ (l) - He System	131
6. ClF ₅ (l) - C ₆ F ₆ (l) - He(g) System	132
7. ClF ₅ (l) - CS ₂ (l) - He(g) System	133
8. F ₂ -H ₂ -He System; Product Composition vs Temperature at 5 Mole Percent F Atom	134
9. F ₂ -H ₂ -He System; Product Composition vs Temperature at 10 Mole Percent F Atom	135
10. ClF ₅ -NH ₃ -He System; Product Composition vs Temperature at 5 Mole Percent F Atom	136
11. ClF ₅ -NH ₃ -He System; Product Composition vs Temperature at 10 Mole Percent F Atom	137
12. ClF ₅ -C ₆ H ₆ -He System; Product Composition vs Temperature at 5 Mole Percent F Atom	138
13. ClF ₅ -C ₆ H ₆ -He System; Product Composition vs Temperature at 10 Mole Percent F Atom	139
14. ClF ₅ -C ₆ F ₆ -He System; Product Composition vs Temperature at 5 Mole Percent F Atom	140
15. ClF ₅ -C ₆ F ₆ -He System; Product Composition vs Temperature at 10 Mole Percent F Atom	141
16. ClF ₅ -CS ₂ -He System; Product Composition vs Temperature at 5 Mole Percent F Atom	142
17. ClF ₅ -CS ₂ -He System; Product Composition vs Temperature at 10 Mole Percent F Atoms	143
18. HF Concentration vs Temperature at 5 Mole Percent F Atoms	144
19. HF Concentration vs Temperature at 10 Mole Percent F Atoms	145
20. Nitrogen Oxide Systems; F-Atom Concentration and Temperature as a Function of Reactant Ratios	146

21.	N_2O-F_2 System; Product Composition vs Temperature	147
22.	N_2O-NF_3 System; Product Composition vs Temperature	148
23.	$NO-NF_3$ System; Product Composition vs Temperature	149
24.	N_2O-ClF_5 System; Product Composition vs Temperature	150
25.	$NO-ClF_5$ System; Product Composition vs Temperature	151
26.	N_2O-SF_6 System; Product Composition vs Temperature	152
27.	$NO-SF_6$ System; Product Composition vs Temperature	153
28.	Comparison of Heats of Formation of $SO_x F_{(6-2x)}$ Compounds	154
29.	Effect of Temperature on Thermodynamically Favored Combustion Products	155
30.	Case I: $F_2-D_2-He-H_2$ (F = 10%, 1500 K, Series I) Gas Static and Stagnation Temperature	156
31.	Case II: $F_2-D_2-He-HCl$ (F = 10%, 1500 K, Series I) Gas Static and Stagnation Temperature	157
32.	Case III: $F_2-C_6F_6-He-H_2$ (F = 10%, 1500 K, Series I) Gas Static and Stagnation Temperature	158
33.	Case IV: $F_2-C_6F_6-He-HCl$ (F = 10%, 1500 K, Series I) Gas Static and Stagnation Temperature	159
34.	Case V: $ClF_5-ND_3-He-H_2$ (F = 10%, 1500 K, Series I) Gas Static and Stagnation Temperature	160
35.	Case VI: $ClF_5-ND_3-He-HCl$ (F = 10%, 1500 K, Series I) Gas Static and Stagnation Temperature	161
36.	Case VII: $ClF_5-C_6F_6-He-H_2$ (F = 10%, 1500 K, Series I) Gas Static and Stagnation Temperature	162
37.	Case VIII: $ClF_5-C_6F_6-He-HCl$ (F = 10%, 1500 K, Series I) Gas Static and Stagnation Temperature	163
38.	Case I: $F_2-D_2-He-H_2$ (F = 10%, 1500 K, Series I) Gas Mach Number	164
39.	Case II: $F_2-D_2-He-HCl$ (F = 10%, 1500 K, Series I) Gas Mach Number	165
40.	Case III: $F_2-C_6F_6-He-H_2$ (F = 10%, 1500 K, Series I) Gas Mach Number	166
41.	Case IV: $F_2-C_6F_6-He-HCl$ (F = 10%, 1500 K, Series I) Gas Mach Number	167

42. Case V: $\text{ClF}_5\text{-ND}_3\text{-He-H}_2$ (F = 10%, 1500 K, Series I)	
Gas Mach Number	168
43. Case VI: $\text{ClF}_5\text{-ND}_3\text{-He-HCl}$ (F = 10%, 1500 K, Series I)	
Gas Mach Number	169
44. Case VII: $\text{ClF}_5\text{-C}_6\text{F}_6\text{-He-H}_2$ (F = 10%, 1500 K, Series I)	
Gas Mach Number	170
45. Case VIII: $\text{ClF}_5\text{-C}_6\text{F}_6\text{-He-HCl}$ (F = 10%, 1500 K, Series I)	
Gas Mach Number	171
46. Case I: $\text{F}_2\text{-D}_2\text{-He-H}_2$ (F = 10%, 1500 K, Series I)	
Species Plot	172
47. Case II: $\text{F}_2\text{-D}_2\text{-He-HCl}$ (F = 10%, 1500 K, Series I)	
Species Plot	173
48. Case III: $\text{F}_2\text{-C}_6\text{F}_6\text{-He-H}_2$ (F = 10%, 1500 K, Series I)	
Species Plot	174
49. Case IV: $\text{F}_2\text{-C}_6\text{F}_6\text{-He-HCl}$ (F = 10%, 1500 K, Series I)	
Species Plot	175
50. Case V: $\text{ClF}_5\text{-ND}_3\text{-He-H}_2$ (F = 10%, 1500 K, Series I)	
Species Plot	176
51. Case VI: $\text{ClF}_5\text{-ND}_3\text{-He-HCl}$ (F = 10%, 1500 K, Series I)	
Species Plot	177
52. Case VII: $\text{ClF}_5\text{-C}_6\text{F}_6\text{-He-H}_2$ (F = 10%, 1500 K, Series I)	
Species Plot	178
53. Case VIII: $\text{ClF}_5\text{-C}_6\text{F}_6\text{-He-HCl}$ (F = 10%, 1500 K, Series I)	
Species Plot	179
54. Case I: $\text{F}_2\text{-D}_2\text{-He-H}_2$ (F = 10%, 1500 K, Series I)	
Pumping Reaction, $\text{F} + \text{H}_2 \rightarrow \text{HF(V)} + \text{H}$	180
55. Case II: $\text{F}_2\text{-D}_2\text{-He-HCl}$ (F = 10%, 1500 K, Series I)	
Pumping Reaction, $\text{F} + \text{H}_2 \rightarrow \text{HF(V)} + \text{Cl}$	181
56. Case III: $\text{F}_2\text{-C}_6\text{F}_6\text{-He-H}_2$ (F = 10%, 1600 K, Series I)	
Pumping Reaction, $\text{F} + \text{H}_2 \rightarrow \text{HF(V)} + \text{H}$	182
57. Case IV: $\text{F}_2\text{-C}_6\text{F}_6\text{-He-HCl}$ (F = 10%, 1500 K, Series I)	
Pumping Reaction, $\text{F} + \text{HCl} \rightarrow \text{HF(V)} + \text{Cl}$	183
58. Case V: $\text{ClF}_5\text{-ND}_3\text{-He-H}_2$ (F = 10%, 1500 K, Series I)	
Pumping Reaction, $\text{F} + \text{H}_2 \rightarrow \text{HF(V)} + \text{H}$	184

59.	Case VI: $\text{ClF}_5\text{-ND}_3\text{-He-HCl}$ (F = 10%, 1500 K, Series I)	
	Pumping Reaction, $\text{F} + \text{HCl} \rightarrow \text{HF(V)} + \text{Cl}$	185
60.	Case VII: $\text{ClF}_5\text{-C}_6\text{F}_6\text{-He-H}_2$ (F = 10%, 1500 K, Series I)	
	Pumping Reaction, $\text{F} + \text{H}_2 \rightarrow \text{HF(V)} + \text{H}$	186
61.	Case VIII: $\text{ClF}_5\text{-C}_6\text{F}_6\text{-He-HCl}$ (F = 10%, 1500 K, Series I)	
	Pumping Reaction, $\text{F} + \text{HCl} \rightarrow \text{HF(V)} + \text{Cl}$	187
62.	Case I: $\text{F}_2\text{-D}_2\text{-He-H}_2$ (F = 10%, 1500 K, Series I)	
	Computed Gain; Zero Power	188
63.	Case II: $\text{F}_2\text{-D}_2\text{-He-HCl}$ (F = 10%, 1500 K, Series I)	
	Computed Gain, Zero Power	189
64.	Case III: $\text{F}_2\text{-C}_6\text{F}_6\text{-He-H}_2$ (F = 10%, 1500 K, Series I)	
	Computed Gain, Zero Power	190
65.	Case IV: $\text{F}_2\text{-C}_6\text{F}_6\text{-He-HCl}$ (F = 10%, 1500 K, Series I)	
	Computed Gain, Zero Power	191
66.	Case V: $\text{ClF}_5\text{-ND}_3\text{-He-H}_2$ (F = 10%, 1500 K, Series I)	
	Computed Gain, Zero Power	192
67.	Case VI: $\text{ClF}_5\text{-ND}_3\text{-He-HCl}$ (F = 10%, 1500 K, Series I)	
	Computed Gain, Zero Power	193
68.	Case VII: $\text{ClF}_5\text{-C}_6\text{F}_6\text{-He-H}_2$ (F = 10%, 1500 K, Series I)	
	Computed Gain, Zero Power	194
69.	Case VIII: $\text{ClF}_5\text{-C}_6\text{F}_6\text{-He-HCl}$ (F = 10%, 1500 K, Series I)	
	Computed Gain, Zero Power	195
70.	$\text{F}_2\text{-D}_2\text{-He-H}_2$ System, Computed Zero Power Gain	
	on $\text{HF(1)} \rightarrow \text{HF(0)}$ Lines	196
71.	$\text{F}_2\text{-D}_2\text{-He-H}_2$ System, Computed Zero Power Gain	
	on $\text{HF(2)} \rightarrow \text{HF(1)}$ Lines	197
72.	$\text{F}_2\text{-D}_2\text{-He-H}_2$ System, Computed Zero Power Gain on Higher Lines	198
73.	$\text{F}_2\text{-D}_2\text{-He-C}_3\text{H}_8$ System, Computed Zero Power Gain	
	on $\text{HF(1)} \rightarrow \text{HF(0)}$ Lines	199
74.	$\text{F}_2\text{-D}_2\text{-He-C}_3\text{H}_8$ System, Computed Zero Power Gain	
	on $\text{HF(2)} \rightarrow \text{HF(1)}$ Lines	200
75.	$\text{F}_2\text{-D}_2\text{-He-C}_3\text{H}_8$ System, Computed Zero Power Gain on Higher Lines	201
76.	$\text{F}_2\text{-D}_2\text{-He-H}_2$ System, Rates of Pumping Reactions	202
77.	$\text{F}_2\text{-D}_2\text{-He-C}_3\text{H}_8$ System, Rates of Pumping Reactions	203

78.	$F_2-D_2-He-H_2$ System, Gas Static and Stagnation Temperatures	204
79.	$F_2-D_2-He-C_3H_8$ System, Gas Static and Stagnation Temperatures	205
80.	$F_2-D_2-He-H_2$ System, Gas Mach Number	206
81.	$F_2-D_2-He-C_3H_8$ System, Gas Mach Number	207
82.	$F_2-D_2-He-H_2$ System, Relative Area of Flow	208
83.	$F_2-D_2-He-C_3H_8$ System, Relative Area of Flow	209
84.	$F_2-D_2-He-H_2$ System, Species Plot	210
85.	$F_2-D_2-He-C_3H_8$ System, Species Plot	211
86.	$F_2-D_2-He-H_2$ System, Rates of Formation of HF(2) by Various Types of Processes	212
87.	$F_2-D_2-He-H_2$ System, Rates of Formation of HF(1) by Various Types of Processes	213
88.	$F_2-D_2-He-H_2$ System, Rates of Formation of HF(0) by Various Types of Processes	214
89.	$F_2-D_2-He-H_2$ System, Rates of Formation of HF(2) by Various V-V Processes	215
90.	$F_2-D_2-He-H_2$ System, Rates of Formation of HF(1) by Various V-V Processes	216
91.	$F_2-D_2-He-H_2$ System, Rates of Formation of HF(1) by Various V-T Processes	217
92.	$F_2-D_2-He-H_2$ System, Rates of Formation of HF(0) via Scrambling Reactions	218
93.	$F_2-D_2-He-C_3H_8$ System, Rates of Formation of HF(2) by Various Types of Processes	219
94.	$F_2-D_2-He-C_3H_8$ System, Rates of Formation of HF(1) by Various Types of Processes	220
95.	$F_2-D_2-He-C_3H_8$ System, Rates of Formation of HF(0) by Various Types of Processes	221
96.	$F_2-D_2-He-C_3H_8$ System, Rates of Formation of HF(2) by Various V-V Processes	222
97.	$F_2-D_2-He-C_3H_8$ System, Rates of Formation of HF(1) by Various V-V Processes	223
98.	$F_2-D_2-He-C_3H_8$ System, Rates of Formation of HF(2) by Various V-T Processes	224

99.	$F_2-D_2-He-C_3H_8$ System, Rates of Formation of HF(1) by Various V-T Processes	225
100.	$F_2-D_2-He-H_2$ System, Gas Static and Stagnation Temperature	226
101.	$F_2-(CN)_2-He-H_2$ System, Gas Static and Stagnation Temperatures	227
102.	$F_2-D_2-He-HBr$ System, Gas Static and Stagnation Temperatures	228
103.	$F_2-(CN)_2-He-HBr$ System, Gas Static and Stagnation Temperatures	229
104.	$F_2-D_2-He-H_2$ System, Gas Mach Number	230
105.	$F_2-(CN)_2-He-H_2$ System, Gas Mach Number	231
106.	$F_2-D_2-He-HBr$ System, Gas Mach Number	232
107.	$F_2-(CN)_2-He-HBr$ System, Gas Mach Number	233
108.	$F_2-D_2-He-H_2$ System, Relative Area of Flow	234
109.	$F_2-(CN)_2-He-H_2$ System, Relative Area of Flow	235
110.	$F_2-D_2-He-HBr$ System, Relative Area of Flow	236
111.	$F_2-(CN)_2-He-HBr$ System, Relative Area of Flow	237
112.	$F_2-D_2-He-H_2$ System, Species Plot	238
113.	$F_2-(CN)_2-He-H_2$ System, Species Plot	239
114.	$F_2-D_2-He-HBr$ System, Species Plot	240
115.	$F_2-(CN)_2-He-HBr$ System, Species Plot	241
116.	$F_2-D_2-He-H_2$ System, Computed Zero Power Gain on HF(1) \rightarrow HF(0) Lines	242
117.	$F_2-(CN)_2-He-H_2$ System, Computed Zero Power Gain on HF(1) \rightarrow HF(0) Lines	243
118.	$F_2-D_2-He-HBr$ System, Computed Zero Power Gain on HF(1) \rightarrow HF(0) Lines	244
119.	$F_2-(CN)_2-He-HBr$ System, Computed Zero Power Gain on HF(1) \rightarrow HF(0) Lines	245
120.	$F_2-D_2-He-H_2$ System, Computed Zero Power Gain on HF(2) \rightarrow HF(1) Lines	246
121.	$F_2-(CN)_2-He-H_2$ System, Computed Zero Power Gain on HF(2) \rightarrow HF(1) Lines	247
122.	$F_2-D_2-He-HBr$ System, Computed Zero Power Gain on HF(2) \rightarrow HF(1) Lines	248
123.	$F_2-(CN)_2-He-HBr$ System, Computed Zero Power Gain on HF(2) \rightarrow HF(1) Lines	249

124.	F_2 - D_2 -He- H_2 System, Computed Zero Power Gain on Higher Lines . . .	250
125.	F_2 -(CN) $_2$ -He- H_2 System, Computed Zero Power Gain on Higher Lines . . .	251
126.	F_2 - D_2 -He-HBr System, Computed Zero Power Gain on Higher Lines . . .	252
127.	F_2 -(CN) $_2$ -He-HBr System, Computed Zero Power Gain on Higher Lines	253
128.	CWLL Schematic	258
129.	Gas Delivery System	260
130.	CWLL Exterior	261
131.	CWLL Interior	262
132.	Computed Thermal Characteristics for Subscale F_2/D_2 Chemical Laser Combustor	265
133.	Inert Mixing Characteristics of Concentric Element Injector	266
134.	Regenerative/Dump-Cooled CWLL Combustor	268
135.	Concentric Injector Element	269
136.	Precombustor, Prior to Assembly	270
137.	Precombustor Assembled	270
138.	Cross Section of Small, Continuous-Wave Laser Nozzle System	274
139.	Definition of Symbols	276
140.	CWLL H_2O Cooled Nozzle Arrays	278
141.	High Molecular Weight Nozzle	279
142.	Assembled Laser Hardware	281
143.	Flow Field With H_2	282
144.	Spatial Relationship of Laser Beam to Nozzle Geometry	283
145.	Laser Power Measurement With 5-Degree-Cant, AR-Coated Al_2O_3 Window	285
146.	Measured Transmission of AR-Coated, 0-Degree Al_2O_3 Window	286
147.	High Q Cavity/Resonator Configuration	286
148.	Brewster Angle Fittings With Windows Mounted	287
149.	Laser Emission Spectra at 0.25 Inch Downstream With Increasing Precombustor Temperature A Through D	288
150.	Laser Emission Spectrum 0.25-Inch Downstream	289
151.	High Q Cavity With Hole Outcoupler Configuration	290
152.	Low-Loss Optical Resonator Configuration	291

153.	Burn Pattern Display of Mode Structure	292
154.	HF Laser Beam Diagnostics	293
155.	Power Measurement	294
156.	Power Scan Schematic	296
157.	Spatial Relationship of Laser Beam to Nozzle Geometry	297
158.	Power Scan Data for F + HCl	298
159.	High-Resolution Spectroscopy	299
160.	Time-Resolved Emission Spectroscopy	300
161.	Typical Oscilloscope Display of Rapid-Scan Spectra	302
162.	Power Out vs Downstream Position	305
163.	Flow Fields With n-C ₃ H ₈ Cavity Fuel	308
164.	Power Scan Data for F + n-Propane	311
165.	Power Scan Data for F + c-Propane	312
166.	Power Scan Data for F + n-Butane	313
167.	Power Scan Data for F + H ₂	314
168.	Power Scan Data for F + n-Propane	315
169.	Relative Spatial Positions of Mode Diameter to Gain Regions Giving Maxima in Power Scans	317
170.	Aperture Experiment Schematic	319
171.	Mode Diameter--Gain Distribution Spatial Relationship Schematic for Aperture Experiment Argument	319
172.	Laser Emission Spectra at 0.25-Inch Downstream With Increasing Precombustor Temperature A Through D	320
173.	Laser Emission Spectrum 0.25-Inch Downstream	322
174.	Laser Emission Spectra 0.90-Inch Downstream	323
175.	High Q Cavity With Hole Outcoupler Configuration	324
176.	Facility Flow Schematic, TARE Stand	332
177.	TARE Facility	333
178.	Experimental Copper Injector	335
179.	Precombustor Assembly, Uncooled Material: 304L CRES	335
180.	Uncooled Copper Combustor	337
181.	Copper Combustor	338
182.	H ₂ O Cooled Copper Workhorse Nozzle	339
183.	Secondary (Staging) Diluent Injector, CWLL	183

184.	Comparative Chamber Pressure Traces for $F_2/H_2/He$ and $F_2/C_3F_8/He$ Tests With CWLL Combustor	345
185.	Schematic of Injector, Combustor, and Nozzle Used in Tests 10 Through 14	346
186.	Comparative Chamber Pressure Traces for $F_2/C_3F_8/He$ Tests With 7.8 and 14.4 Percent Helium Solution	348
187.	Chamber Pressure Traces for Helium Injection Tests, C_4F_8/F_2	351
188.	Swirler Schematic	352
189.	DF-free Combustor Experimental Results	358
190.	$D_2/F_2/He$ Baseline Tests	364
191.	$C_4F_8/F_2/He$ Baseline Test	365
192.	Burn Patterns, $D_2/F_2/He$ Baseline Test	366
193.	Fast Flow Reactor - Mach Number vs Distance	381
194.	Schematic of Fast-Flow-EPR System	388
195.	Titration Experiment, $F + H_2 \rightarrow HF + H$	393
196.	Determination of Reaction Rate Constant	399
197.	Experimental Data, $F + HBr \rightarrow HF + Br$	403
198.	Experimental Data, $F + HI \rightarrow HF + I$	409

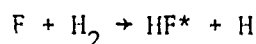
TABLES

I.	Fluorine Dissociation as a Function of Temperature and Total Partial Pressure	35
II.	Oxidizer/Fuel Combustor Reactant Systems	38
III.	Relative Precombustor Product Concentrations Under Various Conditions	42
IV.	Rate of Deactivation of HF(l) by Various Species at 300 K	43
V.	Oxidizer Dissociation Reactions	54
VI.	Fuel Combustion Reactions	55
VII.	Diluent Enthalpy Changes	56
VIII.	Maximum Attainable Mole Percentage of F-Atoms for Various Oxidizer/Fuel Combinations at 1500 and 2000 K	60
IX.	Combustor Reactant Ratios and Product Distributions at Selected Temperatures and Mole Percent F Atoms for Various Oxidizers With Hydrogen Fuel and Helium Diluent	62
X.	Combustor Reactant Ratios and Product Distributions at Selected Temperatures and 10 Mole Percent F Atoms for Various Fuels with Fluorine Oxidizer and Helium Diluent	63
XI.	Combustor Reactant Ratios and Product Distributions at Selected Temperatures and 10 Mole Percent F Atoms for Various Fuels with NF ₃ Oxidizer and Helium Diluent	64
XII.	Mass Fraction of F-Atoms at 1500 K as a Function of Mole Fraction F-Atom	66
XIII.	Reaction Types Included in Series I Kinetic Calculations	82
XIV.	Rate Constants Employed in Series I Kinetic Calculations	84
XV.	Detailed Kinetic Analysis for System ClF ₅ -ND ₃ -He-HCl at 0.10 cm	88
XVI.	Summary of Detailed Kinetic Analysis for System ClF ₅ -ND ₃ -He-HCl at 0.10 cm	95
XVII.	Summary of Detailed Kinetic Analysis, Case I: F ₂ -D ₂ -He-H ₂ at 0.20 cm	101

XVIII.	Summary of Detailed Kinetic Analysis, Case II:	
	$F_2-D_2-He-HCl$ at 0.10 cm	107
XIX.	Summary of Detailed Kinetic Analysis, Case V:	
	$ClF_5-ND_3-He-H_2$ at 0.15 cm	113
XX.	Summary of Detailed Kinetic Analysis, Case VI:	
	$ClF_5-ND_3-He-HCl$ at 0.05 cm	119
XXI.	Revised Rate Constants Used in Series II Kinetic Calculations	125
XXII.	Rate Constants Used in Series III Kinetic Calculations	126
XXIII.	$H_2/F_2/He$ Summary Sheet	272
XXIV.	Baseline 30-1X Nozzle Array	275
XXV.	Operating Conditions of HBr - F_2 Nozzle Pair	280
XXVI.	Cavity Fuels Evaluated	303
XXVII.	Summary of Preliminary Test Results of F + HR	306
XXVIII.	Cavity Fuel Comparison	307
XXIX.	Results of $F + HR \rightarrow HF + R$ Tests	309
XXX.	Pumping, k_g , and Deactivation Rates for Some Cavity Fuels	325
XXXI.	Results of Chemical Analyses of Hydrocarbon Cavity Fuels	328
XXXII.	$C_3F_6/F_2/He$ Test Data	343
XXXIII.	C_4F_8/F_2 Initial Test Series	350
XXXIV.	C_4F_8/F_2 Test Data	353
XXXV.	C_4F_8/F_2 Test Data	354
XXXVI.	Operating Chart - C_4F_8/F_2	357
XXXVII.	Chemical Laser Comparison Operating Chart	357
XXXVIII.	Flow Conditions Summary Sheet, Baseline 30-1X Nozzle	362
XXXIX.	Spectral Content Summary Sheet	363
XL.	Flow Conditions, High Molecular Weight Nozzle	372
XLI.	Effect of Axial Diffusion on Radial Mole Fraction Gradients for the Reaction $F + H_2$	387
XLII.	Diffusion Coefficients of Reactant in Helium	397
XLIII.	Rate Data for $F + H_2 \rightarrow HF + H$ at 298 K	398
XLIV.	Rate Data for $F + HBr \rightarrow HF + Br$ at 298 K	402
XLV.	Rate Data for $F + CF_3H \rightarrow H + CF_3$ at 298 K	405
XLVI.	Rate Data for $F + C_3H_8 \rightarrow C_3H_7$ at 298 K	407
XLVII.	Summary of Measured Global Rate Constants	410

INTRODUCTION

When this program was initially formulated, state-of-the-art combustion-driven HF chemical laser systems were typified by a precombustor that combusted D_2 and F_2 in excess, with He as a diluent, to obtain the high temperature that dissociates F_2 to generate F atoms. (In this discussion, the term HF laser refers to an HF or a DF laser. In the DF laser, H_2 would be used in the precombustor and D_2 would be the cavity fuel.) This mixture is then mixed, in supersonic flow, with the cavity fuel, H_2 , to initiate the "cold" pumping reaction:



which provides vibrationally excited HF in sufficient quantities to produce the inversion (partial) required for a laser.

The overall objective of this program was to find and evaluate reactant systems for a combustion-driven chemical HF laser system that are more readily handled than the F_2 (which is toxic and corrosive) and the H_2 and D_2 (which require cryogenic storage) that were utilized in demonstrating that an HF chemical laser is a viable device. Toward this end, a comprehensive program was formulated in which alternate precombustor and cavity fuel reactants were to be investigated theoretically (Phase I) and experimentally (Phase II). It was realized that alternate precombustor reactants would generate and introduce into the laser cavity combustion byproducts different from those introduced by the baseline $F_2/D_2/He$ precombustor, and the effect of these on laser performance (through deactivation kinetics) is an important issue. Furthermore, the substitution of an H-atom donor other than H_2 for the cavity fuel would result in different activation kinetics which would affect laser performance. Thus, determination of laser performance potential (Phase II) became part of the program.

Also, because of the above and because there was initially a dearth of kinetic data, a substantial part of the original program formulation was devoted to the determination of appropriate kinetic rate constants, both activation and deactivation (Phase III).

Another important aspect is that of the diluent. Helium is a difficult species to store compactly, so alternate diluents were to be considered as well as alternate reactants.

During the execution of the program, several changes in program direction (from the original plan) were suggested and approved as information relevant to the overall objective was obtained in this program and from outside sources. Most of these changes were connected to the question of kinetic rates. First, measurement of rates of deactivation of HF by a wide variety of collision partners became available from the literature, as several investigators pursued this subject prior to the scheduled measurement of such rates in this program. Therefore, this effort was dropped. Second, measurements of the relative rates of formation (activation) of HF in energetically accessible vibrational states from a variety of $F + HR$ pumping reactions also emerged from the literature prior to the scheduled measurement of such rates in this program and, therefore, this effort was dropped. Noticably absent, however, were the very important overall (global) rates of HF generation from $F + HR$ reactions, so this part of the original kinetic effort was retained, as reported later.

In the original plan, the effect of precombustor byproducts on laser performance was to be determined with small-scale CW laser experiments by "seeding" the baseline $F_2/D_2/He$ combustor with the appropriate species, e.g., for NF_3 oxidizer in place of F_2 and a fluorocarbon fuel in place of D_2 , the species N_2 and CF_4 would be introduced in appropriate concentration and laser performance monitored. However, as measured deactivation rates became available, it became clear that this technique would not be feasible because the high deactivation rate of DF (on HF) compared to N_2 or CF_4 , coupled with the relatively high concentration of DF produced by the baseline precombustor, would render the effect of N_2 or CF_4 unmeasurable. Thus it became clear that the issue of deactivation could be pursued in this manner only if a DF-free combustor could be developed. Therefore, the effort

in kinetic rates that was dropped was directed toward the development of a DF-free combustor. This would accomplish two objectives:

1. The acquisition of a baseline combustor for deactivation effect measurements
2. An alternate reactant precombustor would be demonstrated which partially satisfies the end objective of the program, directly

A further redirection in the precombustor reactant investigation effort occurred late in the program when NF_3 itself became readily available and with the demonstration (with in-house funds) that NF_3 could be used in place of F_2 in the sub-scale-sized precombustor utilized in the small-scale laser experiment. This permitted direct evaluation of NF_3 rather than by simulation.

Another important issue recognized in the early stages of the program is connected with fluid dynamics. The test hardware was designed to be optimum for the baseline reactant system. Nozzle contours were designed specifically for H_2 cavity fuel and for the molecular weight and gamma of the $\text{F}_2/\text{D}_2/\text{He}$ precombustor effluent. Thus, when small-scale laser test hardware was utilized with alternate reactant systems, performance was not expected to be optimum. Therefore, in the late program redirection in which HBr was tested further, provision was made to make tests with another nozzle system designed to improve performance of high molecular weight cavity fuels.

The technical considerations outlined above, which led to program redirection several times during the course of the program, will be discussed in greater detail in the appropriate section of this report. Additional introductory remarks on advanced reactants for chemical lasers are presented below.

PRECOMBUSTOR REACTANTS

The first purely chemical HF and DF lasers reacted F_2 and NO in a precombustor to generate F atoms for subsequent reaction with the fuel molecules in a secondary combustion zone (Ref. 1). The supersonic HF lasers that are currently under

investigation generally burn D_2 and F_2 in a subsonic precombustor to generate sufficient heat to dissociate F_2 to F atoms which subsequently are reacted with D_2 in a secondary reaction zone (or cavity). The positions at which the H_2 and D_2 are introduced are reversed if an HF laser is desired. The precombustor for a supersonic laser is usually operated under conditions that result in the nearly complete dissociation of the unburned F_2 to F atoms (i.e., temperatures above 1400 K).

There are several disadvantages of the $F_2/D_2/He$ combustor system. The reactants and the diluent are not storable as liquids at ambient temperatures. Fluorine is a toxic, highly corrosive species and D_2 is flammable and potentially explosive when mixed with air. Furthermore, the heat-generating reaction forms DF, which is believed to be relatively effective in deactivating the vibrationally excited states of HF that are formed in the cavity. The problem of the precombustor-generated DF-absorbing light of lasing frequency is circumvented by using the conjugate isotopes of hydrogen as the precombustor and cavity fuels; however, the potential problem of the mutual deactivation of HF and DF cannot be avoided completely unless a hydrogen-free fuel can be used in the precombustor.

The baseline cavity fuel (H_2) suffers from the same storage and hazard characteristics as D_2 . Furthermore, in the pumping reaction, H atoms are formed. The production of H atoms in the laser cavity has potential deleterious effects. First, the H atom is apparently a rapid deactivator of vibrationally excited HF. Second, if there is DF produced by the precombustor, exchange reactions produce ground state HF which absorbs HF laser light and increases the deactivation rate, particularly through V-V transfers. The types of lasers of interest to this program usually involve the use of three reactants in addition to diluent. These will be referred to as the precombustor fuel, the oxidizer, and the cavity fuel.

To evaluate the potential of a given reactant system for an F-atom generator, the critical parameters with respect to operating conditions and product stream composition must be established. Unfortunately, the state of the art, with respect

to modeling of the overall laser system, has not yet advanced to the point where all of the effects of a change in the precombustor reactants and/or operating conditions can be determined. Changing the precombustor conditions could affect: (1) the supersonic mixing processes, (2) the pumping and energy-transfer processes leading to the inversion, (3) deactivation rates of the excited states of HF, (4) cavity temperature and pressure, (5) beam quality, and (6) the amount of heat released before the product gases reach the diffuser. The considerations involved in determining the favorable precombustor parameters are sometimes quite complex and may involve information and experimental data that are not available.

PRECOMBUSTOR TEMPERATURE

To attain the current design goal of keeping the concentration of undissociated F_2 to a minimum to suppress the hot reaction, precombustor exhaust temperatures on the order of 1400 to 1500 K are required to thermodynamically favor F atoms. In addition, there are indications that somewhat higher precombustor temperatures result in even higher laser efficiency. This observation is contrary to expectations, because inversions in the vibrational energy levels of HF are more easily attainable at lower rotational temperatures and illustrates the eventual need for an overall model of the laser system that contains all of the important parameters and processes. The beneficial effect of higher precombustor temperatures may result rather simply from the occurrence of less F-atom recombination as the hotter precombustor products pass through the cavity nozzle, or from a more subtle effect such as the effects of temperature on the supersonic mixing process.

DILUENT CONCENTRATION

Empirical results also show that optimum laser performance occurs when 4 to 8 moles of diluent are present in the cavity per mole of HF or DF formed (i.e., per mole of F atom present in the precombustor exhaust). This diluent generally is introduced through the precombustor, presumably to keep the cavity temperature up.

The reason that diluent considerations are very important to this analysis of the precombustor is that, in current H_2-F_2 precombustors, 50 to 70 percent of the heat of combustion is used to heat the diluent rather than to heat and dissociate F_2 . This results in the generation of considerable HF (or DF).

It may not be possible to reduce the diluent requirement of the cavity significantly in advanced designs. If lower temperatures in the cavity are found to be suitable in future systems, some of the diluent might be brought in with the fuel or be mixed with the precombustor exhaust just before expansion. This would permit the primary combustion zone to be maintained above 1400 K to dissociate F_2 . The dilution of the exhaust stream would have to occur after expansion or just before to prevent F-atom recombination at the lower temperature and higher pressure.

HF CONCENTRATION

The amount of HF that can be tolerated in the precombustor products of a DF laser is not known. It will be seen that the results of the thermochemical analysis indicate that, if the current levels of HF seriously degrade laser performance, the HF concentration can be reduced by a factor of three by replacing the H_2 with ethylene or kerosene, by a factor of five by employing acetylene or benzene, and HF could be eliminated from the precombustor exhaust if a hydrogen-free fuel such as C_3F_6 could be used. The use of a hydrogen-free fuel would have another advantage in that an HF laser could be fired without using deuterium or any deuterated compounds.

OTHER PRECOMBUSTOR PRODUCTS

The final constraint on the precombustor that will be considered is that the other products of combustion must not be detrimental to laser operation. The results of the thermochemical analysis indicate that, at temperatures around 1500 K, the only products that are thermodynamically stable to any appreciable extent are HF, N_2 , F, ClF, CF_4 , and SF_6 if the only elements introduced are H, F, N, Cl, S, and C. A few percent of the F_2 remains undissociated but this can be eliminated by a

further increase in temperature. Other species such as NF_3 , NF_2 , ClF_3 , and ClF_5 will not be present in the exhaust if the combustion conditions are such that the reactions proceed to equilibrium.

None of the potential product species (except HF) are expected to be detrimental with respect to deactivation of vibrationally excited HF or DF in the cavity. Each of these species has been employed satisfactorily in HF lasers operated under pulsed conditions (Ref. 2 and 3), and the rates at which most of these species deactivate HF(1) have been measured. The situation as to whether certain species that are generated in the precombustor are detrimental to the overall system is more complex. Undissociated F_2 is considered detrimental because it can react with H atoms and H_2 downstream of the oscillator, causing heat to be generated and thereby reducing the efficiency of the diffuser.

The rate at which a given species generated in the precombustor reacts when it is in the cavity will determine if it is a suitable precombustor product. In the case of F_2 , the hot reaction occurs too slowly to contribute significantly to the laser power (based on currently accepted rate constants). If this is the case, the hot reaction is undesirable because it would release heat (downstream) without contributing to the output of the laser. In the case of atom abstraction, such as $\text{H} + \text{CF}_4 \rightarrow \text{HF} + \text{CF}_3$ ($\Delta H = -5$) and $\text{H} + \text{SF}_6 \rightarrow \text{HF} + \text{SF}_5$, there is a good chance that sufficient activation energy will be involved that these reactions will not occur at the moderate temperatures encountered in the cavity. Firm conclusions regarding the overall roles of CF_4 and SF_6 in a CW laser system cannot be made, however, until they have been tested.

The thermochemical calculations to be discussed indicate that if ClF_5 is employed as the oxidizer, considerable amounts of ClF will be formed in the precombustor. ClF may be expected to behave differently than F_2 in two respects. First, the heat release of the hot reactions resulting from the reaction of H and ClF is less than 60 percent of that of the F_2 hot reaction. Second, the $\text{H} + \text{ClF}$ reactions may be fast enough that they will permit part of the excited HF formed from the ClF to contribute to the output of the laser. Sufficient rate data are not available to permit quantitative conclusions on this point to be made.

The above considerations are inconclusive regarding the possible role of the ClF formed in the precombustor from ClF_5 with respect to the overall efficiency of the laser. However, ClF is not expected to reduce laser output.

This discussion of the various constraints that are imposed on the precombustor parameters has served to indicate the types of considerations that are important in assessing the potential of advanced oxidizers and precombustor fuels. Firm conclusions cannot be made at present concerning many of these constraints because of the diverse and complex manner in which the precombustor parameters can affect the cavity reactions and the overall laser performance. It appears that the requirement for the precombustor to heat considerable diluent gas and maintain exhaust temperatures well in excess of 1400 K should not necessarily be expected to be decreased in future systems. The amount of HF that can be tolerated in the precombustor products is unknown, but a decrease in precombustor-formed HF will probably be required to optimize the system. The N_2 and CF_4 that are produced in the precombustor reactions when nitrogen and carbon are present in the reactants are not expected to be detrimental. The ClF that is formed when ClF_5 is employed is not expected to reduce the output of the laser, but this must be established experimentally.

CAVITY FUELS

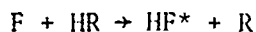
The basis for the consideration of alternate cavity fuels is replacement of H_2 with another H atom-bearing reactant. Reactants considered for this substitution must react with F atoms with sufficient energy to produce vibrational excitation in the HF product, preferably about 32 kcal/mole or greater to compete with H_2 , and must be more readily handled and/or stored than H_2 . Classes of reactants considered are hydrogen halides, hydrocarbons, and partially halogenated hydrocarbons.

The heats of reaction available for vibrational excitation of HF for the hydrogen halide that will be considered are:

	<u>ΔH, kcal/mole (298 K)</u>
$F + HCl \rightarrow HF(0) + Cl$	-33
$F + HBr \rightarrow HF(0) + Br$	-49
$F + HI \rightarrow HF(0) + I$	-65

The heat of reaction of F atoms with HCl is about the same as with H_2 , and that with HBr and HI is greater. Thus, it is expected that these reactions would provide vibrationally excited HF and both pulsed laser (HCl, HBr, and HI) and CW laser results (HCl or HBr) have shown this to be the case. All of these hydrogen halides can be considered as storable, although there may be decomposition problems with HI.

A variety of hydrocarbons can be considered in the reaction



The heat of this type of reaction is expected to be near that of $F + H_2$, thus providing sufficient energy to produce vibrationally excited HF. Several such reactions have been shown to produce lasing in pulsed chemical lasers (Ref. 4 and 5) and a list of those selected for this program is shown later. The absence of H atoms, a species that can deactivate HF^* readily, is expected to be beneficial to laser performance.

Those reactants shown above and the partially halogenated hydrocarbons are relatively easily handled and some are readily stored. Determining whether a specific reactant produces sufficient inversion of excited vibrational states for lasing is the subject of investigation under Phase II of this program.

PROGRAM

To accomplish the evaluation of new reactants for the CW HF chemical laser, the work on the program was divided into three phases, each being further divided into tasks as follows:

Phase I: Thermochemical and Kinetic Analysis

Task I-1. Thermochemical Analysis (Precombustor)

Task I-2. Kinetic Analysis (Cavity)

Phase II: Experimental Laser Tests

HF-Free Combustor Tests

Small-Scale Laser Tests

- Cavity Fuel Evaluation
- Advanced Fuel Evaluation

Phase III: Kinetic Measurements--Global Pumping Rates

The work reported herein is organized in the same fashion.

PHASE I: THERMOCHEMICAL AND KINETIC ANALYSIS

To determine which advanced precombustor and cavity reactants warrant experimental study, the first phase of the program was a theoretical analysis of the thermochemistry of F-atom-generating combustion processes and of the kinetics and mechanisms of cavity reactions. The specific objectives of this phase were: (1) to determine the expected composition of the precombustor gas when reactants other than the baseline reactants F_2 - D_2 -He are employed and (2) to predict the effects of the precombustor products and the use of cavity fuels other than H_2 on the kinetics of the very fast pumping and deactivation reactions that occur in the cavity and on the zero power gain of the HF laser.

The thermochemical calculations permit the final gas composition and temperature to be predicted, assuming that all chemical reactions go to completion and the reactor is adiabatic. The temperature and composition of the exhaust from an actual combustor will, of course, be affected somewhat by heat losses and combustion efficiency (i.e., the degree to which the chemical reactions approach equilibrium). Most of the systems under consideration are expected to demonstrate satisfactory combustion efficiencies if the adiabatic flame temperatures are approached but, with some of the reactant combinations (e.g., N_2O - F_2), it may be difficult to obtain ignition and/or sustained combustion. These practical considerations will not be discussed further in this section.

There are some uncertainties in the thermochemical data, particularly in the heat of formation of SOF_4 but, in most cases, the thermochemical calculations should indicate the F-atom concentrations and temperatures that can be approached if relatively efficient combustion can be achieved. In addition, the major combustion products will be identified so that consideration can be given to their possible detrimental effects on laser efficiency. A detailed thermochemical analysis was conducted which permits the thermochemical properties of the individual fuels, oxidizers, and diluents to be related to the reactant ratios and temperature required to obtain a given concentration of F-atoms. A summary of the results of the thermochemical analysis to be described in this section has been reported elsewhere (Ref. 6).

Although only deuterated or hydrogen-free combustor fuels can be considered for an HF laser (because the introduction of ground-state HF into the cavity would be very detrimental to laser efficiency), the thermochemical analysis was carried out for nondeuterated fuels. The isotope effect on combustor thermochemistry (zero-point energy differences) is small enough that the conclusions obtained will be approximately correct for deuterated fuels. The calculations apply exactly to a DF laser, since it does not require deuterated combustor fuels, and to an HF laser when only hydrogen-free fuels are considered.

The kinetic code calculations conducted under this program of the rates of the various cavity reactions were completed before an efficient mixing-kinetic code had become available. The results obtained using the premixed approximation give some insight into which chemical and energy transfer processes are the more important to laser efficiency, but neglect certain physical processes that may be more important or even efficiency limiting (e.g., effects of molecular weight on mixing within the cavity). Also, the predictions made from the kinetic code calculations must be considered as approximate because rate parameters had not been measured for many of the important chemical and energy transfer processes requiring that estimates be employed. Values for several of these rate constants have become available since the initial calculations were made. Some of these new kinetic data were obtained in experiments conducted under Phase III of this program.

The kinetic discussion in this section is intended to apply mainly to an HF laser in which deuterated fuels (or other hydrogen atom-free reactants) are employed in the precombustor. This choice was made because the estimated rate constants that were available applied mainly to such a system. The results of the kinetic calculations are expected to relate generally to DF lasers also, but some rather large isotope effects may be involved in the initial distribution of vibrational energy and in the rates of the energy transfer (deactivation) processes.

TASK I-1. THERMOCHEMICAL ANALYSIS (PRECOMBUSTOR)

Because only cavity pumping reactions of the type:



are of interest to this program, the precombustor conditions required to dissociate F_2 almost completely to atoms will be considered. This will be followed by an analysis of the thermochemistry involved in the production of F-atoms from various combinations of advanced fuels and oxidizers.

Conditions for F_2 Dissociation

Because the fluorine molecule has a bond dissociation energy of only 38 kcal/mole (Ref. 7), F_2 dissociates almost completely to atoms at moderate temperatures. F_2 is 99 percent dissociated at 1560 K, for example, if chemical equilibrium prevails and the fluorine atom partial pressure is 1 psia. It is possible therefore, to generate large concentrations of F-atoms in combustion processes and this has been recognized for some time. For example, in the F_2 - Cl_2 flame, which has a maximum speed when the reactants contain 9.6-percent excess F_2 (Ref. 8), the calculated equilibrium F-atom partial pressure reaches its maximum (about 1.5 psia, Fig. 1) at this mixture ratio with the F_2 about two-thirds dissociated at an adiabatic flame temperature of 1250 K and a total pressure of 1 atmosphere.

The equilibrium constant for the reaction:



is defined as $K_p = P_F^2 / P_{F_2}$ where P_F and P_{F_2} are the partial pressures of F-atom and F_2 , respectively. The value of K_p was calculated at various temperatures from available thermochemical data (Ref. 9) and the extent of dissociation

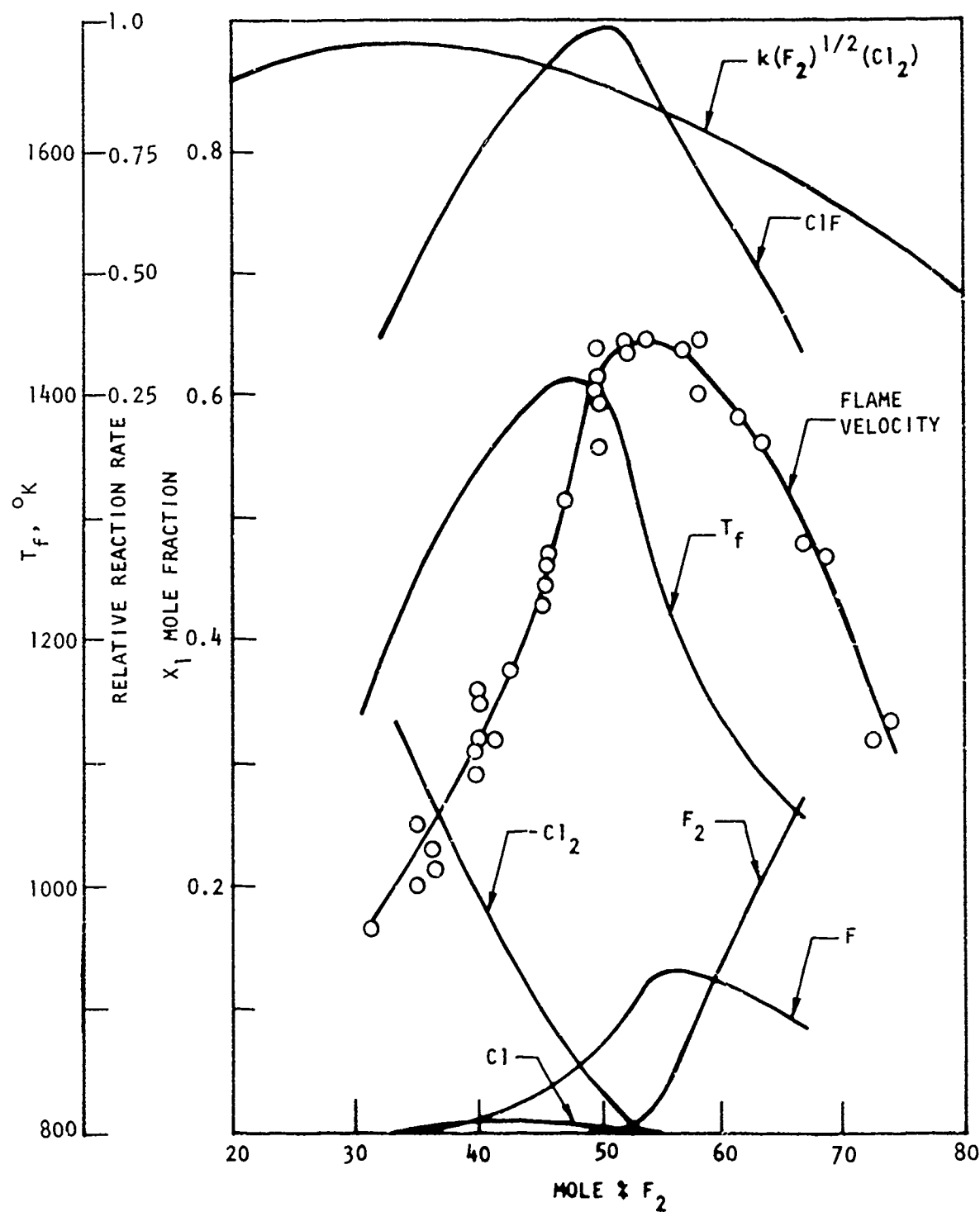


Figure 1. Properties of Chlorine-Fluorine Flames (Rei s,

calculated using the stoichiometric relationship and the above equilibrium expression. Such calculations gave the results plotted in Fig. 2 for the extent of dissociation of fluorine as a function of temperature and total partial pressure of F_2 and F . The format of this semilog plot is designed to permit both large and small extents of dissociation to be read accurately. The percent F_2 dissociated is plotted on a logarithmic scale up to 50-percent dissociation and then the percent F_2 undissociated is plotted for larger extents of dissociation. Thus, the portions of the curves with positive slope represent percent F_2 dissociated and those portions with negative slope denote percent undissociated. The individual curves represent total partial pressure ($P_F + P_{F_2}$) of from 0.01 to 100 psia.

The extent of dissociation increases with temperature and decreases with increasing total partial pressure of F and F_2 . A typical combustor condition of 30 psia and 10 mole percent F -atom corresponds to the 3-psia curve when the F_2 is mostly dissociated. Under these conditions, 90 percent of the F_2 is dissociated at 1410 K, 95 percent at 1490 K, and 99 percent at 1710 K. Other selected results, read from Fig. 2, are listed in Table I where it can be seen that increasing the total combustor pressure or the extent of F_2 dissociation affects the combustor temperature required to give a 10-percent F -atom concentration as follows:

Percent F_2 Dissociated	$P_t = 3$ psia $P_F = 0.3$	$P_t = 30$ psia $P_F = 3$	$P_t = 300$ psia $P_F = 30$
95	1280*	1490*	1800*
99	1430	1710	2130
99.9	1710	2130	2800

TABLE I. FLUORINE DISSOCIATION AS A FUNCTION OF TEMPERATURE AND TOTAL PARTIAL PRESSURE ($P_F + P_{F_2}$)

$P_t + P_{F_2}$		Temperature, K (For Given Percent Dissociation)								
psia	torr	0.1	1	5	10	50	90	95	99	99.9
100	5210	765	930	1100	1190	1510	1870	2030	2430	>3000
50	1560	730	880	1030	1110	1390	1690	1800	2130	2800
10	521	700	840	980	1050	1290	1540	1650	1910	2440
3	156	670	800	920	985	1200	1410	1490	1710	2130
1	52.1	645	765	880	940	1130	1310	1370	1560	1910
0.3	15.6	625	730	830	885	1050	1220	1280	1430	1710
0.1	5.21	610	700	795	845	1000	1135	1190	1310	1560
0.03	1.6	580	670	755	800	940	1070	1110	1220	1430
0.01	0.52	560	640	725	765	890	1000	1040	1140	1325

* $P_F + P_{F_2} = 1.026 P_F$ at 95-percent dissociation, but neglecting the presence of the F_2 results in a temperature error of only a few degrees.

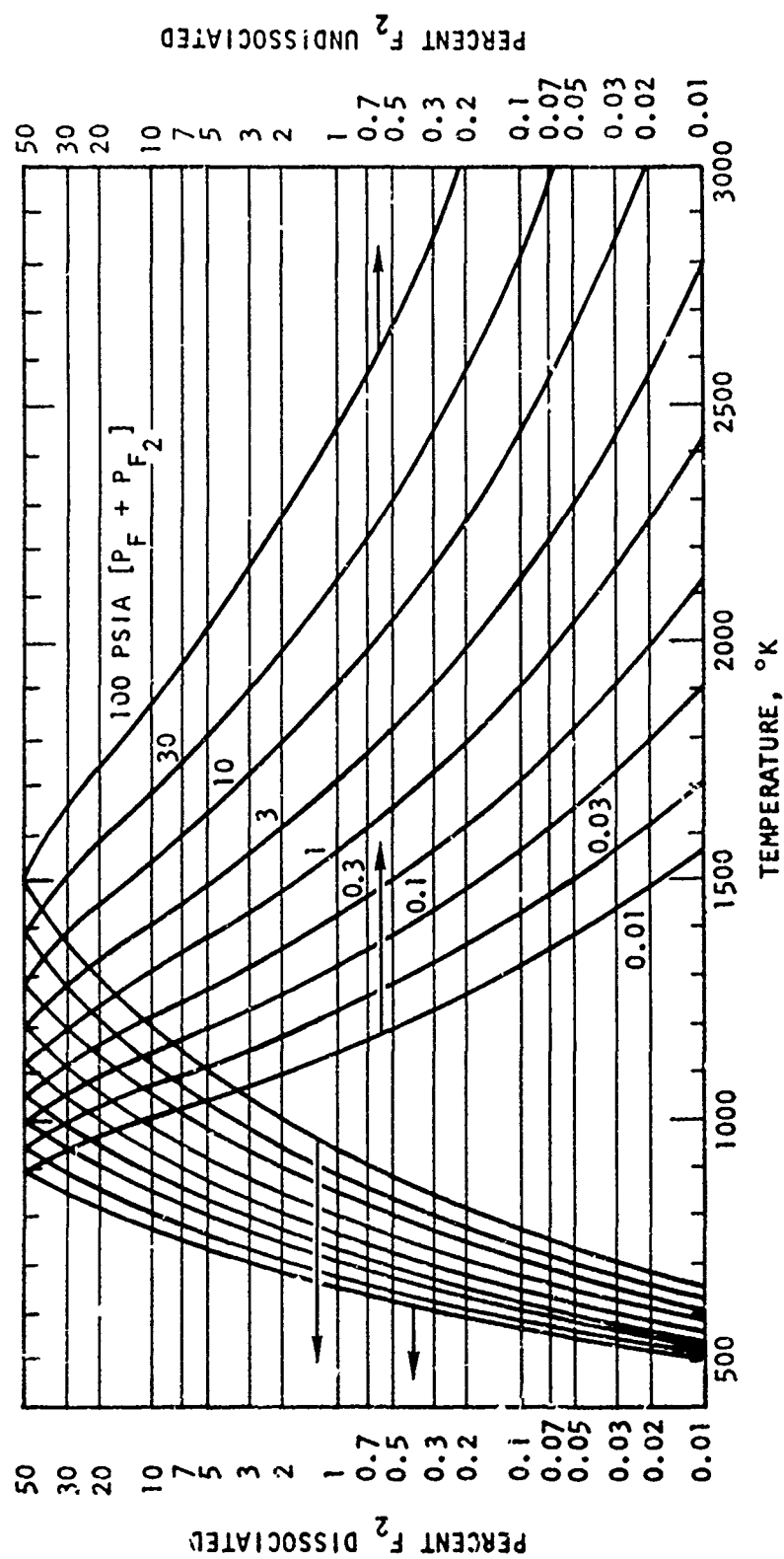


Figure 2. Extent of Fluorine Dissociation at Chemical Equilibrium as a Function of Temperature and Total Pressure of F atoms and F_2 Molecules

At large extents of F_2 dissociation, the percent F_2 undissociated is approximately proportional to the F-atom concentration at a given temperature. At 1900 K, for example, 0.01 percent is undissociated when $P_F = 0.1$ psia (Fig. 2), 0.1 percent at 1 psia, 1 percent at 10 psia, and about 9 percent at $P_F = 94.5$ psia ($P_F + P_{F_2} = 100$). This relationship can be predicted by changing the equilibrium expression, $K_p = P_F^2/P_{F_2}$, to the form $200 \cdot P_{F_2}/P_F = 200 \cdot P_F/K_p$ and noting that K_p is constant at a given temperature ($K_p = 1920$ psia at 1900 K) and the percent F_2 undissociated is equal to $200 \cdot P_{F_2}/(P_F + 2 \cdot P_{F_2})$, which becomes approximately $200 \cdot P_{F_2}/P_F$ at large extents of dissociation.

Dissociation of F_2 to the extent of 95 to 99 percent is believed to be sufficient for satisfactory laser operation. Therefore, temperatures in excess of 2000 K would not be required even if combustor pressures as high as 300 psia were employed.

Advanced Precombustor Reactants

Oxidizers and fuels of potential interest for the chemical generation of F-atoms are listed in Table II. It will be shown that the major exothermic combustion reactions in the presence of excess oxidizer are those in which the strong bonds C-F, H-F, S-F, and N≡N (N_2) are formed. PF_3 is also included in Table II because it can be oxidized exothermically to PF_5 . It will be shown that the decomposition of the nitrogen oxides, N_2O and NO , to N_2 and O_2 is also a potential source of heat for dissociating the oxidizers to F-atoms. It may be difficult, however, to sustain a nitrogen oxide adiabatic decomposition flame.

TABLE II. OXIDIZER/FUEL COMBUSTOR REACTANT SYSTEMS

Oxidizers	Fuels
F_2	H_2
N_2F_4	N_2H_4
NF_3	NH_3
ClF_5	CS_2
ClF_3	$(CN)_2$
	PF_3
	Hydrocarbons:
	CH_4 , methane
	$(CH_2)_x(CH_3)_2$, saturated
	$(CH_2)_x$, alkenes and cyclic saturated
	$(CH)_x$, Acetylene and benzene
	Perfluorohydrocarbons (fluorocarbons)

The number of promising oxidizers is limited. NF_3 is much less reactive and toxic than is fluorine and there is considerable interest in this oxidizer for those reasons. The oxidizers ClF_5 and ClF_3 have been developed as storable rocket propellants. They are at least as reactive as fluorine and their use involves similar hazards. However, ClF_5 and ClF_3 can be stored as liquids at ambient temperature, leading to the possibility of development of a liquid-reactant chemical HF or DF laser. The use of ClF_5 as the oxidizer in conjunction with liquid fuels for the precombustor and cavity could eliminate the need for low-temperature or high-pressure storage conditions except for the diluent. N_2F_4 is partially condensible but its availability is limited.

The number of precombustor fuels that can be considered is almost limitless because all of the hydrocarbons and fluorocarbons have the potential to undergo strongly exothermic reactions with any of the oxidizers. It should be possible,

therefore, to choose a precombustor fuel with almost any desired physical properties. It will be shown that the combustion of hydrazine or ammonia produces as much or more of the undesirable precombustor product HF as does H_2 . However, HF production would be greatly reduced if a hydrocarbon were employed as the fuel, the greatest reduction being achieved with the least saturated of the hydrocarbons, and eliminated if a hydrogen-free fuel (such as CS_2 , cyanogen, PF_3 , or a fluorocarbon) were used.

Adiabatic Temperature and F-Atom Concentration

In an idealized combustor in which (1) all reactants are introduced at the same temperature*, (2) the reactor is adiabatic, and (3) the final pressure is defined, there are two independent variables in a three-component oxidizer/fuel/diluent system. Therefore, a given final temperature can be attained with an indefinite number of reactant ratios (provided the temperature does not exceed the maximum attainable). If, however, both the final temperature and F-atom concentration are defined, only one set of reactant mole fractions can give this condition.

A series of calculations was made with the Rocketdyne Thermochemical Computer Code to investigate the temperatures and F-atom concentrations that can be attained with various reactant mixture ratios. These data should be useful in determining precombustor conditions for the testing of advanced reactant systems. Five reactant systems were selected for these calculations: $F_2(g)-H_2(g)-He(g)$, $ClF_5(l)-NH_3(l)-He(g)$, $ClF_5(l)-C_6H_6(l)-He(g)$, $ClF_5(l)-C_6F_6(l)-He(g)$, and $ClF_5(l)-CS_2(l)-He(g)$. The computer code, described in Appendix A, minimizes the free energy of the system at constant enthalpy.

The results of these calculations, made at a pressure of 30 psia, are plotted in terms of F-atom concentration as a function of temperature in Fig. 3 through 7**, The calculations were carried out at fixed oxidizer-to-fuel molar ratios (the

*All reactants are assumed to be at 298 K in the calculations carried out in this section.

**For convenience, Fig. 3 through 127 have been placed at the end of Phase I, starting on page 129.

solid curves in the figures) at various mole percent helium (the intersections of the solid and dotted curves). Interpolation of these curves permits the mixture ratios to be estimated that are required to obtain a given combustor exhaust condition. It can be seen from Fig. 3, for example, that to achieve a temperature of 1800 K and 5 mole percent F-atoms, the F_2/H_2 ratio must be about 1.37 with 84 percent helium. To attain this condition with ClF_5 and benzene (Fig. 5) requires a ClF_5/C_6H_6 ratio of about 8.1 and 91 mole percent helium.

Listed at the intersections of the curves in these plots is information regarding the concentrations of selected reactor products relative to the F-atom concentration at that condition. These values show some interesting trends. In Fig. 3, for example, it can be seen that increasing the F-atom concentration at a fixed temperature of 1800 K decreases the ratio HF/F . This is because the F_2/H_2 ratio increases and the helium concentration decreases to maintain constant temperature. On the other hand, increasing temperature at constant F-atom concentration increases HF/F because both the F_2/H_2 ratio and the mole fraction of helium must decrease.

Precombustor Products as a Function of Temperature

Two series of calculations were made with each of the selected reactant systems to determine the complete product distributions as a function of temperature under conditions (reactant mixture ratios) that produce 5 and 10 percent F-atoms, respectively. The conditions were selected by interpolation of Fig. 3 through 7. A subroutine was added to the Thermochemical Computer Code to store the results of each calculation and then plot automatically the product distributions for each series. These plots are shown in Fig. 8 through 17.

The thermochemical calculations established that at temperatures between 1000 and 1500 K, none of the products except F_2 are appreciably dissociated. The thermodynamically favored products in this temperature range (in the absence of oxygen) are HF , N_2 , ClF , CF_4 , and SF_6 . As the temperature of the calculations is increased

above 1500 K, the species Cl, Cl₂, and SF₄ begin to appear in appreciable quantities as the following endothermic reactions shift to the right:



The use of ClF₅ in place of F₂ increases the fraction of available fluorine that must be combusted to attain a given temperature (see later discussion), thereby requiring the formation of more HF when H₂ or NH₃ is employed as the precombustor fuel. The amount of HF formed can be reduced, however, by the use of a hydrocarbon fuel because much of the heat of combustion then comes from the formation of CF₄. This situation is demonstrated in Fig. 18 and 19. These curves are reproduced from the previous figures in the series for comparison on a single plot. It may be seen also from the results of these calculations (Fig. 10 through 17) that ClF does not dissociate at temperatures up to about 1600 K, resulting in large amounts of ClF being introduced into the cavity if ClF₅ were to be employed as the oxidizer. It is not known if ClF has a detrimental effect on laser efficiency but it has a potential to undergo reaction with H atoms and with Cl atoms in the cavity. The deactivation of HF(1) by ClF has been reported (Ref. 10) to have a rate constant of only 730 torr/sec (or $1.4 \times 10^{10} \text{ (mole/cc)}^{-1} \text{ sec}^{-1}$). Direct deactivation by ClF in the cavity should not be a problem.

The relative product concentrations from Fig. 8 through 17 are compared in Table III at 1500 and 2000 K. The species concentrations are listed relative to the F-atom concentration at the same condition. This ratio is used because nearly every F-atom is expected to form an excited HF (or DF) molecule in the cavity. Therefore, the precombustor ClF/F ratio, for example, will be approximately the ClF/HF ratio in the cavity. It can be seen from Table III that ClF₅-NH₃ forms even more HF than does F₂-H₂, but the production of HF can be reduced by more than a factor of 4 by using benzene as the fuel rather than ammonia. Nearly all of the chlorine in ClF₅ forms ClF at 1500 K, but most of it forms Cl atoms at 2000 K. All of the carbon forms CF₄ (in these oxygen-free systems) with more

TABLE III. RELATIVE PRECOMBUSTOR PRODUCT CONCENTRATIONS UNDER VARIOUS CONDITIONS

Product Ratio	Temperature, K	Percent F atoms	Reactant System			
			F_2-H_2-He	ClF_5-NH_3-He	$ClF_5-C_6H_6-He$	$ClF_5-C_6F_6-He$
HF/F	1500	5	2.3	3.6	0.76	--
	1500	10	1.2	2.1	0.46	--
	2000	5	3.3	5.4	1.20	--
	2000	10	1.7	3.1	0.70	--
ClF/F	1500	5	--	1.14	1.16	1.34
	1500	10	--	0.80	0.85	0.95
	2000	5	--	0.30	0.31	0.34
	2000	10	--	0.30	0.33	0.37
Cl/F	1500	5	--	0.018	0.018	0.024
	1500	10	--	0.006	0.006	0.008
	2000	5	--	0.80	0.86	1.02
	2000	10	--	0.43	0.47	0.55
CF ₄ /F	1500	5	--	--	0.76	0.31
	1500	10	--	--	0.46	0.18
	2000	5	--	--	1.20	0.64
	2000	10	--	--	0.70	0.37
SF ₆ /F	1500	5	--	--	--	0.57
	1500	10	--	--	--	0.36
	2000	5	--	--	--	<0.001
	2000	10	--	--	--	<0.001
SF ₄ /F	1500	5	--	--	--	0.024
	1500	10	--	--	--	0.003
	2000	5	--	--	--	1.06
	2000	10	--	--	--	0.67

being formed at 2000 K because more fuel must be combusted to reach this temperature. Any sulfur present in the reactants forms SF_6 at 1500 K and SF_4 at 2000 K.

The rates at which various species deactivate $\text{HF}(1)$ at 300 K are listed in Table IV. The rates in this table are the sum of V-T-R and V-V processes (except for HF). It can be seen that the expected precombustor products ClF , CF_4 , N_2 , O_2 , SF_6 , and He are relatively ineffective in deactivating vibrationally excited HF and should not, therefore, be detrimental to laser efficiency. ClF , CF_4 , N_2 , and O_2 do deactivate HF faster than does helium but considerable concentrations of these species can probably be tolerated. On the other hand, HF and DF deactivate HF sufficiently rapidly (via V-T,R processes) that their presence in the precombustor exhaust is very likely to be detrimental.

TABLE IV. RATE OF DEACTIVATION OF $\text{HF}(1)$ BY VARIOUS SPECIES AT 300 K (V-V + V-T,R except for HF)

Species	Rate Constant		References
	$\text{torr}^{-1} \text{sec}^{-1}$	$(\text{mole/cc})^{-1} \text{sec}^{-1}$	
H_2O	4×10^6	7×10^{13}	41
ClF_3	1.1×10^5	2.0×10^{12}	19
DF	7×10^4	1.3×10^{12}	14, 16
	1.3×10^5	2.6×10^{12}	21
HF	$6.1-8.7 \times 10^4$	$1.1-1.6 \times 10^{12}$	15,18,19
cyclo- C_3H_6	3.2×10^5	6×10^{12}	19
n- C_4H_{10}	1.7×10^5	3.2×10^{12}	19
C_2H_6 , C_3H_8	$5-13 \times 10^4$	$9-24 \times 10^{11}$	19, 44
CH_4 , C_2H_2 , C_2H_4	$4-6 \times 10^4$	$7-11 \times 10^{11}$	19, 44
CO_2	$4-7 \times 10^4$	$7-13 \times 10^{11}$	14,13,42
H_2	2×10^4	4×10^{11}	14,16,42,44
HCl	$1.7-2.9 \times 10^4$	$3-5 \times 10^{11}$	14, 21
HBr	7500	1.4×10^{11}	14, 21
NO	6100	1.1×10^{11}	14,43
HI	3500	7×10^{10}	21
CO	1800-2500	$3.3-4.6 \times 10^{10}$	14, 43
ClF	730	1.4×10^{10}	10
CF_4	420	8×10^9	19
N_2	140	3×10^9	14, 42
O_2	350	7×10^9	43
	45	8×10^8	14
NF_3	< 300	$< 6 \times 10^9$	19
F_2	< 100	$< 2 \times 10^9$	19, 45
SF_6 , He, Ar	< 60	$< 1.1 \times 10^9$	16,18,19,42

Nitrogen Oxide-Oxidizer Reactant Systems

The nitrogen oxides NO and N_2O decompose exothermically forming products that are relatively thermodynamically stable in the presence of F-atoms.* The theoretical adiabatic decomposition temperature is 1930 K for N_2O and >2500 K for NO. Therefore, in a mixture containing a minor amount of fluorine oxidizer, the oxidizer will be dissociated to F-atoms if all chemical reactions proceed to equilibrium. Thermochemical calculations were conducted for N_2O -oxidizer and NO-oxidizer systems although it has not been demonstrated that such systems will undergo steady-state combustion.**

These two component systems have only one independent variable. Therefore, specifying any one of the parameters (mixture ratio, final temperature, or F-atom concentration) determines the others. Plotted in Fig. 20 are the F-atom concentrations (calculated using the Thermochemical Computer Code) that can be attained at various temperatures with the systems N_2O-F_2 , N_2O-NF_3 , N_2O-ClF_5 , N_2O-SF_6 ***, NO- NF_3 , and NO- ClF_5 and NO- SF_6 . The small numbers listed on these curves at various points represent the molar mixture ratio of reactants (nitrogen oxide to fluorine compound) required to reach a given temperature. It can be noted that at high molar ratios, each curve becomes linear with a slope such that it would intersect the abscissa at the adiabatic flame temperature if extrapolated to zero F-atom concentration (pure nitrogen oxide).

The theoretical reaction products are plotted as a function of temperature for these systems in Fig. 21 through 27. In all systems, the concentration of FNO decreases rapidly with temperature as the endothermic reaction:



*It will be shown that small amounts of FNO do form theoretically from F, N_2 , and O_2 at lower combustion temperatures.

**The thermal decomposition of N_2O is catalyzed by halogens (Ref. 11 and 12) suggesting that an N_2O -oxidizer mixture may burn better than N_2O alone.

*** SF_6 is classed as an "oxidizer" in this discussion.

shifts toward NO. In the N_2O-ClF_5 and $NO-ClF_5$ systems, the ClF again dissociates mainly to Cl atoms at the higher temperature. In the N_2O-SF_6 system, the F-atom concentration increases with temperature below about 1600 K, even though the fraction of SF_6 in the reactants is decreasing. This is because SF_6 is stable at 1500 K but dissociates appreciably at 1600 K.

The NO-oxidizer systems yield higher calculated F-atom concentrations (Fig. 20) because the larger heat of decomposition of NO permits a given temperature to be attained with a much higher fraction of oxidizer in the reactant mixture. Also, the $NO-SF_6$ system reaches maximum F-atom concentration at a higher temperature than N_2O-SF_6 because the molar reactant ratio increases more slowly with temperature.

Heat of Formation of SOF_4

The results of the thermochemical calculations on the systems N_2O-SF_6 and $NO-SF_6$ depend on the heat of formation that is assigned to SOF_4 . Calculations with the Thermochemical Code indicate that, if the ΔH_{298} of SOF_4 is -254 kcal/mole, as estimated by Wilkins (Ref. 13), SOF_4 is the expected major sulfur-containing product from the binary reactant systems N_2O-SF_6 and $NO-SF_6$. However, unpublished data obtained by C. M. Merrill indicate that the heat of formation of SOF_4 cannot be more negative than about -228 kcal/mole. In addition, thermochemical calculations made at AFRPL show that revision of this heat of formation to -230 or greater results in SO_2F_2 being favored thermodynamically over SOF_4 .

This situation has been reviewed in some detail and the results obtained, which are in agreement with the calculations made at AFRPL, are presented below. It will be shown that possible empirical methods for estimating the heat of formation of SOF_4 lead to a wide range of predicted values (none of which approach the value of -254), but structural considerations suggest a value less negative than -235 in agreement with the experimental observations. The Rocketdyne thermochemical data tape has been changed to include a value of -225 kcal/mole for the heat of formation of SOF_4 and this value was used in the calculations shown in Fig. 20, 26, and 27.

Experimental Stability of SOF₄. Dr. C. M. Merrill of AFRPL synthesized SOF₄ some years ago while at the University of Washington. He observed that when SOF₄ was held overnight at 521 C it converted spontaneously and apparently quantitatively to a mixture of SO₂F₂ and SF₆, via the reaction:



The absence of unreacted SOF₄ was determined by infrared analysis. This method can detect a concentration of less than 1 percent. The following table illustrates the effect of the heat of formation of SOF₄ on the heat of the above reaction and on the mole fraction of SOF₄ remaining at equilibrium at 800 K (assuming that the other thermochemical data used in the calculation are accurate).

Mole Fraction SOF ₄ at Equilibrium	ΔH (Eq. I-8)	ΔH _{f,298} ^{SOF₄}
0.0001	-32.5	-220.3
0.0001	-25.2	-224.0
0.01	-17.9	-227.7
0.10	-10.2	-231.5
0.25	-6.8	-233.2
0.50	-3.3	-235.0
0.75	+0.2	-236.7
0.90	+3.7	-238.5
0.95	+6.1	-239.6
0.99	+11.3	-242.3
0.999	+18.7	-245.9

If the detectability limit for SOF₄ were 1 percent, the lower limit calculated for ΔH_{f,298} SOF₄ would be -227.7 kcal/mole

Estimated Stability of SOF₄. The experimental heats of formation of SO₃(g), SO₂F₂(g), and SF₆(g) (Ref. 9) are plotted in Fig. 28 for comparison with the values for SOF₄ estimated by the following possible methods.

Method A. Assuming reaction I-8 to be thermoneutral, a heat of formation for SOF₄ of -237 kcal/mole is obtained. This is equivalent to a linear interpolation between SO₂F₂ and SF₆ in Fig. 28. This method presumes that the relative

bond strengths are the same in species that have structures that are tetrahedral (SO_2F_2), trigonal bipyramidal (SOF_4), and octahedral (SF_6), respectively. General experience with related compounds indicates that trigonal bipyramidal compounds are less stable and exhibit weaker bonds than compounds with tetrahedral and octahedral structures. Thus, the heat of formation of SOF_4 is not likely to be as negative as -237 kcal/mole and reaction I-8 would be expected to be exothermic.

Method B. If the heats of formation of SO_2F_2 and SOF_4 were to be estimated using the average S-O and S-F bond energies in SO_3 and SF_6 , respectively, they would be equal to those obtained by linear interpolation between SO_3 and SF_6 (dashed line in Fig. 28). This is equivalent to assuming that the reactions



and



are thermoneutral. The heat of formation of SO_2F_2 , obtained by such a linear interpolation, is -161 kcal/mole, whereas the experimental value is -181.3. This may be interpreted as indicating that there is a total strengthening of bond energies in SO_2F_2 , relative to those in SO_3 and SF_6 , of 20 kcal per mole. Thus, reaction I-9 is exothermic by 61 kcal/mole. The value obtained for the heat of formation of SOF_4 , using linear interpolations between SO_3 and SF_6 , is -227 kcal/mole which is the lower limit obtained from Merrill's observation. This suggests that reaction I-10 is thermoneutral or even endothermic.

Method C. If an arc is drawn through the experimental points in Fig. 28, the heat of formation of SOF_4 estimated by this nonlinear interpolation technique is -244 kcal/mole. Inherent in this estimating method is the assumption that the strengthening of the bonds in SOF_4 with respect to those in SO_3 and SF_6 is similar to the observed strengthening in SO_2F_2 . In fact, this assumption requires that reaction I-8 be endothermic by 16 kcal/mole. Since this nonlinear interpolation technique predicts stability trends that are opposite from those predicted from

the structural considerations discussed above, this method cannot be given serious consideration. But even this method does not give a value as negative as that suggested in Ref. 13.

Method D. Assuming that the heat of the reaction $\text{SF}_4 + \text{O} = \text{SOF}_4$ is equal to that of $\text{SO}_2 + \text{O} = \text{SO}_3$ provides another possible method for estimating the heat of formation of SOF_4 . This method is equivalent to assuming that the reaction $\text{SF}_4 + \text{SO}_3 = \text{SOF}_4 + \text{SO}_2$ is thermoneutral, and is also questionable on the grounds that the types of molecular bonding are not the same in these compounds. The value obtained, -210.2, is compatible with the experimental observation. This method was tested by estimating the heat of formation of POF_3 from the heats of formation of P_2O_3 , P_2O_5 , and PF_3 . The value obtained (-270) was 16 kcal/mole higher than the experimental value (-286) indicating again that such methods are not reliable.

In summary, any heat of formation estimate that is based on an empirical interpolation involving bond strengths and their trends must be considered very approximate unless nearly identical types of molecular orbital bonding are involved. Thus, the only reliable estimate for the heat of formation of SOF_4 is that obtained from the cited experimental observation which indicates that the value cannot be more negative than -227 kcal/mole. However, the empirical estimates suggest that this experimental value is reasonable, and strongly indicate that Wilkins' estimated heat of formation is not.

It can be seen from the results in Fig. 26 and 27, obtained using a heat of formation of SOF_4 of -225 kcal/mole, that SF_6 should be the major sulfur-containing species at lower temperatures, and most of the sulfur should form SO_2F_2 at higher temperatures. SOF_4 is not predicted to be an important product when the less negative value for its heat of formation is used.

Detailed Thermochemical Analysis

The calculations made with the Thermochemical Computer Code are exact within the accuracy of the available thermochemical data, but do not define directly the important thermochemical properties of the individual oxidizers, fuels, and

diluents. The following detailed analysis, although somewhat less rigorous, gives additional insight into the thermochemistry involved in the precombustor reactions.

Effect of Temperature on Product Distributions. Considering again the temperature ranges in which various potential products are favored thermodynamically, this can be approached more directly by simply calculating the equilibrium positions of the following reactions as a function of temperature:



The results of such calculations are plotted in Fig. 29. Curve 1 was taken from the curve in Fig. 2 for $P_F + P_{F_2} = 3$ psia. The other curves were calculated for conditions where $P_F = 3$ psia at equilibrium.* For these curves, the fraction of a given species which is converted to the product shown is independent of the concentration of the species or its products (holding $P_F = 3$). For example, the equilibrium constant for Eq. I-12 is equal to $P_{SF_4} \cdot P_F^2 / P_{SF_6}$. At a given temperature and F-atom concentration, the ratio P_{SF_4} / P_{SF_6} is the same regardless of the amount of sulfur in the system. Thus, the fraction of SF_6 converted to SF_4 (at $P_F = 3$) is independent of the total concentration of sulfur-containing species ($P_{SF_6} + P_{SF_4}$). It can be shown in this manner that curves 2 and 4 through 7

(Fig. 29) are general for any combustor that attains equilibrium and forms F-atoms at a partial pressure of 3 psia. The results represented by curve 3 in Fig. 29 are not as general because they are dependent on the final oxygen concentration as well. Curve 3 was calculated for the case in which the combustor

*Equivalent to a 30-psia precombustor forming 10 percent F-atoms.

total pressure is 30 psia, the products contain 10 percent r-atom, and the oxygen and CF_4 are initially at 20 and 7 mole percent, respectively (i.e., 20 to 16.5 mole percent O_2).

The following conclusions can be drawn from Fig. 29:

1. All of the hydrogen in the reactant species will be converted to HF even at temperatures above 3000 K.
2. In the absence of oxygen, all carbon will be present as CF_4 up to temperatures above 2500 K. If considerable oxygen is present (e.g., if air were used as diluent), the carbon would exist as CF_4 at 1500 K but mainly as COF_2 above about 1900 K.
3. Chlorine, which would be present if ClF_5 were the oxidizer, exists as ClF at 1500 K, but mainly as Cl atoms above 1900 K. It can be seen from Fig. 10, for example, that some Cl_2 molecules will also be present at 1900 K, but their concentration will not exceed about 20 percent of the chlorine in the system.
4. In the absence of oxygen, SF_6 is the major sulfur-containing product at 1500 K but SF_4 suddenly becomes favored at slightly higher temperatures. It can be seen from Fig. 16 that SF_4 dissociates above 2100 K to SF_2 , Si_2 , and SF . It was shown earlier (Fig. 26) that in the presence of O_2 , Si_4 is converted to SO_2F_2 above about 1500 K.
5. The combustion reaction $\text{PF}_3 + \text{F}_2 = \text{PF}_5$ cannot be used to obtain temperatures above about 2200 K because PF_5 will not form at the higher temperatures.

Effect of Reactant Properties on Thermochemistry. It can be shown from Fig. 10 and 29 (and similar equilib. calculations) that the only major combustion products at 1500 K are F^* , HF , CF_4 , ClF , O_2 , SF_6 , PF_5 , and N_2 . If no chlorine, oxygen, phosphorous, or sulfur species are in the reactants, the only products

The few percent F_2 that remains undissociated at 1500 K is ignored in the following discussion.

that form in the temperature range of 1500 to 2500 K are F, HF, CF_4 , and N_2 . The fact that each element goes almost exclusively to a single product under these conditions permits the thermochemistry of the combustor reactions to be analyzed in some detail. Also, if chlorine or sulfur are present in the reactants, e.g., as ClF_5 or CS_2 , the following simplified analysis can be carried out at 1500 K where ClF and SF_6 are formed almost exclusively (Fig. 29).

For this theoretical analysis, the overall combustion process can be considered as occurring in two thermochemical stages. In one stage, the fuel and part of the oxidizer react to form hot combustion products, at temperature T, and heat:

$$n_{\text{fuel}} \cdot \text{fuel}(298) + n_{\text{ox}} \cdot \text{oxid}(298) = n_{\text{prod}}^c \cdot \text{prod}(T), \Delta H_c \quad (\text{I-18})$$

where* n_{fuel} and n_{ox} are the moles of fuel and oxidizer, respectively, that react in the combustion reaction per mole of fluorine atom combusted, and n_{prod}^c is the total moles of combustion product(s) formed in this amount of reaction.** The heat generated in Eq. I-18 for a given fuel/oxidizer combination is defined as $-\Delta H_c$, the "heat of combustion" per mole of fluorine atom combusted.

In the second thermochemical stage, the heat of combustion is consumed entirely in dissociating the excess oxidizer and in heating the diluent:

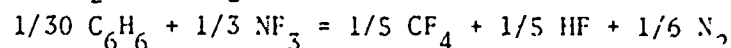
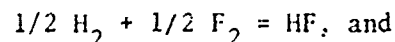
$$n_{\text{ox}} \cdot \text{oxid}(298) = F(T) + n_{\text{prod}}^{\text{oxid}} \cdot \text{prod}(T), \Delta H_{\text{ox}} \quad (\text{I-19})$$

$$\text{diluent}(298) = \text{diluent}(T), \Delta H_{\text{dil}} \quad (\text{I-20})$$

where n_{ox} represents the moles of oxidizer that must be dissociated to form one mole of F-atom (and has the same value as in Eq. I-18) and $n_{\text{prod}}^{\text{oxid}}$ the total moles

*A nomenclature list is given at the end of the report.

**Examples of Eq. I-18 are:



For the first, $n_{\text{fuel}} = n_{\text{ox}} = 1/2$ and $n_{\text{prod}}^c = 1$. For the second, $n_{\text{fuel}} = 1/30$, $n_{\text{ox}} = 1/3$, and $n_{\text{prod}}^c = 17/30$.

of products that are formed in addition to the F-atom, if any.* ΔH_{ox} is the oxidizer "heat of dissociation," as defined in Eq. I-19, and ΔH_{dil} is the heat required to increase the temperature of one mole of diluent from 298 K to the final combustor temperature, T.

The thermochemical properties of the fuels and oxidizers can be considered individually by dividing the combustion reaction (Eq. I-18) into two hypothetical half-reactions, one of which (Eq. I-19) is the dissociation of oxidizer to form 1 mole of F-atoms at temperature, T, and the other is the combustion of 1 mole of F-atoms:

$$n_{ox} \cdot \text{oxid}(298) = F(T) + n_{prod}^{oxid} \cdot \text{prod}(T), \Delta H_{ox} \quad (I-19)$$

$$n_{fuel} \cdot \text{fuel}(298) + F(T) = n_{prod}^{fuel} \cdot \text{prod}(T), \Delta H_{fuel} \quad (I-21)$$

$$n_{fuel} \cdot \text{fuel}(298) + n_{ox} \cdot \text{oxid}(298) = n_{prod}^c \cdot \text{prod}(T), \Delta H_c \quad (I-18)$$

ΔH_{fuel} is the heat released when 1 mole of F-atoms is combusted with a given fuel as defined in Eq. I-21 and $\Delta H_c = \Delta H_{ox} + \Delta H_{fuel}$. Also, $n_{prod}^c = n_{prod}^{oxid} + n_{prod}^{fuel}$. The half-reactions are chosen in this manner so that the combustion reaction can be considered as dissociation of oxidizer to form F-atoms followed by the combustion of F-atoms with the fuel.** This permits the thermochemical properties of the oxidizers and fuels to be considered individually.

*For example, in the dissociation reaction $1/4 \text{ClF}_5(298) = F(T) + 1/4 \text{ClF}(T)$,

$$n_{ox} = 1/4 \text{ and } n_{prod}^{oxid} = 1/4.$$

**For example, the half-reactions for the combustion of CS_2 and NF_3 at 1500 K are:

$$1/3 \text{NF}_3(298) = F(1500) + 1/6 \text{N}_2(1500)$$

$$1/16 \text{CS}_2(298) + F(1500) = 1/16 \text{CF}_4(1500) + 1/8 \text{SF}_6(1500)$$

$$1/3 \text{NF}_3 + 1/16 \text{CS}_2 = 1/6 \text{N}_2 + 1/16 \text{CF}_4 + 1/8 \text{SF}_6$$

where $n_{prod}^{oxid} = 1/6$, $n_{prod}^{fuel} = 3/16$, and $n_{prod}^c = 17/48$.

It can now be seen that the more endothermic the oxidizer dissociation reaction per mole of F-atom formed (as defined in Eq. I-19), the larger the fraction of the "available fluorine"* that must be combusted to achieve a given temperature and F-atom concentration with any fuel. This is because not only is more heat required to dissociate the excess oxidizer (Eq. I-19), but a lower heat of combustion is obtained with any given fuel (Eq. I-18). Likewise, a fuel that reacts more exothermically in Eq. I-21 will have a higher heat of combustion with any given oxidizer.

The oxidizer dissociation reactions are listed in Table V along with the associated enthalpy changes, ΔH_{ox} , and the stoichiometric factors from Eq. I-19, n_{ox} and n_{prod} . F_2 and N_2F_4 have appreciably smaller heats of dissociation than do NF_3 , ClF_5 , and ClF_3 . Therefore, F_2 and N_2F_4 will consume less heat in the dissociation process as well as burn hotter with any given fuel. The unfavorable thermodynamic properties of NF_3 and the interhalogens do not necessarily preclude their use but indicate that more of the available fluorine must be burned with these oxidizers causing the formation of higher concentrations of combustion products such as HF (or DF) and CF_4 . Also listed in Table V are the percentages of available fluorine that must be combusted, with H_2 as the fuel, to obtain a temperature of 1500 K and 10 mole percent F-atoms (helium diluent). These values were calculated, assuming an adiabatic combustor, by a procedure that will be described later in this section.

In Table VI, the conjugate half-reactions for a number of potential combustor fuels are listed. The values of ΔH_{fuel} at 1500 K (in units of kcal per mole of F combusted) range from -83.9 for PF_3 and C_2F_4 to -60.9 for C_2F_6 . The percentage of available fluorine that must be combusted to obtain a temperature of 1500 K (with F_2 as the fuel and forming 10 mole percent F-atoms) ranges from 54.9 for

*Some of the possible combustor reactants contain F-atoms that do not form new bonds during combustion and, therefore, do not contribute to the heat of combustion. Specifically, these are one F-atom in ClF_5 and ClF_3 and all of the F-atoms in the perfluorohydrocarbons. Such F-atoms are defined as "unavailable fluorine."

TABLE V. OXIDIZER DISSOCIATION REACTIONS

Half Reaction	ΔH_{ox} , kcal/mole		Percent Fluorine Combusted at 1500 K*	Stoichiometric Factors	
	1500 K	2000 K		n_{ox}	n_{prod}^{oxid}
$1/2 F_2, g(298) = F(T)$	+25.05	+27.55	55.8	1/2	0
$1/4 N_2F_4, g(298) = F(T) + 1/4 N_2(T)$	+27.84	+31.41	56.7	1/4	1/4
$1/3 NF_3, g(298) = F(T) + 1/6 N_2(T)$	+36.44	+39.66	63.1	1/3	1/6
$1/4 ClF_5, l(298) = F(T) + 1/4 ClF(T)$	+39.74	--	65.1	1/4	1/4
$1/2 ClF_3, l(298) = F(T) + 1/2 ClF(T)$	+46.44	--	68.8	1/2	1/2

*Fraction of available fluorine in oxidizer that is combusted (rather than dissociated to F-atoms) when the oxidizer is reacted with H_2 in helium at reactant ratios that give 10 mole percent F-atoms at 1500 K.

N_2H_4 to 65.3 for C_2F_6 . There is a general correlation between low values for the magnitude of ΔH_{fuel} and large values for percent available fluorine combusted. However, those fuels with larger values of n_{prod}^{fuel} require less fluorine combusted at a given value of ΔH_{fuel} because the combustion products replace some of the required diluent (helium in these examples). The results in the following tabulation demonstrate further the higher fraction of fluorine that must be combusted with the cooler-burning reactant combinations (at 1500 K and forming 10 mole percent F-atom):

Reactants	ΔH_c , 1500 K	Percent Fluorine Combusted	
		Diluent = He	Diluent = N_2
F_2-H_2	-56.5	56	62
NF_3-H_2	-45.1	63	68
F_2-CS_2	-45.0	63	70
NF_3-CS_2	-33.6	71	76

TABLE VI. FUEL COMBUSTION REACTIONS

Half Reaction	ΔH_{fuel} kcal/mole		Percent Fluorine Combusted at 1500 K ⁽⁴⁾	Stoichiometric Factors	
	1500 K	2000 K		n_{fuel}	n_{prod}
$1/2 \text{ H}_2, \text{ g}(298) + \text{F}(\text{T}) = \text{HF}(\text{T})$	-81.53	-80.07	55.8	1/2	1
$1/4 \text{ N}_2\text{H}_4, \text{ l}(298) + \text{F}(\text{T}) = \text{HF}(\text{T}) + 1/4 \text{ N}_2(\text{T})$	-82.24	-79.725	54.9	1/4	3/4
$1/3 \text{ NH}_3, \text{ l}(298) + \text{F}(\text{T}) = \text{HF}(\text{T}) + 1/6 \text{ N}_2(\text{T})$	-74.76	-72.59	58.2	1/3	7/6
$1/16 \text{ CS}_2, \text{ l}(298) + \text{F}(\text{T}) = 1/16 \text{ CF}_4(\text{T}) + 1/8 \text{ SF}_6(\text{T})$	70.05	----	63.1	1/16	3/16
$1/8 \text{ (CN)}_2, \text{ l}(298) + \text{F}(\text{T}) = 1/4 \text{ CF}_4(\text{T}) + 1/8 \text{ N}_2(\text{T})$	-82.24	-81.09	57.0	1/8	3/8
$1/2 \text{ PF}_3, \text{ g}(298) + \text{F}(\text{T}) = 1/2 \text{ PF}_5(\text{T})$	-83.89	-78.61	56.0	1/2	1/2
$1/4 \text{ CO}, \text{ g}(298) + \text{F}(\text{T}) = 1/4 \text{ CF}_4(\text{T}) + 1/8 \text{ O}_2(\text{T})$	-66.34	----	64.4	1/4	3/8
$1/14 \text{ C}_2\text{H}_6, \text{ g}(298) + \text{F}(\text{T}) = 3/7 \text{ HF}(\text{T}) + 1/7 \text{ CF}_4(\text{T})$	-75.87	-74.89	59.2	1/14	4/7
$1/10 \text{ C}_2\text{H}_2, \text{ g}(298) + \text{F}(\text{T}) = 1/5 \text{ HF}(\text{T}) + 1/5 \text{ CF}_4(\text{T})$	-81.05	-80.26	57.4	1/10	2/5
$1/30 \text{ C}_6\text{H}_6, \text{ l}(298) + \text{F}(\text{T}) = 1/5 \text{ HF}(\text{T}) + 1/5 \text{ CF}_4(\text{T})$	-76.02	-75.23	59.6	1/30	2/5
$1/2 \text{ C}_2\text{F}_6, \text{ l}(298) + \text{F}(\text{T}) = \text{CF}_4(\text{T})$	-60.89	-50.88	65.3	1/2	1
$1/4 \text{ C}_2\text{F}_4, \text{ g}(298) + \text{F}(\text{T}) = 1/2 \text{ CF}_4(\text{T})$	-83.92	-80.17	56.0	1/4	1/2
$1/6 \text{ C}_3\text{F}_6^{(1)} \text{ g}(298) + \text{F}(\text{T}) = 1/2 \text{ CF}_4(\text{T})$	-79.43	-75.68	57.9	1/6	1/2
$1/8 \text{ C}_4\text{F}_8^{(2)} \text{ g}(298) + \text{F}(\text{T}) = 1/2 \text{ CF}_4(\text{T})$	-77.08	-73.33	58.9	1/8	1/2
$1/18 \text{ C}_6\text{F}_6^{(3)} \text{ l}(298) + \text{F}(\text{T}) = 1/3 \text{ CF}_4(\text{T})$	-76.08	-74.42	59.8	1/18	1/3

⁽¹⁾ Perfluoropropylene⁽²⁾ Perfluorocyclopropane⁽³⁾ Perfluorobenzene⁽⁴⁾ Fraction of available fluorine that is combusted (rather than dissociated to F atoms) when the fuel is reacted with F₂ in helium at reactant ratios that give 10 mole percent F atoms at 1500 K.

It is apparent, therefore, that in most cases a penalty must be paid in terms of the quantity of reactants burned to generate a given quantity of F-atoms, when reactants other than F_2-H_2-He are employed.

Listed in Table VII are the enthalpies, ΔH_{dil} , required to heat 1 mole of diluent from 298 to 1500 and 2000 K, respectively. Of course, the specific heat of N_2 is considerably greater than that of He. The effect of this is to increase the fraction fluorine combusted when N_2 is the diluent as shown in the above tabulation

TABLE VII. DILUENT ENTHALPY CHANGES

Diluent	ΔH_{dil} , kcal/mole	
	1500 K	2000 K
$He(298) = He(T)$	5.971	8.455
$N_2(298) = N_2(T)$	0.179	13.418

In some applications, the use of larger quantities of oxidizer and fuel may not be a major drawback. A more serious limitation would be if the products formed in the combustor reaction were detrimental to laser efficiency. For example, DF deactivates vibrationally excited HF moderately rapid (Table IV). Thus, increasing the quantity of DF or HF in the combustor products by employing a cooler-burning oxidizer would not be desirable and the elimination of DF may be beneficial.

The data contained in Tables V through VII can be used to calculate the required reactant ratios and the product compositions obtained for conditions where the products are exactly those listed in the tables. It can be seen from Fig. 29 that, at 1500 K, there will be a small error in the calculated results because about 5 percent of the F_2 is not dissociated. However, for systems that contain only the elements C, H, F, N, and He, the products will be almost entirely F, CF_4 , HF , N_2 , and He from 1700 to 2500 K. Exact thermochemical calculations can

be made for any reactant system at any temperature using the Rocketdyne Thermochemical Computer Code, but the following procedure gives additional insight into the thermochemistry involved at temperatures where the analysis applies.

Assuming an adiabatic reactor, the reactant ratios and product compositions can be calculated by solving the energy balance and stoichiometric equations as follows. If R_1 is defined as moles of F combusted per mole of F-atom formed and R_2 as moles of diluent in the products per mole of F-atom formed, the following reactions will occur (per mole of F-atom formed):

$$(1 + R_1) \cdot \left[n_{ox} \cdot \text{oxid}(298) + F(T) = n_{prod}^{ox} \cdot \text{prod}(T) \right] \quad (\text{I-22})$$

$$(R_1) \cdot \left[n_{fuel} \cdot \text{fuel}(298) + F(T) = n_{prod}^{fuel} \cdot \text{prod}(T) \right] \quad (\text{I-23})$$

$$(R_2) \cdot \left[\text{diluent}(298) = \text{diluent}(T) \right] \quad (\text{I-24})$$

The heat balance of the system requires

$$R_1(\Delta H_c) + \Delta H_{ox} + R_2(\Delta H_{dil}) = 0 \quad (\text{I-25})$$

If the final mole fraction of F-atom is defined as X_F , the following stoichiometric relationships exist in the products (the calculations are made per mole of F-atom formed):

$$\text{Moles of diluent}^* = R_2 \quad (\text{I-26})$$

$$\text{Moles of reaction products} = n_{prod}^{ox} + R_1 \left(n_{prod}^{ox} + n_{prod}^{fuel} \right) \quad (\text{I-27})$$

$$\text{Total moles} = 1 + n_{prod}^{ox} + R_1 \left(n_{prod}^{ox} + n_{prod}^{fuel} \right) + R_2 = 1/X_F \quad (\text{I-28})$$

*If the diluent is N_2 , this equation does not include the N_2 that may be formed as a reaction product.

Solving Eq. I-25 for R_1 gives

$$R_1 = -(\Delta H_c)^{-1} \cdot (H_{ox} + R_2 \cdot \Delta H_{dil}) \quad (I-29)$$

Solving Eq. I-28 for R_2 and substituting for R_1 from Eq. I-29 gives the following expression for R_2 :

$$R_2 = \left[\frac{1}{X_F} - 1 - n_{prod}^{oxid} + (\Delta H_{ox}/\Delta H_c) \cdot (n_{prod}^{oxid} + n_{prod}^{fuel}) \right] \div \left[1 - (\Delta H_{dil}/\Delta H_c) \cdot (n_{prod}^{oxid} + n_{prod}^{fuel}) \right] \quad (I-30)$$

For a given oxidizer-fuel-diluent-temperature- X_F combination, R_2 can be obtained from Eq. I-30 and then R_1 from Eq. I-29. It can be seen from Eq. I-22 through I-24 that the mole fractions of reactants are given by:

$$X_{oxid} = \left[n_{ox}(1 + R_1) \right] \div \left[n_{ox}(1 + R_1) + n_{fuel}(R_1) + R_2 \right] \quad (I-31)$$

$$X_{fuel} = \left[n_{fuel}(R_1) \right] \div \left[n_{ox}(1 + R_1) + n_{fuel}(R_1) + R_2 \right] \quad (I-32)$$

$$X_{dil} = 1 - X_{oxid} - X_{fuel} \quad (I-33)$$

The mole fractions of the various reaction products can be obtained in a similar manner from Eq. I-22 through I-24 by separating n_{prod}^{oxid} and n_{prod}^{fuel} into the terms of the individual product species as shown in the chemical equations in Tables V and VI. Taking, for example, the system NF_3 - CS_2 -He:

$$n_{prod}^{oxid} = n_{N_2}^{oxid} = 1/6 \quad (I-34)$$

$$n_{prod}^{fuel} = n_{CF_4}^{fuel} + n_{SF_6}^{fuel} = 1/16 + 1/8 \quad (I-35)$$

$$\text{Total moles} = 1/X_F \text{ (from Eq. I-28)} \quad (I-36)$$

$$\begin{aligned} X_{N_2} &= (1 + R_1) \cdot (1/6) / (\text{total moles}) \\ &= (1 + R_1) \cdot (1/6) \cdot (X_F) \end{aligned} \quad (I-37)$$

$$X_{CF_4} = (R_1) \cdot (1/16) \cdot (X_F) \quad (I-38)$$

$$X_{SF_6} = (R_1) \cdot (1/8) \cdot (X_F) \quad (I-39)$$

$$X_{He} = R_2 (X_F) \quad (I-40)$$

The mass fractions of reactants and products can be obtained by multiplying the mole fraction of each species by its molecular weight and normalizing to total mass fraction of one. Finally, the fraction of available fluorine that is combusted is given by the expression:

$$\text{Fraction Combusted} = R_1 / (1 + R_1) \quad (I-41)$$

Comparison of Combustor Reactant Systems. Thermochemical calculations of the type described in the previous section will now be used to examine the conditions that can be attained with various oxidizer-fuel-diluent systems and the concentrations at which chemical species will be present in the reaction products (if chemical equilibrium is achieved and the reactor is adiabatic). The above equations were set up in a form that permits determination of the reactant ratios required to obtain a given temperature and a given value of X_F .

The thermochemical properties of the reactants set an upper limit on the maximum mole fraction of F-atoms that can be obtained at any temperature as well as the maximum attainable temperature (the adiabatic flame temperature of the oxidizer/fuel combination). If the desired value of X_F exceeds the thermochemically allowed value, negative diluent mole fractions will be calculated in Eq. I-33 and I-40. The maximum value of X_F at any given temperature would be obtained in the absence of any diluent. The maximum F-atom concentration that can be attained at any temperature (in the absence of diluent) can be calculated by solving Eq. I-25 for R_1 and then Eq. I-28 for X_F after setting $R_2=0$ in both of these equations. In the absence of diluent, there is one independent variable and a given temperature can be attained only with a single reactant ratio. The results of such calculations are listed in Table VIII for various oxidizer/fuel combinations at 1500 and 2000 K. All of the reactant systems are capable of generating sufficient

TABLE VIII. MAXIMUM ATTAINABLE MOLE PERCENTAGE OF F-ATOMS FOR VARIOUS
OXIDIZER/FUEL COMBINATIONS AT 1500 AND 2000 K (NO DILUENT)

Fuels	Oxidizers									
	F ₂ , g		N ₂ F ₄ , g		NF ₃ , g		ClF ₅ , l		ClF ₃ , l	
	1500 K	2000 K	1500 K	2000 K	1500 K	2000 K	1500 K	2000 K	1500 K	2000 K
H ₂ , g	69.3	65.6	52.7	48.6	47.4	43.3	41.0		28.7	
N ₂ H ₄ , l	64.6	60.2	49.6	44.9	43.6	38.9	37.7		26.5	
NH ₃ , l	63.0	58.4	47.8	42.9	41.1	36.1	35.0		23.6	
CS ₂ , l	90.6		65.0		64.5		54.8		35.1	
(CN) ₂ , l	85.9	83.8	63.7	60.8	62.6	59.3	54.5		38.0	
PF ₃ , g	82.5	78.7	61.6	57.2	59.6	54.2	51.9		36.5	
CO, g	81.5		58.8		54.7		45.8		28.2	
C ₂ H ₆ , g	78.0	75.0	57.9	54.2	54.1	50.1	46.4		31.3	
C ₂ H ₂ , g	84.8	82.7	62.9	60.0	61.4	58.1	53.3		36.9	
C ₆ H ₆ , l	83.6	81.2	61.5	58.3	59.2	55.6	51.0		34.3	
C ₂ F ₆ , g	58.9	45.8	43.4	30.6	34.4	18.9	27.8		15.8	
C ₂ F ₄ , g	82.5	79.2	61.6	57.7	59.6	55.0	52.0		36.5	
C ₃ F ₆ , g	81.3	77.7	60.4	56.1	57.7	52.6	50.0		34.4	
C ₄ F ₈ , g	80.6	76.9	59.7	55.2	56.7	51.2	48.8		33.2	
C ₆ F ₆ , l	85.9	83.6	63.0	59.7	61.5	57.6	53.0		35.6	

quantities of F-atoms (in the absence of diluent). Even the very-cold-burning combination $\text{NF}_3\text{-C}_2\text{F}_6$, which has a heat of combustion at 1500 K of only -24.4 kcal/mole F combusted compared with -56.5 for $\text{F}_2\text{-H}_2$, can generate 34 mole percent F-atoms at 1500 K.

The thermochemical calculations described in the previous section were carried out for a number of reactant systems (with helium as diluent) by use of a computer program. The results obtained are presented in Tables IX through XI. In Table IX, the five oxidizers are compared in the systems oxidizer- H_2 -He at 1500 and 2000 K and reactant ratios that form 10 and 20 mole percent F-atoms. The major combustion product with H_2 as the fuel is HF with from 0.8 to 2.3 moles forming per mole of F-atom. About 50 percent more HF is formed from the cooler-burning oxidizers NF_3 and ClF_5 than from F_2 or N_2F_4 . It may also be seen that the use of ClF_5 or ClF_3 as the oxidizer would, in addition, lead to the formation of appreciable concentrations of ClF at 1500 K (or Cl atoms at higher temperatures). The 15 fuels are similarly compared in Table X for the systems F_2 -fuel-He at 1500 and 2000 K and reactant ratios that give 10 mole percent F-atoms. Similar amounts of HF are formed from the fuels H_2 , N_2H_4 , and NH_3 . The amount of HF that is formed is decreased by a factor of 2 when the fuel is a saturated hydrocarbon and by more than a factor of 4 with $(\text{CH})_x$ hydrocarbons such as acetylene or benzene. Most of the combusted fluorine forms CF_4 with the hydrocarbon fuels. Of course, fuels that do not contain hydrogen do not form HF but, instead, form CF_4 , SF_6 (at 1500 K), or PF_5 .

The systems NF_3 -fuel-He are compared in Table XI. The product distributions are quite similar to those obtained with F_2 except that higher concentrations of products are formed (about 50 percent higher) and, of course, some nitrogen is formed.

Detailed Analyses of Nitrogen Oxide Systems. A detailed thermochemical analysis has not been conducted for all of the nitrogen oxide systems. The heat of combustion in these systems is supplied by the decomposition of the nitrogen oxide. Taking the $\text{N}_2\text{O-F}_2$ system as an example, the detailed thermochemistry can be considered as follows. The major reaction products at 1600 K, as calculated using

TABLE IX. COMBUSTOR REACTANT RATIOS AND PRODUCT DISTRIBUTIONS AT SELECTED TEMPERATURES (1500 AND 2000 K) AND MOLE PERCENT F ATOMS (10 AND 20) FOR VARIOUS OXIDIZERS WITH HYDROGEN FUEL AND HELIUM DILUENT*

Temperature	1500 K												
	Reactants, Mole Percent	Oxidizer/Fuel Reactants	F ₂ ,g H ₂ ,g	N ₂ F ₄ ,g H ₂ ,g	NF ₃ ,g H ₂ ,g	ClF ₅ ,l H ₂ ,g	ClF ₃ ,l H ₂ ,g	F ₂ ,g H ₂ ,g	N ₂ F ₄ ,g H ₂ ,g	NF ₃ ,g H ₂ ,g	ClF ₅ ,l H ₂ ,g	ClF ₃ ,l H ₂ ,g	
		Oxidizer	11.9	6.9	10.5	8.9	20.3	19.8	12.7	18.8	16.8	39.1	
2000 K	Products, Mole Percent	Fuel	6.6	7.9	10.0	11.6	14.0	8.7	11.4	15.1	18.7	23.6	
		Helium	81.5	85.2	79.5	79.5	65.7	71.5	75.9	66.1	64.5	37.3	
		F	10.0	10.0	10.0	10.0	10.0	20.0	20.0	20.0	20.0	20.0	
		He	77.4	71.1	68.4	64.2	51.9	64.3	54.5	50.1	43.5	24.1	
		HF	12.6	13.1	17.1	18.6	22.1	15.7	16.4	22.8	25.2	30.6	
		CF ₄	--	--	--	--	--	--	--	--	--	--	
		ClF	--	--	--	7.2	16.0	--	--	--	11.3	25.3	
		N ₂	--	5.8	4.5	--	--	--	9.11	7.13	--	--	
	SF ₆	--	--	--	--	--	--	--	--	--	--		
PF ₅	--	--	--	--	--	--	--	--	--	--			
Fraction Fluorine Combust-ed		0.558	0.567	0.631	0.651	0.688	0.439	0.451	0.533	0.558	0.605		
2000 K	Reactants, Mole Percent	Oxidizer	14.2	8.6	13.0				22.3	14.9	22.0		
		Fuel	9.0	11.0	13.5				11.2	15.4	19.4		
		He	76.8	80.5	73.5				66.5	69.7	58.6		
	Products, Mole Percent	F	10.0	10.0	10.0				20.0	20.0	20.0		
		He	73.0	65.3	61.8				59.9	48.4	43.2		
		HF	17.0	17.8	22.7				20.1	21.3	28.7		
		CF ₄	--	--	--				--	--	--		
		ClF	--	--	--				--	--	--		
		N ₂	--	6.9	5.5				--	10.3	8.11		
		SF ₆	--	--	--				--	--	--		
PF ₅	--	--	--				--	--	--				
Fraction Fluorine Combusted		0.630	0.640	0.695				0.502	0.516	0.589			

*The combustor is assumed to be adiabatic and the few percent P₂ molecules that are present at 1500 K are neglected.

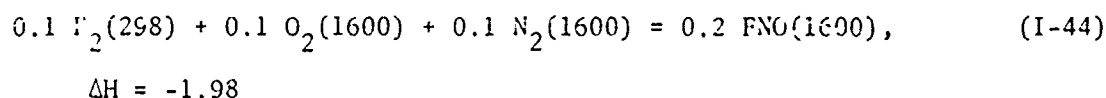
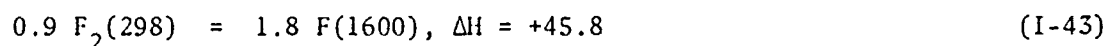
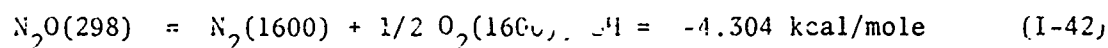
TABLE X. COMBUSTOR REACTANT RATIOS AND PRODUCT DISTRIBUTIONS AT SELECTED TEMPERATURES (1500 AND 2000 K) AND 10 MOLE PERCENT F ATOMS FOR VARIOUS FUELS WITH FLUORINE OXIDIZER AND HELIUM DILUENT

Temperature		Reactants, Mole Percent	Reactant Ratios															
			Oxidizer/Fuel Reactants	F ₂ ,g H ₂ ,g	F ₂ ,g N ₂ H ₄ ,l	F ₂ ,g NH ₃ ,l	F ₂ ,g CS ₂ ,l	F ₂ ,g (CH ₃) ₂ ,g	F ₂ ,g PF ₃ ,g	F ₂ ,g CO,g	F ₂ ,g C ₂ H ₆ ,g	F ₂ ,g C ₂ H ₂ ,g	F ₂ ,g C ₆ H ₆ ,l	F ₂ ,g C ₂ F ₆ ,g	F ₂ ,g C ₂ F ₄ ,g	F ₂ ,g C ₃ F ₈ ,g	F ₂ ,g C ₄ F ₈ ,g	F ₂ ,g C ₆ F ₆ ,l
			Oxidizer	11.9	12.5	13.2	13.4	11.8	11.2	13.8	12.9	12.0	12.8	15.2	11.6	12.2	12.6	12.6
			Fuel	6.64	3.43	5.13	1.05	1.69	6.28	4.45	1.09	1.38	0.51	9.92	3.24	2.35	1.85	8.40
1500 K	Products, Mole Percent	Helium	F	81.5	84.1	81.7	85.6	86.5	82.5	81.8	86.0	86.6	86.7	74.9	85.2	85.5	85.6	86.5
				10.0	10.0	10.0	10.0	10.0	10.0	10.0	10.0	10.0	10.0	10.0	10.0	10.0	10.0	10.0
				77.4	74.8	73.8	86.8	85.0	83.6	83.2	81.7	84.6	84.1	71.2	83.6	83.1	82.8	85.0
				12.6	12.2	13.9	--	--	--	--	6.23	2.70	2.95	--	--	--	--	--
				--	--	--	1.07	3.31	--	4.52	2.08	2.70	2.95	18.8	6.37	6.87	7.16	4.95
				--	--	--	--	--	--	--	--	--	--	--	--	--	--	--
				--	3.05	2.32	--	1.66	--	--	--	--	--	--	--	--	--	--
				--	--	--	2.14	--	--	--	--	--	--	--	--	--	--	--
				--	--	--	--	--	6.37	--	--	--	--	--	--	--	--	--
				--	--	--	--	--	--	2.26	--	--	--	--	--	--	--	--
2000 K	Products, Mole Percent	Fraction Fluorine Combusted	F	0.558	0.549	0.582	0.631	0.570	0.560	0.644	0.592	0.574	0.596	0.653	0.560	0.579	0.589	0.598
				14.2	15.3	16.3	--	14.2	13.8	--	15.7	14.4	15.5	22.4	14.2	15.2	15.7	15.5
				8.95	4.76	7.09	--	2.29	8.98	--	1.49	1.87	0.683	17.2	4.58	3.36	2.66	1.16
				76.8	80.0	75.6	--	83.5	77.2	--	82.8	83.7	83.8	60.4	81.2	81.5	81.6	83.3
				10.0	10.0	10.0	--	10.0	10.0	--	10.0	10.0	10.0	10.0	10.0	10.0	10.0	10.0
				75.0	69.3	68.0	--	83.1	80.6	--	78.6	82.6	81.9	57.4	80.9	80.1	79.6	83.0
				17.0	16.5	18.9	--	--	--	--	8.52	3.70	4.06	--	--	--	--	--
				--	--	--	--	4.57	--	--	2.84	3.70	4.06	32.6	9.12	9.9	10.4	6.95
				--	--	--	--	--	--	--	--	--	--	--	--	--	--	--
				--	4.13	3.15	--	2.28	--	--	--	--	--	--	--	--	--	--
2000 K	Products, Mole Percent	Fraction Fluorine Combusted	F	0.630	0.623	0.654	--	0.646	0.652	--	0.665	0.649	0.670	0.765	0.646	0.664	0.675	0.676
				--	--	--	--	--	--	--	--	--	--	--	--	--	--	--
				--	--	--	--	--	--	--	--	--	--	--	--	--	--	--
				--	--	--	--	--	--	--	--	--	--	--	--	--	--	--
				--	--	--	--	--	--	--	--	--	--	--	--	--	--	--
				--	--	--	--	--	--	--	--	--	--	--	--	--	--	--
				--	--	--	--	--	9.37	--	--	--	--	--	--	--	--	--
				--	--	--	--	--	--	--	--	--	--	--	--	--	--	--
				--	--	--	--	--	--	--	--	--	--	--	--	--	--	--
				--	--	--	--	--	--	--	--	--	--	--	--	--	--	--

TABLE XI. COMBUSTOR REACTANT RATIOS AND PRODUCT DISTRIBUTIONS AT SELECTED TEMPERATURES (1500 AND 2000 K) AND 10 MOLE PERCENT F ATOMS FOR VARIOUS FUELS WITH NF_3 OXIDIZER AND HELIUM DILUENT

Temperature	1500 K																		
	Reactants, Mole Percent	Oxidizer/Fuel Reactants	NF ₃ , H ₂ , H<																

the Thermochemical Computer Code (Fig. 21), are N_2 , O_2 , F-atoms, and FNO at a concentration of about one-tenth that of the F-atoms. Thus, the overall heats of reaction per mole of N_2O and F_2 reacted, respectively, are:



The molar $N_2O:F_2$ ratio required to give a temperature of 1600 K should be equal to $(45.8 - 1.98)/4.30 = 10.2$. It can be seen that this is in agreement with the ratio listed in Fig. 20 at 1600 K which was calculated by the more exact procedure. Reactions I-42 through I-44 include, therefore, all of the important thermochemical processes in this reactant system.

Reactant Weight Considerations. The use of advanced precombustor reactants will result in a weight penalty over the baseline system F_2-H_2-He . In addition, the use of nitrogen or air as diluent would result in a further weight penalty. This could be important in some applications and will have to be considered in future system efficiency calculations. To investigate this effect briefly, the calculated F-atom mass fractions are compared in Table XII. It can be seen from these results that the use of the ClF_5 -fuel reactant systems decreases the F-atom mass fractions by about a factor of 2 (with helium) over the baseline system, and the use of N_2 in place of helium results in another decrease of about a factor of 2.

Conclusions from Thermochemical Analysis

It is apparent from this analysis that a number of reactant systems have favorable thermochemical properties and thus appear promising for use in the combustor of a DF continuous wave laser provided that efficient combustion can be attained. The oxidizers NF_3 and ClF_5 burn colder than F_2 forming, therefore, slightly higher concentrations of combustion products. In addition, ClF_5 forms considerable ClF or Cl atoms, depending on the temperature.

TABLE XII. MASS FRACTION OF F-ATOMS AT 1500 K AS A
FUNCTION OF MOLE FRACTION F-ATOM

System	Mole Fraction F			
	0.05	0.10	0.15	0.20
	Mass Fraction			
F_2-H_2-He	0.145	0.253	0.335	0.400
$F_2-H_2-N_2$	0.036	0.074	0.113	0.154
$ClF_5(1)-NH_3(1)-He$	0.086	0.139	0.175	0.202
$ClF_5(1)-NH_3(1)-N_2$	0.034	0.069	0.104	0.140
$ClF_5(1)-C_6H_6(1)-He$	0.082	0.133	0.168	0.193
$ClF_5(1)-C_6H_6(1)-N_2$	0.029	0.058	0.086	0.113
$ClF_5(1)-C_6F_6(1)-He$	0.072	0.087	0.149	0.171
$ClF_5(1)-C_6F_6(1)-N_2$	0.027	0.054	0.079	0.103
$ClF_5(1)-CS_2(1)-He$	0.070	0.114	0.144	0.165
$ClF_5(1)-CS_2(1)-N_2$	0.027	0.052	0.076	0.099
$ClF_5(1)-N_2H_4(1)-He$	0.091	0.146	0.185	0.212
$ClF_5(1)-N_2H_4(1)-N_2$	0.034	0.069	0.104	0.140

A large number of fuels may be considered as replacement for hydrogen. Ammonia and hydrazine produce quantities of HF even greater than those formed in the present F_2-H_2-He system. The use of a hydrocarbon fuel would greatly reduce the amount of HF that is formed. If fluorocarbons can be made to burn efficiently with an oxidizer, they will have the advantage that no HF is formed. The use of carbon-containing fuels would lead to the formation of CF_4 as a combustion product. CS_2 and PF_3 are also potential hydrogen-free fuels. The use of these fuels requires that consideration be given to the possible effects of the products SF_6 , SF_4 , and PF_5 .

The nitrogen oxide-oxidizer reactant systems have satisfactory thermochemical properties also. Their utility will depend not only on their combustion properties but on the suitability of N_2-O_2 mixtures as diluents in place of the lighter and inert diluent helium.

TASK I-2. KINETIC ANALYSIS (CAVITY)

An analysis was made of the effects of advanced reactant systems on the kinetics of cavity reactions. Using available data and best estimates for the rate constants of the many elementary reactions that may occur in the cavity, the reaction rates for a number of reactant systems were integrated using the Rocketdyne VIREL Computer Code* described in Appendix B. Estimates were obtained of the expected conditions and zero-power gain as a function of distance from the injector. The premixed approximation was made although, as mentioned earlier, this ignores the important effects of mixing. The calculations do, however, permit the roles of various chemical and energy-transfer processes to be examined. The composition of the mixture at the start of the integration was obtained by determining the composition of the precombustor gas from the results of the thermochemical analysis (for 10 percent F-atom and 1500 K) and then adding cavity fuel (H_2 , HCl, propane, or HBr) at a concentration that is three times that of the F-atom.

Three series of kinetic calculations were conducted during the course of the program. In the first series, the cavity fuels H_2 and HCl were compared using the baseline precombustor system F_2-D_2-He and a DF-free system $F_2-C_6F_6-He$. These cavity fuels were also compared with liquid precombustor systems using ClF_5 as the oxidizer and ND_3 and C_6F_6 as the combustor fuels. In the second series, the cavity fuels H_2 and propane were compared using the baseline precombustor. Finally, HBr and H_2 were compared using both the baseline precombustor and a DF-free reactant system. Because the kinetic calculations were made over a period of about 2 years, somewhat different kinetic parameters were used for each series.

Series I Kinetic Calculations, Comparison of Systems:

$F_2-D_2-He-H_2/HCl$, $F_2-C_6F_6-H_2/HCl$, $ClF_5-ND_3-He-H_2/HCl$ and $ClF_5-C_6F_6-He-H_2/HCl$

Kinetic calculations were conducted for these eight reactant systems choosing precombustor conditions that produce 10 percent F-atoms at 1500K. In each case, the mixture was assumed to be at a temperature of 250 K and a Mach number of about 3.5 at the start of the integration.

*Test calculations have been run to compare the VIREL code with the RESALE program developed at Aerospace Corporation. Equivalent results were obtained.

The calculated static and stagnation temperatures for these conditions are plotted in Fig. 30 through 37* as a function of distance. It will be seen that the faster rates of temperature rise in the HCl systems result from the assignment of a larger rate constant to the $F + HCl$ pumping reaction. The calculated Mach numbers are plotted in Fig. 38 through 45.

The reaction types included in the first kinetics analysis are outlined in Table XIII*. The nomenclature employed is arbitrary. The reactions $HF(V) + H = HF(V-1) + H$ are designated in this table as V-T reactions, while the reactions $HF(V) + H = HF(V-2)$, $(V-3)$, etc. + H are designated as scrambling-deactivation reactions.

The rate constants employed in this kinetics analysis are defined in Table XIV. These rate parameters were obtained from discussion with Dr. Norm Cohen of Aerospace Corporation, and with Dr. Wayne Solomon, then of AFRPL. For those reactions contained in Dr. Cohen's compilation of recommended rate parameters, his values were used. Some of the rate expressions contained in Table XIV are simply estimates. It is assumed in Table XIV that the very exothermic Reaction VI-B goes only to $HF(O)$. In the VIREL program, the excited states of HF are assumed to form in Reaction VI-B in proportion to the concentrations in which they are present. Neither of these assumptions appears to be reasonable, so a product distribution should be estimated for Reaction VI-B in future calculations.

Because N_2 was in the program but CF_4 was not, it was expedient in the Series I calculations to use N_2 to account for CF_4 deactivation, but the rate constant used for N_2 (Table XIV) was lower than the value that has since been measured for CF_4 by about a factor of 1000 (see Table IV). However, the deactivation rate obtained for CF_4 was so small that it would not represent a significant deactivation path even if the larger rate constant had been used.

Presented in Fig. 46 through 53 are the predicted species plots generated directly by the VIREL program. These plots show the general trend of increased pumping rates with HCl as the cavity fuel. The individual pumping reactions are plotted in Fig. 54 through 61. These rates are in units of mole fraction per cm. In all cases where HCl is the cavity fuel, the reaction that pumps the $HF(3)$ level reverses

*For convenience, Fig. 3 through 127 and Tables XIII through XXII are placed at the end of Phase I.

(dotted curve), whereas this does not occur (by the end of the graph) for the reaction $F + H_2 \rightarrow HF(3) + H$.

The calculated zero-power gain curves are presented in Fig. 62 through 69 for the lines P(3), P2(4), P1(4), P1(5), and P1(6). Although not shown, most of the P3 lines did not reach threshold. The position of maximum gain occurs closer to the nozzle as the theoretical pumping rate is increased by employing HCl as the cavity fuel*. However, the maximum power calculated for the P2 lines is essentially independent of whether the fuel is H_2 or HCl (the HCl reached its maximum gain so rapidly that it may have been greater than that calculated at 0.05 cm, the first printout position). On the other hand, the P1 gains increase by factors of about 1.5 to 3 when the H_2 is replaced by HCl.

Detailed Kinetic Analysis. To gain further insight into the effects of various species on the kinetics of the cavity reactions, a computer routine was written to explore, in detail, the rates of specific reactions and reaction types. Using the composition at a given distance from the injector as calculated by the VIREL program, this routine calculates the rate for each reaction and sums the rates of various classes of reactions. When desired, the rates of the individual reactions can be listed. An example of such a listing for reactant system VI, ClF_5 - ND_3 -He-HCl, is shown in Table XV**. In Table XV the rate constants are in units of $(\text{mole/cc})^{-1} \text{ sec}^{-1}$. KF and KR are the rate constants for the forward and reverse directions, respectively, for the reaction as written. Therefore, KF/KR is the equilibrium constant. RF and RR are the calculated reaction rates, in units of moles per cc per sec, in the forward and reverse directions.

Perhaps an even more informative output format for this computer routine are the rate summaries presented in Tables XVI through XX. The downstream positions chosen for these calculations were those at which either the P1 or P2 lines achieve maximum calculated zero-power gain. The following examples will illustrate the type of information that is contained in these tables. In case I, the baseline case, it can be seen from Table XVII that the HF(1) and HF(2) levels are increasing at the same rate and the HF(0) is increasing more slowly. This is in agreement with the P2

*More recent data indicate that the $F + HCl$ reaction is slower by about a factor of 20 than the rates employed in these calculations.

**Results presented in Tables XV and XVIII are for conditions attained with a pre-combustor that formed 5 percent F-atoms. All other kinetic calculations in this report were based on 10 percent F-atoms in the combustor exhaust (before mixing in cavity fuel).

gains being at their maxima, while the P1 gains are still increasing (Fig. 62). The loss of HF(2) is about one-half the rate at which it is being pumped. This loss is mostly from HF-HF V-V processes, particularly: $\text{HF}(2) + \text{HF}(2) \rightarrow \text{HF}(1) + \text{HF}(3)$. The HF(1) level is being pumped more slowly but gains overall from V-T and V-V processes in a cascading effect. The HF(0) is not formed in the pumping reaction but is formed from deactivation of the higher levels, mainly via $\text{H} + \text{HF}(2) = \text{H} + \text{HF}(0)$ and $\text{H} + \text{HF}(3) = \text{H} + \text{HF}(0)$. Therefore, based on the rate constants used, H_2 is not particularly detrimental in the baseline system but H atom reactions and the inherent energy transfer between HF species are the limiting processes. The reaction $\text{HF}(2) + \text{HF}(2) = \text{HF}(1) + \text{HF}(3)$ does not remove appreciable vibrational energy but distributes it to levels where the gains are inherently lower.

When the H_2 in the baseline system is replaced by HCl (Table XVIII), thereby eliminating the detrimental effect of H-atoms, the HF(0) is again formed at an undesirable rate. About two-thirds is formed from the HF-HF V-V deactivation of higher levels. More HF(0) is formed directly in the pumping reactions than in V-T processes. In systems containing both H_2 and ClF_5 , the reaction of H and ClF_5 occurs quite rapidly but an assessment of the effect of this reaction or the overall gain cannot be made until the specific pumping rates to the various levels of HCl and HF have been determined.

No obvious detrimental effects of the use of advanced reactant systems are indicated and the results suggest that the elimination of H_2 (H-atoms) would be beneficial if the new pumping reaction does not form appreciable ground-state HF.

Series II Kinetic Calculations, Comparison of Systems:

$\text{F}_2\text{-D}_2\text{-He-H}_2$ and $\text{F}_2\text{-D}_2\text{-He-C}_3\text{H}_8$

Kinetic calculations were later conducted to compare H_2 and C_3H_8 as cavity fuels. The baseline precombustor was selected for these calculations. The rate constants used in these calculations were updated from the Series I set (Table XIV) based on additional data that became available and discussions with several people interested in this area.

Rate Constants. The revised rate constants used in the Series II kinetic calculations are listed in Table XXI.

V-T Rate Constants. The first term in the rate expression for the V-T reactions $\text{HF(V)} + \text{M} = \text{HF(V-1)} + \text{M}$ with $\text{M} = \text{HF}$ was increased giving the following expression:

$$k_{V-T}(\text{M}=\text{HF}) = 10^{14.23} V T^{-0.8} + 2.5 V T^{3.5} \quad (\text{I-45})$$

which matches the experimental value (Ref. 18 through 21) at a temperature of 300 K. For $\text{M} = \text{DF}$, the pre-exponential factor was increased to fit the rate data then available. The following rate expression was then obtained by separating the HF-DF V-V rate, which was estimated as $10^{11.48} V$:

$$k_{V-T}(\text{M}=\text{DF}) = 10^{6.5} V T^{1.7} - 10^{11.48} V \quad (\text{I-46})$$

The rate of deactivation of HF by propyl radical was assumed to be the same as the rate measured by Green and Hancock for propane (Ref. 19*). Because our book-keeping system defines these processes as V-T, the following rate expression was obtained:

$$k_{V-T}(\text{M}=\text{C}_3\text{H}_8 + \text{C}_3\text{H}_7) = 10^{7.47} V T^2 \quad (\text{I-47})$$

HF-HF V-V Rate Constants. The Series I calculations indicated that the rates of the HF-HF V-V reactions are much faster than any of the HF-M V-T (or V-T,R) reactions. The more recent results of Osgood, Sackett, and Javan (Ref. 22) indicate that some of these HF-HF V-V reactions may be much faster than the rates obtained using the previously estimated rate constants. Based on these results, the rate constant for the reaction $\text{HF(1)} + \text{HF(1)} = \text{HF(0)} + \text{HF(2)}$ was increased slightly to

$$k = 1.9 \times 10^{12} \times T^{1/2} \quad (\text{I-48})$$

and the rate the reaction $\text{HF(1)} + \text{HF(2)} = \text{HF(3)} + \text{HF(0)}$ was increased by a factor of 12 to

$$k = 9.2 \times 10^{12} \times T^{1/2} \quad (\text{I-49})$$

*A lower value was reported by Anlaub et al. at 320 K (Ref. 44).

The rate constant obtained from Eq. I-49 approaches the collision frequency. It is not likely, therefore, that the rates of the HF-HF V-V reactions will increase further for the higher vibrational levels of HF. Therefore, the rate constants for the higher levels were also set equal to Eq. I-49 (in the faster, exothermic, direction).

Pumping Reaction. The rate of the reaction $F + C_3H_8 = HF + C_3H_7$ was taken as that reported in Ref. 23 and was assumed to be constant with temperature because the activation energy is unknown. This global pumping rate, 3.4×10^{13} , is slightly lower than the rate of 5×10^{13} measured later under this program (Phase III).

The distribution of vibrational energy in the HF formed was taken to be the same as in the $F + H_2$ reaction (Table XIV).

Conditions Employed in Series II Kinetic Calculations. The precombustor product composition was taken as that which would be obtained from the baseline F_2 - D_2 -He precombustor system if chemical equilibrium were attained at a temperature of 1500 K with reactant ratios such that 10 mole percent F atoms are present in the precombustor exhaust. To this hypothetical mixture, fuel (H_2 or C_3H_8) was added at a fuel/F molar ratio of 3. This gave an initial premixed composition of He = 59.5 mole percent, F = 7.69, DF = 9.69, and fuel = 23.1. Similar initial compositions were used in the Series I and Series III kinetic calculations.

The mixtures were assumed to be initially at 250 K and the cavity pressure was 0.01 atm (7.6 torr). With H_2 the velocity was 2.488×10^5 cm/sec (initial Mach number of 3.5) while in the propane case it was 1.468×10^5 cm/sec (Mach 3.85). Recent experiments conducted at Rocketdyne and calculations made on the kinetic-mixing code being developed under a company-funded project indicate that higher temperatures may actually exist in the mixing zone. Unfortunately, the rates of many of the important processes have been measured at ambient temperature only and their temperature coefficients have not yet been established.

Results of Series II Kinetic Calculations. The theoretical comparison of propane and hydrogen as cavity fuels gave the following results.

Calculated Zero Power Gain. The zero power gain curves calculated for various HF lines are plotted in Fig. 70 through 72 for H_2 and Fig. 73 through 75 for propane. Because of the increased HF V-V rates used, maximum gain is reached in a much shorter distance for the baseline case than in the Series I Calculations (Fig. 62). The following approximate equations will be useful in the discussion of these quantitative results. At maximum gain, G_{\max} , the rates of the pumping and deactivation reactions are approximately equal:

$$k_p \cdot (F) \cdot (\text{Fuel}) \cong k_d [\text{HF}^*]^2 \quad (\text{I-50})$$

If the very crude approximations are made that the pumping reaction rate is constant up to the point of maximum gain, and the gain is proportional to the concentration of excited HF, the following qualitative relationship is obtained:

$$G_{\max} \propto (k_p/k_d)^{1/2} \quad (\text{I-51})$$

Because the V-V deactivation rates are proportional to the square of the HF^* concentration, they will not become a serious loss until the gain approaches its maximum value. This gives the approximate relationship for the time t_{\max} required to reach maximum gain:

$$t_{\max} \propto (\text{HF}^*)_{\max}/k_p \quad G_{\max}/k_p \quad (\text{I-52})$$

Comparison of Fig. 70 and 71 with Fig. 62 indicates that increasing the HF-HF V-V rates markedly decreases the gains calculated on the $\text{HF}(2) \rightarrow \text{HF}(1)$ lines with H_2 as the cavity fuel. The gains on the $\text{HF}(1) \rightarrow \text{HF}(0)$ lines are also decreased, but only slightly. These trends are in qualitative agreement with Eq. I-51. The V-V deactivation rates for the higher HF levels were increased by about an order of magnitude, and those for $\text{HF}(1)$ by a much smaller amount.

The calculated zero power gains are higher by about a factor of two when propane replaces H_2 as the cavity fuel. This is true for both the P1 and P2 lines. The average ratio of the pumping rate constant for propane to that for H_2 is about 4 over the temperature range of 250 to 300 K. This ratio is the same for the pumping of both $\text{HF}(2)$ and $\text{HF}(1)$. Thus, this quantitative result is also in agreement with the qualitative Eq. I-51.

With both fuels, the P1 lines reach their maximum at a distance from the nozzle that is about twice as great as the distance where the P2 lines reach their maxima. Since the P2 gains are higher than those for HF(1) by a factor of 3.4, Eq.I-52 indicates that the time to reach maximum P1 should be longer by a factor of 1.35. Because the gas velocity with H_2 is 1.7 of that with propane, the predicted distance factor is 2.3 in qualitative agreement with the results in Fig. 70 and 71 and in Fig. 73 and 74.

The gain curves with propane reach their maxima in about one-third the distance compared with H_2 . Substituting into Eq.I-52 that G_{max} with propane is higher by about a factor of 2 and k_p is higher by a factor of 4, the H_2 should take twice as long to reach maximum gain. Thus, the qualitatively predicted distance factor is 2×1.7 or about 3.4, in agreement with the more exact calculations.

Pumping Rates. Figures 76 and 77 show that the pumping rates at a temperature of 250 K are nearly an order of magnitude faster with propane than with H_2 , but this difference becomes smaller as the temperature increases because of the difference in the assigned activation energy. It should be noted that the rates plotted in Fig. 76 and 77 and later figures are in units of mole fraction per centimeter and involve distance units rather than the usual time units. The rate constants for pumping from propane are faster by a factor of 5.2 at 250 K than the rate constants for pumping from H_2 . Since the gas velocity in the H_2 case was chosen to be 1.7 times that of the propane case (to give similar Mach numbers), the pumping rates in distance units are in the ratio of 8.8 to 1 as shown in Fig. 76 and 77.

Gas Temperature, Mach Number, and Relative Areas of Flow. Figures 78 through 83 are plots of the gas temperature, Mach number, and relative area of flow as a function of distance for the two cases. The temperature rises faster with propane but, with either fuel, the temperature increases only about 50 degrees before maximum gain is reached.

Species Plots. The calculated mole fractions of the various species as a function of distance are shown in Fig. 84 and 85. Because the excited states of

HF were assumed to form in the same ratio in both pumping reactions, these figures are quite similar. With propane in place of H_2 , the propyl radical replaces H atom as the species that builds up from the pumping reaction. The further reactions of the propyl radical with F-atoms (e.g., to form HF and propylene) were not included because they would not greatly affect the results in this calculation (because of the large excess of propane) unless a product was obtained that was extremely efficient in deactivating HF. The arrows at the bottom of these two figures indicate (for comparison purposes) the distances at which the calculated zero power gain curves reach their maxima.

Detailed Kinetic Analysis. A very detailed kinetic analysis was presented for the Series I calculations. The purpose of such an analysis is to identify the more important reactions of the many which can occur in these reaction systems. The numerical analysis method that was developed is quite informative, but rather difficult to use. For this reason, additions were made to the VIREL code so that rates of various reactions and classes of reactions could be machine-plotted as a function of distance. These plots are simpler to review and have the added advantage that the analysis is not limited to a single distance from the injector.

The four curves in Fig. 86 demonstrate the types of reactions that are most important with respect to the formation and loss of the species HF(2). The reaction rates are plotted on a linear scale with positive rates indicating the formation of HF(2) and negative rates the loss of HF(2). These curves were obtained with H_2 as the cavity fuel. In agreement with the species plot (Fig. 84), the total rate of formation of HF(2) becomes zero at a distance of about 2.4 mm. The detailed analysis shows however, that HF(2) is still being pumped at a rapid rate, but the rate of V-V deactivation has increased to the point where the deactivation rate equals the pumping rate. It can also be seen from Fig. 86 that the V-T and scrambling reactions* are not fast enough to affect the concentration of HF(2).

Similar plots are presented in Fig. 87 and 88 for the species HF(1) and HF(0). It can be seen that the rate of formation of HF(1) becomes equal to the rate of

Scrambling reactions have been arbitrarily defined as the reactions of H- and D-atoms with HF and HF in which isotope exchange occurs or $\Delta V > 1$. Therefore, the reaction $H + HF(2) = HF(0) + H$ is defined as a scrambling reaction while $H + HF(2) = HF(1) + H$ is a V-T reaction.

of formation of HF(2), a point just before the HF(2) \rightarrow HF(1) transitions reach maximum gain. A similar situation is demonstrated with HF(1) and HF(0).

In Fig. 89 and 90 are plots of V-V rates only for the species HF(2) and HF(1). The "total" V-V curves in these plots are the same as the V-V curves on the previous plots. Also shown, however, are the rates of the individual V-V reactions HF-HF, HF-H₂, and HF-DF. It can be concluded from these plots that the HF-HF V-V reactions are the dominant energy-transfer process in an HF laser.

Figure 91 compares the rates of individual V-T reactions of HF(1). The deactivation by DF is the main V-T reaction. All of the V-T processes are slow compared to the V-V processes.

The rates of formation of HF(0) by various scrambling reactions are shown in Fig. 92. Of these, H + DF(0) \rightarrow HF(0) + D is dominant, but the rate is quite slow until well beyond the point of maximum gain.

The results of a similar detailed kinetic analysis for the propane system are plotted in Fig. 93 through 99. The results obtained were similar to those of the H₂ system. HF-HF V-V reactions dominate the energy-transfer processes. Deactivation by C₃H₈ and C₃H₇ is the fastest of the V-T reactions, but is slow compared with the V-V reactions, especially in the case of the species HF(2).

This kinetic analysis demonstrates that the theoretically limiting "deactivation" processes are HF-HF V-V reactions whether the cavity fuel is H₂ or propane. The faster rate of the pumping reaction from propane accounts for the larger theoretical zero power gain that was obtained in the computations described earlier. Because the HF-HF V-V rates used in these calculations are so large, deactivation by other species, including DF, is found not to be an important process. There is experimental evidence, however, that the presence of DF may be detrimental in real systems.

Series III Kinetic Calculations, Comparison of H₂ and HBr
as Cavity Fuels With Baseline and DF-Free Precombustor

The Series III kinetic calculations compared the predicted zero-power gains for the cavity fuels (H₂ and HBr), using both the baseline F₂-D₂-He precombustor and a DF-free precombustor (F₂-(CN)₂-He) employing again the premixed approximation. The calculated gas temperatures, Mach number, and relative areas of flow are plotted in Fig. 100 through 111.

The rate constant employed in this series of calculations are listed in Table XXII. The rate of F + HBr pumping reaction is that measured in Phase III of this program (see later section). The HF-HF V-V rates are about an order-of-magnitude smaller than the rates measured by Osgood, et al. These rates were selected because calculations made using the Rocketdyne kinetic-mixing code indicated that agreement with experiment could be obtained only if the slower V-V rates were used. The deactivation of HF by HBr was assumed to be entirely a V-T,R process for the purposes of these calculations. The rate at 298 K is 1.4×10^{11} (mole/cc)⁻¹ sec⁻¹, in agreement with the rate measurements of both Bott and Cohen, and Ahl and Cool (Table IV). Ahl and Cool found the rate at 350 K to be lower by a factor of about 2 than at 300 K.

The species plots are presented in Fig. 112 through 115. The species CF₄ and N₂ are not shown in these plots. In Fig. 116 through 127, the calculated zero power gain curves are compared for selected lines. Maximum gain was reached in a shorter distance with HBr because of the faster pumping rate. The presence of DF had little effect on the calculated gain. The gain curves for the baseline fuel, H₂, were similar to those obtained in the Series I calculations because the slower HF-HF V-V rates were again employed.

The calculated gains on the HF(1) → HF(0) lines were smaller by a factor of 2 for HBr compared to H₂ (see Fig. 116 and 118). The maximum gains are higher for H₂ by a factor of 3 on the P2(3), and P2(4) lines and a factor of 2 on P2(5) and P2(6) (Fig. 120 and 122). The gains calculated on the HF(3) → HF(2) lines are much greater for HBr (see Fig. 126 and 127) because the F + HBr pumping reaction is more exothermic. A detailed kinetic analysis was not conducted for the HBr systems.

Conclusions and Recommendations

The following conclusions are indicated by the results of the kinetic analysis:

1. The fast HF-HF V-V processes dominate energy transfer in the cavity.
2. Species such as CF_4 and SF_6 , that are formed from advanced precombustor fuels, do not deactivate HF nearly as rapidly as does DF. Therefore, based on the mechanisms used in the calculations, advanced precombustor reactant systems should have no detrimental effect on laser efficiency except for those combinations that generate increased amounts of DF (e.g., $\text{NF}_3 + \text{ND}_3$). The effects of some potential cavity reactions, such as the reaction of H atom with ClF or O_2 formed in the precombustor, were not evaluated.
3. Cavity fuels that undergo faster pumping reactions with F atoms give higher zero-power gains provided that the energy distribution of the pumping reaction is favorable (in particular, if little ground-state HF is formed).
4. The zero-power gains are calculated to be higher by a factor of 2 when propane replaces H_2 as the cavity fuel. Most of this increase results from the pumping rate (faster by a factor of 4) although some minor benefits are obtained from the elimination of H atom. This prevents the occurrence of reactions such as $\text{H} + \text{DF} = \text{HF}(0) + \text{D}$ and $\text{H} + \text{HF}(2) = \text{H} + \text{HF}(0)$.
5. The cavity fuels HCl and HBr have the potential for improved performance over H_2 but the calculations made on these fuels were not conclusive in this respect. HCl and HBr do not form H atoms, which can undergo the detrimental reactions mentioned above, and the HBr pumping reaction is faster and 50 percent more exothermic than the H_2 pumping reaction. Because the distributions of the excited states of HF formed are different from the distribution from H_2 , the comparison of zero-power gains does not yield directly a figure of merit. Extracted power calculations would give a more definitive rating.

The energy distribution in the $F + HCl$ pumping reaction is somewhat less favorable than in the $F + H_2$ reaction because more ground-state HF and less HF(3) is formed. The conclusions that can be drawn from the HCl calculations, which were conducted early in the program, are limited also by the use of too large a rate constant for the $F + HCl$ pumping reaction.

The $F + HBr$ global pumping rate is faster by a factor of 3 than the $F + H_2$ rate (see Phase III of this report). The $F + HBr$ pumping reaction is exothermic by 40.5 kcal/mole compared with 31.9 for the $F + H_2$ reaction. This leads to a more favorable energy distribution in the higher levels: 20 percent in HF(4), 27 percent in HF(3), 30 percent in HF(2), and 18 percent in HF(1). However, about 6 percent of the HF molecules are formed in the ground vibrational state.

The limited effect of DF on the zero-power gains that were calculated resulted, in part, from the use of premixed approximation and partly from the assignment of most of the deactivation by DF to V-V processes (i.e., the excited DF formed may be returning part of its vibrational energy to HF in a subsequent V-V exchange). Recent calculations at Rocketdyne using a kinetic-mixing code indicate that DF is more detrimental in the cavity of an HF laser by several fold than is indicated by calculations using the premixed approximation. This is in agreement with experimental observations on DF. Also, although the rate of deactivation of HF(1) by DF is known fairly accurately, the relative magnitudes of the V-V and V-T, R processes are not certain (Ref. 15 and 16).

This analysis represents a step in the attainment of an understanding of the cavity mechanisms and demonstrates both the analytical procedures and the detailed rate data that are required. It is recommended that future calculations of this type be made with kinetic mixing codes and that power calculations be used to compare cavity fuels whose pumping reactions have different energy distributions.

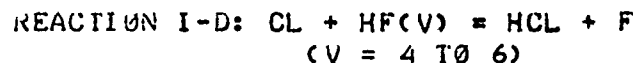
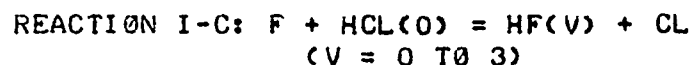
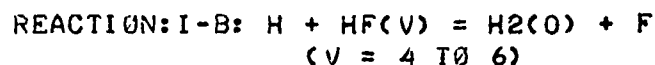
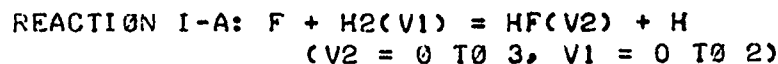
The thermochemical calculations demonstrated that the use of advanced precombustor reactants, with better physical properties than D_2 and F_2 , will not lead to reduced laser performance if efficient combustion can be achieved, and may lead to improved

performance be reducing the amount of DF introduced into the cavity. The kinetic calculations indicate that the use of cavity fuels with pumping rates that are faster than the pump rate with H_2 should give improved performance under pre-mixed conditions. However, in an actual laser, mixing of the higher molecular weight cavity fuels is a problem, as shown in the following experimental section.*

*Text resumes on page 254.

TABLE XIII. REACTION TYPES INCLUDED IN SERIES I KINETIC CALCULATIONS

TYPE I, COLD PUMPING



TYPE II, HOT PUMPING



TYPE III, V-V ENERGY TRANSFER

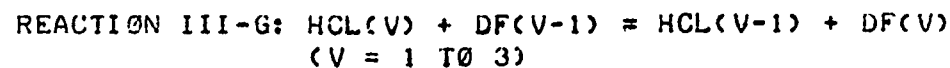
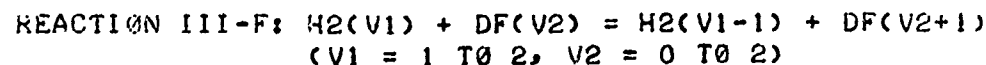
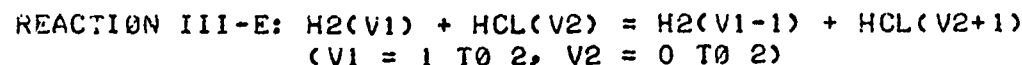
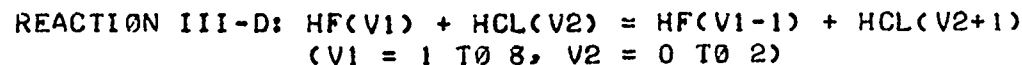
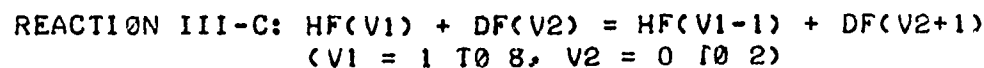
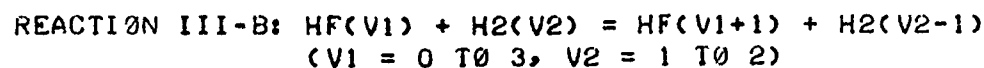
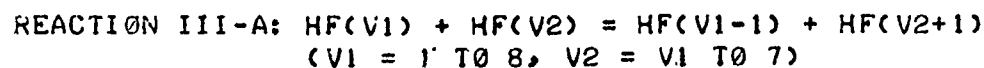
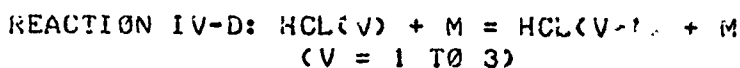
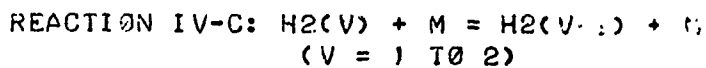
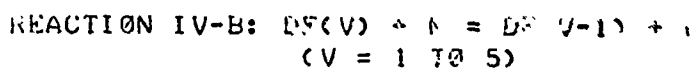
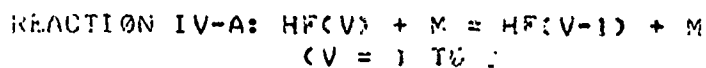
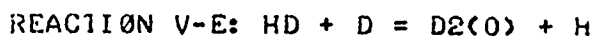
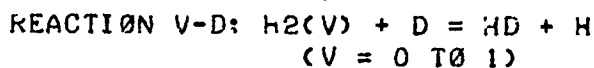
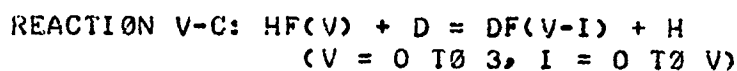
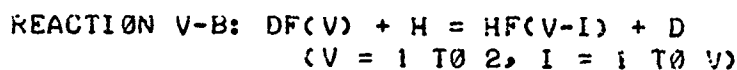
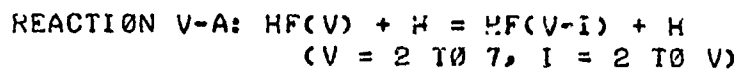


TABLE XIII. (Concluded)

TYPE IV, V-T DEACTIVATION



TYPE V, SCRAMBLING-DEACTIVATION



TYPE VI, MISC.

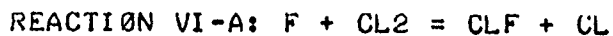


TABLE XIV. RATE CONSTANTS EMPLOYED IN SERIES I
KINETIC CALCULATIONS*

F + H₂ Pumping (Reaction I-A) and Reverse (I-B):

$F + H_2 = HF(1) + H$	$k = 10^{13.41} \exp(-1600/RT)$
$F + H_2 = HF(2) + H$	$k = 10^{13.94} \exp(-1600/RT)$
$F + H_2 = HF(3) + H$	$k = 10^{13.64} \exp(-1600/RT)$
$H + HF(4) = H_2(0) + F$	$k = 10^{13.23} \exp(-540/RT)$
$H + HF(5) = H_2(0) + F$	$k = 10^{13.32} \exp(-570/RT)$
$H + HF(6) = H_2(0) + F$	$k = 10^{13.81} \exp(-510/RT)$

F + HCl Pumping (Reaction I-C) and Reverse (I-D):

$F + HCl(0) = HF(0) + Cl$	$k = 10^{13.28} \exp(-900/RT)$
$F + HCl(0) = HF(1) + Cl$	$k = 10^{13.93} \exp(-900/RT)$
$F + HCl(0) = HF(2) + Cl$	$k = 10^{14.11} \exp(-900/RT)$
$F + HCl(0) = HF(3) + Cl$	$k = 10^{13.28} \exp(-900/RT)$
$Cl + HF(4) = HCl + F$	Not included
$Cl + HF(5) = HCl + F$	
$Cl + HF(6) = HCl + F$	

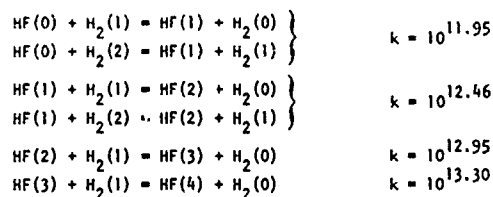
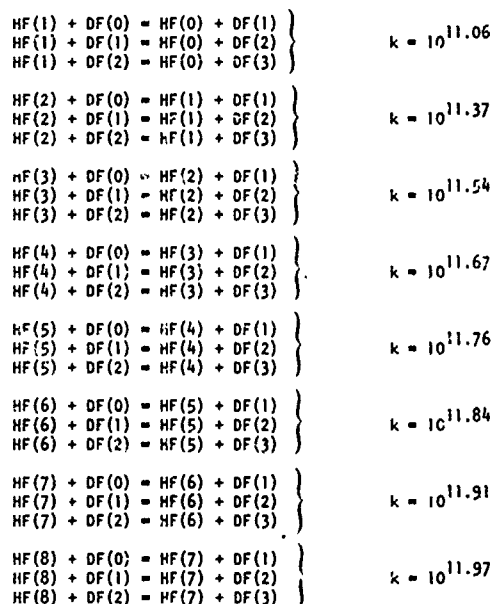
H + F₂ Pumping (Reaction II):

$H + F_2 = HF(0) + F$	$k = 10^{12.04} \exp(-2400/RT)$
$H + F_2 = HF(1) + F$	$k = 10^{12.40} \exp(-2400/RT)$
$H + F_2 = HF(2) + F$	$k = 10^{12.54} \exp(-2400/RT)$
$H + F_2 = HF(3) + F$	$k = 10^{12.56} \exp(-2400/RT)$
$H + F_2 = HF(4) + F$	$k = 10^{13.20} \exp(-2400/RT)$
$H + F_2 = HF(5) + F$	$k = 10^{13.56} \exp(-2400/RT)$
$H + F_2 = HF(6) + F$	$k = 10^{13.68} \exp(-2400/RT)$
$H + F_2 = HF(7) + F$	$k = 10^{12.74} \exp(-2400/RT)$
$H + F_2 = HF(8) + F$	$k = 10^{12.40} \exp(-2400/RT)$

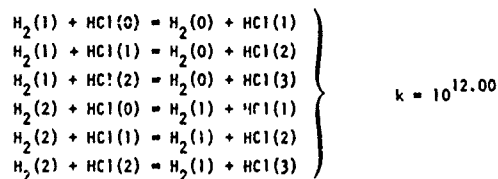
HF - HF V-V Processes (Reaction III-A):

$\left. \begin{aligned} HF(1) + HF(1) &= HF(0) + HF(2) \\ HF(2) + HF(2) &= HF(1) + HF(3) \\ HF(3) + HF(3) &= HF(2) + HF(4) \\ HF(4) + HF(4) &= HF(3) + HF(5) \\ HF(5) + HF(5) &= HF(4) + HF(6) \\ HF(6) + HF(6) &= HF(5) + HF(7) \\ HF(7) + HF(7) &= HF(6) + HF(8) \end{aligned} \right\}$	$k = 10^{12.18} T^{0.5}$
$\left. \begin{aligned} HF(1) + HF(2) &= HF(0) + HF(3) \\ HF(2) + HF(3) &= HF(1) + HF(4) \\ HF(3) + HF(4) &= HF(2) + HF(5) \\ HF(4) + HF(5) &= HF(3) + HF(6) \\ HF(5) + HF(6) &= HF(4) + HF(7) \\ HF(6) + HF(7) &= HF(5) + HF(8) \end{aligned} \right\}$	$k = 10^{11.88} T^{0.5}$
$\left. \begin{aligned} HF(1) + HF(3) &= HF(0) + HF(4) \\ HF(2) + HF(4) &= HF(1) + HF(5) \\ HF(3) + HF(5) &= HF(2) + HF(6) \\ HF(4) + HF(6) &= HF(3) + HF(7) \\ HF(5) + HF(7) &= HF(4) + HF(8) \end{aligned} \right\}$	$k = 10^{11.57} T^{0.5}$
$\left. \begin{aligned} HF(1) + HF(4) &= HF(0) + HF(5) \\ HF(2) + HF(5) &= HF(1) + HF(6) \\ HF(3) + HF(6) &= HF(2) + HF(7) \\ HF(4) + HF(7) &= HF(3) + HF(8) \end{aligned} \right\}$	$k = 10^{11.27} T^{0.5}$

TABLE XIV. (Continued)

HF - H₂ V-V Processes (Reaction III-B):HF - DF V-V Processes (Reaction III-C):HF - HCl V-V Processes (Reaction III-D):

These rate constants were assigned the same values as for the HF - DF V-V processes above.

H₂ - HCl V-V Processes (Reaction III-E):H₂ - DF V-V Processes (Reaction III-F):

These rate constants were assigned the same values as for the H₂ - HCl V-V processes above.

TABLE XIV. (Continued)

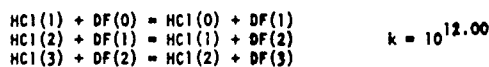
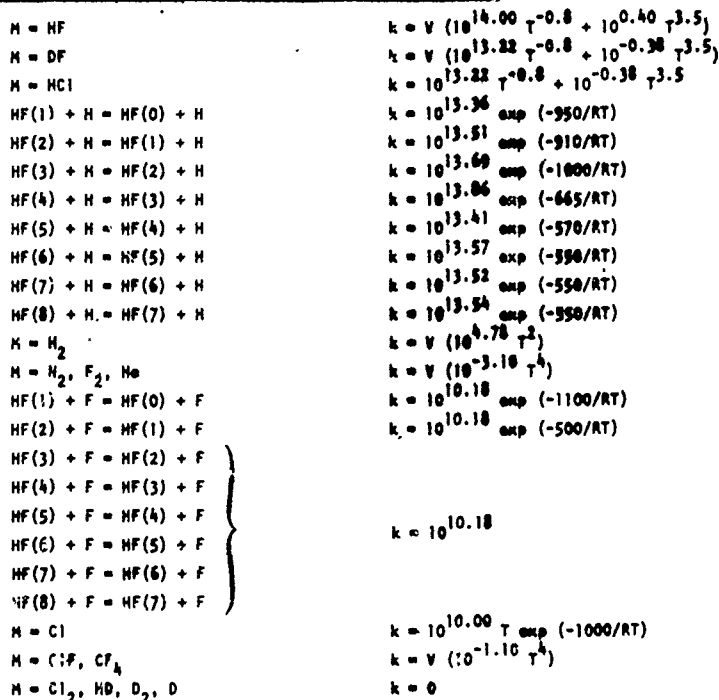
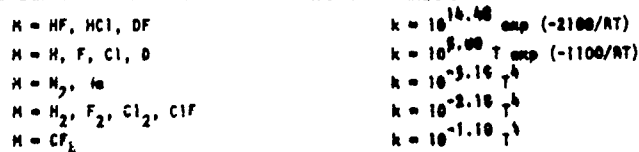
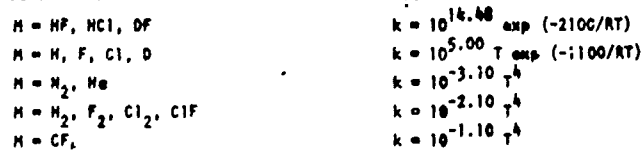
HCl - DF V-V Processes (Reaction 111-6):HF(V) + M = HF (V-1) + M V - T, R Processes (Reaction 1V-A):DF(V) + M = DF (V-1) + M V - T, R Processes (Reaction 1V-B):H₂ (V) + M = H₂ (V-1) + M V - T, R Processes (Reaction 1V-C):HCl(V) + M = HCl (V-1) + M V - T, R Processes (Reaction 1V-D):

TABLE XIV. (Concluded)

HF(V) + H = HF(V') + H Scrambling-Deactivation (Reaction V-A)

HF(2) + H = HF(0) + H	$k = 10^{13.68} \exp(-910/RT)$
HF(3) + H = HF(1) + H	$k = 10^{13.68} \exp(-1000/RT)$
HF(3) + H = HF(0) + H	$k = 10^{13.82} \exp(-1000/RT)$
HF(4) + H = HF(2) + H	$k = 10^{13.62} \exp(-665/RT)$
HF(4) + H = HF(1) + H	$k = 10^{13.42} \exp(-665/RT)$
HF(4) + H = HF(0) + H	$k = 10^{13.59} \exp(-665/RT)$
HF(5) + H = HF(3) + H	$k = 10^{13.29} \exp(-570/RT)$
HF(5) + H = HF(2) + H	$k = 10^{13.70} \exp(-570/RT)$
HF(5) + H = HF(1) + H	$k = 10^{13.31} \exp(-570/RT)$
HF(5) + H = HF(0) + H	$k = 10^{13.51} \exp(-570/RT)$
HF(6) + H = HF(4) + H	$k = 10^{13.45} \exp(-550/RT)$
HF(6) + H = HF(3) + H	$k = 10^{13.29} \exp(-550/RT)$
HF(6) + H = HF(2) + H	$k = 10^{13.27} \exp(-550/RT)$
HF(6) + H = HF(1) + H	$k = 10^{13.21} \exp(-550/RT)$
HF(6) + H = HF(0) + H	
HF(7) + H = HF(5) + H	
HF(7) + H = HF(4) + H	
HF(7) + H = HF(3) + H	$k = 10^{13.52} \exp(-550/RT)$
HF(7) + H = HF(2) + H	
HF(7) + H = HF(1) + H	
HF(7) + H = HF(0) + H	

DF(V) + H = HF(V') + D Scrambling-Deactivation (Reaction V-B and -C):

DF(1) + H = HF(0) + D	$k = 10^{13.00} \exp(-500/RT)$
DF(2) + H = HF(1) + D	
DF(2) + H = HF(0) + D	
HF(0) + D = DF(0) + H	
HF(1) + D = DF(1) + H	
HF(1) + D = DF(0) + H	
HF(2) + D = DF(2) + H	
HF(2) + D = DF(1) + H	
HF(2) + D = DF(0) + H	
HF(3) + D = DF(3) + H	
HF(3) + D = DF(2) + H	
HF(3) + D = DF(1) + H	
HF(3) + D = DF(0) + H	
HF(4) + D = DF(4) + H	
HF(4) + D = DF(3) + H	
HF(4) + D = DF(2) + H	
HF(4) + D = DF(1) + H	
HF(4) + D = DF(0) + H	
HF(5) + D = DF(5) + H	
HF(5) + D = DF(4) + H	
HF(5) + D = DF(3) + H	
HF(5) + D = DF(2) + H	
HF(5) + D = DF(1) + H	
HF(5) + D = DF(0) + H	

H₂(V) + D = HD + H Scrambling-Deactivation (Reaction V-D):

H ₂ (1) + D = HD + H	$k = 10^{12.70}$
H ₂ (0) + D = HD + H	

HD + D = D₂ + H Scrambling (Reaction V-E):

HD + D = D ₂ (0) + H	$k = 10^{12.70}$
---------------------------------	------------------

Miscellaneous Reactions (VI-A through VI-D):

F + Cl ₂ = ClF + Cl	$k = 10^{14.70} \exp(-1400/RT)$
H + ClF = HF + Cl	$k = 10^{14.48} \exp(-2100/RT)$
H + ClF = HCl(0) + F	$k = 10^{14.48} \exp(-2100/RT)$
D + ClF = DF(0) + Cl	$k = 10^{14.48} \exp(-2100/RT)$

Reactions are written in exothermic direction. Rate constants are in units of (mole/cc)⁻¹ sec⁻¹.

TABLE XV. DETAILED KINETIC ANALYSIS FOR SYSTEM $\text{ClF}_5\text{-ND}_3\text{-HE-HCl}$ at 0.10 CM
(0.60 microsecond, the position of maximum gain on P2 lines;
precombustor: 1500 K and 5 percent F-atom)*

REACTION I-A: $\text{F} + \text{H}_2(\text{V}) = \text{HF}(\text{V}) + \text{H}$ (H_2 COLD PUMPING)

		KF	KR	RF	RP	RF-RP
1	$\text{H}_2(0) \text{ HF}(1)$	$2.22\text{E}+12$	$6.23\text{E}-02$	$4.44\text{E}-38$	$2.67\text{E}-47$	$4.44\text{E}-38$
2	$\text{H}_2(1) \text{ HF}(1)$	$2.22\text{E}+12$	$7.25\text{E}-10$	0	$3.10\text{E}-55$	$-3.10\text{E}-55$
3	$\text{H}_2(2) \text{ HF}(1)$	$2.22\text{E}+12$	$2.34\text{E}-17$	0	$1.00\text{E}-62$	$-1.00\text{E}-62$
4	$\text{H}_2(0) \text{ HF}(2)$	$7.53\text{E}+12$	$3.59\text{E}+06$	$1.50\text{E}-37$	$2.06\text{E}-39$	$1.48\text{E}-37$
5	$\text{H}_2(1) \text{ HF}(2)$	$7.53\text{E}+12$	$4.18\text{E}-02$	0	$2.40\text{E}-47$	$-2.40\text{E}-47$
6	$\text{H}_2(2) \text{ HF}(2)$	$7.53\text{E}+12$	$1.35\text{E}-09$	0	$7.77\text{E}-55$	$-7.77\text{E}-55$
7	$\text{H}_2(0) \text{ HF}(3)$	$3.76\text{E}+12$	$1.46\text{E}+13$	$7.52\text{E}-38$	$1.73\text{E}-33$	$-1.73\text{E}-33$
8	$\text{H}_2(1) \text{ HF}(3)$	$3.76\text{E}+12$	$1.70\text{E}+05$	0	$2.01\text{E}-41$	$-2.01\text{E}-41$
9	$\text{H}_2(2) \text{ HF}(3)$	$3.76\text{E}+12$	$5.51\text{E}-03$	0	$6.50\text{E}-49$	$-6.50\text{E}-49$

REACTION I-B: $\text{H} + \text{HF}(\text{V}) = \text{H}_2(0) + \text{F}$ (REVERSE H_2 COLD PUMPING, $\text{V}=4-6$)

		KF	KR	RF	RR	RF-RR
10	$\text{HF}(4)$	$7.41\text{E}+12$	$4.78\text{E}+05$	$3.03\text{E}-35$	$9.55\text{E}-45$	$3.03\text{E}-35$

REACTION I-C: $\text{F} + \text{HCl}(0) = \text{HF}(\text{V}) + \text{Cl}$ (HCl PUMPING)

		KF	KR	RF	RP	RF-RP
11	$\text{HF}(0)$	$4.77\text{E}+12$	$8.36\text{E}-10$	$6.65\text{E}-04$	$1.30\text{E}-26$	$6.65\text{E}-04$
12	$\text{HF}(1)$	$2.13\text{E}+13$	$1.36\text{E}-01$	$2.98\text{E}-03$	$7.19\text{E}-18$	$2.98\text{E}-03$
13	$\text{HF}(2)$	$3.26\text{E}+13$	$3.53\text{E}+06$	$4.55\text{E}-03$	$2.51\text{E}-10$	$4.55\text{E}-03$
14	$\text{HF}(3)$	$4.77\text{E}+12$	$4.21\text{E}+12$	$6.65\text{E}-04$	$6.15\text{E}-05$	$6.04\text{E}-04$

*Gas static temperature, 327.5 K; species concentrations are listed in Table XVI.

TABLE XV. (Continued)

REACTION III-A: $\text{HF}(\text{V1}) + \text{HF}(\text{V2}) = \text{HF}(\text{V1-1}) + \text{HF}(\text{V2+1})$ (HF-HF V-V)

		KF	KR	RF	RR	RF-RR
20	1+1 = 0+2	2.71E+13	1.27E+13	5.01E-04	9.24E-05	4.08E-04
21	1+2 = 0+3	1.36E+13	3.05E+12	3.36E-04	4.54E-06	3.31E-04
22	1+3 = 0+4	6.79E+12	7.46E+11	3.45E-05	3.84E-03	3.45E-05
23	1+4 = 0+5	3.39E+12	1.85E+11	5.27E-07	0	5.97E-07
24	2+2 = 1+3	2.71E+13	1.30E+13	9.02E-04	6.61E-05	8.36E-04
25	2+3 = 1+4	1.36E+13	3.18E+12	9.26E-05	5.58E-07	9.20E-05
26	2+4 = 1+5	6.79E+12	7.87E+11	1.60E-04	0	1.60E-04
27	3+3 = 2+4	2.71E+13	1.33E+13	3.80E-05	3.13E-06	3.49E-05
28	3+4 = 2+5	1.36E+13	3.29E+12	6.58E-07	0	6.58E-07
29	4+4 = 3+5	2.71E+13	1.34E+13	4.55E-08	0	4.55E-08

REACTION III-B: $\text{HF}(\text{V1}) + \text{H}_2(\text{V2}) = \text{HF}(\text{V1+1}) + \text{H}_2(\text{V2-1})$ (HF-H₂ V-V)

		KF	KR	RF	RR	RF-RR
30	0+1 = 1+0	9.00E+11	3.79E+11	0	8.49E-39	-8.49E-39
31	0+2 = 1+1	9.00E+11	1.06E+12	0	0	0
32	1+1 = 2+0	2.90E+12	5.74E+11	0	1.72E-38	-1.72E-38
33	1+2 = 2+1	2.90E+12	1.60E+12	0	0	0
34	2+1 = 3+0	9.00E+12	8.53E+11	0	5.26E-39	-5.26E-39
35	2+2 = 3+1	0	0	0	0	0
36	3+1 = 4+0	2.00E+13	9.27E+11	0	1.98E-40	-1.98E-40
37	3+2 = 4+1	0	0	0	0	0

REACTION III-C: $\text{HF}(\text{V1}) + \text{DF}(\text{V2}) = \text{HF}(\text{V1-1}) + \text{DF}(\text{V2+1})$ (HF-DF V-V)

		KF	KR	RF	RR	RF-RR
38	1+0 = 0+1	1.16E+11	1.12E+09	2.80E-05	7.37E-11	2.80E-05
39	1+1 = 0+2	1.16E+11	7.54E+08	2.60E-08	0	2.60E-08
40	1+2 = 0+3	1.16E+11	5.06E+08	0	0	0
41	2+0 = 1+1	2.32E+11	4.79E+09	7.52E-05	1.07E-09	7.52E-05
42	2+1 = 1+2	2.32E+11	3.21E+09	6.97E-02	0	6.97E-02
43	2+2 = 1+3	2.32E+11	2.15E+09	0	0	0
44	3+0 = 2+1	3.48E+11	1.50E+10	2.32E-05	4.51E-09	2.32E-05
45	3+1 = 2+2	3.48E+11	1.01E+10	2.15E-08	0	2.15E-08
46	3+2 = 2+3	3.48E+11	6.75E+09	0	0	0
47	4+0 = 3+1	4.64E+11	4.09E+10	1.07E-06	2.52E-09	1.07E-06
48	4+1 = 3+2	4.64E+11	2.75E+10	9.90E-10	0	9.90E-10
49	4+2 = 3+3	4.64E+11	1.84E+10	0	0	0
50	5+0 = 4+1	5.80E+11	1.03E+11	0	2.20E-10	-2.20E-10
51	5+1 = 4+2	5.80E+11	6.93E+10	0	0	0
52	5+2 = 4+3	5.80E+11	4.64E+10	0	0	0

TABLE XV. (Continued)

REACTION III-D: $\text{HF}(V1) + \text{HCL}(V2) = \text{HF}(V1-1) + \text{HCL}(V2+1)$ (HF-HCL V-V)

		KF	KR	RF	RR	RF-RR
53	1+0 = 0+1	1.16E+11	1.02E+09	1.81E-05	4.31E-11	1.81E-05
54	1+1 = 0+2	1.16E+11	6.48E+08	1.67E-08	0	1.67E-08
55	1+2 = 0+3	1.16E+11	4.12E+08	0	0	0
56	2+0 = 1+1	2.32E+11	4.35E+09	4.87E-05	6.26E-10	4.87E-05
57	2+1 = 1+2	2.32E+11	2.76E+09	4.48E-08	0	4.48E-08
58	2+2 = 1+3	2.32E+11	1.75E+09	0	0	0
59	3+0 = 2+1	3.48E+11	1.36E+10	1.50E-05	2.63E-09	1.50E-05
60	3+1 = 2+2	3.48E+11	8.64E+09	1.38E-08	0	1.38E-08
61	3+2 = 2+3	3.48E+11	5.49E+09	0	0	0
62	4+0 = 3+1	4.64E+11	3.72E+10	6.92E-07	1.47E-09	6.90E-07
63	4+1 = 3+2	4.64E+11	2.36E+10	6.36E-10	0	6.36E-10
64	4+2 = 3+3	4.64E+11	1.50E+10	0	0	0
65	5+0 = 4+1	5.80E+11	9.39E+10	0	1.29E-10	-1.29E-10
66	5+1 = 4+2	5.80E+11	5.95E+10	0	0	0
67	5+2 = 4+3	5.80E+11	3.78E+10	0	0	0

REACTION IV-A: $\text{HF}(V) + \text{M} = \text{HF}(V-1) + \text{M}$ (HF DEACTIVATION, V-T)

		KF	KR	RF	RR	RF-RR
68	V=1 M=HF(0)	9.74E+11	2.69E+04	5.26E-06	4.25E-14	5.26E-06
69	V=1 M=HF(1)	9.74E+11	2.69E+04	1.80E-05	1.45E-13	1.80E-05
70	V=1 M=HF(2)	9.74E+11	2.69E+04	2.41E-05	1.95E-13	2.41E-05
71	V=1 M=HF(3)	9.74E+11	2.69E+04	4.95E-06	4.00E-14	4.95E-06
72	V=1 M=DF(0)	1.62E+11	4.48E+03	3.92E-05	3.17E-13	3.92E-05
73	V=1 M=DF(1)	1.62E+11	4.48E+03	3.63E-08	2.93E-16	3.63E-08
74	V=1 M=DF(2)	1.62E+11	4.48E+03	0	0	0
75	V=1 M=DF(3)	1.62E+11	4.48E+03	0	0	0
76	V=1 M=HCL(0)	1.62E+11	4.48E+03	2.54E-05	2.05E-13	2.54E-05
77	V=1 M=HCL(1)	1.62E+11	4.48E+03	2.33E-08	1.89E-16	2.33E-08
78	V=1 M=HCL(2)	1.62E+11	4.48E+03	0	0	0
79	V=1 M=HCL(3)	1.62E+11	4.48E+03	0	0	0
80	V=1 M=H	5.32E+12	1.47E+05	2.28E-33	1.84E-41	2.28E-33
81	V=1 M=H2(0)	6.44E+09	1.78E+02	1.44E-40	1.16E-48	1.44E-40
82	V=1 M=H2(1)	6.44E+09	1.78E+02	0	0	0
83	V=1 M=H2(2)	6.44E+09	1.78E+02	0	0	0

TABLE XV. (Continued)

84	V=1	M=N2	9.20E+06	2.54E-01	3.84E-10	3.10E-18	3.84E-10
85	V=1	M=F2	9.20E+06	2.54E-01	1.50E-16	1.21E-24	1.50E-16
86	V=1	M=HF	9.20E+06	2.54E-01	8.82E-09	7.13E-17	8.82E-09
87	V=1	M=F	9.06E+11	2.50E+04	1.49E-05	1.21E-13	1.49E-05
88	V=1	M=CL	7.04E+11	1.94E+04	3.74E-05	3.02E-12	3.74E-05
89	V=1	M=CLF	9.20E+08	2.54E+01	7.09E-08	5.73E-14	7.09E-08
90	V=1	M=CF4	9.20E+08	2.54E+01	0	0	0
91	V=1	M=CL2	0	0	0	0	0
92	V=2	M=HF(0)	1.95E+12	1.14E+05	1.41E-05	6.18E-13	1.41E-05
93	V=2	M=HF(1)	1.95E+12	1.14E+05	4.82E-05	2.11E-12	4.82E-05
94	V=2	M=HF(2)	1.95E+12	1.14E+05	6.47E-05	2.83E-12	6.47E-05
95	V=2	M=HF(3)	1.95E+12	1.14E+05	1.33E-05	5.81E-13	1.33E-05
96	V=2	M=DF(0)	3.25E+11	1.91E+04	1.05E-04	4.61E-12	1.05E-04
97	V=2	M=DF(1)	3.25E+11	1.91E+04	9.75E-08	4.27E-15	9.75E-08
98	V=2	M=DF(2)	3.25E+11	1.91E+04	0	0	0
99	V=2	M=DF(3)	3.25E+11	1.91E+04	0	0	0
100	V=2	M=HCL(0)	1.62E+11	9.53E+03	3.41E-05	1.49E-12	3.41E-05
101	V=2	M=HCL(1)	1.62E+11	9.53E+03	3.13E-08	1.37E-15	3.13E-08
102	V=2	M=HCL(2)	1.62E+11	9.53E+03	0	0	0
103	V=2	M=HCL(3)	1.62E+11	9.53E+03	0	0	0
104	V=2	M=H	8.08E+12	4.74E+05	4.64E-33	2.03E-40	4.64E-33
105	V=2	M=H2(0)	1.29E+10	7.56E+02	3.87E-40	1.69E-47	3.87E-40
106	V=2	M=H2(1)	1.29E+10	7.56E+02	0	0	0
107	V=2	M=H2(2)	1.29E+10	7.56E+02	0	0	0
108	V=2	M=N2	1.84E+07	1.08	1.03E-09	4.51E-17	1.03E-09
109	V=2	M=F2	1.84E+07	1.08	4.03E-16	1.76E-23	4.03E-16
110	V=2	M=HF	1.84E+07	1.08	2.37E-08	1.04E-15	2.37E-08
111	V=2	M=F	2.28E+12	1.34E+05	5.03E-05	2.20E-12	5.03E-05
112	V=2	M=CL	7.04E+11	4.14E+04	5.02E-05	2.20E-12	5.02E-05
113	V=2	M=CLF	1.84E+09	1.08E+02	1.90E-07	8.33E-15	1.90E-07
114	V=2	M=CF4	1.84E+09	1.08E+02	0	0	0
115	V=2	M=CL2	0	0	0	0	0

TABLE XV. (Continued)

116	V=3	M=HF(0)	2.92E+12	3.58E+05	4.35E-06	2.60E-12	4.35E-06
117	V=3	M=HF(1)	2.92E+12	3.58E+05	1.48E-05	8.87E-12	1.48E-05
118	V=3	M=HF(2)	2.92E+12	3.58E+05	1.99E-05	1.19E-11	1.99E-05
119	V=3	M=HF(3)	2.92E+12	3.58E+05	4.09E-06	2.44E-12	4.09E-06
120	V=3	M=DF(0)	4.87E+11	5.97E+04	3.24E-05	1.94E-11	3.24E-05
121	V=3	M=DF(1)	4.87E+11	5.97E+04	3.00E-08	1.79E-14	3.00E-08
122	V=3	M=DF(2)	4.87E+11	5.97E+04	0	0	0
123	V=3	M=DF(3)	4.87E+11	5.97E+04	0	0	0
124	V=3	M=HCL(0)	1.62E+11	1.99E+04	7.00E-06	4.18E-12	7.00E-06
125	V=3	M=HCL(1)	1.62E+11	1.99E+04	6.43E-09	3.84E-15	6.43E-09
126	V=3	M=HCL(2)	1.62E+11	1.99E+04	0	0	0
127	V=3	M=HCL(3)	1.62E+11	1.99E+04	0	0	0
128	V=3	M=H	1.06E+13	1.30E+06	1.25E-33	7.48E-40	1.25E-33
129	V=3	M=H2(0)	1.93E+10	2.37E+03	1.19E-40	7.11E-47	1.19E-40
130	V=3	M=H2(1)	1.93E+10	2.37E+03	0	0	0
131	V=3	M=H2(2)	1.93E+10	2.37E+03	0	0	0
132	V=3	M=N2	2.76E+07	3.39	3.17E-10	1.90E-16	3.17E-10
133	V=3	M=F2	2.76E+07	3.39	1.24E-16	7.41E-23	1.24E-16
134	V=3	M=HE	2.76E+07	3.39	7.30E-09	4.36E-15	7.30E-09
135	V=3	M=F	4.91E+12	6.02E+05	2.23E-05	1.33E-11	2.23E-05
136	V=3	M=CL	7.04E+11	8.64E+04	1.03E-05	6.15E-12	1.03E-05
137	V=3	M=CLF	2.76E+09	3.39E+02	5.86E-08	3.50E-14	5.86E-08
138	V=3	M=CF4	2.76E+09	3.39E+02	0	0	0
139	V=3	M=CL2	0	0	0	0	0

TABLE XV. (Continued)

REACTION V-A: $\text{HF}(V) + \text{H} = \text{HF}(V-1) + \text{H}$ (SCRAMBLING-DEACTIVATION)

			KF	KR	RF	RR	RF-RR
140	I=2	V=2	1.18E+13	1.91E-02	6.79E-33	2.40E-48	6.79E-33
141	I=2	V=3	1.03E+13	7.42E-02	1.22E-33	3.18E-47	1.22E-33
143	I=3	V=3	1.42E+13	2.82E-09	1.62E-33	3.54E-55	1.62E-33

REACTION V-B: $\text{DF}(V) + \text{H} = \text{HF}(V-1) + \text{D}$ (SCRAMBLING-DEACTIVATION)

			KF	KR	RF	RR	RF-RR
146	I=1	V=1	4.64E+12	7.33E+07	2.41E-35	4.57E-41	2.41E-35
147	I=1	V=2	4.64E+12	1.13E+10	0	2.40E-38	-2.40E-38
148	I=2	V=2	4.64E+12	3.11E+02	0	1.94E-46	-1.94E-46

REACTION V-C: $\text{HF}(V) + \text{D} = \text{DF}(V-1) + \text{H}$ (SCRAMBLING-DEACTIVATION)

			KF	KR	RF	RR	RF-RR
149	I=0	V=0	4.64E+12	9.34E+11	2.89E-36	4.68E-33	-4.68E-33
150	I=0	V=1	4.64E+12	8.09E+09	9.86E-36	4.20E-38	2.82E-36
151	I=1	V=1	4.64E+12	2.30E+04	9.86E-36	1.29E-40	9.86E-36
152	I=0	V=2	4.64E+12	1.12E+08	1.32E-35	0	1.32E-35
153	I=1	V=2	4.64E+12	4.75E+02	1.32E-35	2.47E-45	1.32E-35
154	I=2	V=2	4.64E+12	1.35E-03	1.32E-35	7.55E-48	1.32E-35
155	I=0	V=3	4.64E+12	2.17E+06	2.72E-36	0	2.72E-36
156	I=1	V=3	4.64E+12	1.37E+01	2.72E-36	0	2.72E-36
157	I=2	V=3	4.64E+12	5.83E-05	2.72E-36	3.03E-52	2.72E-36
158	I=3	V=3	4.64E+12	1.66E-10	2.72E-36	9.30E-55	2.72E-36
159	I=1	V=4	4.64E+12	5.45E-01	9.40E-38	0	9.40E-38
160	I=2	V=4	4.64E+12	3.45E-06	9.40E-38	0	9.40E-38
161	I=3	V=4	4.64E+12	1.46E-11	9.40E-38	7.60E-59	9.40E-38
162	I=4	V=4	4.64E+12	4.16E-17	9.40E-38	2.33E-61	9.40E-38

TABLE XV. (Concluded)

REACTION VI-A: $F + Cl_2 = ClF + Cl$

	KF	KR	FF	RR	RF-RR
163	6.40E+13	1.09E+12	4.86E-05	2.42E-04	-1.93E-04

REACTION VI-B: $H + ClF = HF(O) + Cl$

	KF	KR	RF	RR	RF-RR
164	1.19E+13	6.96E-39	2.13E-32	1.08E-55	2.13E-32

REACTION VI-C: $H + ClF = HCl(O) + F$

	KF	KR	RF	RR	RF-RR
165	1.19E+13	3.97E-17	2.13E-32	5.54E-33	1.58E-32

REACTION VI-D: $D + ClF = DF(O) + Cl$

	KF	KR	RF	RR	RF-RR
166	1.19E+13	1.25E-39	1.06E-34	8.70E-55	1.06E-34

TABLE XVI. SUMMARY OF DETAILED KINETIC ANALYSIS FOR SYSTEM $\text{ClF}_5\text{-ND}_3\text{-HE-HCl}$
 AT 0.10 CM (0.60 microsecond, the position of maximum gain on P2 lines;
 precombustor: 1500 K and 5 percent F-atom)

CONDITIONS:

TEMPERATURE, DEG K: 327.5
 PRESSURE, ATM: .01
 PRESSURE, TORR: 7.6

MOLE PERCENTS:

HF(0)=	0.3380	DF(0)=	15.1170	H=	0.0000
HF(1)=	1.1540	DF(1)=	0.0140	D=	0.0000
HF(2)=	1.5490	DF(2)=	0.0000	CL=	3.3200
HF(3)=	0.3180	DF(3)=	0.0000	F=	1.0300
HF(4)=	0.0110	DF(4)=	0.0000	F2=	0.0000
HF(5)=	0.0000	DF(5)=	0.0000	CLF=	4.8200
HF(6)=	0.0000	H2(0)=	0.0000	CL2=	0.0533
HF(7)=	0.0000	H2(1)=	0.0000	CF4=	0.0000
HF(8)=	0.0000	H2(2)=	0.0000	N2=	2.6100
HCL(0)=	9.7850	D2(0)=	0.0000	HE=	60.0000
HCL(1)=	0.0090	HD=	0.0000		
HCL(2)=	0.0000				
HCL(3)=	0.0000				

TABLE XVI.. (Continued)

SPECIES: HF(0)

PUMPING:	GAIN=	6.65E-04	LOSS=	1.30E-26	NET=	6.65E-04
V-1(TOT):	GAIN=	1.69E-04	LOSS=	1.37E-12	NET=	1.69E-04
H:	GAIN=	2.28E-33	LOSS=	1.84E-41	NET=	2.28E-33
CL:	GAIN=	3.74E-05	LOSS=	3.02E-13	NET=	3.74E-05
HP:	GAIN=	1.44E-40	LOSS=	1.16E-48	NET=	1.44E-40
HCL:	GAIN=	2.54E-05	LOSS=	2.05E-13	NET=	2.54E-05
HF:	GAIN=	5.25E-05	LOSS=	4.24E-13	NET=	5.25E-05
DF:	GAIN=	3.93E-05	LOSS=	3.17E-13	NET=	3.93E-05
CLF:	GAIN=	7.09E-08	LOSS=	5.73E-16	NET=	7.09E-08
V-V(TOT):	GAIN=	9.18E-04	LOSS=	9.70E-05	NET=	8.21E-04
HF:	GAIN=	8.72E-04	LOSS=	9.70E-05	NET=	7.75E-04
DF:	GAIN=	2.81E-05	LOSS=	7.37E-11	NET=	2.81E-05
HP:	GAIN=	8.49E-39	LOSS=	0	NET=	8.49E-39
HCL:	GAIN=	1.82E-05	LOSS=	4.31E-11	NET=	1.82E-05
SCP, (TOT):	GAIN=	1.32E-32	LOSS=	2.29E-36	NET=	1.32E-32
H+HF:	GAIN=	9.52E-33	LOSS=	2.40E-48	NET=	9.52E-33
H+DF:	GAIN=	4.71E-33	LOSS=	2.89E-36	NET=	4.70E-33
MIS, H+CLF:	GAIN=	2.13E-32	LOSS=	1.08E-55	NET=	2.13E-32
TOTAL	GAIN=	1.75E-03	LOSS=	9.70E-05	NET=	1.65E-03

TABLE XVI. (Continued)

SPECIES: HF(1)

PUMPING:	GAIN=	2.98E-03	LOSS=	7.19E-18	NET=	2.98E-03
V-T(TOT):	GAIN=	3.81E-04	LOSS=	1.69E-04	NET=	2.12E-04
H:	GAIN=	4.64E-33	LOSS=	2.28E-32	NET=	2.37E-33
CL:	GAIN=	5.02E-05	LOSS=	3.74E-05	NET=	1.28E-05
H2:	GAIN=	3.87E-40	LOSS=	1.44E-40	NET=	2.43E-40
HCL:	GAIN=	3.41E-05	LOSS=	2.54E-05	NET=	8.70E-06
HF:	GAIN=	1.41E-04	LOSS=	5.25E-05	NET=	8.84E-05
DF:	GAIN=	1.05E-04	LOSS=	3.93E-05	NET=	6.61E-05
CLF:	GAIN=	1.90E-07	LOSS=	7.09E-08	NET=	1.19E-07
V-V(TOT):	GAIN=	1.31E-03	LOSS=	1.49E-03	NET=	-1.80E-04
HF:	GAIN=	1.19E-03	LOSS=	1.44E-03	NET=	-2.50E-04
DF:	GAIN=	7.53E-05	LOSS=	2.81E-05	NET=	4.72E-05
H2:	GAIN=	1.72E-38	LOSS=	2.49E-39	NET=	8.71E-39
HCL:	GAIN=	4.87E-05	LOSS=	1.82E-05	NET=	3.05E-05
SCR,(TOT):	GAIN=	1.25E-33	LOSS=	1.97E-35	NET=	1.23E-33
H+HF:	GAIN=	1.25E-33	LOSS=	3.18E-47	NET=	1.25E-33
H+DF:	GAIN=	4.22E-38	LOSS=	1.97E-35	NET=	-1.97E-35
MIS,H+CLF:	GAIN=	0	LOSS=	0	NET=	0
TOTAL	GAIN=	4.67E-03	LOSS=	1.66E-03	NET=	3.01E-03

TABLE XVI.. (Continued)

SPECIES: H₂(g)

PUMPING:	GAIN=	4.55E-03	LOSS=	2.51E-10	NET=	4.55E-03
V-T(TOT):	GAIN=	1.15E-04	LOSS=	3.81E-04	NET=	-2.66E-04
H:	GAIN=	1.25E-33	LOSS=	4.64E-33	NET=	-3.39E-33
CL:	GAIN=	1.03E-05	LOSS=	5.02E-05	NET=	-3.99E-05
H2:	GAIN=	1.19E-40	LOSS=	3.87E-40	NET=	-2.68E-40
HCL:	GAIN=	7.00E-06	LOSS=	3.41E-05	NET=	-2.71E-05
HF:	GAIN=	4.34E-05	LOSS=	1.41E-04	NET=	-9.75E-05
DF:	GAIN=	3.25E-05	LOSS=	1.05E-04	NET=	-7.29E-05
CLF:	GAIN=	5.86E-08	LOSS=	1.90E-07	NET=	-1.32E-07
V-V(TOT):	GAIN=	7.15E-04	LOSS=	2.45E-03	NET=	-1.73E-03
HF:	GAIN=	6.77E-04	LOSS=	2.33E-03	NET=	-1.65E-03
DF:	GAIN=	2.32E-05	LOSS=	7.53E-05	NET=	-5.21E-05
H2:	GAIN=	5.26E-39	LOSS=	1.72E-38	NET=	-1.19E-38
HCL:	GAIN=	1.50E-05	LOSS=	4.87E-05	NET=	-3.37E-05
SCR,(TOT):	GAIN=	6.14E-35	LOSS=	6.83E-33	NET=	-6.77E-33
H+HF:	GAIN=	6.14E-35	LOSS=	6.79E-33	NET=	-6.73E-33
H+DF:	GAIN=	2.48E-45	LOSS=	3.97E-35	NET=	-3.97E-35
MIS,H+CLF:	GAIN=	0	LOSS=	0	NET=	0
TOTAL	GAIN=	5.39E-03	LOSS=	2.83E-03	NET=	2.55E-03

TABLE XVI.. (Continued)

SPECIES: HF(3)

PUMPING:	GAIN=	6.65E-04	LOSS=	6.15E-05	NFT=	6.03E-04
V-T(TOT):	GAIN=	4.87E-06	LOSS=	1.15E-04	NET=	-1.11E-04
H:	GAIN=	1.06E-34	LOSS=	1.25E-33	NET=	-1.15E-33
CL:	GAIN=	3.56E-07	LOSS=	1.03E-05	NET=	-9.94E-06
H2:	GAIN=	5.49E-42	LOSS=	1.19E-40	NET=	-1.14E-40
HCL:	GAIN=	2.42E-07	LOSS=	7.00E-06	NET=	-6.76E-06
HF:	GAIN=	2.00E-06	LOSS=	4.34E-05	NET=	-4.14E-05
DF:	GAIN=	1.50E-06	LOSS=	3.25E-05	NET=	-3.10E-05
CLF:	GAIN=	2.70E-09	LOSS=	5.86E-08	NET=	-5.59E-08
V-V(TOT):	GAIN=	1.25E-03	LOSS=	3.13E-04	NET=	9.37E-04
HF:	GAIN=	1.24E-03	LOSS=	2.74E-04	NFT=	9.66E-04
DF:	GAIN=	1.07E-06	LOSS=	2.32E-05	NET=	-2.21E-05
H2:	GAIN=	1.98E-40	LOSS=	5.26E-39	NET=	-5.06E-39
HCL:	GAIN=	6.95E-07	LOSS=	1.50E-05	NFT=	-1.43E-05
SCR,(TOT):	GAIN=	3.18E-47	LOSS=	2.90E-33	NFT=	-2.90E-33
H+HF:	GAIN=	3.18E-47	LOSS=	2.89E-33	NET=	-2.89E-33
H+DF:	GAIN=	3.04E-52	LOSS=	1.09E-35	NFT=	-1.09E-35
MIS,H+CLF:	GAIN=	0	LOSS=	0	NET=	0
TOTAL	GAIN=	1.91E-03	LOSS=	4.89E-04	NET=	1.43E-03

TABLE XVI.. (Concluded)

SPECIES: HF(4)

PUMPING:	GAIN=	1.52E-40	LOSS=	3.03E-35	NET=	-3.03E-35
V-T(TCT):	GAIN=	3.53E-11	LOSS=	4.87E-06	NET=	-4.87E-06
H:	GAIN=	7.67E-40	LOSS=	1.06E-34	NET=	-1.06E-34
CL:	GAIN=	2.58E-12	LOSS=	3.56E-07	NET=	-3.56E-07
H2:	GAIN=	3.98E-47	LOSS=	5.49E-42	NET=	-5.49E-42
HCL:	GAIN=	1.76E-12	LOSS=	2.22E-07	NET=	-2.22E-07
HF:	GAIN=	1.45E-11	LOSS=	2.00E-06	NET=	-2.00E-06
DF:	GAIN=	1.09E-11	LOSS=	1.50E-06	NET=	-1.50E-06
CLF:	GAIN=	1.96E-14	LOSS=	2.70E-09	NET=	-2.70E-09
V-V(TCT):	GAIN=	1.65E-04	LOSS=	2.44E-04	NET=	1.57E-04
HF:	GAIN=	1.65E-04	LOSS=	6.67E-06	NET=	1.52E-04
DF:	GAIN=	2.52E-09	LOSS=	1.07E-06	NET=	-1.07E-06
H2:	GAIN=	0	LOSS=	1.98E-40	NET=	-1.98E-40
HCL:	GAIN=	1.47E-09	LOSS=	6.92E-07	NET=	-6.91E-07
ECT, (TCT):	GAIN=	2.66E-46	LOSS=	1.58E-34	NET=	-1.52E-34
H+HF:	GAIN=	2.66E-46	LOSS=	1.57E-34	NET=	-1.57E-34
H+DF:	GAIN=	7.62E-59	LOSS=	3.76E-37	NET=	-3.76E-37
MIS, H+CLF:	GAIN=	0	LOSS=	0	NET=	0
TOTAL	GAIN=	1.65E-04	LOSS=	1.33E-05	NET=	1.52E-04

TABLE XVII. SUMMARY OF DETAILED KINETIC ANALYSIS, CASE I: $F_2-D_2-HE-H_2$ AT 0.20 CM
(0.78 microsecond, the position of maximum gain on P2 lines;*
precombustor: 1500 K and 10 percent F-atoms)

CONDITIONS:

TEMPERATURE, DEG K: 319.9
PRESSURE, ATM: .01
PRESSURE, Torr: 7.6

MOLE PERCENTS:

HF(0)= 9.4600	DF(0)= 9.4350	H= 3.4400
HF(1)= 0.3680	DF(1)= 0.0190	D= 0.2350
HF(2)= 1.7110	DF(2)= 0.0020	CL= 0.0000
HF(3)= 0.8270	DF(3)= 0.0010	F= 4.0200
HF(4)= 0.0430	DF(4)= 0.0000	F2= 0.0000
HF(5)= 0.0010	DF(5)= 0.0000	CLF= 0.0000
HF(6)= 0.0000	H2(0)= 19.2690	CL2= 0.0000
HF(7)= 0.0000	H2(1)= 0.1710	CF4= 0.0000
HF(8)= 0.0000	H2(2)= 0.0020	N2= 0.0000
HCL(0)= 0.0000	D2(0)= 0.0000	HE= 59.5000
HCL(1)= 0.0000	HD= 0.0000	
HCL(2)= 0.0000		
HCL(3)= 0.0000		

*See Fig. 46 and 62.

TABLE XVII. (Continued)

SPECIES: HF(O)

PUMPING:	GAIN=	1.07E-11	LOSS=	1.20E-74	NET=	1.07E-11
V-T(TOT):	GAIN=	3.36E-04	LOSS=	3.24E-12	NET=	3.36E-04
H:	GAIN=	2.23E-04	LOSS=	2.15E-12	NET=	2.23E-04
CL:	GAIN=	0	LOSS=	0	NET=	0
H2:	GAIN=	1.50E-06	LOSS=	1.45E-14	NET=	1.50E-06
HCL:	GAIN=	0	LOSS=	0	NET=	0
HF:	GAIN=	4.89E-05	LOSS=	4.72E-13	NET=	4.89E-05
DF:	GAIN=	1.97E-05	LOSS=	1.90E-13	NET=	1.97E-05
CLF:	GAIN=	0	LOSS=	0	NET=	0
V-V(TOT):	GAIN=	7.61E-04	LOSS=	1.59E-04	NET=	3.02E-04
HF:	GAIN=	6.54E-04	LOSS=	1.58E-04	NET=	4.96E-04
DF:	GAIN=	1.38E-05	LOSS=	1.40E-10	NET=	1.38E-05
H2:	GAIN=	9.26E-05	LOSS=	1.04E-06	NET=	9.16E-05
HCL:	GAIN=	0	LOSS=	0	NET=	0
SOL(TOT):	GAIN=	1.94E-03	LOSS=	7.15E-06	NET=	1.94E-03
H+HF:	GAIN=	1.57E-03	LOSS=	1.89E-19	NET=	1.57E-03
H+DF:	GAIN=	3.73E-04	LOSS=	7.15E-06	NET=	3.65E-04
MIS,H+CLF:	GAIN=	0	LOSS=	0	NET=	0
TOTAL	GAIN=	3.04E-03	LOSS=	1.66E-04	NET=	2.87E-03

TABLE XVII. (Continued)

SPECIES: HF(1)

PUMPING:	GAIN=	2.38E-03	LOSS=	1.23E-18	NET=	2.38E-03
V-T(TOT):	GAIN=	1.16E-03	LOSS=	3.36E-04	NET=	8.26E-04
H:	GAIN=	6.67E-04	LOSS=	2.23E-04	NET=	4.45E-04
CL:	GAIN=	0	LOSS=	0	NET=	0
H2:	GAIN=	5.93E-06	LOSS=	1.50E-06	NET=	4.43E-06
HCL:	GAIN=	0	LOSS=	0	NET=	0
HF:	GAIN=	1.93E-04	LOSS=	4.89E-05	NET=	1.44E-04
DF:	GAIN=	7.77E-05	LOSS=	1.97E-05	NET=	5.80E-05
CLF:	GAIN=	0	LOSS=	0	NET=	0
V-V(TOT):	GAIN=	2.05E-03	LOSS=	1.19E-03	NET=	8.60E-04
HF:	GAIN=	1.72E-03	LOSS=	1.08E-03	NET=	6.40E-04
DF:	GAIN=	5.45E-05	LOSS=	1.38E-05	NET=	4.07E-05
H2:	GAIN=	2.72E-04	LOSS=	9.89E-05	NET=	1.73E-04
HCL:	GAIN=	0	LOSS=	0	NET=	0
SCR,(TOT):	GAIN=	4.30E-04	LOSS=	2.70E-05	NET=	4.03E-04
H+HF:	GAIN=	4.30E-04	LOSS=	1.43E-18	NET=	4.30E-04
H+DF:	GAIN=	4.61E-07	LOSS=	2.70E-05	NET=	-2.65E-05
MIS,H+CLF:	GAIN=	0	LOSS=	0	NET=	0
TOTAL	GAIN=	6.02E-03	LOSS=	1.55E-03	NET=	4.47E-03

TABLE XVII. (Continued)

SPECIES: HF(2)

PUMPING:	GAIN=	8.06E-03	LOSS=	2.07E-10	NET=	8.06E-03
V-T(TOT):	GAIN=	8.54E-04	LOSS=	1.16E-03	NET=	-3.08E-04
H:	GAIN=	4.22E-04	LOSS=	6.67E-04	NET=	-2.45E-04
CL:	GAIN=	0	LOSS=	0	NET=	0
H2:	GAIN=	4.30E-06	LOSS=	5.93E-06	NET=	-1.63E-06
HCL:	GAIN=	0	LOSS=	0	NET=	0
HF:	GAIN=	1.40E-04	LOSS=	1.93E-04	NET=	-5.30E-05
DF:	GAIN=	5.63E-05	LOSS=	7.77E-05	NET=	-2.14E-05
CLF:	GAIN=	0	LOSS=	0	NET=	0
V-V(TOT):	GAIN=	1.08E-03	LOSS=	3.37E-03	NET=	-2.29E-03
HF:	GAIN=	8.43E-04	LOSS=	3.01E-03	NET=	-2.16E-03
DF:	GAIN=	3.95E-05	LOSS=	5.45E-05	NET=	-1.50E-05
H2:	GAIN=	1.93E-04	LOSS=	3.09E-04	NET=	-1.16E-04
HCL:	GAIN=	0	LOSS=	0	NET=	0
SCR.(TOT):	GAIN=	3.15E-05	LOSS=	1.06E-03	NET=	-1.02E-03
H+HF:	GAIN=	3.15E-05	LOSS=	9.76E-04	NET=	-9.44E-04
H+DF:	GAIN=	8.47E-12	LOSS=	7.97E-05	NET=	-7.97E-05
MIS,H+CLF:	GAIN=	0	LOSS=	0	NET=	0
TOTAL	GAIN=	1.00E-02	LOSS=	5.59E-03	NET=	4.44E-03

TABLE XVII. (Continued)

SPECIES: HFC3

POPI NG:	GAIN=	4.03E-03	LOSS=	5.96E-04	NET=	3.43E-03
V-T(TOT):	GAIN=	3.02E-05	LOSS=	8.54E-04	NET=	-7.74E-04
H:	GAIN=	5.43E-05	LOSS=	4.22E-04	NET=	-3.68E-04
CL:	GAIN=	0	LOSS=	0	NET=	0
H2:	GAIN=	2.98E-07	LOSS=	4.30E-06	NET=	-4.00E-06
HCL:	GAIN=	0	LOSS=	0	NET=	0
HF:	GAIN=	9.63E-06	LOSS=	1.40E-04	NET=	-1.30E-04
DF:	GAIN=	3.90E-06	LOSS=	5.63E-05	NET=	-5.24E-05
CLF:	GAIN=	0	LOSS=	0	NET=	0
V-V(T-T):	GAIN=	1.51E-03	LOSS=	1.30E-03	NET=	2.10E-04
H:	GAIN=	1.46E-03	LOSS=	1.03E-03	NET=	4.30E-04
DF:	GAIN=	2.75E-06	LOSS=	3.95E-05	NET=	-3.67E-05
H2:	GAIN=	4.36E-05	LOSS=	2.28E-04	NET=	-1.79E-04
HCL:	GAIN=	0	LOSS=	0	NET=	0
SO2(T-T):	GAIN=	7.47E-14	LOSS=	1.03E-03	NET=	-1.03E-03
H+HF:	GAIN=	1.43E-13	LOSS=	9.76E-04	NET=	-9.76E-04
H+DF:	GAIN=	7.47E-14	LOSS=	5.14E-05	NET=	-5.14E-05
H2+H+CLF:	GAIN=	0	LOSS=	0	NET=	0
TOTAL	GAIN=	5.62E-03	LOSS=	3.78E-03	NET=	1.84E-03

TABLE XVII. (Concluded)

SPECIES: HF(4)

PUMPING:	GAIN=	5.07E-10	LOSS=	1.56E-05	NET=	-1.56E-05
V-T(TOT):	GAIN=	2.70E-10	LOSS=	8.02E-05	NET=	-8.02E-05
H:	GAIN=	1.83E-10	LOSS=	5.43E-05	NET=	-5.43E-05
CL:	GAIN=	0	LOSS=	0	NET=	0
H2:	GAIN=	1.00E-12	LOSS=	2.98E-07	NET=	-2.98E-07
HCL:	GAIN=	0	LOSS=	0	NET=	0
HF:	GAIN=	3.26E-11	LOSS=	9.68E-06	NET=	-9.68E-06
DF:	GAIN=	1.31E-11	LOSS=	3.90E-06	NET=	-3.90E-06
CLF:	GAIN=	0	LOSS=	0	NET=	0
V-V(TOT):	GAIN=	6.53E-04	LOSS=	4.61E-05	NET=	6.07E-04
HF:	GAIN=	6.12E-04	LOSS=	3.30E-05	NET=	5.79E-04
DF:	GAIN=	8.92E-08	LOSS=	2.74E-06	NET=	-2.65E-06
H2:	GAIN=	4.11E-05	LOSS=	1.04E-05	NET=	3.07E-05
HCL:	GAIN=	0	LOSS=	0	NET=	0
SCR.(TOT):	GAIN=	1.84E-17	LOSS=	8.34E-05	NET=	-8.34E-05
H+HF:	GAIN=	1.84E-17	LOSS=	8.07E-05	NET=	-8.07E-05
H+DF:	GAIN=	1.31E-20	LOSS=	2.67E-06	NET=	-2.67E-06
MIS,H+CLF:	GAIN=	0	LOSS=	0	NET=	0
TOTAL	GAIN=	6.53E-04	LOSS=	2.25E-04	NET=	4.28E-04

TABLE XVIII. SUMMARY OF DETAILED KINETIC ANALYSIS, CASE II: $F_2-D_2-HE-HCl$ AT 0.10 CM
(0.60 microsecond, the position of maximum gain on P1 lines;*
precombustor: 1500 K and 10 percent F-atoms)

CONDITIONS:

TEMPERATURE, DEG K: 424.2
PRESSURE, ATM: .01
PRESSURE, TORR: 7.6

MOLE PERCENTS:

HF(0)= 0.3920	DF(0)= 9.6750	H= 0.0000
HF(1)= 2.3970	DF(1)= 0.0170	D= 0.0000
HF(2)= 2.9540	DF(2)= 0.0000	CL= 7.1200
HF(3)= 0.8120	DF(3)= 0.0000	F= 0.5750
HF(4)= 0.0610	DF(4)= 0.0000	F2= 0.0000
HF(5)= 0.0010	DF(5)= 0.0000	CLF= 0.0000
HF(6)= 0.0000	H2(0)= 0.0000	CL2= 0.0000
HF(7)= 0.0000	H2(1)= 0.0000	CF4= 0.0000
HF(8)= 0.0000	H2(2)= 0.0000	N2= 0.0000
HCL(0)=15.9800	D2(0)= 0.0000	HE= 59.5000
HCL(1)= 0.0230	HD= 0.0000	
HCL(2)= 0.0000		
HCL(3)= 0.0000		

*See Fig. 47 and 63

TABLE XVIII. (Continued)

SPECIES: HF(0)

PUMPING:	GAIN=	4.95E-04	LOSS=	6.66E-21	NET=	4.95E-04
V-T(TOT):	GAIN=	3.81E-04	LOSS=	2.07E-10	NET=	3.81E-04
H:	GAIN=	3.89E-27	LOSS=	2.11E-33	NET=	3.89E-27
CL:	GAIN=	1.82E-04	LOSS=	9.90E-11	NET=	1.82E-04
H2:	GAIN=	6.60E-34	LOSS=	3.58E-40	NET=	6.60E-34
HCL:	GAIN=	4.19E-05	LOSS=	2.28E-11	NET=	4.19E-05
HF:	GAIN=	1.12E-04	LOSS=	6.07E-11	NET=	1.12E-04
DF:	GAIN=	2.54E-05	LOSS=	1.38E-11	NET=	2.54E-05
CLF:	GAIN=	1.35E-30	LOSS=	7.34E-37	NET=	1.35E-30
V-V(TOT):	GAIN=	2.56E-03	LOSS=	4.05E-04	NET=	2.15E-03
HF:	GAIN=	2.50E-03	LOSS=	4.05E-04	NET=	2.09E-03
DF:	GAIN=	2.22E-05	LOSS=	4.05E-10	NET=	2.22E-05
H2:	GAIN=	2.82E-32	LOSS=	0	NET=	2.82E-32
HCL:	GAIN=	3.67E-05	LOSS=	6.20E-10	NET=	3.67E-05
SCR.(TOT):	GAIN=	1.77E-26	LOSS=	1.70E-30	NET=	1.77E-26
H+HF:	GAIN=	1.43E-26	LOSS=	1.21E-38	NET=	1.43E-26
H+DF:	GAIN=	3.37E-27	LOSS=	1.70E-30	NET=	3.37E-27
MIS,H+CLF:	GAIN=	1.43E-49	LOSS=	3.07E-43	NET=	-3.07E-43
TOTAL	GAIN=	3.43E-03	LOSS=	4.05E-04	NET=	3.03E-03

TABLE XVIII. (Continued)

SPECIES: HFC1

PCAF18:	GAIN=	2.22E-03	LOSS=	5.49E-14	NET=	2.22E-03
V-TCOT:	GAIN=	6.64E-04	LOSS=	3.81E-04	NET=	2.83E-04
H:	GAIN=	7.18E-27	LOSS=	3.39E-27	NET=	3.29E-27
CL:	GAIN=	2.25E-04	LOSS=	1.82E-04	NET=	4.24E-05
HE:	GAIN=	1.63E-33	LOSS=	6.60E-34	NET=	9.67E-34
HCL:	GAIN=	5.17E-05	LOSS=	4.19E-05	NET=	9.75E-06
HF:	GAIN=	2.76E-04	LOSS=	1.12E-04	NET=	1.64E-04
DF:	GAIN=	6.26E-05	LOSS=	2.54E-05	NET=	3.72E-05
CLF:	GAIN=	3.34E-30	LOSS=	1.35E-30	NET=	1.98E-30
V-VCOT:	GAIN=	3.47E-03	LOSS=	4.31E-03	NET=	-8.40E-04
HF:	GAIN=	3.32E-03	LOSS=	4.25E-03	NET=	-9.30E-04
DF:	GAIN=	5.48E-05	LOSS=	2.22E-05	NET=	3.26E-05
H2:	GAIN=	6.26E-32	LOSS=	2.82E-32	NET=	3.44E-32
HCL:	GAIN=	9.06E-05	LOSS=	3.67E-05	NET=	5.39E-05
CO2(TOT):	GAIN=	2.76E-27	LOSS=	9.18E-30	NET=	2.75E-27
H+HF:	GAIN=	2.76E-27	LOSS=	9.25E-38	NET=	2.76E-27
H+DF:	GAIN=	1.69E-31	LOSS=	9.18E-30	NET=	-9.01E-30
H2,H+CLF:	GAIN=	0	LOSS=	0	NET=	0
TOTAL	GAIN=	6.34E-03	LOSS=	4.69E-03	NET=	1.65E-03

TABLE XVIII. (Continued)

SPECIES: HF(2)

PUMPING:	GAIN=	3.39E-03	LOSS=	3.96E-08	NET=	3.39E-03
V-T(TOT):	GAIN=	2.40E-04	LOSS=	6.64E-04	NET=	-4.24E-04
H:	GAIN=	2.67E-27	LOSS=	7.18E-27	NET=	-4.50E-27
CL:	GAIN=	6.18E-05	LOSS=	2.25E-04	NET=	-1.63E-04
H2:	GAIN=	6.71E-34	LOSS=	1.63E-33	NET=	-9.56E-34
HCL:	GAIN=	1.42E-05	LOSS=	5.17E-05	NET=	-3.75E-05
HF:	GAIN=	1.14E-04	LOSS=	2.76E-04	NET=	-1.62E-04
DF:	GAIN=	2.58E-05	LOSS=	6.26E-05	NET=	-3.68E-05
CLF:	GAIN=	1.38E-30	LOSS=	3.34E-30	NET=	-1.96E-30
V-V(TOT):	GAIN=	2.30E-03	LOSS=	6.22E-03	NET=	-3.92E-03
HF:	GAIN=	2.24E-03	LOSS=	6.07E-03	NET=	-3.83E-03
DF:	GAIN=	2.26E-05	LOSS=	5.48E-05	NET=	-3.22E-05
H2:	GAIN=	3.02E-32	LOSS=	6.26E-32	NET=	-3.24E-32
HCL:	GAIN=	3.73E-05	LOSS=	9.06E-05	NET=	-5.33E-05
SCR.(TOT):	GAIN=	2.53E-28	LOSS=	1.05E-26	NET=	-1.03E-26
H+HF:	GAIN=	2.53E-28	LOSS=	1.05E-26	NET=	-1.02E-26
H+DF:	GAIN=	4.42E-37	LOSS=	1.69E-29	NET=	-1.69E-29
MIS,H+CLF:	GAIN=	0	LOSS=	0	NET=	0
TOTAL	GAIN=	5.93E-03	LOSS=	6.88E-03	NET=	-9.54E-04

TABLE XVIII. (Concluded)

SPECIES: HF(3)

PUMPING:	GAIN=	4.95E-04	LOSS=	3.45E-04	NET=	1.50E-04
V-T(TØT):	GAIN=	2.15E-05	LOSS=	2.40E-04	NET=	-2.19E-04
H:	GAIN=	4.37E-28	LOSS=	2.67E-27	NET=	-2.24E-27
CL:	GAIN=	4.64E-06	LOSS=	6.18E-05	NET=	-5.72E-05
H2:	GAIN=	6.72E-35	LOSS=	6.71E-34	NET=	-6.04E-34
HCL:	GAIN=	1.07E-06	LOSS=	1.42E-05	NET=	-1.31E-05
HF:	GAIN=	1.14E-05	LOSS=	1.14E-04	NET=	-1.02E-04
DF:	GAIN=	2.59E-06	LOSS=	2.58E-05	NET=	-2.32E-05
CLF:	GAIN=	1.38E-31	LOSS=	1.38E-30	NET=	-1.24E-30
V-V(TØT):	GAIN=	3.19E-03	LOSS=	1.14E-03	NET=	2.05E-03
HF:	GAIN=	3.19E-03	LOSS=	1.08E-03	NET=	2.11E-03
DF:	GAIN=	2.28E-06	LOSS=	2.26E-05	NET=	-2.03E-05
H2:	GAIN=	2.90E-33	LOSS=	3.02E-32	NET=	-2.73E-32
HCL:	GAIN=	3.76E-06	LOSS=	3.74E-05	NET=	-3.36E-05
SCR.(TØT):	GAIN=	9.25E-38	LOSS=	6.19E-27	NET=	-6.19E-27
H+HF:	GAIN=	9.25E-38	LOSS=	6.18E-27	NET=	-6.18E-27
H+DF:	GAIN=	2.04E-42	LOSS=	6.19E-30	NET=	-6.19E-30
MIS,H+CLF:	GAIN=	0	LOSS=	0	NET=	0
TØTAL	GAIN=	3.71E-03	LOSS=	1.73E-03	NET=	1.98E-03

TABLE XIX. SUMMARY OF DETAILED KINETIC ANALYSIS, CASE V: $\text{ClF}_5\text{-ND}_3\text{-HE-H}_2$ AT 0.15 CM
(0.83 microsecond, the position of maximum gain on P1 lines*;
precombustor: 1500 K and 10 percent F-atoms)

CONDITIONS:

TEMPERATURE, DEG K: 393
PRESSURE, ATM: .01
PRESSURE, TORR: 7.6

MOLE PERCENTS:

HF(0)= 0.7310	DF(0)= 16.5020	H= 3.0400
HF(1)= 1.1220	DF(1)= 0.0360	D= 0.3720
HF(2)= 2.0920	DF(2)= 0.0050	CL= 0.4820
HF(3)= 0.9990	DF(3)= 0.0020	F= 3.8000
HF(4)= 0.0590	DF(4)= 0.0000	F2= 0.0000
HF(5)= 0.0010	DF(5)= 0.0000	CLF= 5.3600
HF(6)= 0.0000	H2(0)= 18.9190	CL2= 0.0088
HF(7)= 0.0000	H2(1)= 0.2010	CF4= 0.0000
HF(8)= 0.0000	H2(2)= 0.0020	N2= 2.7700
HCL(0)= 0.2940	D2(0)= 0.0000	HE= 43.4000
HCL(1)= 0.0000	HD= 0.0000	
HCL(2)= 0.0000		
HCL(3)= 0.0000		

*See Fig. 50 and 66

TABLE XIX. (Continued)

SPECIES: HF(O)

PUMPING:	GAIN=	6.38E-05	LOSS=	2.85E-23	NET=	6.38E-05
V-T(TOT):	GAIN=	3.56E-04	LOSS=	1.40E-10	NET=	3.56E-04
H:	GAIN=	2.20E-04	LOSS=	8.64E-11	NET=	2.20E-04
CL:	GAIN=	5.70E-06	LOSS=	2.23E-12	NET=	5.70E-06
H2:	GAIN=	1.91E-06	LOSS=	7.50E-13	NET=	1.91E-06
HCL:	GAIN=	4.31E-07	LOSS=	1.69E-13	NET=	4.31E-07
HF:	GAIN=	4.40E-05	LOSS=	1.72E-11	NET=	4.40E-05
DF:	GAIN=	2.42E-05	LOSS=	9.50E-12	NET=	2.42E-05
CLF:	GAIN=	1.13E-07	LOSS=	4.44E-14	NET=	1.13E-07
V-V(TOT):	GAIN=	8.74E-04	LOSS=	2.62E-04	NET=	6.12E-04
HF:	GAIN=	7.64E-04	LOSS=	2.61E-04	NET=	5.03E-04
DF:	GAIN=	2.02E-05	LOSS=	7.12E-10	NET=	2.02E-05
H2:	GAIN=	7.02E-05	LOSS=	1.25E-06	NET=	8.89E-05
HCL:	GAIN=	3.59E-07	LOSS=	0	NET=	3.59E-07
SCR,(TOT):	GAIN=	2.11E-03	LOSS=	1.36E-05	NET=	2.10E-03
H+HF:	GAIN=	1.46E-03	LOSS=	2.13E-16	NET=	1.46E-03
H+DF:	GAIN=	6.53E-04	LOSS=	1.36E-05	NET=	6.39E-04
MIS,H+CLF:	GAIN=	3.22E-03	LOSS=	3.77E-47	NET=	3.22E-03
TOTAL	GAIN=	6.63E-03	LOSS=	2.76E-04	NET=	6.35E-03

TABLE XIX. (Continued)

SPECIES: HF(1)

PUMPING:	GAIN=	2.63E-03	LOSS=	1.03E-15	NET=	2.63E-03
V-T(TOT):	GAIN=	1.13E-03	LOSS=	3.56E-04	NET=	7.71E-04
H:	GAIN=	6.17E-04	LOSS=	2.20E-04	NET=	3.97E-04
CL:	GAIN=	1.06E-05	LOSS=	5.70E-06	NET=	4.93E-06
H2:	GAIN=	7.13E-06	LOSS=	1.91E-06	NET=	5.22E-06
HCL:	GAIN=	8.03E-07	LOSS=	4.31E-07	NET=	3.72E-07
HF:	GAIN=	1.64E-04	LOSS=	4.40E-05	NET=	1.20E-04
DF:	GAIN=	9.03E-05	LOSS=	2.42E-05	NET=	6.61E-05
CLF:	GAIN=	4.22E-07	LOSS=	1.13E-07	NET=	3.09E-07
V-V(TOT):	GAIN=	2.39E-03	LOSS=	1.41E-03	NET=	9.80E-04
HF:	GAIN=	2.02E-03	LOSS=	1.29E-03	NET=	7.30E-04
DF:	GAIN=	7.53E-05	LOSS=	2.02E-05	NET=	5.51E-05
H2:	GAIN=	2.92E-04	LOSS=	9.64E-05	NET=	1.96E-04
HCL:	GAIN=	1.34E-06	LOSS=	3.59E-07	NET=	9.81E-07
SCR,(TOT):	GAIN=	4.05E-04	LOSS=	4.17E-05	NET=	3.63E-04
H+HF:	GAIN=	4.04E-04	LOSS=	9.97E-16	NET=	4.04E-04
H+DF:	GAIN=	7.89E-07	LOSS=	4.17E-05	NET=	-4.09E-05
MIS,H+CLF:	GAIN=	0	LOSS=	0	NET=	0
TOTAL	GAIN=	6.55E-03	LOSS=	1.81E-03	NET=	4.74E-03

TABLE XIX. (Continued)

SPECIES: HF(2)

PUMPING:	GAIN=	8.37E-03	LOSS=	4.80E-09	NET=	8.37E-03
V-TOT:	GAIN=	8.02E-04	LOSS=	1.13E-03	NET=	-3.25E-04
H:	GAIN=	3.96E-04	LOSS=	6.17E-04	NET=	-2.21E-04
CL:	GAIN=	5.07E-06	LOSS=	1.06E-05	NET=	-5.55E-06
H2:	GAIN=	5.11E-06	LOSS=	7.13E-06	NET=	-2.02E-06
HCL:	GAIN=	3.83E-07	LOSS=	8.03E-07	NET=	-4.19E-07
HF:	GAIN=	1.17E-04	LOSS=	1.64E-04	NET=	-4.65E-05
DF:	GAIN=	6.47E-05	LOSS=	9.03E-05	NET=	-2.56E-05
CLF:	GAIN=	3.02E-07	LOSS=	4.22E-07	NET=	-1.20E-07
V-V(TOT):	GAIN=	1.31E-03	LOSS=	3.74E-03	NET=	-2.43E-03
HF:	GAIN=	1.02E-03	LOSS=	3.34E-03	NET=	-2.32E-03
DF:	GAIN=	5.39E-05	LOSS=	7.53E-05	NET=	-2.14E-05
H2:	GAIN=	2.36E-04	LOSS=	3.26E-04	NET=	-9.00E-05
HCL:	GAIN=	9.58E-07	LOSS=	1.34E-06	NET=	-3.82E-07
SCR(TOT):	GAIN=	3.03E-05	LOSS=	1.02E-03	NET=	-9.88E-04
H+HF:	GAIN=	3.03E-05	LOSS=	9.02E-04	NET=	-8.72E-04
H+DF:	GAIN=	1.28E-10	LOSS=	1.16E-04	NET=	-1.16E-04
MIS,H+CLF:	GAIN=	0	LOSS=	0	NET=	0
TOTAL	GAIN=	1.05E-02	LOSS=	5.89E-03	NET=	4.62E-03

TABLE XIX. (Continued)

SPECIES: HF(3)

PUMPING:	GAIN=	4.03E-03	LOSS=	4.90E-04	NET=	3.54E-03
V-T(TOT):	GAIN=	7.99E-05	LOSS=	8.02E-04	NET=	-7.22E-04
H:	GAIN=	5.22E-05	LOSS=	3.96E-04	NET=	-3.44E-04
CL:	GAIN=	3.00E-07	LOSS=	5.07E-06	NET=	-4.77E-06
H2:	GAIN=	4.02E-07	LOSS=	5.11E-06	NET=	-4.71E-06
HCL:	GAIN=	2.26E-08	LOSS=	3.83E-07	NET=	-3.61E-07
HF:	GAIN=	9.25E-06	LOSS=	1.17E-04	NET=	-1.08E-04
DF:	GAIN=	5.10E-06	LOSS=	6.47E-05	NET=	-5.96E-05
CLF:	GAIN=	2.38E-08	LOSS=	3.02E-07	NET=	-2.79E-07
V-V(TOT):	GAIN=	1.66E-03	LOSS=	1.46E-03	NET=	2.00E-04
HF:	GAIN=	1.60E-03	LOSS=	1.14E-03	NET=	4.60E-04
DF:	GAIN=	4.27E-06	LOSS=	5.40E-05	NET=	-4.97E-05
H2:	GAIN=	5.22E-05	LOSS=	2.67E-04	NET=	-2.15E-04
HCL:	GAIN=	7.55E-08	LOSS=	9.58E-07	NET=	-8.82E-07
SCR,(TOT):	GAIN=	1.99E-12	LOSS=	9.91E-04	NET=	-9.91E-04
H+HF:	GAIN=	9.97E-16	LOSS=	9.17E-04	NET=	-9.17E-04
H+DF:	GAIN=	1.99E-12	LOSS=	7.41E-05	NET=	-7.41E-05
MIS,H+CLF:	GAIN=	0	LOSS=	0	NET=	0
TOTAL	GAIN=	5.77E-03	LOSS=	3.74E-03	NET=	2.03E-03

TABLE XIX. (Concluded)

SPECIES: HF(4)

PUMPING:	GAIN=	7.86E-09	LOSS=	1.44E-05	NET=	-1.44E-05
V-T(TOT):	GAIN=	5.01E-09	LOSS=	7.99E-05	NET=	-7.99E-05
H:	GAIN=	3.28E-09	LOSS=	5.22E-05	NET=	-5.22E-05
CL:	GAIN=	1.88E-11	LOSS=	3.00E-07	NET=	-3.00E-07
H2:	GAIN=	2.52E-11	LOSS=	4.02E-07	NET=	-4.02E-07
HCL:	GAIN=	1.42E-12	LOSS=	2.26E-08	NET=	-2.26E-08
HF:	GAIN=	5.80E-10	LOSS=	9.25E-06	NET=	-9.25E-06
DF:	GAIN=	3.20E-10	LOSS=	5.10E-06	NET=	-5.10E-06
CLF:	GAIN=	1.49E-12	LOSS=	2.38E-08	NET=	-2.38E-08
V-V(TOT):	GAIN=	6.90E-04	LOSS=	6.48E-05	NET=	6.25E-04
HF:	GAIN=	6.52E-04	LOSS=	4.37E-05	NET=	6.08E-04
DF:	GAIN=	1.14E-07	LOSS=	4.25E-06	NET=	-4.14E-06
H2:	GAIN=	3.77E-05	LOSS=	1.67E-05	NET=	2.10E-05
HCL:	GAIN=	1.60E-09	LOSS=	7.55E-08	NET=	-7.39E-08
SCR.(TOT):	GAIN=	8.19E-15	LOSS=	8.20E-05	NET=	-8.20E-05
H+HF:	GAIN=	8.19E-15	LOSS=	7.76E-05	NET=	-7.76E-05
H+DF:	GAIN=	7.37E-18	LOSS=	4.37E-06	NET=	-4.37E-06
MIS,H+CLF:	GAIN=	0	LOSS=	0	NET=	0
TOTAL	GAIN=	6.90E-04	LOSS=	2.41E-04	NET=	4.49E-04

TABLE XX. SUMMARY OF DETAILED KINETIC ANALYSIS, CASE VI: $\text{ClF}_5\text{-ND}_3\text{-HE-HCl}$ AT 0.05 CM
(0.36 microsecond, the position of maximum gain on P1 lines*;
Precombustor: 1500 K and 10 percent F-atoms)

CONDITIONS:

TEMPERATURE, DEG K: 385.2
PRESSURE, ATM: .01
PRESSURE, TORR: 7.6

MOLE PERCENTS:

HF(0)= 0.6200	DF(0)= 16.9060	H= 0.0000
HF(1)= 2.1130	DF(1)= 0.0150	D= 0.0000
HF(2)= 2.8490	DF(2)= 0.0000	CL= 6.0700
HF(3)= 0.5960	DF(3)= 0.0000	F= 1.6200
HF(4)= 0.0220	DF(4)= 0.0000	F2= 0.0000
HF(5)= 0.0000	DF(5)= 0.0000	CLF= 6.0300
HF(6)= 0.0000	H2(0)= 0.0000	CL2= 0.1400
HF(7)= 0.0000	H2(1)= 0.0000	CF4= 0.0000
HF(8)= 0.0000	H2(2)= 0.0000	N2= 2.7700
HCL(0)=16.9300	D2(0)= 0.0000	HE= 43.4000
HCL(1)= 0.0150	HD= 0.0000	
HCL(2)= 0.0000		
HCL(3)= 0.0000		

*See Fig. 51 and 67.

TABLE XX (Continued)

TABLE: H(CO)

TABLE: H(CO)	GAIN=	1.61E-03	LOSS=	7.79E-23	NET=	1.61E-03
TABLE: H(CO)	GAIN=	3.96E-04	LOSS=	4.34E-11	NET=	3.96E-04
TABLE: H(CO)	GAIN=	3.60E-29	LOSS=	3.95E-36	NET=	3.60E-29
TABLE: H(CO)	GAIN=	1.34E-04	LOSS=	1.47E-11	NET=	1.34E-04
TABLE: H(CO)	GAIN=	1.58E-36	LOSS=	1.73E-43	NET=	1.58E-36
TABLE: H(CO)	GAIN=	5.12E-05	LOSS=	5.62E-12	NET=	5.12E-05
TABLE: H(CO)	GAIN=	1.12E-04	LOSS=	1.23E-11	NET=	1.12E-04
TABLE: H(CO)	GAIN=	5.11E-05	LOSS=	5.61E-12	NET=	5.11E-05
TABLE: H(CO)	GAIN=	2.25E-07	LOSS=	2.46E-14	NET=	2.25E-07
TABLE: H(CO)	GAIN=	2.38E-03	LOSS=	2.89E-04	NET=	2.09E-03
TABLE: H(CO)	GAIN=	2.30E-03	LOSS=	2.89E-04	NET=	2.01E-03
TABLE: H(CO)	GAIN=	4.15E-05	LOSS=	2.10E-10	NET=	4.15E-05
TABLE: H(CO)	GAIN=	7.66E-35	LOSS=	0	NET=	7.66E-35
TABLE: H(CO)	GAIN=	4.16E-05	LOSS=	1.93E-10	NET=	4.16E-05
TABLE: H(CO)	GAIN=	1.91E-28	LOSS=	1.10E-32	NET=	1.91E-28
TABLE: H(CO)	GAIN=	1.25E-28	LOSS=	6.18E-42	NET=	1.35E-28
TABLE: H(CO)	GAIN=	5.55E-29	LOSS=	1.10E-32	NET=	5.55E-29
TABLE: H(CO)	GAIN=	2.99E-23	LOSS=	1.63E-47	NET=	2.99E-23
TABLE: H(CO)	GAIN=	4.39E-03	LOSS=	2.89E-04	NET=	4.10E-03

Best Available Copy

TABLE XX (Continued)

SPECIES: HFC1)

U-M (ING):	GAIN=	7.20E-03	LOSS=	3.13E-15	NET=	7.20E-03
V-T(TOT):	GAIN=	8.30E-04	LOSS=	3.96E-04	NET=	4.34E-04
H:	GAIN=	7.30E-29	LOSS=	3.60E-29	NET=	3.70E-29
CL:	GAIN=	1.81E-04	LOSS=	1.34E-04	NET=	4.66E-05
H2:	GAIN=	4.26E-36	LOSS=	1.58E-36	NET=	2.68E-36
HCL:	GAIN=	6.90E-05	LOSS=	5.12E-05	NET=	1.78E-05
HF:	GAIN=	3.03E-04	LOSS=	1.12E-04	NET=	1.91E-04
DF:	GAIN=	1.38E-04	LOSS=	5.11E-05	NET=	8.67E-05
CLF:	GAIN=	6.06E-07	LOSS=	2.25E-07	NET=	3.81E-07
V-V(TOT):	GAIN=	3.43E-03	LOSS=	3.90E-03	NET=	-4.70E-04
HF:	GAIN=	3.21E-03	LOSS=	3.31E-03	NET=	-6.00E-04
DF:	GAIN=	1.12E-04	LOSS=	4.15E-05	NET=	7.05E-05
H2:	GAIN=	1.75E-34	LOSS=	7.66E-35	NET=	9.84E-35
HCL:	GAIN=	1.12E-04	LOSS=	4.16E-05	NET=	7.04E-05
SCR, (TOT):	GAIN=	2.05E-29	LOSS=	7.55E-32	NET=	2.04E-29
H+HF:	GAIN=	2.05E-29	LOSS=	6.67E-41	NET=	2.05E-29
H+DF:	GAIN=	9.74E-34	LOSS=	7.55E-32	NET=	-7.45E-32
MIS, H+CLF:	GAIN=	0	LOSS=	0	NET=	0
TOTAL	GAIN=	1.14E-02	LOSS=	4.30E-03	NET=	7.13E-03

TABLE XX (Continued)

SPECIES: HF(2)

PUMPING:	GAIN=	1.10E-02	LØSS=	9.21E-09	NET=	1.10E-02
V-I(TØT):	GAIN=	2.47E-04	LØSS=	8.30E-04	NET=	-5.83E-04
H:	GAIN=	2.05E-29	LØSS=	7.30E-29	NET=	-5.25E-29
CL:	GAIN=	3.78E-05	LØSS=	1.81E-04	NET=	-1.43E-04
H2:	GAIN=	1.34E-36	LØSS=	4.26E-36	NET=	-2.92E-36
HCL:	GAIN=	1.44E-05	LØSS=	6.90E-05	NET=	-5.46E-05
HF:	GAIN=	9.51E-05	LØSS=	3.03E-04	NET=	-2.08E-04
DF:	GAIN=	4.33E-05	LØSS=	1.38E-04	NET=	-9.46E-05
CLF:	GAIN=	1.90E-07	LØSS=	6.06E-07	NET=	-4.16E-07
V-V(TØT):	GAIN=	1.91E-03	LØSS=	6.43E-03	NET=	-4.52E-03
HF:	GAIN=	1.84E-03	LØSS=	6.21E-03	NET=	-4.37E-03
DF:	GAIN=	3.51E-05	LØSS=	1.12E-04	NET=	-7.69E-05
H2:	GAIN=	6.07E-35	LØSS=	1.75E-34	NET=	-1.14E-34
HCL:	GAIN=	3.52E-05	LØSS=	1.12E-04	NET=	-7.68E-05
SCR,(TØT):	GAIN=	9.92E-31	LØSS=	1.07E-28	NET=	-1.06E-28
H+HF:	GAIN=	9.92E-31	LØSS=	1.07E-28	NET=	-1.06E-28
H+DF:	GAIN=	6.93E-40	LØSS=	1.52E-31	NET=	-1.52E-31
MIS,H+CLF:	GAIN=	0	LØSS=	0	NET=	0
TOTAL	GAIN=	1.31E-02	LØSS=	7.26E-03	NET=	5.89E-03

TABLE XX (Continued)

SPECIES: HF(3)

PUMPING:	GAIN=	1.61E-03	LOSS=	2.12E-04	NET=	1.40E-03
V-T(TOT):	GAIN=	1.08E-05	LOSS=	2.47E-04	NET=	-2.36E-04
H:	GAIN=	1.71E-30	LOSS=	2.05E-29	NET=	-1.88E-29
CL:	GAIN=	1.39E-06	LOSS=	3.78E-05	NET=	-3.64E-05
H2:	GAIN=	6.57E-38	LOSS=	1.34E-36	NET=	-1.27E-36
HCL:	GAIN=	5.33E-07	LOSS=	1.44E-05	NET=	-1.39E-05
HF:	GAIN=	4.68E-06	LOSS=	9.51E-05	NET=	-9.04E-05
DF:	GAIN=	2.13E-06	LOSS=	4.33E-05	NET=	-4.11E-05
CLF:	GAIN=	9.36E-09	LOSS=	1.90E-07	NET=	-1.81E-07
V-V(TOT):	GAIN=	3.31E-03	LOSS=	8.38E-04	NET=	2.47E-03
HF:	GAIN=	3.30E-03	LOSS=	7.68E-04	NET=	2.53E-03
DF:	GAIN=	1.74E-06	LOSS=	3.51E-05	NET=	-3.34E-05
H2:	GAIN=	2.71E-36	LOSS=	6.07E-35	NET=	-5.80E-35
HCL:	GAIN=	1.74E-06	LOSS=	3.52E-05	NET=	-3.35E-05
SCR.(TOT):	GAIN=	6.67E-41	LOSS=	4.74E-29	NET=	-4.74E-29
H+HF:	GAIN=	6.67E-41	LOSS=	4.73E-29	NET=	-4.73E-29
H+DF:	GAIN=	9.21E-46	LOSS=	4.25E-32	NET=	-4.25E-32
MIS,H+CLF:	GAIN=	0	LOSS=	0	NET=	0
TOTAL	GAIN=	4.92E-03	LOSS=	1.30E-03	NET=	3.62E-03

TABLE XX: (Concluded)

SPECIES: HF(4)

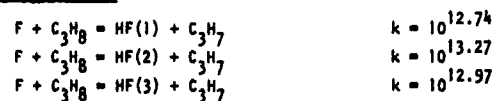
PUMPING:	GAIN=	2.51E-36	LOSS=	4.75E-31	NET=	-4.75E-31
V-T(TOT):	GAIN=	7.16E-10	LOSS=	1.08E-05	NET=	-1.08E-05
H:	GAIN=	1.13E-34	LOSS=	1.71E-30	NET=	-1.71E-30
CL:	GAIN=	9.24E-11	LOSS=	1.39E-06	NET=	-1.39E-06
H2:	GAIN=	4.35E-42	LOSS=	6.57E-38	NET=	-6.57E-38
HCL:	GAIN=	3.53E-11	LOSS=	5.33E-07	NET=	-5.33E-07
HF:	GAIN=	3.10E-10	LOSS=	4.68E-06	NET=	-4.68E-06
DF:	GAIN=	1.41E-10	LOSS=	2.13E-06	NET=	-2.13E-06
CLF:	GAIN=	6.20E-13	LOSS=	9.36E-09	NET=	-9.36E-09
V-V(TOT):	GAIN=	4.48E-04	LOSS=	2.42E-05	NET=	4.24E-04
HF:	GAIN=	4.48E-04	LOSS=	2.07E-05	NET=	4.27E-04
DF:	GAIN=	5.27E-09	LOSS=	1.73E-06	NET=	-1.72E-06
H2:	GAIN=	0	LOSS=	2.71E-36	NET=	-2.71E-36
HCL:	GAIN=	4.36E-09	LOSS=	1.73E-06	NET=	-1.73E-06
SCR, (TOT):	GAIN=	4.18E-40	LOSS=	2.54E-30	NET=	-2.54E-30
H+HF:	GAIN=	4.18E-40	LOSS=	2.54E-30	NET=	-2.54E-30
H+DF:	GAIN=	2.25E-51	LOSS=	1.57E-33	NET=	-1.57E-33
MIS, H+CLF:	GAIN=	0	LOSS=	0	NET=	0
TOTAL	GAIN=	4.48E-04	LOSS=	3.50E-05	NET=	4.13E-04

TABLE XXI. REVISED RATE CONSTANTS USED IN SERIES II
KINETIC CALCULATIONS*

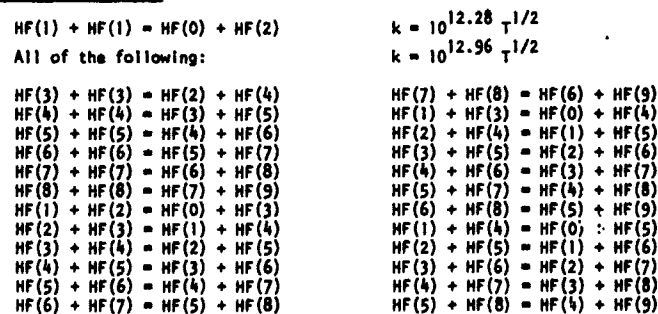
Reverse of F + H₂ Pumping:



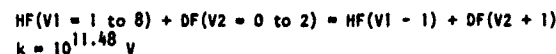
F + C₃H₈ Pumping:



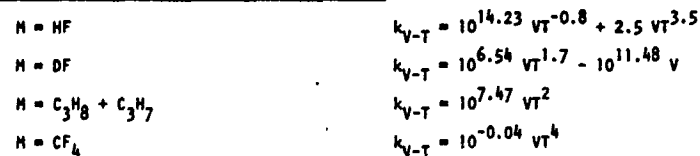
HF - HF V-V Processes:



HF - DF V-V Processes:



HF(V) + M = HF(V - 1) + M V - T, R Processes:



*Other rate constants were as listed in Table XIII. Reactions are written in exothermic direction. Rate constants are in units of (mole/cc)⁻¹ sec⁻¹.

TABLE XXII. RATE CONSTANTS USED IN SERIES III
KINETIC CALCULATIONS*

F + H₂ Pumping and Reverse:

$F + H_2 = HF(1) + H$	$k = 10^{13.41} \exp(-1600/RT)$
$F + H_2 = HF(2) + H$	$k = 10^{13.94} \exp(-1600/RT)$
$F + H_2 = HF(3) + H$	$k = 10^{13.64} \exp(-1600/RT)$
$H + HF(4) = H_2(0) + F$	$k = 10^{12.57} \exp(-510/RT)$
$H + HF(4) = H_2(1) + F$	$k = 10^{12.57} \exp(-510/RT)$
$H + HF(5) = H_2(0) + F$	$k = 10^{12.60} \exp(-510/RT)$
$H + HF(5) = H_2(1) + F$	$k = 10^{12.85} \exp(-510/RT)$
$H + HF(6) = H_2(0) + F$	$k = 10^{12.60} \exp(-560/RT)$
$H + HF(6) = H_2(1) + F$	$k = 10^{12.60} \exp(-560/RT)$
$H + HF(6) = H_2(2) + F$	$k = 10^{13.04} \exp(-560/RT)$
$H + HF(7) = H_2(0) + F$	$k = 10^{12.60} \exp(-560/RT)$
$H + HF(7) = H_2(1) + F$	$k = 10^{12.90} \exp(-560/RT)$
$H + HF(7) = H_2(2) + F$	$k = 10^{13.08} \exp(-560/RT)$

F + HBr Pumping:

$F + HBr = HF(0) + Br$	$k = 10^{12.95} \exp(-1000/RT)$
$F + HBr = HF(1) + Br$	$k = 10^{13.45} \exp(-1000/RT)$
$F + HBr = HF(2) + Br$	$k = 10^{13.65} \exp(-1000/RT)$
$F + HBr = HF(3) + Br$	$k = 10^{13.61} \exp(-1000/RT)$
$F + HBr = HF(4) + Br$	$k = 10^{13.48} \exp(-1000/RT)$

H + F₂ Pumping:

$H + F_2 = HF(0) + F$	$k = 10^{12.04} \exp(-2400/RT)$
$H + F_2 = HF(1) + F$	$k = 10^{12.40} \exp(-2400/RT)$
$H + F_2 = HF(2) + F$	$k = 10^{12.54} \exp(-2400/RT)$
$H + F_2 = HF(3) + F$	$k = 10^{12.56} \exp(-2400/RT)$
$H + F_2 = HF(4) + F$	$k = 10^{13.20} \exp(-2400/RT)$
$H + F_2 = HF(5) + F$	$k = 10^{13.56} \exp(-2400/RT)$
$H + F_2 = HF(6) + F$	$k = 10^{13.68} \exp(-2400/RT)$
$H + F_2 = HF(7) + F$	$k = 10^{12.74} \exp(-2400/RT)$
$H + F_2 = HF(8) + F$	$k = 10^{12.40} \exp(-2400/RT)$

HF(V) + H = HF(V') + H V - T, R Processes:

For V = 1 to 8:

$M = HF, \Delta V = -1$	$k = V (10^{14.48} T^{-1} + 10^{4.53} T^{2.26})$
$M = H_2, \Delta V = -1$	$k = V (10^{4.20} T^{2.28})$
$M = H, \Delta V = -1 \text{ to } -V$	$k = 10^{13.26} \exp(-700/RT)$
$M = D, \Delta V = -1 \text{ to } -V$	$k = 10^{14.95} \exp(-700/RT)$
$M = F, \Delta V = -1 \text{ to } -V$	$k = V [10^{12.90} \exp(-1840/RT)]$
$M = HBr, \Delta V = -1$	$k = V (10^{13.65} T^{-1} + 10^{4.53} T^{2.26})$

DF(V) + H = DF(V-1) + H V - T, R Processes

$M = HF, F \text{ and } DF$	$k = 10^{12.00} \exp(-600/RT)$
$M = H \text{ and } D$	$k = 10^{12.70} \exp(-600/RT)$

TABLE XXII. (Continued)

H₂(V) + M = H(V-1) + M V ~ T, R Processes:

M = HF, DF, and F

$$k = 10^{-3.60} T^{-4.3}$$

M = H₂ and H

$$k = 10^{-2.00} T^{-4.3}$$

HF ~ HF V-V Processes:

$$\text{HF}(1) + \text{HF}(1) = \text{HF}(2) + \text{HF}(0)$$

$$k = 10^{15.90} T^{-1}$$

$$\left. \begin{array}{l} \text{HF}(2) + \text{HF}(1) = \text{HF}(3) + \text{HF}(0) \\ \text{HF}(2) + \text{HF}(2) = \text{HF}(3) + \text{HF}(1) \end{array} \right\}$$

$$k = 10^{16.50} T^{-1}$$

$$\left. \begin{array}{l} \text{HF}(3) + \text{HF}(1) = \text{HF}(4) + \text{HF}(0) \\ \text{HF}(3) + \text{HF}(2) = \text{HF}(4) + \text{HF}(1) \\ \text{HF}(3) + \text{HF}(3) = \text{HF}(4) + \text{HF}(2) \end{array} \right\}$$

$$k = 10^{16.85} T^{-1}$$

$$\left. \begin{array}{l} \text{HF}(4) + \text{HF}(1) = \text{HF}(5) + \text{HF}(0) \\ \text{HF}(4) + \text{HF}(2) = \text{HF}(5) + \text{HF}(1) \\ \text{HF}(4) + \text{HF}(3) = \text{HF}(5) + \text{HF}(2) \\ \text{HF}(4) + \text{HF}(4) = \text{HF}(5) + \text{HF}(3) \end{array} \right\}$$

$$k = 10^{17.10} T^{-1}$$

$$\left. \begin{array}{l} \text{HF}(5) + \text{HF}(1) = \text{HF}(6) + \text{HF}(0) \\ \text{HF}(5) + \text{HF}(2) = \text{HF}(6) + \text{HF}(1) \\ \text{HF}(5) + \text{HF}(3) = \text{HF}(6) + \text{HF}(2) \\ \text{HF}(5) + \text{HF}(4) = \text{HF}(6) + \text{HF}(3) \\ \text{HF}(5) + \text{HF}(5) = \text{HF}(6) + \text{HF}(4) \end{array} \right\}$$

$$k = 10^{17.26} T^{-1}$$

$$\left. \begin{array}{l} \text{HF}(6) + \text{HF}(1) = \text{HF}(7) + \text{HF}(0) \\ \text{HF}(6) + \text{HF}(2) = \text{HF}(7) + \text{HF}(1) \\ \text{HF}(6) + \text{HF}(3) = \text{HF}(7) + \text{HF}(2) \\ \text{HF}(6) + \text{HF}(4) = \text{HF}(7) + \text{HF}(3) \\ \text{HF}(6) + \text{HF}(5) = \text{HF}(7) + \text{HF}(4) \\ \text{HF}(6) + \text{HF}(6) = \text{HF}(7) + \text{HF}(5) \end{array} \right\}$$

$$k = 10^{17.42} T^{-1}$$

$$\left. \begin{array}{l} \text{HF}(7) + \text{HF}(1) = \text{HF}(8) + \text{HF}(0) \\ \text{HF}(7) + \text{HF}(2) = \text{HF}(8) + \text{HF}(1) \\ \text{HF}(7) + \text{HF}(3) = \text{HF}(8) + \text{HF}(2) \\ \text{HF}(7) + \text{HF}(4) = \text{HF}(8) + \text{HF}(3) \\ \text{HF}(7) + \text{HF}(5) = \text{HF}(8) + \text{HF}(4) \\ \text{HF}(7) + \text{HF}(6) = \text{HF}(8) + \text{HF}(5) \\ \text{HF}(7) + \text{HF}(7) = \text{HF}(8) + \text{HF}(6) \end{array} \right\}$$

$$k = 10^{17.48} T^{-1}$$

$$\left. \begin{array}{l} \text{HF}(8) + \text{HF}(1) = \text{HF}(9) + \text{HF}(0) \\ \text{HF}(8) + \text{HF}(2) = \text{HF}(9) + \text{HF}(1) \\ \text{HF}(8) + \text{HF}(3) = \text{HF}(9) + \text{HF}(2) \\ \text{HF}(8) + \text{HF}(4) = \text{HF}(9) + \text{HF}(3) \\ \text{HF}(8) + \text{HF}(5) = \text{HF}(9) + \text{HF}(4) \\ \text{HF}(8) + \text{HF}(6) = \text{HF}(9) + \text{HF}(5) \\ \text{HF}(8) + \text{HF}(7) = \text{HF}(9) + \text{HF}(6) \\ \text{HF}(8) + \text{HF}(8) = \text{HF}(9) + \text{HF}(7) \end{array} \right\}$$

$$k = 10^{17.53} T^{-1}$$

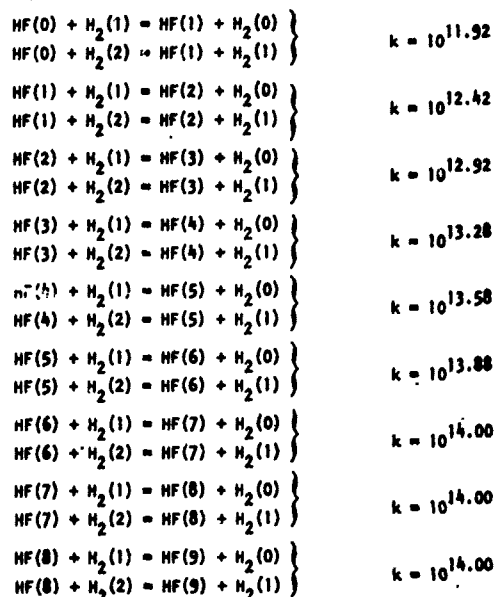
HF ~ DF V-V Processes:

$$\left. \begin{array}{l} \text{HF}(1) + \text{DF}(0) = \text{HF}(0) + \text{DF}(1) \\ \text{HF}(1) + \text{DF}(1) = \text{HF}(0) + \text{DF}(2) \\ \text{HF}(2) + \text{DF}(0) = \text{HF}(1) + \text{DF}(1) \\ \text{HF}(2) + \text{DF}(1) = \text{HF}(1) + \text{DF}(2) \\ \text{HF}(3) + \text{DF}(0) = \text{HF}(2) + \text{DF}(1) \\ \text{HF}(3) + \text{DF}(1) = \text{HF}(2) + \text{DF}(2) \\ \text{HF}(4) + \text{DF}(0) = \text{HF}(3) + \text{DF}(1) \\ \text{HF}(4) + \text{DF}(1) = \text{HF}(3) + \text{DF}(2) \\ \text{HF}(5) + \text{DF}(0) = \text{HF}(4) + \text{DF}(1) \\ \text{HF}(5) + \text{DF}(1) = \text{HF}(4) + \text{DF}(2) \\ \text{HF}(6) + \text{DF}(0) = \text{HF}(5) + \text{DF}(1) \\ \text{HF}(6) + \text{DF}(1) = \text{HF}(5) + \text{DF}(2) \\ \text{HF}(7) + \text{DF}(0) = \text{HF}(6) + \text{DF}(1) \\ \text{HF}(7) + \text{DF}(1) = \text{HF}(6) + \text{DF}(2) \\ \text{HF}(8) + \text{DF}(0) = \text{HF}(7) + \text{DF}(1) \\ \text{HF}(8) + \text{DF}(1) = \text{HF}(7) + \text{DF}(2) \end{array} \right\}$$

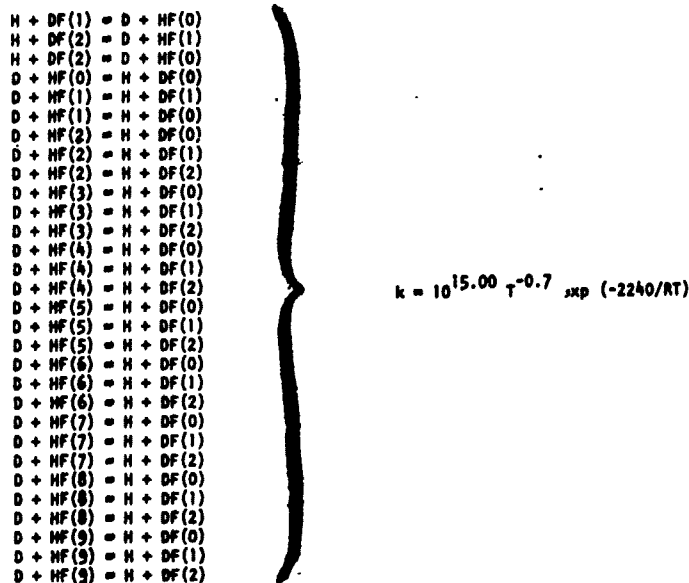
$$k = V (10^{17.00} T^{-2} + 10^{8.79} T)$$

TABLE XXII. (Concluded)

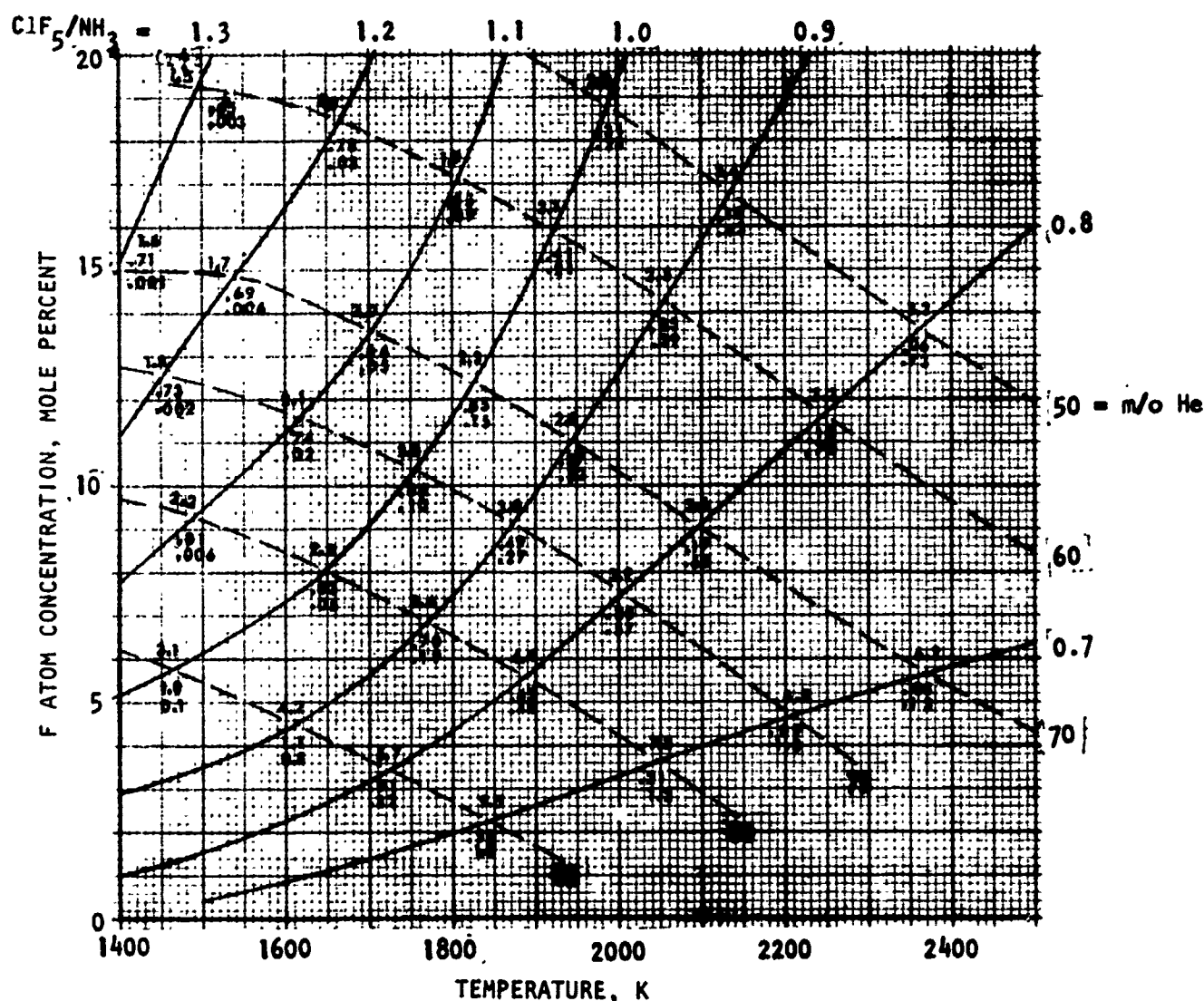
HF - H₂ V-V Processes:



Isotope Exchange Reactions:



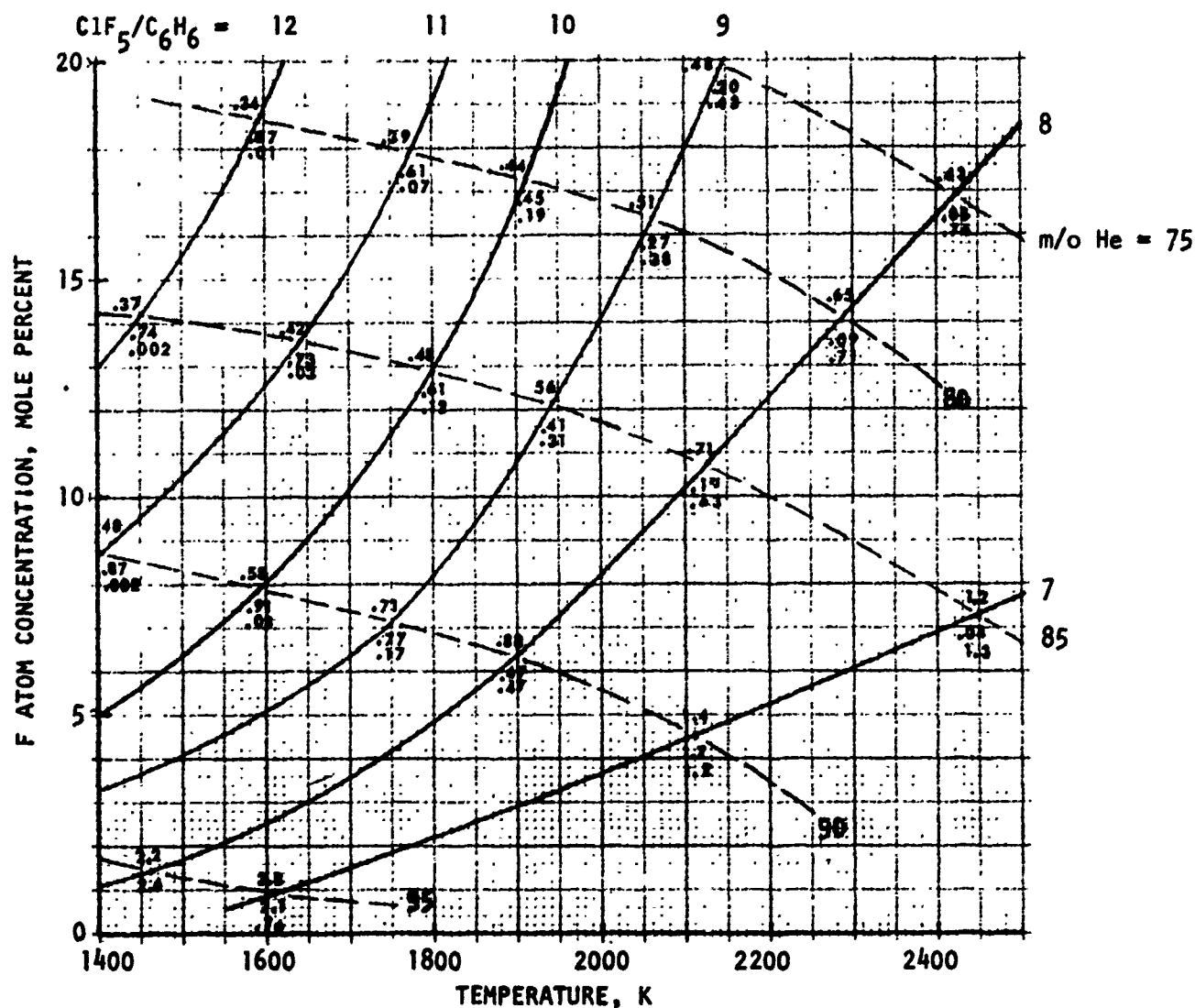
*Reactions are written in exothermic direction; rate constants are in units of (mole/cc)⁻¹ sec⁻¹.



NOTE

Solid lines are fixed ClF_5/NH_3 molar ratios; dashed lines are fixed m/o He. Numbers at intersections denote molar ratios: HF/F, ClF/F, and Cl/F (top to bottom, respectively)

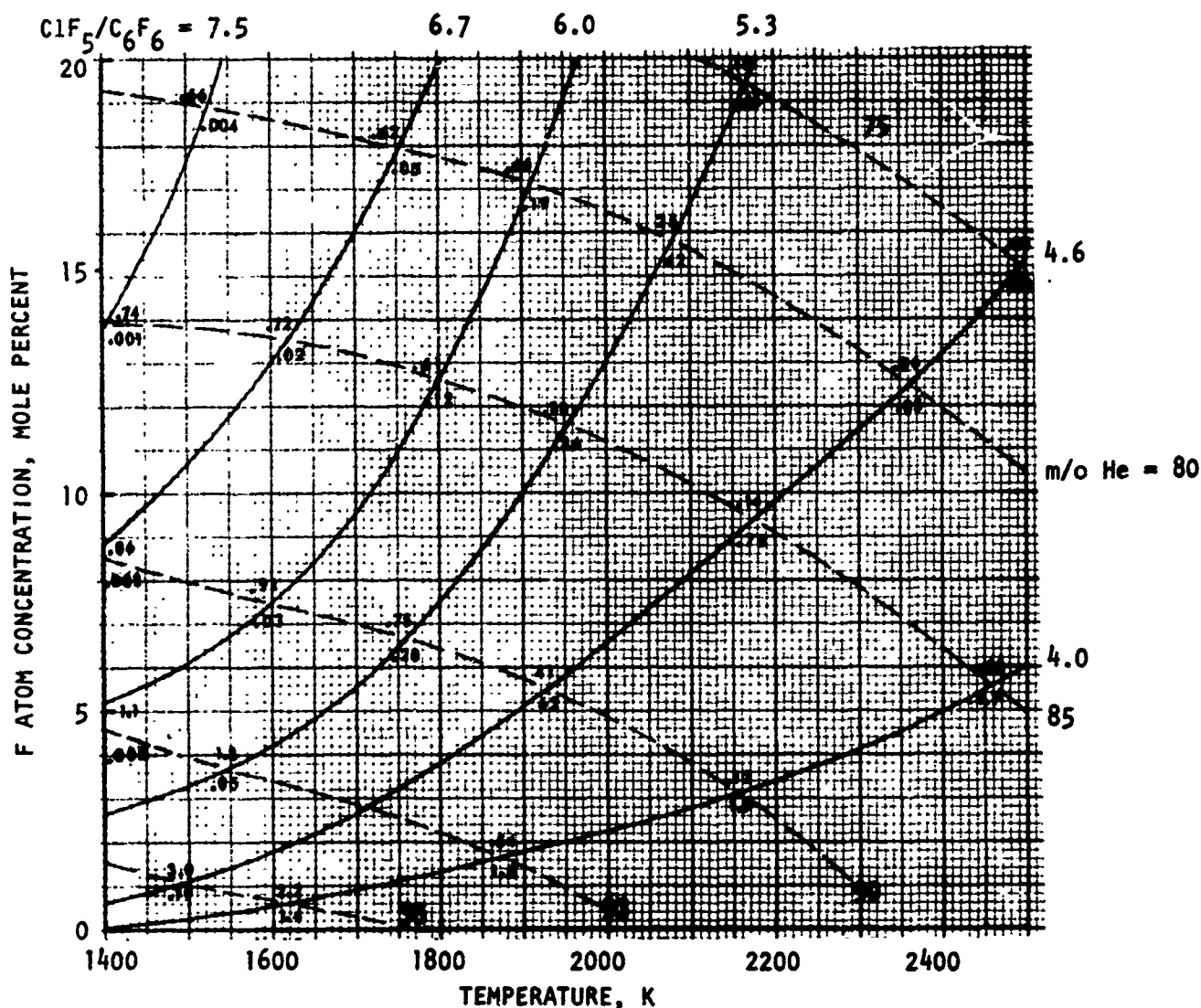
Figure 4. $\text{ClF}_5(l) - \text{NH}_3(l) - \text{He}(g)$ System (F Atom Concentration and Temperature as a Function of Reactant Ratios)



NOTE:

Solid lines are fixed $\text{ClF}_5/\text{C}_6\text{H}_6$ molar ratios; dashed lines are fixed m/o He. Numbers at intersections denote molar ratios: HF/F, ClF/F, and Cl/F (top to bottom, respectively)

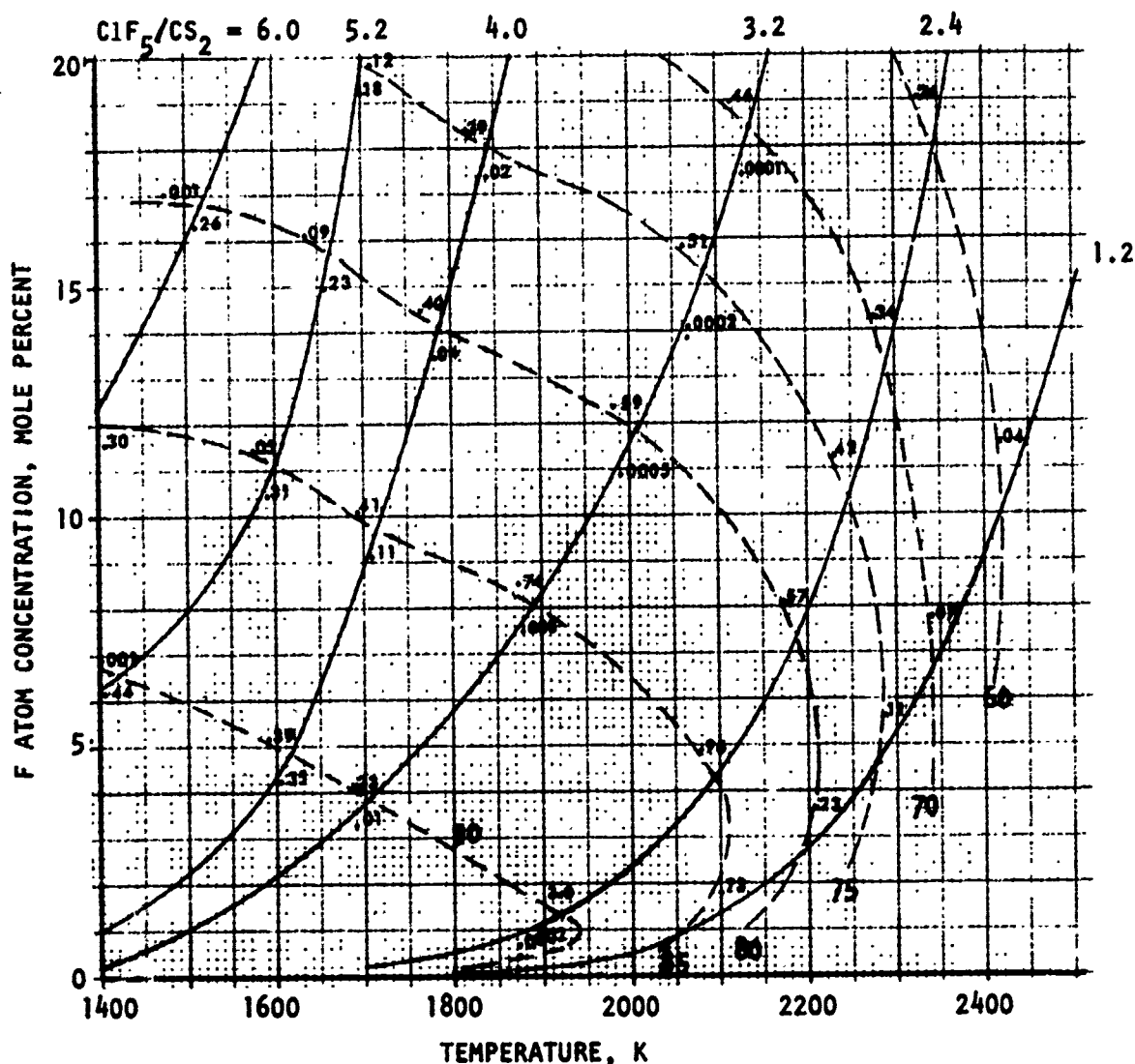
Figure 5. $\text{ClF}_5(1) - \text{C}_6\text{H}_6(1) - \text{He}$ System (F Atom Concentration and Temperature as a Function of Reactant Ratios)



NOTE:

Solid lines are fixed $\text{ClF}_5/\text{C}_6\text{F}_6$ molar ratios; dashed lines are fixed $m/o \text{ He}$. Numbers at intersections denote molar ratios: ClF/F and Cl/F (top and bottom, respectively)

Figure 6. $\text{ClF}_5(1) - \text{C}_6\text{F}_6(1) - \text{He}(g)$ System (F Atom Concentration and Temperature as a Function of Reactant Ratios)



NOTE.

Solid lines are fixed ClF /CS molar ratios; dashed lines are fixed m/o He. Numbers at intersections denote molar ratios: SF₄/F and SF₆/F (top and bottom, respectively)

Figure 7. ClF₅(l) - CS₂(l) - He(g) System (F Atom Concentration and Temperature as a Function of Reactant Ratios)

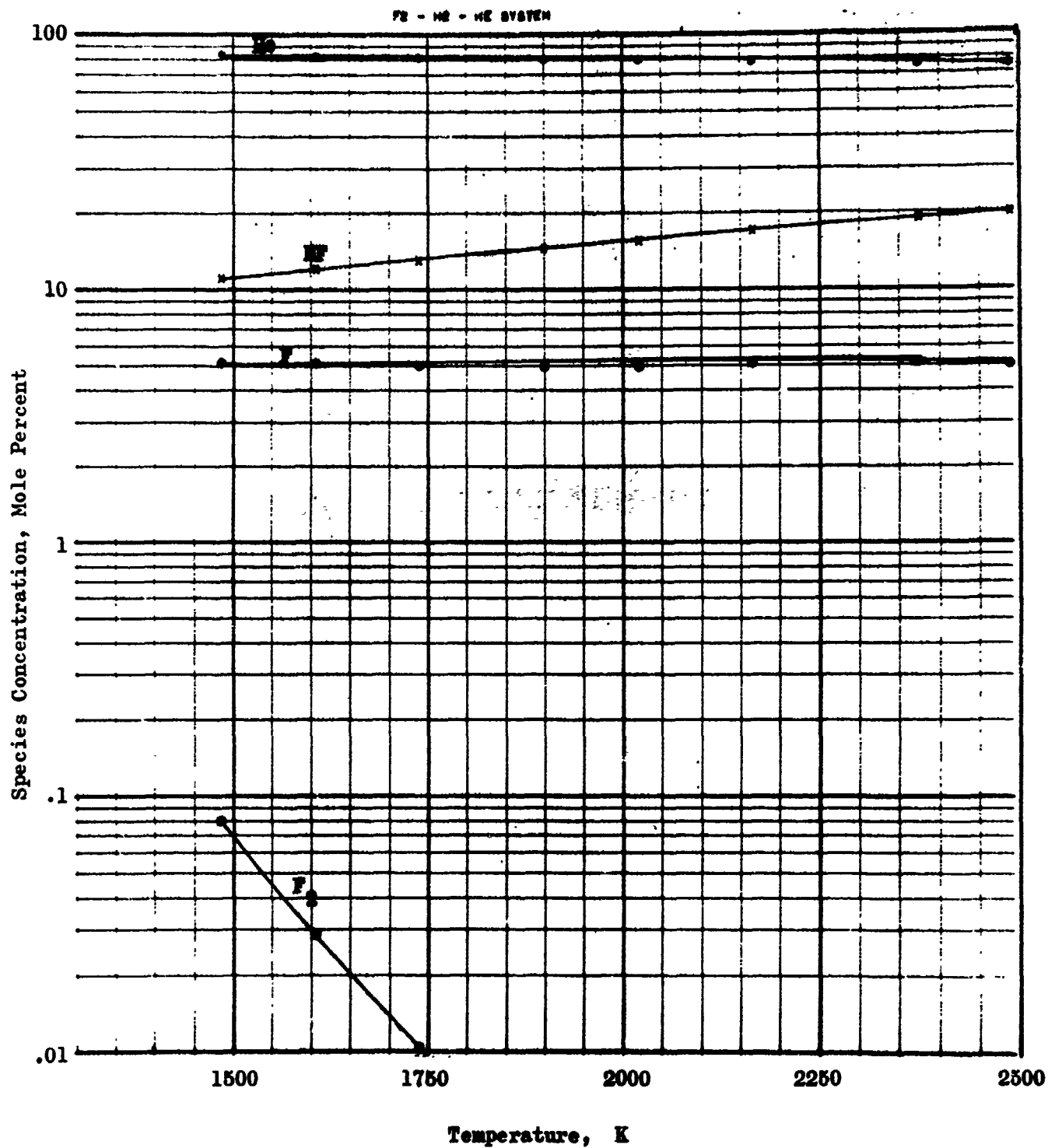


Figure 8. F₂-H₂-He System; Product Composition vs Temperature at 5 Mole Percent F Atom (30 psia)

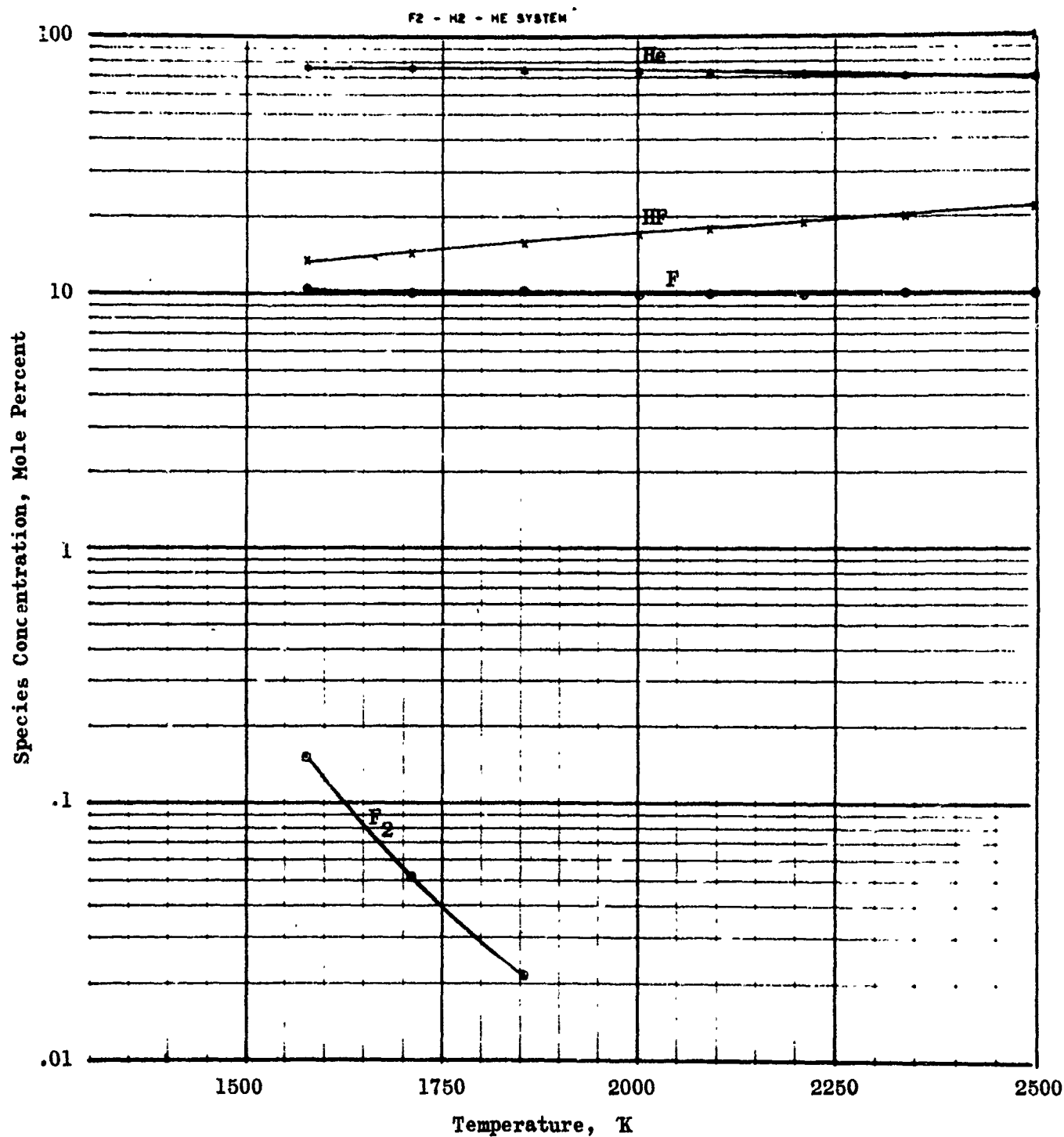


Figure 9. F₂-H₂-He System; Product Composition vs Temperature at 10 Mole Percent F Atoms (30 psia)

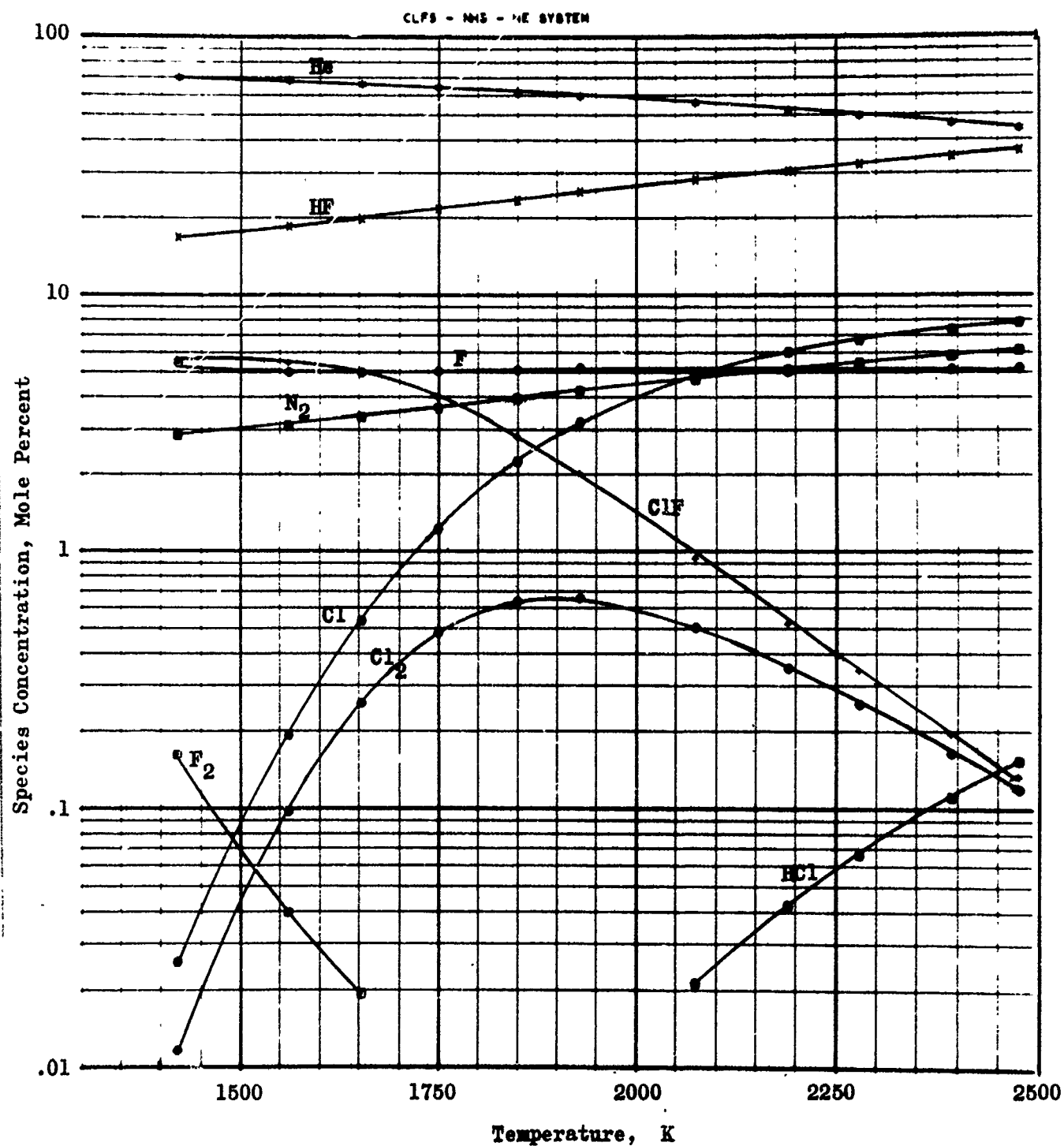


Figure 10. ClF₅-NH₃-He System; Product Composition vs Temperature at 5 Mole Percent F Atom (30 psia)

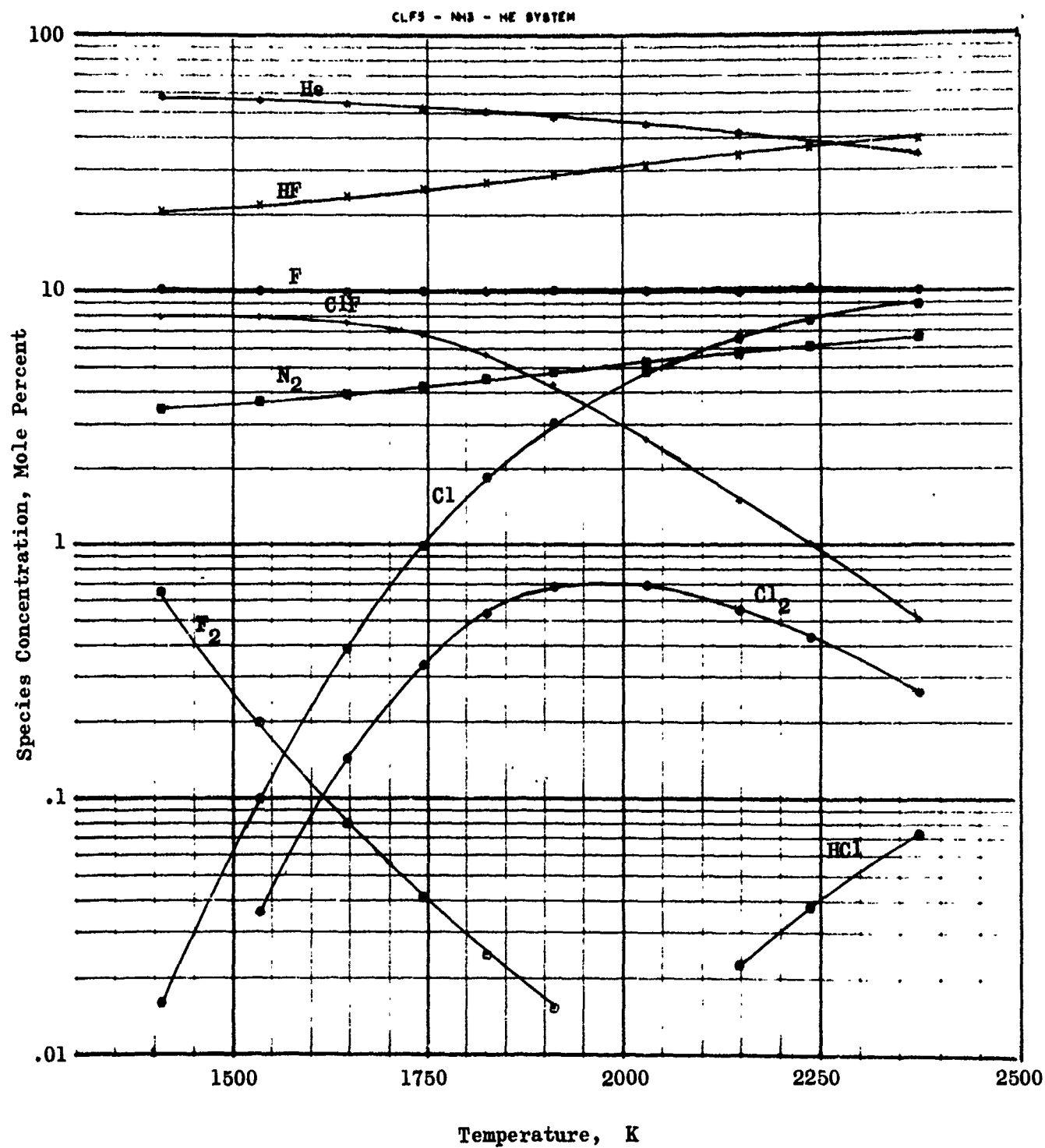


Figure 11. ClF₃-NH₃-He System; Product Composition vs Temperature at 10 Mole Percent F Atoms (30 psia)

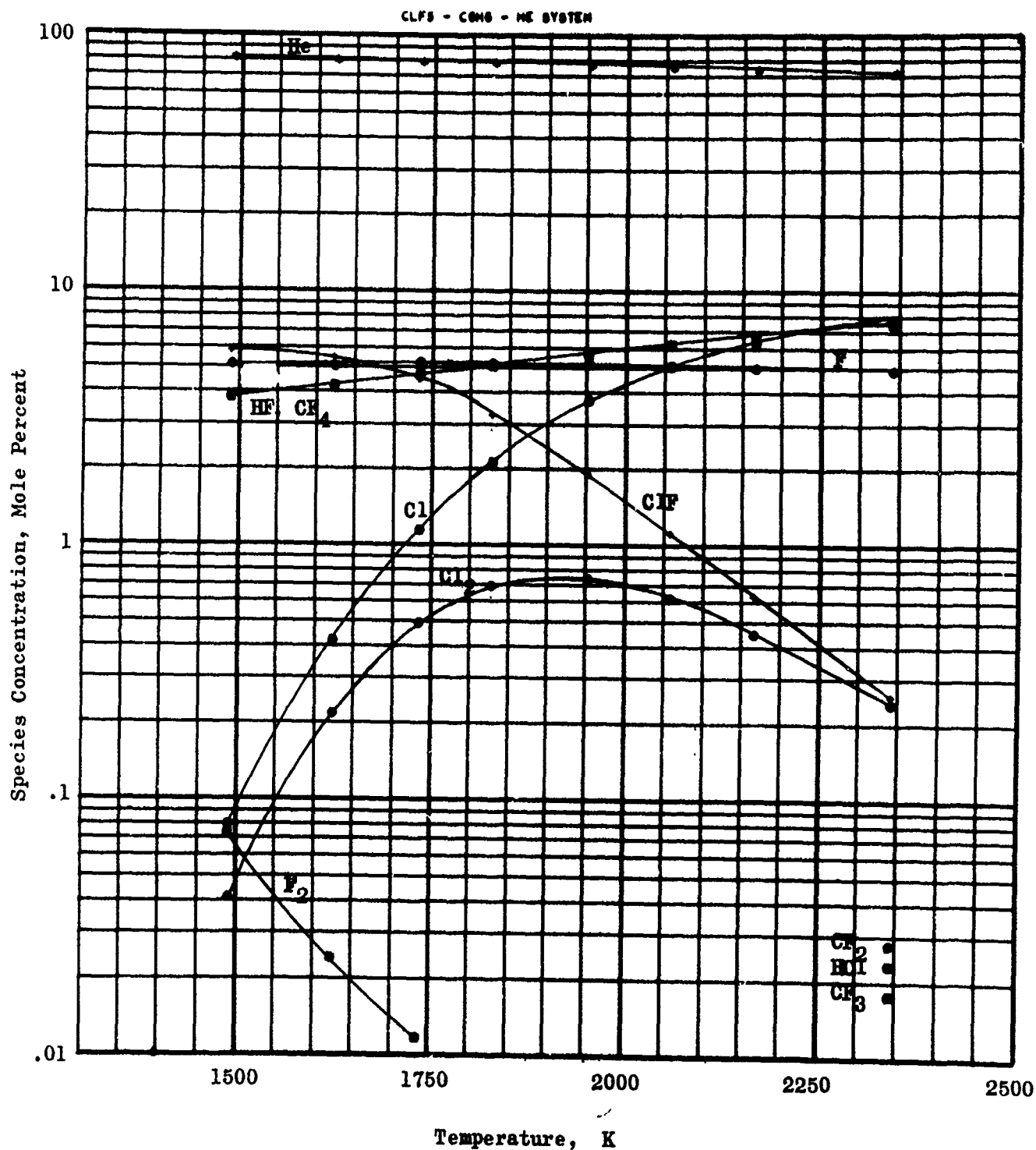


Figure 12. ClF₅-C₆H₆-He System; Product Composition vs Temperature at 5 Mole Percent F Atom (30 psia)

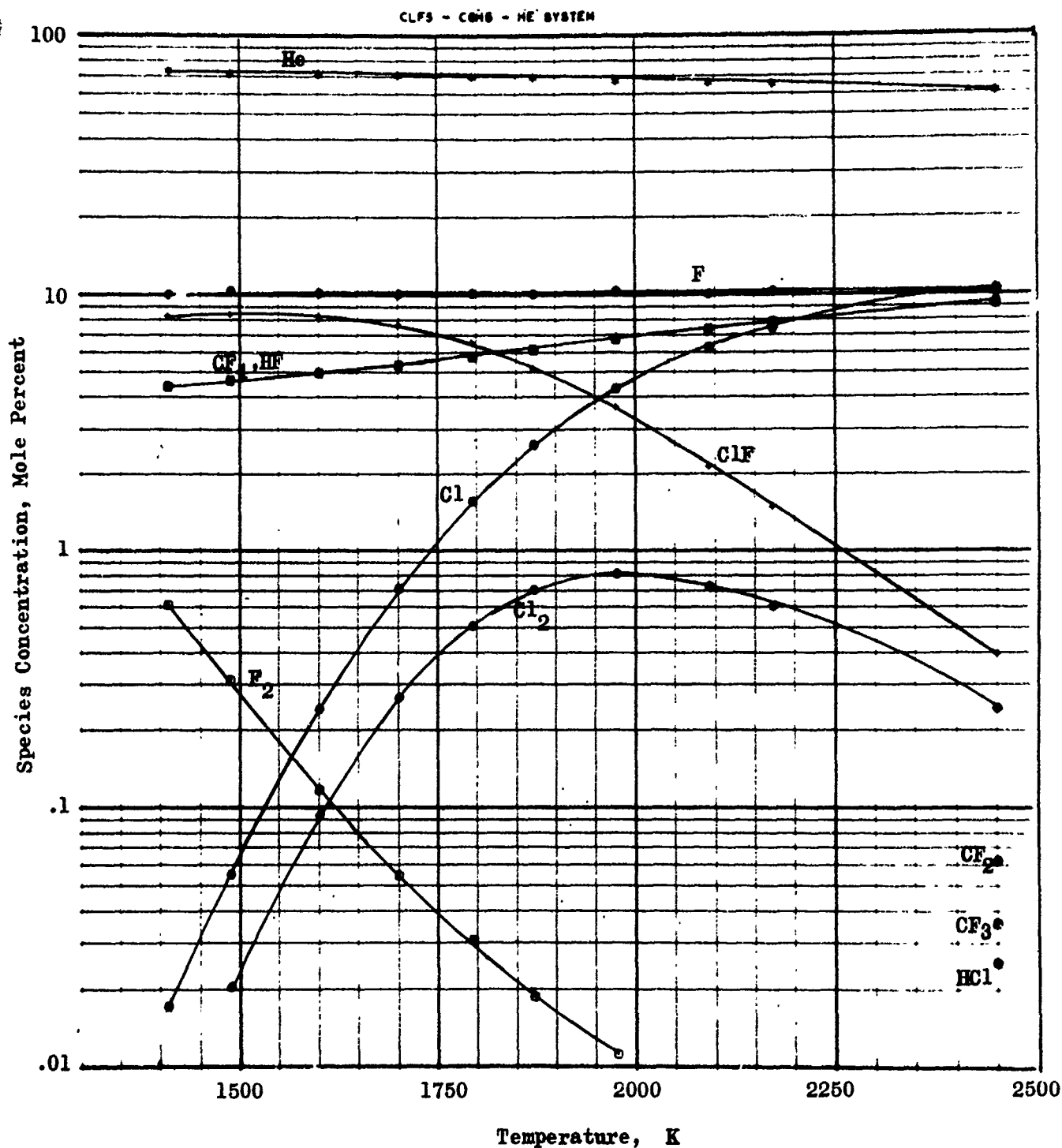


Figure 13. ClF₅-C₆H₆-He System; Product Composition vs Temperature at 10 Mole Percent F Atoms (30 psia)

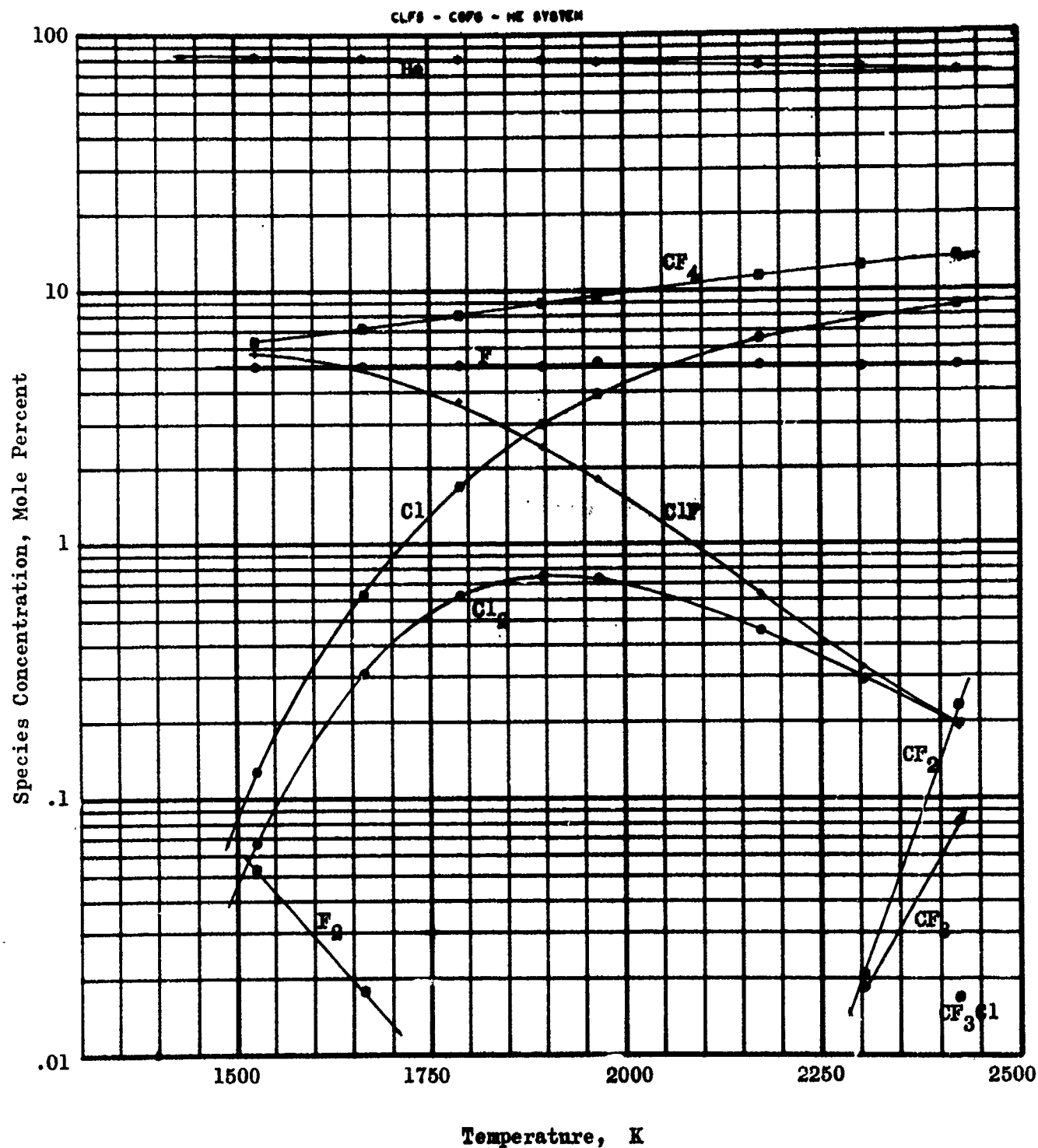


Figure 14. ClF₅-C₆F₆-He System; Product Composition vs Temperature at 5 Mole Percent F Atom (30 psia)

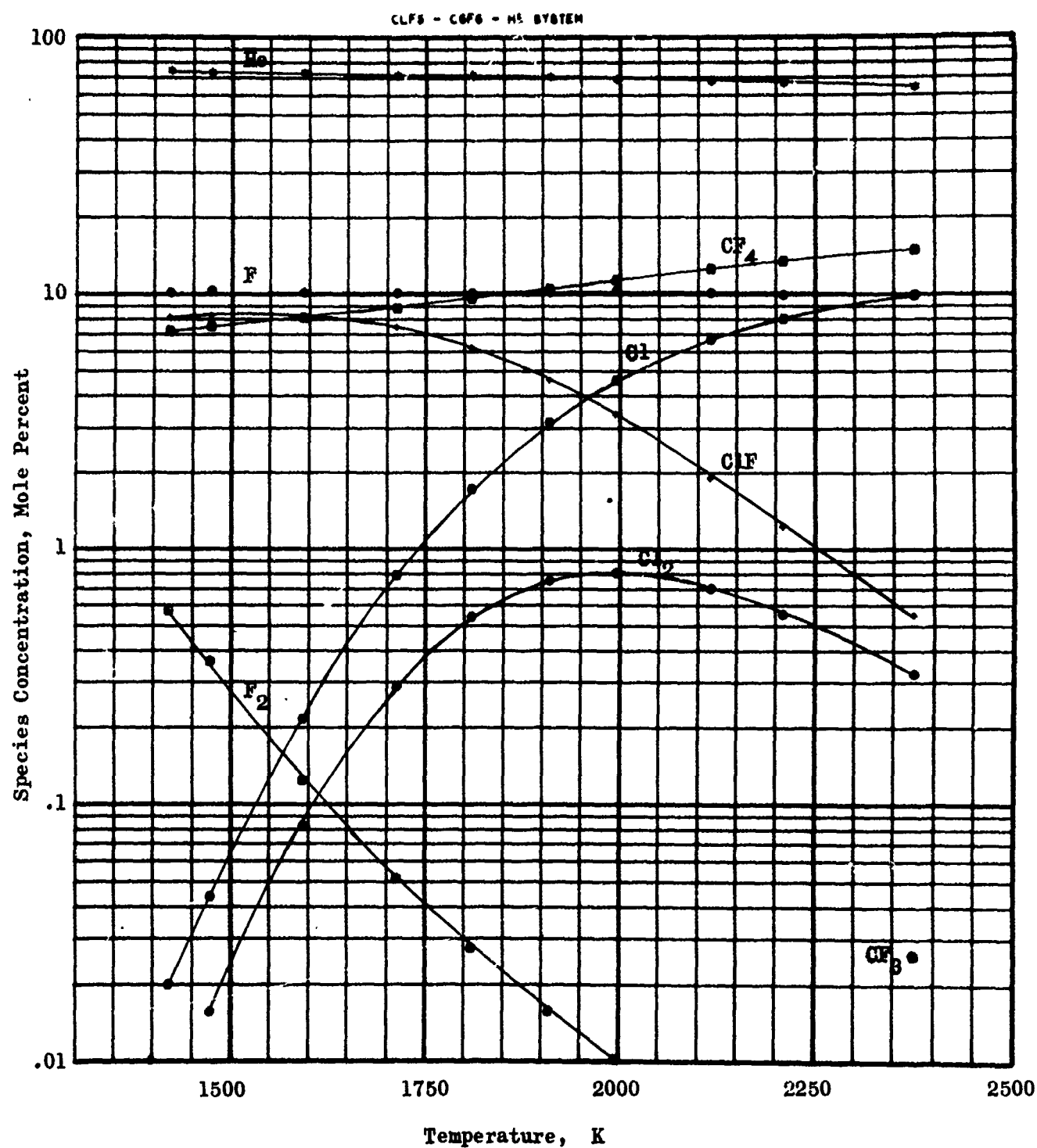


Figure 15. ClF₅ - C₆F₆ - He System; Product Composition versus Temperature at 10 Mole Percent F Atoms (30 psia)

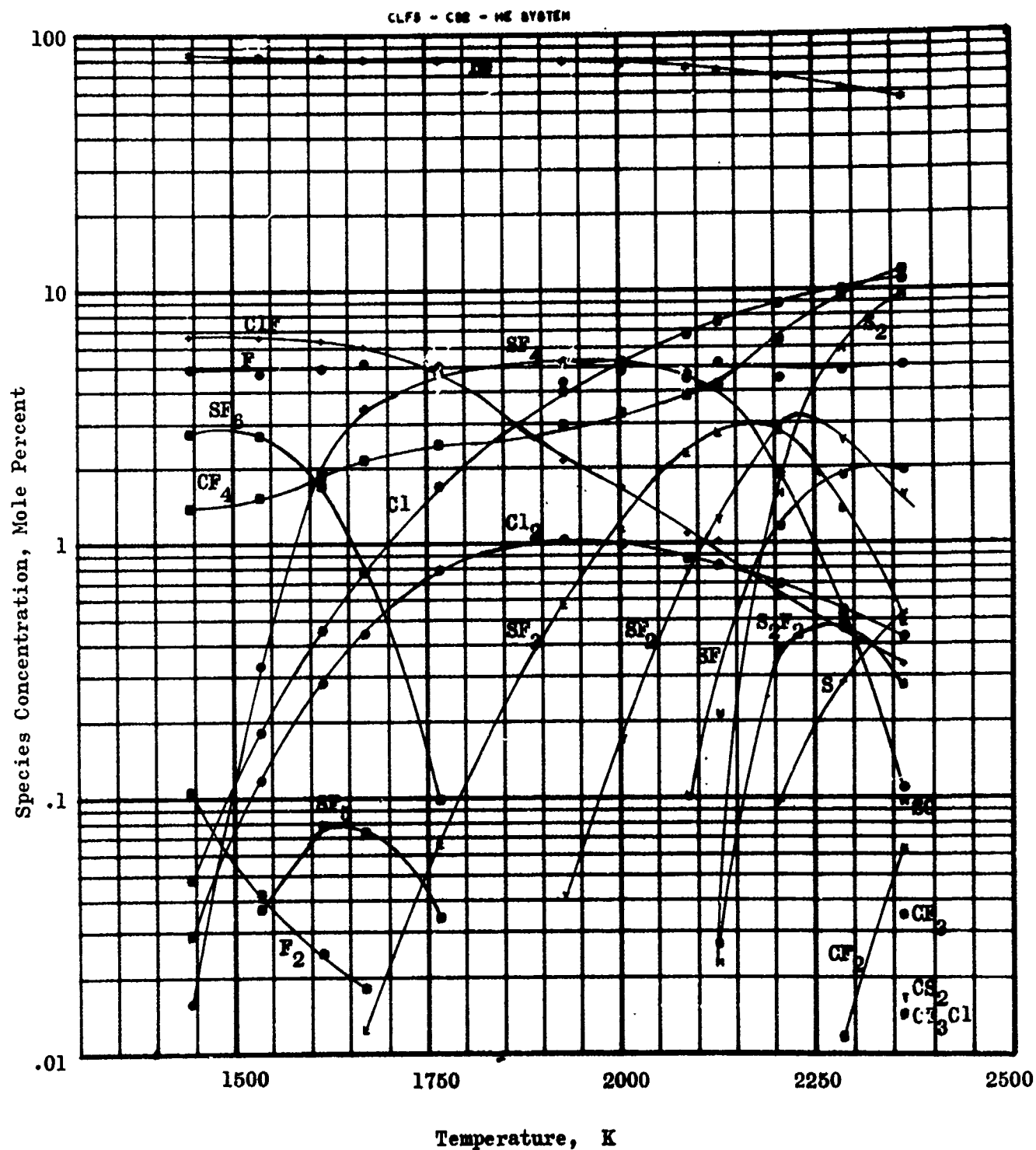


Figure 16. ClF₅-CS₂-He System; Product Composition vs Temperature at 5 Mole Percent F Atom (30 psia)

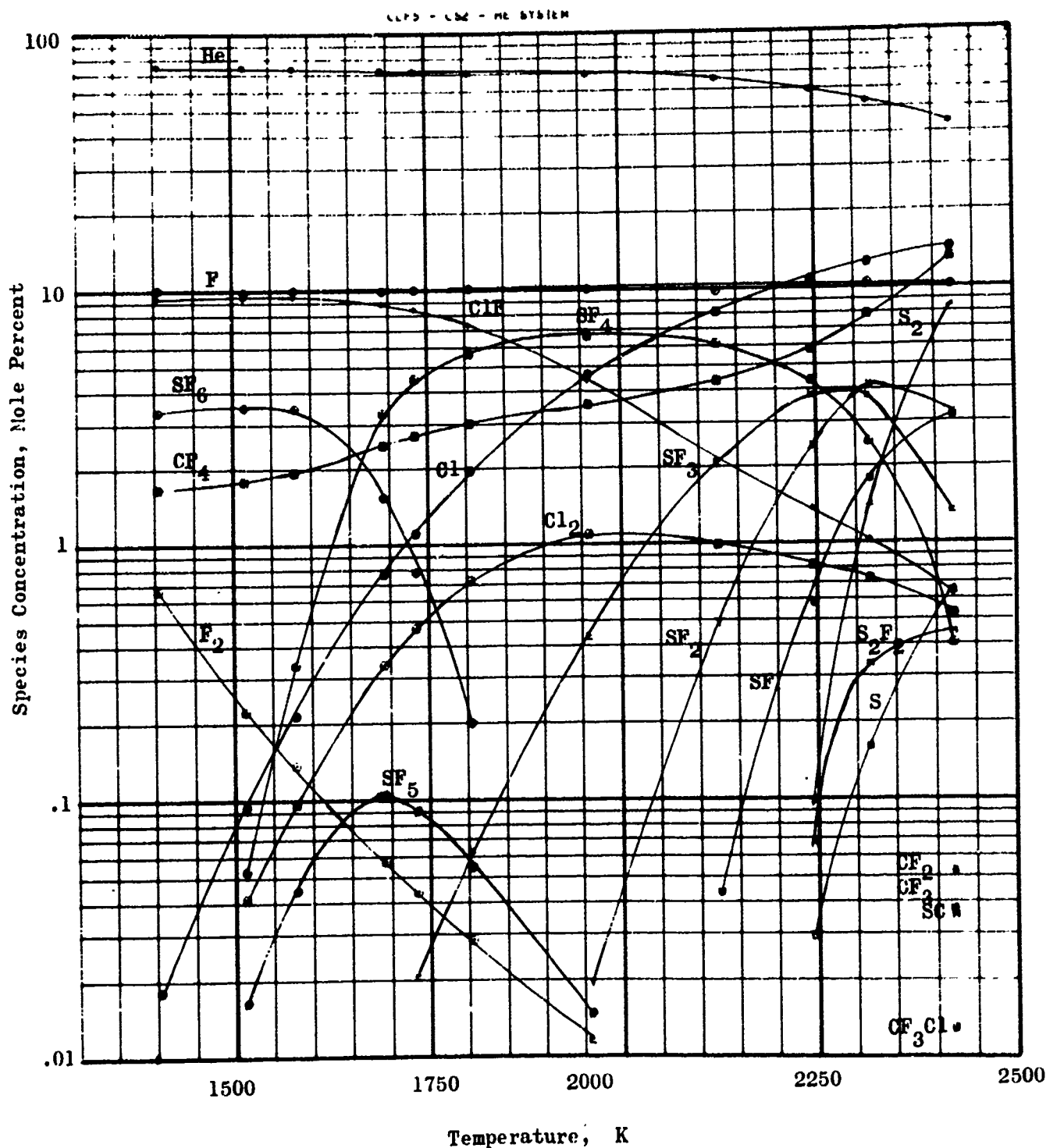


Figure 17. ClF₅-CS₂-He System; Product Composition vs Temperature at 10 Mole Percent F Atoms (30 psia), reproduced from Fig. 15 of Reference 8

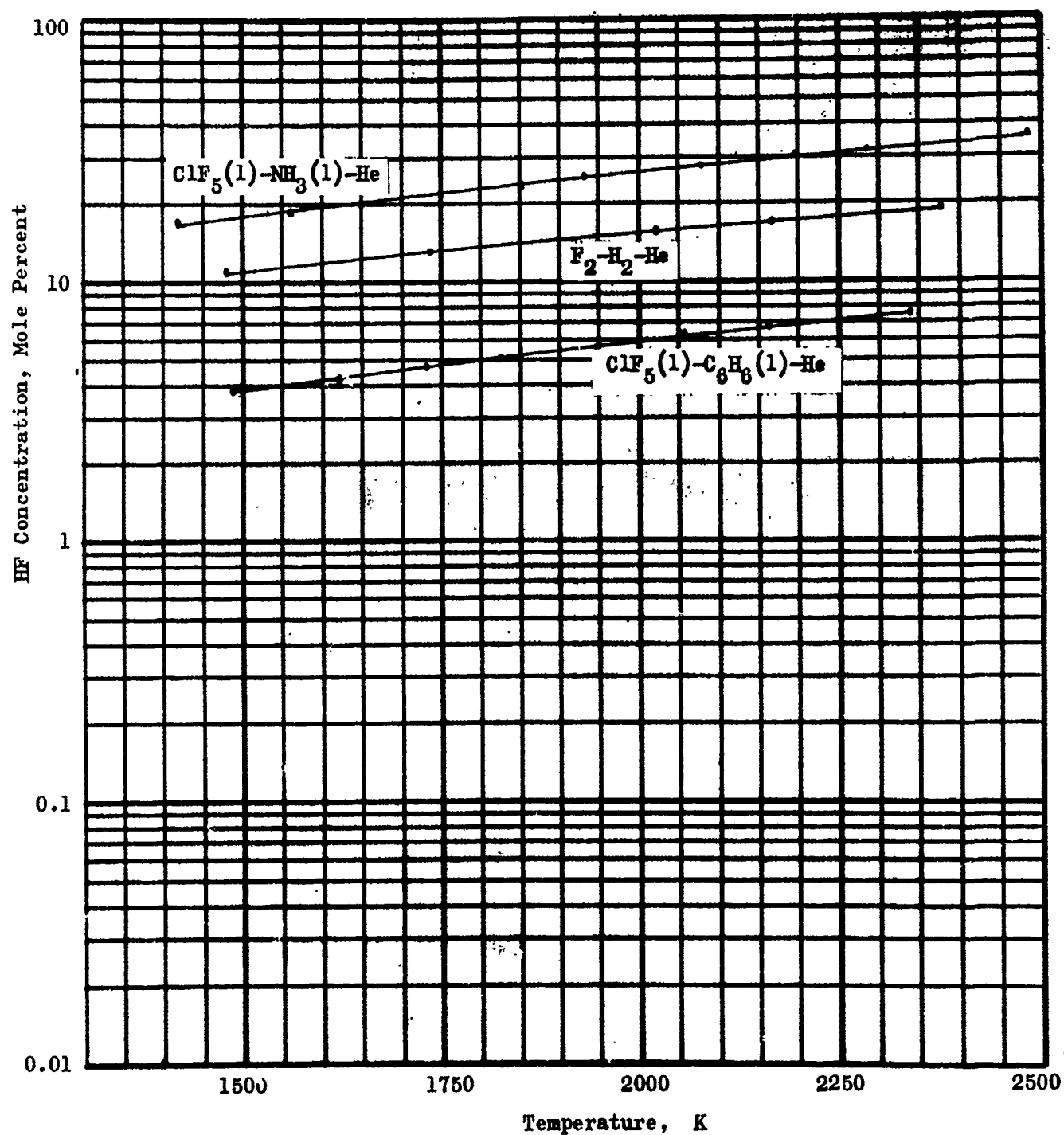


Figure 18. HF Concentration vs Temperature at 5 Mole Percent F Atoms (30 psia)

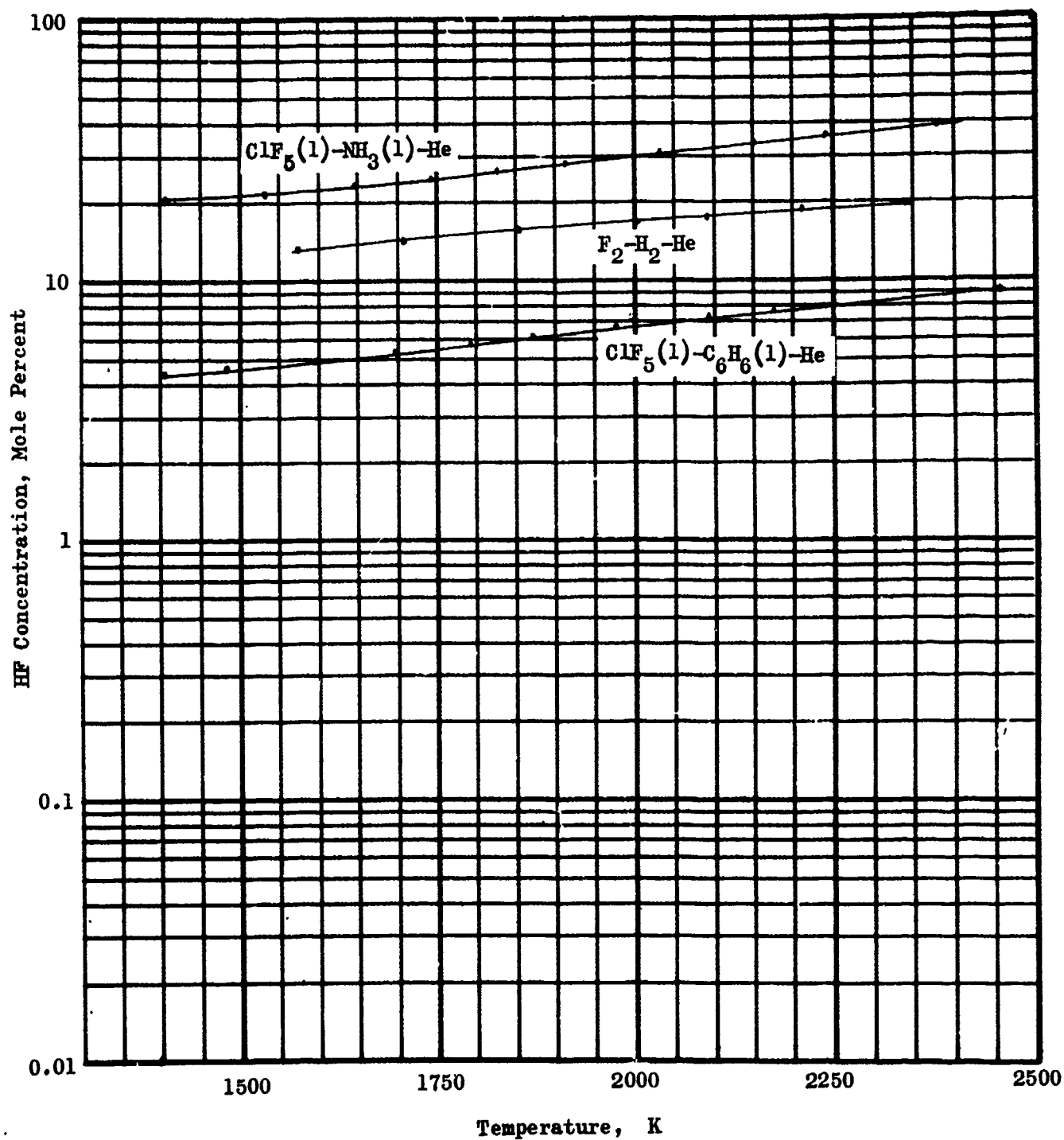


Figure 19. HF Concentration vs Temperature at 10 Mole Percent F Atoms (30 psia)

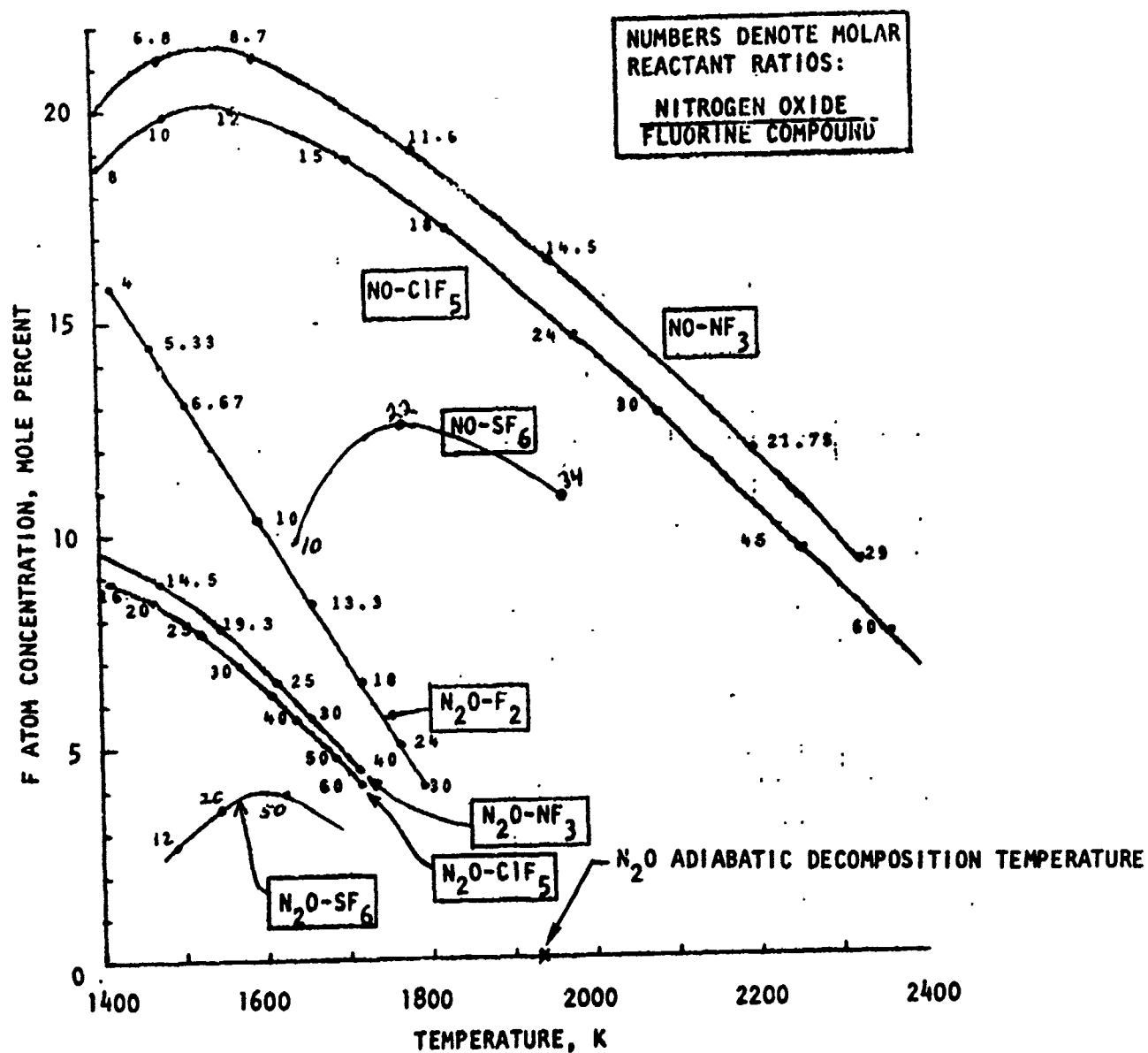


Figure 20. Nitrogen Oxide Systems; F-Atom Concentration and Temperature as a Function of Reactant Ratios (60 psia)

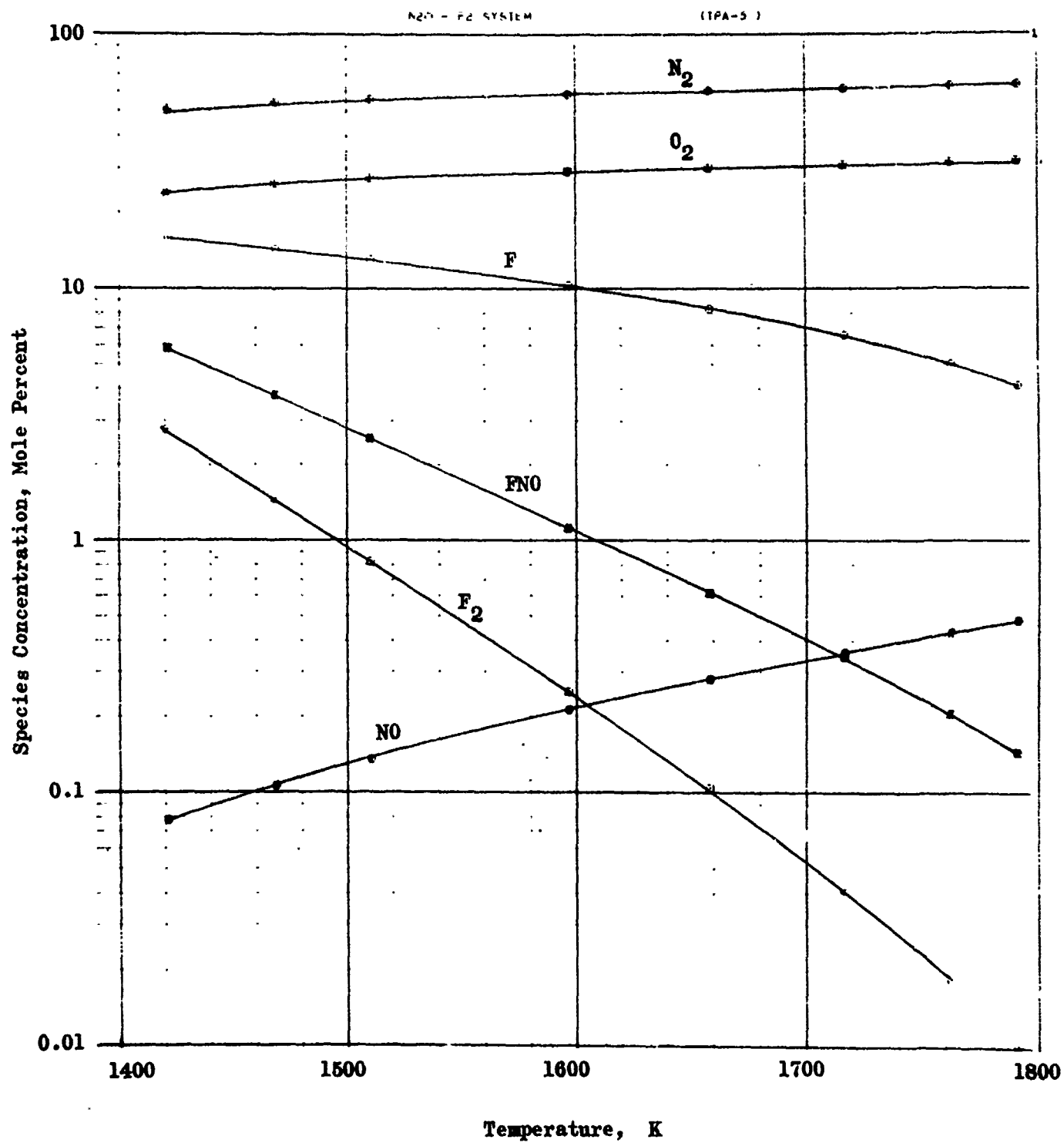


Figure 21. N₂O-F₂ System; Product Composition vs Temperature (60 psia)

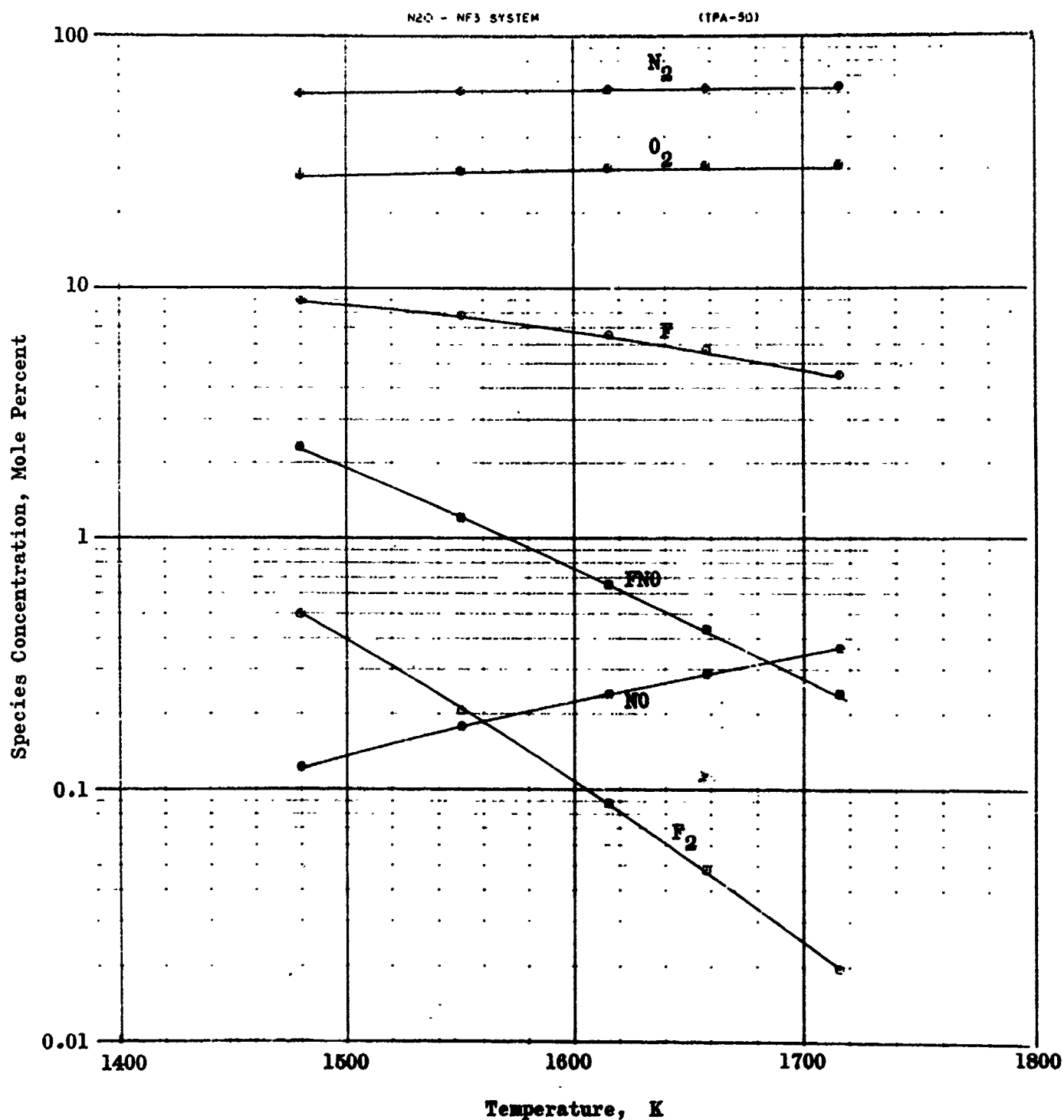


Figure 22. N₂O-NF₃ System; Product Composition vs Temperature (60 psia)

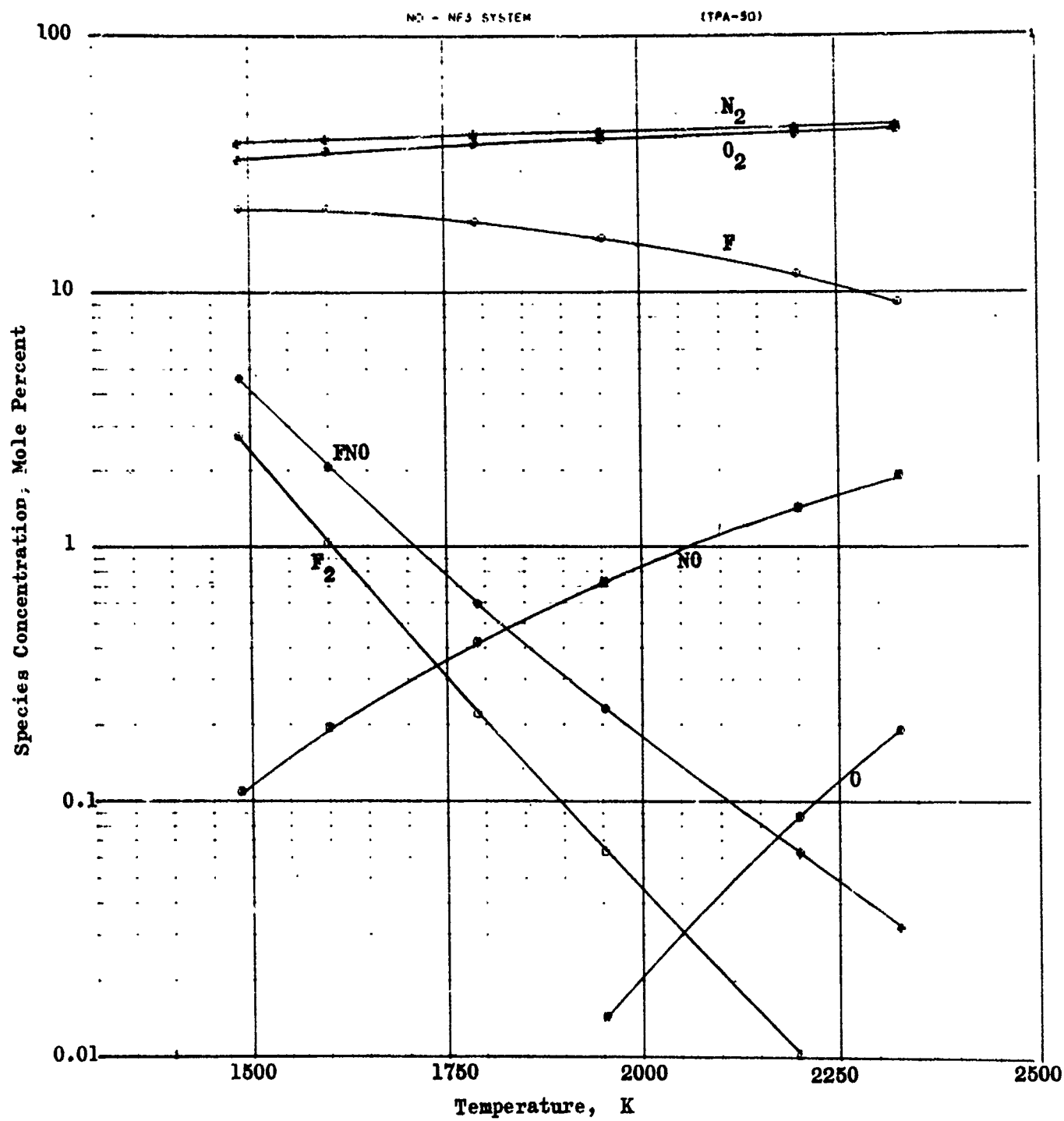


Figure 23. NO-NF₃ System; Product Composition vs Temperature (60 psia)

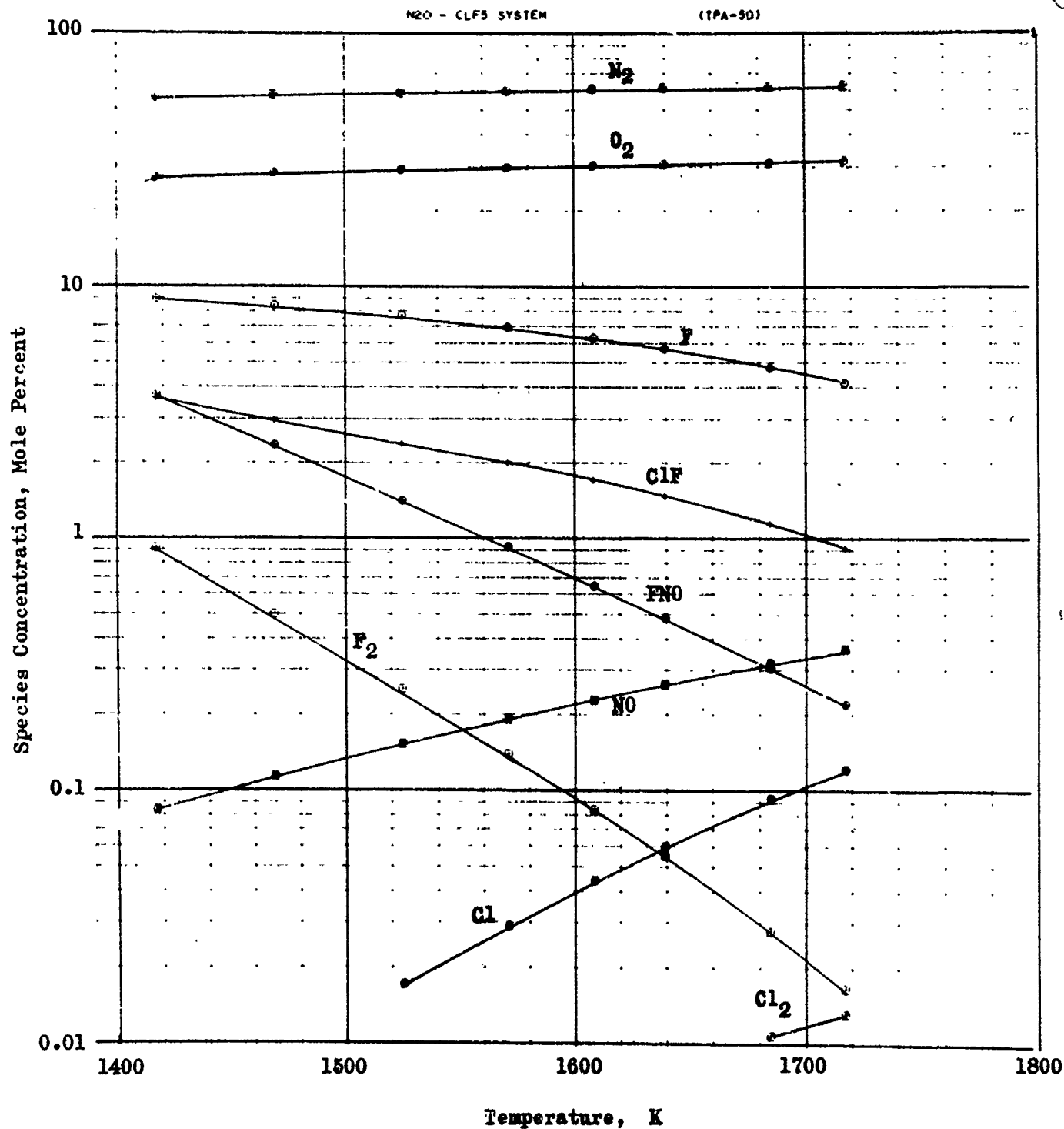


Figure 24. N₂O-ClF₅ System; Product Composition vs Temperature (60 Psia)

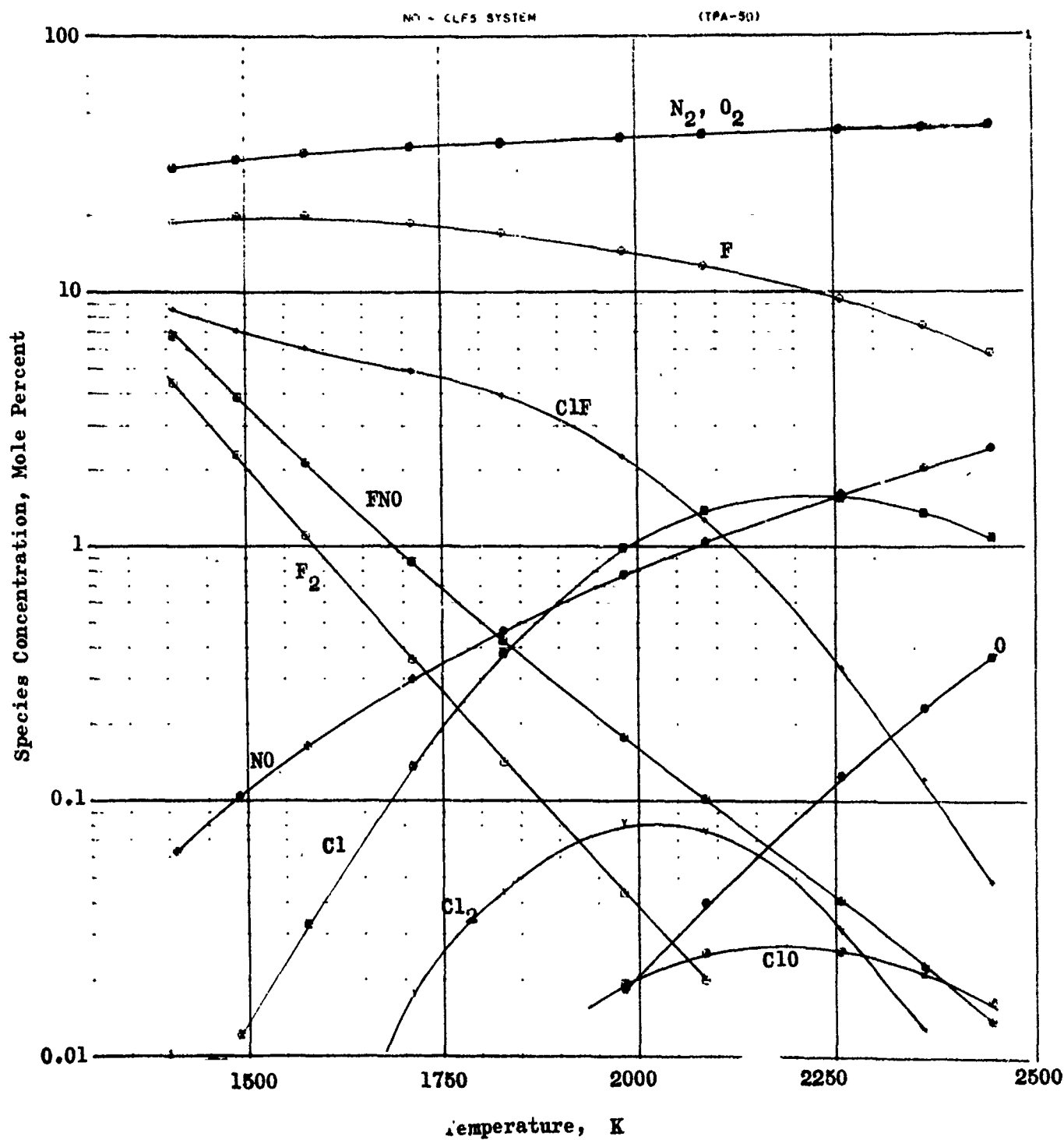


Figure 25. NO-ClF₅ System; Product Composition vs Temperature (60 psia)

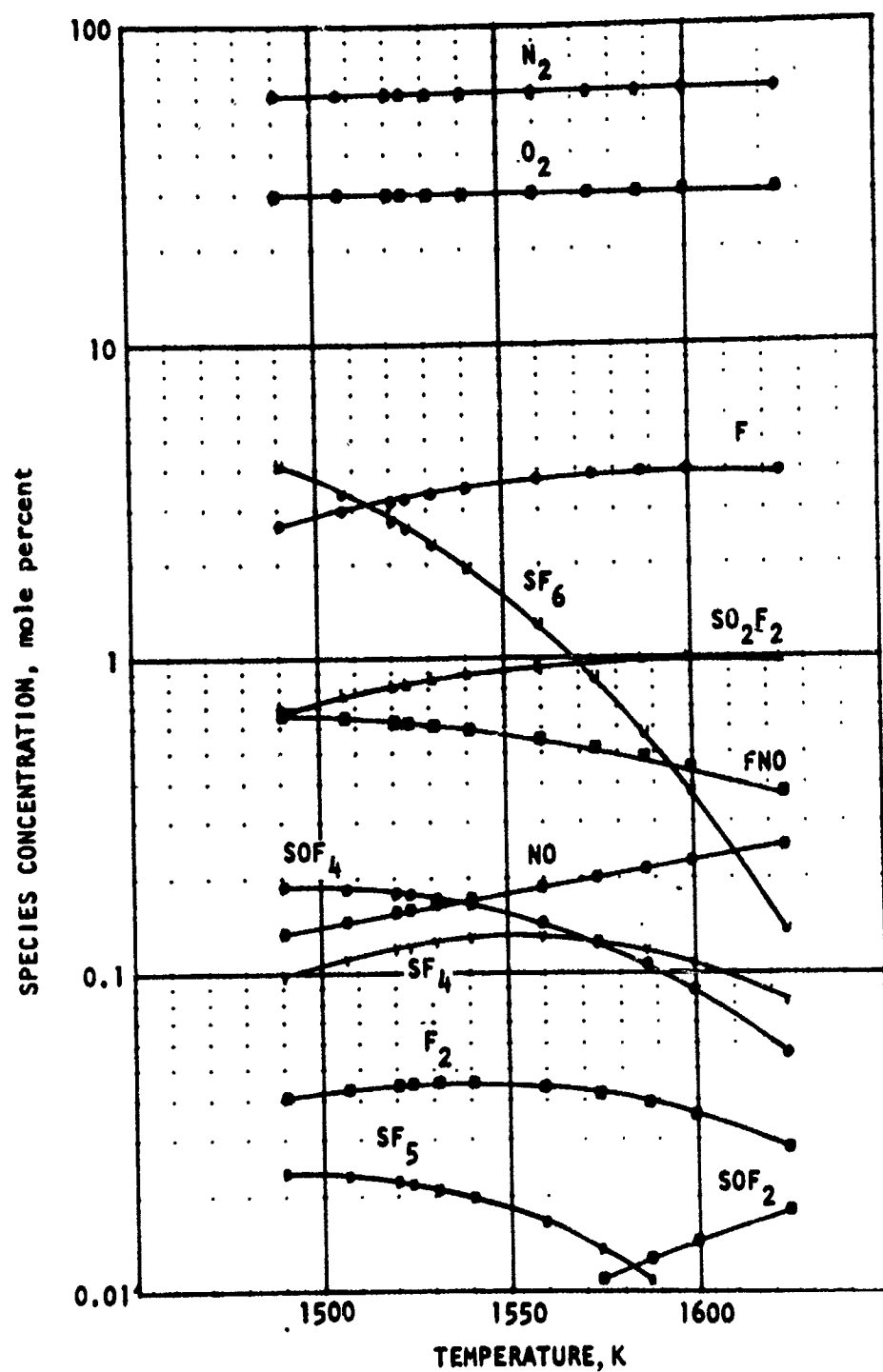


Figure 26. N_2O - SF_6 System; Product Composition versus Temperature (60 psia)

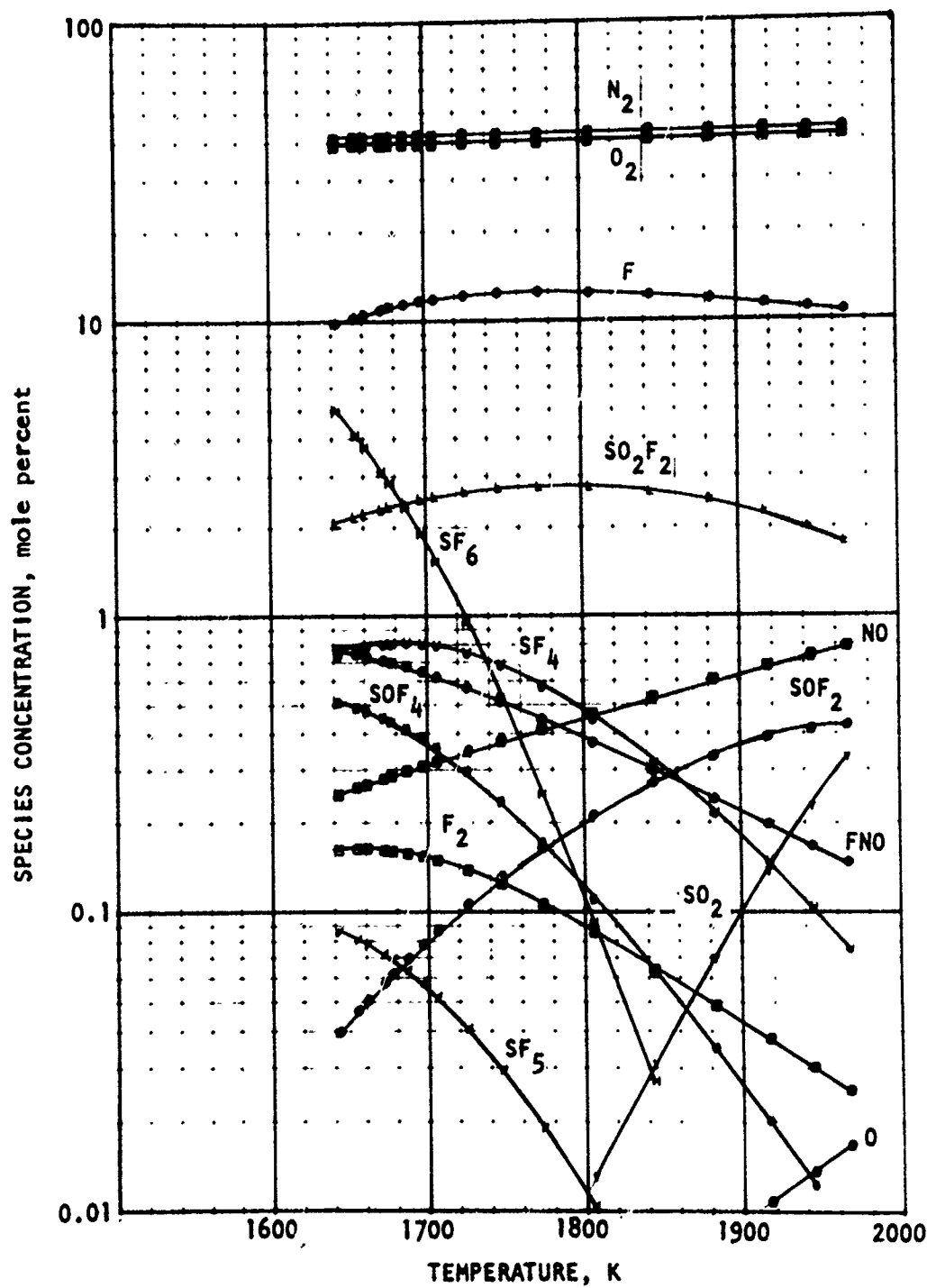


Figure 27. NO-SF₆ System: Product Composition Versus Temperature (60 psia)

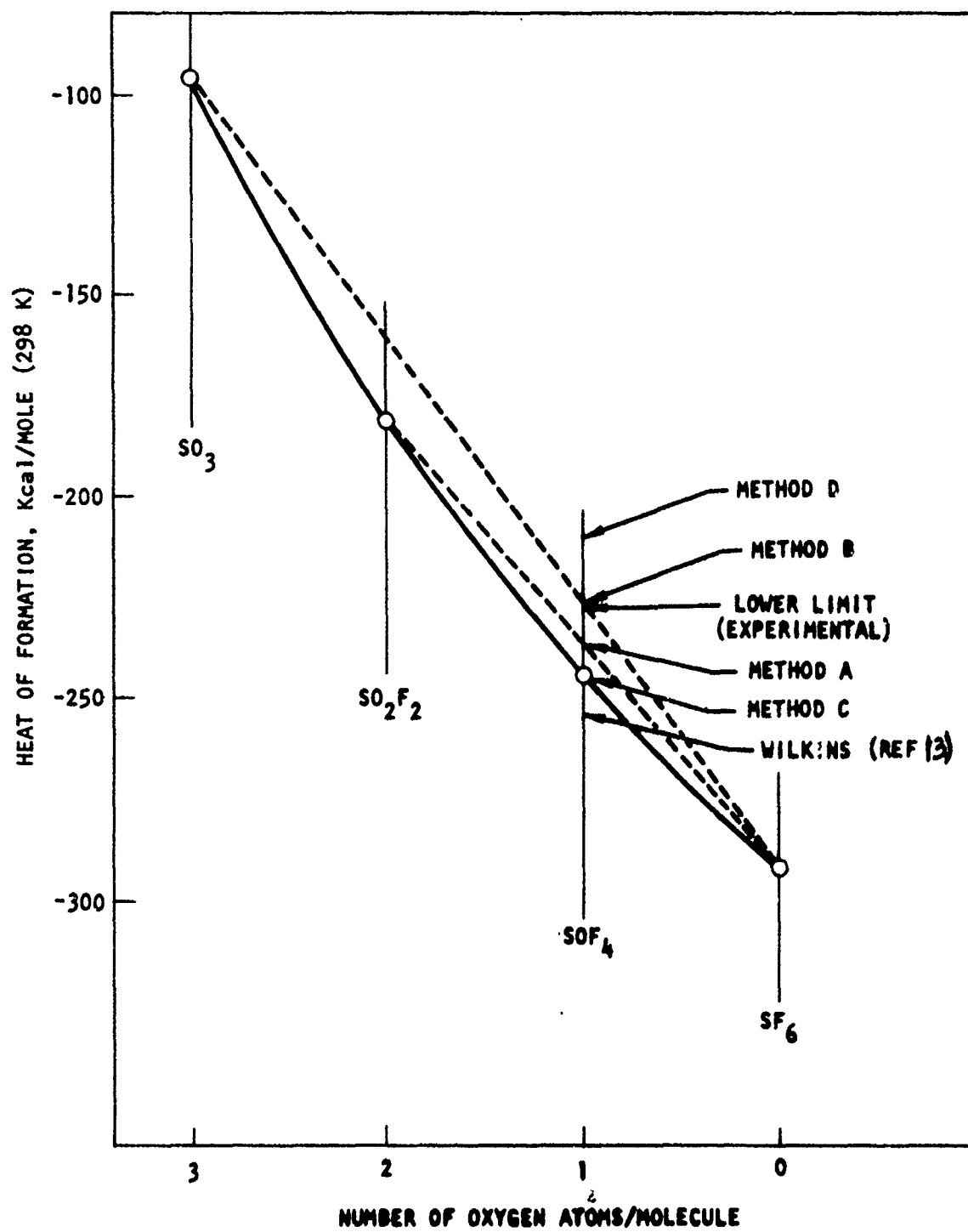


Figure 28. Comparison of Heats of Formation of $\text{SO}_x\text{F}_{(6-2x)}$ Compounds

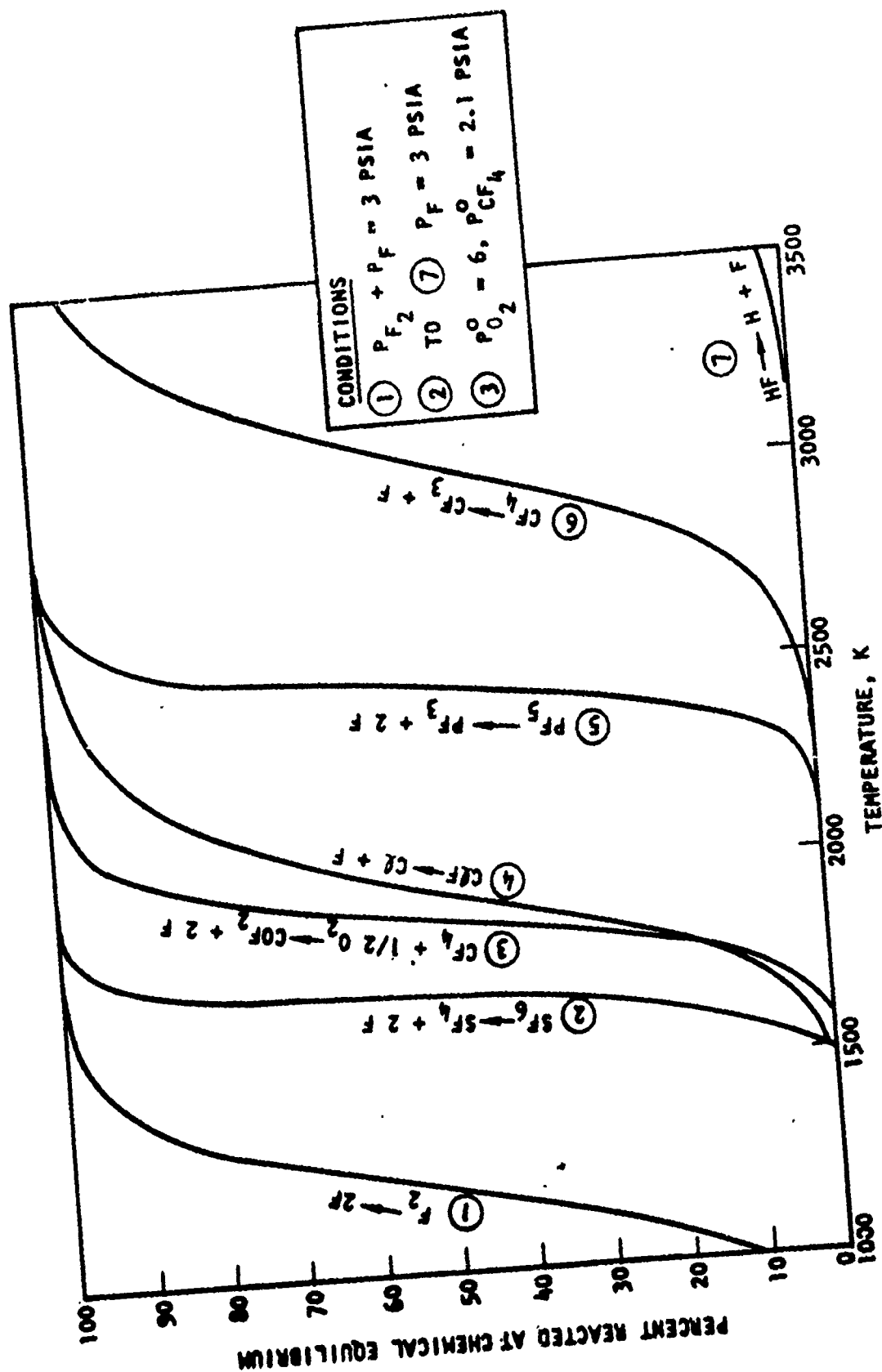


Figure 29. Effect of Temperature on Thermodynamically Favored Combustion Products

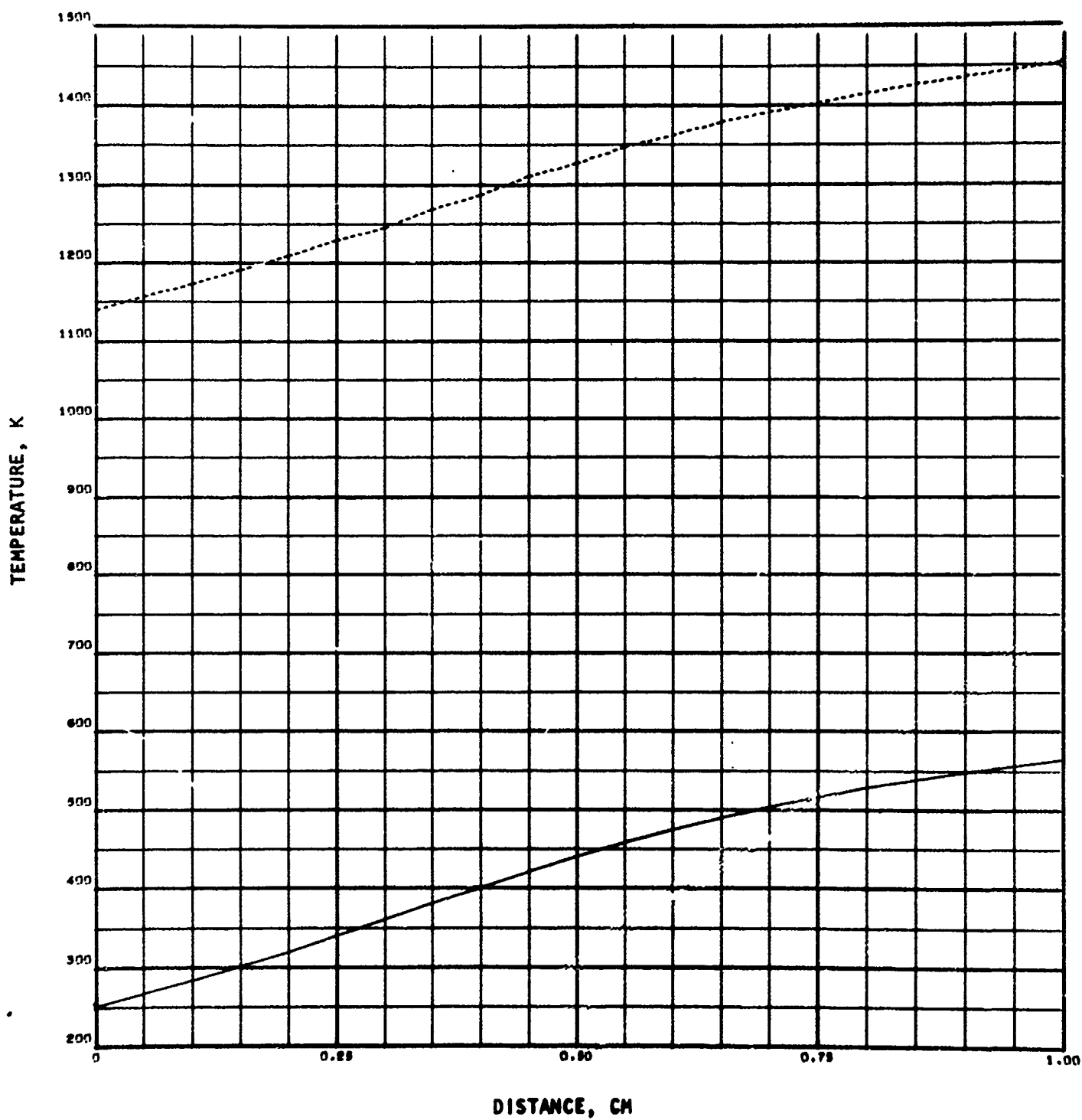


Figure 30. Case I: $F_2-D_2-He-H_2$ ($F = 10\%$, 1500 K, Series I)
Gas Static and Stagnation Temperature

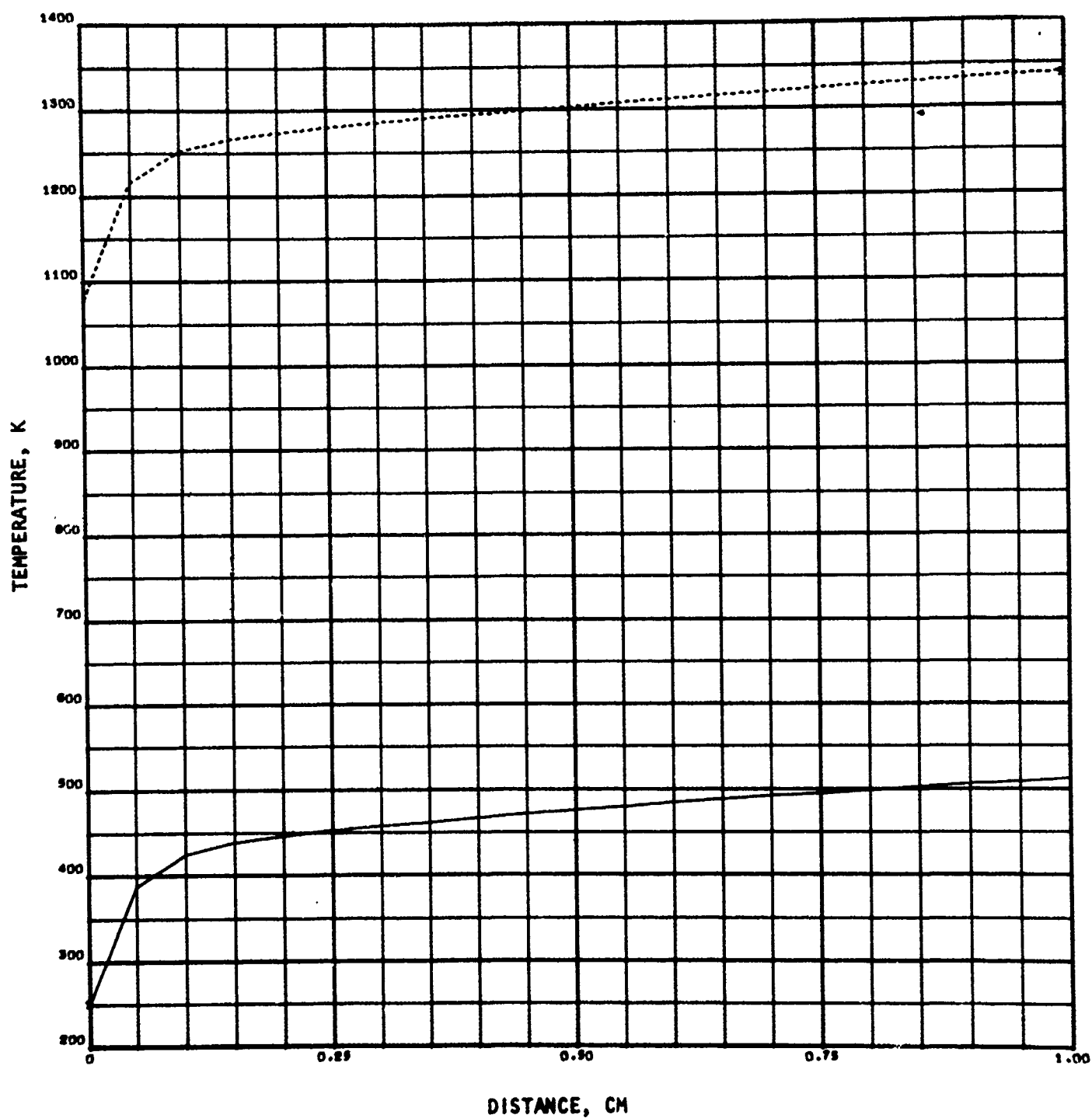


Figure 31. Case II: F_2 - D_2 -He-HCl ($F = 10\%$, 1500 K, Series I)
Gas Static and Stagnation Temperature

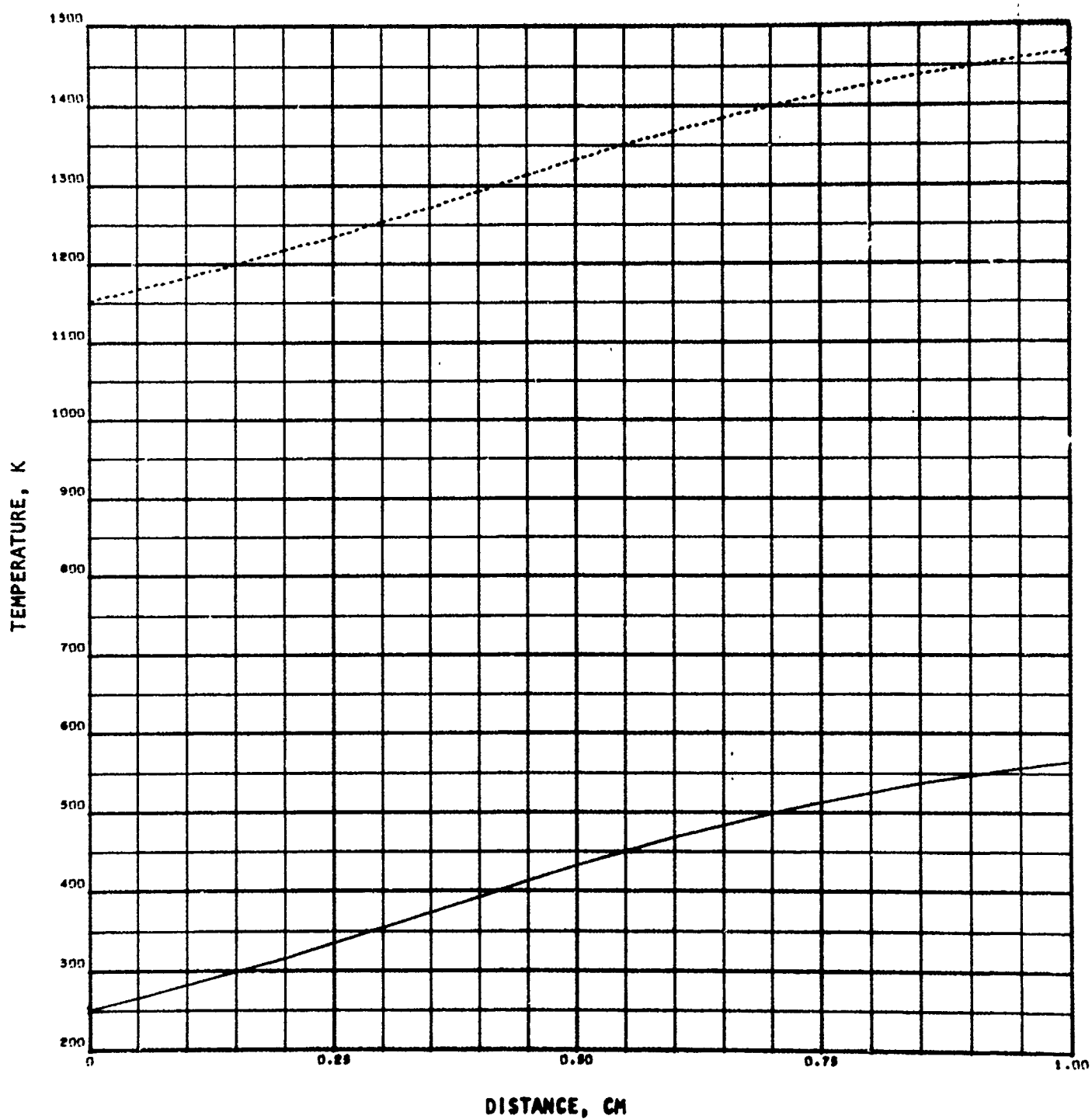


Figure 32. Case III: $F_2-C_6F_6-He-H_2$ ($F = 10\%$, 1500 K, Series I)
Gas Static and Stagnation Temperature

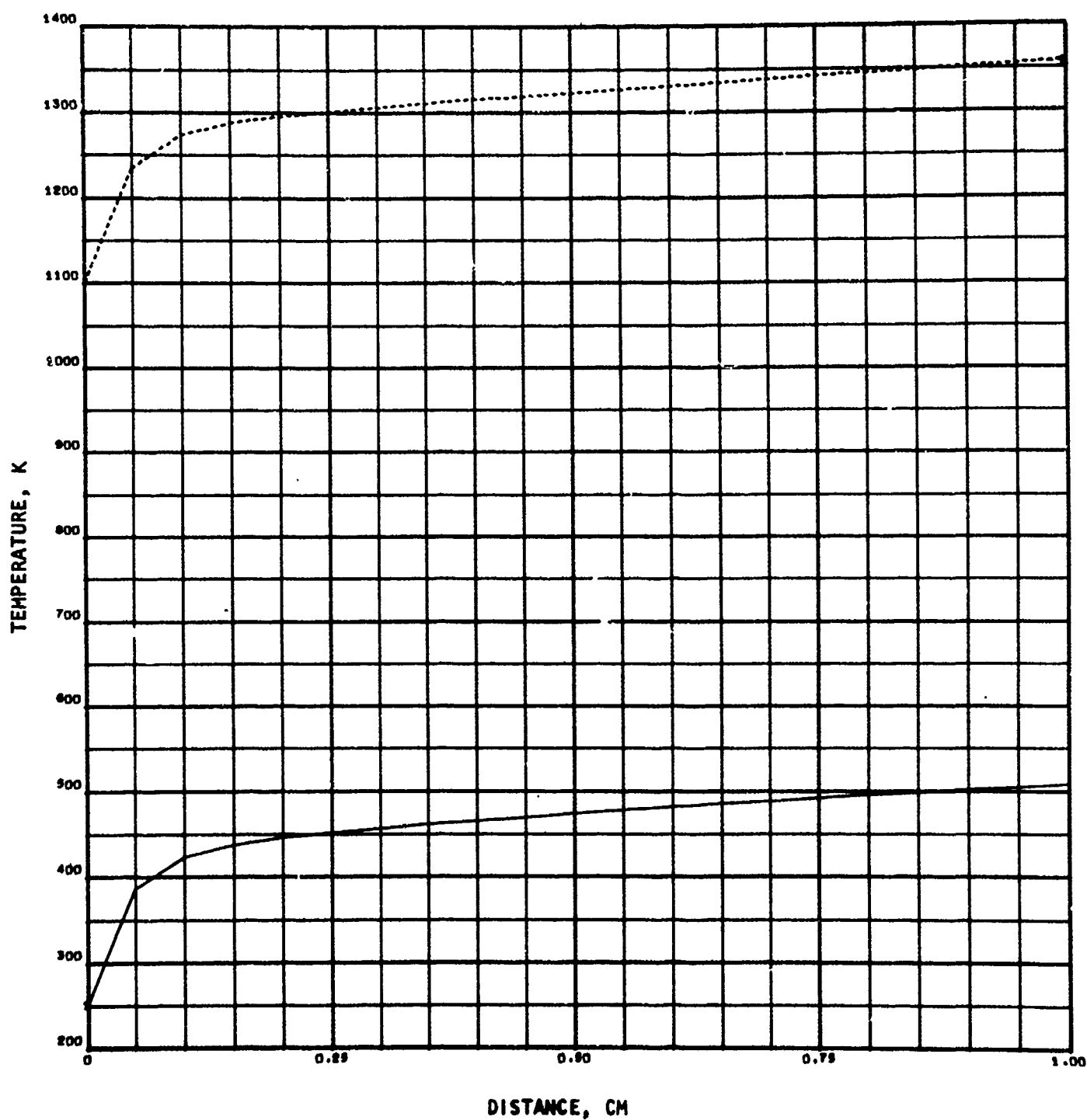


Figure 33. Case IV: $F_2-C_6F_6-He-HCl$ (F = 10%, 1500 K, Series I)
Gas Static and Stagnation Temperature

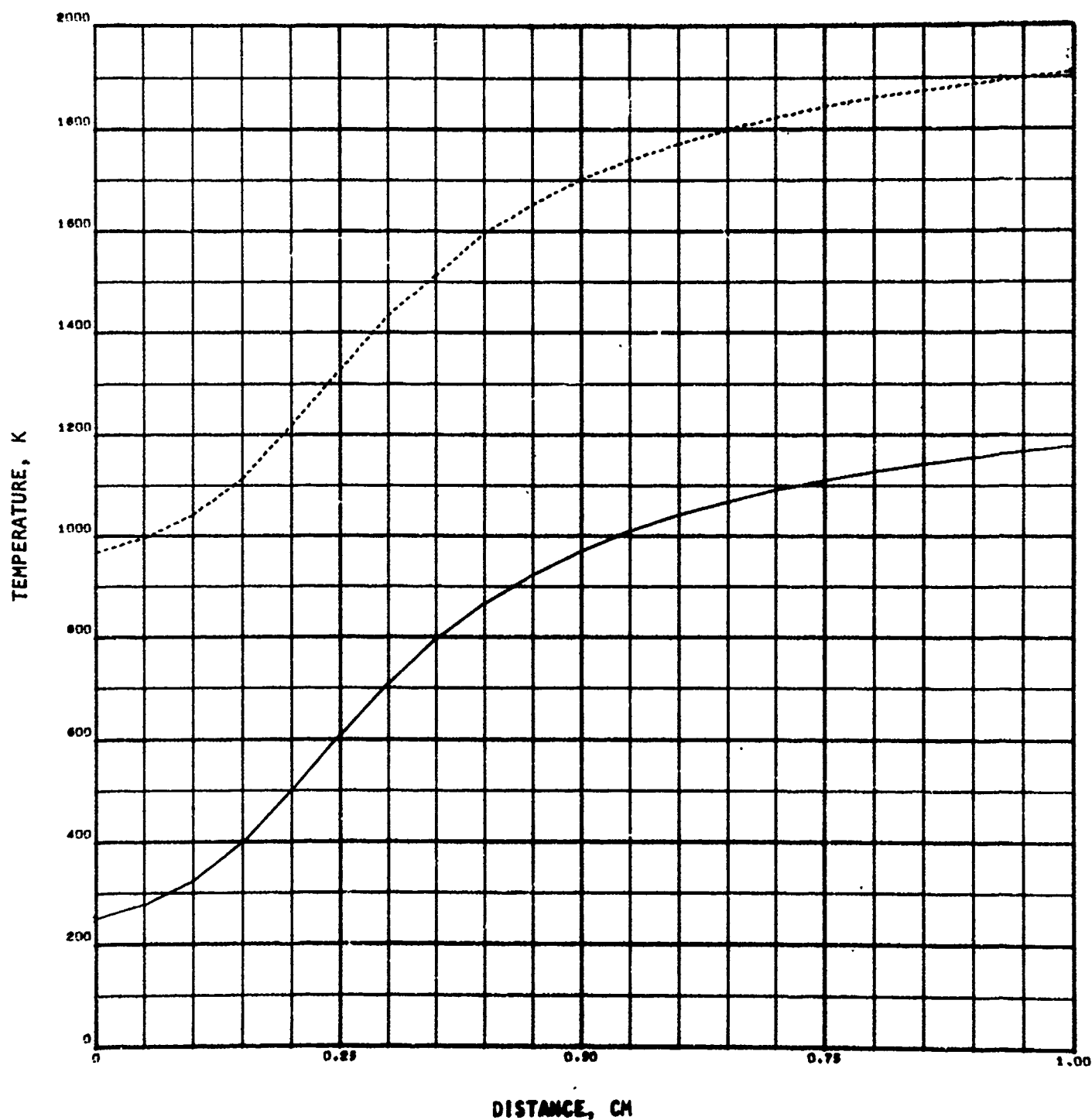


Figure 34. Case V: $\text{ClF}_5\text{-ND}_3\text{-He-H}_2$ ($F = 10\%$, 1500 K, Series I)
Gas Static and Stagnation Temperature

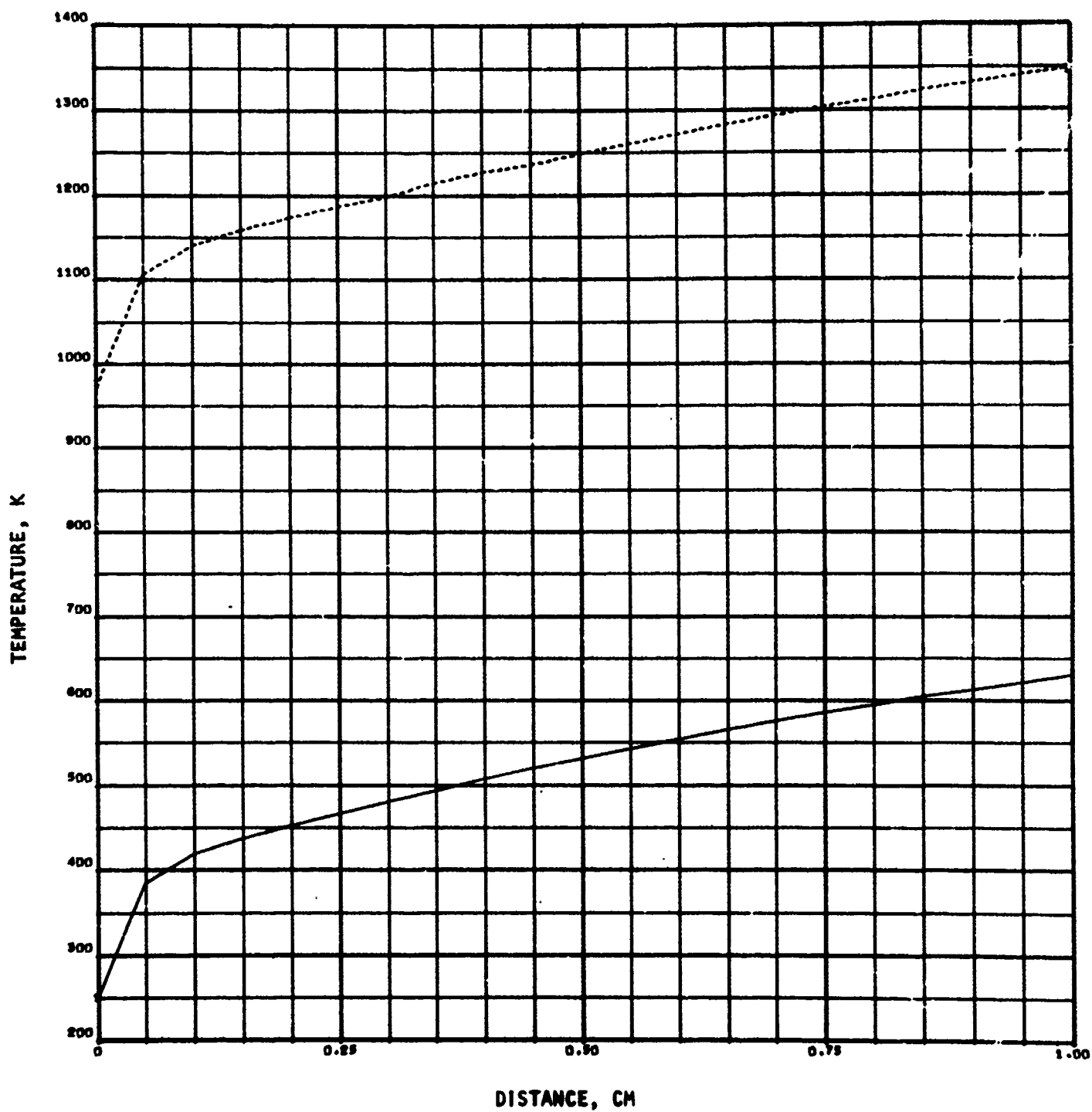


Figure 35. Case VI: $\text{ClF}_5\text{-ND}_3\text{-He-HCl}$ ($F = 10\%$, 1500 K, Series I)
Gas Static and Stagnation Temperature

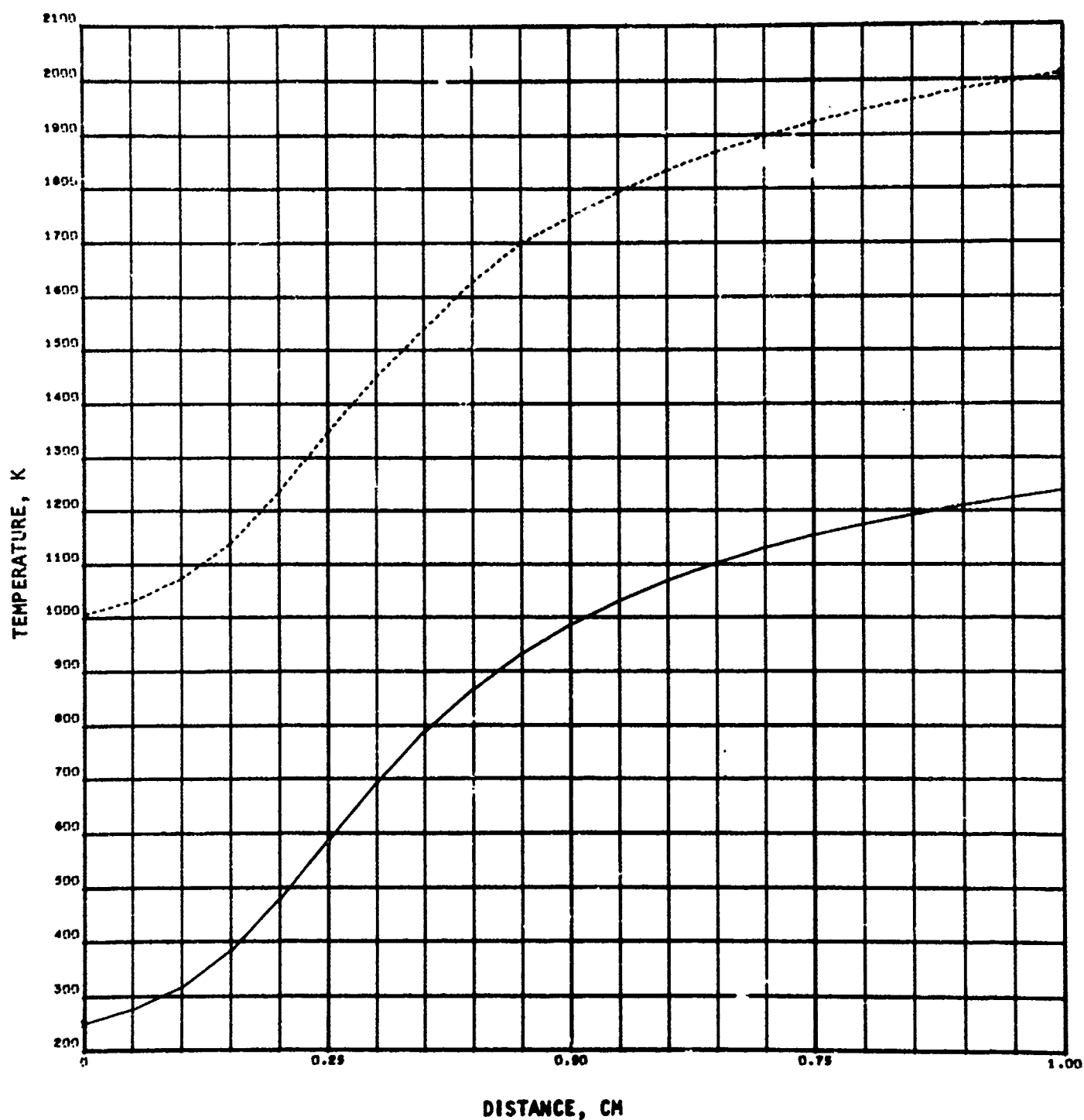


Figure 36. Case VII: $\text{ClF}_5\text{-C}_6\text{F}_6\text{-He-H}_2$ ($F = 10\%$, 1500 K, Series I)
Gas Static and Stagnation Temperature

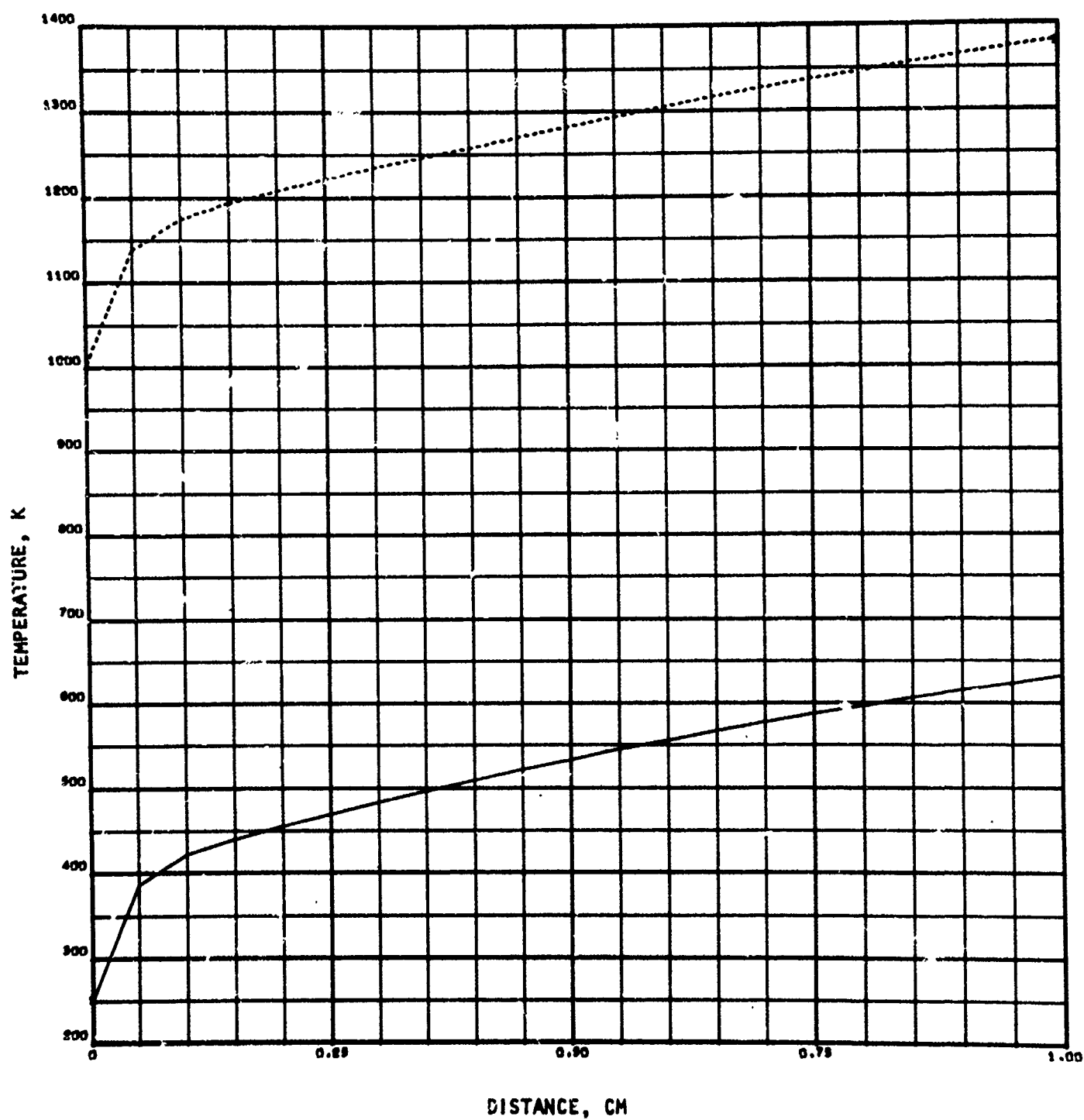


Figure 37. Case VIII: $\text{ClF}_5\text{-C}_6\text{F}_6\text{-He-HCl}$ ($F = 10\%$, 1500 K, Series I)
Gas Static and Stagnation Temperature

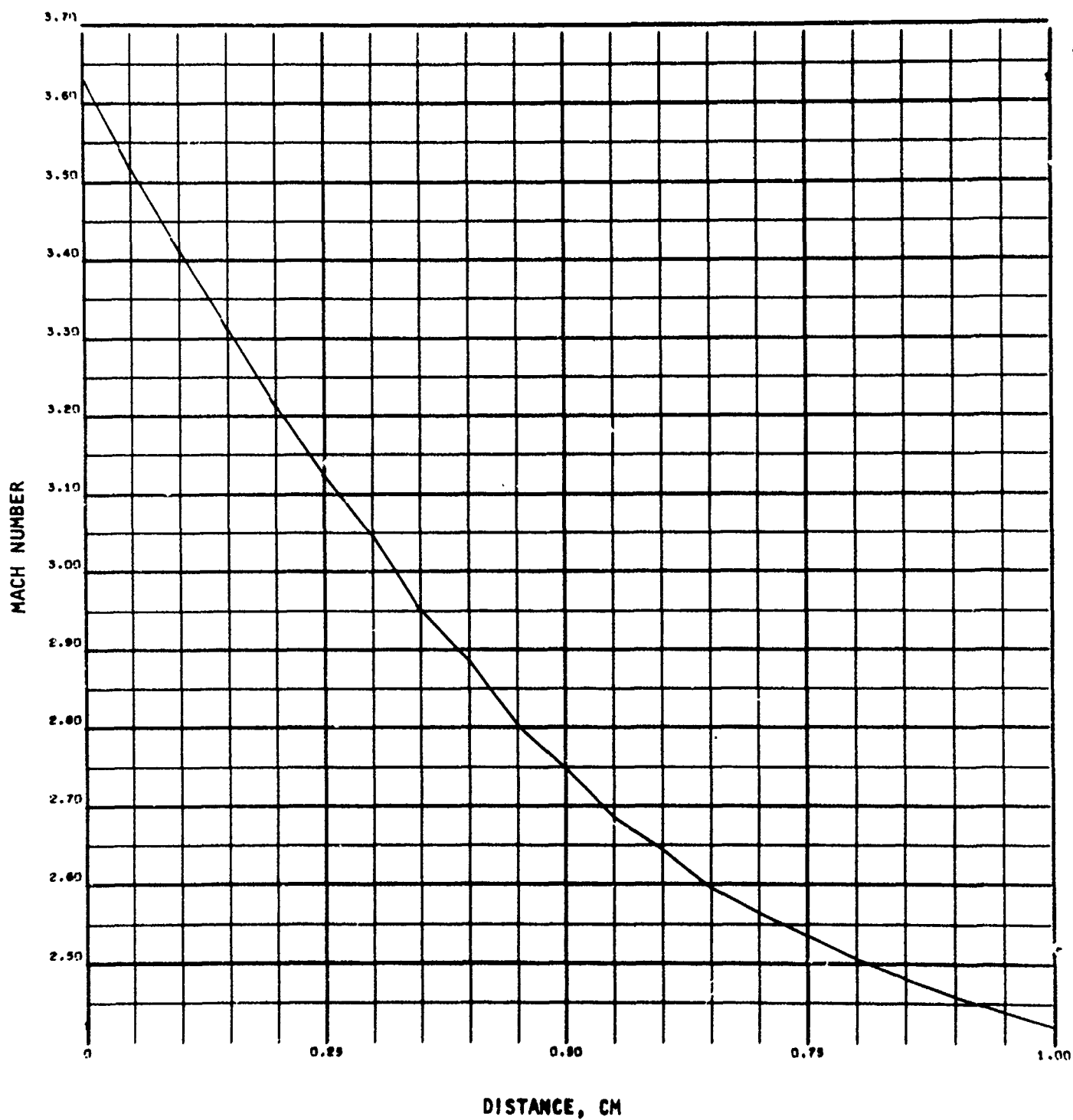


Figure 38. Case I: $F_2-D_2-He-H_2$ ($F = 10\%$, 1500 K, Series I)
Gas Mach Number

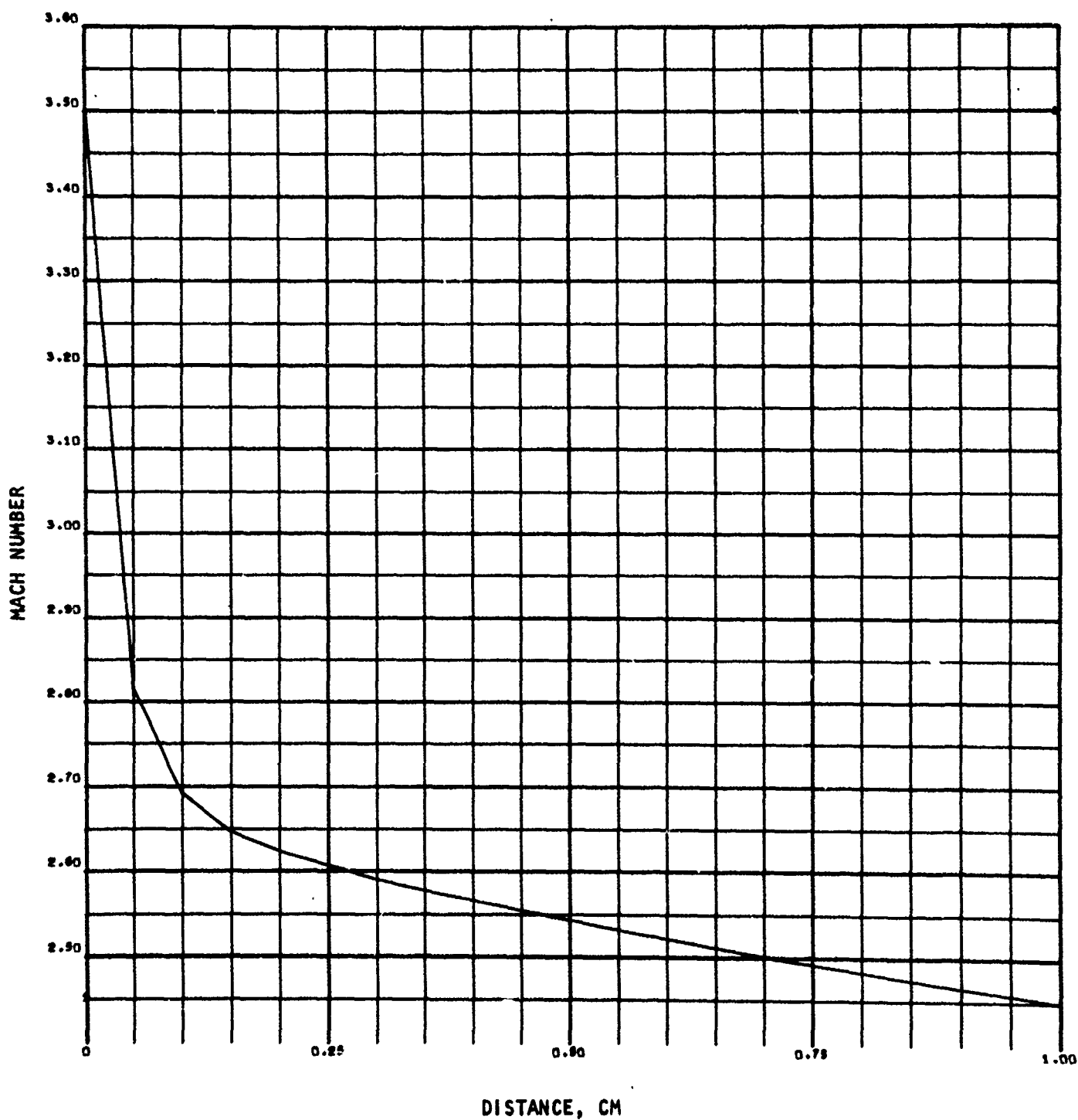


Figure 39. Case II: $F_2-D_2-He-HCl$ ($F = 10\%$, 1500 K, Series I)
Gas Mach Number

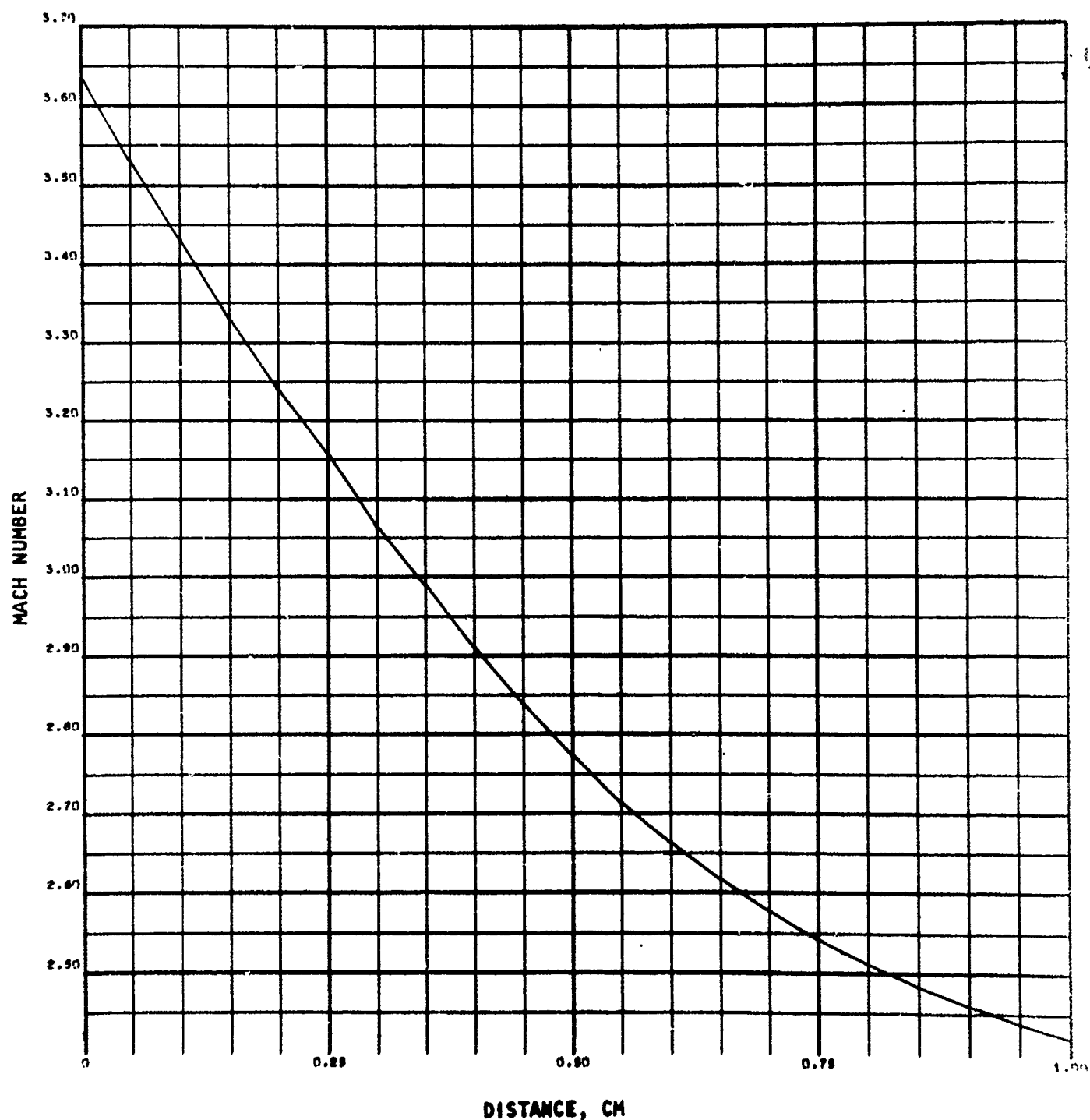


Figure 40. Case III: $F_2-C_6F_6-He-H_2$ (F = 10%, 1500 K, Series I)
Gas Mach Number.

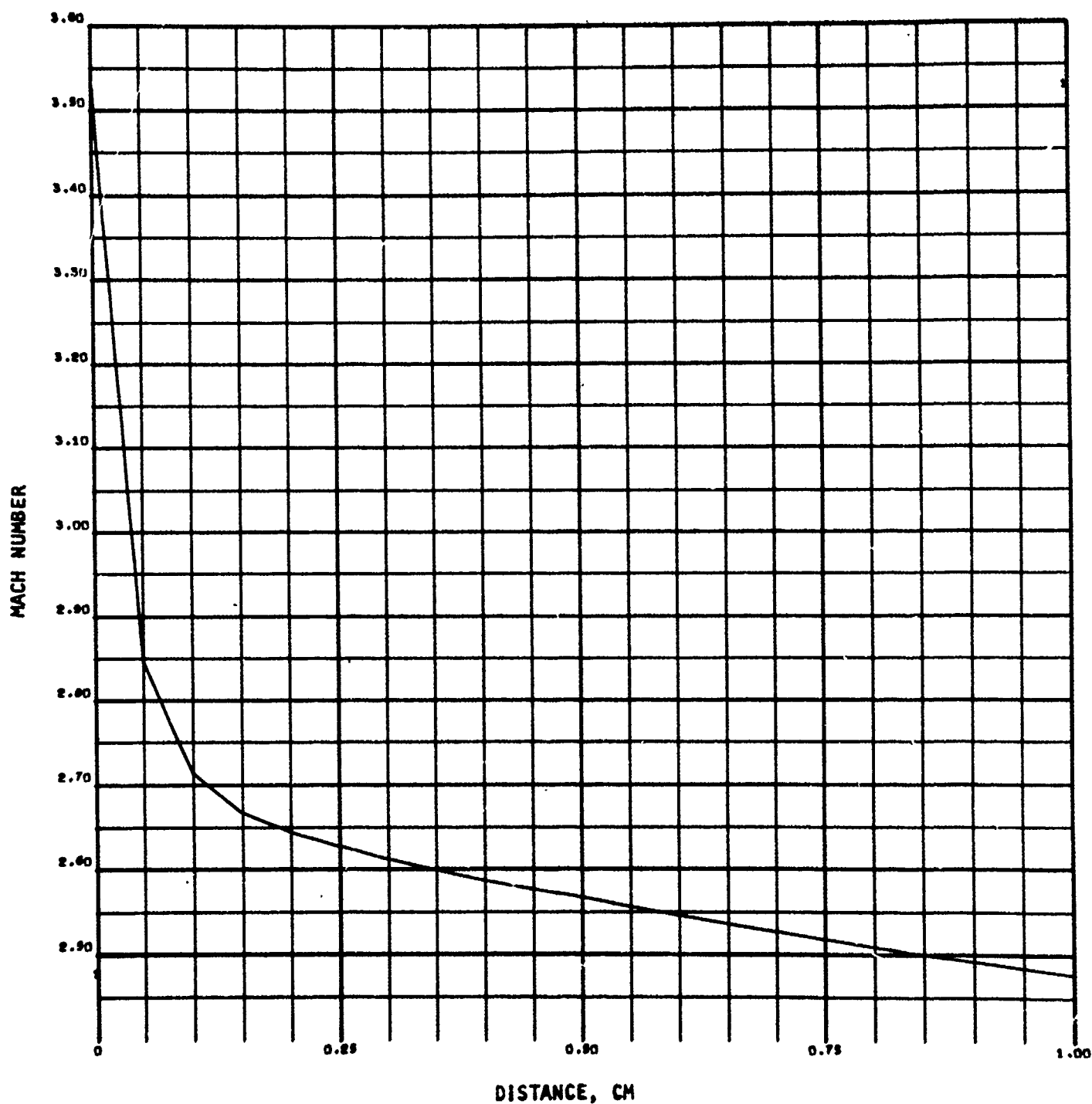


Figure 41. Case IV: $F_2-C_6F_6-He-HCl$ ($F = 10\%$, 1500 K, Series I)
Gas Mach Number

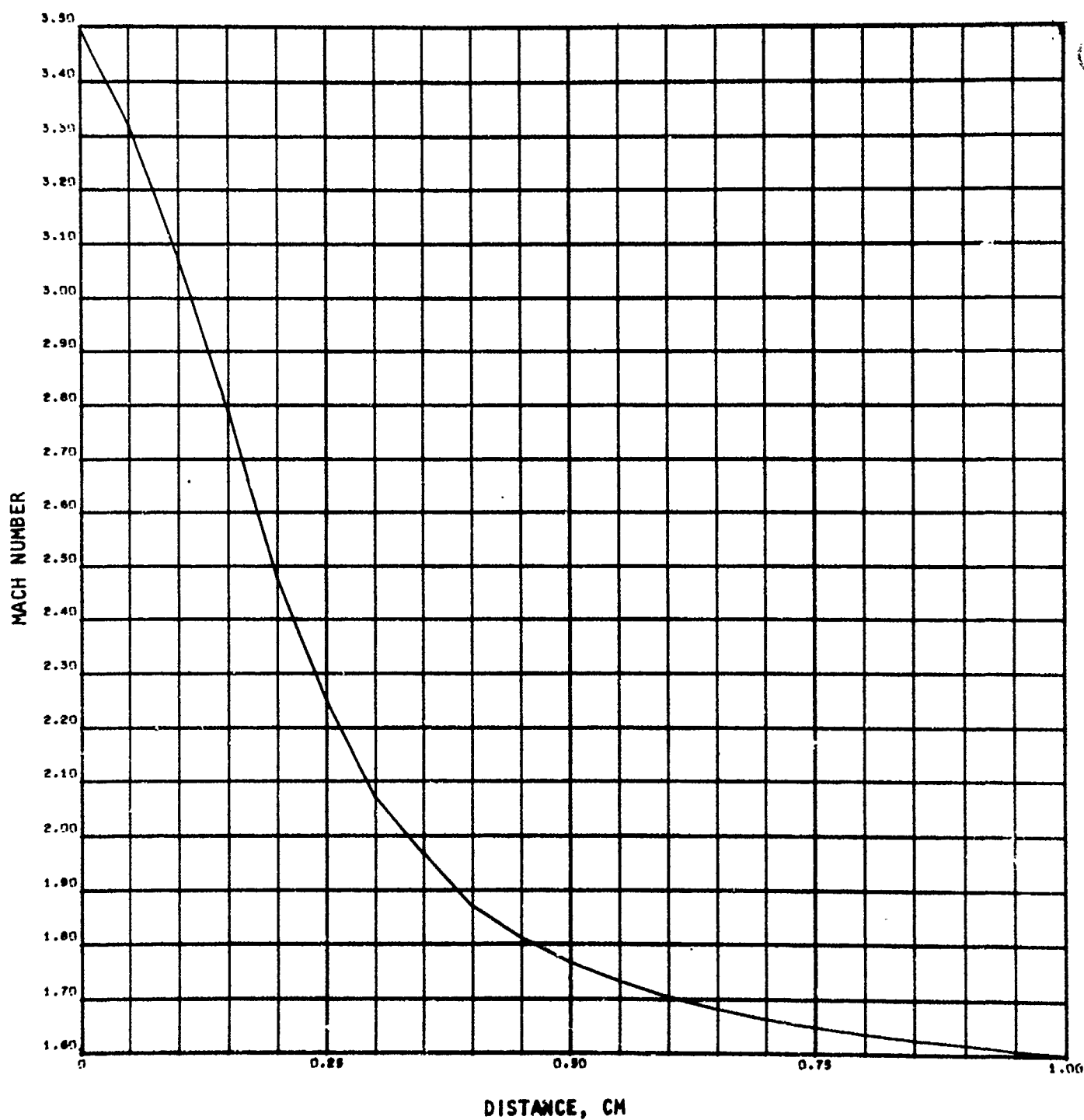


Figure 42. Case V: $\text{ClF}_5\text{-ND}_3\text{-He-H}_2$ ($F = 10\%$, 1500 K, Series I)
Gas Mach Number

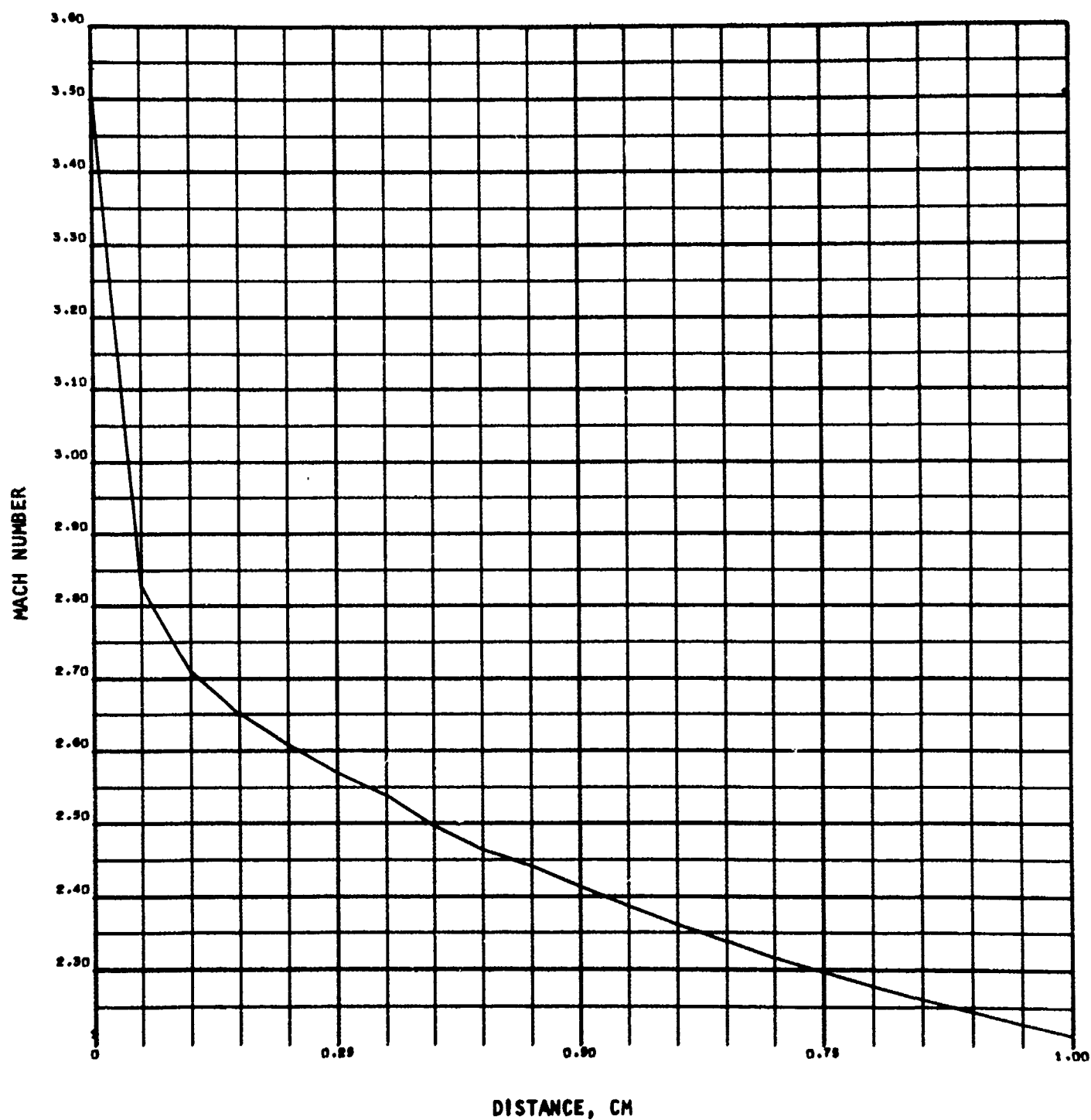


Figure 43. Case VI: $\text{ClF}_5\text{-ND}_3\text{-He-HCl}$ ($F = 10\%$, 1500 K, Series I)
Gas Mach Number

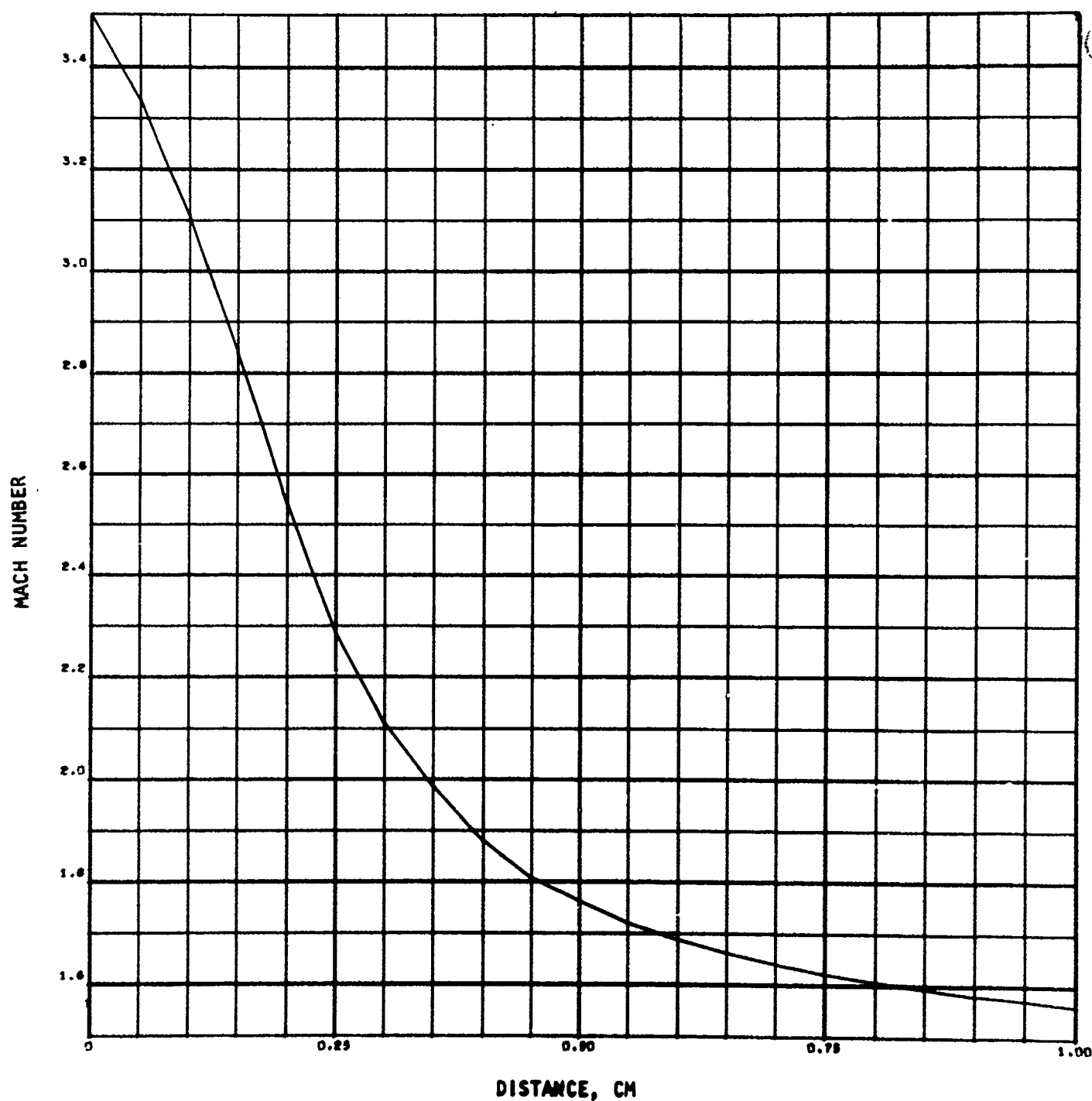


Figure 44. Case VII: $\text{ClF}_5\text{-C}_6\text{F}_6\text{-He-H}_2$ ($F = 10\%$, 1500 K, Series I)
Gas Mach Number

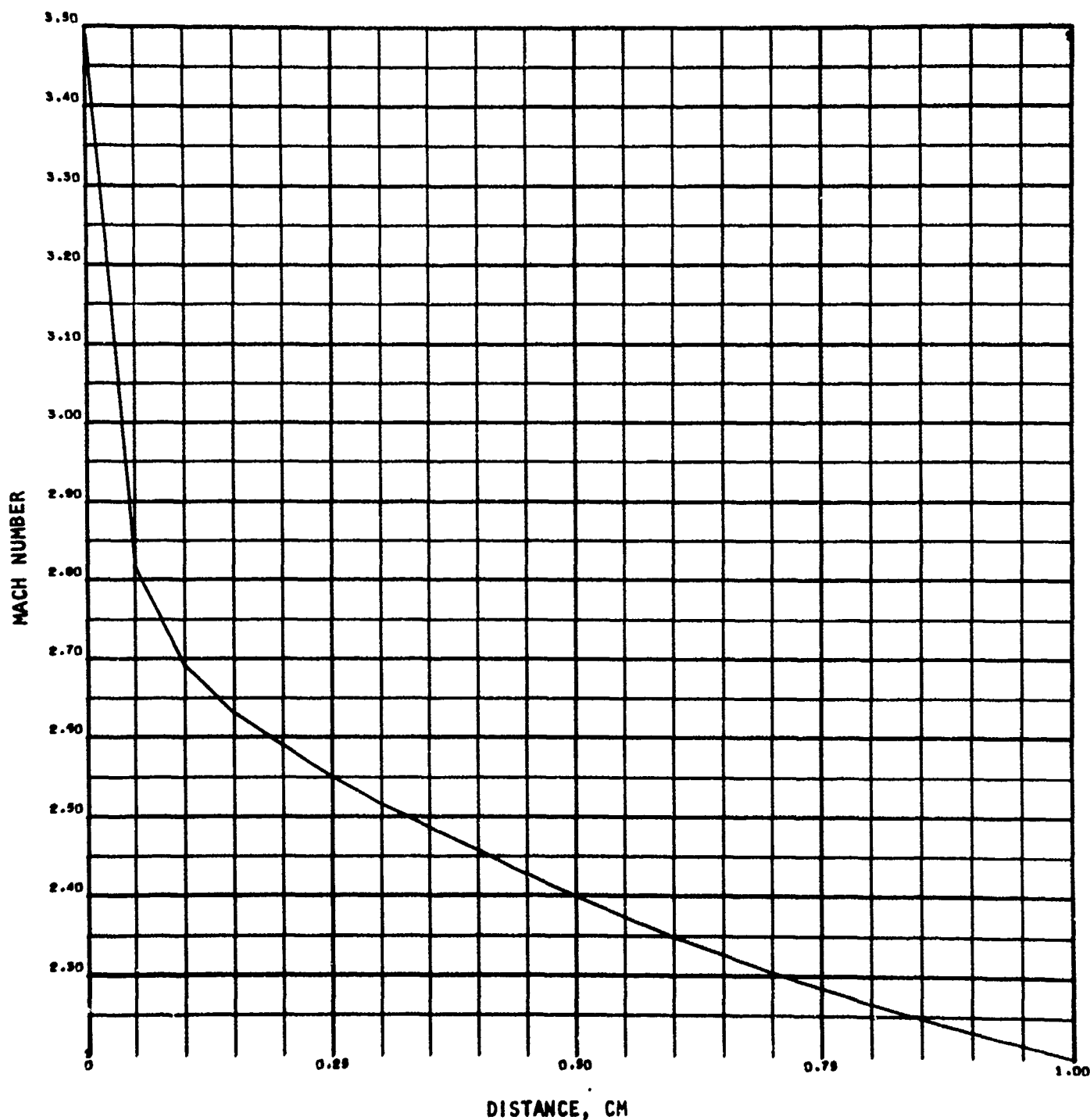


Figure 45. Case VIII: $\text{ClF}_5\text{-C}_6\text{F}_6\text{-He-HCl}$ ($F = 10\%$, 1500 K, Series I)
Gas Mach Number

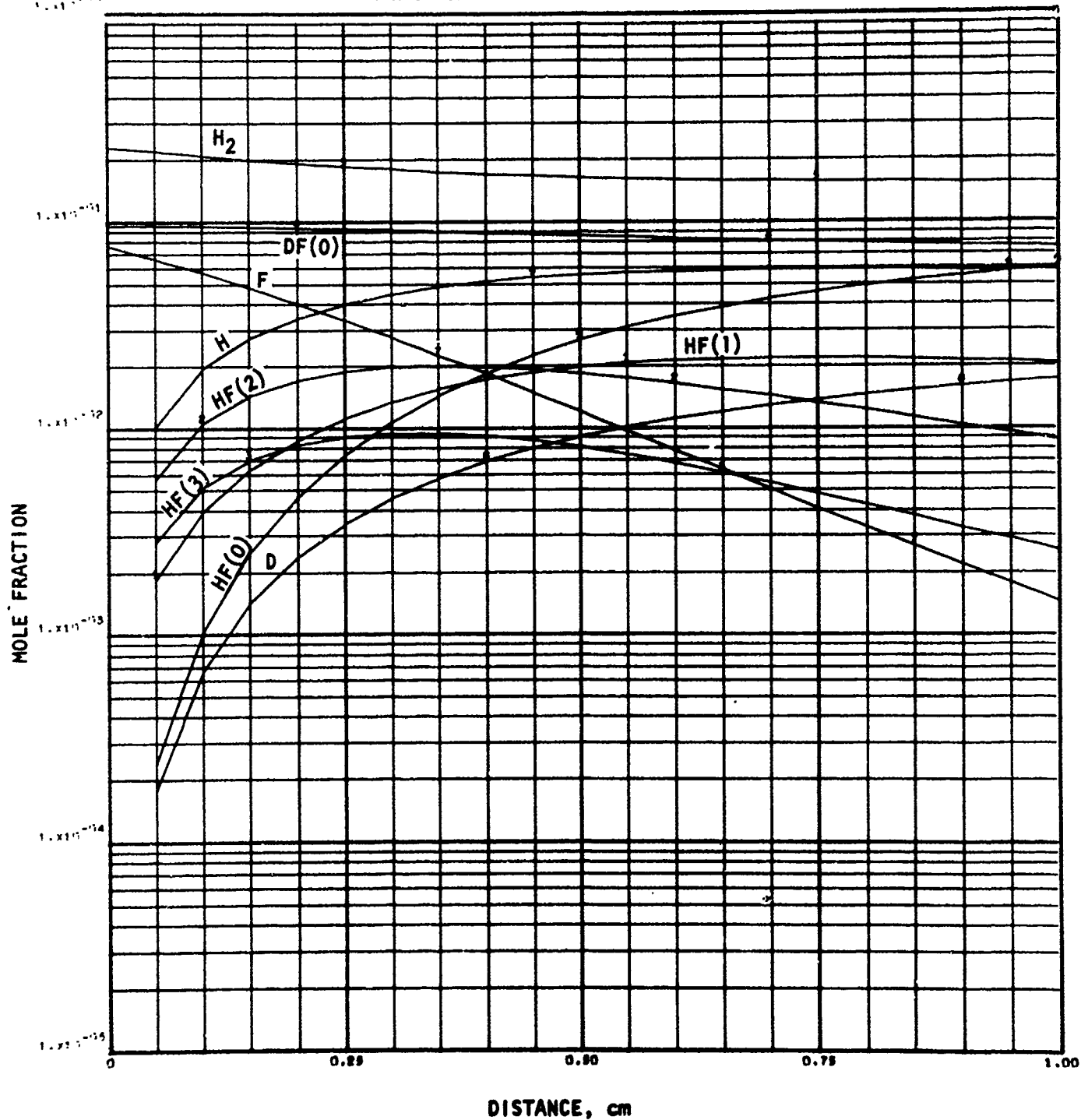
CASE 2 H₂/F=3

Figure 46. Case I: F₂-D₂-He-H₂ (F = 10%, 1500 K, Series I)
Species Plot

55835827
011573 0020

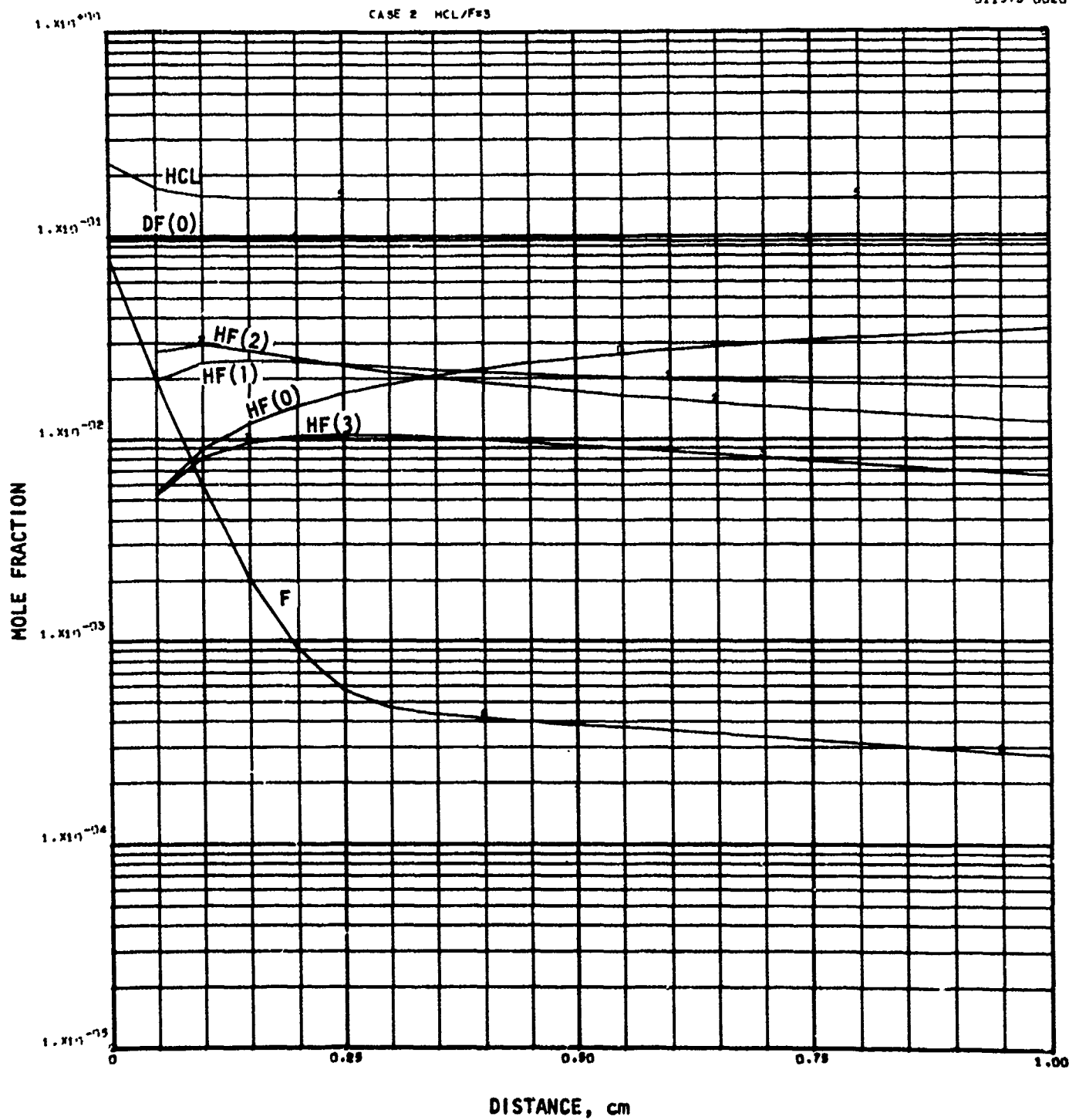


Figure 47. Case II: $F_2-D_2-He-HCl$ ($F = 10\%$, 1500 K, Series I)
Species Plot

CASE 10 H₂/F=3

59035021
011273 0020

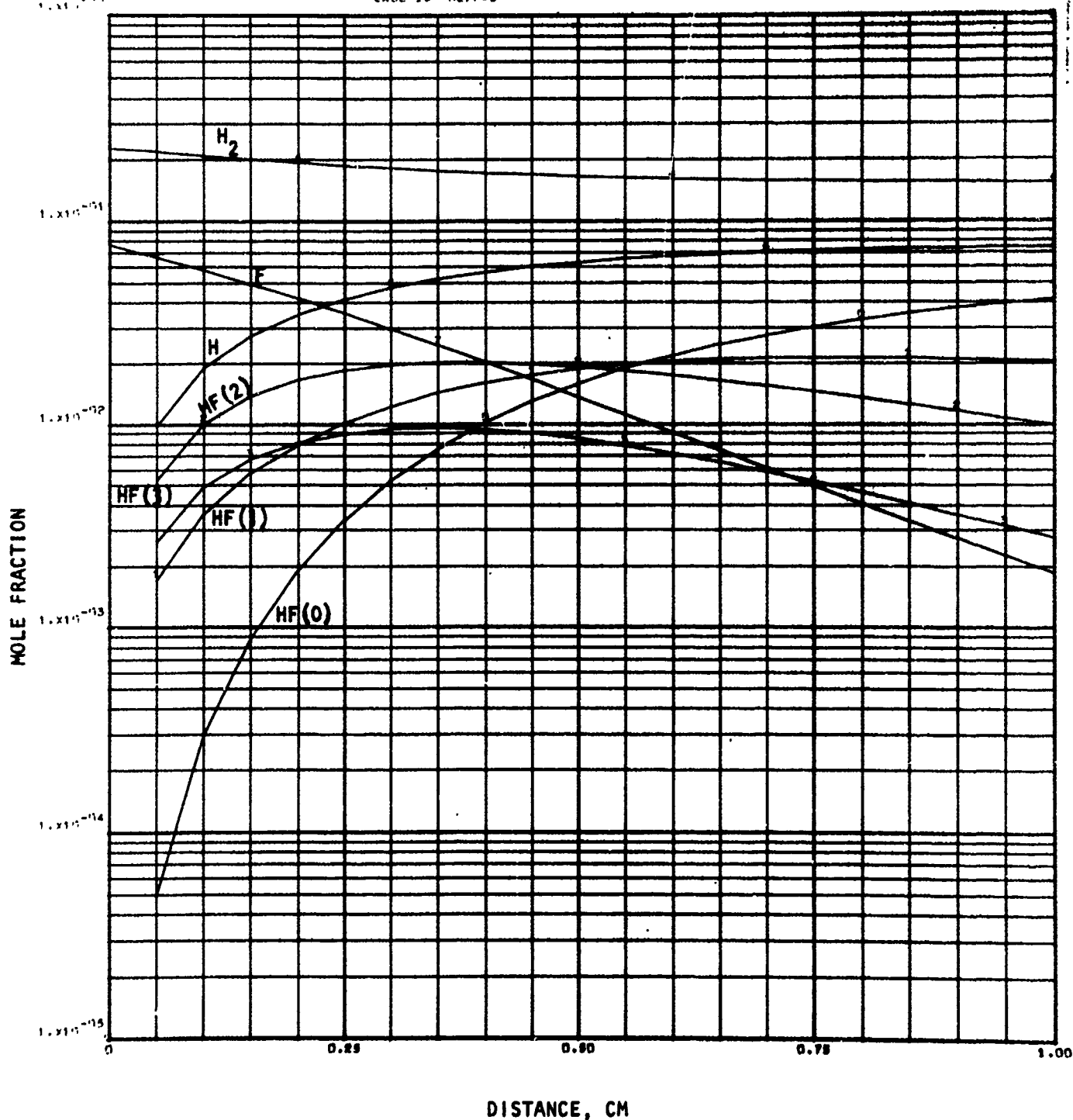


Figure 48. Case III: $F_2-C_6F_6-He-H_2$ (F = 10%, 1500 K, Series I)
Species Plot

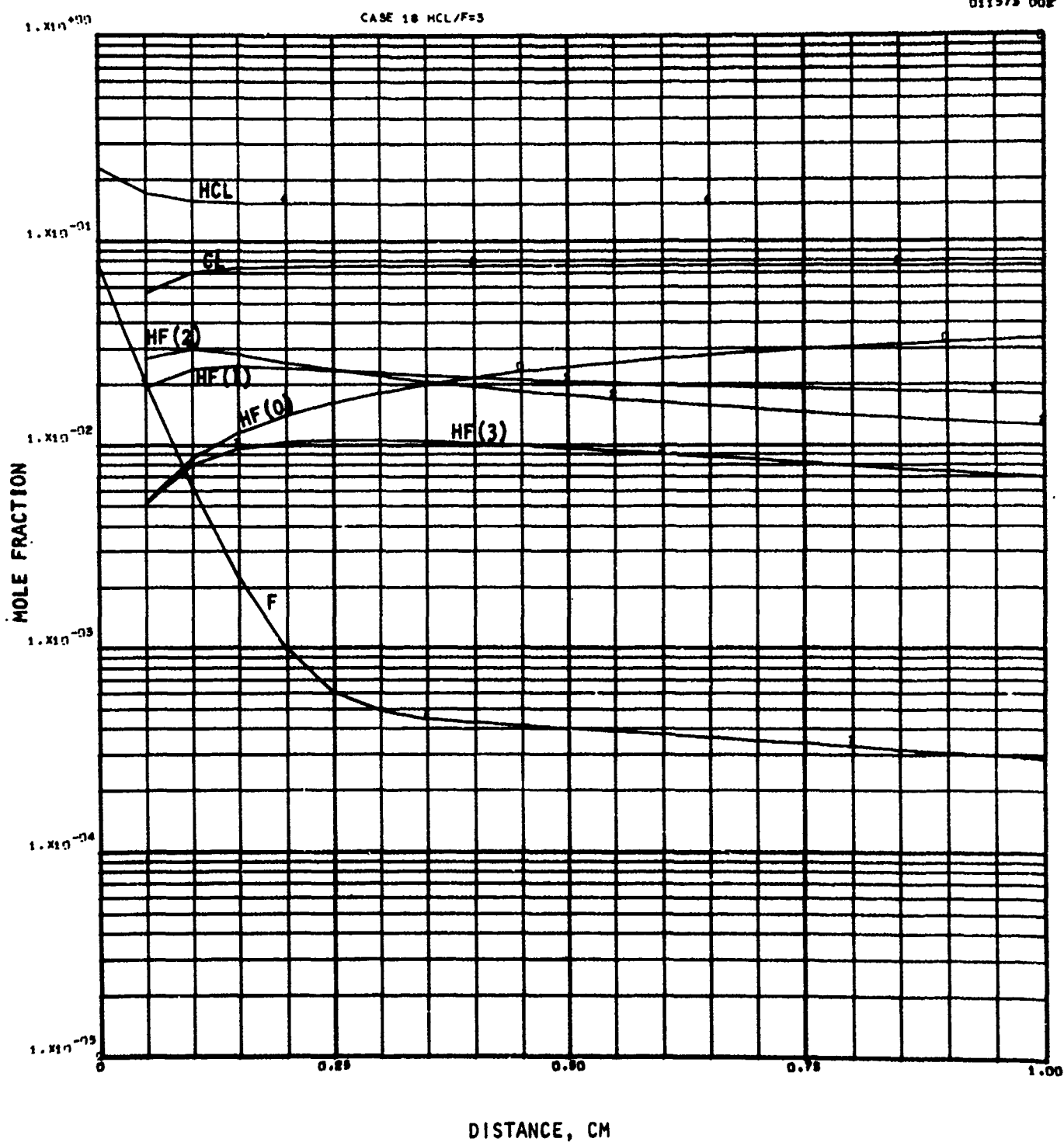


Figure 49. Case IV: $F_2-C_6F_6-He-HCl$ ($F = 10\%$, 1500 K, Series I)
Species Plot

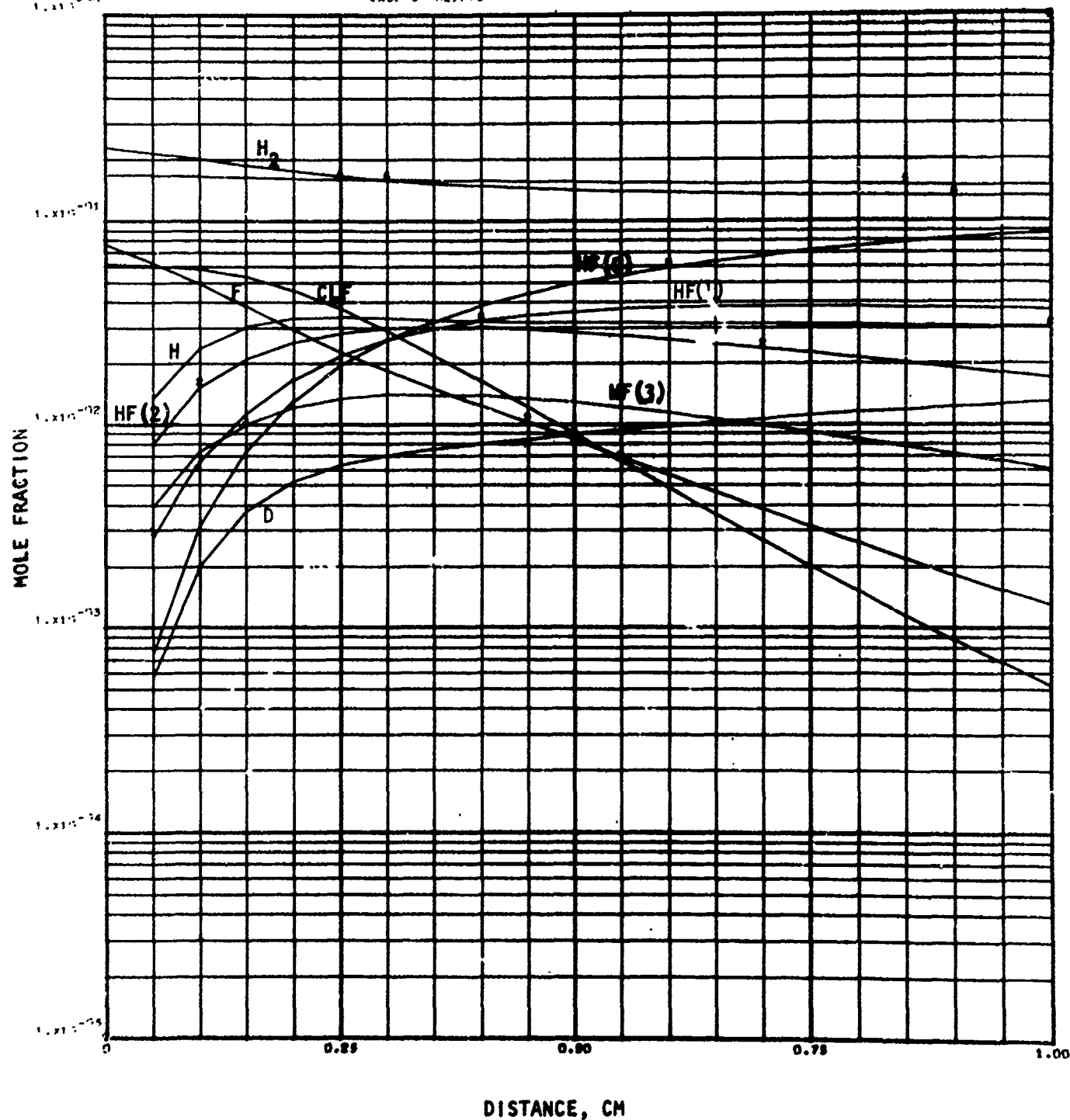


Figure 50. Case V: ClF₅-ND₃-He-H₂ (F = 10%, 1500 K, Series I)
Species Plot

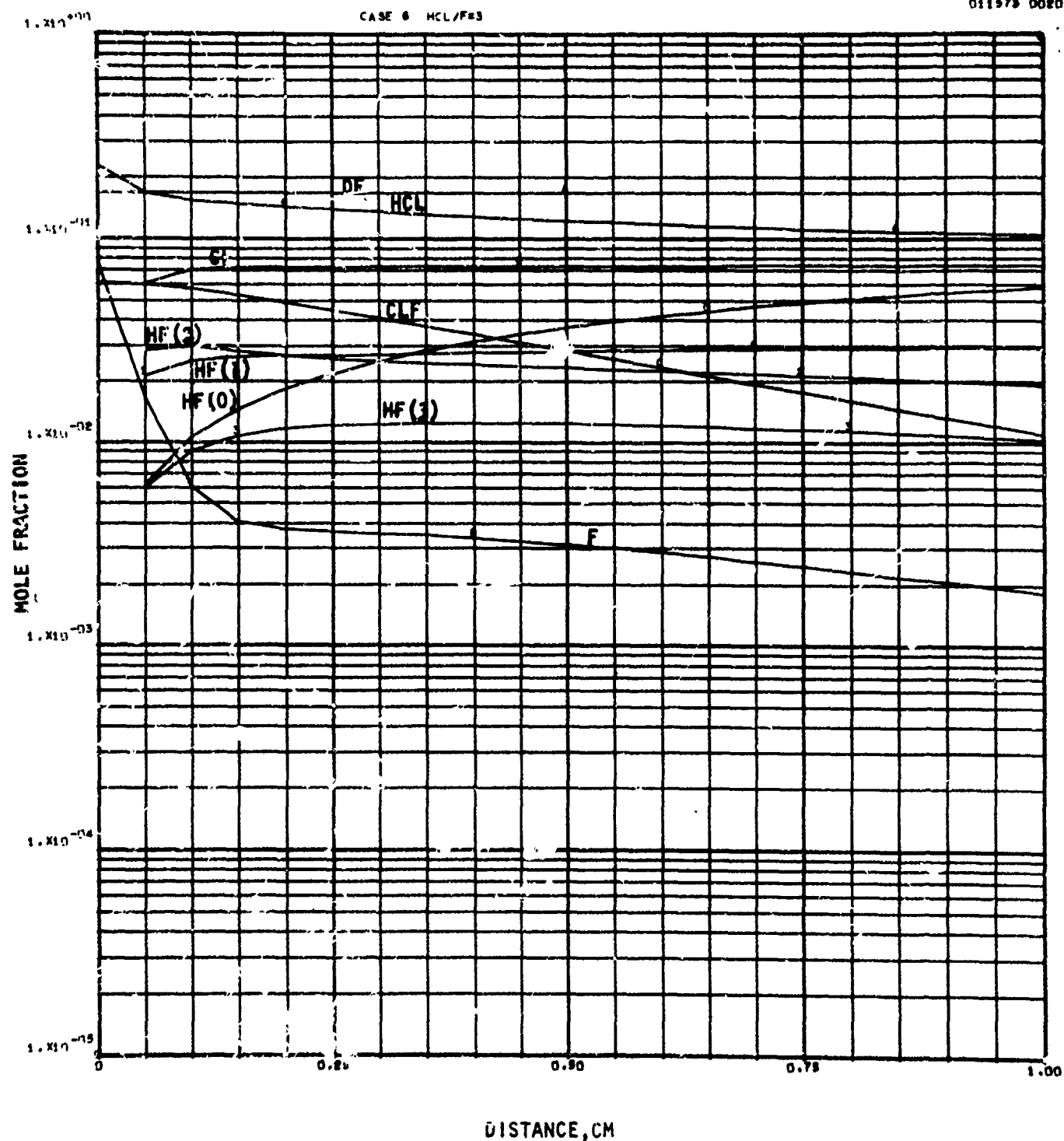


Figure S1. Case VI: $\text{ClF}_5\text{-ND}_3\text{-He-HCl}$ ($F = 10\%$, 1500 K, Series I)
Species Plot

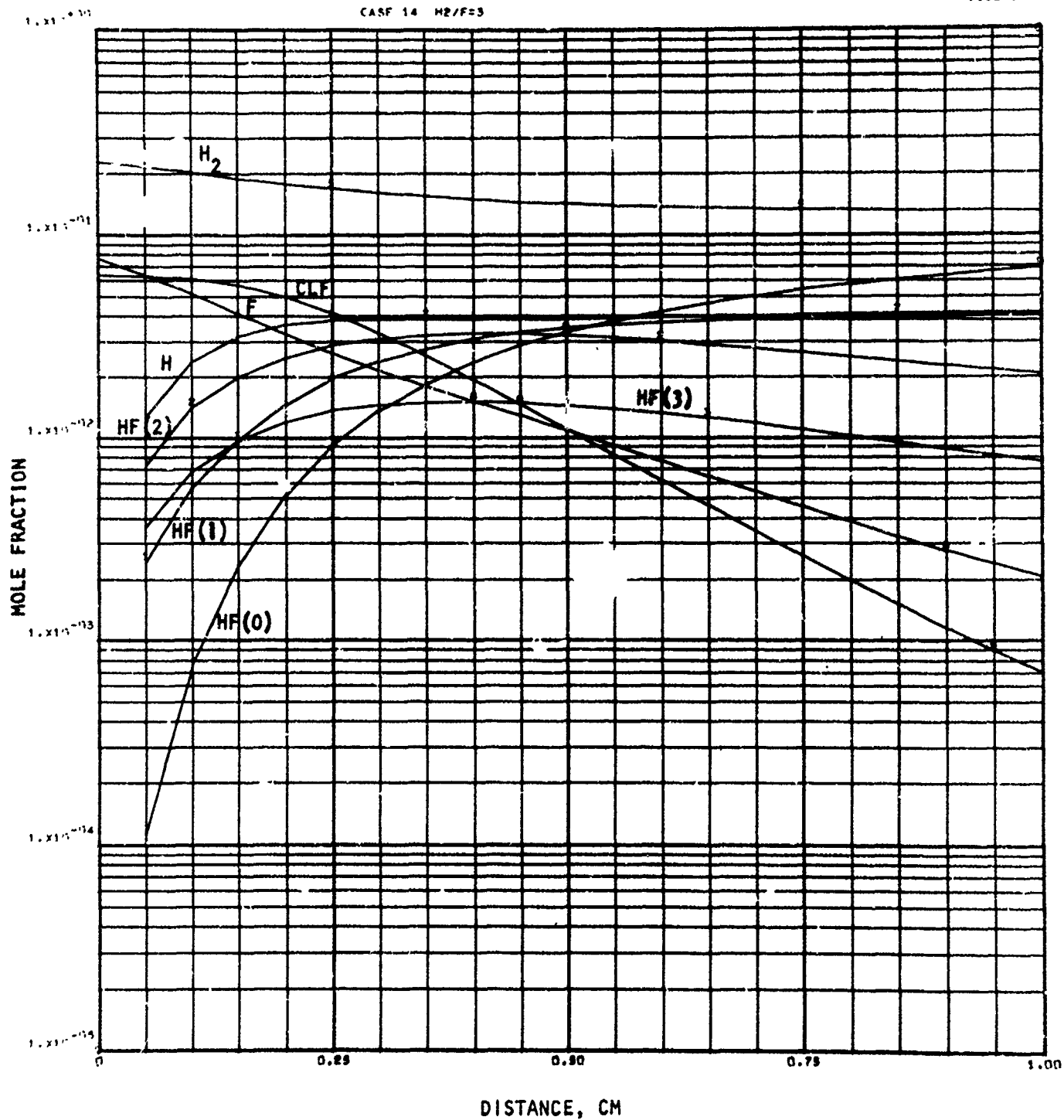
CASE 14 H₂/F=3

Figure 52. Case VII; ClF₅-C₆F₆-He-H₂ (F = 10%, 1500 K, Series I)
Species Plot

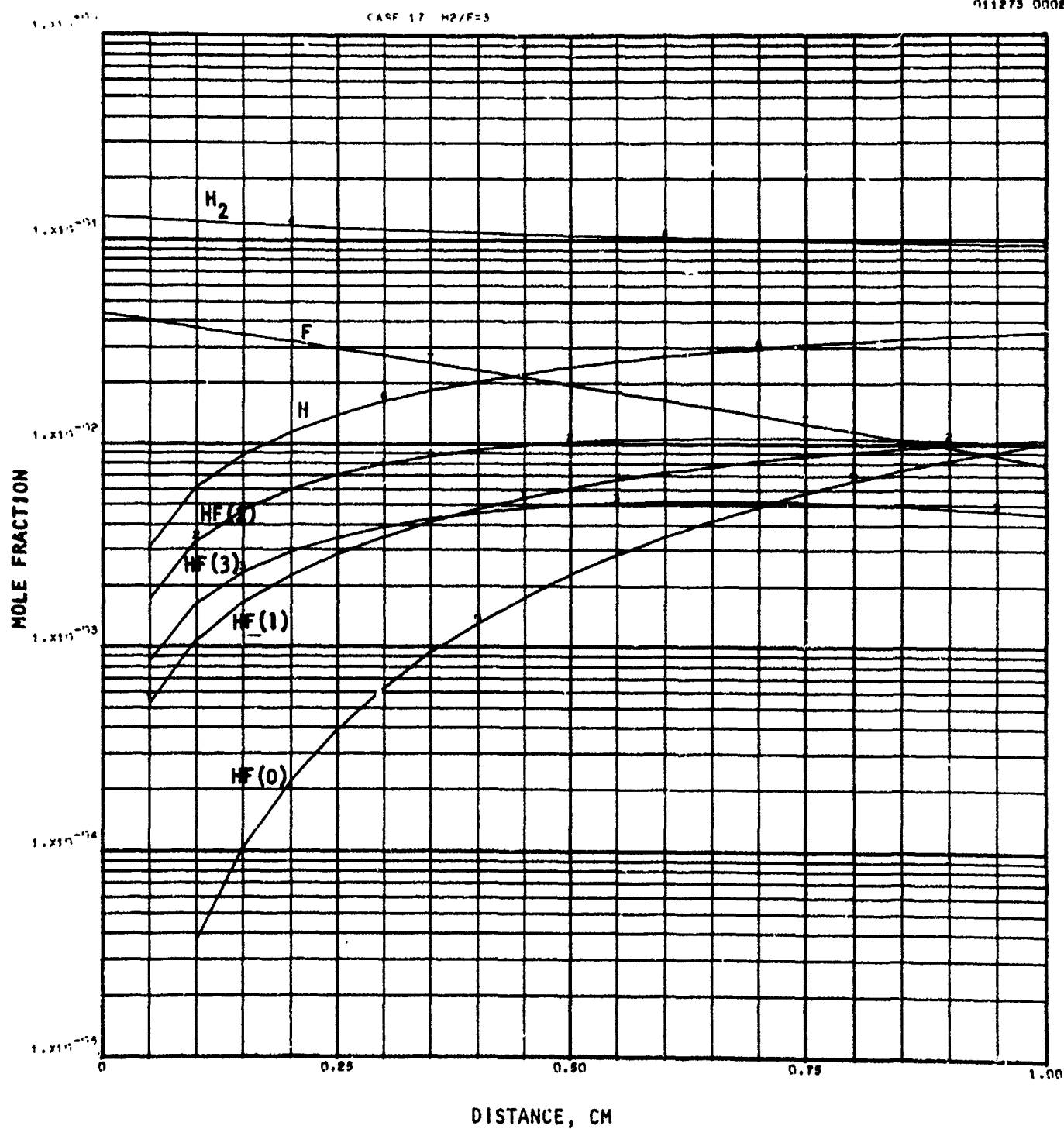


Figure 53. Case VIII: $ClF_5-C_6F_6-He-HCl$ ($F = 10\%$, 1500 K, Series I)
Species Plot

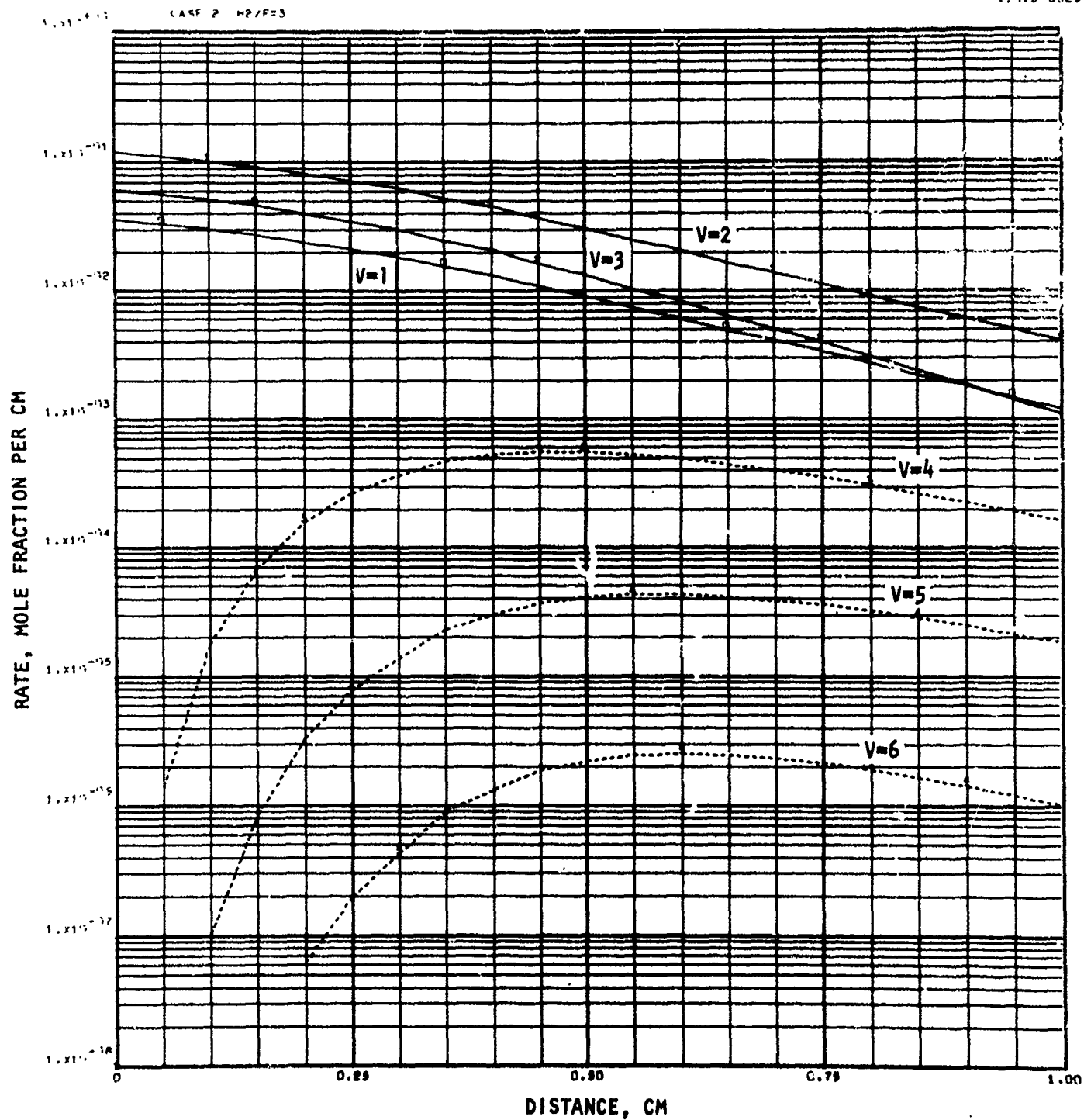


Figure 54. Case I: F_2 -D₂-He-H₂ (F = 10%, 1500 K, Series I)
Pumping Reaction, $F_2 + H_2 \rightarrow HF(V) + H$

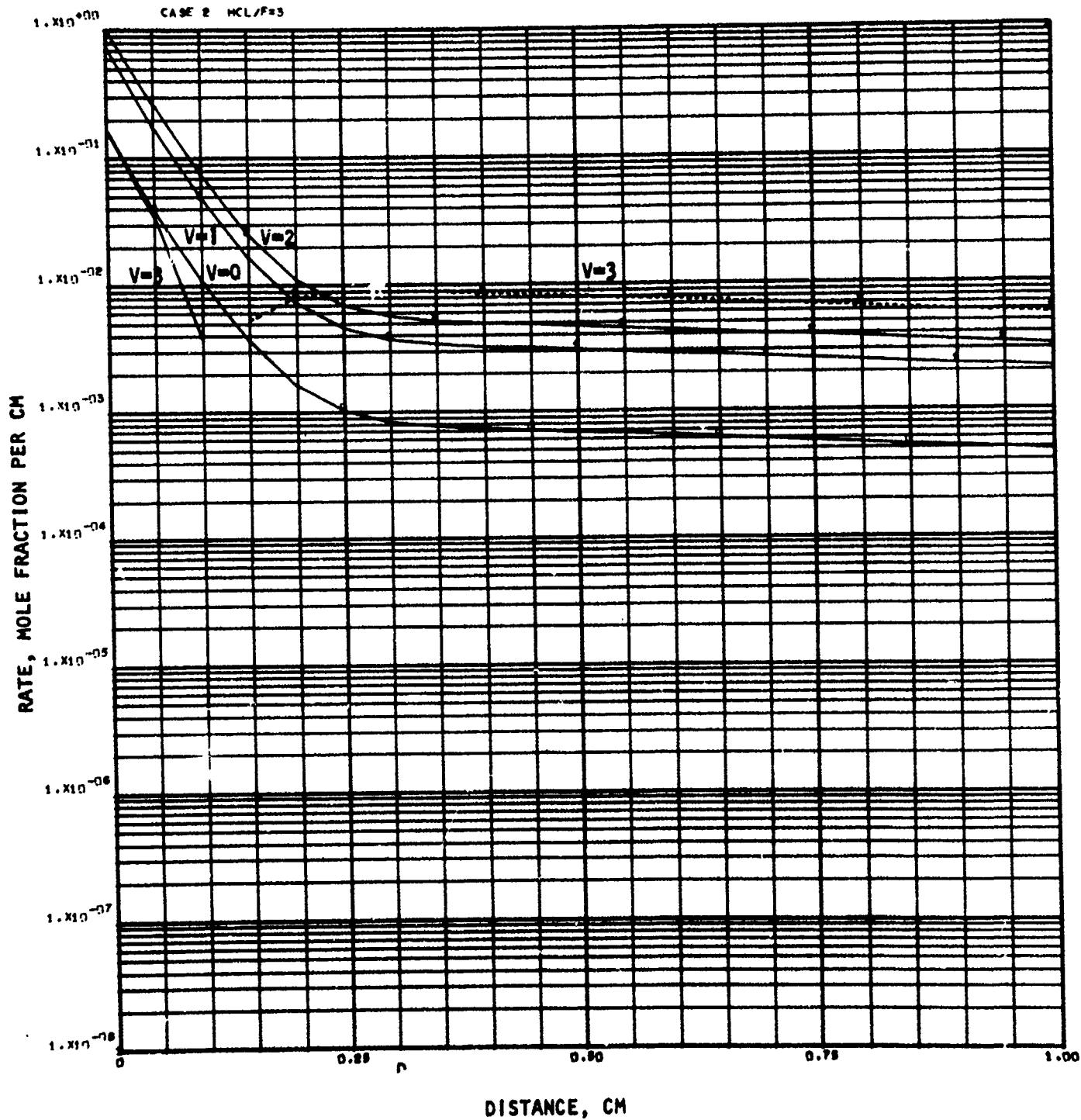


Figure 55. Case II: F_2-D_2 -He-HCl(F = 10%, 1500 K, Series I)
Pumping Reaction, $F + H_2 \rightarrow HF(V) + Cl$

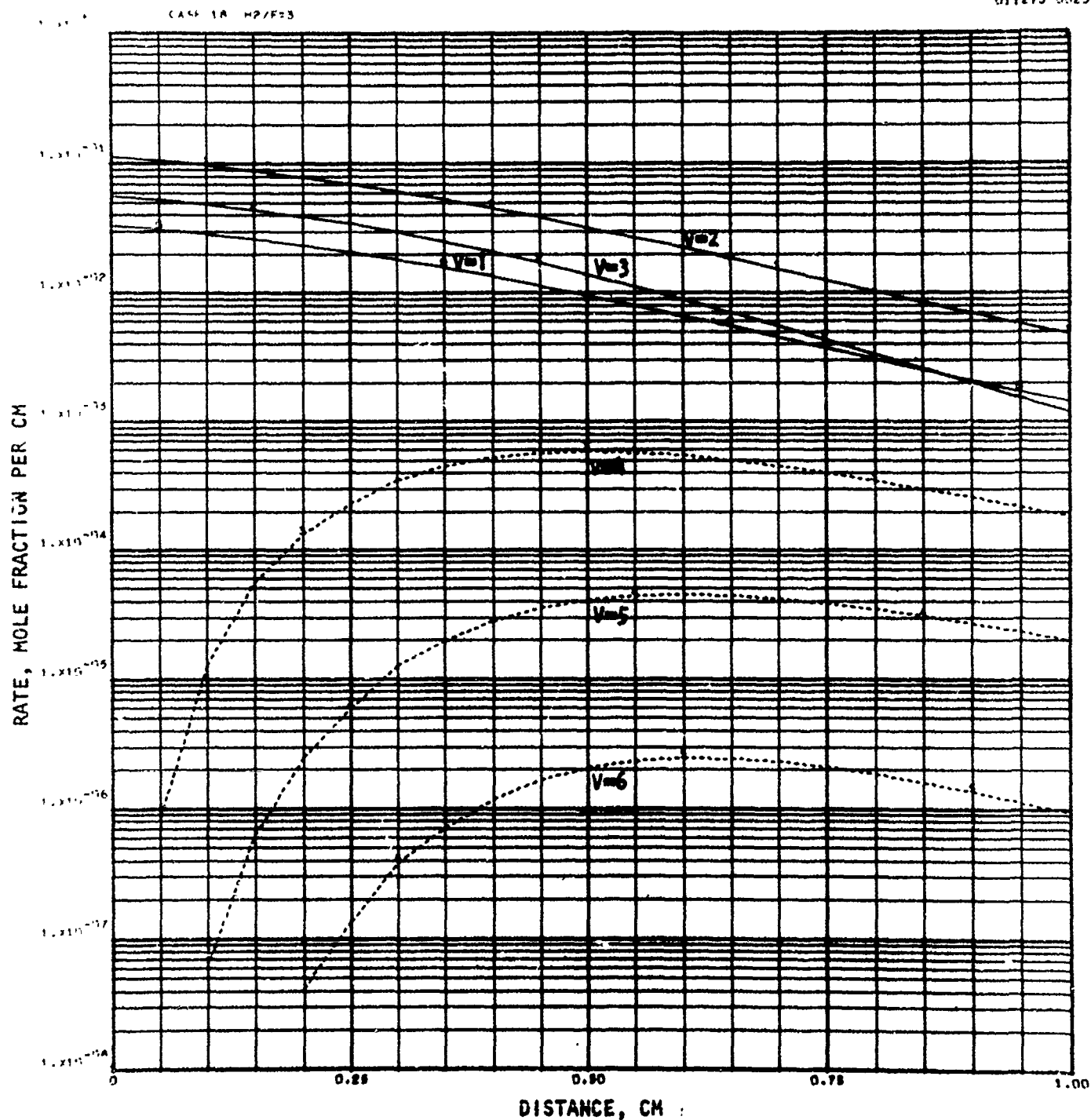


Figure 56. Case III: $F_2-C_6F_6-He-H_2$ ($F = 10\%$, 1500 K, Series I)
Pumping Reaction, ${}_6F + H_2 \rightarrow HF(V) + H$

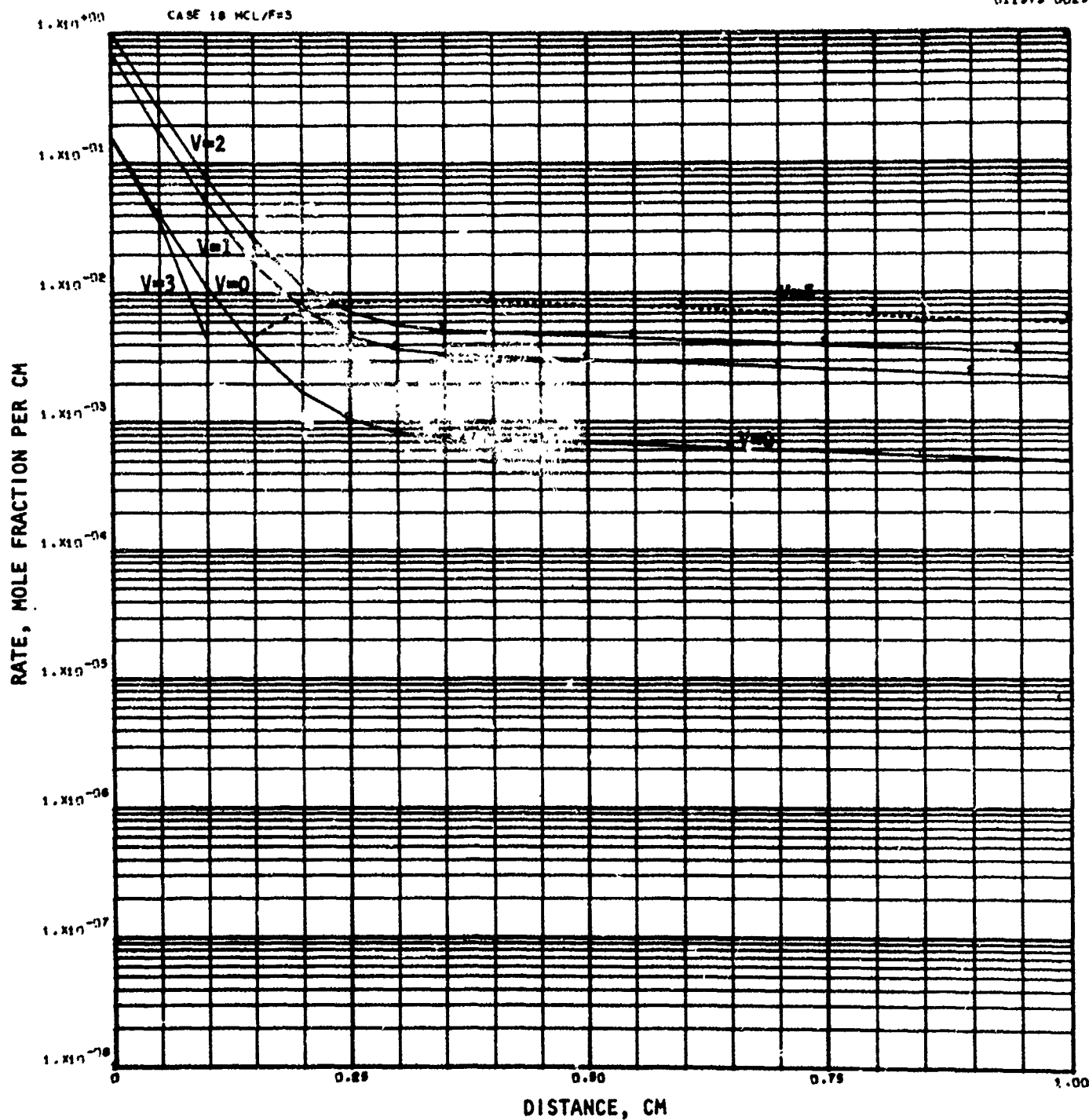


Figure 57. Case IV: $F_2-C_6F_6$ -He-HCl (F = 10%, 1500 K, Series I)
Pumping Reaction, $F + HCl \rightarrow HF(V) + Cl$

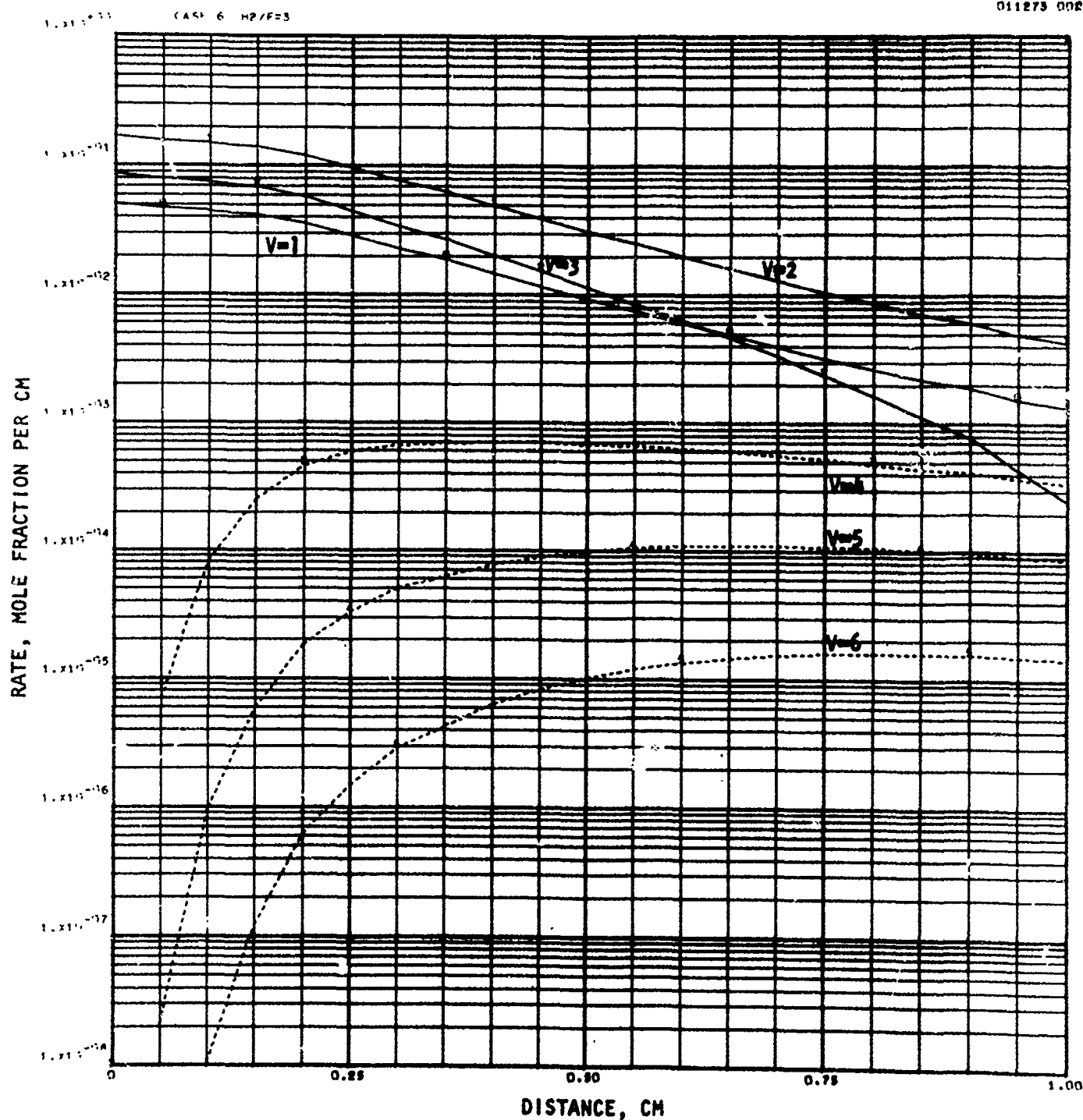


Figure 58. Case V: $\text{ClF}_5\text{-ND}_3\text{-He-H}_2$ (F = 10%, 1500 K, Series I)
Pumping Reaction, $\text{F} + \text{H}_2 \rightarrow \text{HF(V)} + \text{H}$

55035020
011973 0025

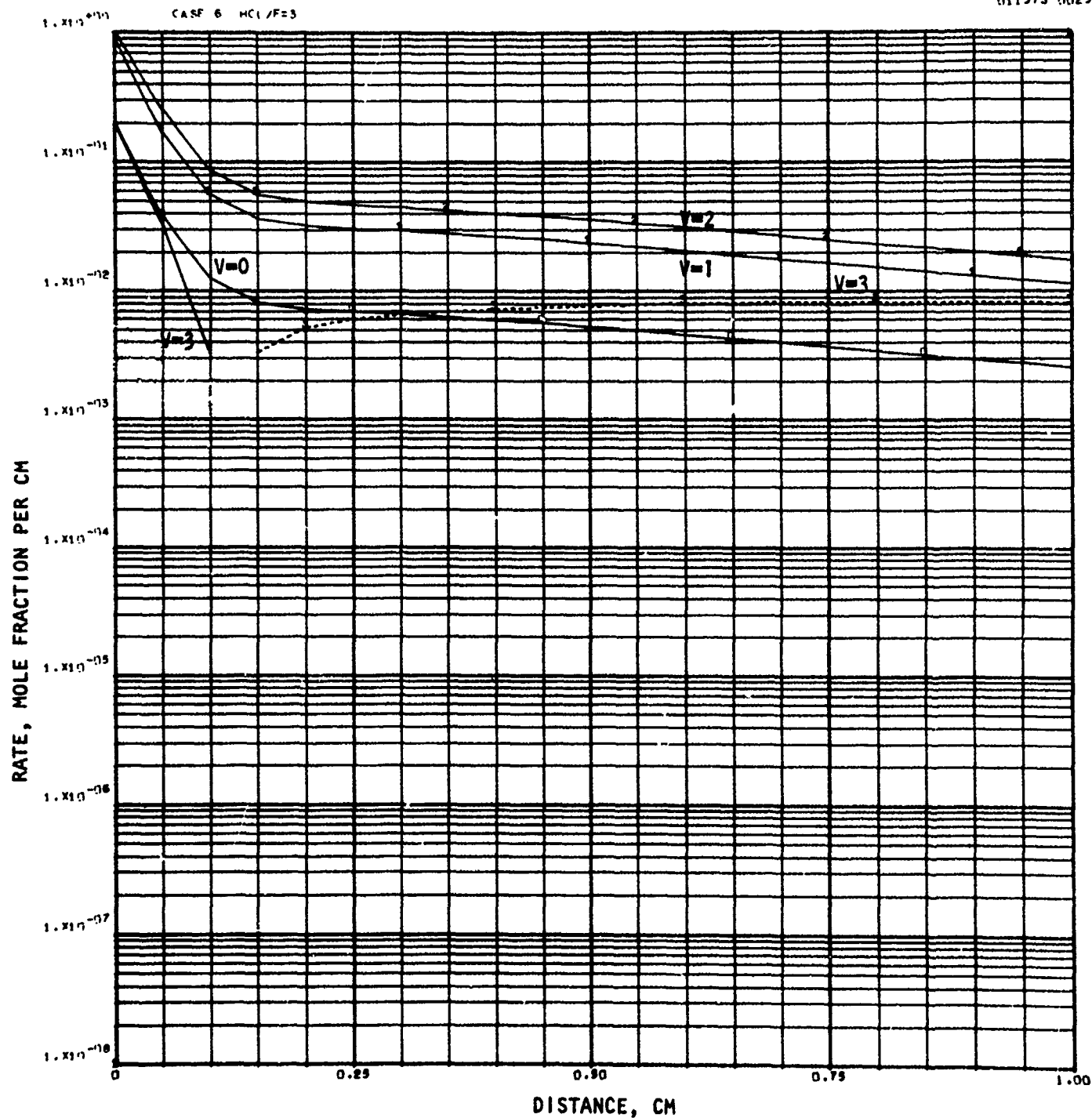


Figure 59. Case VI: $\text{ClF}_5\text{-ND}_3\text{-He-HCl}$ ($F = 10\%$, 1500 K, Series I)
Pumping Reaction, $\text{F} + \text{HCl} \rightarrow \text{HF}(V) + \text{Cl}$

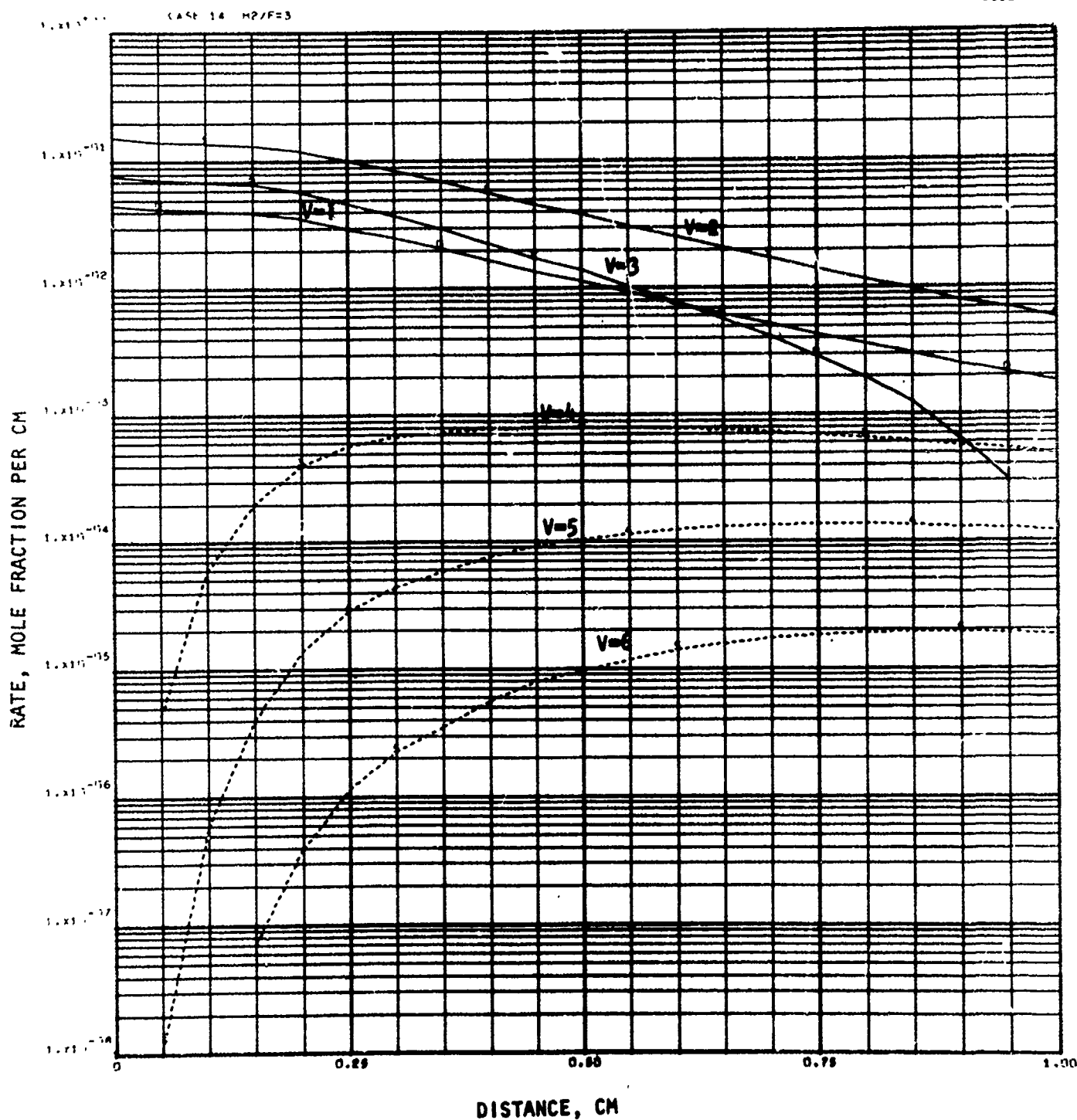


Figure 60. Case VII: $ClF_5-C_6F_6-He-H_2$ ($F = 10\%$, 1500 K, Series I)
Pumping Reaction, $F + H_2 \rightarrow HF(V) + H$

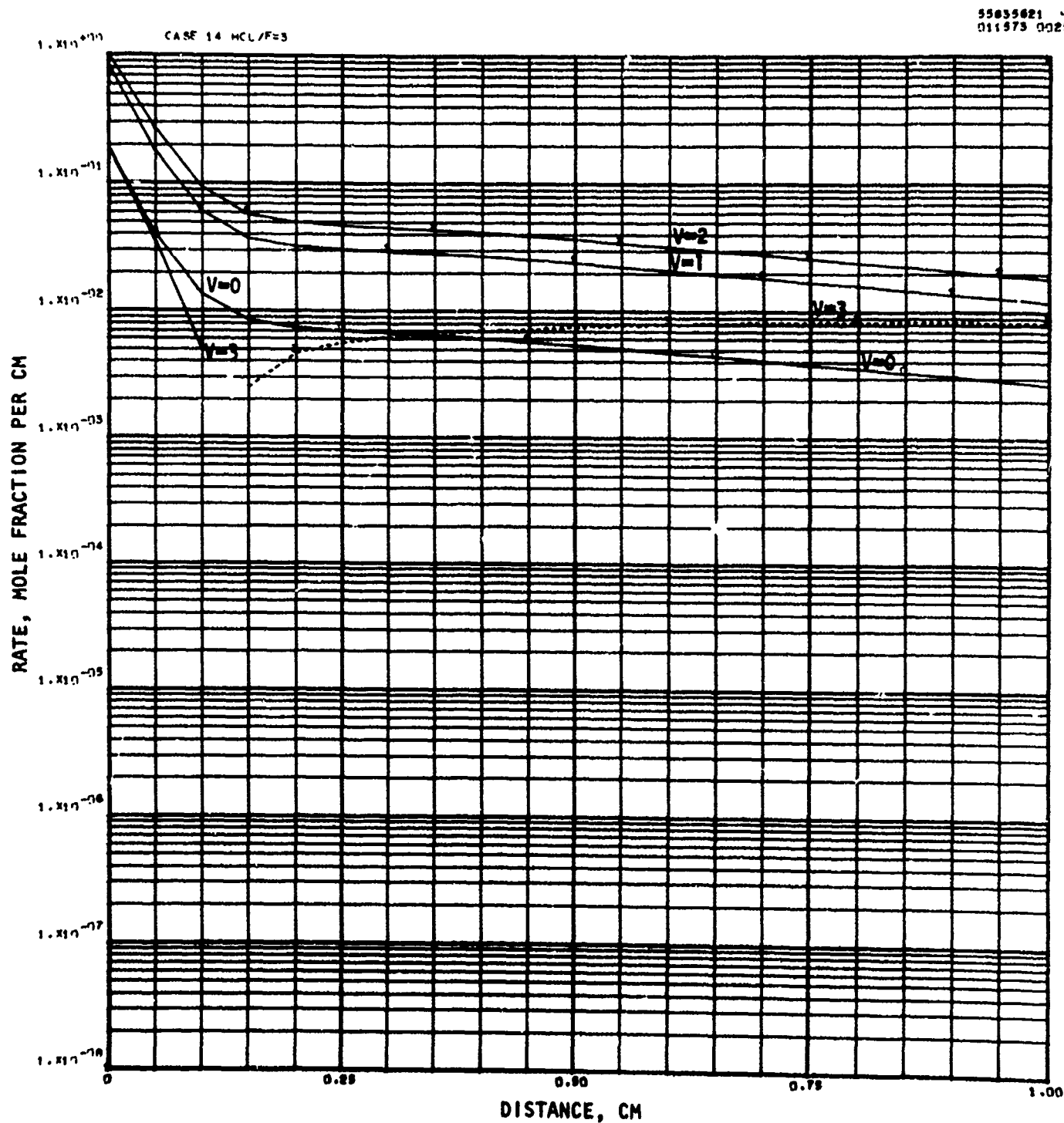


Figure 61. Case VIII: $\text{ClF}_5\text{-C}_6\text{F}_6\text{-He-HCl}$ ($F = 10\%$, 1500 K, Series I)
Pumping Reaction, $\text{F} + \text{HCl} \rightarrow \text{HF(V)} + \text{Cl}$

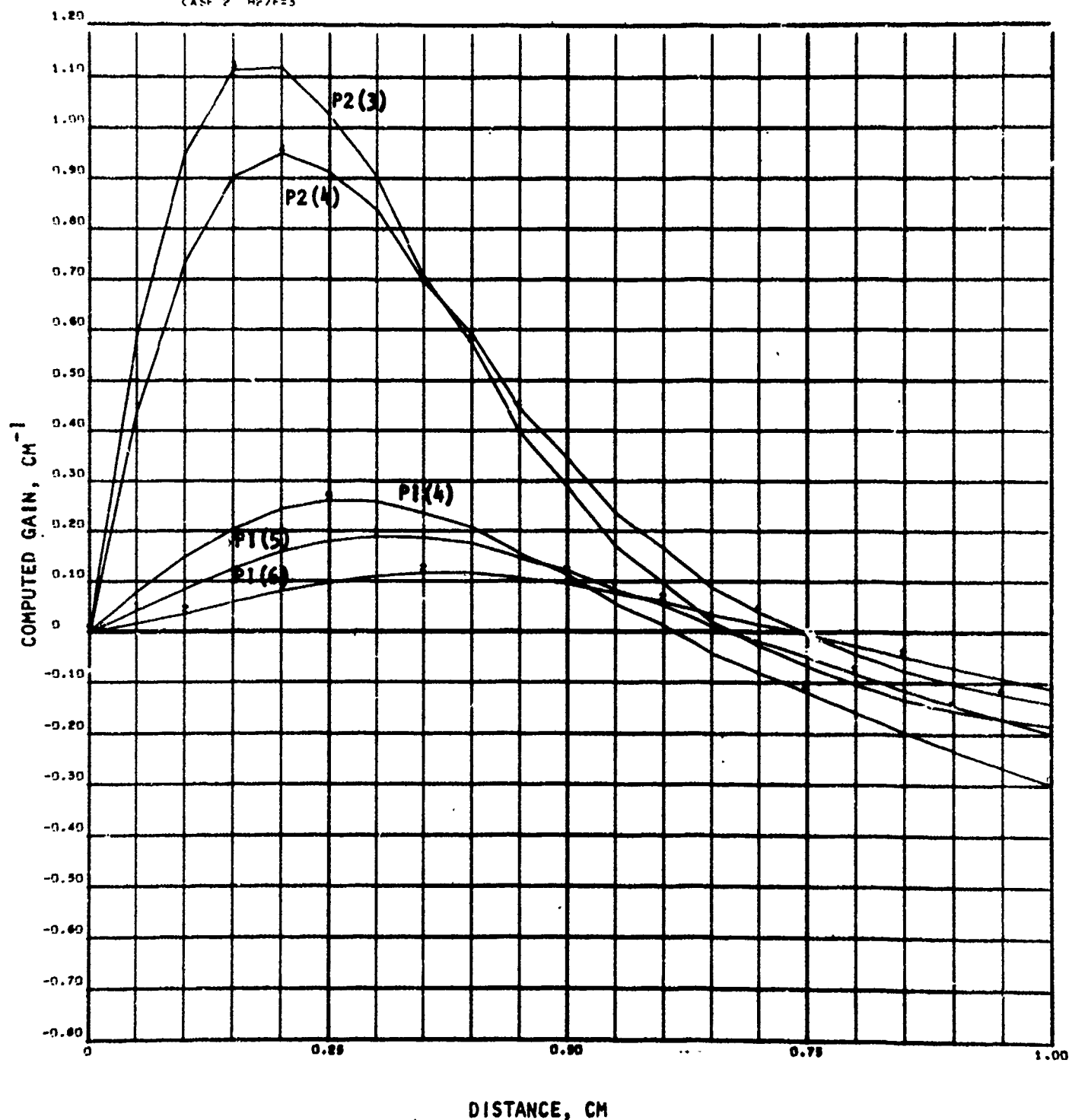


Figure 62. Case I: $F_2-D_2-He-H_2$ ($F = 10\%$, 1500 K, Series I)
Computed Gain, Zero Power

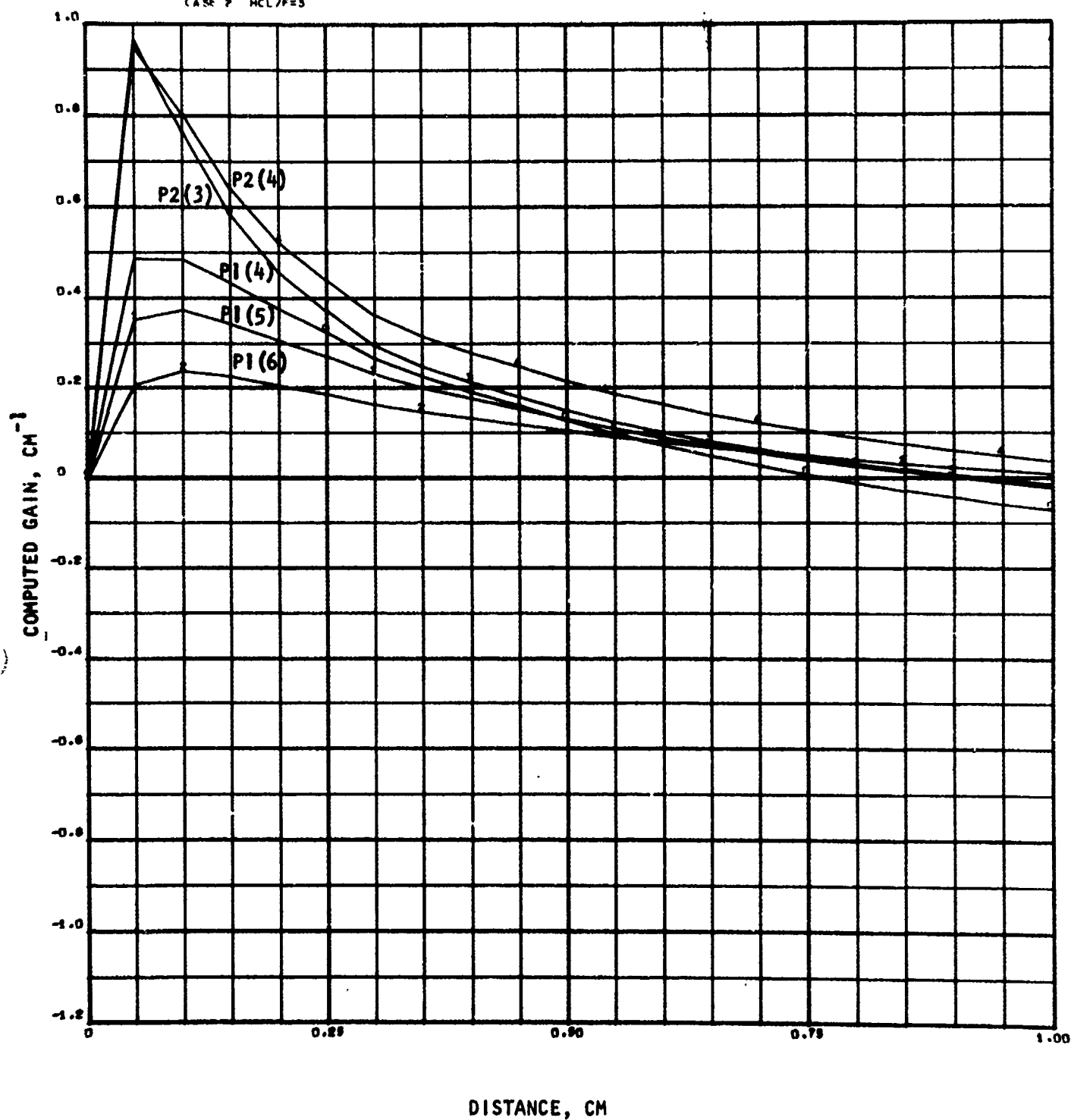


Figure 63. Case II: $\text{F}_2\text{-D}_2\text{-He-HCl}$ ($F = 10\%$, 1500 K, Series I)
Computed Gain; Zero Power

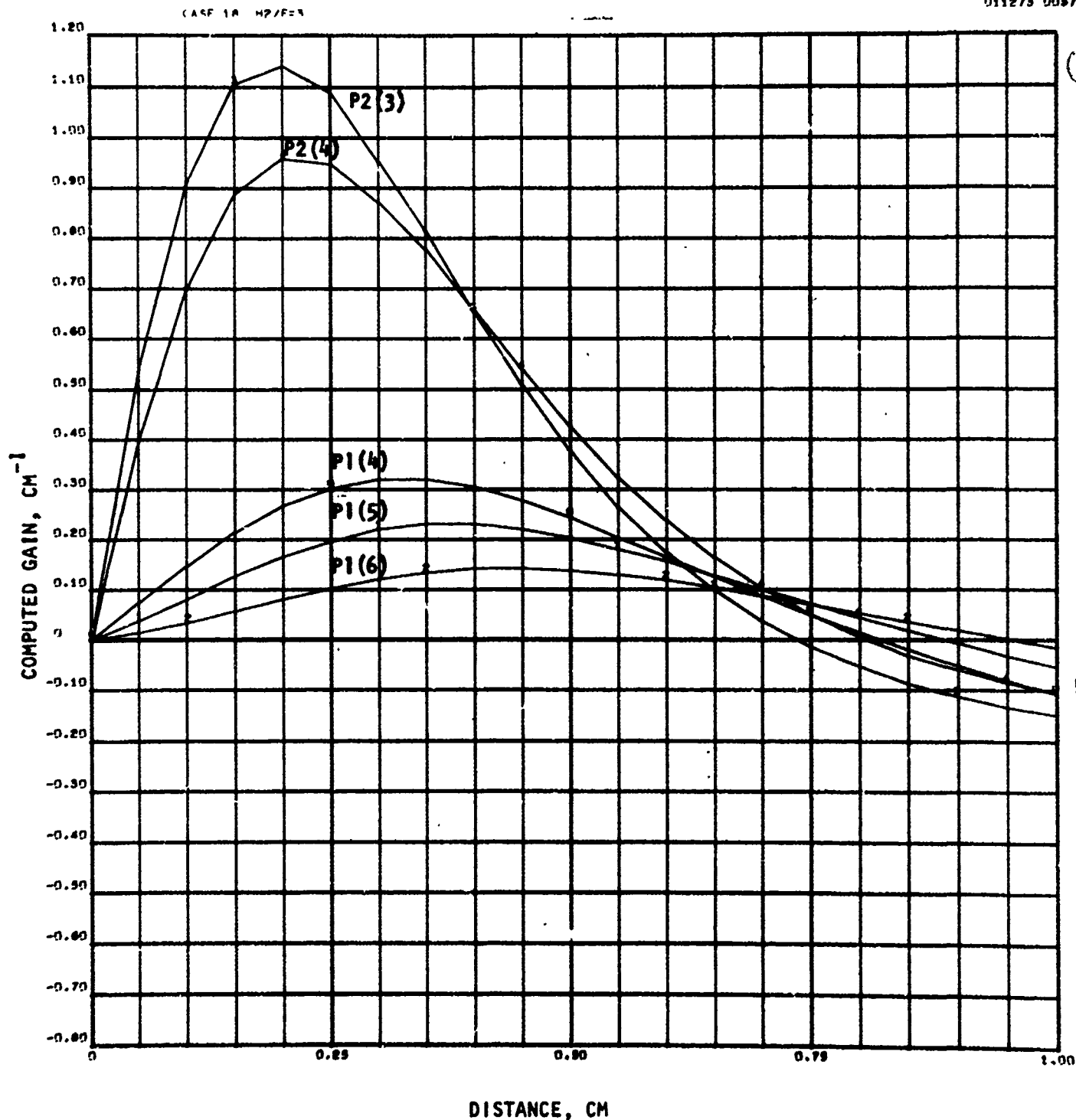


Figure 64. Case III: $\text{F}_2\text{-C}_2\text{F}_6\text{-He-H}_2$ ($F = 10\%$, 1500 K, Series I)
Computed Gain, Zero Power

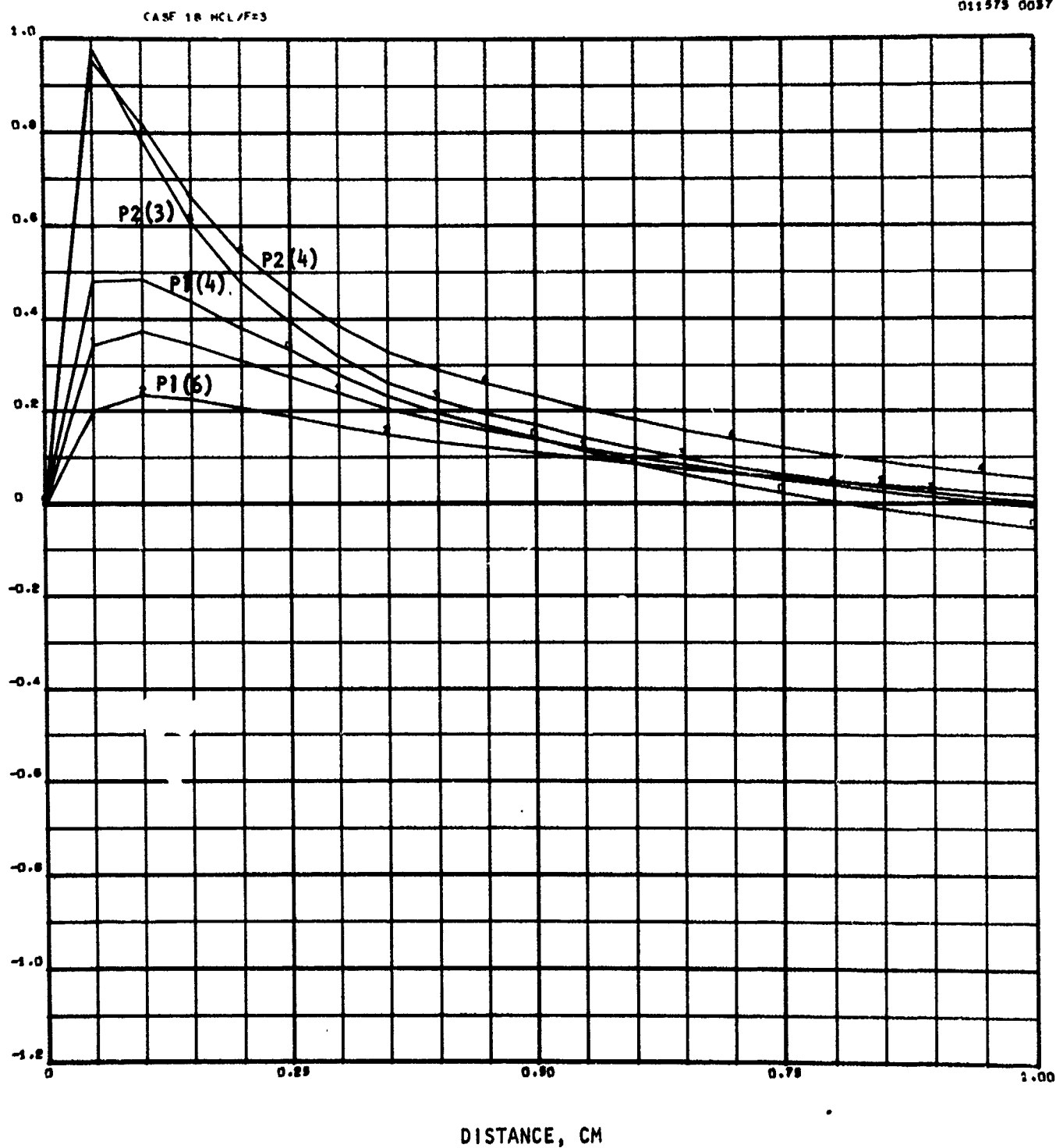


Figure 65. Case IV: $F_2-C_6F_6-He-HCl$ ($F = 10\%$, 1500, K, Series I)
Computed Gain, Zero Power

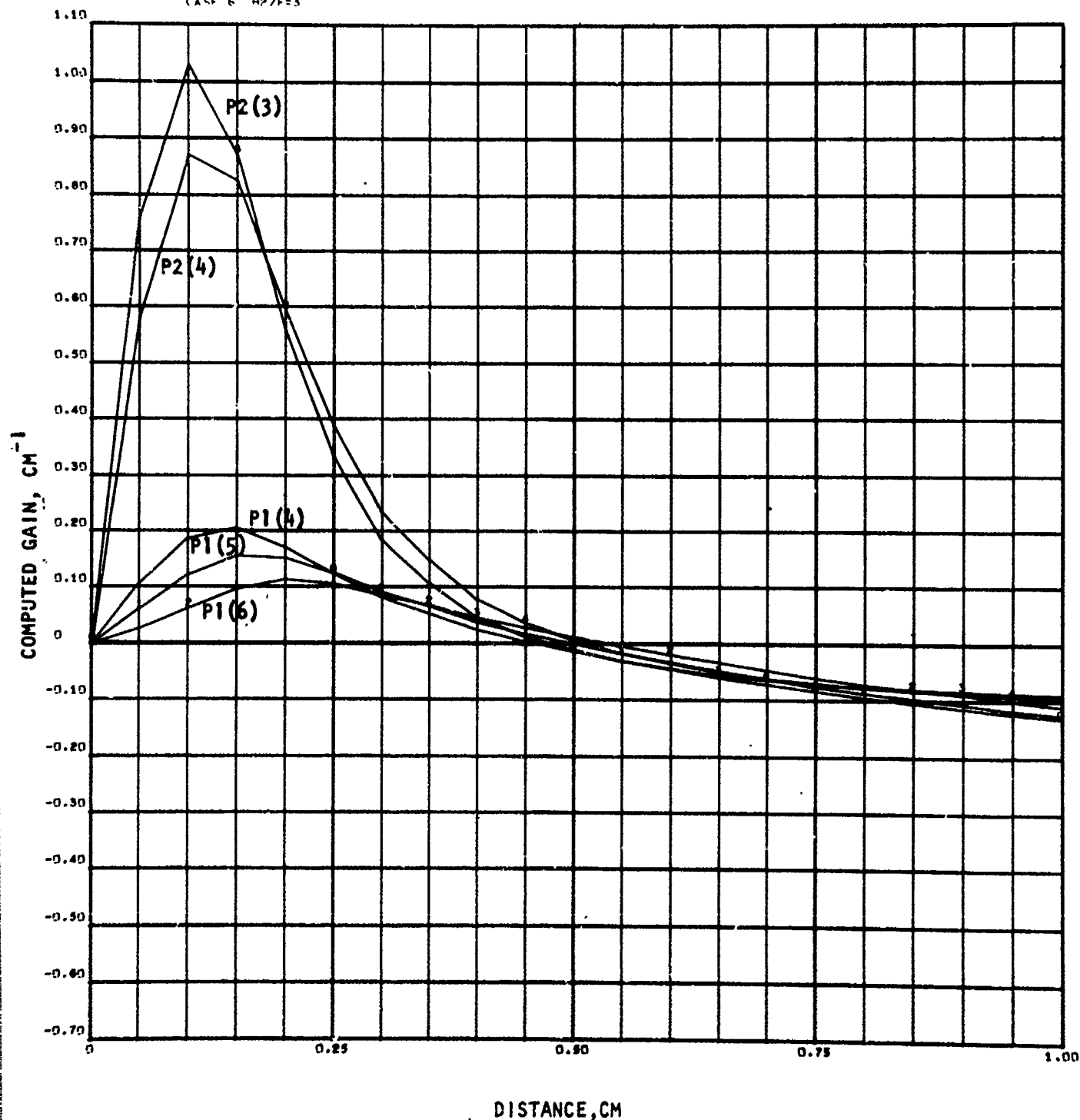


Figure 66. Case V: $\text{ClF}_5\text{-ND}_3\text{-He-H}_2$ ($F = 10\%$, 1500, K, Series I)
Computed Gain, Zero Power

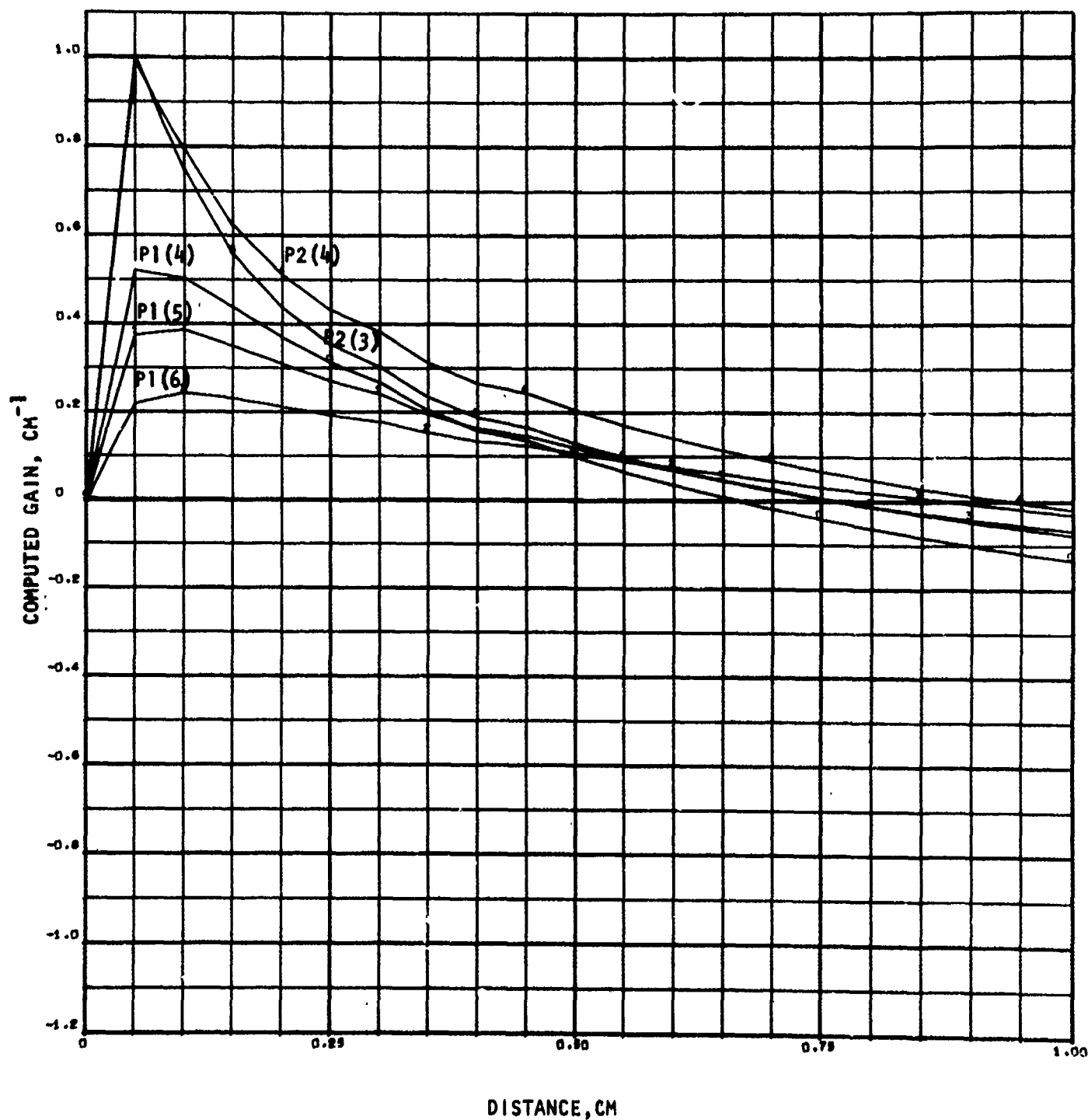


Figure 67. Case VI: $\text{ClF}_5\text{-ND}_3\text{-He-HCl}$ ($F = 10\%$, 1500 K, Series I)
Computed Gain, Zero Power

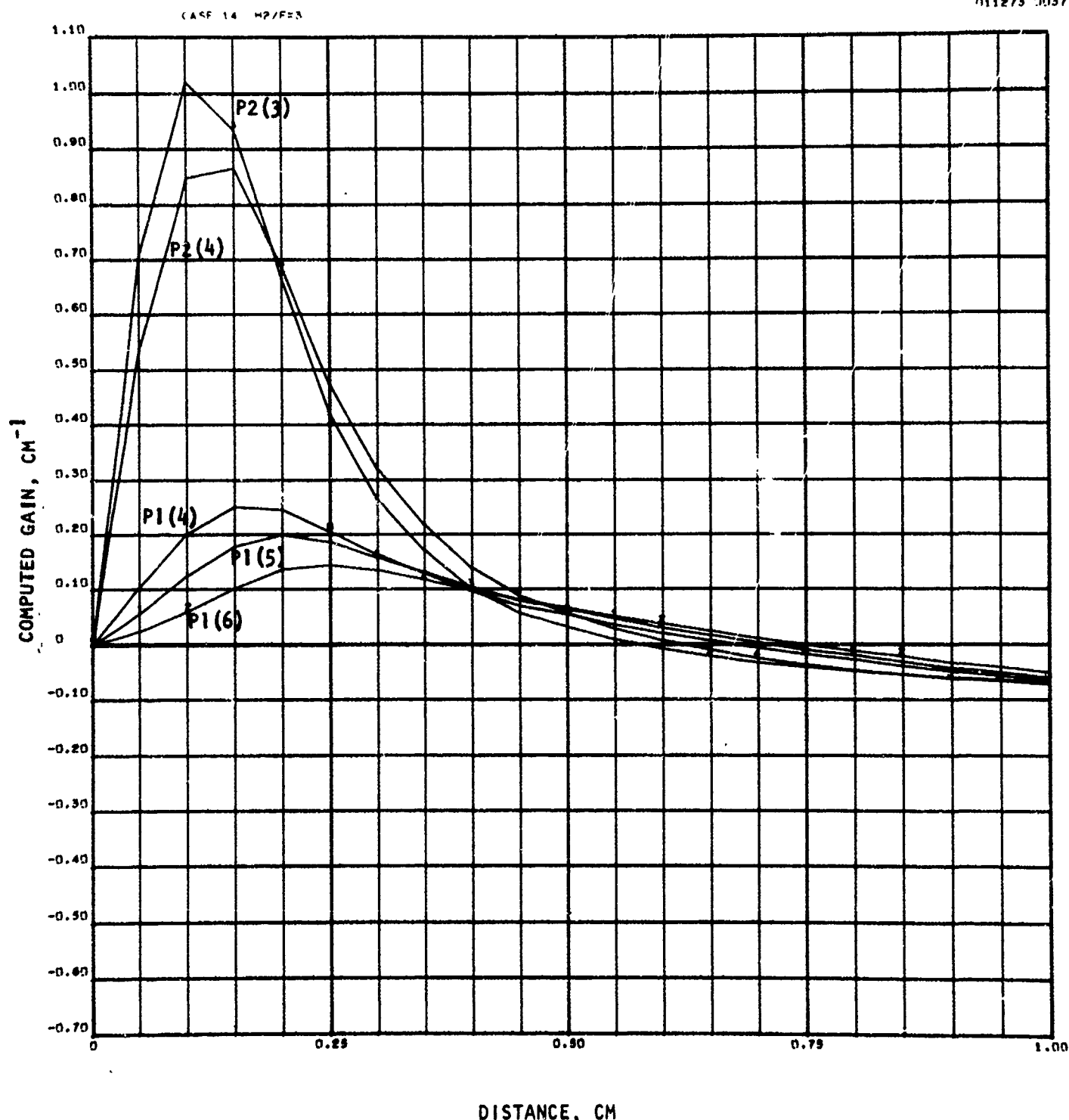


Figure 68. Case VII: $\text{ClF}_5\text{-C}_6\text{F}_6\text{-He-H}_2$ ($F = 10\%$, 1500 K, Series I)
Computed Gain; Zero Power

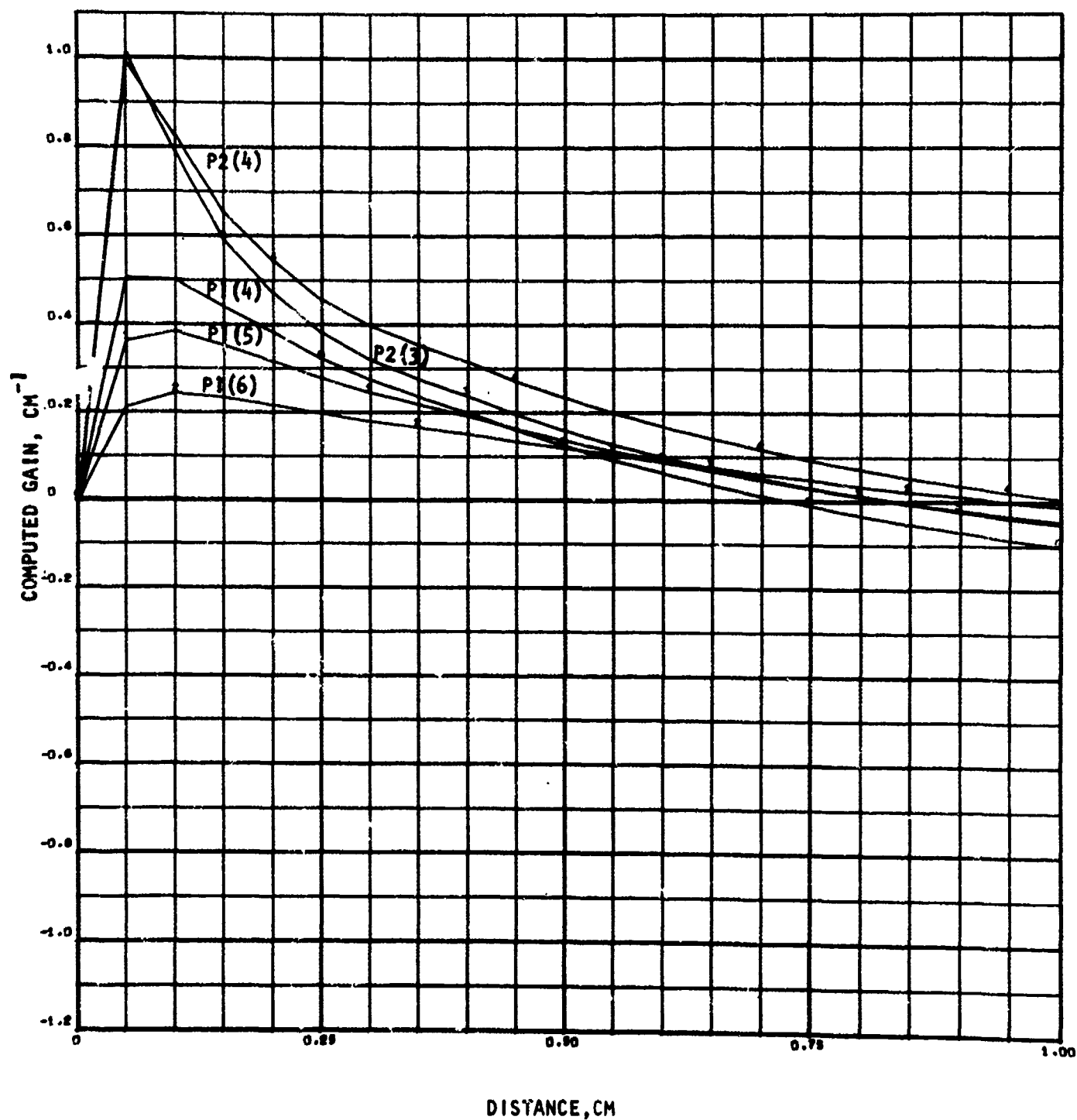


Figure 69. Case VIII: $\text{ClF}_5\text{-C}_6\text{F}_6\text{-He-HCl}$ ($F = 10\%$, 1500 K, Series I)
Computed Gain; Zero Power

CASE 1 H₂/P=3

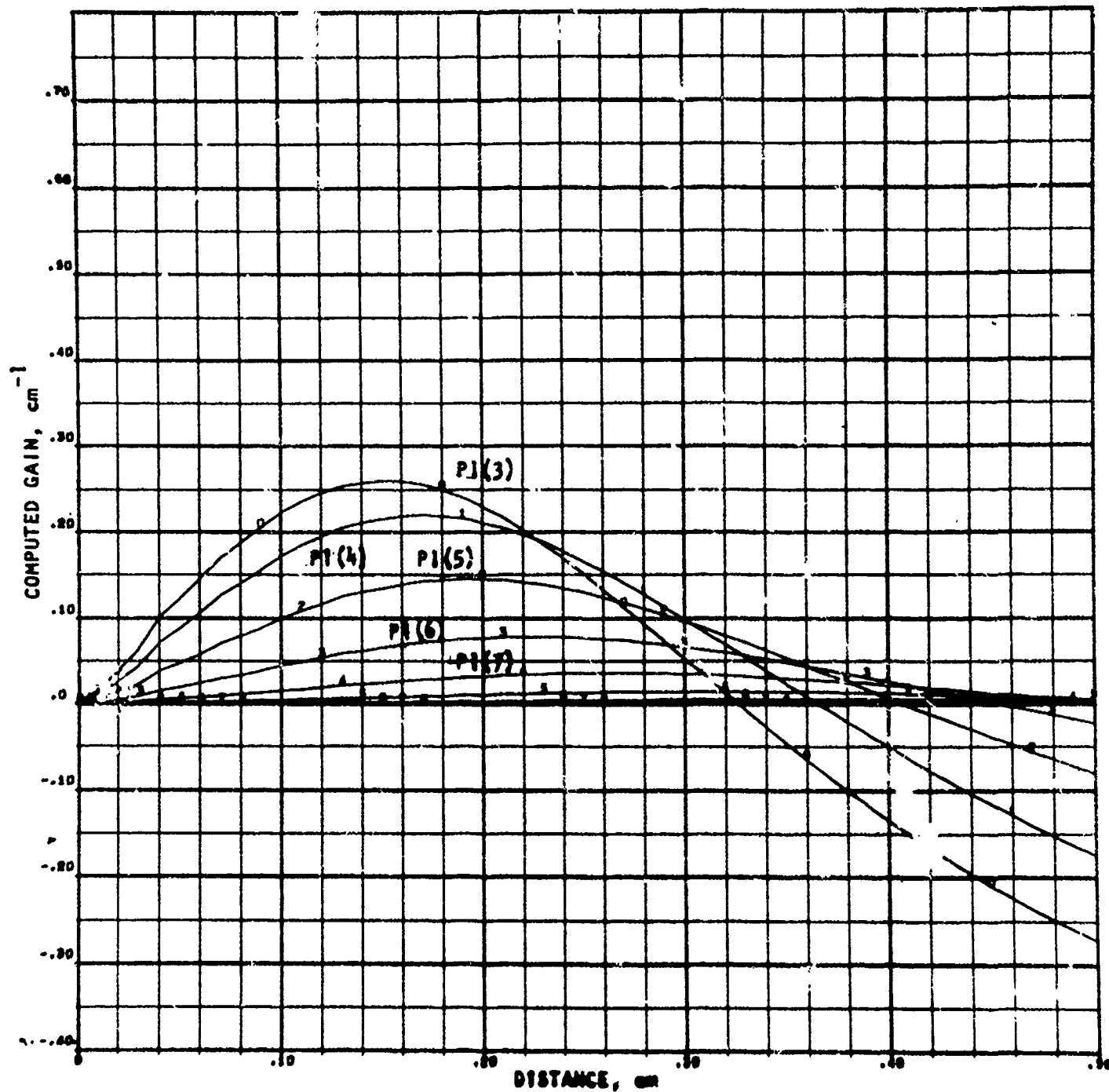


Figure 70. $F_2-D_2-He-H_2$ System, Computed Zero Power Gain on $HF(1) \rightarrow HF(0)$ Lines
($F = 10\%$, 1500 K, Series II)

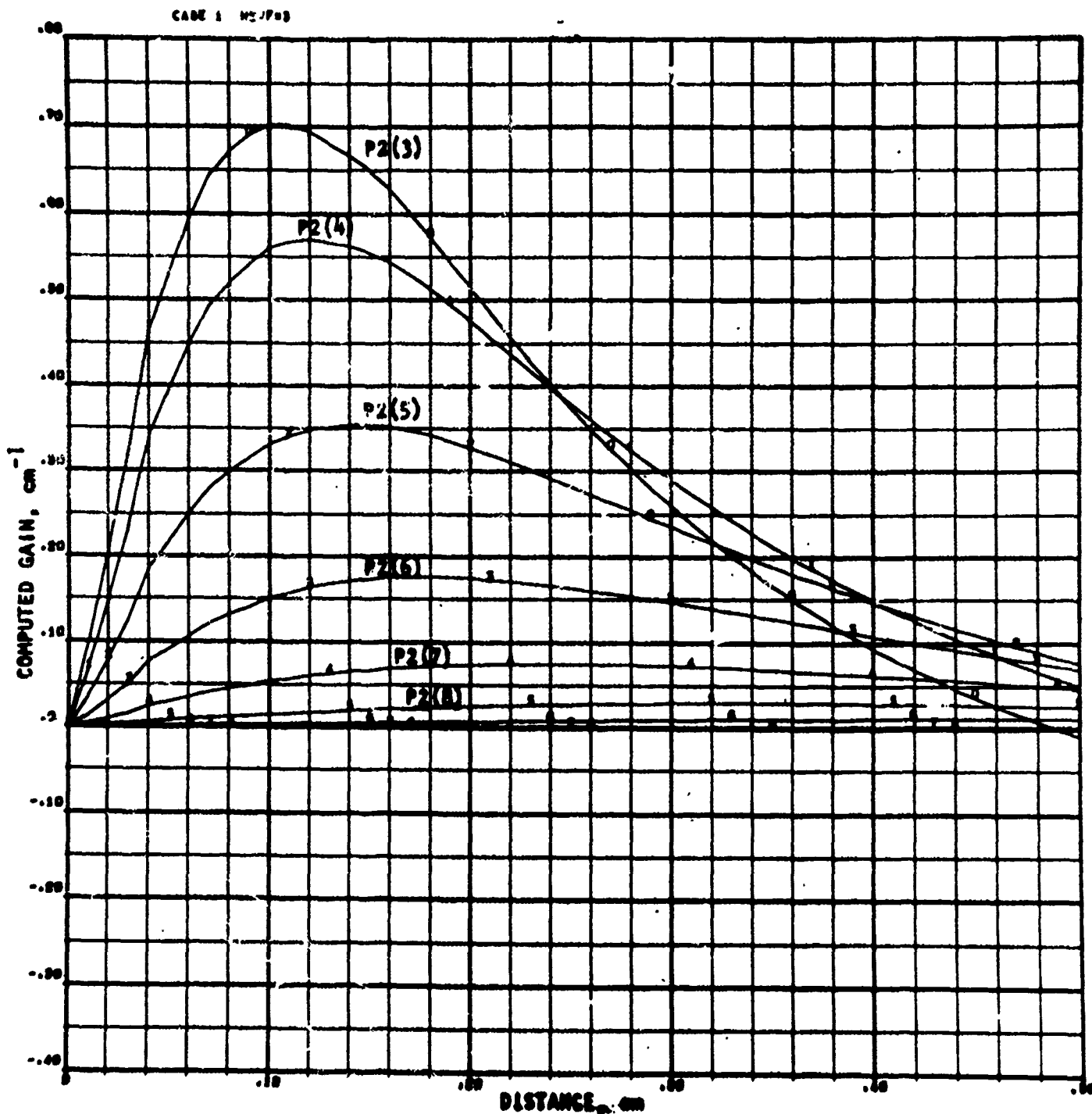


Figure 71. $\text{F}_2\text{-D}_2\text{-He-H}_2$ System, Computed Zero Power Gain on $\text{HF}(2) \rightarrow \text{HF}(1)$ Lines
($F = 10\%$, 1500 K, Series II)

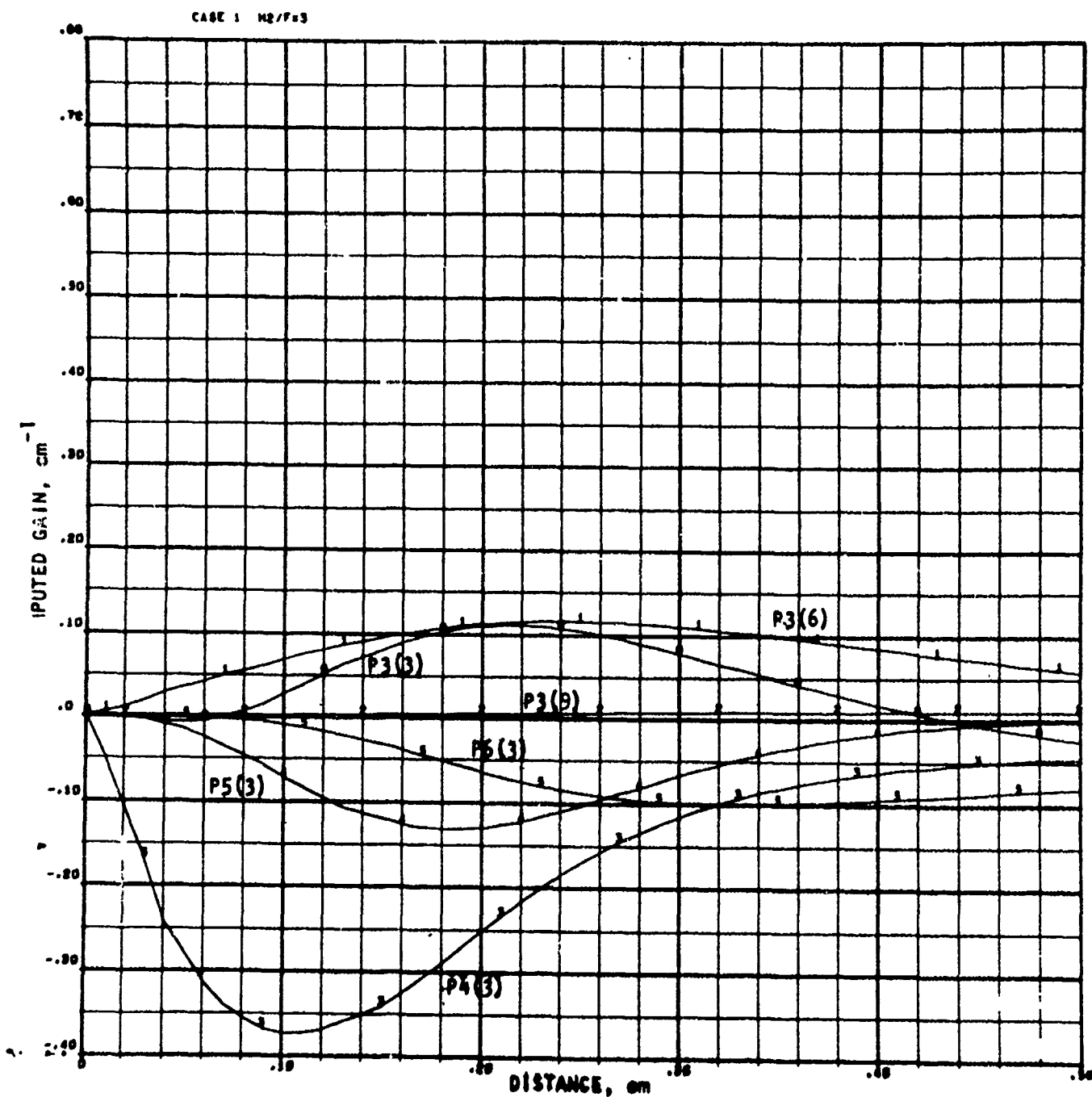


Figure 72. $\text{F}_2\text{-D}_2\text{-He-H}_2$ System, Computed Zero Power
Gain on Higher Lines
($F = 10\%$, 1500 K, Series II)

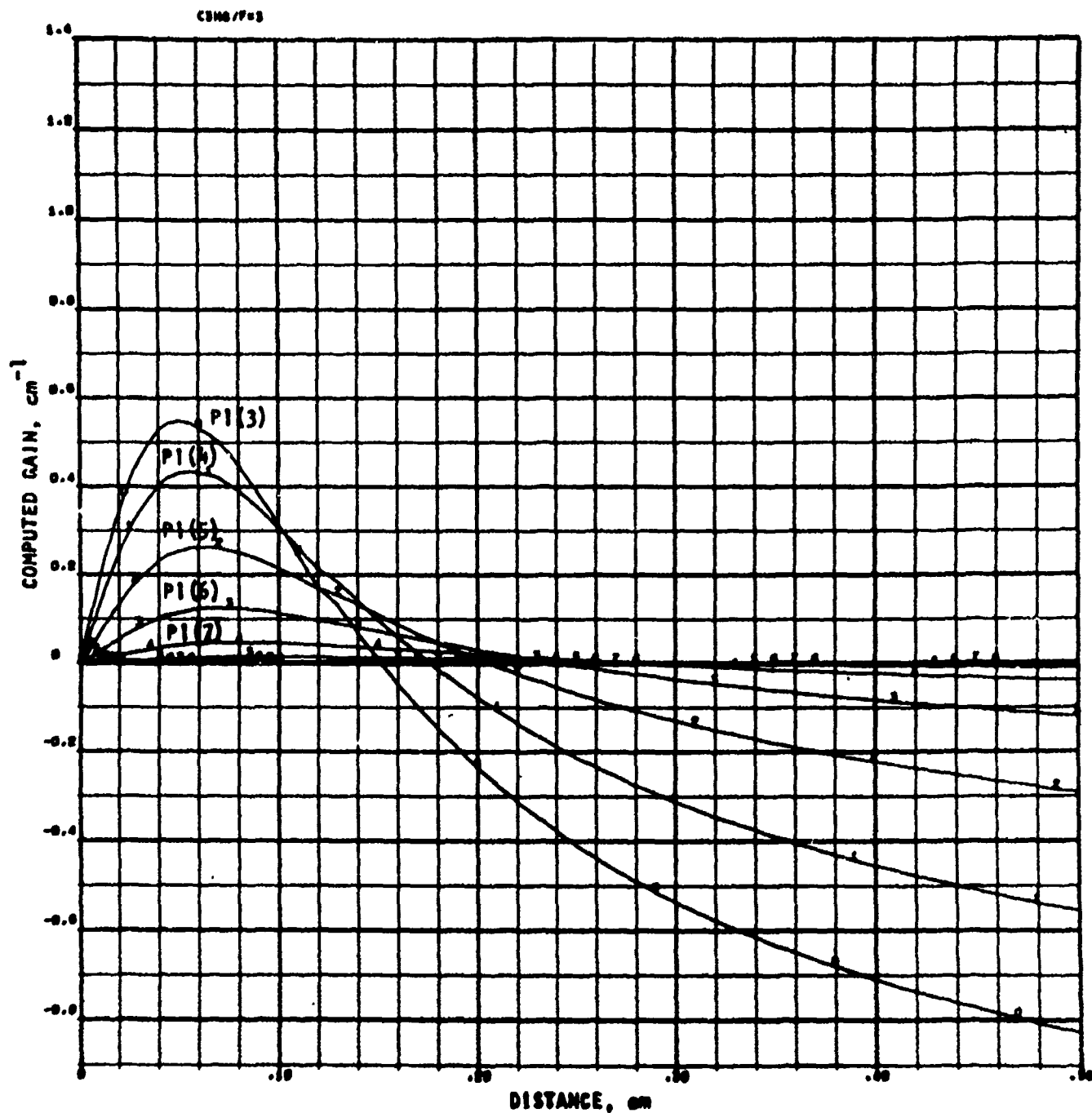


Figure 73. $\text{F}_2\text{-D}_2\text{-He-C}_3\text{H}_8$ System, Computed Zero Power
Gain on $\text{HF}(1) \rightarrow \text{HF}(0)$ Lines
($F = 10\%$, 1500 K, Series II)

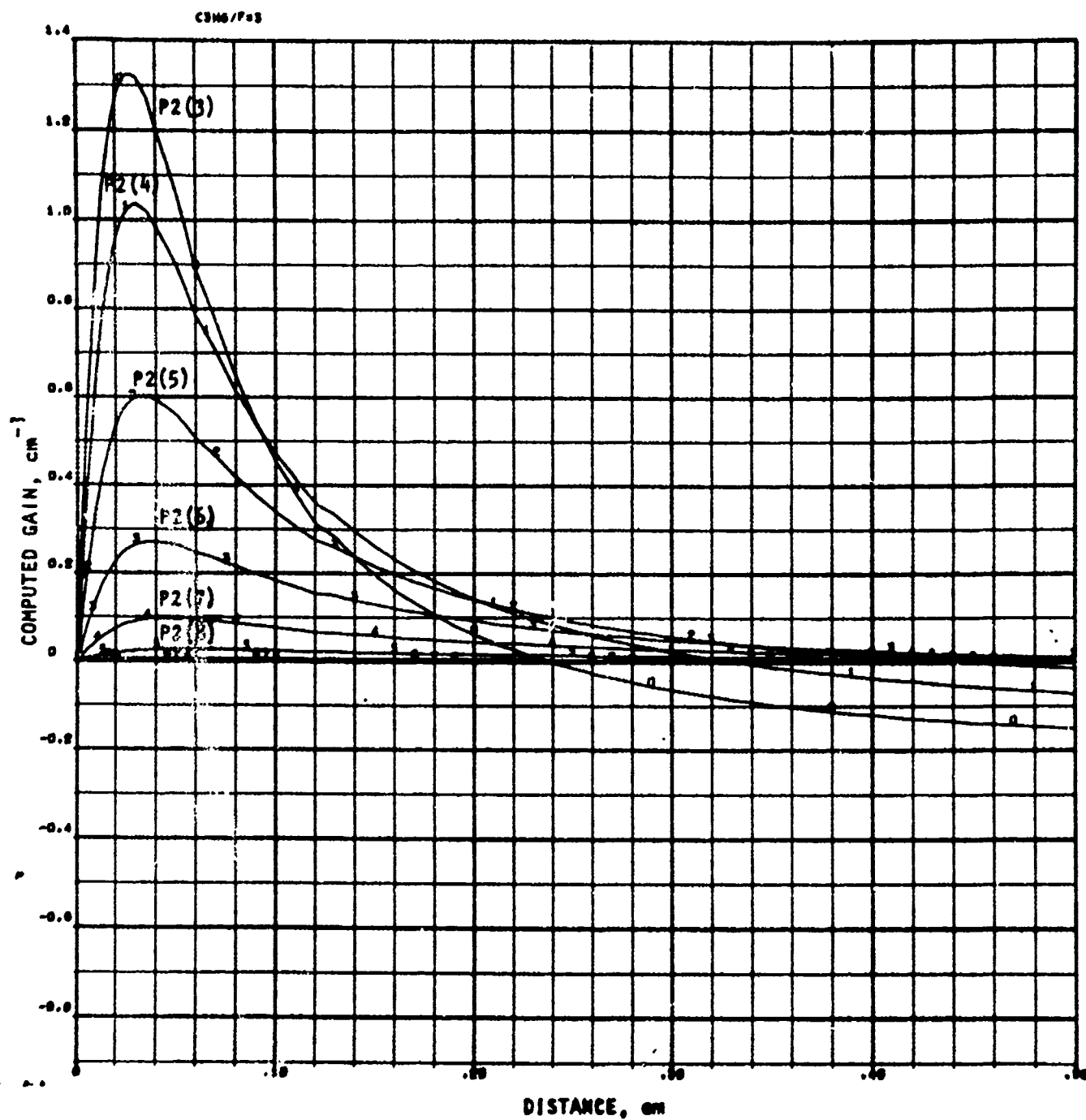


Figure 14. $\text{F}_2\text{-D}_2\text{-He-C}_3\text{H}_8$ System, Computed Zero Power
Gain on $\text{HF}(2) \rightarrow \text{HF}(1)$ Lines
($F = 10\%$, 1500 K, Series II)

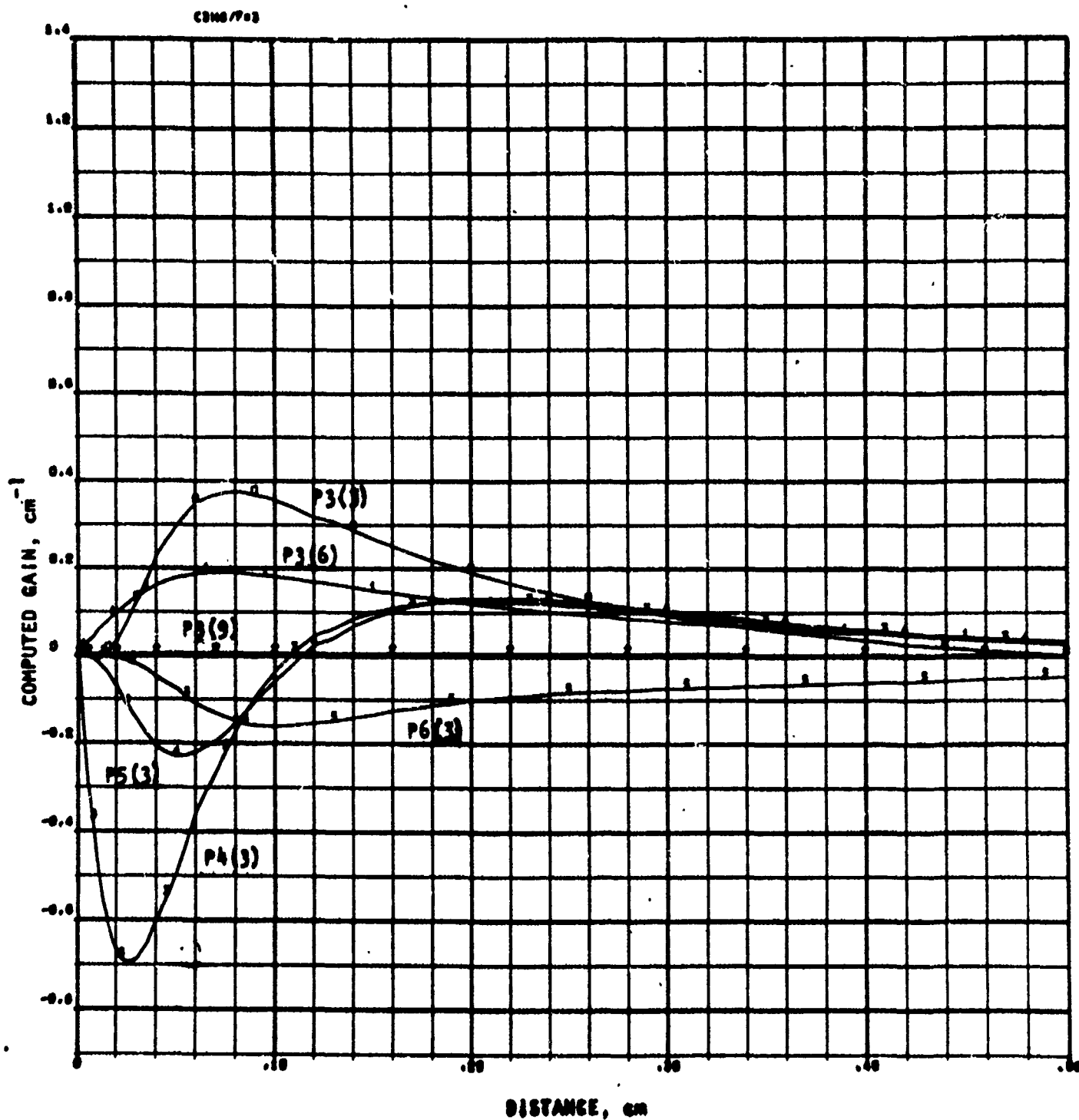


Figure 75. $\text{F}_2\text{-D}_2\text{-He-C}_3\text{H}_8$ System, Computed Zero Power Gain on Higher Lines
($F = 10\%$, 1500 K, Series II)

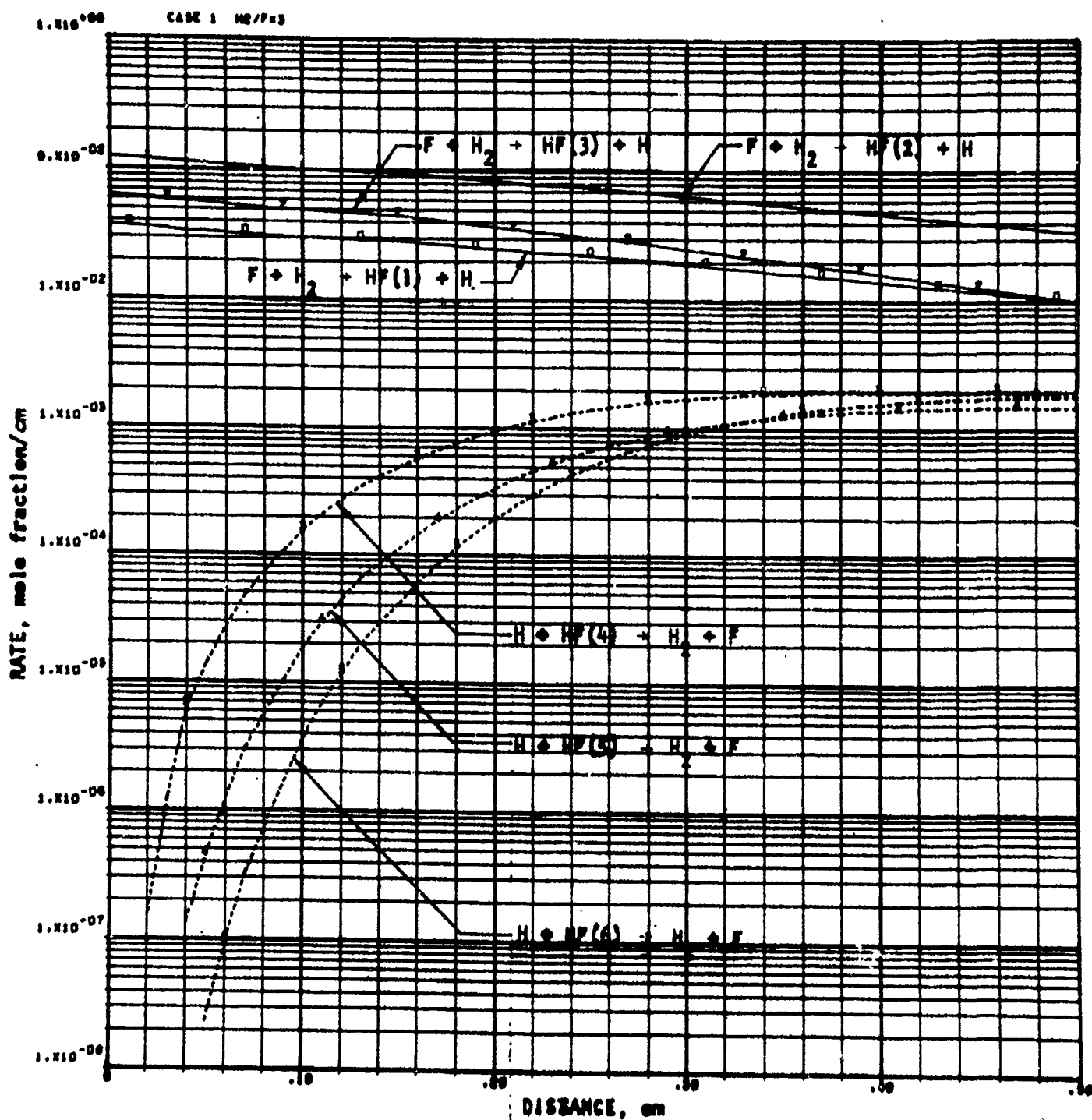


Figure 76. F_2 - D_2 -He- H_2 System, Rates of Pumping Reactions
(F = 10%, 1500 K, Series II)

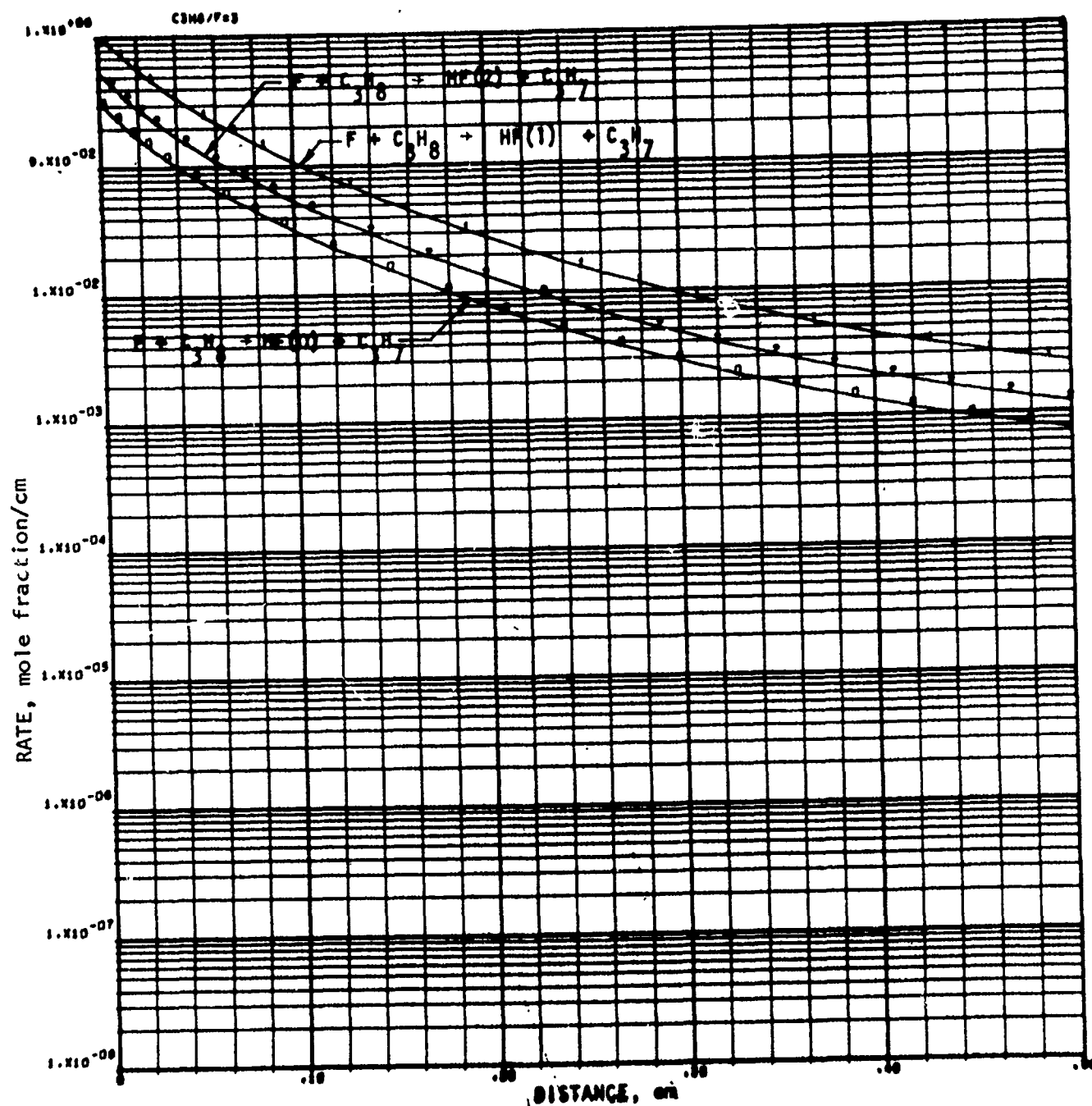


Figure 77. $F_2-D_2-He-C_3H_8$ System, Rates of Pumping Reactions
($F = 10\%$, 1500 K, Series II)

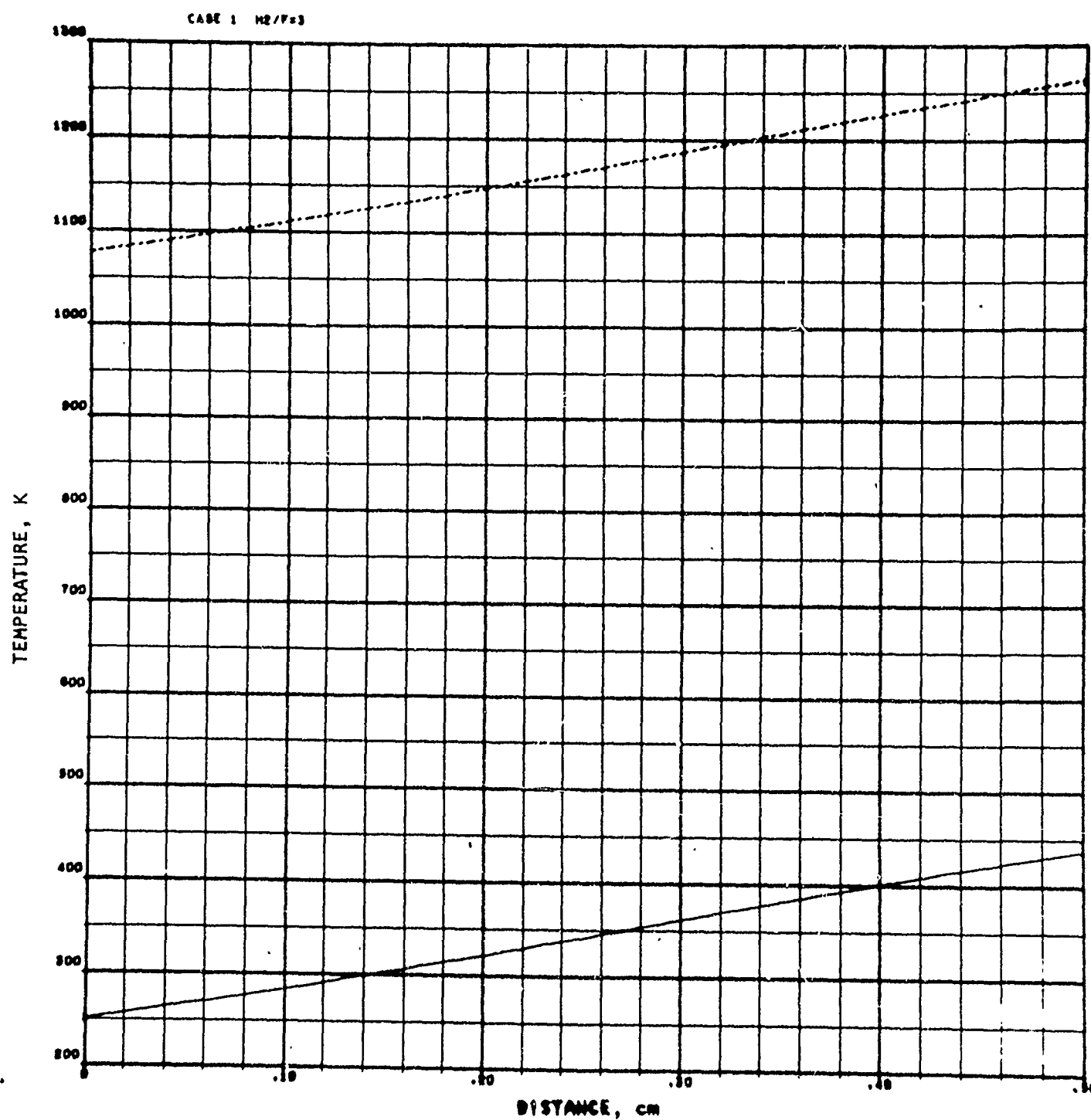


Figure 78. F_2 - D_2 -He- H_2 System, Gas Static and Stagnation Temperatures
($F = 10\%$, 1500 K, Series II)

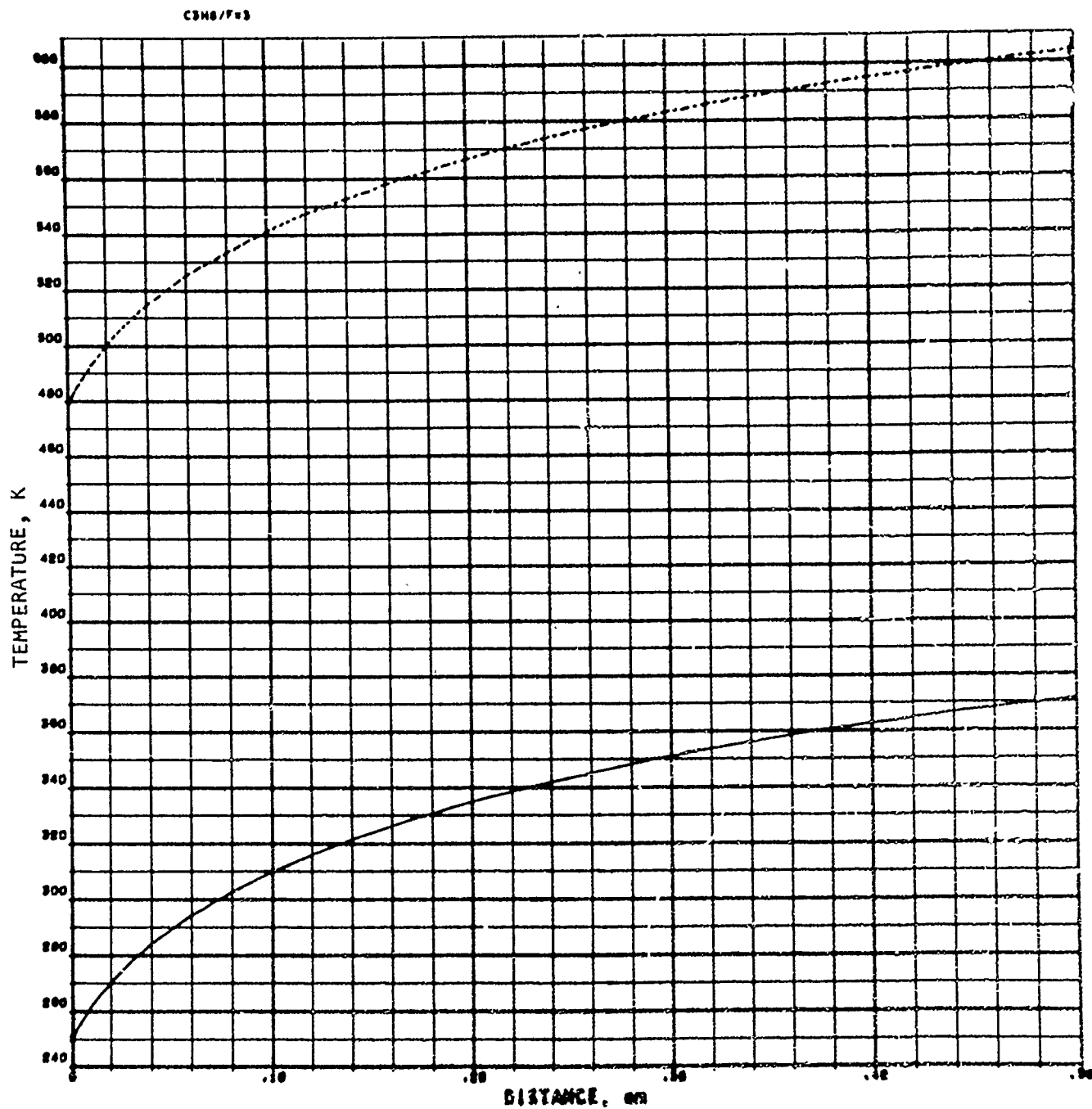


Figure 79. F_2 - D_2 -He- C_3H_8 System, Gas Static and Stagnation Temperatures
($F = 10\%$, 1500 K, Series II)

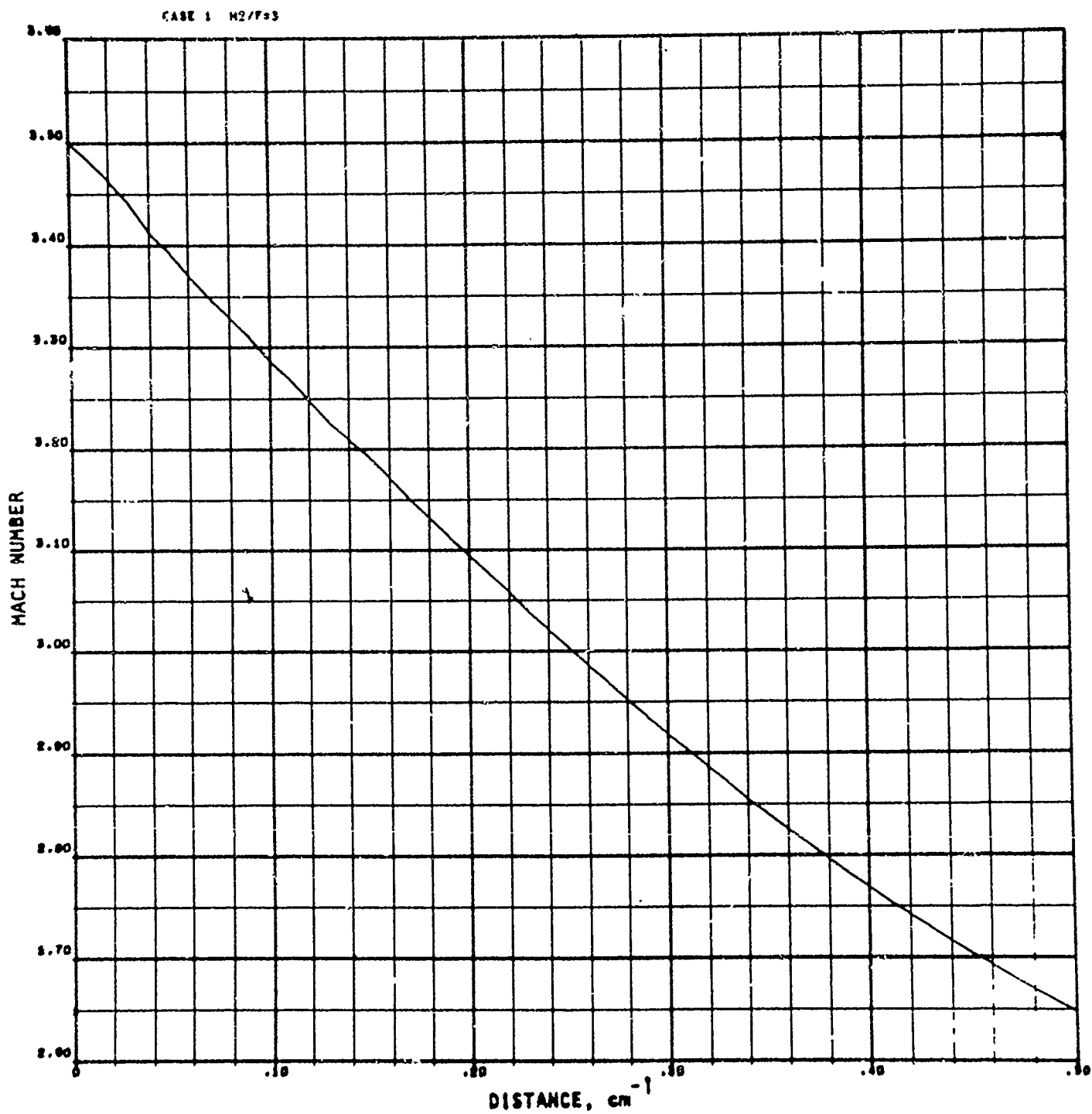


Figure 80. $F_2-D_2-He-H_2$ System, Gas Mach Number
($F = 10\%$, 1500 K, Series II)

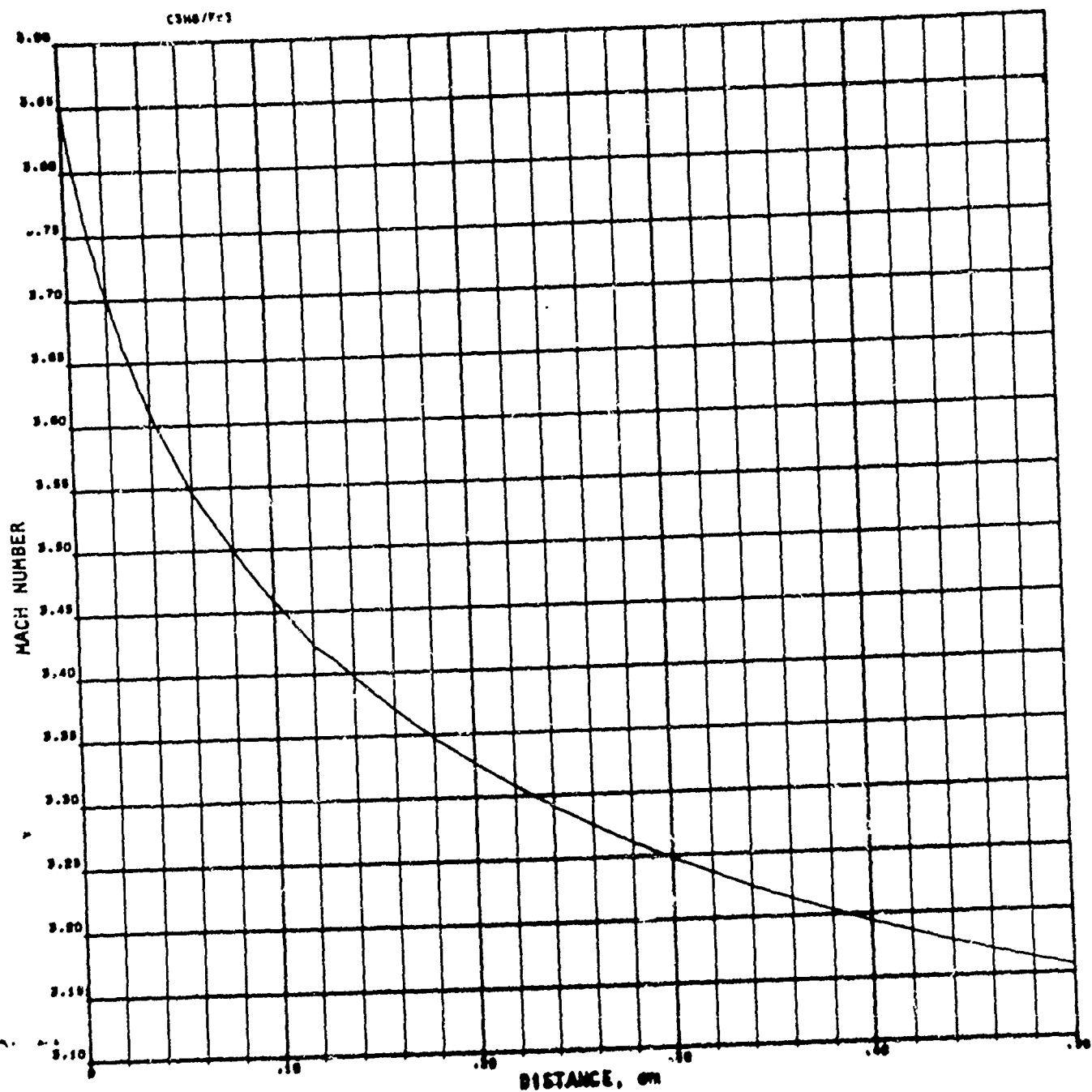


Figure 81. $F_2-D_2-He-C_3H_8$ System, Gas Mach Number
($F = 10\%$, 1500 : , Series II)

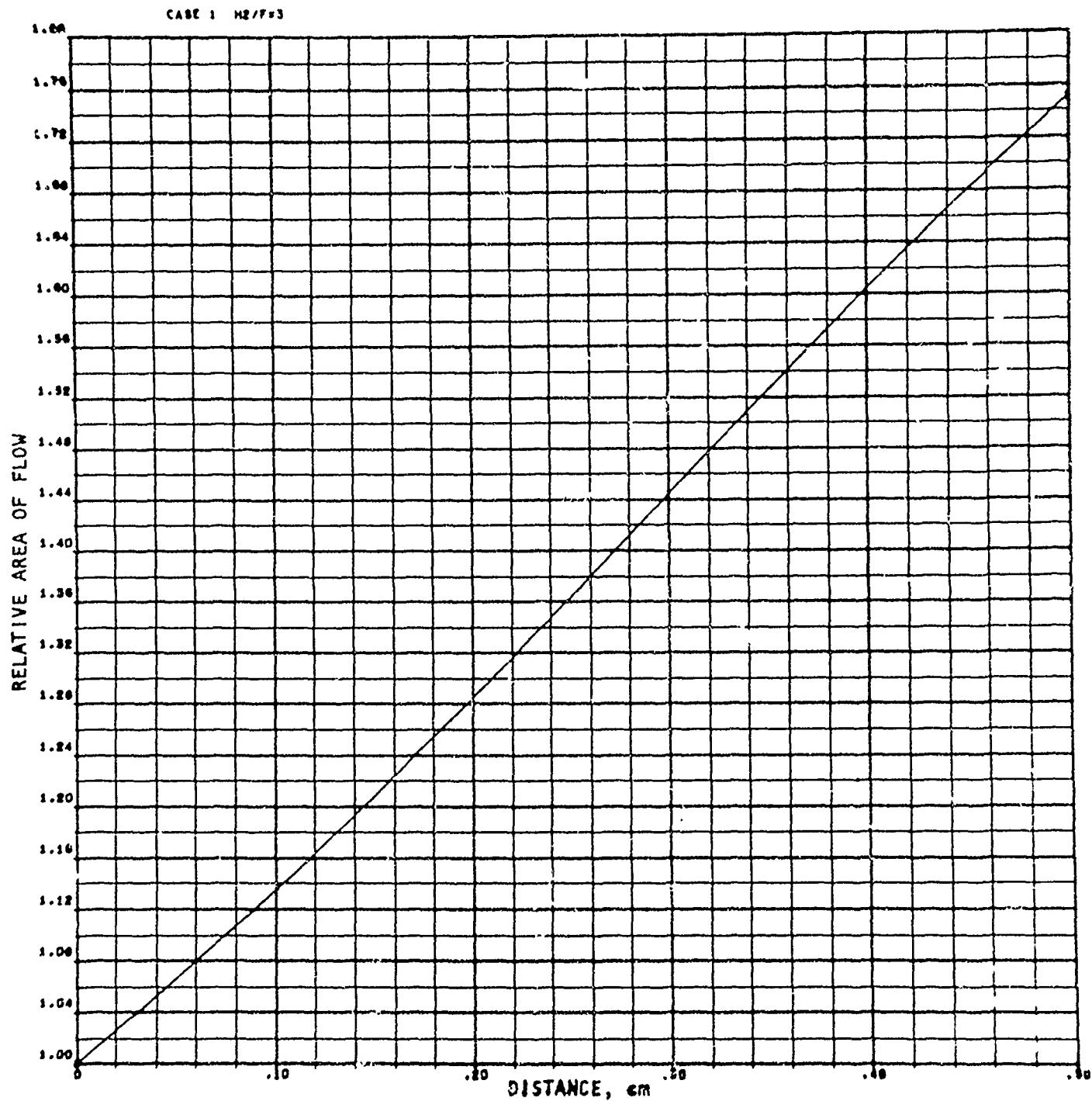


Figure 82. $F_2-D_2-He-H_2$ System, Relative Area of Flow
($F = 10\%$, 1500 K, Series II)

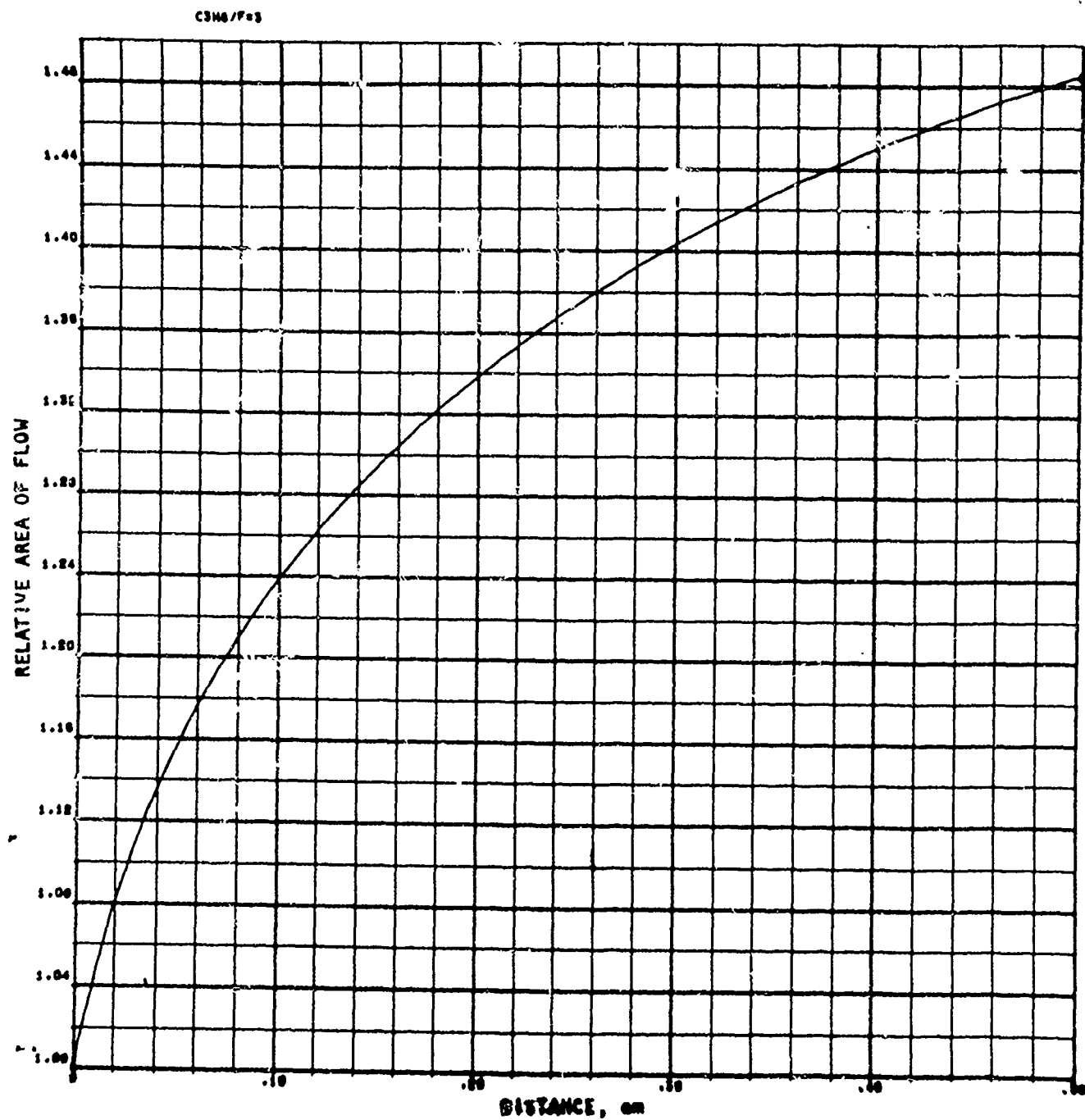


Figure 83. F_2 - D_2 -He- C_3H_8 System, Relative Area of Flow
(F = 10%, 1500 K, Series II)

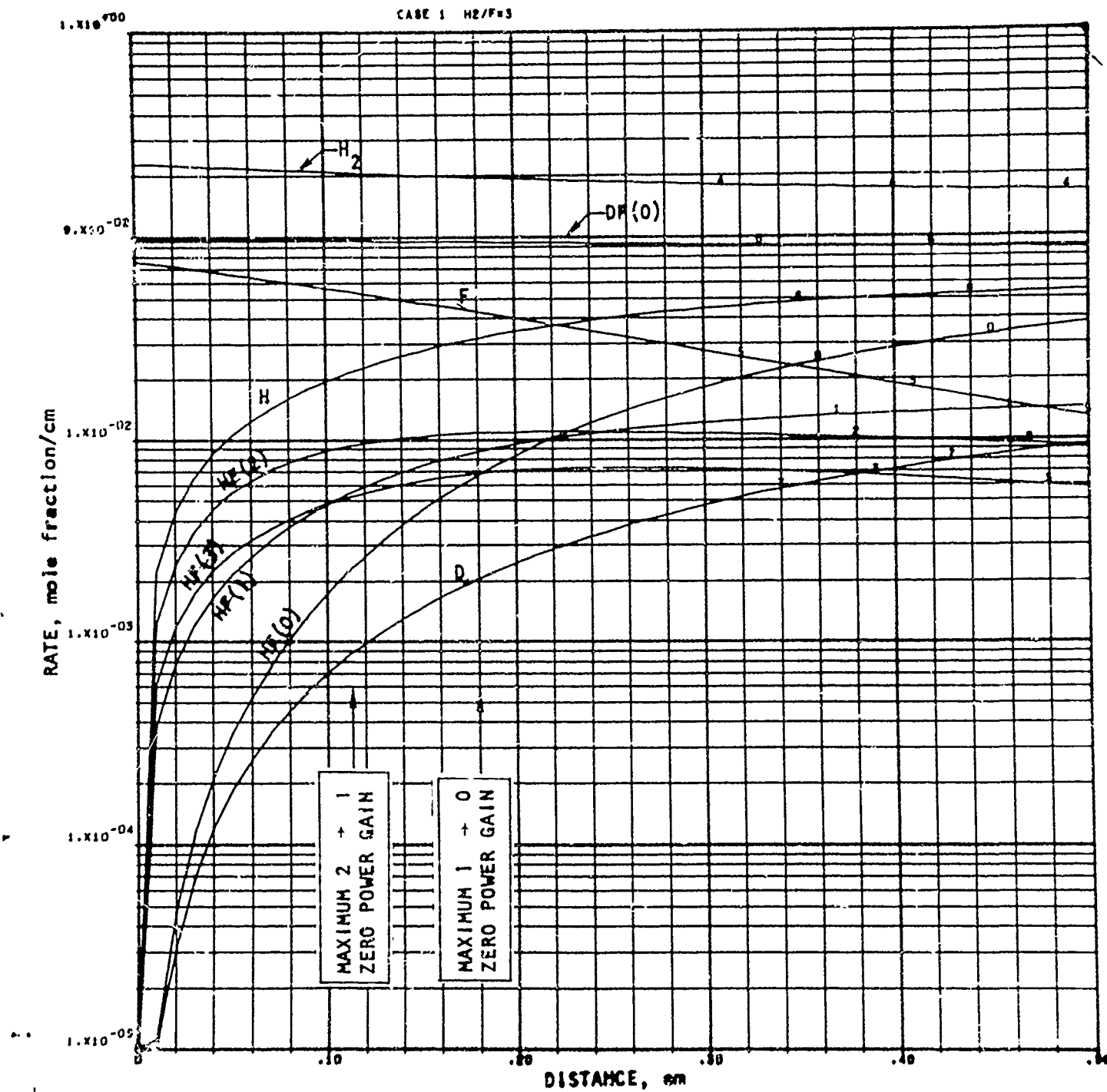


Figure 84. $F_2-D_2-He-H_2$ System, Species Plot
($F = 10\%$, 1500 K, Series II)

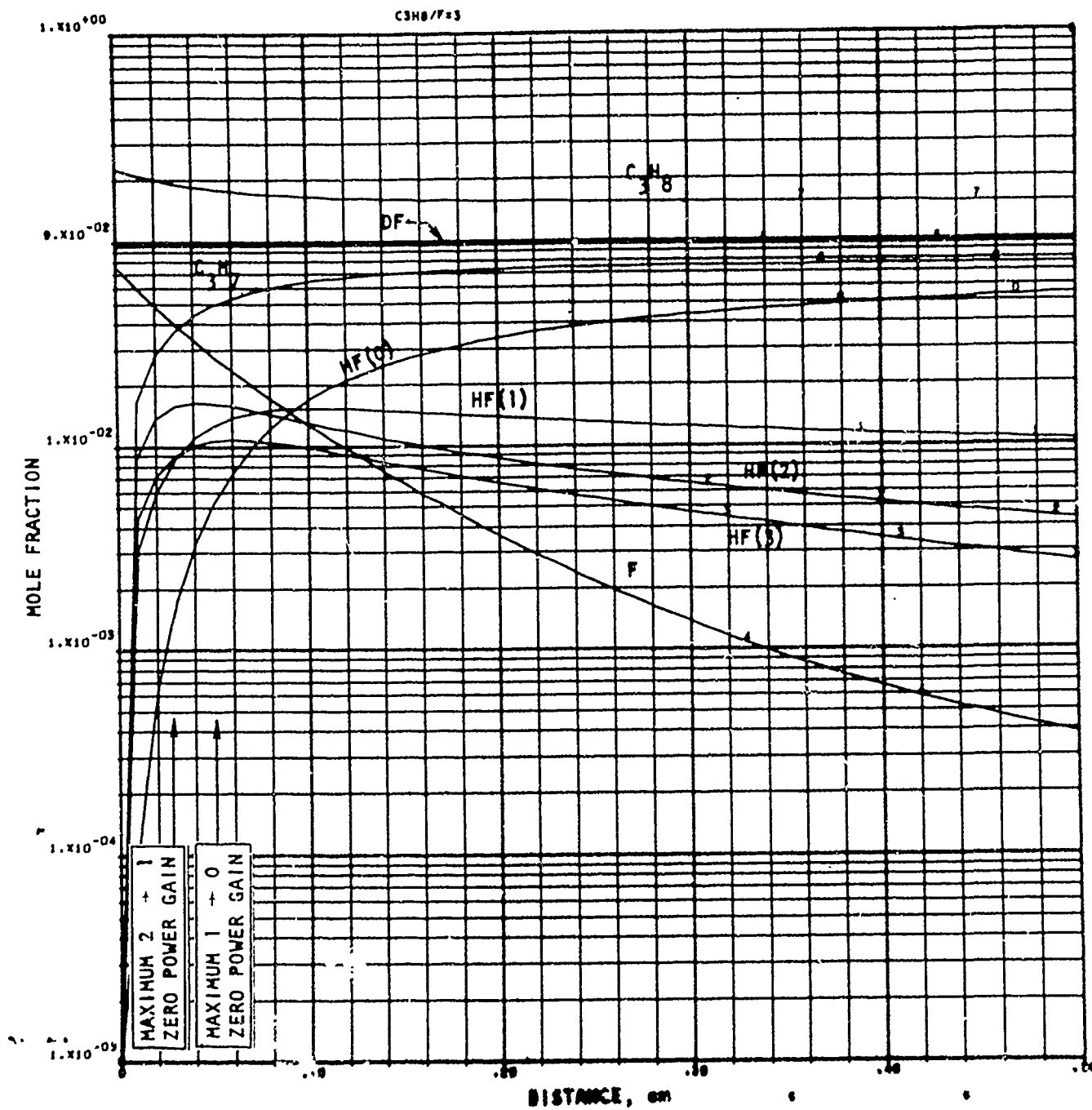


Figure 85. $F_2-D_2-He-C_3H_8$ System, Species Plot
($F = 10\%$, 1500 K, Series II)

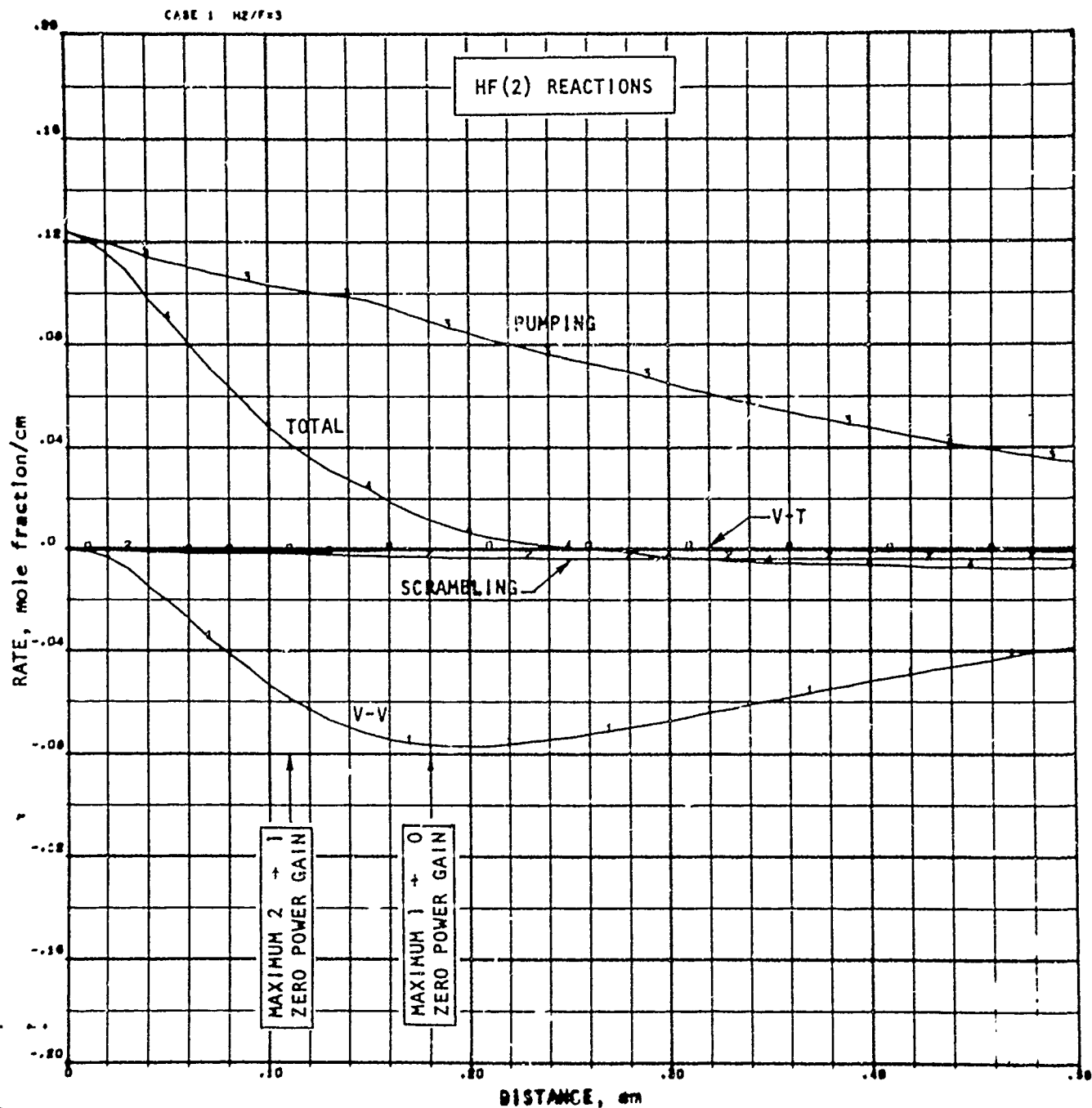


Figure 86. F₂-D₂-He-H₂ System, Rates of Formation of HF(2) by Various Types of Processes
(F = 10%, 1500 K, Series II)

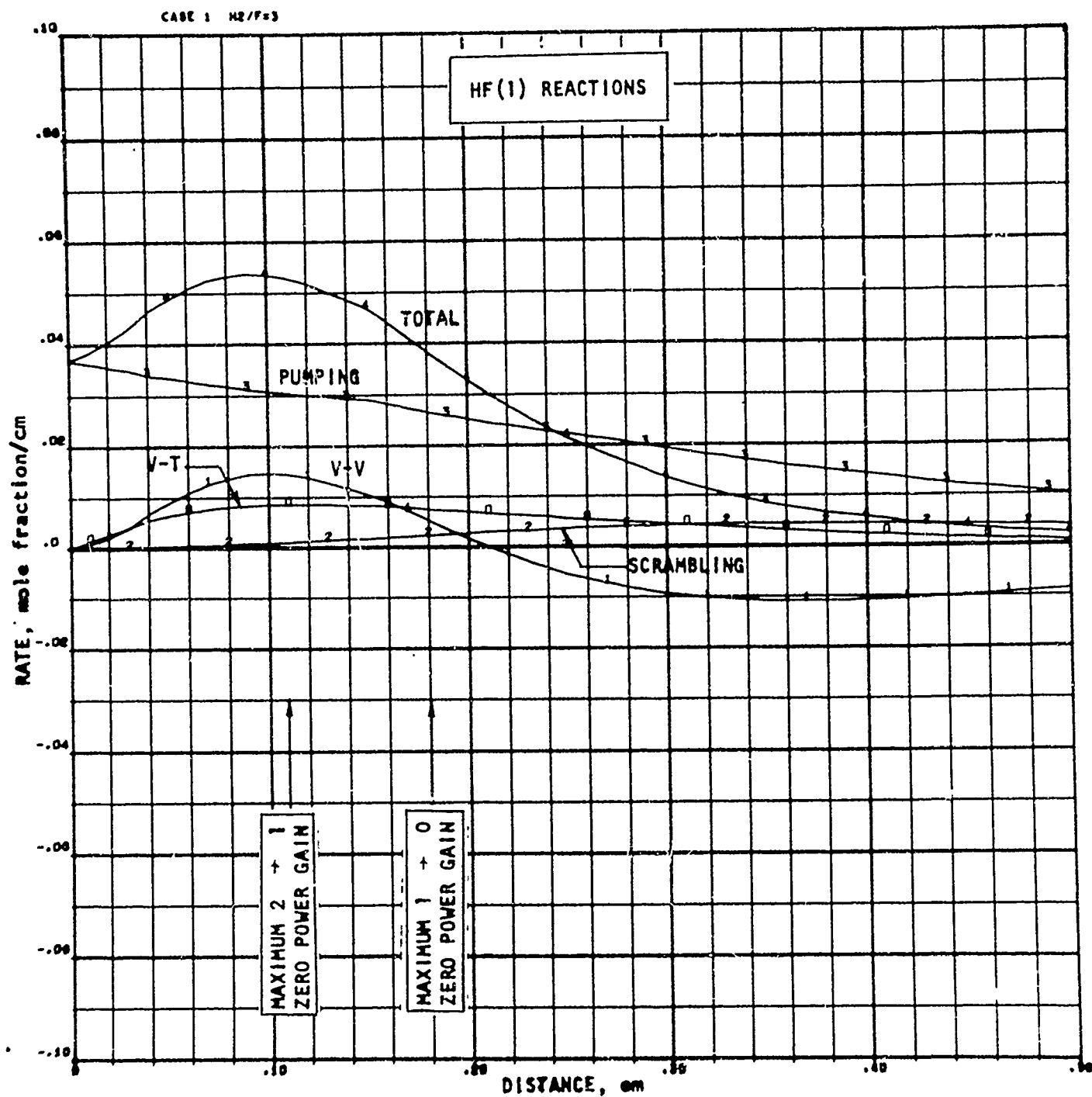


Figure 87. $F_2-D_2-He-H_2$ System, Rates of Formation of HF(1) by Various Types of Processes
($F = 10\%$, 1500 K, Series II)

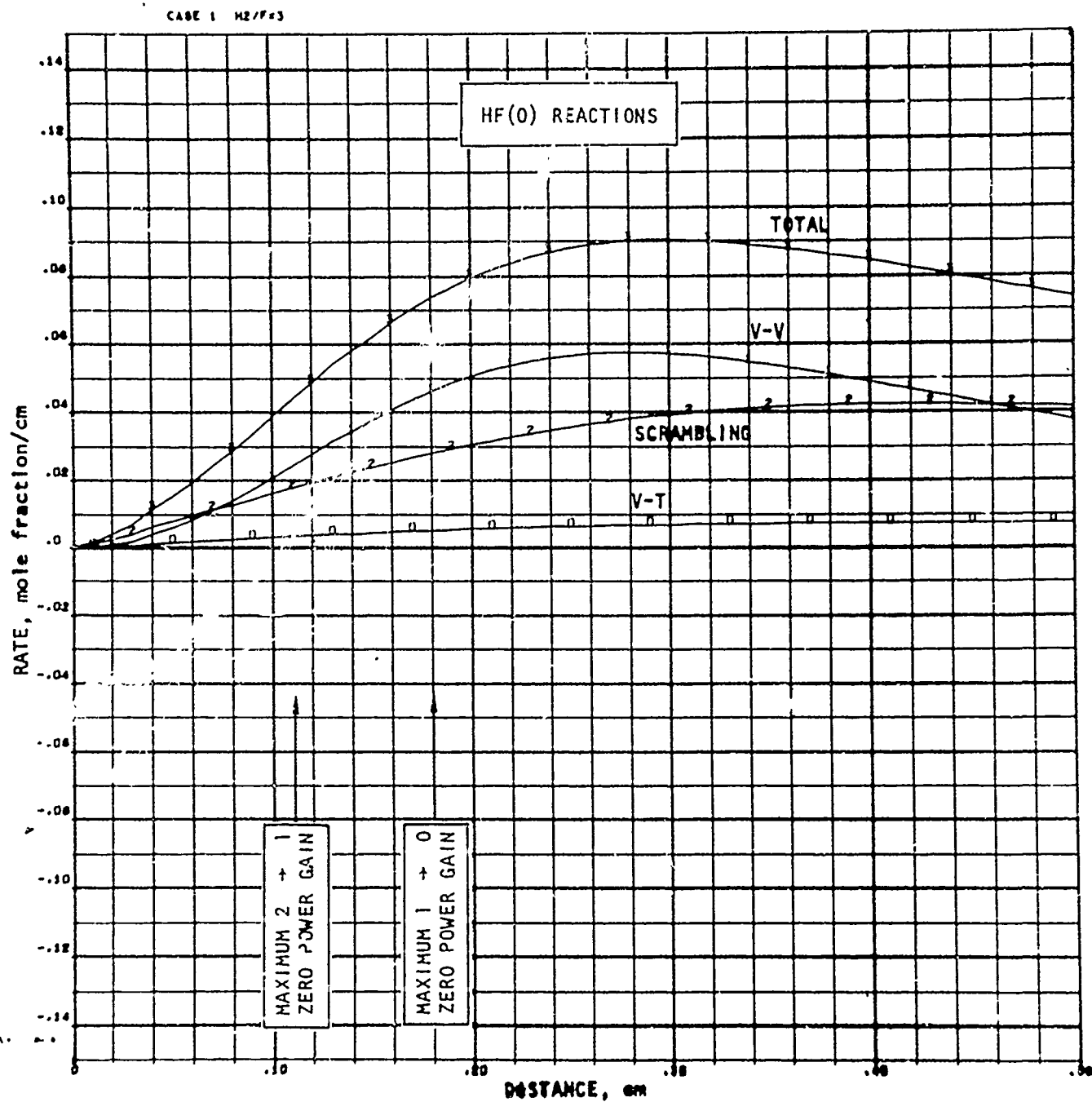


Figure 88. F_2 - D_2 -He- H_2 System, Rates of Formation of $HF(0)$ by Various Types of Processes
($F = 10\%$, 1500 K, Series II)

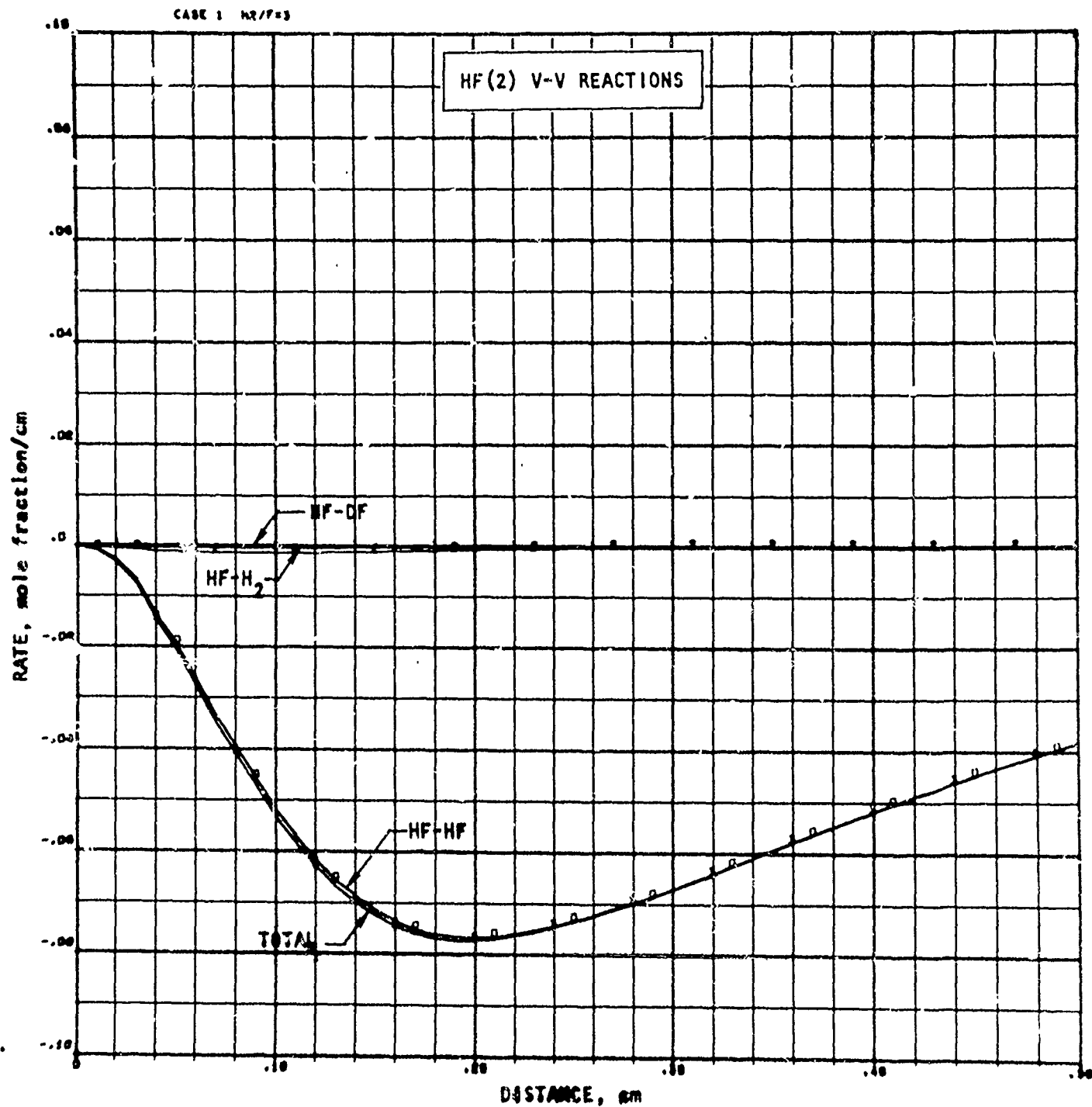


Figure 89. $\text{F}_2\text{-D}_2\text{-He-H}_2$ System, Rates of Formation of $\text{HF}(2)$ by Various V-V Processes
($\text{F} = 10\%$, 1500 K, Series II)

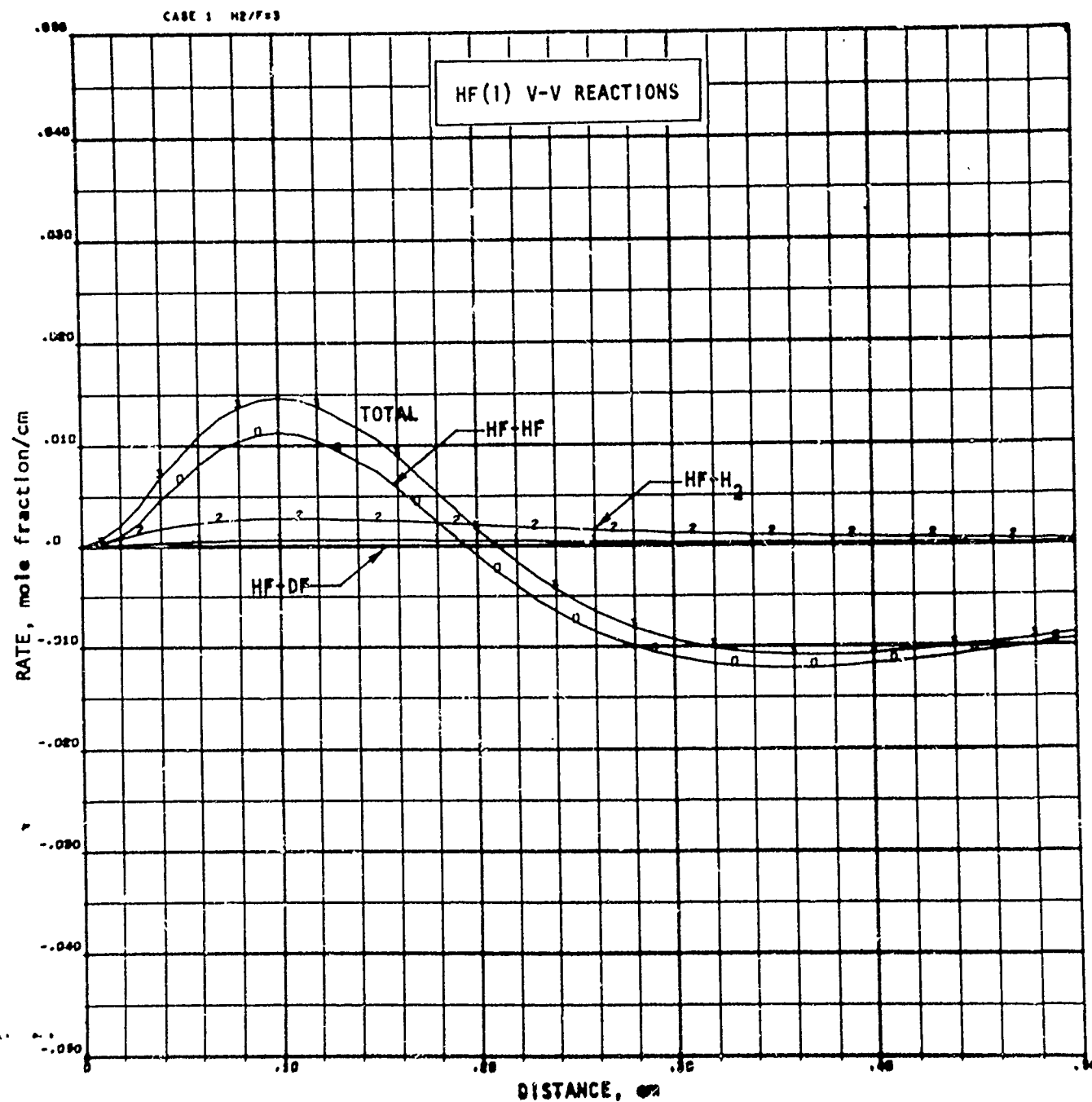


Figure 90. F_2 - D_2 -He- H_2 System, Rates of Formation of HF(1) by Various V-V Processes
($F = 10\%$, 1500 K, Series II)

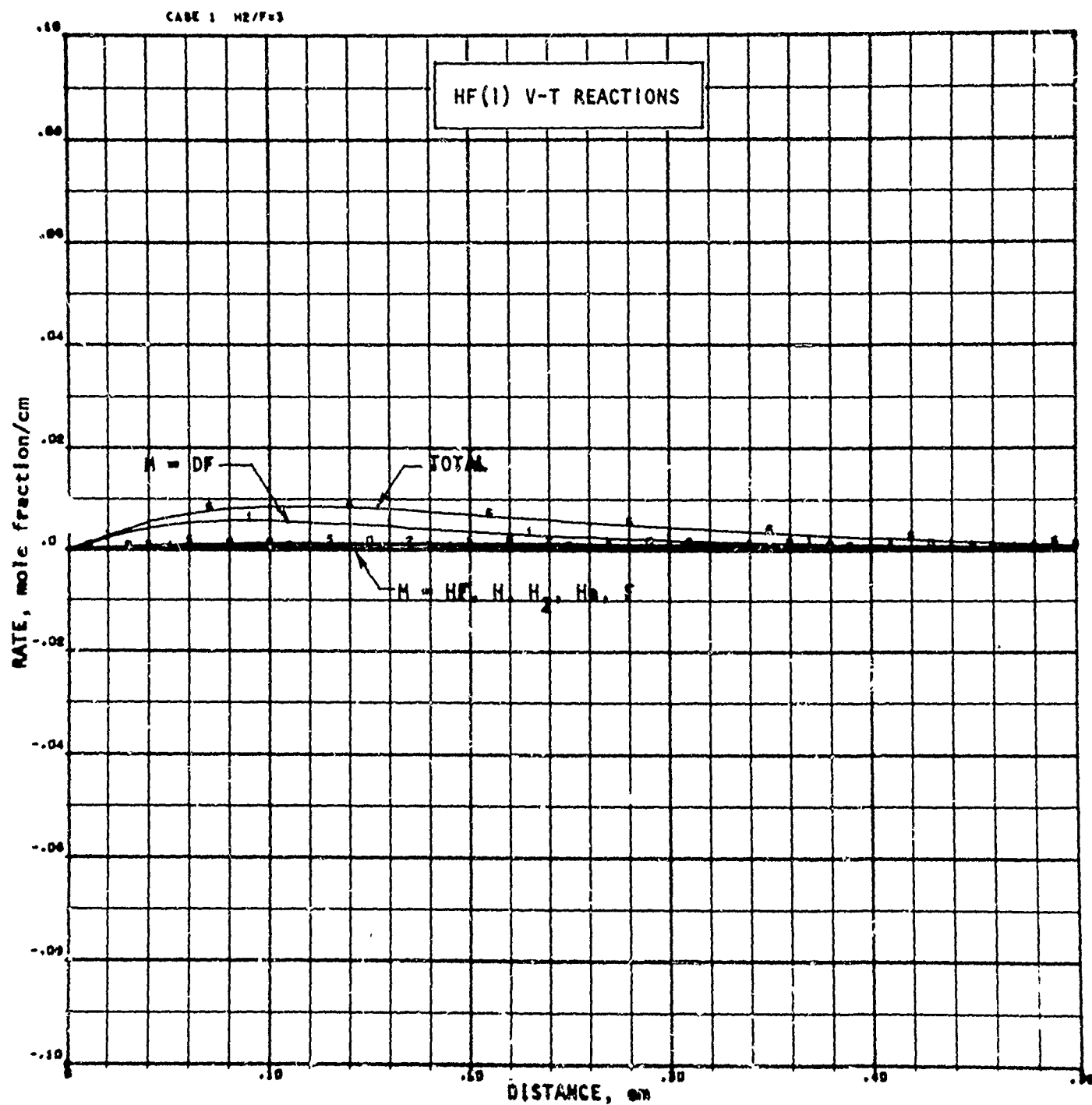


Figure 91. F_2 - D_2 -He- H_2 System, Rates of Formation of HF(1) by Various V-T Processes
($F = 10\%$, 1500 K, Series II)

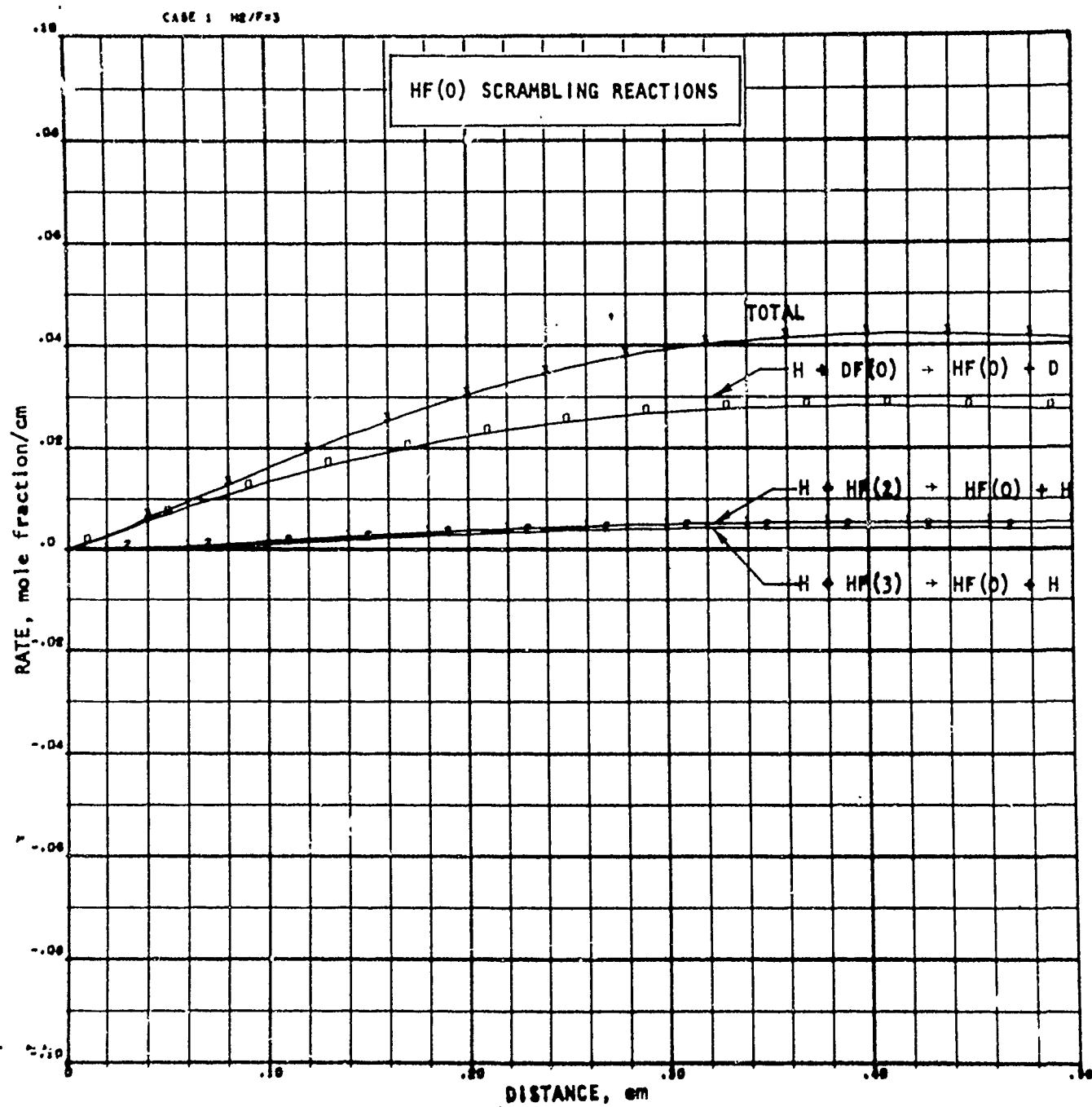


Figure 92. $\text{F}_2\text{-D}_2\text{-He-H}_2$ Systems, Rates of Formation of $\text{HF}(0)$ via Scrambling Reactions
($F = 10\%$, 1500 K, Series II)

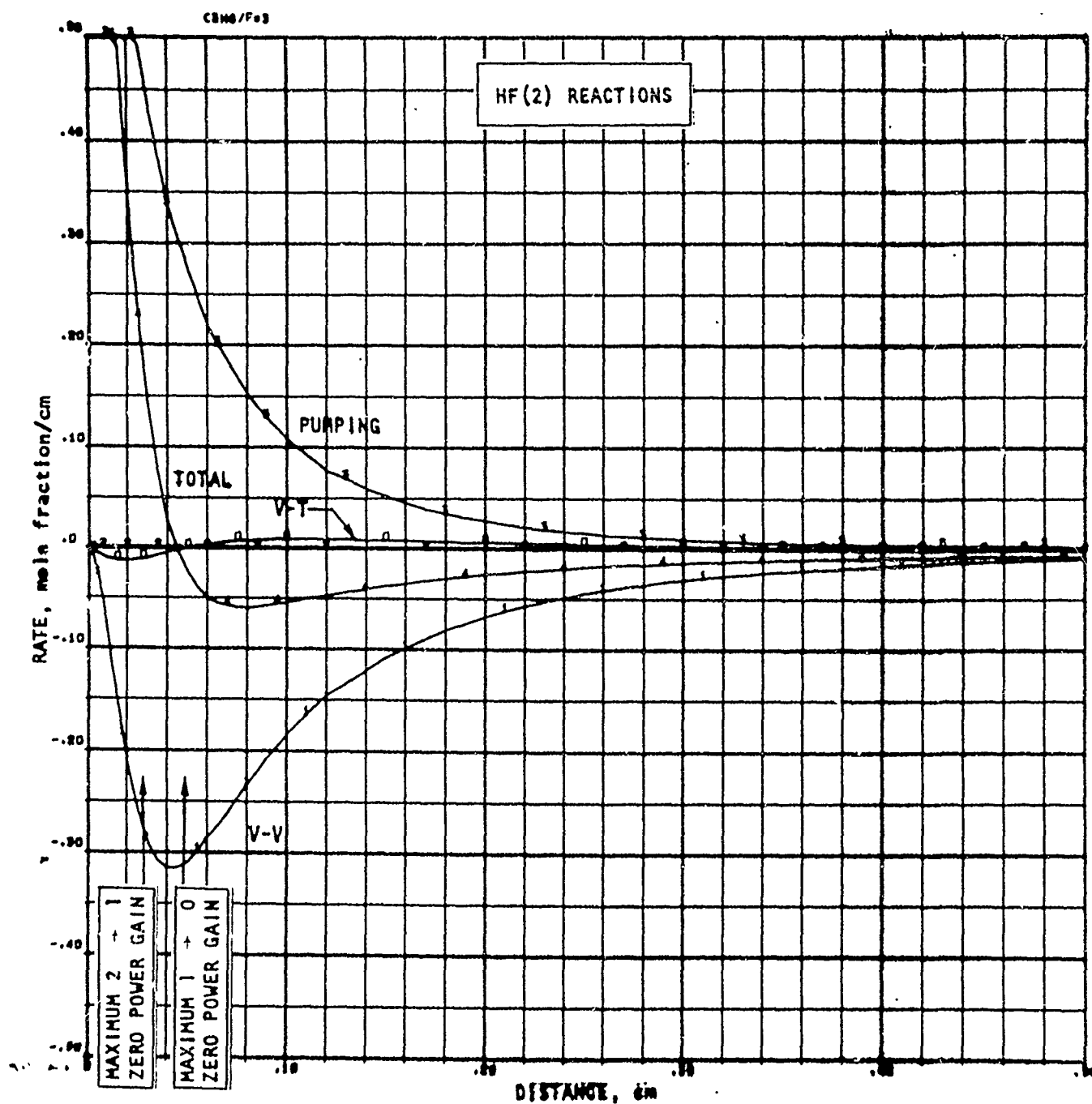


Figure 93. F_2 - D_2 -He- C_3H_8 System, Rates of Formation of HF(2) by Various Types of Processes (F = 10%, 1500 K, Series II)

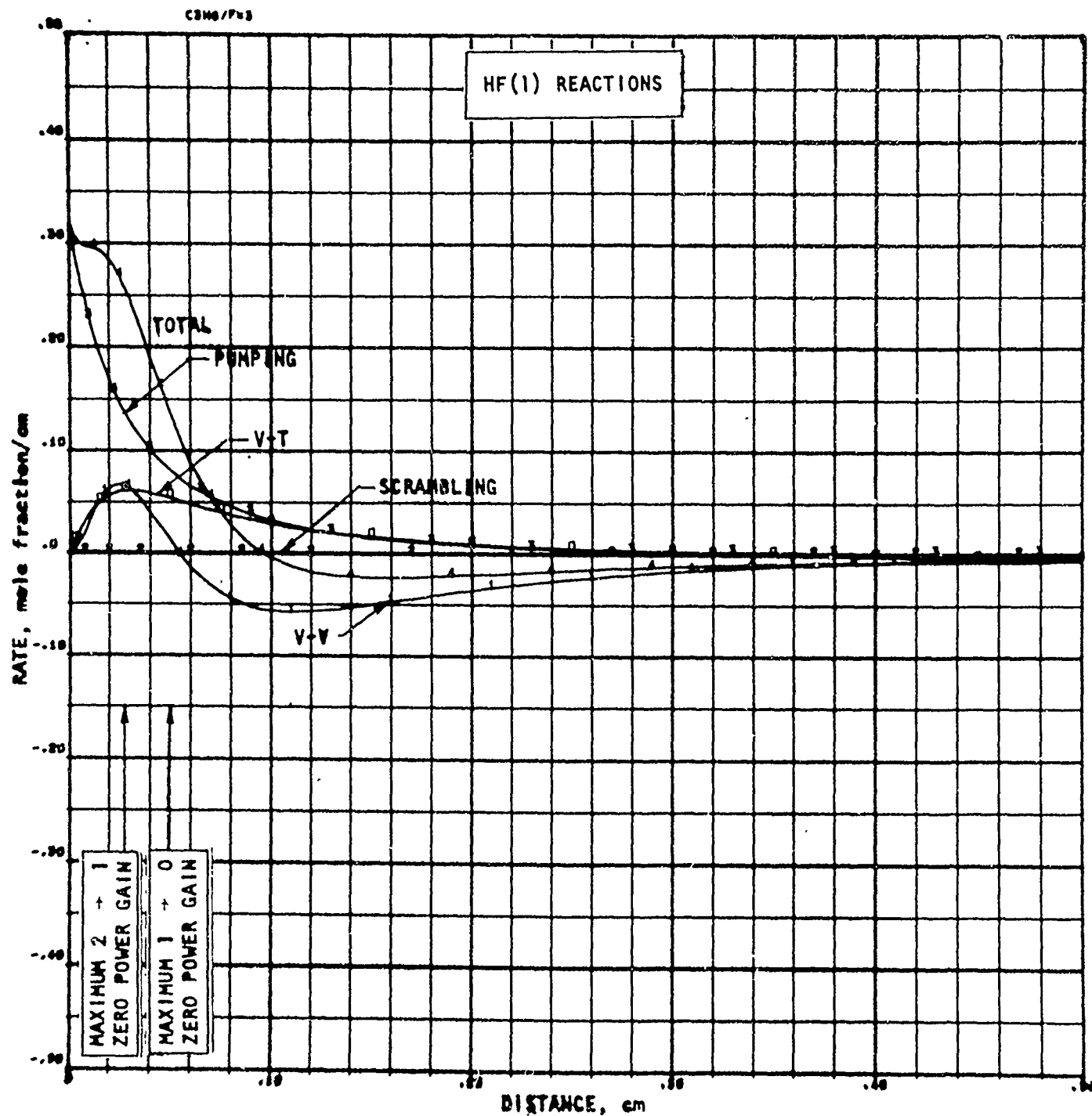


Figure 94. F₂-D₂-He-C₃H₈ Systems, Rates of Formation of HF(1) by Various Types of Reactions (F = 10%, 1500 K, Series II)

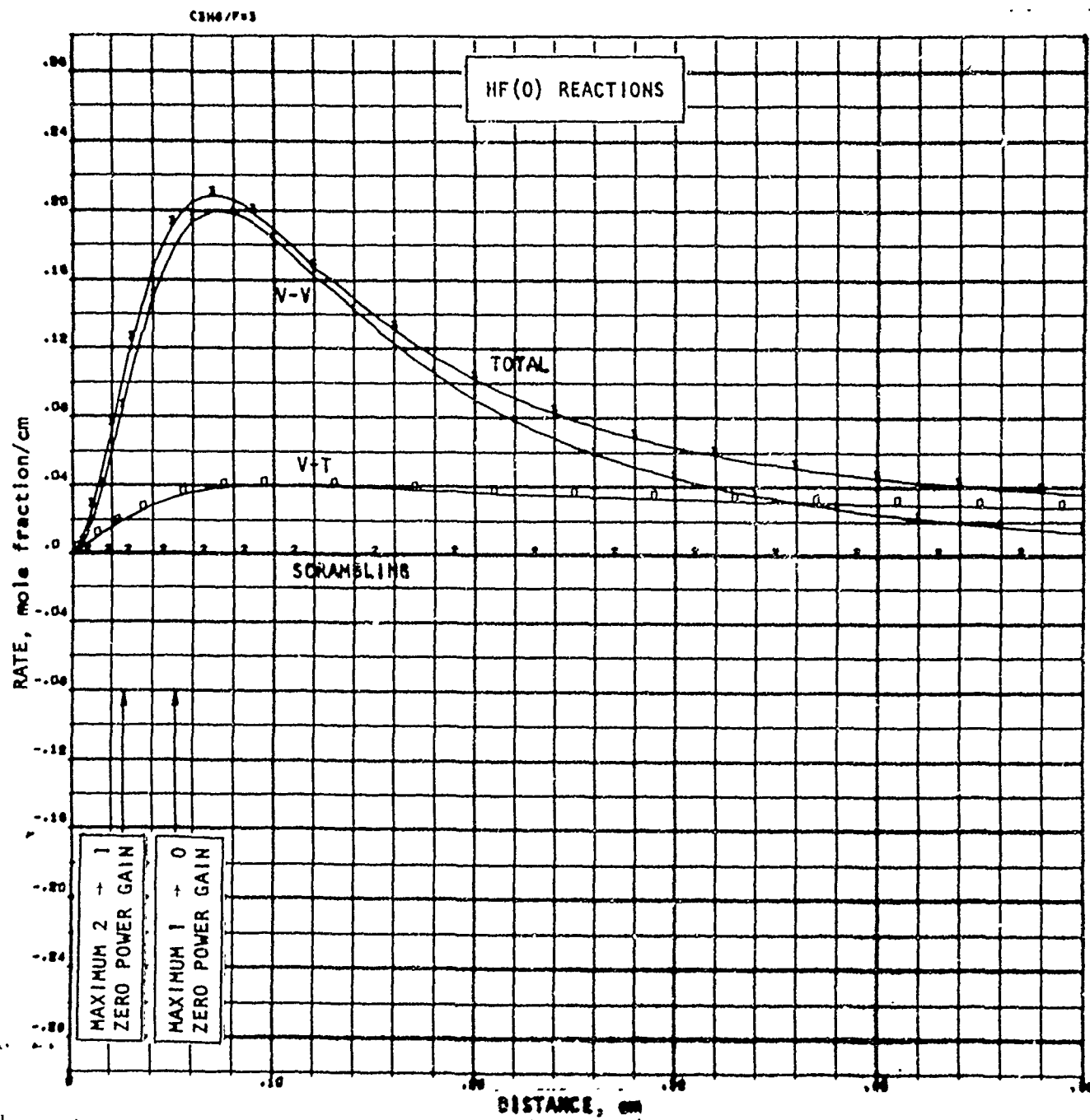


Figure 95. $F_2-D_2-He-C_3H_8$ System, Rates of Formation of HF(0) by Various Types of Processes
(F = 10%, 1500 K, Series II)

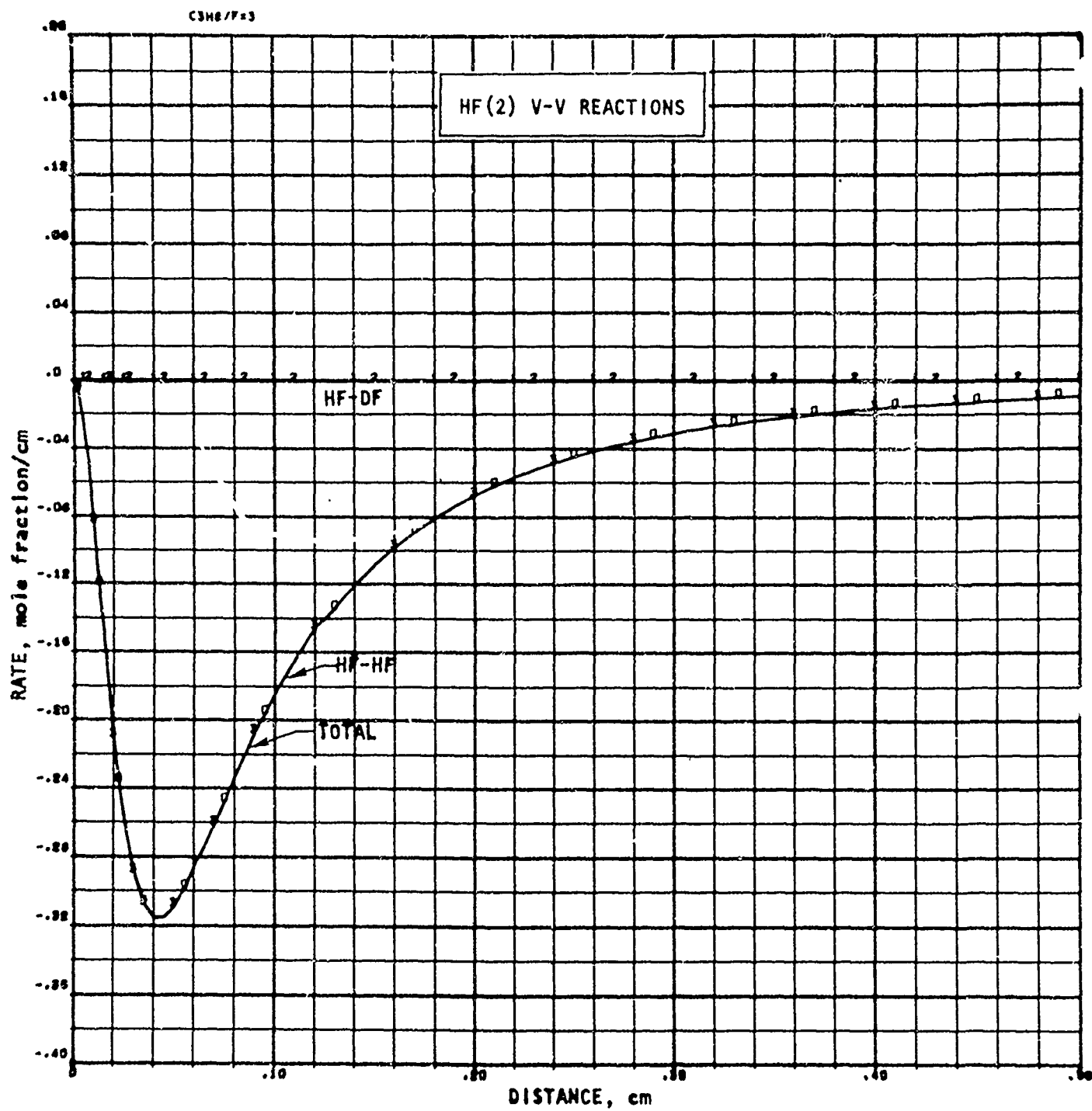


Figure 96. F_2 - D_2 -He- C_3H_8 System, Rates of Formation of $HF(2)$ by Various V-V Processes
($F = 10\%$, 1500 K, Series II)

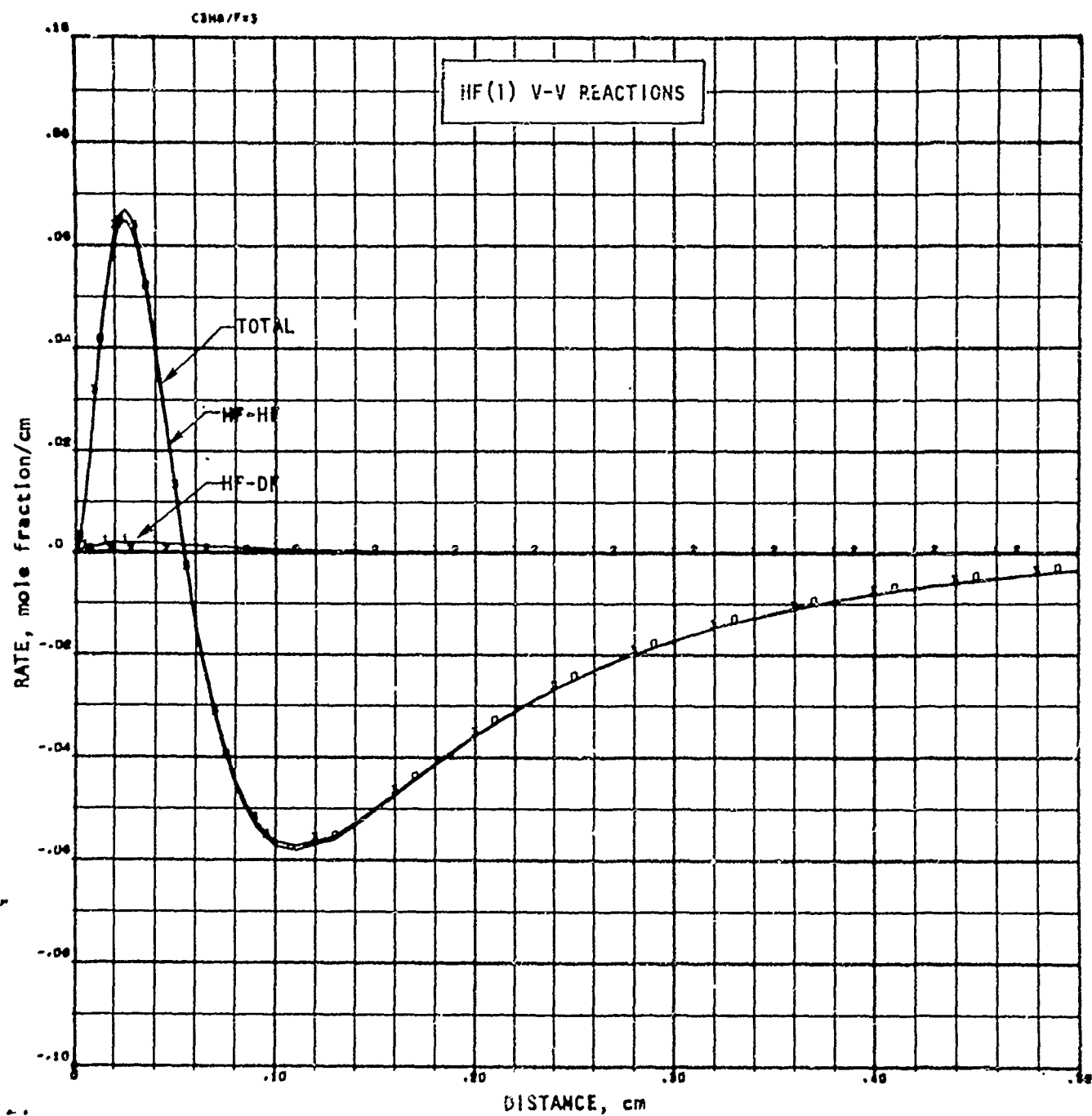


Figure 97. F₂-D₂-He-C₃H₈ System, Rates of Formation of HF(1) by Various V-V Processes (F = 10%, 1500 K, Series II)

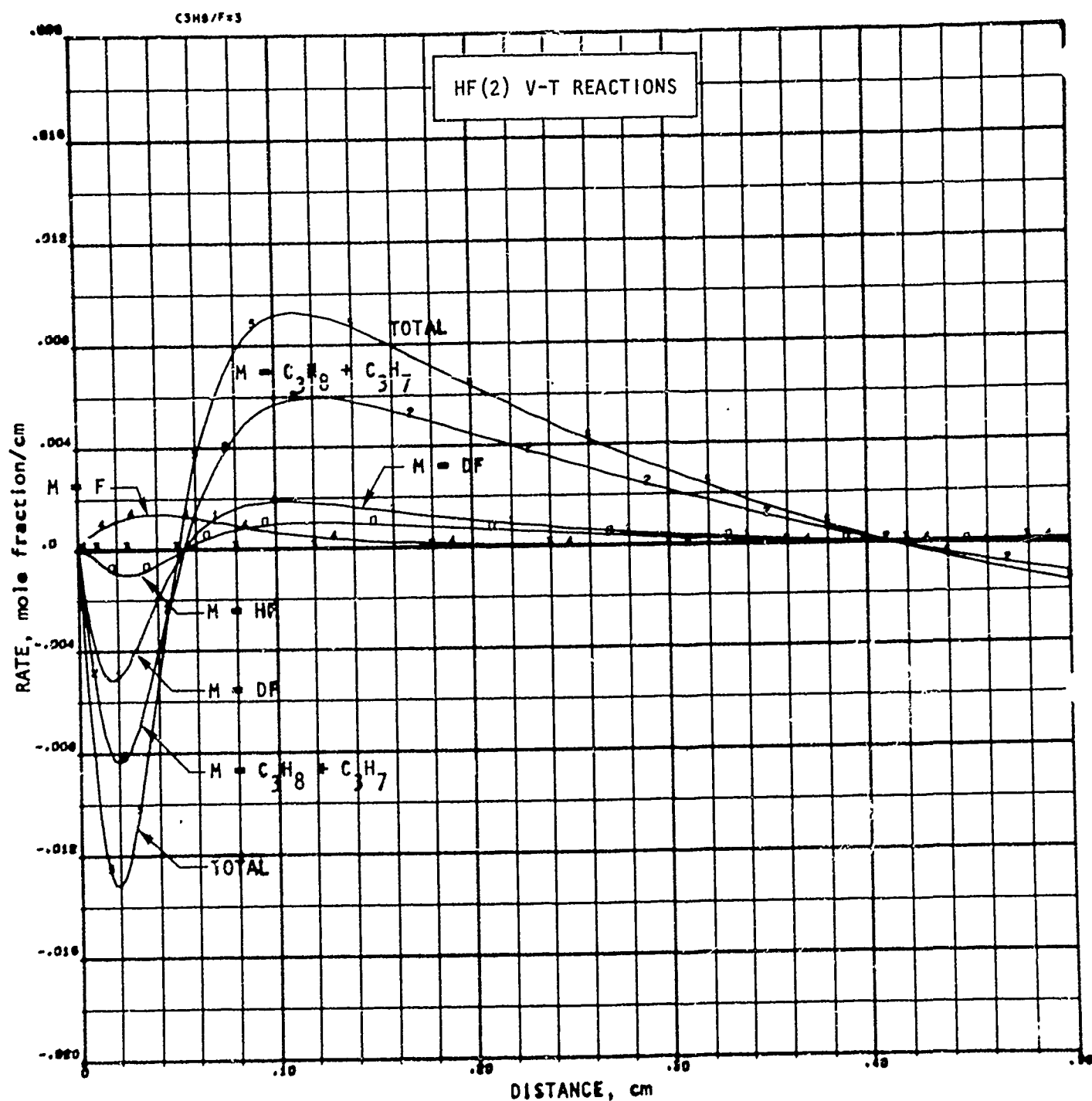


Figure 98. F₂-D₂-He-C₃H₈ System, Rates of Formation of HF(2) by Various V-T Processes (F = 10%, 1500 K, Series II)

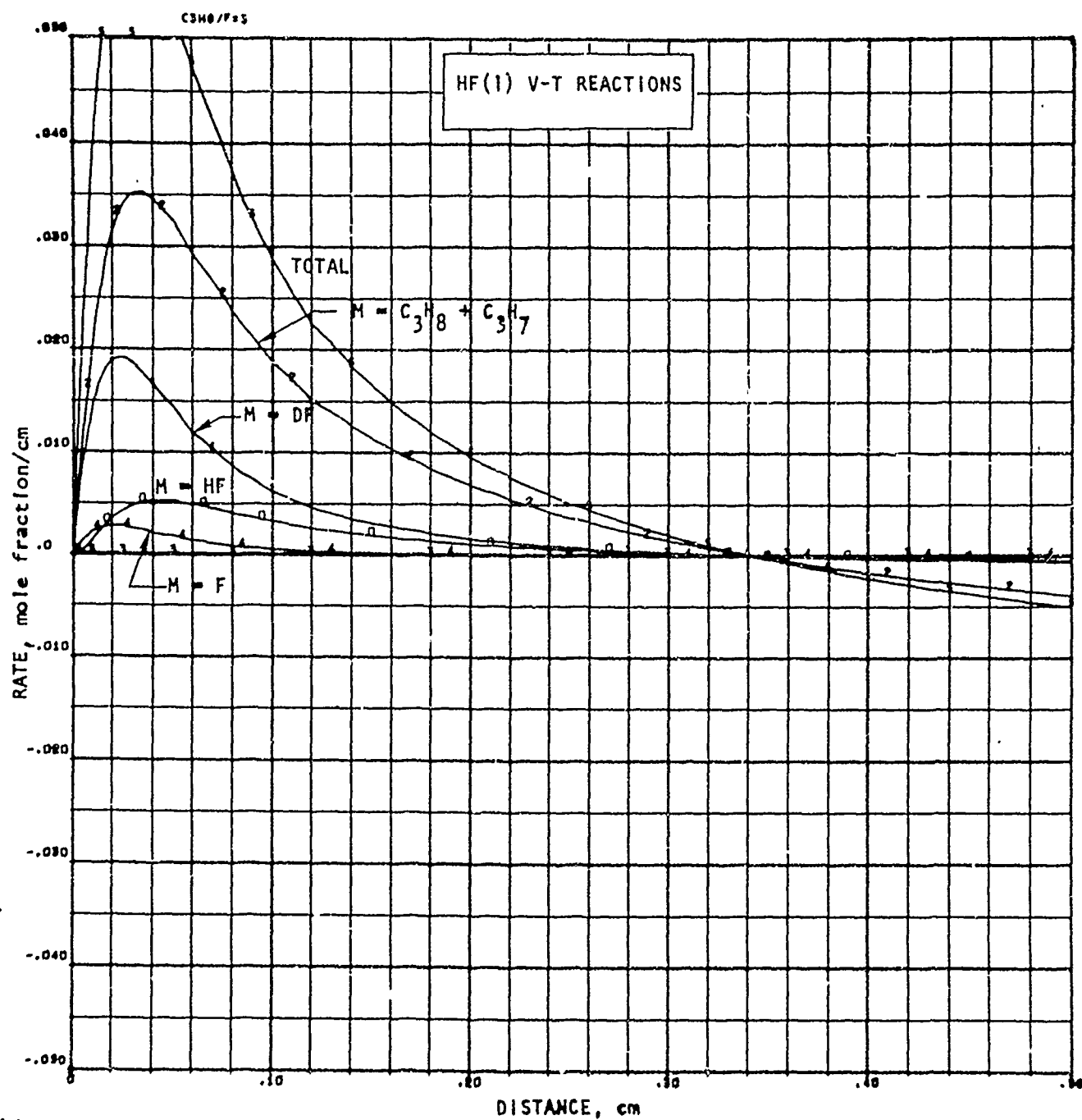


Figure 99. F₂-D₂-He-C₃H₈ System, Rates of Formation of HF(1) by Various V-T Processes (F = 10%, 1500 K, Series II)

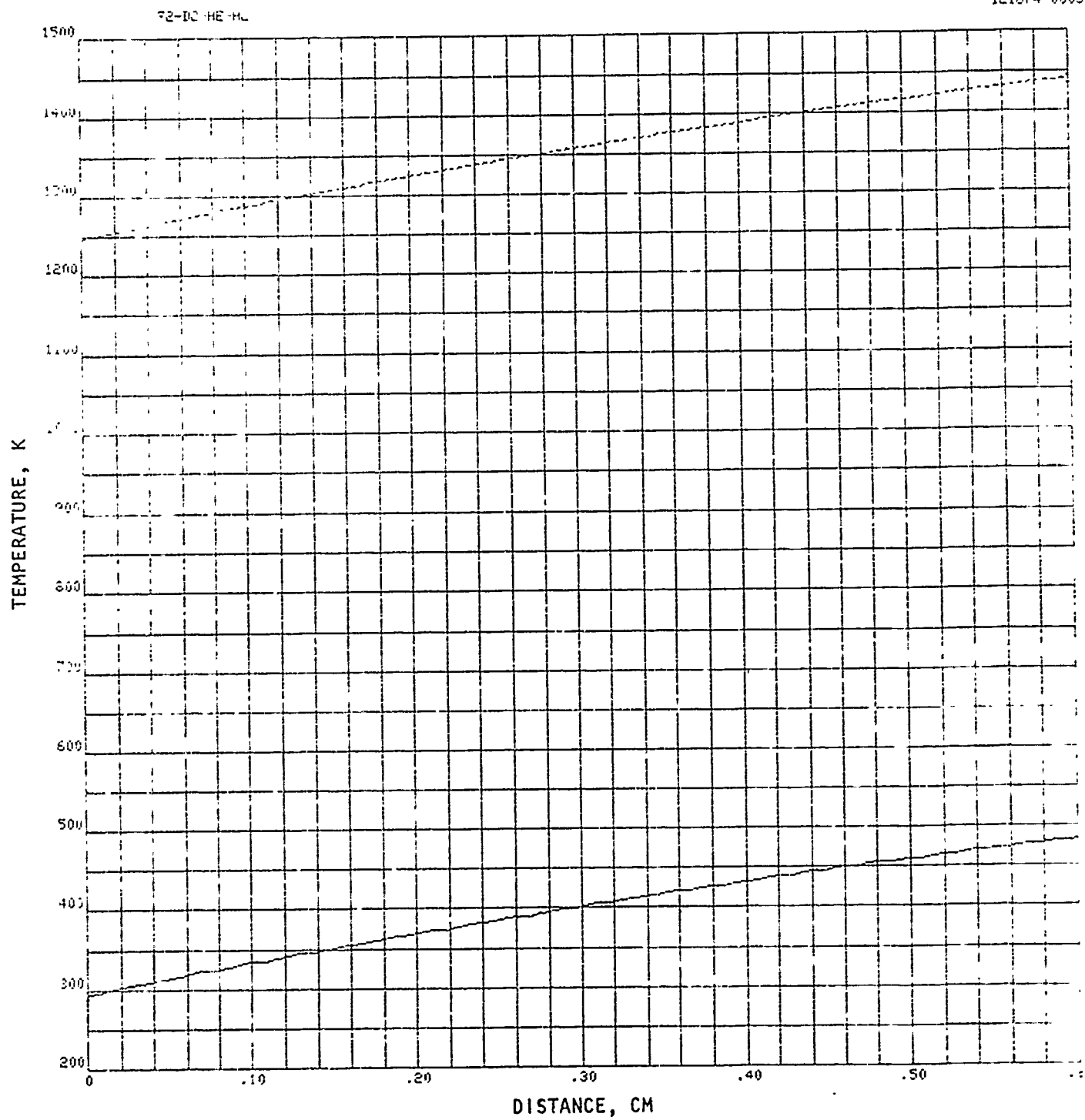


Figure 100. $F_2-D_2-He-H_2$ System, Gas Static and Stagnation Temperatures
($F = 10\%$, 1500 K, Series III)

*055811391
121874 0003

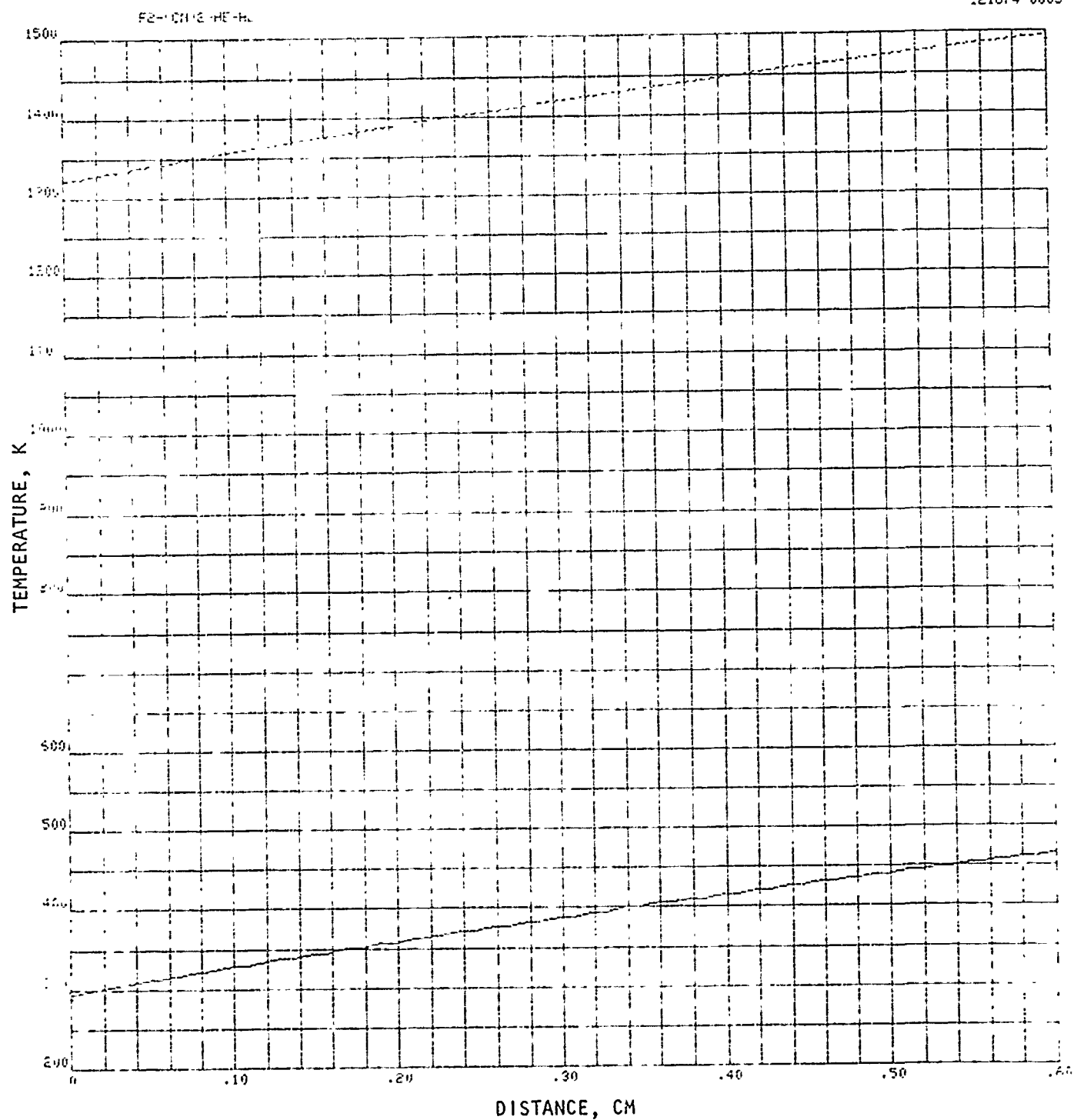


Figure 101. F₂-(CN)₂-He-H₂ System, Gas Static and Stagnation Temperatures
(F = 10%, 1500 K, Series III)

4055811301
121874 6003

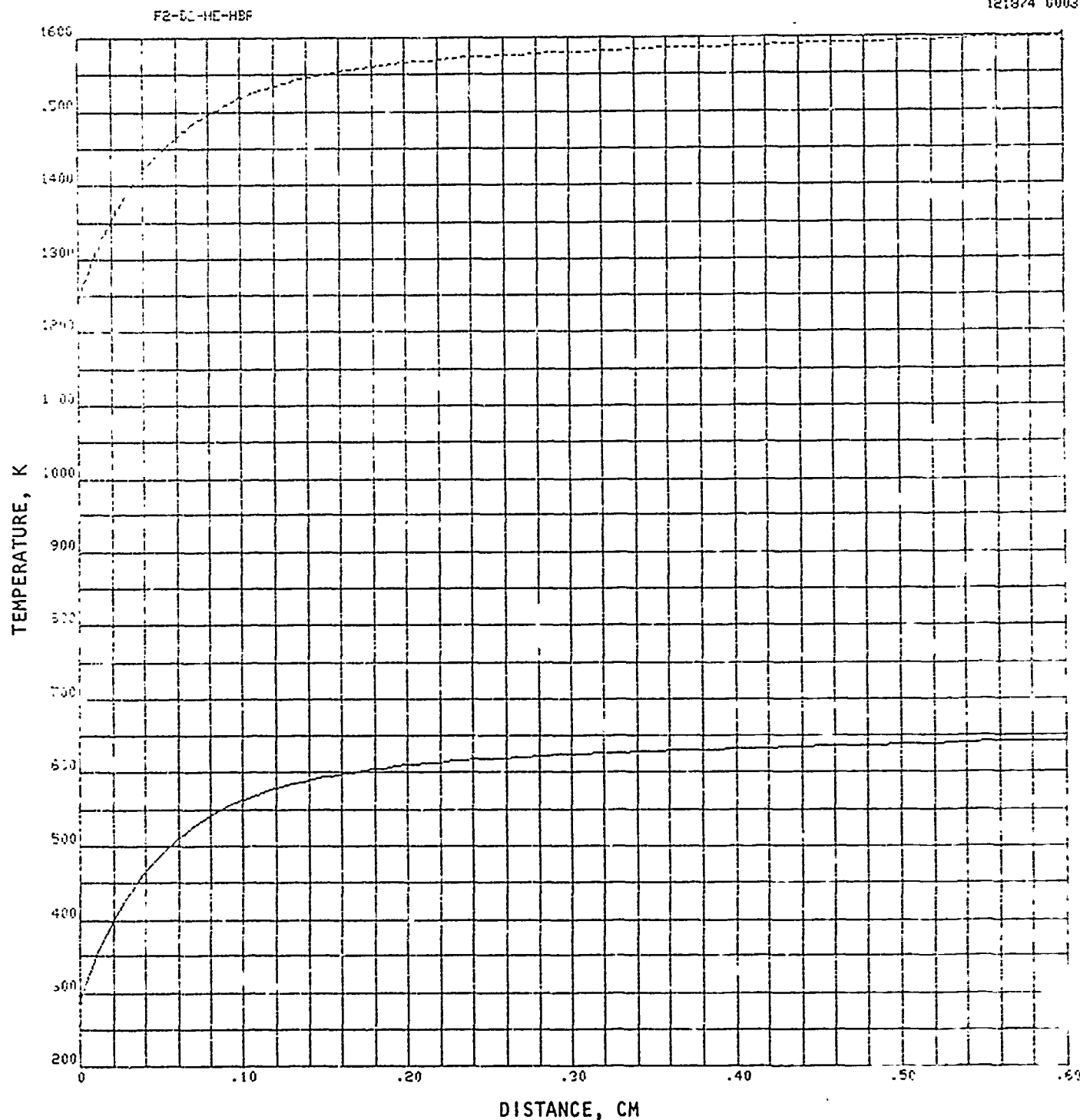


Figure 102. F₂-D₂-He-HBr System, Gas Static and Stagnation Temperatures
(F = 10%, 1500 K, Series III)

1055811301
121874 0003

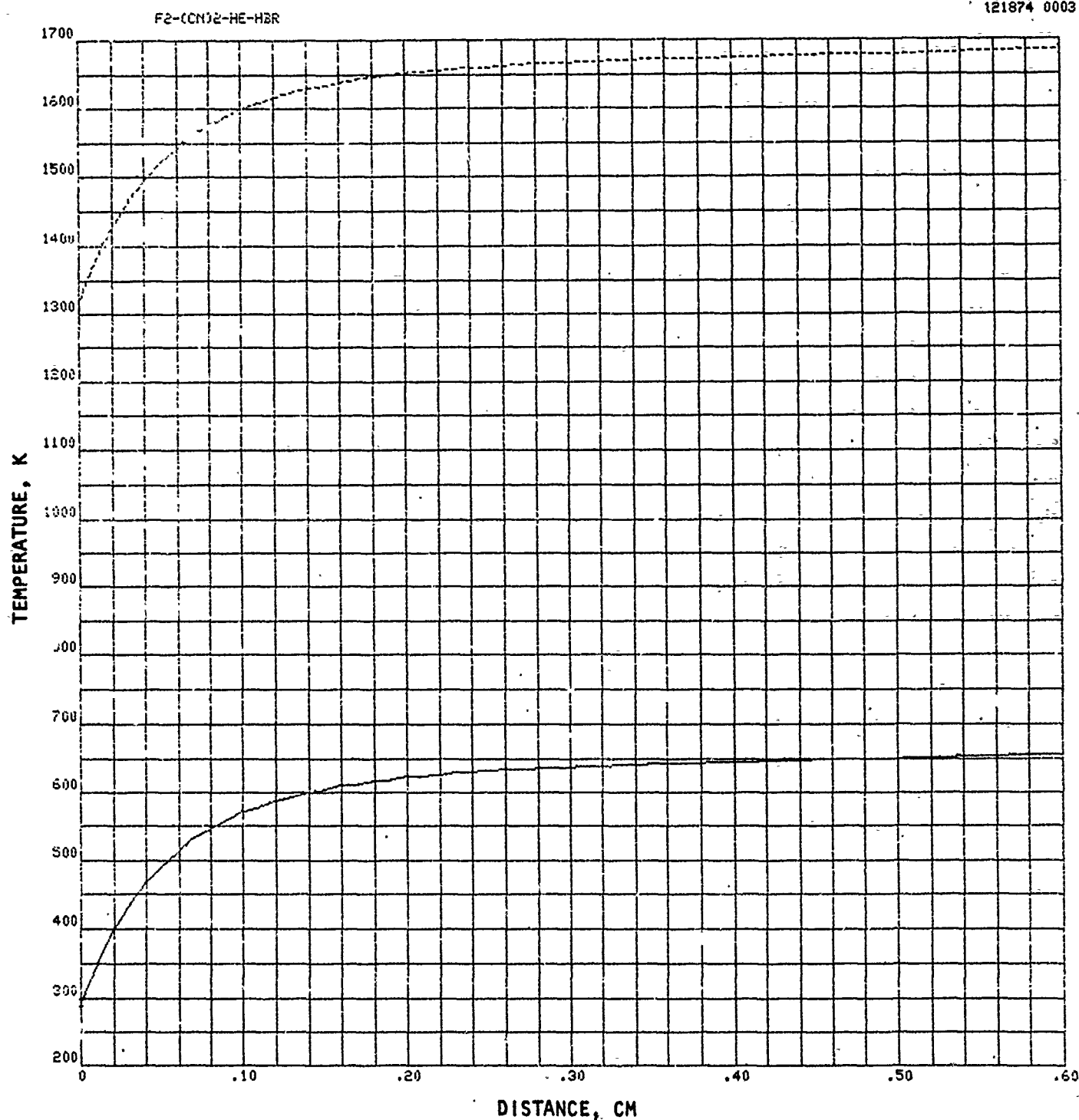


Figure 103. F₂-(CN)₂-He-HBr System, Gas Static and Stagnation Temperatures
(F = 10%, 1500 K, Series III)

1055811301
121874 0005

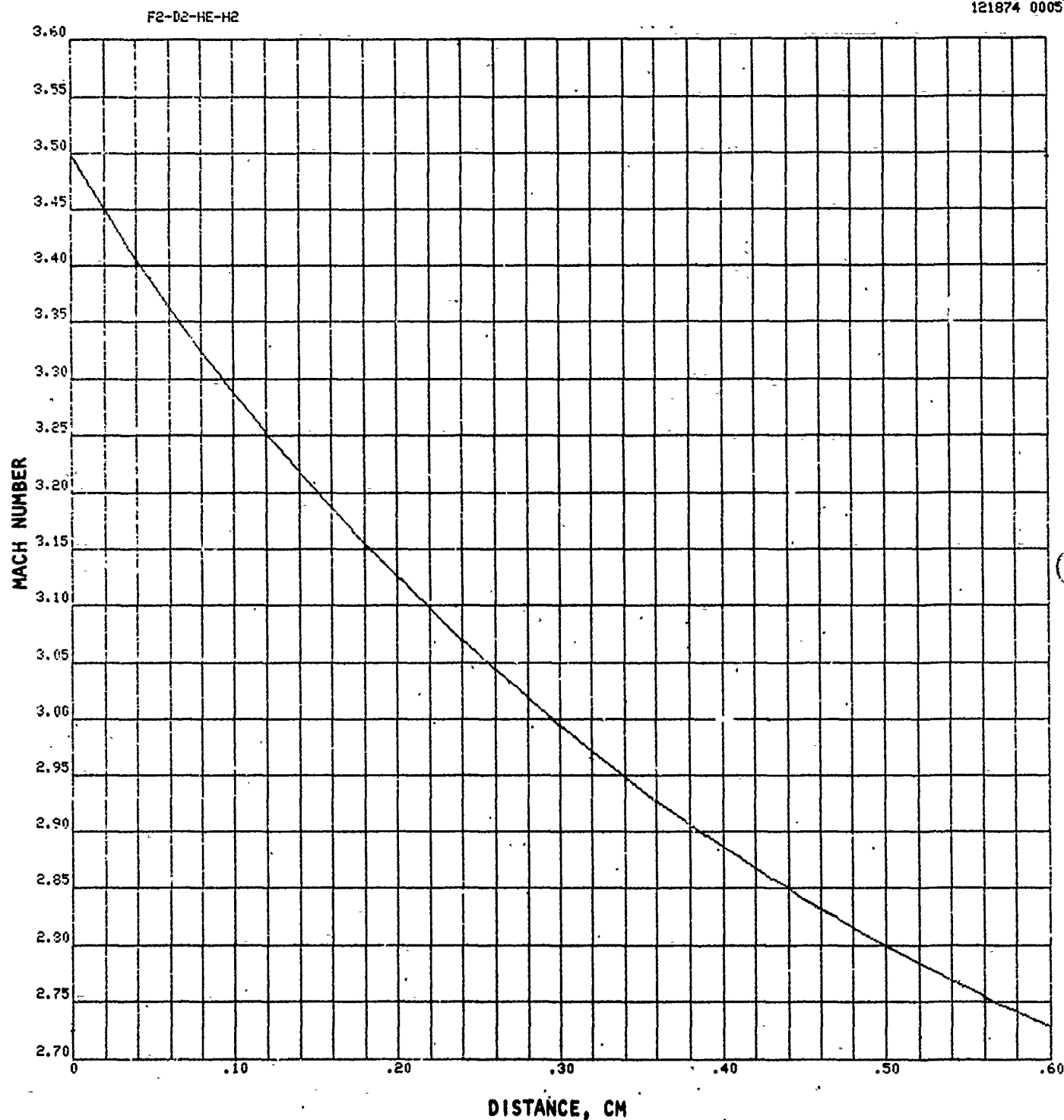


Figure 104. $F_2-D_2-He-H_2$ System, Gas Mach Numbers
($F = 10\%$, 1500 K, Series III)

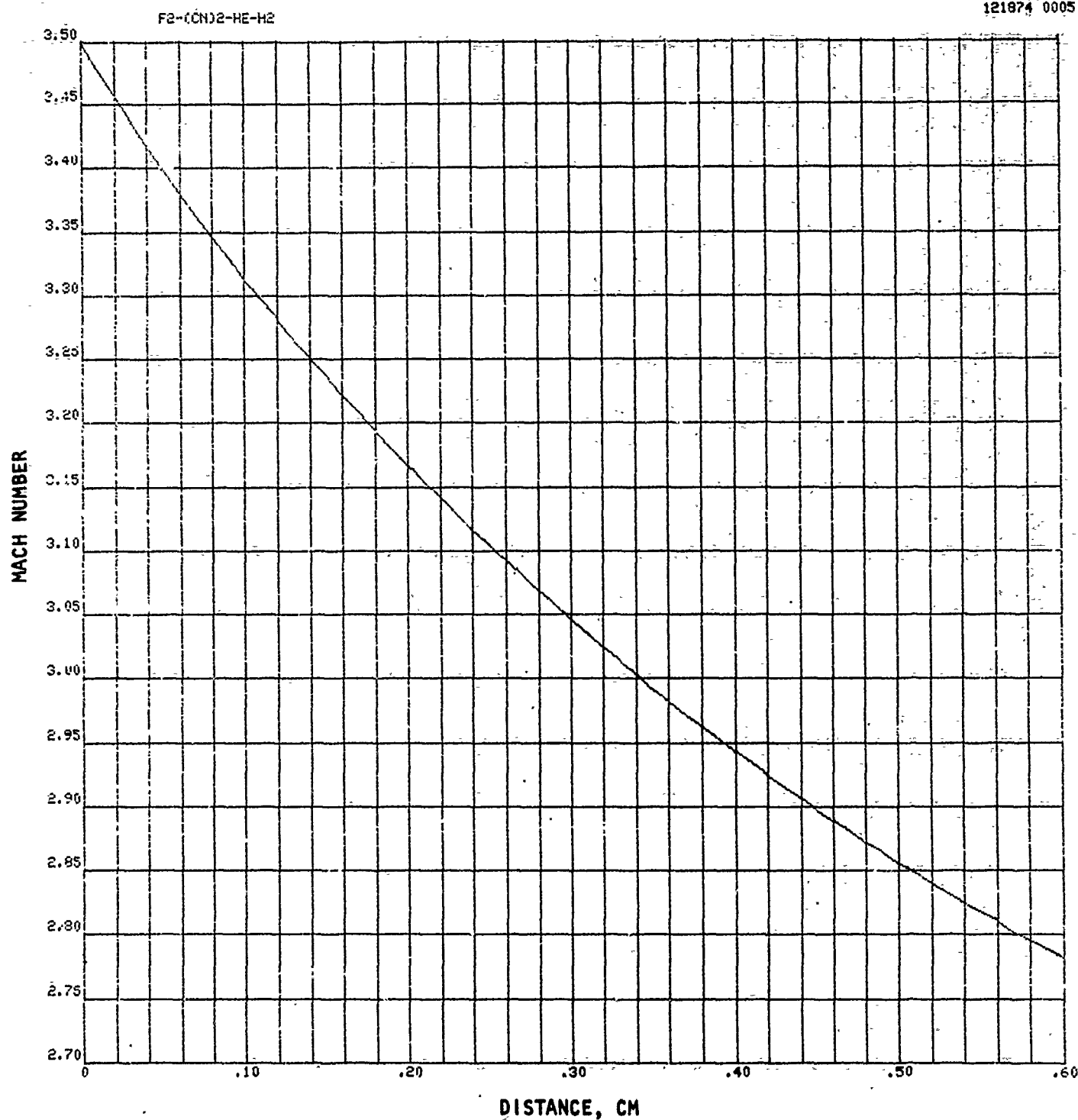


Figure 105. F₂-(CN)₂-He-H₂ System, Gas Mach Number
(F = 10%, 1500 K, Series III).

055611301
121874 0005

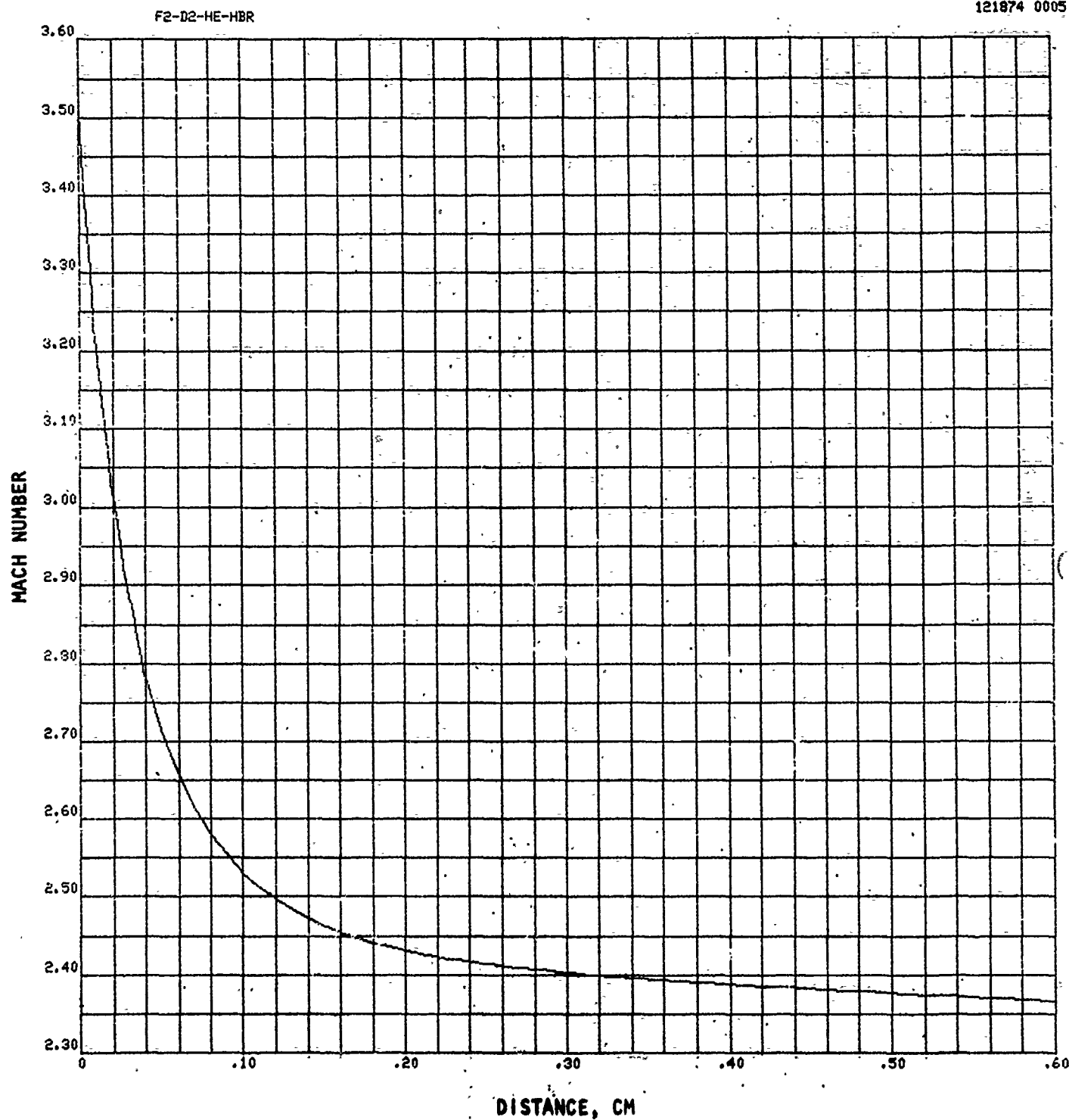


Figure 106. F₂-D₂-He-HBr System, Gas Mach Number
(F = 10%, 1500 K, Series III)

055811301
121874 0005

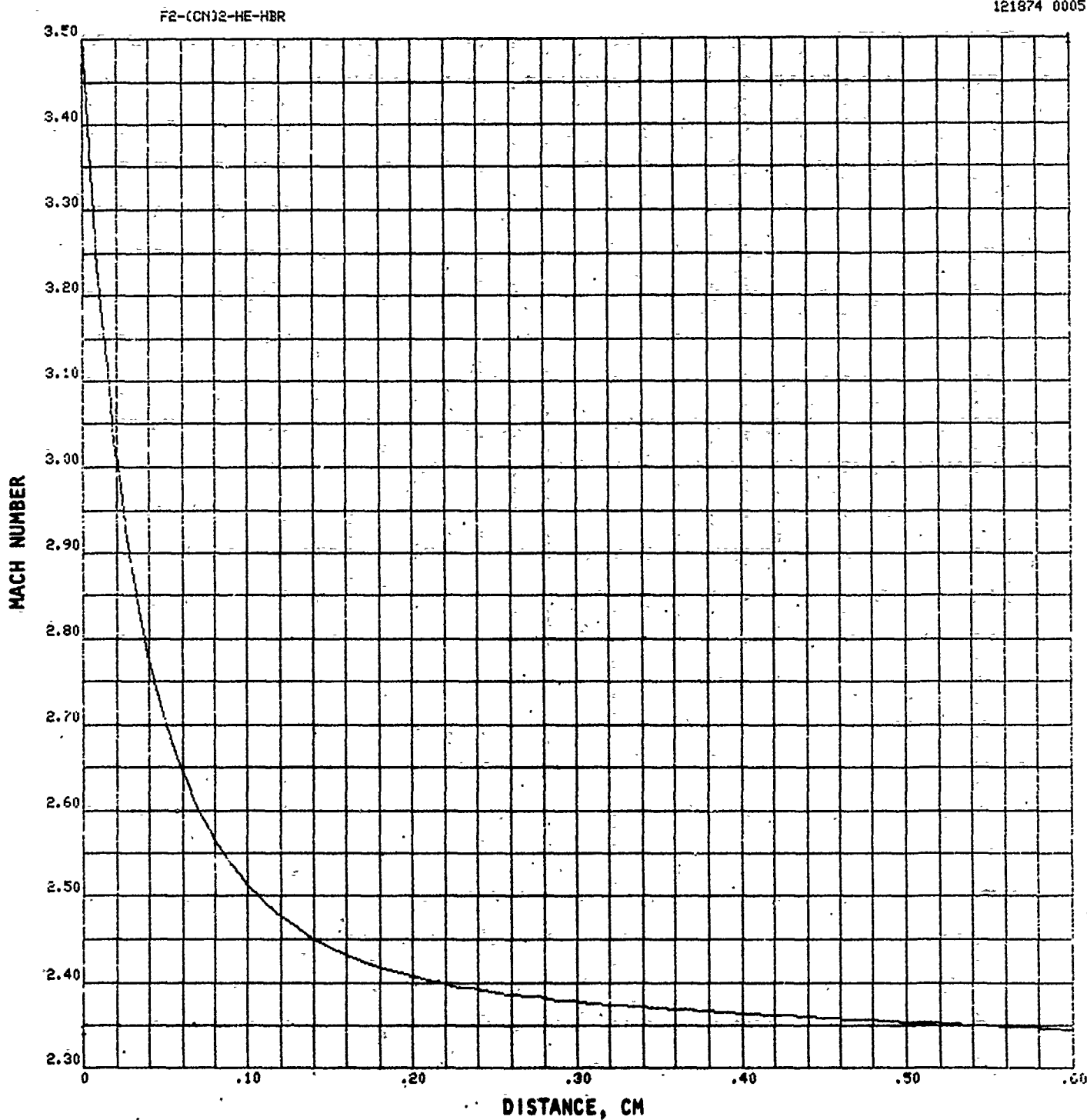


Figure 107. F₂-(CN)₂-He-HBr System, Gas Mach Number
(F = 10%, 1500 K, Series III)

F2-D2-HE-H2

*055811301
121874 0004

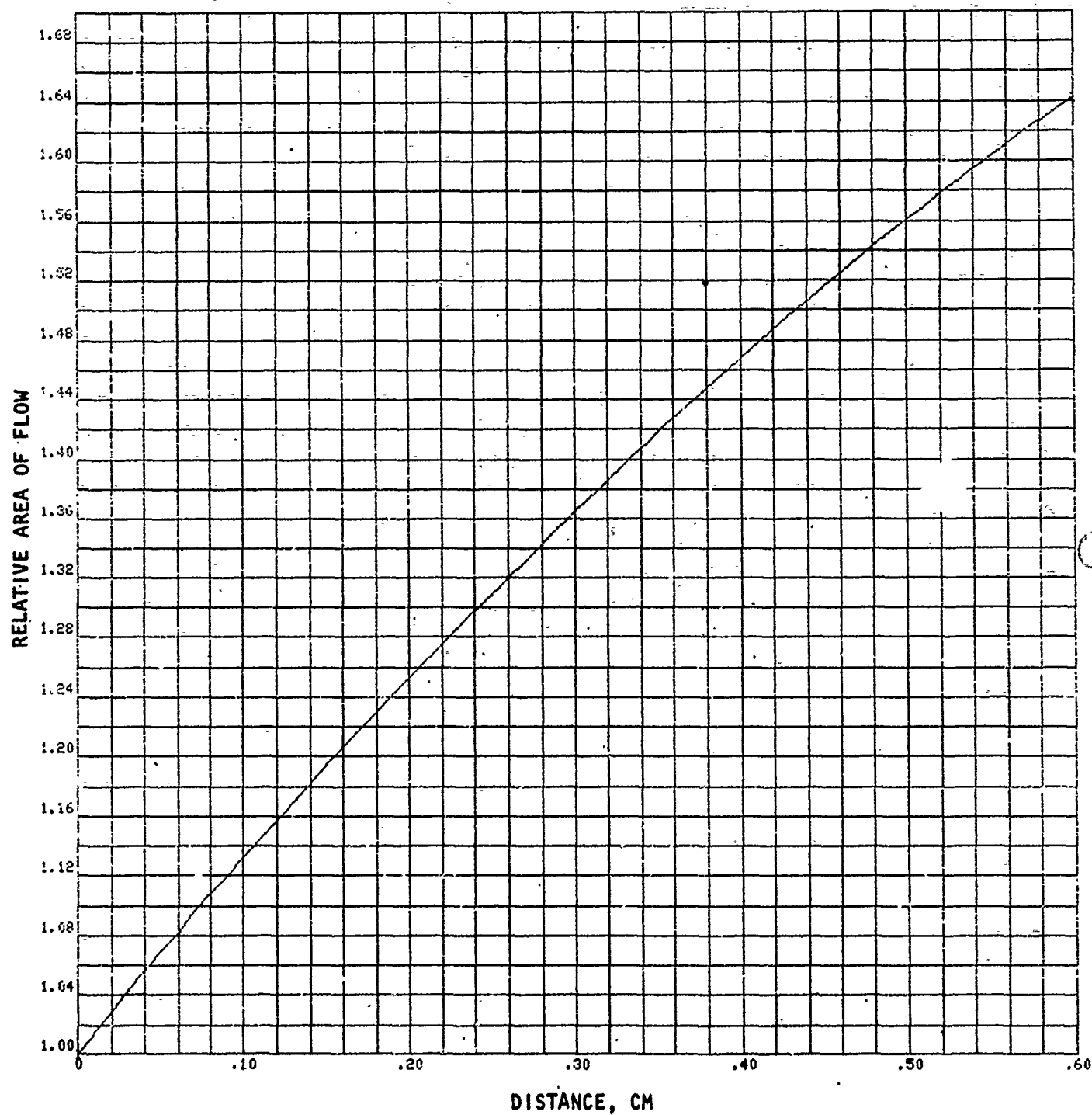


Figure 108. F₂-D₂-He-H₂ System, Relative Area of Flow
(F = 10%, 1500 K, Series III)

*055811304
1C1874 0004

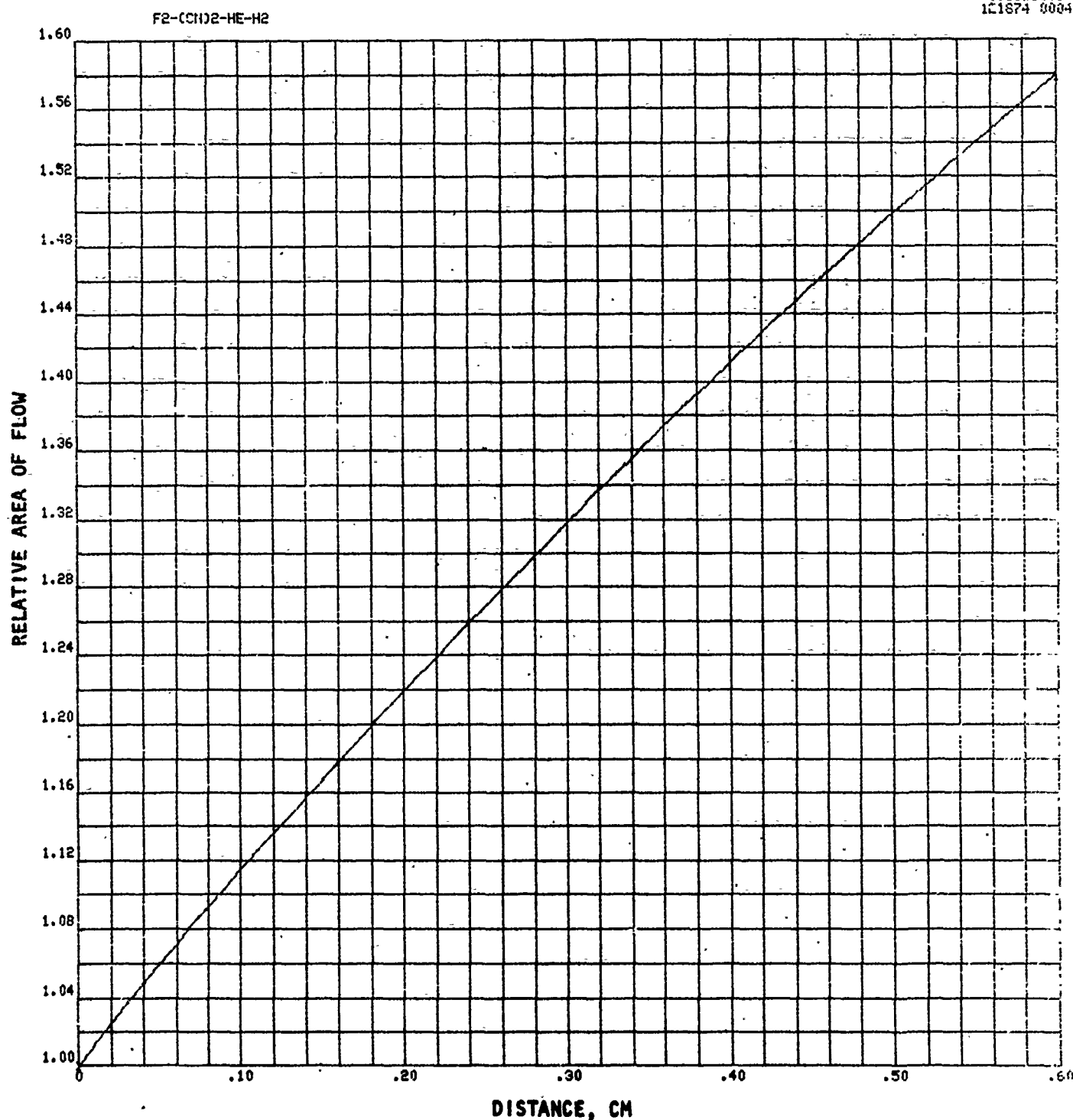


Figure 109. $F_2-(CN)_2-He-H_2$ -System, Relative Area of Flow
($F = 10\%$, 1500 K, Series III)

W055811301
121874 0004

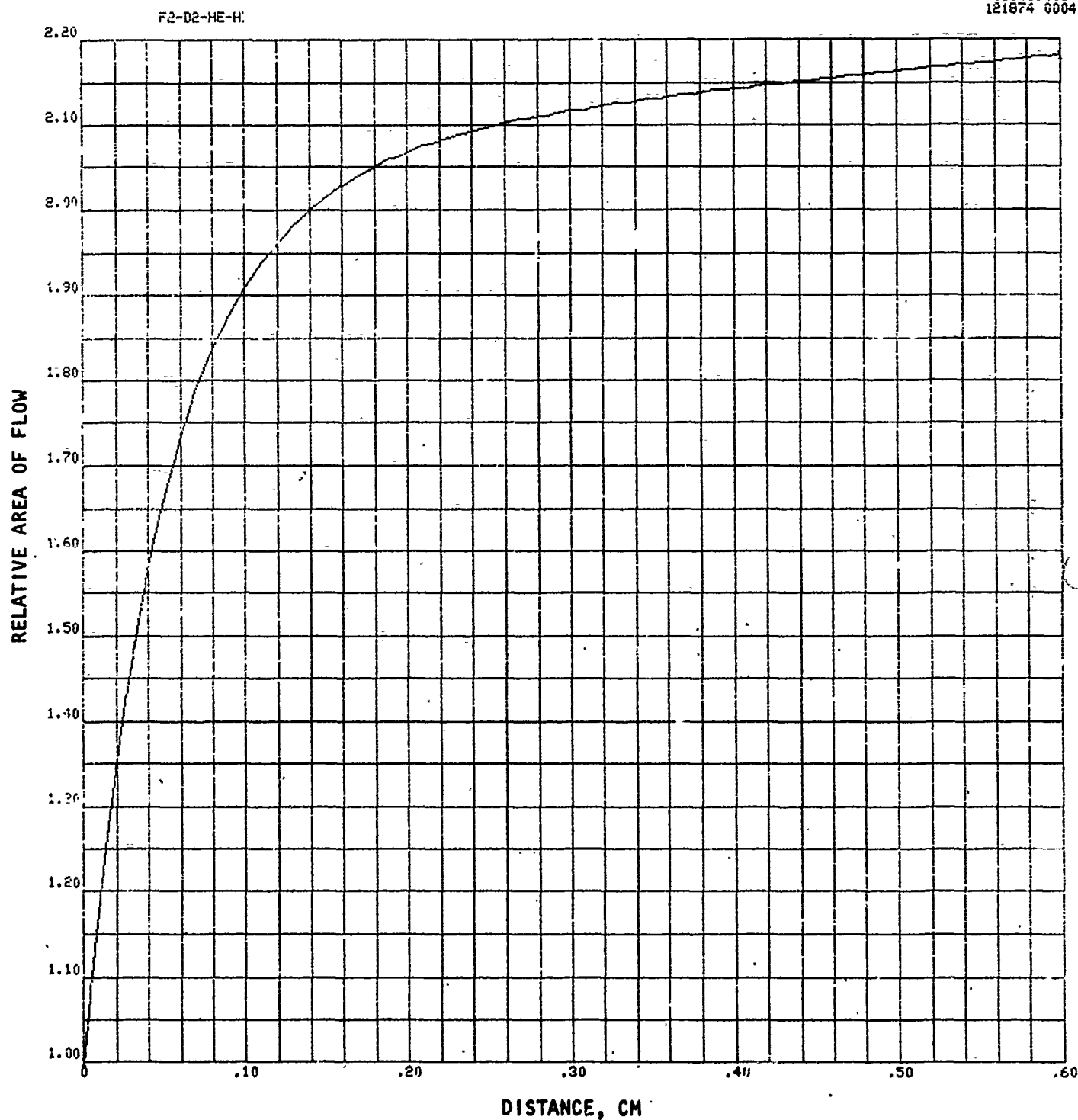


Figure 110. F₂-D₂-He-HBr System, Relative Area of Flow
(F = 10%, 1500 K, Series III)

#055811301
121874 0004

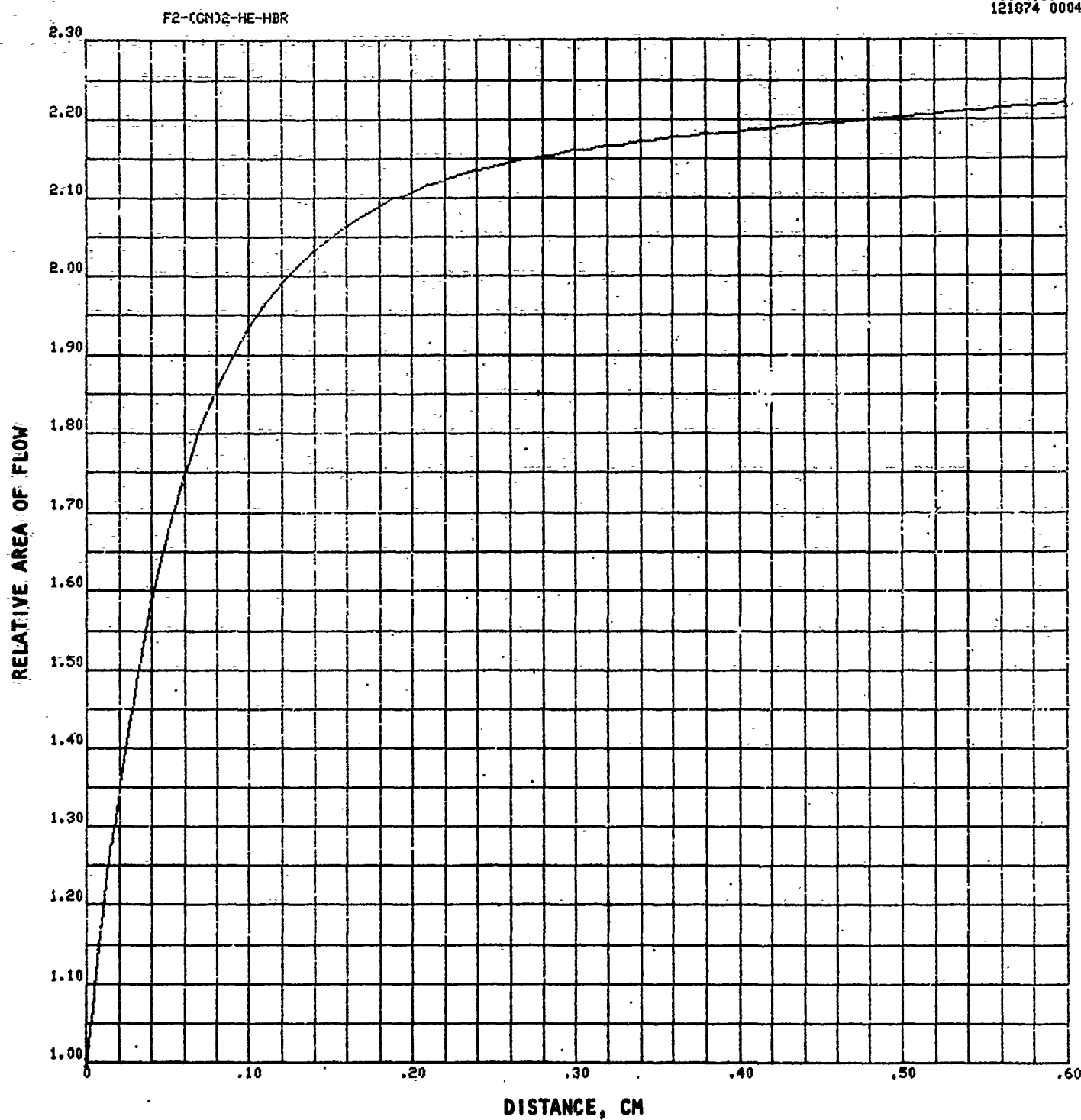


Figure 111. F₂-(CN)₂-He-HBr System, Relative Area of Flow
(F = 10%, 1500 K, Series III)

#055811301
121874 0002

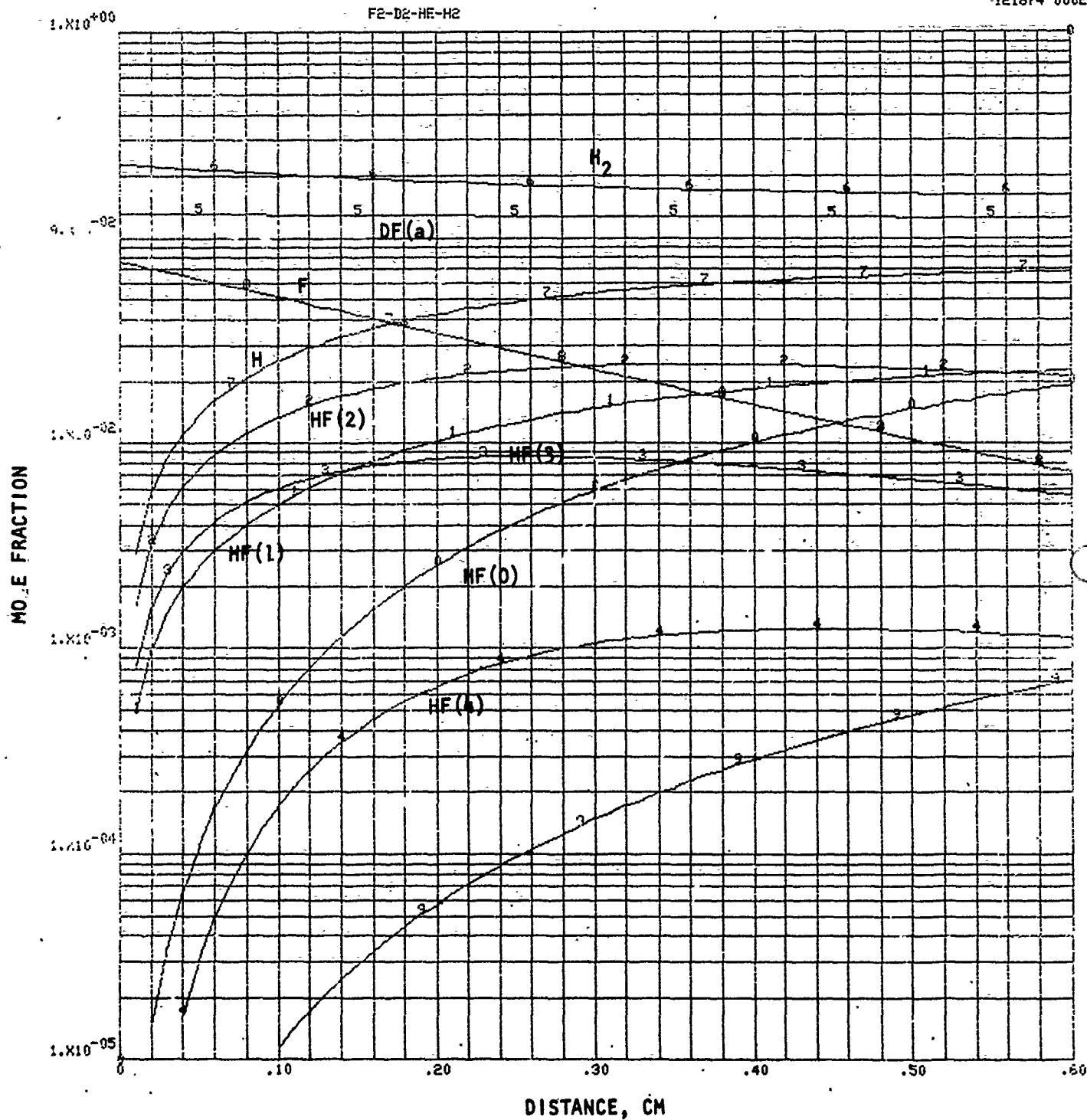


Figure 112. F₂-D₂-He-H₂ System, Species Plot
(F = 10%, 1500 K, Series III)

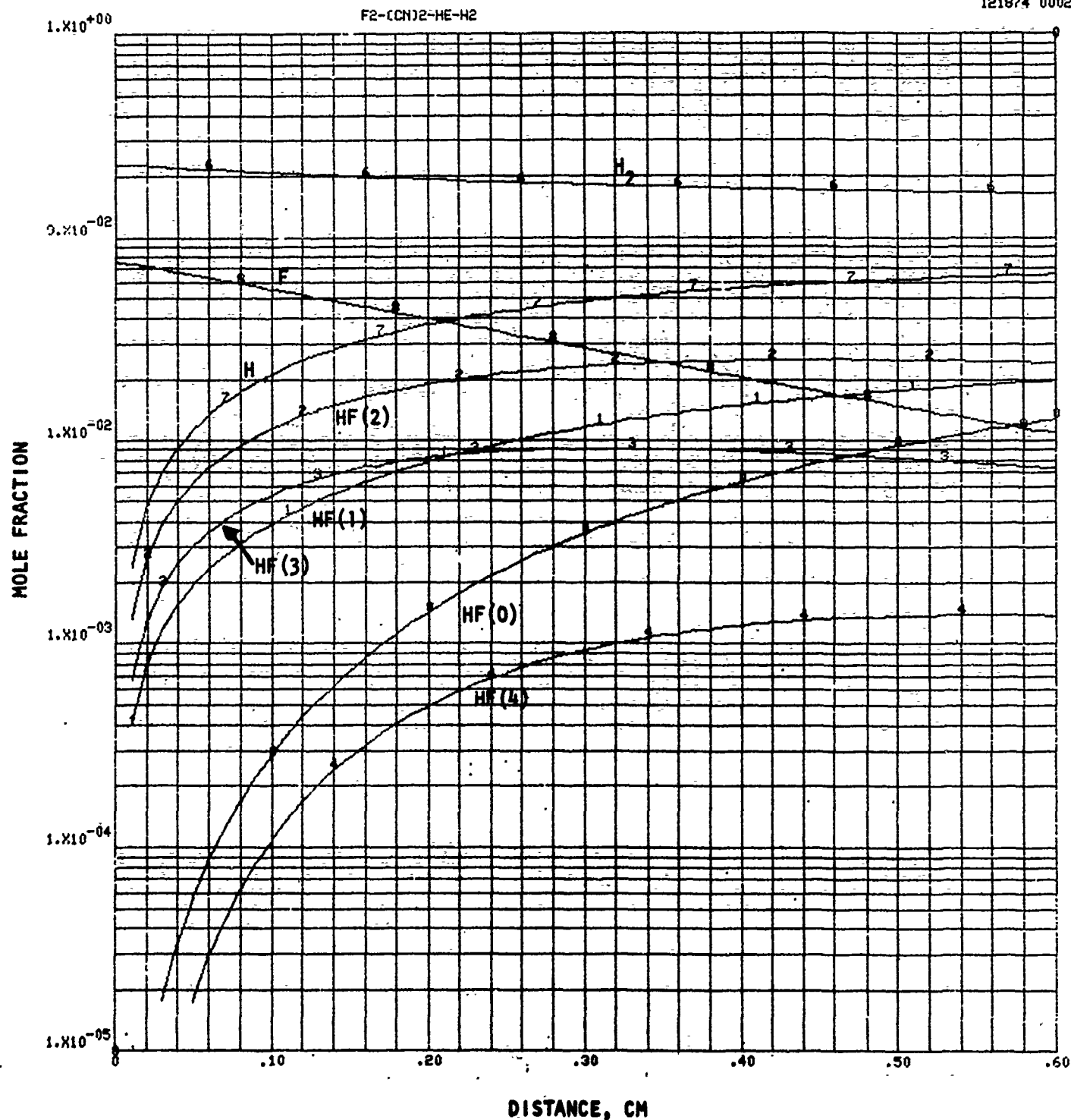


Figure 113. $F_2-(CN)_2-He-H_2$ System, Species Plot
($F = 10\%$, 1500 K, Series III)

#055811301
121874 0002

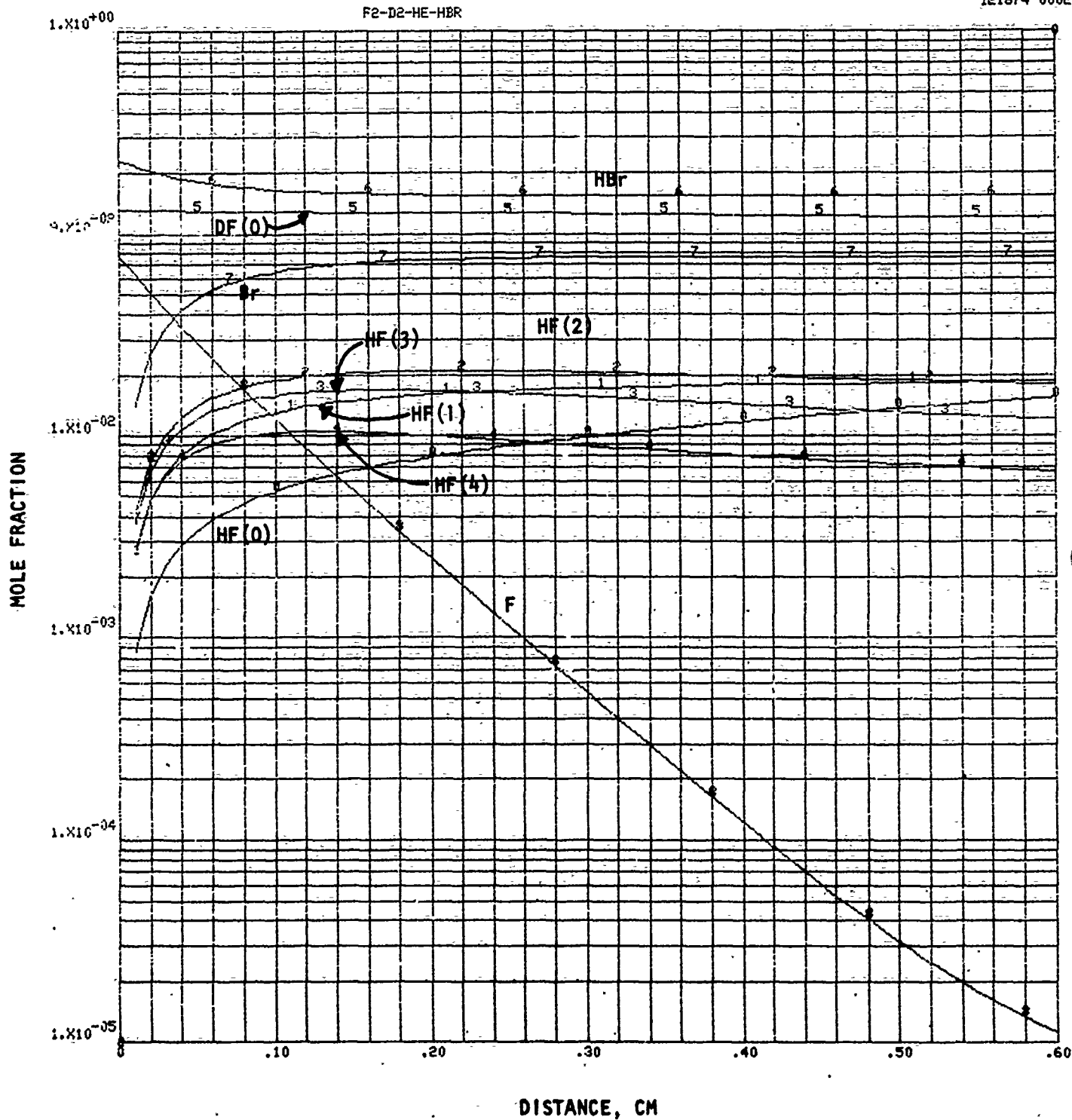


Figure 114. F₂-D₂-He-HBr System, Species Plot
(F = 10%, 1500 K, Series III)

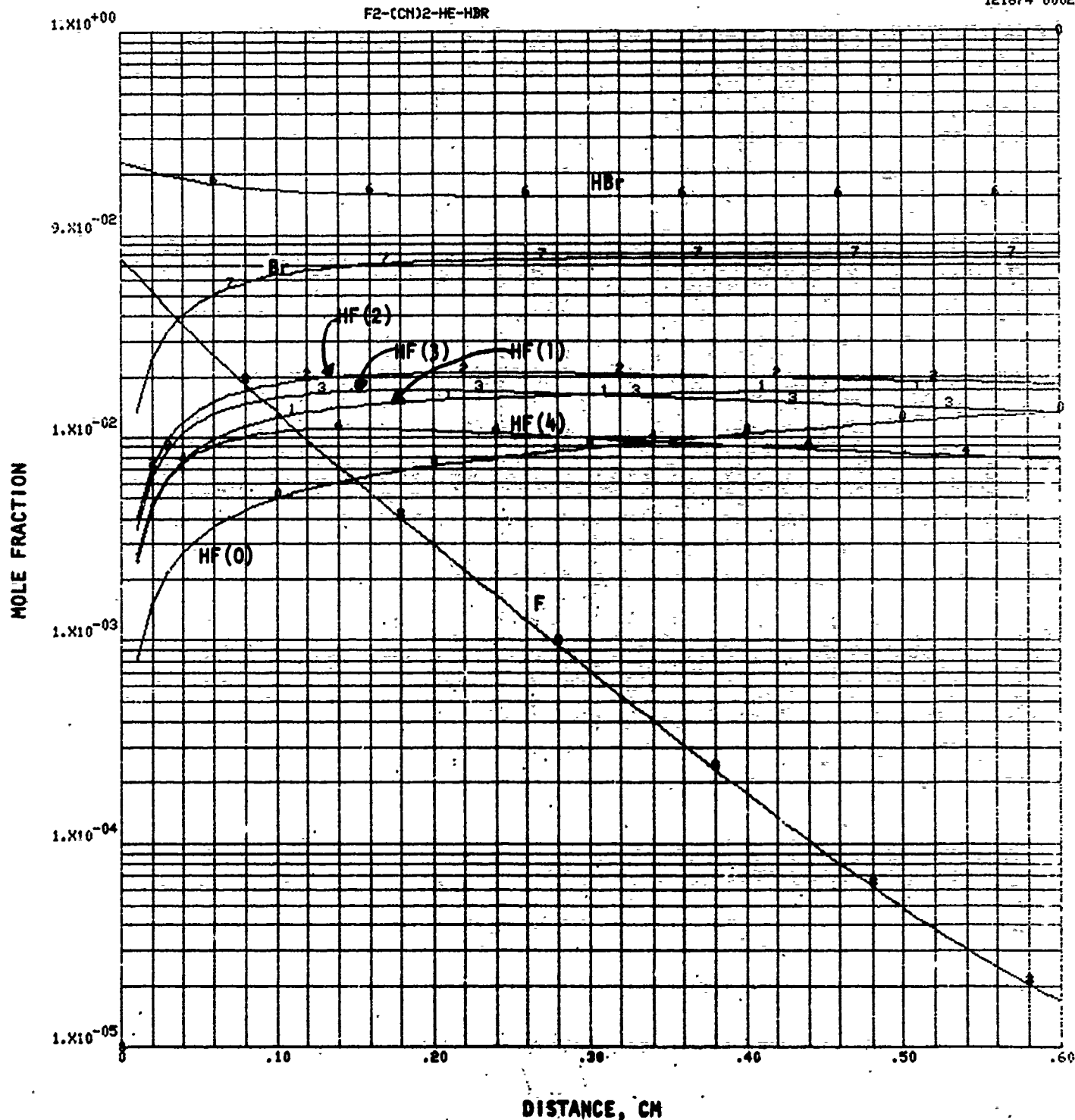


Figure 115. F₂-(CN)₂-He-HBr System, Species Plot
(F = 10%, 1500 K, Series III)

F2-D2-He-H2

THE P1(J)-LINES

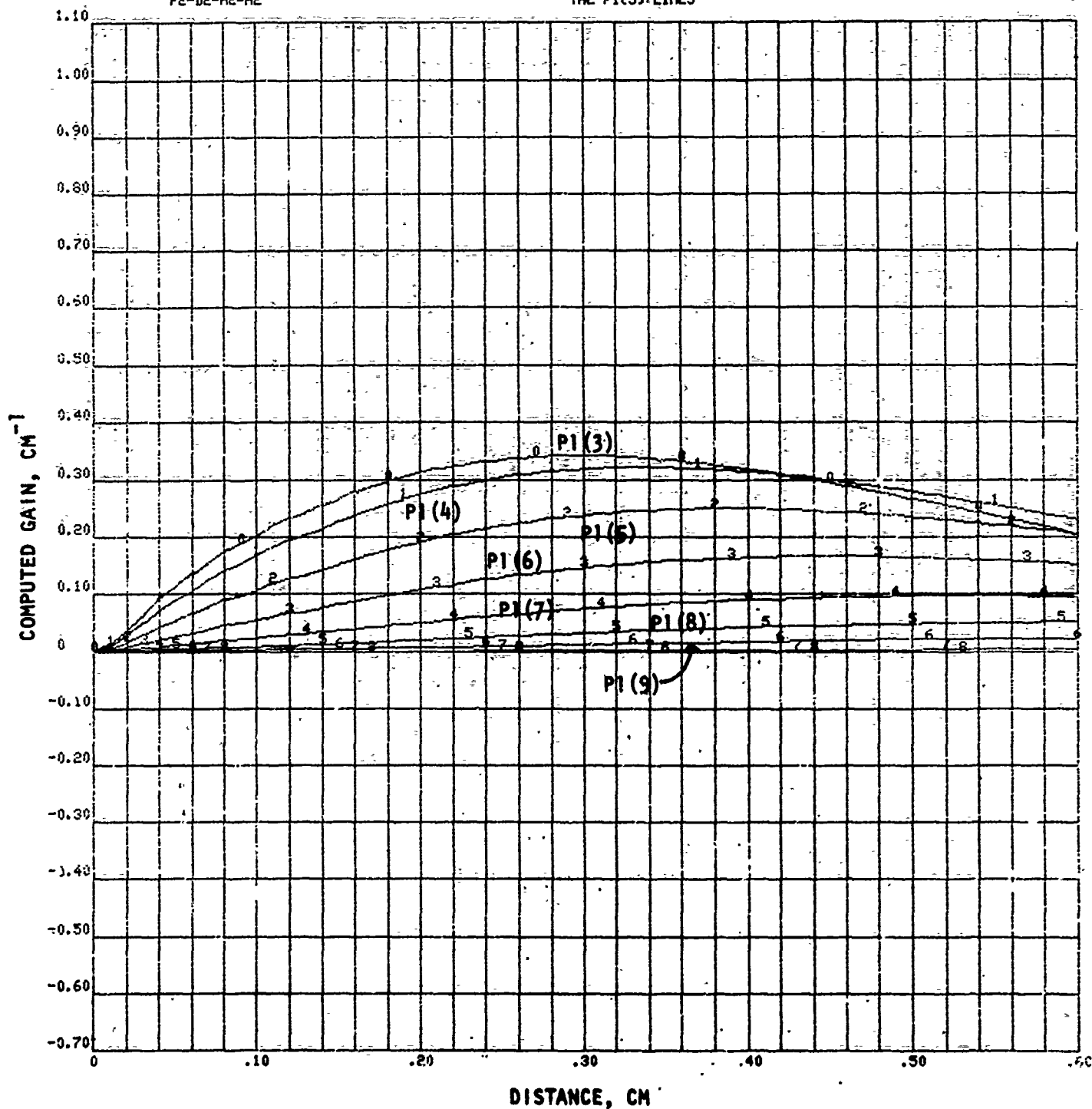
#055811301
121874 0007

Figure 116. F_2-D_2 -He- H_2 System, Computed Zero Power Gain on HF(1) \rightarrow HF(0) Lines
($F = 10\%$, 1500 K, Series III)

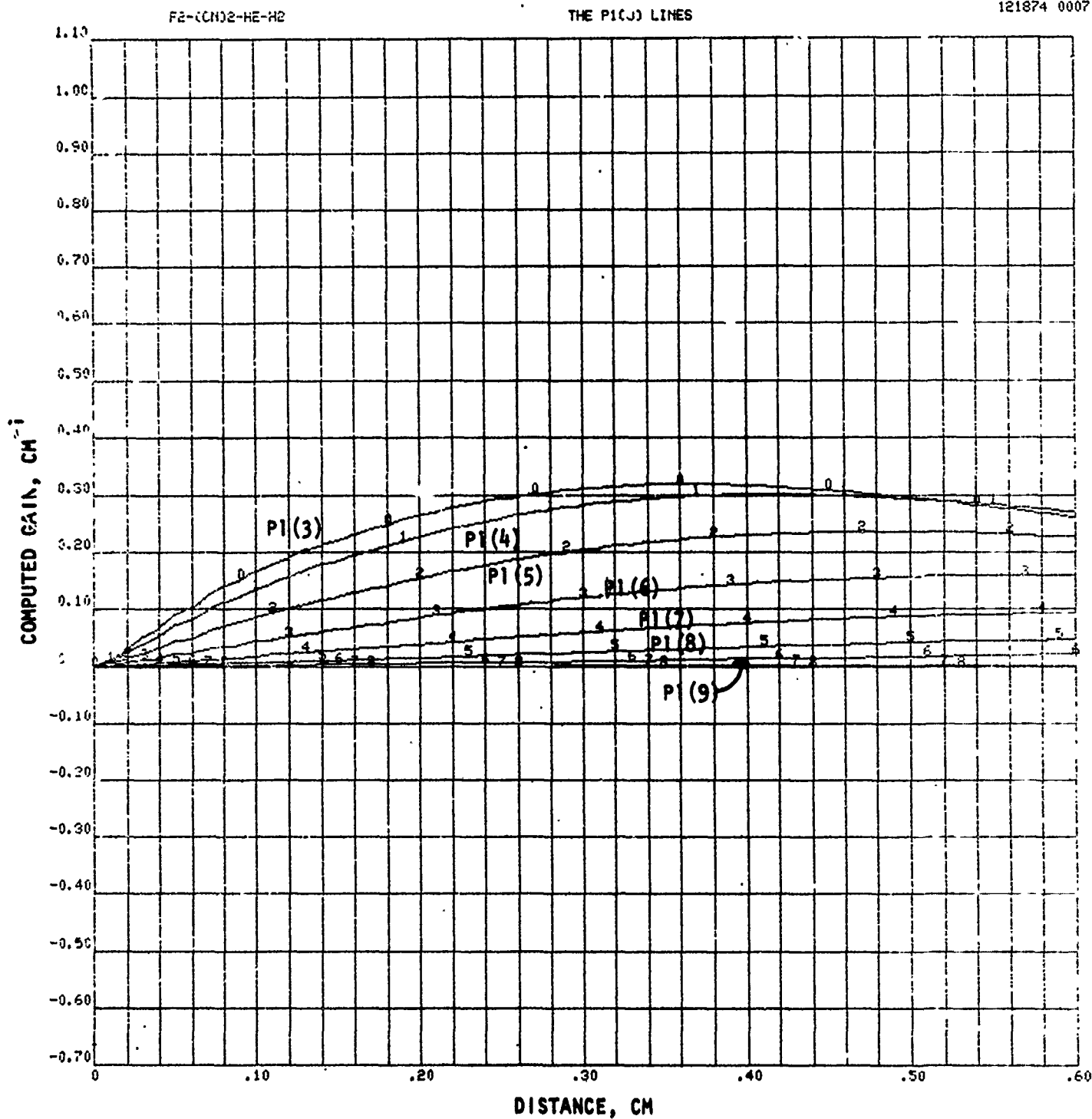


Figure 117. F₂-(CN)₂-He-H₂ System, Computed Zero Power Gain on HF(1) → HF(0) Lines
(F = 10%, 1500 K, Series III)

F2-D2-HE-HBR

THE P1(J) LINES

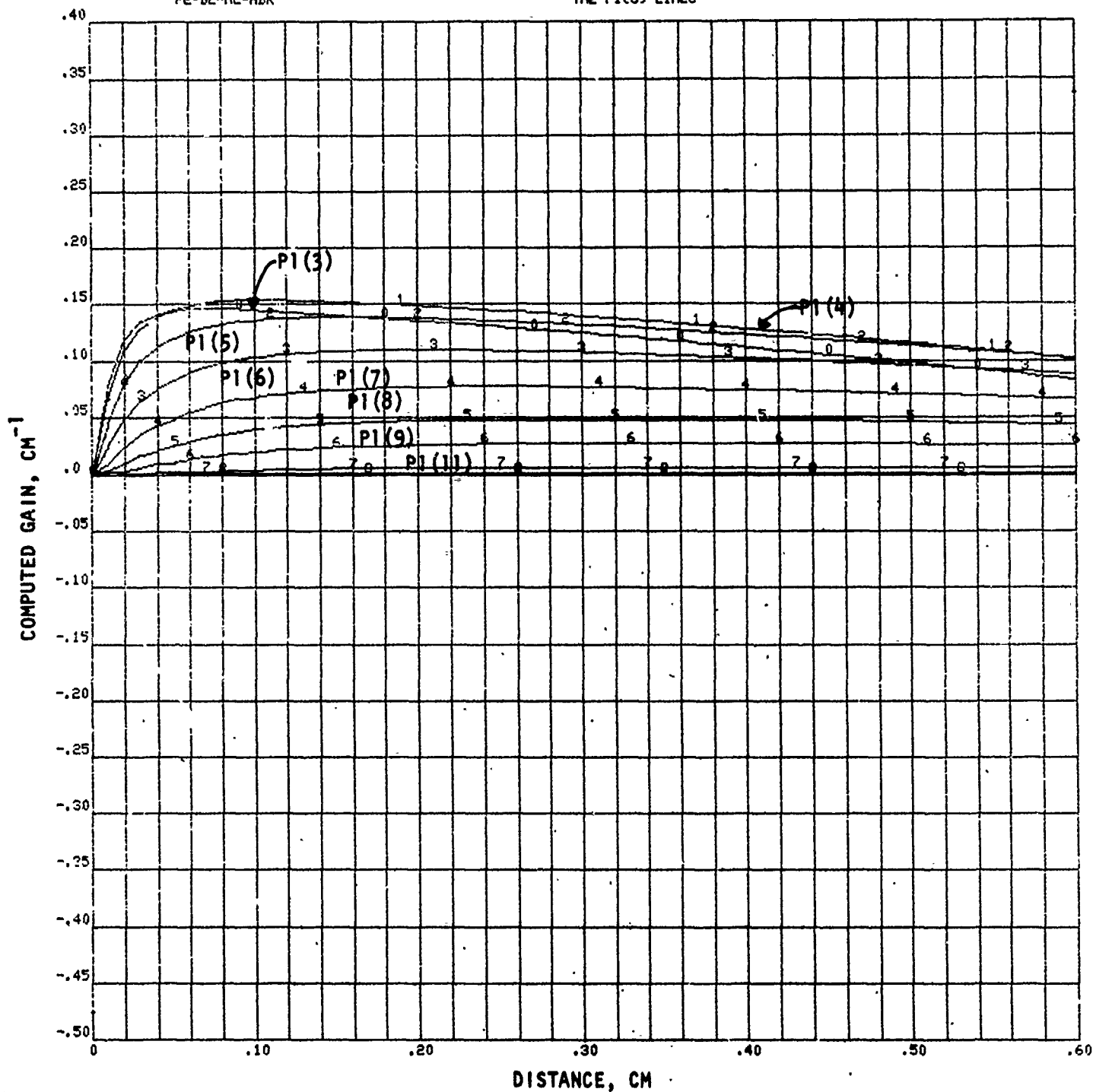
#055811301
121874 0007

Figure 118. F₂-D₂-He-HBr System, Computed Zero Power Gain on HF(1) → HF(0) Lines
(F = 10%, 1500 K, Series III)

F2-(CN)2-HE-HBR

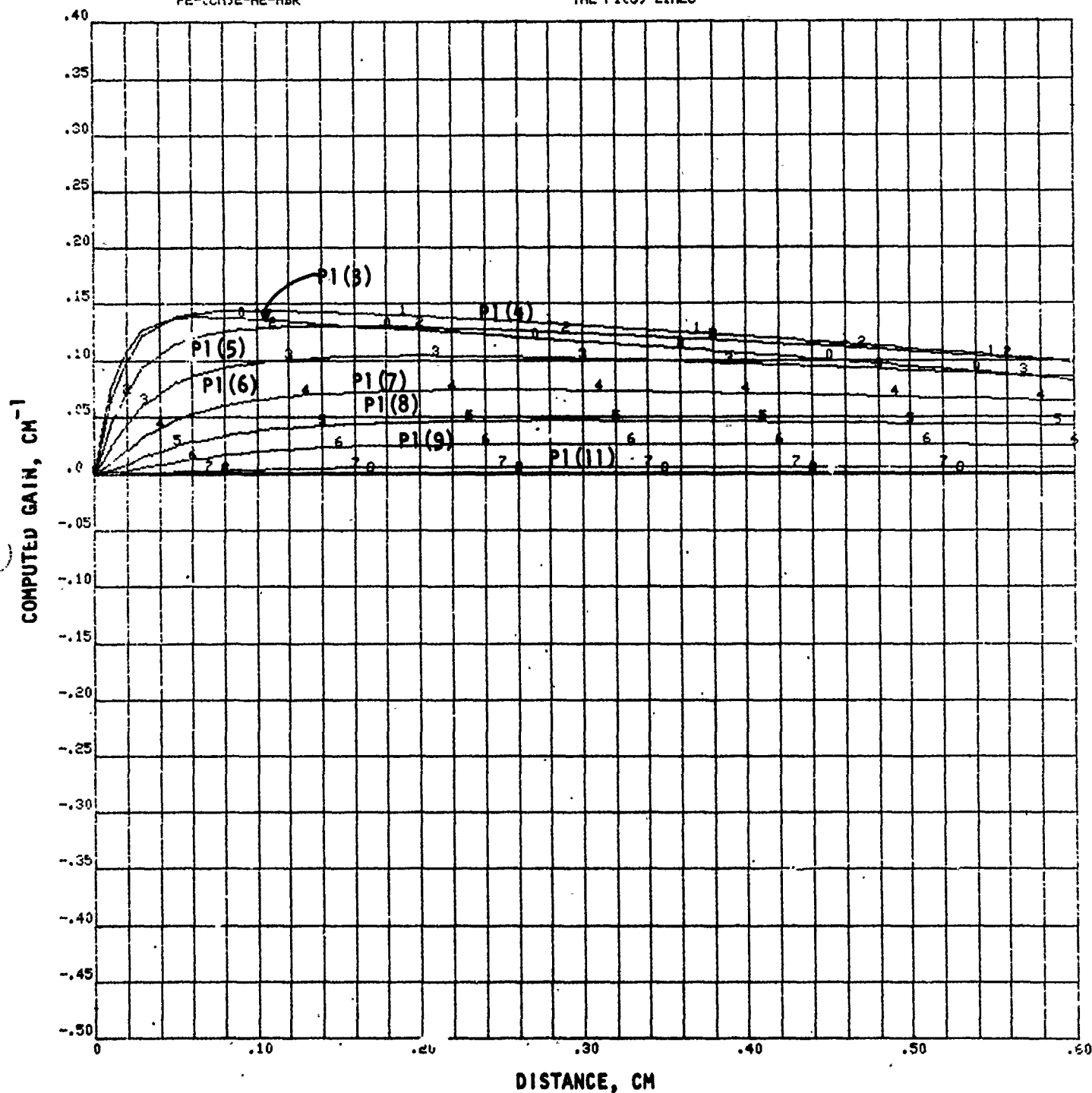
ROCKETDYNE LASER KINETICS CODE
COMPUTED GAIN
THE P1(J) LINESW055811301
121874 0007

Figure 119. $F_2-(CN)_2$ -He-HBr System, Computed Zero Power Gain on HF(1) \rightarrow HF(0) Lines
(F = 10%, 1500 K, Series III)

F2-D2-HE-H2

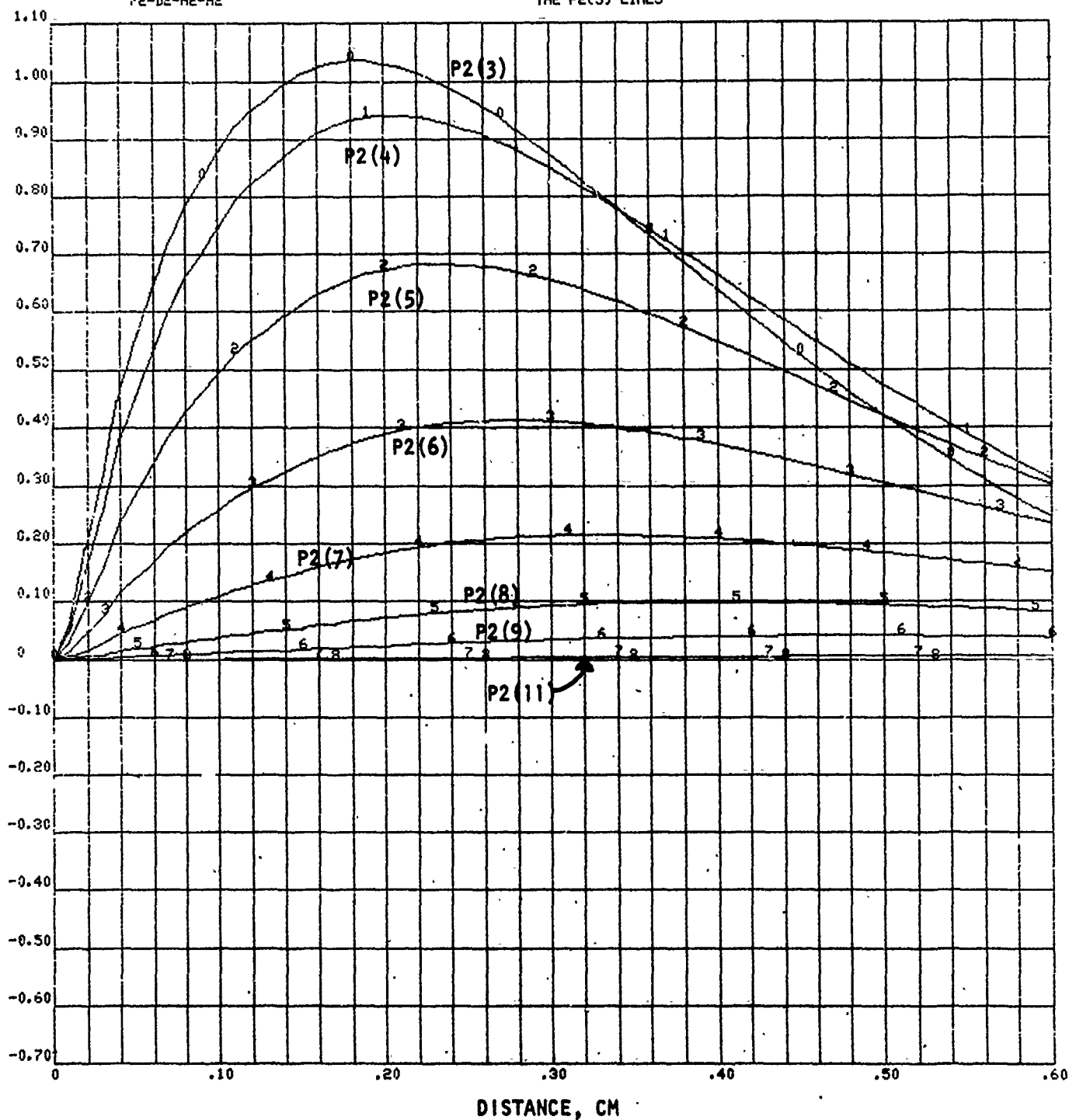
ROCKETDYNE LASER KINETICS CODE COMPUTED GAIN
THE P2(J) LINES*055811301
121874 0009

Figure 120. $F_2-D_2-He-H_2$ System, Computed Zero Power Gain on HF(2) \rightarrow HF(1) Lines
(F = 10%, 1500 K, Series III)

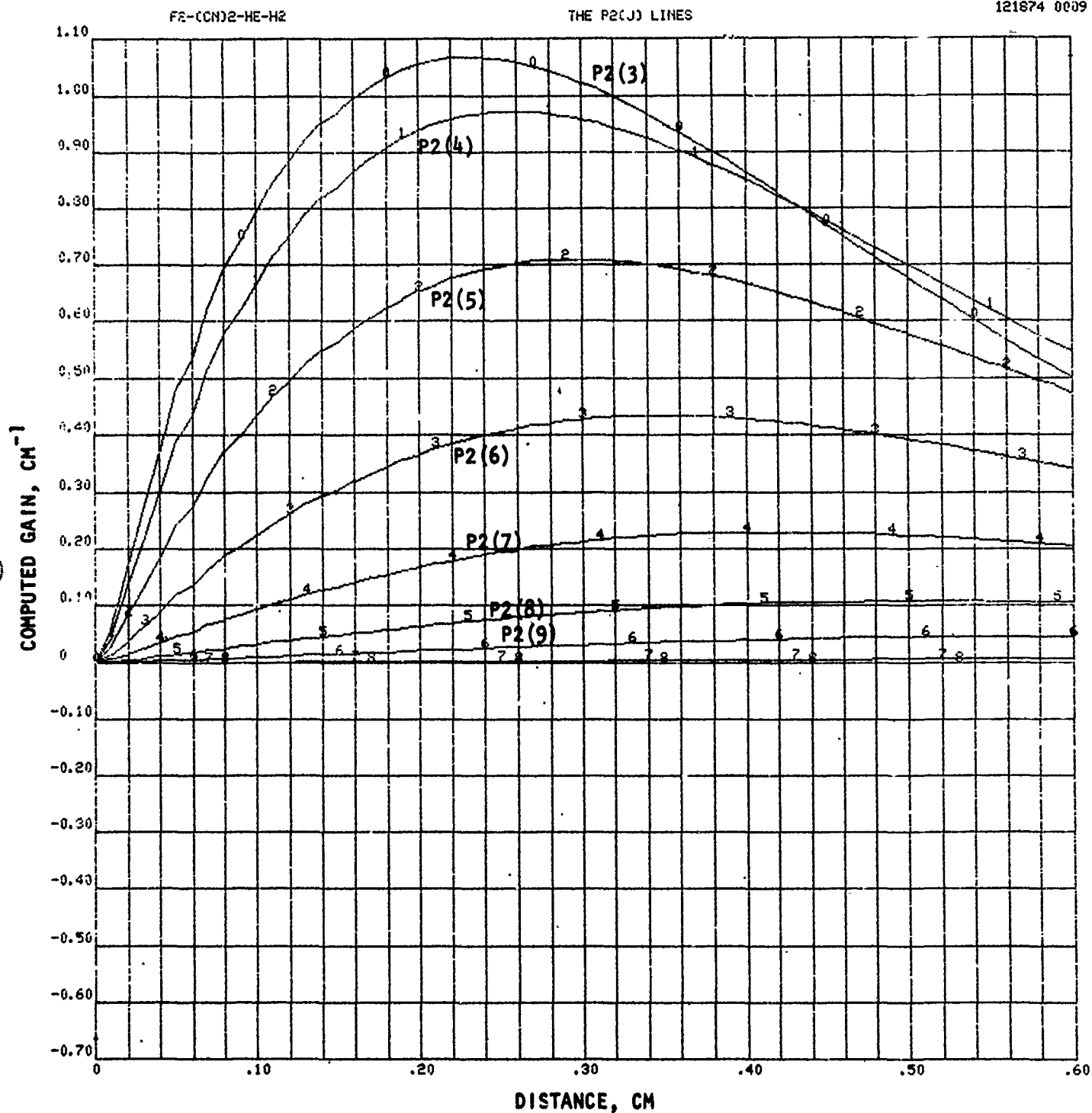


Figure 121. F₂-(CN)₂-He-H₂ System, Computed Zero Power Gain on HF(2) → HF(1) Lines
(F = 10%, 1500 K, Series III)

F2-D2-HE-HBR

THE P2(J) LINES

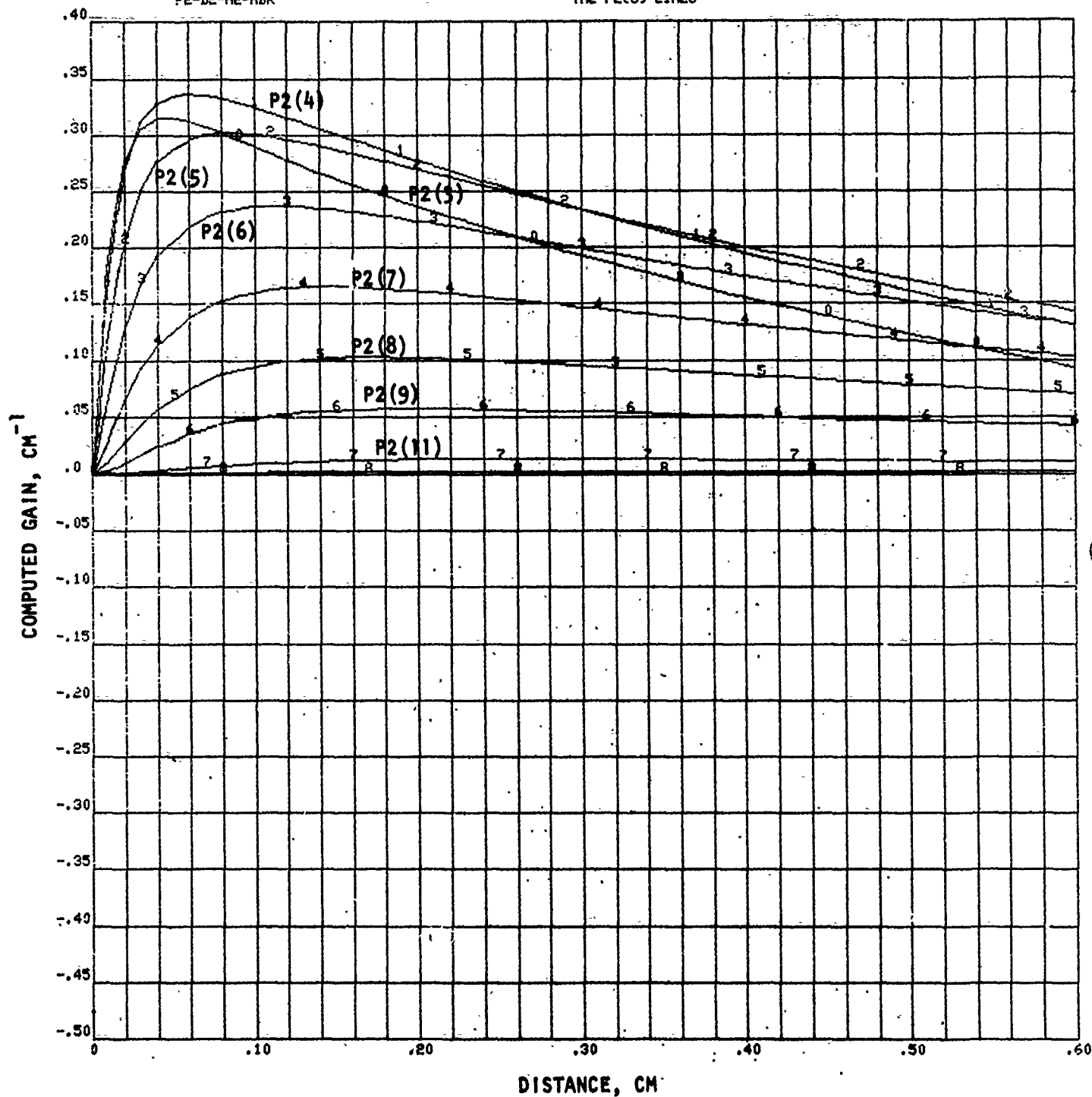
#055811301
121874 0009

Figure 122. $\text{F}_2\text{-D}_2\text{-He-HBr}$ System, Computed Zero Power Gain on $\text{HF}(2) \rightarrow \text{HF}(1)$ Lines
($F = 10\%$, 1500 K, Series III)

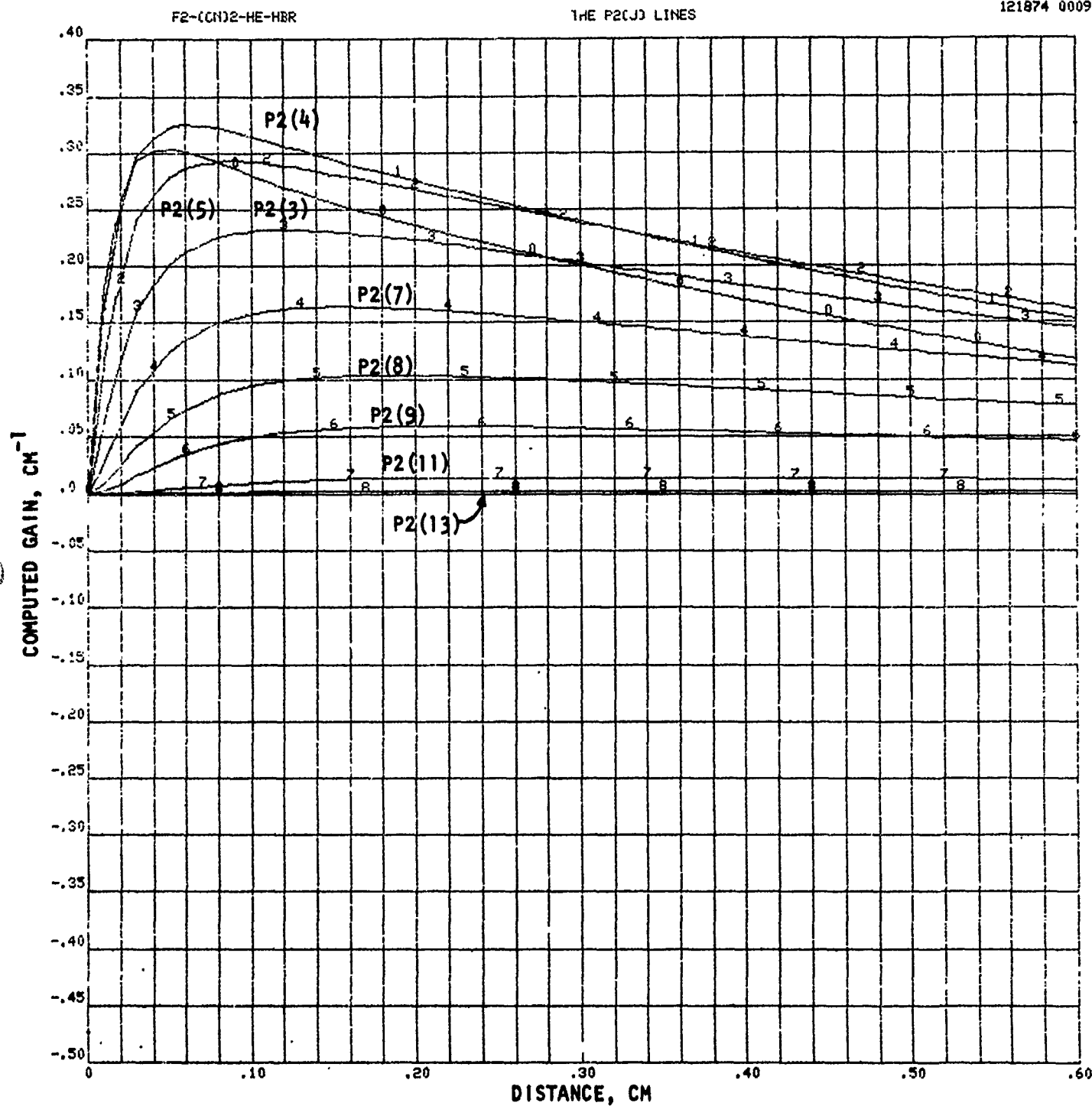


Figure 123. F₂-(CN)₂-He-HBr System, Computed Zero Power Gain on HF(2) → HF(1) Lines
(F = 10%, 1500 K, Series III)

F2-D2-HE-H2

SOME P3(J) LINES ETC

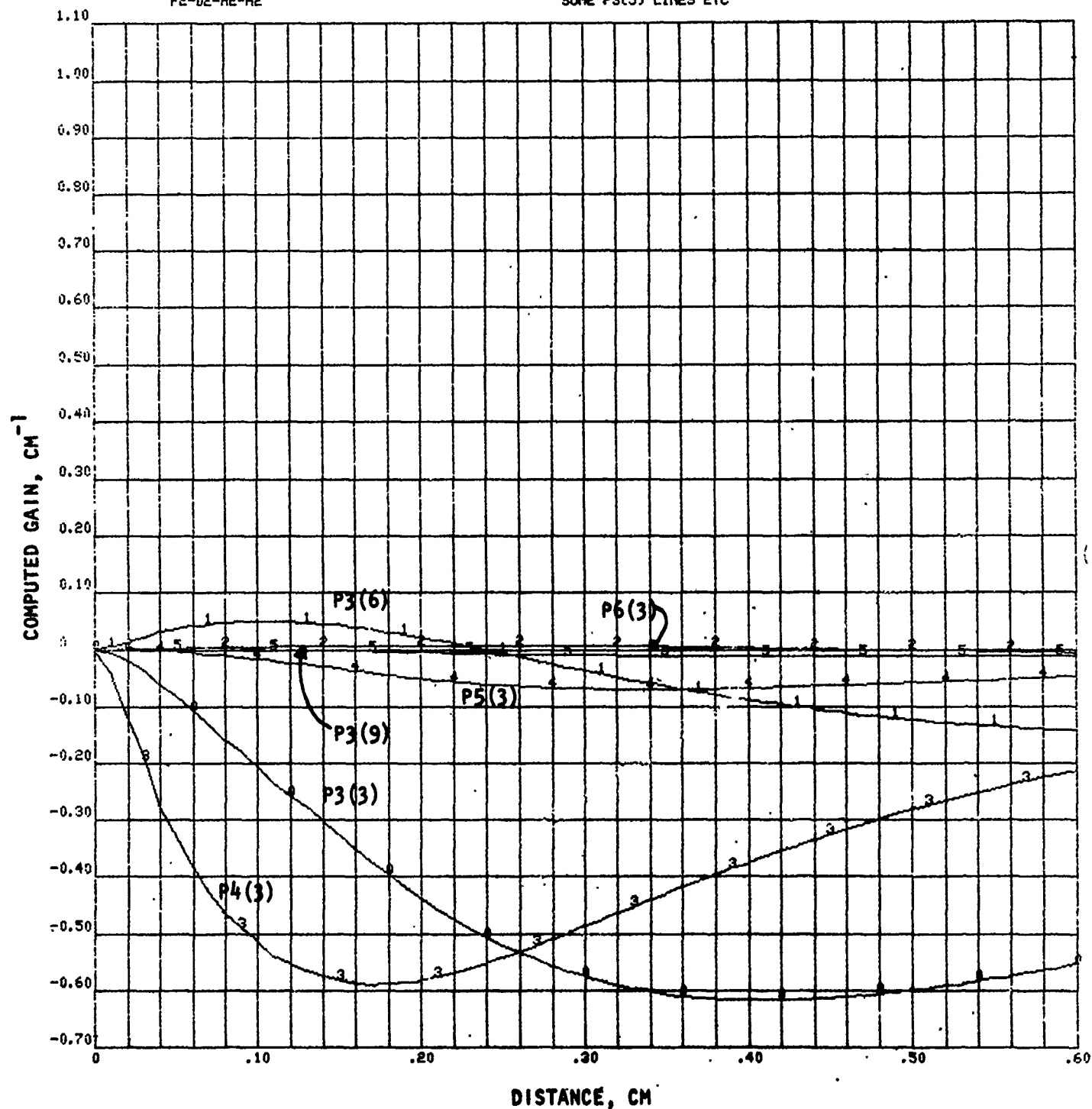
W055611301
121874 0011

Figure 124. $F_2-D_2-He-H_2$ System, Computed Zero Power Gain on Higher Lines
($F = 10\%$, 1500 K, Series III)

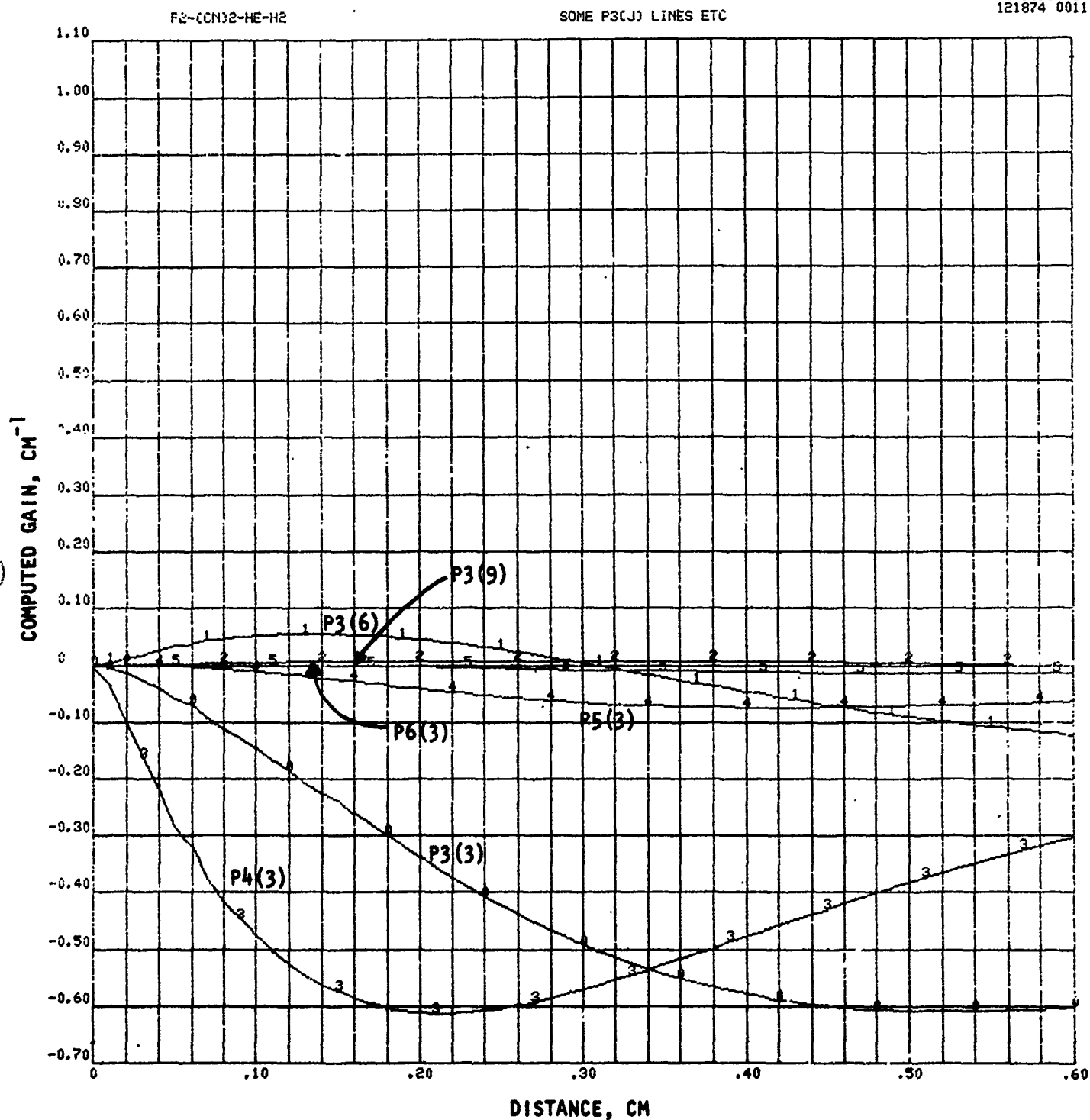


Figure 125. F₂-(CN)₂-He-H₂ System, Computed Zero Power Gain on Higher Lines
(F = 10%, 1500 K, Series III)

F2-D2-HE-HBR

SOME P3(J) LINES ETC

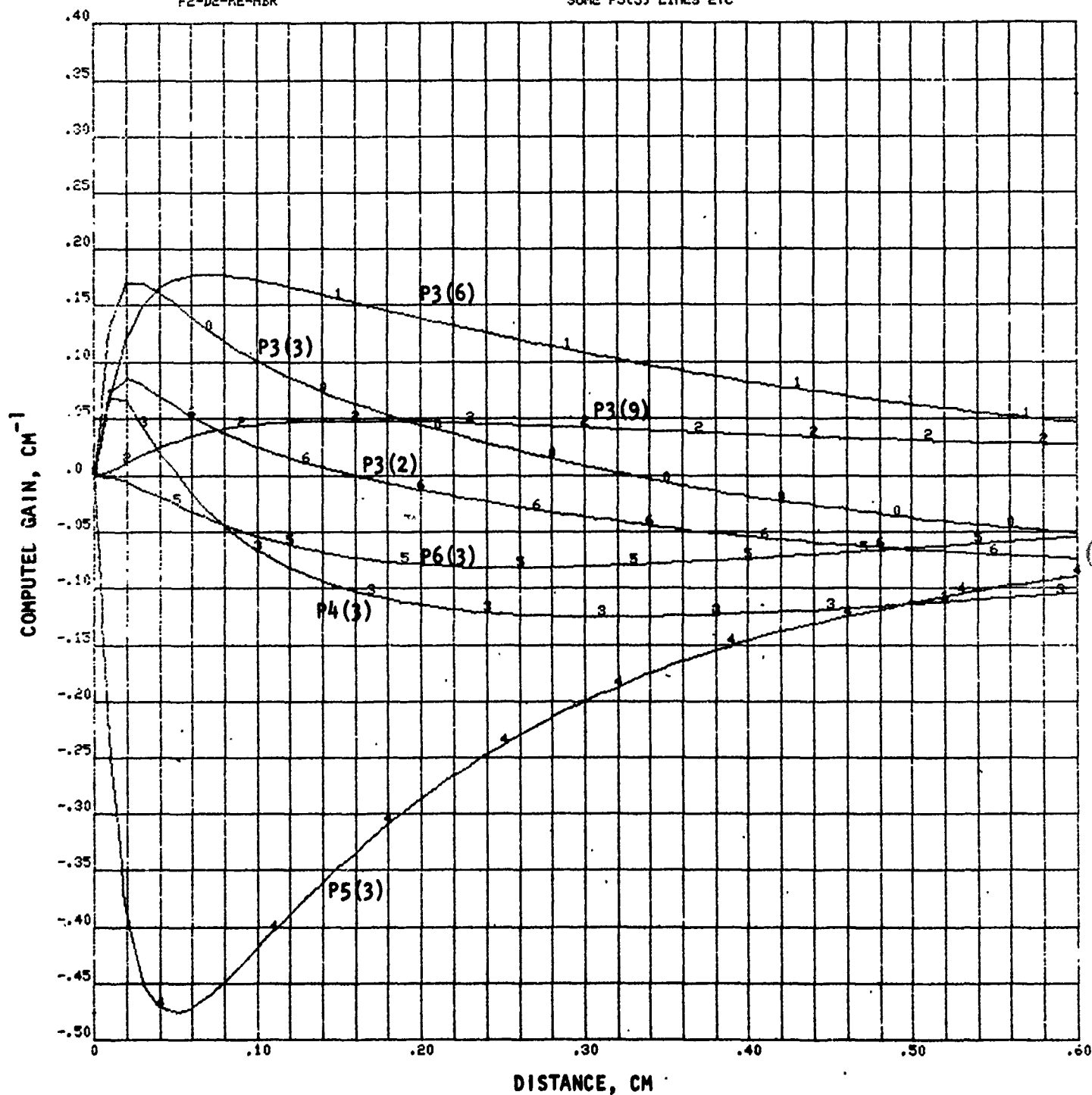
*055811301
121874 0011

Figure 126. F₂-D₂-He-HBr System, Computed Zero Power Gain on Higher Lines
(F = 10%, 1500 K, Series III)

F₂-(CN)₂-HE-HBR

SOME P3(J) LINES ETC

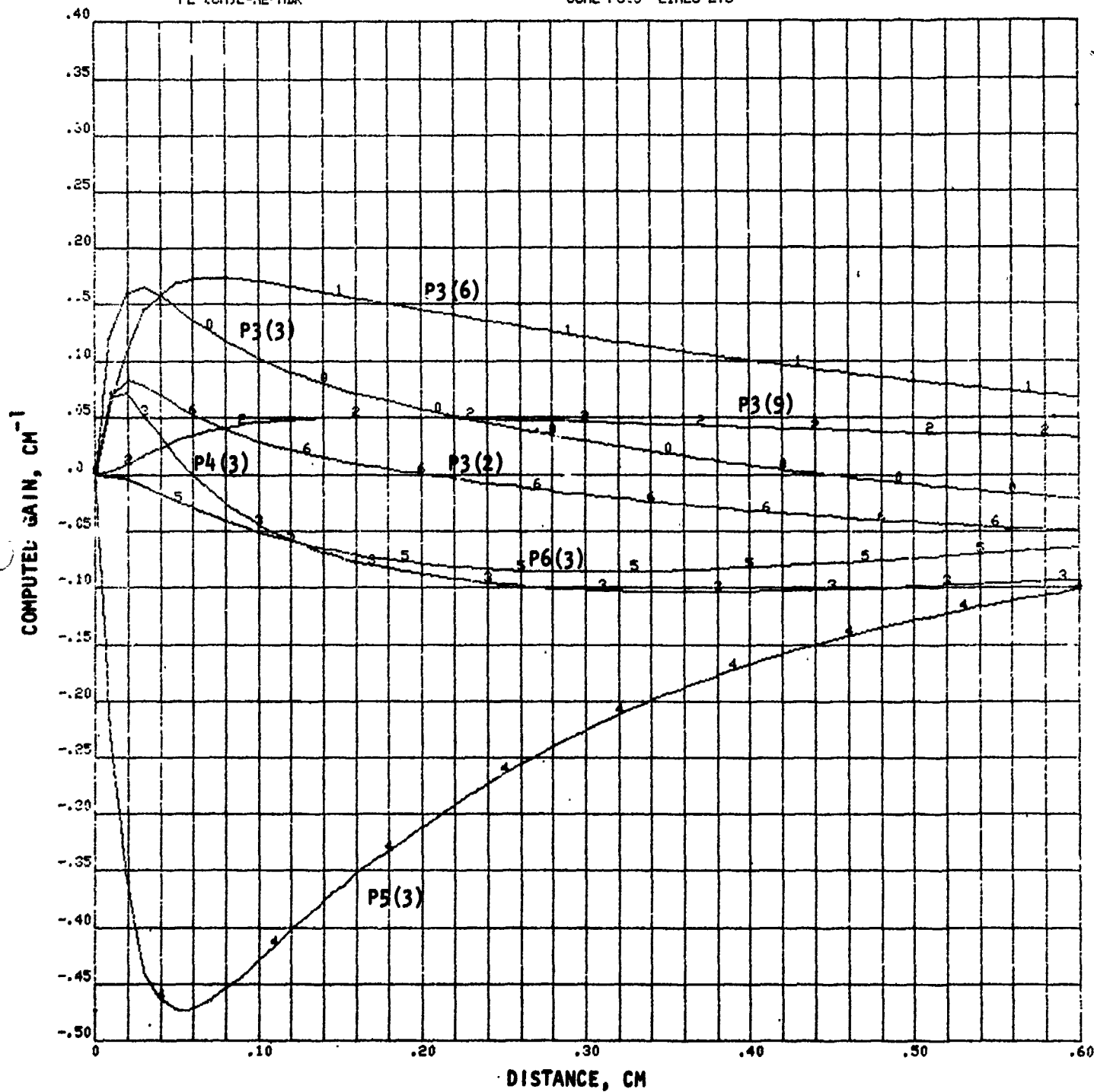


Figure 127. F₂-(CN)₂-He-HBr System, Computed Zero Power Gain on Higher Lines
(F = 10%, 1500 K, Series III)

PHASE II: SMALL SCALE LASER TESTS

INTRODUCTION

The objective of this phase of the program was the direct evaluation of advanced reactants for chemical (HF/DF) lasers utilizing a small-scale CW laser test apparatus. When the program was initiated, chemical laser performance codes were in their infancy and there was a dearth of good kinetic data. Thus, analytic determination of the performance potential, though useful in initial screening of potential advanced reactants, could not be expected to predict performance adequately. Experimental data were clearly required. As the program progressed, analytic performance codes matured and more and better kinetic rate data became available; however, the ability of codes to accurately predict chemical laser performance, *a priori*, is still questionable. The analysis is quite complex, requiring chemical kinetics and fluid mixing at supersonic velocities to be accurately combined. Codes attempting to account directly for all of the phenomena occurring require large amounts of time on digital computers and, therefore, are expensive to run. Even given that the code itself is accurate, large inaccuracies and unknowns still exist in the input data. The evaluation of advanced reactants experimentally is still essential.

In this program, both alternate (to H_2) cavity fuels and (to $F_2/D_2/He$) precombustor fuels were evaluated. The method of cavity fuel evaluation was relatively direct. In the small-scale HF chemical laser, to be described later, alternate cavity fuels were simply substituted for H_2 in the cavity fuel nozzle flow and lasing characteristics determined. It was recognized in the beginning that the performance characteristics would not be directly comparable to H_2 because the cavity fuel nozzle was designed specifically to handle H_2 (low molecular weight) and all other potential cavity fuels would have much greater molecular weight. Thus, mixing characteristics would be expected to be substantially different and data comparing H_2 and alternate cavity fuels would have to be interpreted in this light. However, the intercomparison between alternate cavity fuels is expected to be reasonably reliable because the difference in molecular weight, which is approximately scaled by

the square root, is substantially reduced. The largest variation being $\sqrt{2}$ (HBr to HCl, e.g.) for the alternate cavity fuel as compared to $\sqrt{40}$ (HBr to H_2). Later in the program, tests were run on a second nozzle system which was designed to alleviate (at least in part) the difficulties associated with flowing high molecular weight cavity fuels through the cavity fuel nozzle.

The evaluation of advanced precombustor reactants as initially envisioned was based on a somewhat less direct approach. Thermochemical analysis as described in the previous section predicts the species and concentration of the combustion byproducts that would occur if alternate precombustor reactants were utilized. It was beyond the scope of the program to develop precombustors for several advanced precombustor reactant combinations; therefore, a simulation procedure was planned. In this procedure, the combustor byproducts (CF_4 , N_2 , or SF_6 , e.g.) would be introduced into the baseline $F_2/D_2/He$ combustor by mixing the appropriate concentration of the species into the He diluent prior to the flowing of the diluent into the precombustor. Laser performance would then be monitored using the baseline (H_2) cavity fuel. At that time, rates of HF^* deactivation were not well known so that this approach was designed to provide the most efficient means of evaluating the effect on laser performance (in relation to deactivation effects) of advanced precombustor reactants. As the program progressed and the role of DF as a deactivator became better understood, and as deactivation rates for other species such as CF_4 , SF_6 , and N_2 become available, it became evident that the simulation method as initially planned would not be feasible. The high deactivation rate of DF, compared to CF_4 , SF_6 , N_2 , and other species, coupled with the relatively high concentration of DF produced in the baseline $F_2/D_2/He$ precombustor, would serve to completely mask any deactivation by the "seeded" species so that effects on performance would not be determinable. Furthermore, comparison measurements between power developed by arc-driven (therefore DF-free) and combustion driven chemical lasers in the Mesa program strongly suggested that DF deactivation was playing a large role in performance degradation. Based on the Mesa tests and measured rate of deactivation it was clear that the "game" plan for evaluation of advanced precombustor reactants evaluation based on simulation experiments utilizing the baseline $F_2/D_2/He$ precombustor had to be changed, and it was.

The new plan was keyed to the development of a DF-free precombustor and effort was redirected to do just this. Fluorocarbon fuels were selected in combination with F_2 to develop a precombustor that would generate *no* DF. This effort was successful and is described in this section. Not only did this effort provide the small-scale laser experiments with a DF-free precombustor, it also established the viability of a readily stored, nontoxic, nonflammable precombustor fuel directly, thus satisfying the objectives of the program in part. This new precombustor could then be used in simulation experiments as originally conceived provided that deactivation characteristics of other advanced reactant species such as N_2 and SF_6 had deactivation rates comparable to or greater than CF_4 . Furthermore, this precombustor could then be utilized to evaluate effects of DF via the simulation technique.

During the development of the F_2 /fluorocarbon/He precombustor, an alternate method of introducing the diluent into the precombustor was developed which has much greater versatility. Ordinarily, diluent has been introduced by mixing with the F_2 or the D_2 , or both, prior to injection into the precombustor. In this effort, secondary (staged) diluent injection was developed. This permits less reactive fuels to be utilized and decouples the diluent source from the combustion region, permitting much greater flexibility in operation. Also, during the course of the development of the DF-free precombustor, pure NF_3 became readily available in the modest quantities required for this program, so it became possible to consider the direct use of NF_3 rather than simulating its use. In-house sponsored tests showed that the precombustor hardware that initially utilized F_2/D_2 /He and, then, when modified, F_2/C_xF_y /He, could be used, as modified, with NF_3/D_2 /He and NF_3/C_xF_y /He, thus paving the way to direct evaluation of NF_3 as an oxidizer with both baseline (D_2) and advanced (C_xF_y) fuels. Therefore, near the end of the program, some effort was redirected to the utilization of NF_3 directly.

The final redirection of the effort was prompted by the success in utilizing NF_3 and C_4F_8 in the precombustor hardware. In this effort, several small-scale laser tests were conducted in the investigation of laser performance with the test device utilizing only advanced reactants. For example, the precombustor would be run with NF_3 and C_4F_8 , adding nitrogen rather than He, and HBr would be used as a cavity fuel in place of H_2 . Furthermore, to gain additional data on the high molecular

weight cavity fuel a new nozzle system was employed in which the cavity fuel nozzle was modified to permit greater flow with contours designed on the basis of the molecular weight and gamma of HBr. These tests yielded many interesting results and generated at least as many interesting questions.

The structuring of this part of the report, Phase II, is somewhat complex because of the evolutionary character of the program as it was executed. First, the experimental apparatus, facility, and diagnostics used for the small-scale laser tests will be described. Following this, the effort in evaluating advanced cavity fuels utilizing the $F_2/D_2/He$ baseline precombustor will be described. Then, the effort in evaluating advanced precombustor fuels will be described. Included in this discussion is the development of the DF-free precombustor and the facility and apparatus used in this development effort. Finally, the most recent tests, designed to investigate laser performance using advanced reactants entirely is discussed. This is followed with a summary of results and conclusions for the work carried out in this phase of the program.

EXPERIMENTAL APPARATUS

The small-scale CW HF chemical laser utilized in this program was constructed and checked out on Rocketdyne-sponsored funds and operated in the CWLL (Continuous Wave Laser Laboratory) located at Rocketdyne's Santa Susana Field Laboratory. This facility, the baseline test hardware, and diagnostics utilized in this program are described below. Some changes in the baseline configuration were made in connection with certain test series. These changes are described in the test series discussion.

Facility

The CWLL facility was set up explicitly for the operation and testing of small CW chemical lasers. It consists principally of a pumping station, a gas control system, an operations and instrumentation console, and a vibration isolation optical table which encloses all but one side of the test station. Figure 128 shows a schematic of the facility.

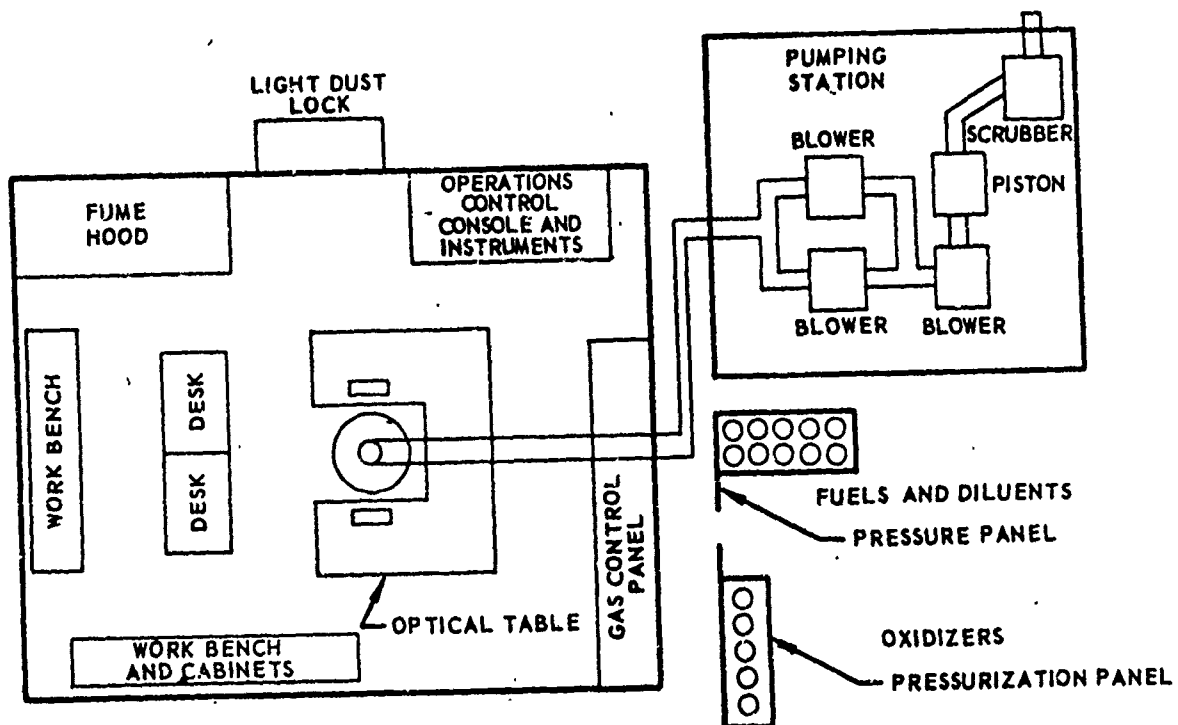


Figure 128. CWLL Schematic

The pumping system includes three rotary, positive-displacement pumps with inter-stage heat exchangers, and a piston-type backing pump. The exhaust of the pumping system is passed through a scrubber. There is another heat exchanger located between the test station and the pumping system.

Reactant and diluent gases are supplied from "K" bottles located outside the laboratory. These gases are fed to the laboratory at reduced pressure from exterior pressurization panels. The exterior pressure panel for F_2 also includes a remote readout flowmeter and a remote control pressure regulator. The other gases are pressure controlled and metered at the interior gas control panel. Feed lines then run through a ramp from the bottom of the gas control panel to the bottom of the test station. The test station, the gas control panel, and the ramp are fully enclosed and positively exhausted to the exterior of the laboratory. The gas delivery system is shown schematically in Figure 129.

Gases are turned on (and off) in selected sequence by electrically initiated pneumatic valves either automatically or manually at the operations console. This console also contains instrumentation for monitoring the operating parameters of the test device, such as precombustor pressure, cavity pressure, and pertinent temperatures, as well as the F_2 flow.

The test station is surrounded on three sides by a Lansing gas cushion vibration isolation table that supports the optical resonator for the CW HF laser and optical diagnostic equipment.

A photograph of the exterior of the facility is shown in Fig. 130. A photograph of the interior, before the test hardware has been mounted, is shown in Fig. 131.

CW HF Chemical Laser

The laser device used in this program consists of a precombustor for producing F atoms, a supersonic nozzle array for injecting the precombustor effluent into an optical cavity, a supersonic nozzle array for introducing the cavity fuel (H_2 for the baseline case) into the optical cavity, an optical resonator, and a means of outcoupling some of the optical flux from the resonator.

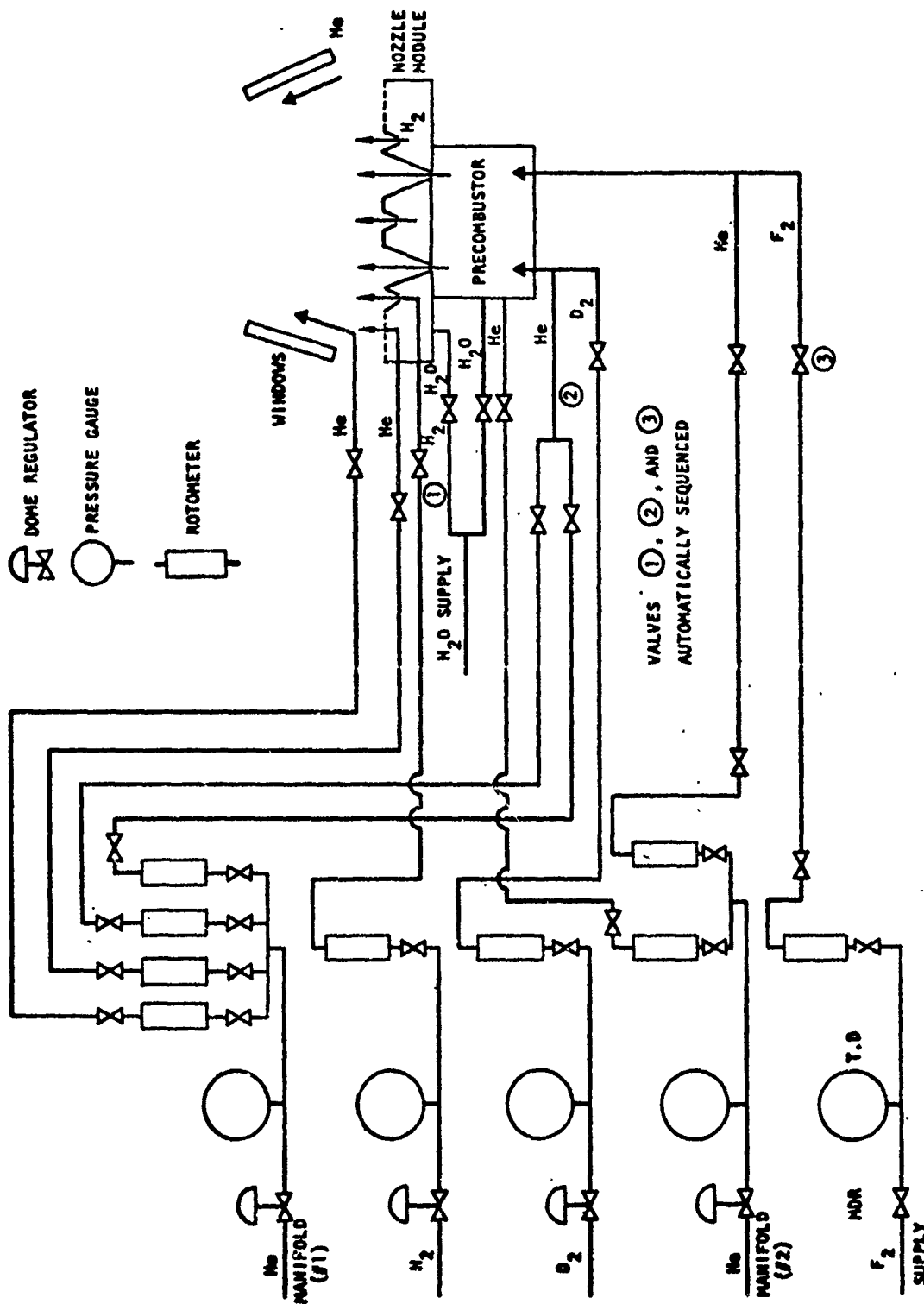
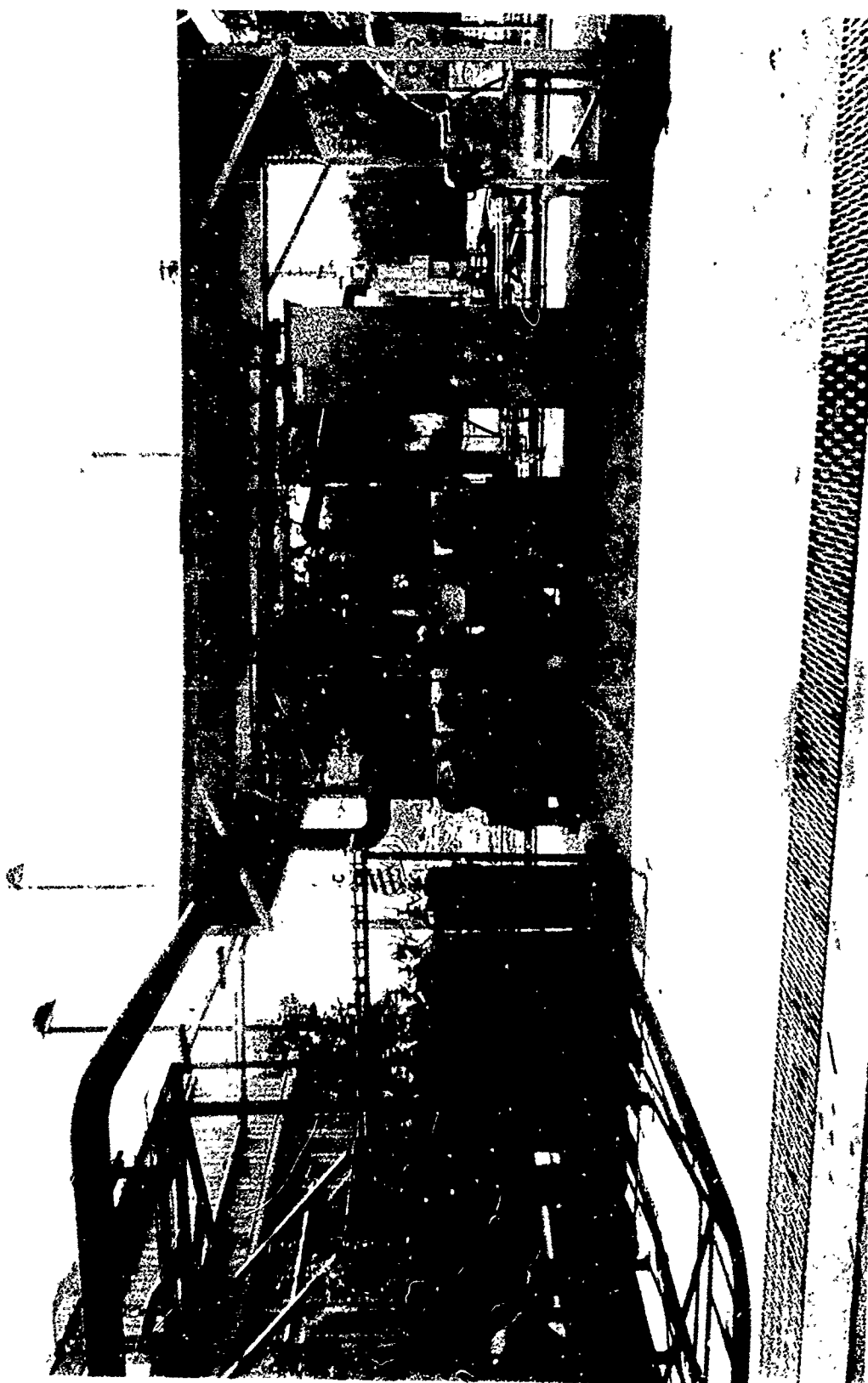
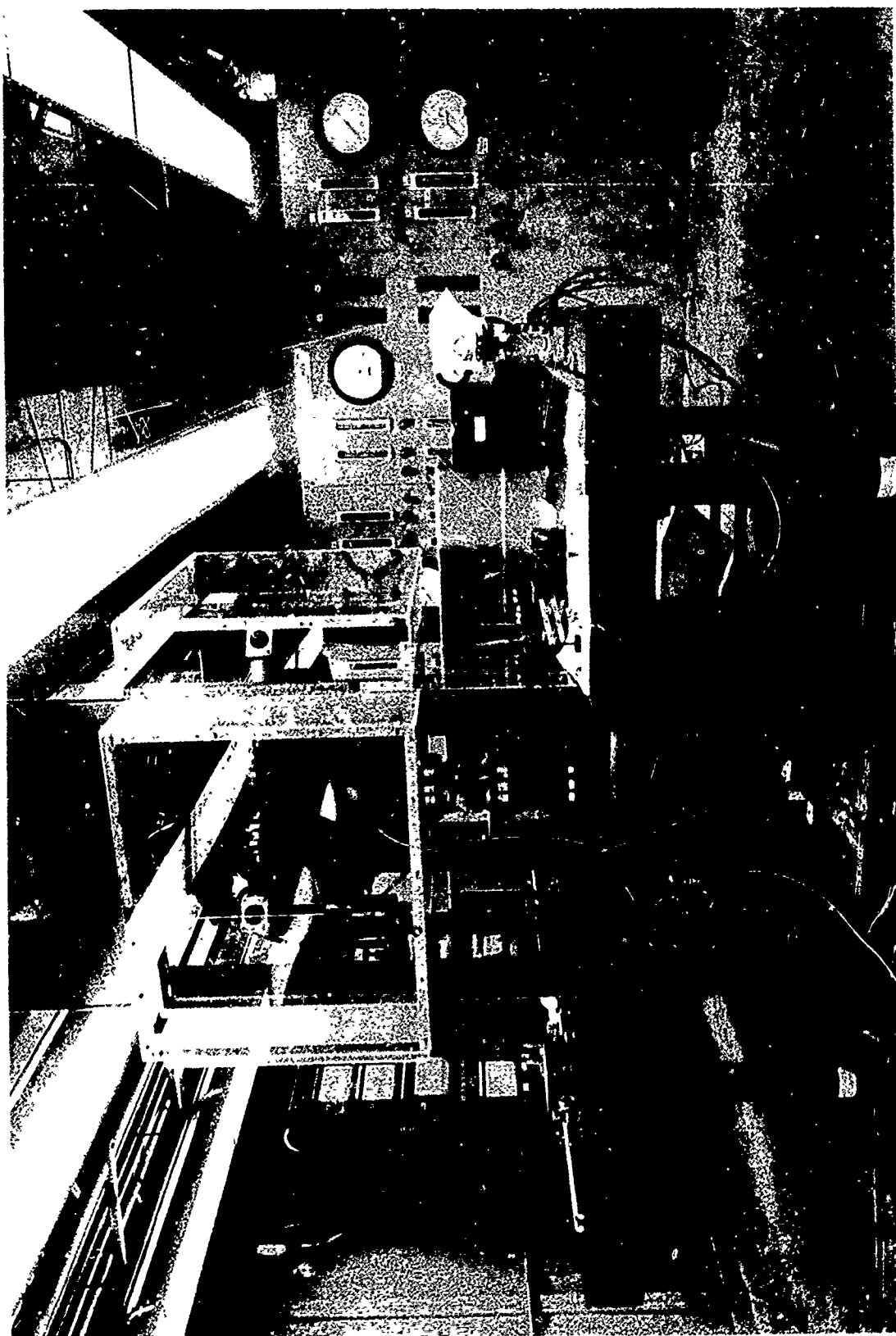


Fig. 129. Gas Delivery System



5AJ33-9/12/72-S1A*

Figure 130. CWLL Exterior



5AJ33-9/12/72-SIH*

Figure 131. CWLL Interior

Precombustor.

Conditions. A detailed design analysis was conducted for the subscale F_2/D_2 chemical laser combustor. The nominal design specifications on which the design analysis was based are as follows:

Chamber Pressure, psia	31.76
F_2 Flowrate, gm/sec	0.953
D_2 Flowrate, gm/sec	0.070
He Flowrate, gm/sec	0.783
Nozzle Inlet Temperature, K	1800

Combustion Chamber. The basic internal chamber geometry was defined as a rectangular volume approximately 2.5 inches long having a flow cross section measuring approximately 0.5 by 1 inch. A minimum chamber length was desired to reduce the amount of heat transferred to the chamber. As a first approximation, the Dittus-Boelter expression for the heat-transfer coefficient was used to compute the nominal hot-side heat transfer coefficient. This value, based on the given geometry and on the known equilibrium properties at nominal design conditions, was further modified to reflect actual heat transfer characteristics determined empirically for similar chamber configurations and operating characteristics.

At the outset of the analysis, it was assumed that high-purity nickel would be used for the chamber. Nickel 200 was selected in preference to other materials because of its proved compatibility in a high-temperature fluorine environment. Its conductivity and reasonable maximum working temperature were considered assets in comparison with other candidate materials. Conceptually, the chamber jacket was assumed to feature small rectangular channels in essentially a monolithic material.

Precombustor.

Conditions. A detailed design analysis was conducted for the subscale F_2/D_2 chemical laser combustor. The nominal design specifications on which the design analysis was based are as follows:

Chamber Pressure, psia	31.76
F_2 Flowrate, gm/sec	0.953
D_2 Flowrate, gm/sec	0.070
He Flowrate, gm/sec	0.783
Nozzle Inlet Temperature, K	1800

Combustion Chamber. The basic internal chamber geometry was defined as a rectangular volume approximately 2.5 inches long having a flow cross section measuring approximately 0.5 by 1 inch. A minimum chamber length was desired to reduce the amount of heat transferred to the chamber. As a first approximation, the Dittus-Boelter expression for the heat-transfer coefficient was used to compute the nominal hot-side heat transfer coefficient. This value, based on the given geometry and on the known equilibrium properties at nominal design conditions, was further modified to reflect actual heat transfer characteristics determined empirically for similar chamber configurations and operating characteristics.

At the outset of the analysis, it was assumed that high-purity nickel would be used for the chamber. Nickel 200 was selected in preference to other materials because of its proved compatibility in a high-temperature fluorine environment. Its conductivity and reasonable maximum working temperature were considered assets in comparison with other candidate materials. Conceptually, the chamber jacket was assumed to feature small rectangular channels in essentially a monolithic material.

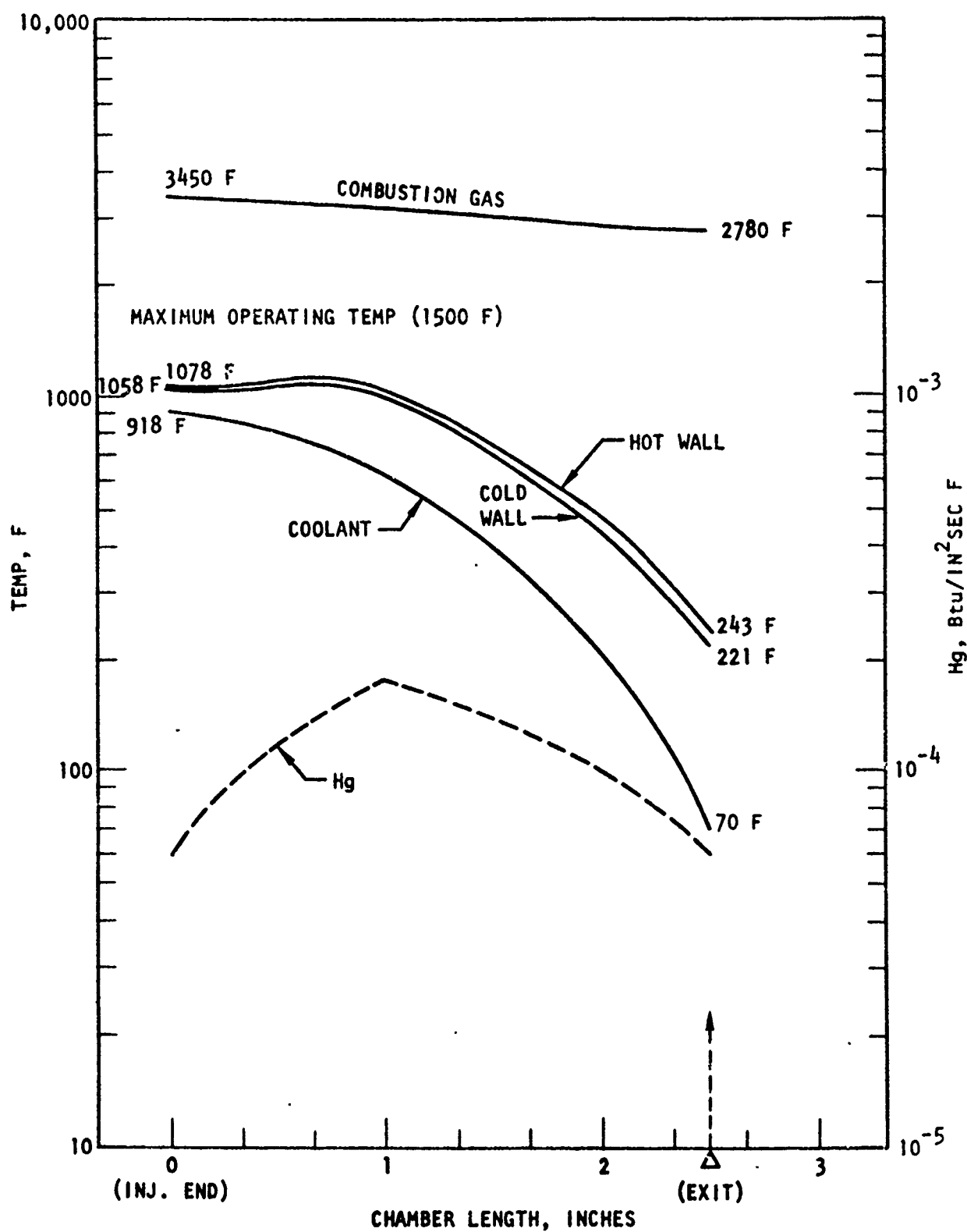


Figure 132. Computed Thermal Characteristics for Subscale F_2/D_2 Chemical Laser Combustor

Self-Cooled Concentric Orifice Injectors. A review of several potential injector design concepts indicated that a concentric element type would be best suited for the relatively small chamber size. Other elements that could possibly provide higher mixing efficiency and performance were generally considered unfavorable because of the confined geometry of the chamber. Impinging types were rejected because of potential misimpingement and maldistribution problems that could seriously jeopardize the structural integrity of the combustion chamber.

From a performance standpoint, selection of a concentric-element design was based primarily on recent results derived from the Space Shuttle APS program. Extensive cold-flow and hot-fire experimental studies were conducted to define the performance characteristics of the concentric-orifice injector. Mixing characteristics were determined from cold-flow studies using simulant inert gases for fuel and oxidizer. A typical curve developed from that study is shown in Fig. 133, wherein mixing efficiency (E_m) is shown as a function of sampling distance. The indicated mixing efficiency of 97 percent at 2 inches would suggest that, with an additional 0.5 inch of chamber length, high-performance precombustor operation would be assumed. It should be noted here that E_m is a nonreactive mixing index and is not necessarily indicative of predicted combustion efficiency with F_2 and D_2 .

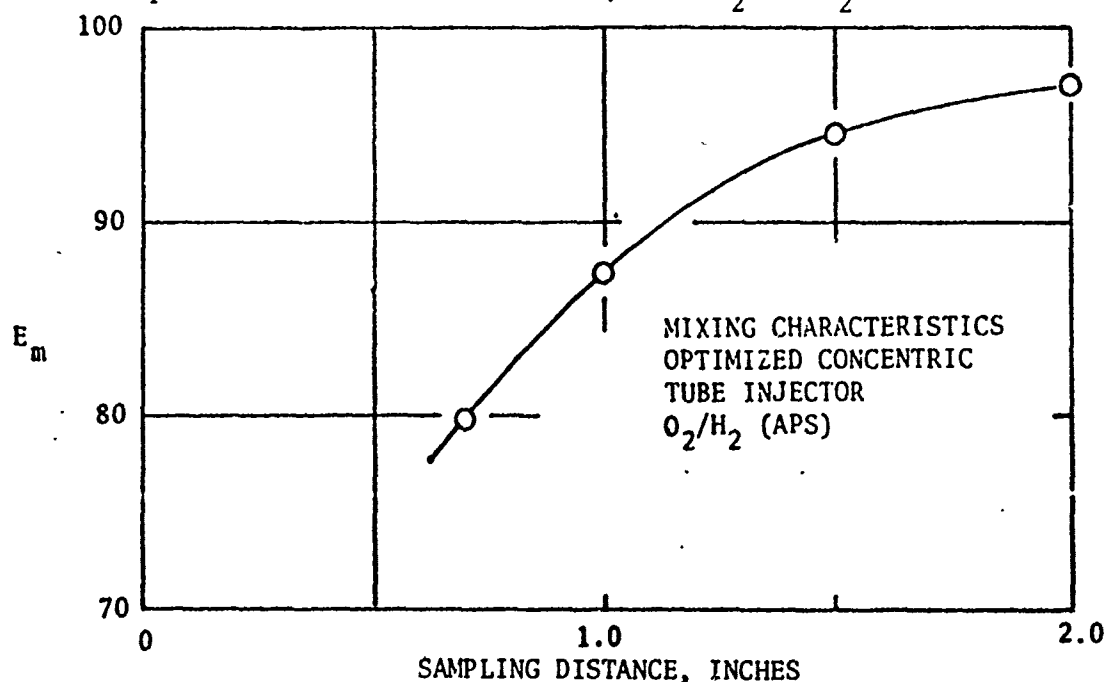


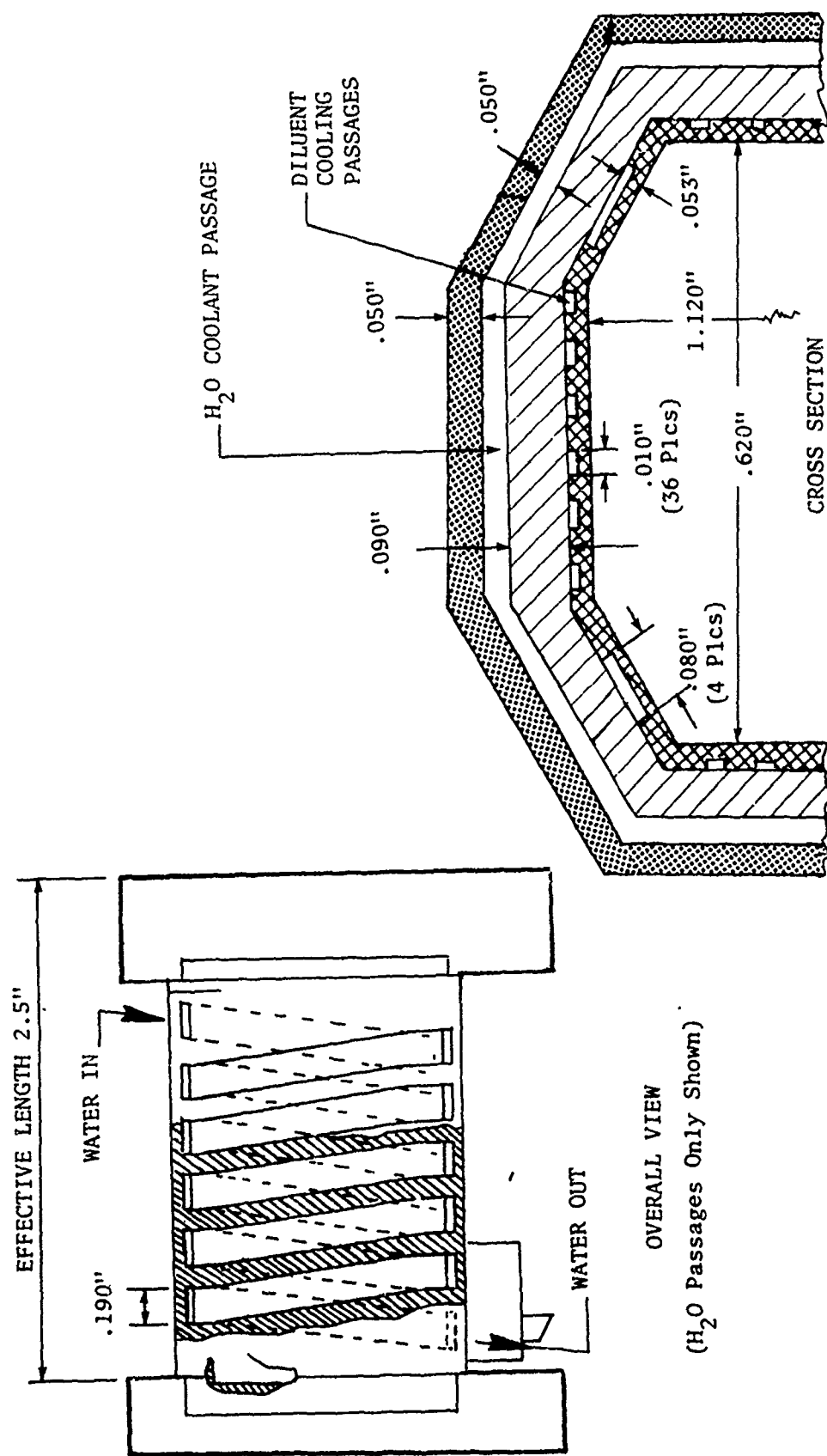
Figure 133. Inert Mixing Characteristics of Concentric Element Injector

Combustion Chamber Fabrication. The precombustor is a welded assembly composed of three principal parts, i.e., the body, the forward manifold assembly, and the rear manifold assembly. The body is initially fabricated from a rectangular block, and the rectangular chamber cavity is electrical-discharge machined (EDM) providing the basic wall thickness of 0.040 inch. The chamber wall design features two integral cooling circuits, as shown in Fig. 134, contained within a monolithic structure of nickel that is electroformed (ELF) on the basic 0.040-inch-thick wall by an electrodeposition process. The forward face of the chamber has two orifices that receive the mating injector posts of the injector assembly (to be discussed later) and form the outer annular wall for this concentric-element-type injector.

The rear manifold assembly is made of machined nickel plate and contains the four-bolt-hole flange for attachment with the nozzle block assembly. It also provides the inlet coolant line and manifold for the inner helium circuit as well as the chamber pressure tap line. The aft face incorporates a metallic O-ring for sealing combustion gases at the interface with the nozzle block assembly. Both the forward and aft manifold flanges are contour milled to minimize the heat sink mass and limit transient heating losses.

During and after the precombustor assembly buildup, leak and flow checks of internal passages were taken to ensure structural weld integrity and nonblockage in the flow passages.

Injector Fabrication. The injector assembly essentially comprises a body, a cover, a deuterium inlet line, and a fluorine inlet line. The body, which is the principal structure member, is constructed of stainless steel because of its lower conductivity and good fluorine compatibility at lower temperatures. It contains a flange for attachment with the precombustor that has been contour milled to reduce heat sink mass. The body also contains the two injector posts that are separate nickel rods accurately positioned to ensure concentric gapping with the combustor orifice holes. The injector posts are EB welded to the body, and their inside and outside diameters are made by EDM after welding to guarantee straightness and concentricity. Two thermocouple fittings are EB welded to the body to monitor



OVERALL VIEW
(H₂O Passages Only Shown)

Figure 134. Regenerative/Dump-Cooled CWLL Combustor

combustor wall temperature and inlet gas temperature. Fluorine is fed through an offset tube that opens to a manifold cavity between the body and cover and enters the inner bore of each injector post. EB welding is used to join the cover, body, and propellant lines. Special manufacturing procedures were maintained for removal of burrs and crevices that are catalytic to fluorine attack, and all internal corners in contact with fluorine were rounded off. In addition, all welded joint surfaces were specially prepared to ensure "through welds" by EB welding so that no back-side crevices would be in contact with fluorine. These preparations are necessary to deter fluorine attack and prolong the life of the hardware. The concentric injector element (there are two elements in the combustor) is shown schematically in Fig. 135.

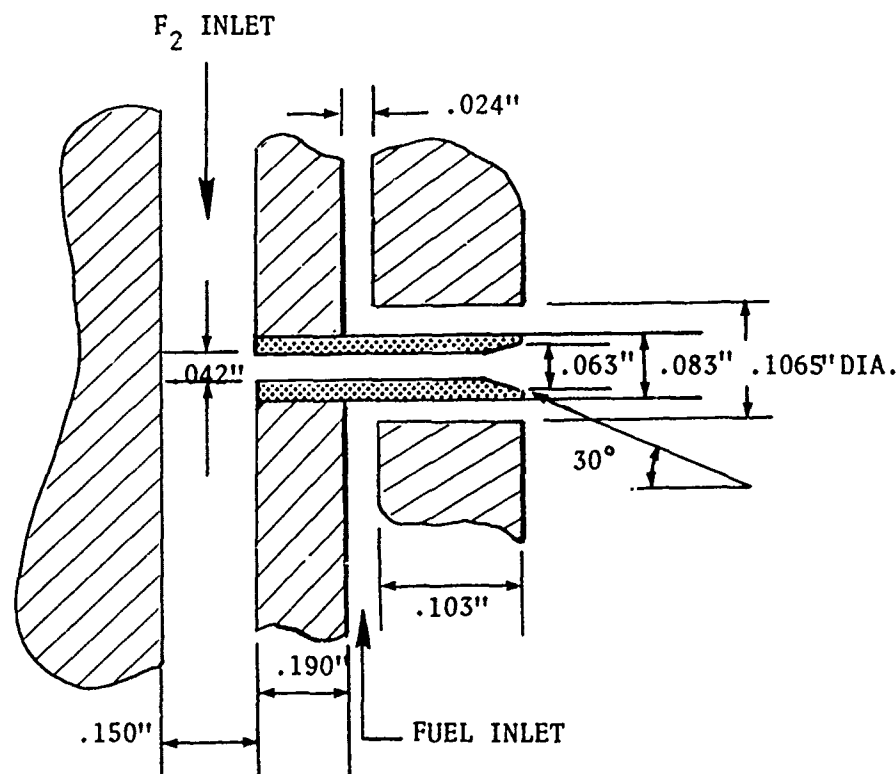


Figure 135. Concentric Injector Element

Precombustor Assembly. Photographs of the precombustor prior to assembly are shown in Fig. 136 and as assembled in Fig. 137. This assembly mates with the nozzle array discussed below. All tests with the precombustor in this program utilized the water-cooled, dumped diluent mode of cooling. .

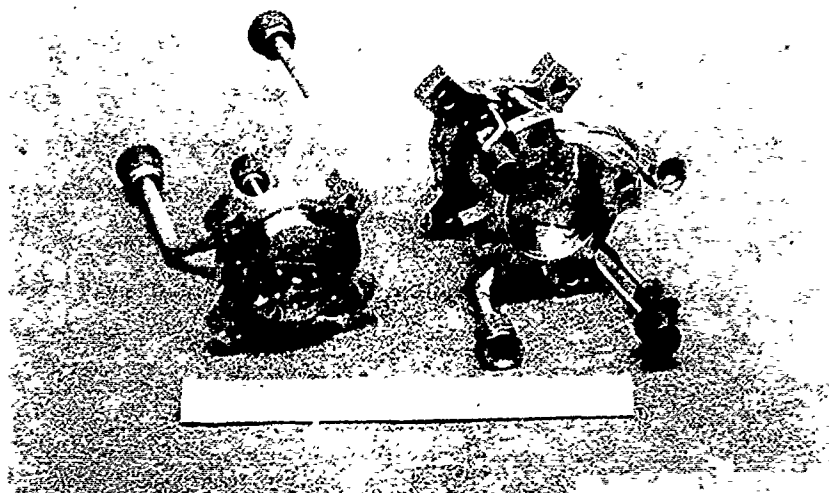


Figure 136. Precombustor, Prior to Assembly

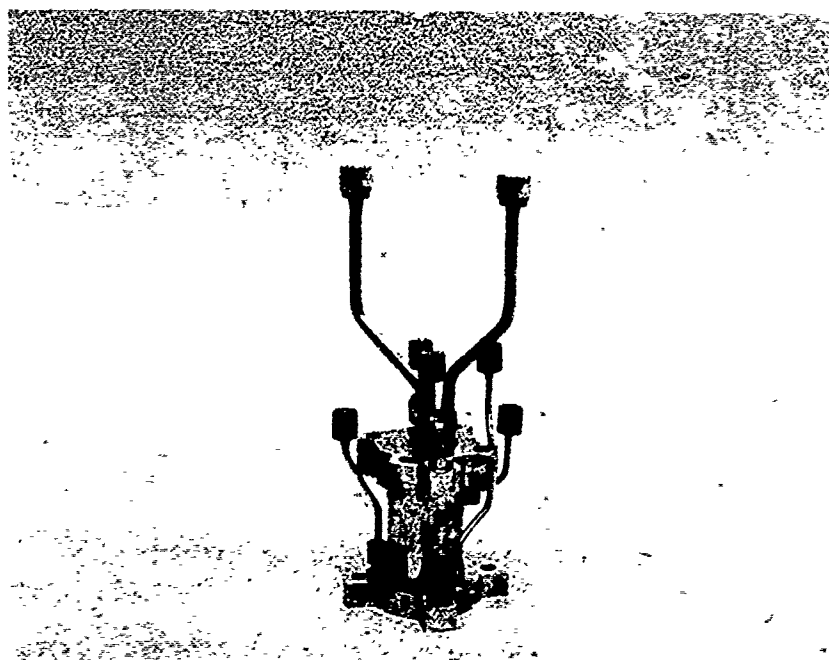


Figure 137. Precombustor Assembled

Baseline Combustor Checkout Experiments ($H_2/F_2/He$). Following fabrication and assembly of the fully cooled laser combustor components, a series of four tests was conducted to make preliminary assessment of performance, heat transfer, and operational characteristics for evaluation preparatory to any programmed use. Conventional strain gage pressure transducers and thermocouples were used for primary measurement. Gas flows were metered through sonic venturis while coolant water flowrates were measured with conventional turbine-type meters. Differential water temperature measurements were accomplished with four-junction iron/constantan thermopiles.

Reduced experimental parameters for these tests are listed in Table XXIII. The basic approach to the design of these tests was to primarily assess combustor operation at gradually increasing combustion temperatures approaching the nominal design conditions of 1800 K nozzle end stagnation temperature. The mass ratio of fluorine to hydrogen (F_2/H_2) was maintained at a nominally constant proportion for these tests, while increases in combustion temperature were accomplished through incremental reduction of helium diluent flowrate. The observed performance characteristics for these experiments are summarized by the calculated c^* efficiencies, which were based on directly measured chamber pressure and propellant flowrates. A nominal uncorrected c^* efficiency of 80 percent was observed for all of the experiments and the corrected combustion efficiency for heat loss was 93 to 102 percent.

Heat transfer measurements for the four tests indicated effective temperature decrements of 22, 33, 36, and 36 percent, respectively. These heat loss measurements indicate effective heat balance for the last three tests, conducted at somewhat lower temperatures, while a lower indicated heat loss is apparent for the first test.

Analysis of the data shows close correspondence to anticipated operational behavior. Indicated heat losses appear quite compatible with each test condition. A nominally constant c^* efficiency would be expected since it should primarily reflect the quality of the injector design itself and not the thermal characteristics.

TABLE XXIII. $H_2/F_2/He$ SUMMARY SHEET

Parameters	Test No.			
	A	B	C	D
$\dot{w}_{FL} \times 10^{-3}$, lb/sec	1.47	1.91	2.24	2.31
$\dot{w}_{H_2} \times 10^{-3}$, lb/sec	0.056	0.076	0.093	0.099
$\dot{w}_{He} \times 10^{-3}$, lb/sec	3.00	2.36	1.74	1.62
Mixture Ratio	26.8	26.2	24.1	23.3
$\dot{w}_{tot} \times 10^{-3}$, lb/sec	4.51	4.35	4.07	4.03
He, percent	66.0	54.3	42.7	40.2
P_c , psia	28.8	29.8	29.7	30.8
c^*_{act} , ft/sec	4888	5295	5031	5903
c^*_{theo} , ft/sec	6080	6640	7080	7430
η_{c^*} uncorr, percent	80.4	79.7	79.5	79.4
① η_{c^*} corr, percent	92.9	98.9	99.8	101.6
T_o^F , K	890	1050	1336	1463
Q_c , cal/sec	297	768	937	983
Q_N , cal/sec	189	252	302	335
Q_T , cal/sec	486	1020	1239	1318
β_c	64.4	46.9	33.4	34.4
MW, gm/mole	5.55	6.32	7.37	5.48
γ	1.63	1.61	1.53	1.57
C_p , Btu/gm-mole	5.16	5.24	5.41	5.49
α	0.21	0.76	0.99	1.00
F_2 avail, gm/sec	0.20	0.22	0.22	0.20

① Corrected for full shifting composition

Nozzle Arrays. There were two nozzle arrays utilized in this program, with the bulk of the effort completed with the nozzle designated as the Baseline 30-1X configuration. At the very end of the program, some tests were run with a nozzle array designed to obtain higher cavity fuel flow for high molecular weight cavity fuels.

Baseline 30-1X Configuration. The Baseline 30-1X configuration, shown schematically in Fig. 138, was based on a two-dimensional analog to an existing Mesa I nozzle (Ref. 46). The array was designed to be 0.4 by 1 inch having the operating parameters defined in Table XXIV. (Refer to Fig. 139 and the Nomenclature for definition of terms.)

The nozzles were designed to produce parallel, uniform exit flow and were truncated to approximately two-thirds full length to reduce the boundary layer thickness at the nozzle exit. The final contour was the inviscid core boundary moved out by the boundary layer displacement thickness. The boundary layer thickness is proportional to the square root of the throat gap; therefore, iteration between the boundary layer program and a program that sized the nozzles in accordance with the selected design parameters was required until the throat gap used in the boundary layer program was equal to the throat gap from the nozzle sizing program. The modules were designed to include relief on the side (noncontoured) walls for the side-wall boundary layer growth. Individual nozzle contours for the multiple injector/nozzle arrays were designed using the method described in Ref. 46. The combustor temperature, core area ratios, cavity pressure, partial pressure of HF, and injector height and width were selected to obtain a high-performance chemical laser based on available test results at the time the selection was made.

The F_2 (F, DF, He, F_2 mixture) nozzles (two) and the H_2 (cavity fuel) nozzles (three) are both 1-inch long. The F_2 nozzle expansion contours were optimized for expansion from a precombustor chamber pressure of 30 psia to a laser cavity pressure of 7.6 torr. For the H_2 nozzles, the contours are designed to expand to 7.6 torr from a plenum pressure of 5 psia. The throat and exit dimensions

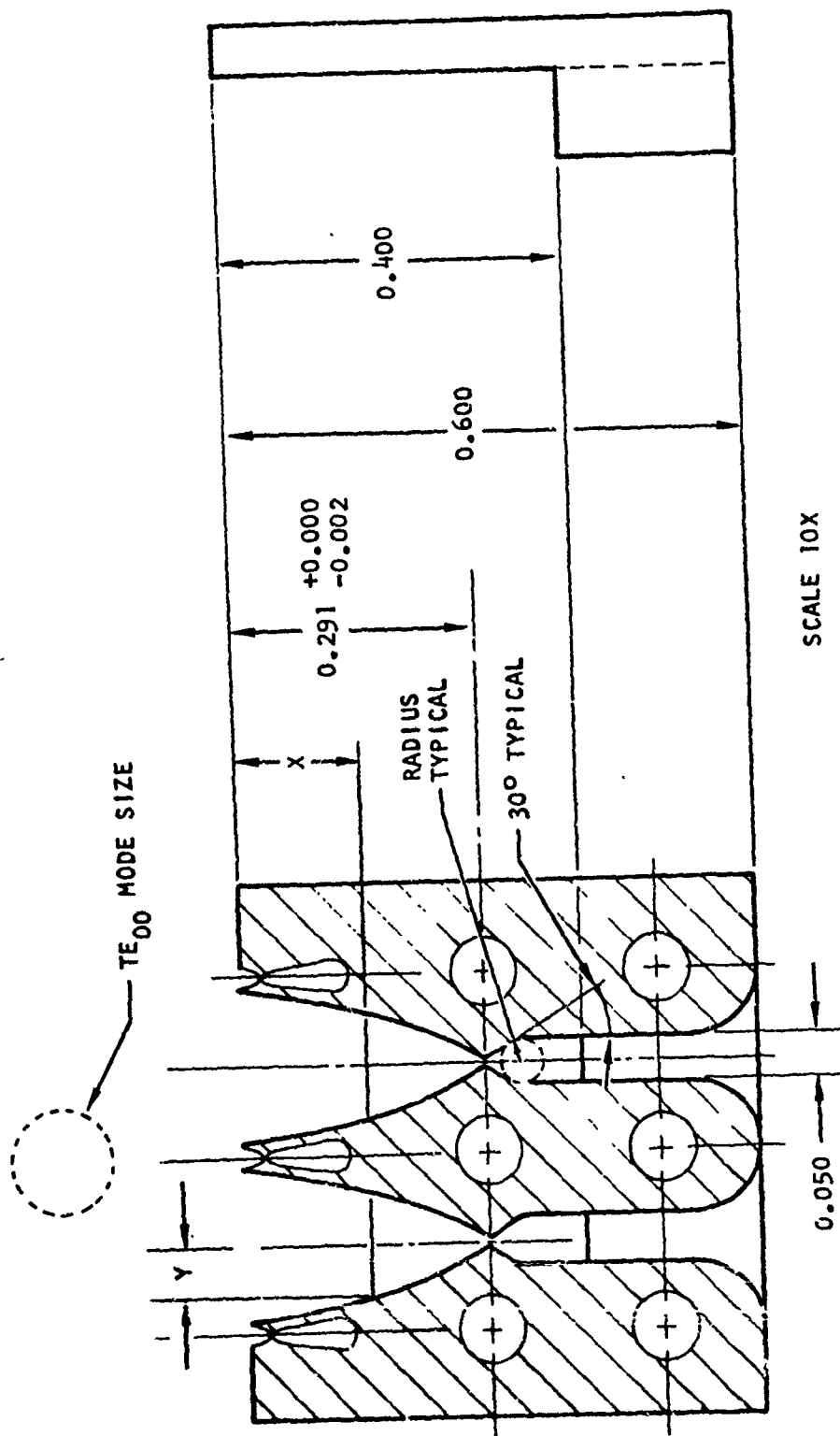


Figure 138. Cross Section of Small, Continuous-Wave Laser Nozzle System

TABLE XXIV. BASELINE 30-1X NOZZLE ARRAY

Parameter	Design Conditions	Fluorine Nozzle	Hydrogen Nozzle
R_L	8.0		
ψ_L	30		
P_{HF}/P_L	0.05		
R_ψ	1.0		
ψ_c	30		
R_c	1.442		
α	1.0		
γ_{NS} , cm	0.0025		
g , cm		0.0305	0.0112
γ_E , cm		0.2197	0.0315
N		2	3
P_o , psia		31.76	4.99
T_o , K		1800	298
MW, gm/mole		7.34	2.0
γ		1.573	1.406
M_e		4.61	2.95
a_e , cm/sec		67,000	79,080
P_L , torr		7.6	7.6
\dot{w}_{D_2} , gm/sec		0.061	
\dot{w}_{F_2} , gm/sec		0.833	
\dot{w}_{He} , gm/sec		0.685	
\dot{w}_{H_2} , gm/sec			0.151

NOTE: See Nomenclature and Fig. 139 for definition of terms.

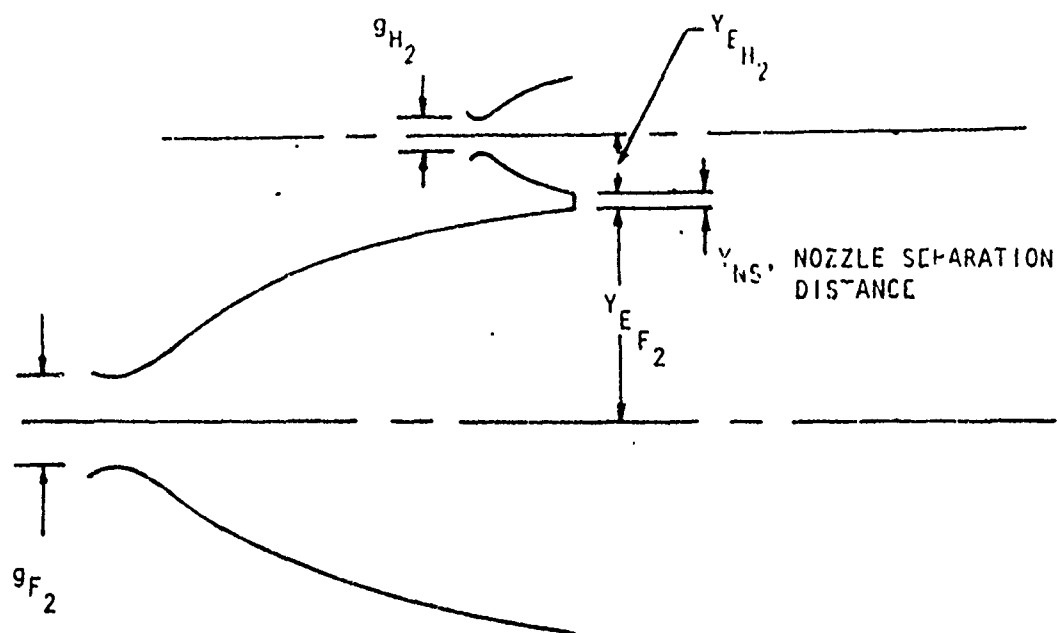


Figure 139. Definition of Symbols

of 0.012 and 0.173 inch, and 0.0044 and 0.0248 inch for the F_2 and H_2 nozzles, respectively, gave respective geometric area ratios of 14.4 and 5.6. Accounting for boundary layers, the respective aerodynamic area ratios are 10 and 4.

The nozzles are fabricated from nickel and assembled with electroformed nickel. Water-cooling channels are provided in the nozzle assembly.

The axis of the laser optics (see later discussion) is parallel to the long dimension of the nozzle, thus providing about a 2.5-cm gain path. Figure 138' shows the approximate low order mode to scale. This nozzle configuration, three H_2 nozzles and two " F_2 " nozzles, was selected because there is symmetry in the flow-field when the laser axis is located directly downstream of the center H_2 nozzle.

A photograph of the assembled precombustor and nozzle is shown in Fig. 142. The Regimesh structure that surrounds the nozzle array is used to introduce a He "base bleed" to minimize recirculation and to reduce end effects.

The entire structure is mounted to a bulkhead which is bolted to the final bottom flange of the "downcomer" at the test station (Fig. 131). This assembly puts the nozzle exit plane just in view of the windows of the optical cavity.

High Molecular Weight Nozzle Array. A high molecular weight cavity fuel and combustor nozzle were selected from several that were considered. The fuel nozzle was designed to flow HBr and the combustor nozzle the products of combustion of D_2 , F_2 , and He. This pair was designed to yield a small distance between the centerlines of the two nozzles, as shown in Fig. 140 to the same scale as the Baseline 30-1X configuration. Nozzle operating conditions are presented in Table XXV. Geometric walls and core geometries are described in Fig. 141. The cavity fuel (HBr) and combustor (F_2) nozzle geometric throat gaps were 0.0103 and 0.0062 inch, respectively, and the core area ratios were 4 and 9.9, respectively. This relatively large throat of the HBr nozzle was required to pass the necessary molar flowrate of this high molecular weight (81) gas. The F_2 nozzle was one-half

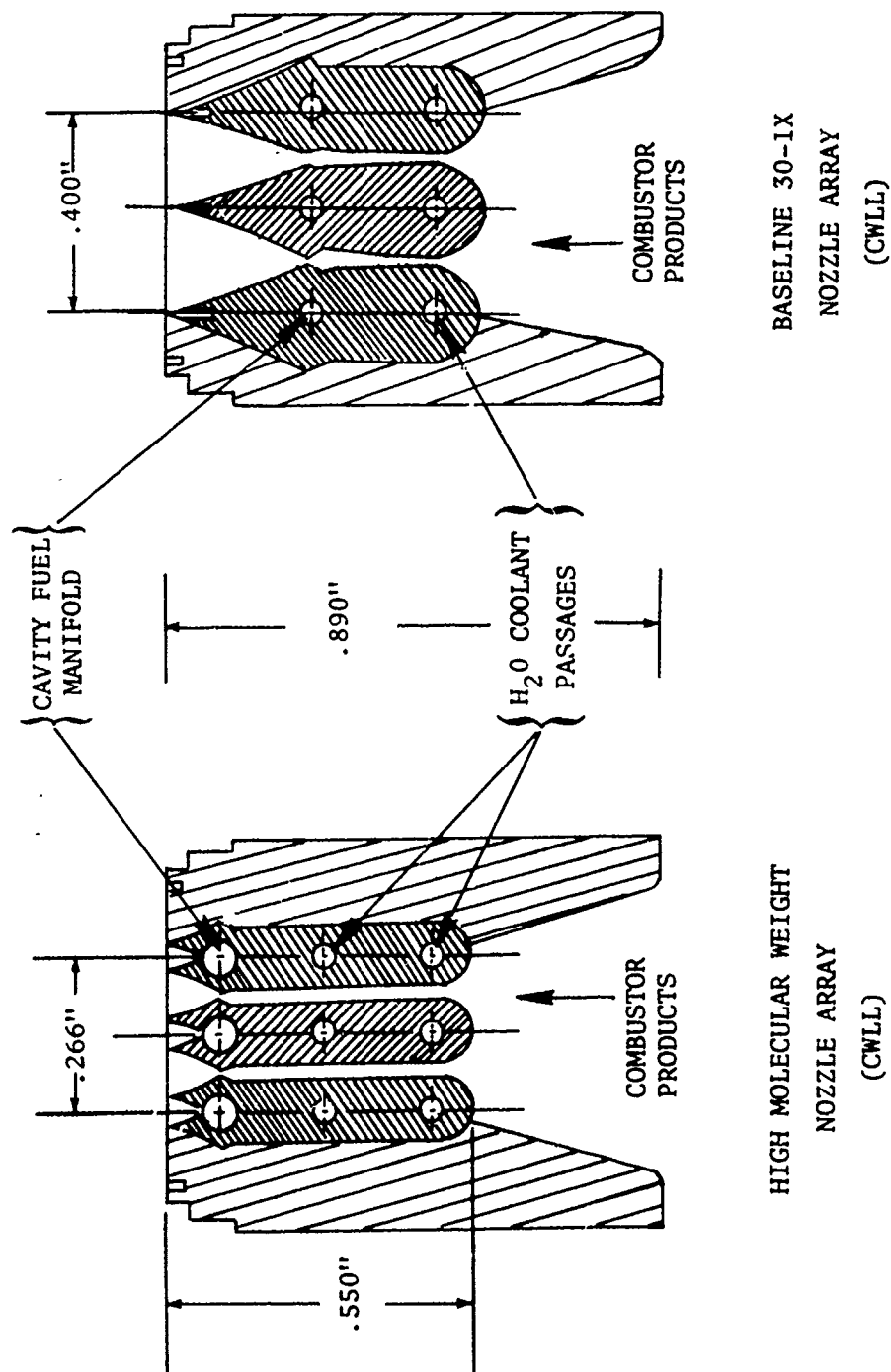
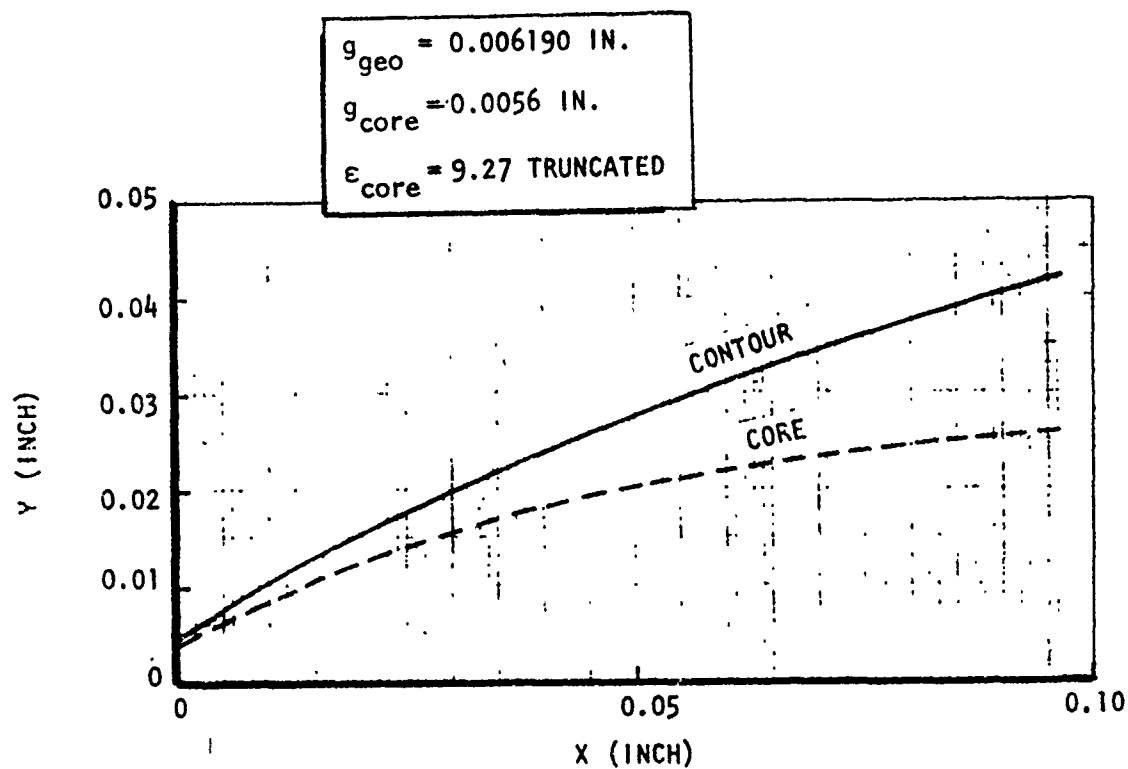
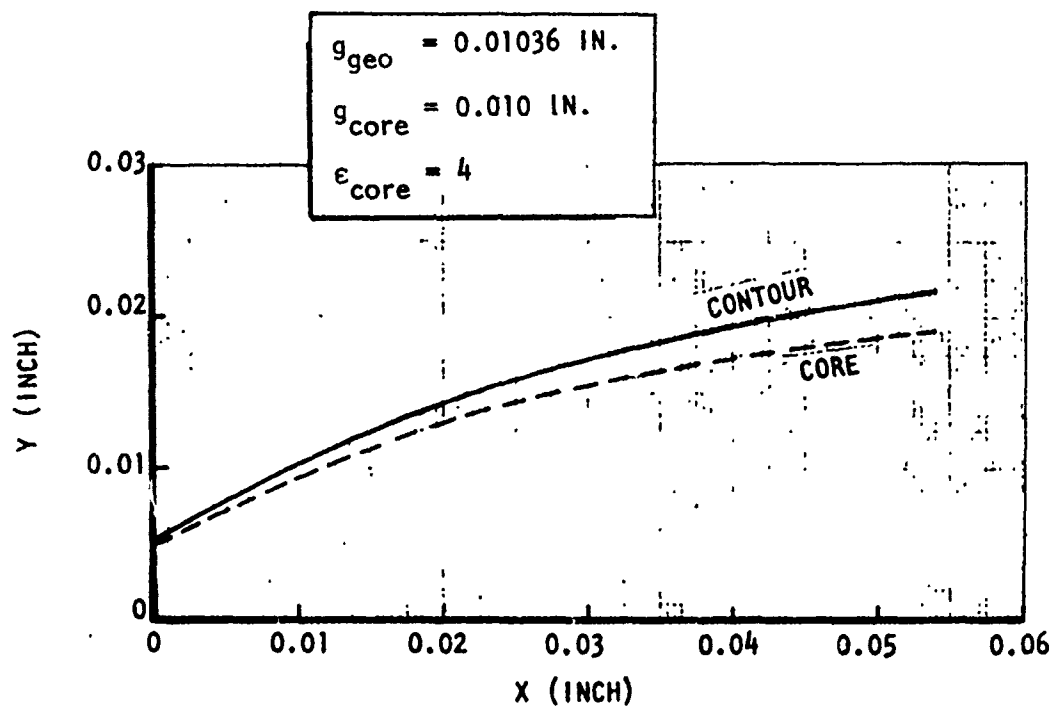


Figure 140. CWLL H₂O Cooled Nozzle Arrays



F₂ NOZZLE



CAVITY FUEL NOZZLE

Figure 141. High Molecular Weight Nozzle

TABLE XXV. OPERATING CONDITIONS OF HBr - F₂ NOZZLE PAIR

	HBr	F ₂
Chamber Pressure, P _c , psia	5	32
Chamber Temperature, T _c , (R)	537	3240
Specific Heat Ratio, γ	1.39	1.573
Molecular Weight, MW	80.9	7.34
Mass Flow		
\dot{m}_{HBr} , g/sec (three nozzles)	2.61	--
\dot{m}_{D_2} , g/sec	--	0.030
\dot{m}_{F_2} , g/sec	--	0.417
\dot{m}_{He} , g/sec	--	0.316

the size of the Baseline 30-1X nozzle. The HBr nozzle is seen to be approximately one-half the size of the F₂ nozzle. The lip thickness between the nozzles was set to be 0.003 inch, which is generally considered a practical minimum. Centerline to centerline distance of the nozzle pair is seen to be 0.0665 inch.

Optical Cavity. In this discussion, the phrase "optical cavity" refers to the evacuated enclosure that houses the laser hardware just downstream of the nozzles. It has an inside diameter of about 4 inches, just sufficient to accept the nozzle array assembly shown in Fig. 142. This enclosure contains four optical windows that are used to view the active medium. The laser optical configuration used on the device is such that the optical resonator is external to the optical cavity so the two windows that are within the optical resonator have a fine optical polish. The optical cavity permits viewing from just upstream of the nozzle exit plane to up to 5 inches downstream from the nozzle exit plane.

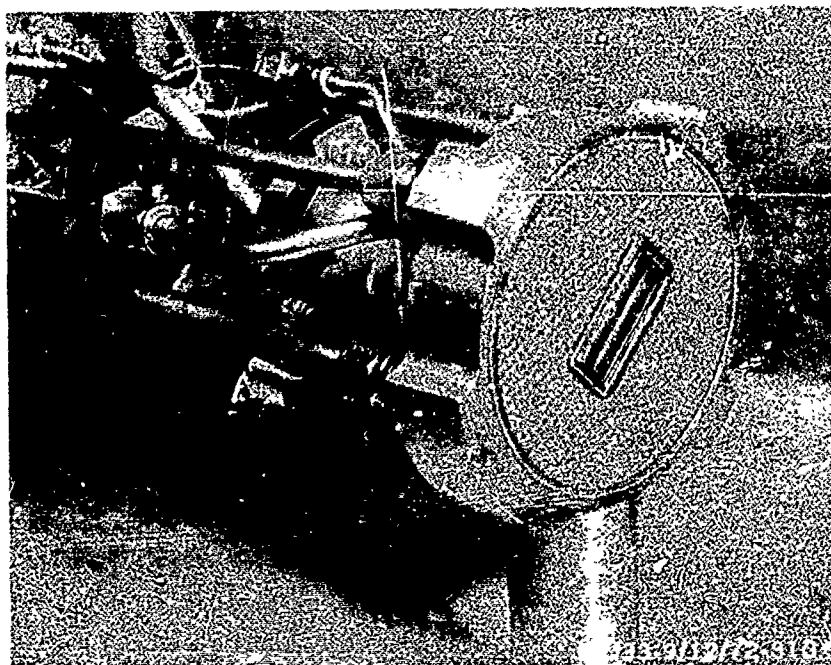
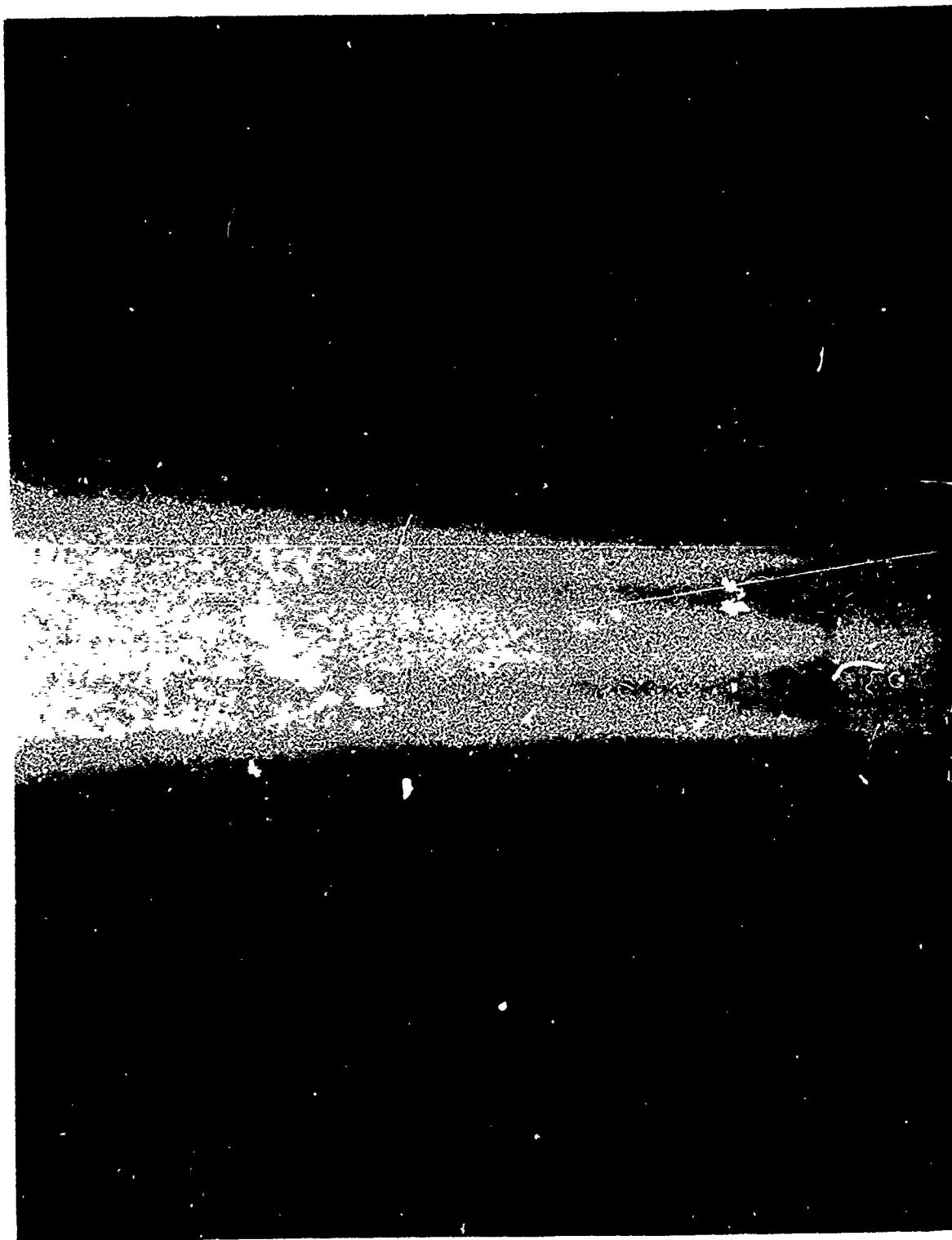


Figure 142. Assembled Laser Hardware

The windows utilized in the optical cavity through which the laser optical axis passes, varied as discussed below. For lasing tests, the two windows perpendicular to the laser axis were plexiglass. All of the window mounts have been provided with an inert gas purge to sweep out any reaction products that might otherwise stagnate in the "dead" space adjacent to the window.

Optical Resonators. The flowfield obtained from the nozzle system described above is depicted in Fig. 143, which is a photograph of the "orange" glow taken through one of the optical cavity windows. In this figure, the long direction of the nozzles is perpendicular to the page. To minimize effects of gain variation and to maximize the gain path for this small laser, the optical axes of all of the resonators utilized in this study were oriented parallel to the long dimension of the nozzles (in the same direction in which the photograph in Fig. 143 was taken). This orientation is shown in the isometric schematic of Fig. 144.



5AA24-2/24/73-S1*

Figure 143. Flow Field With H_2

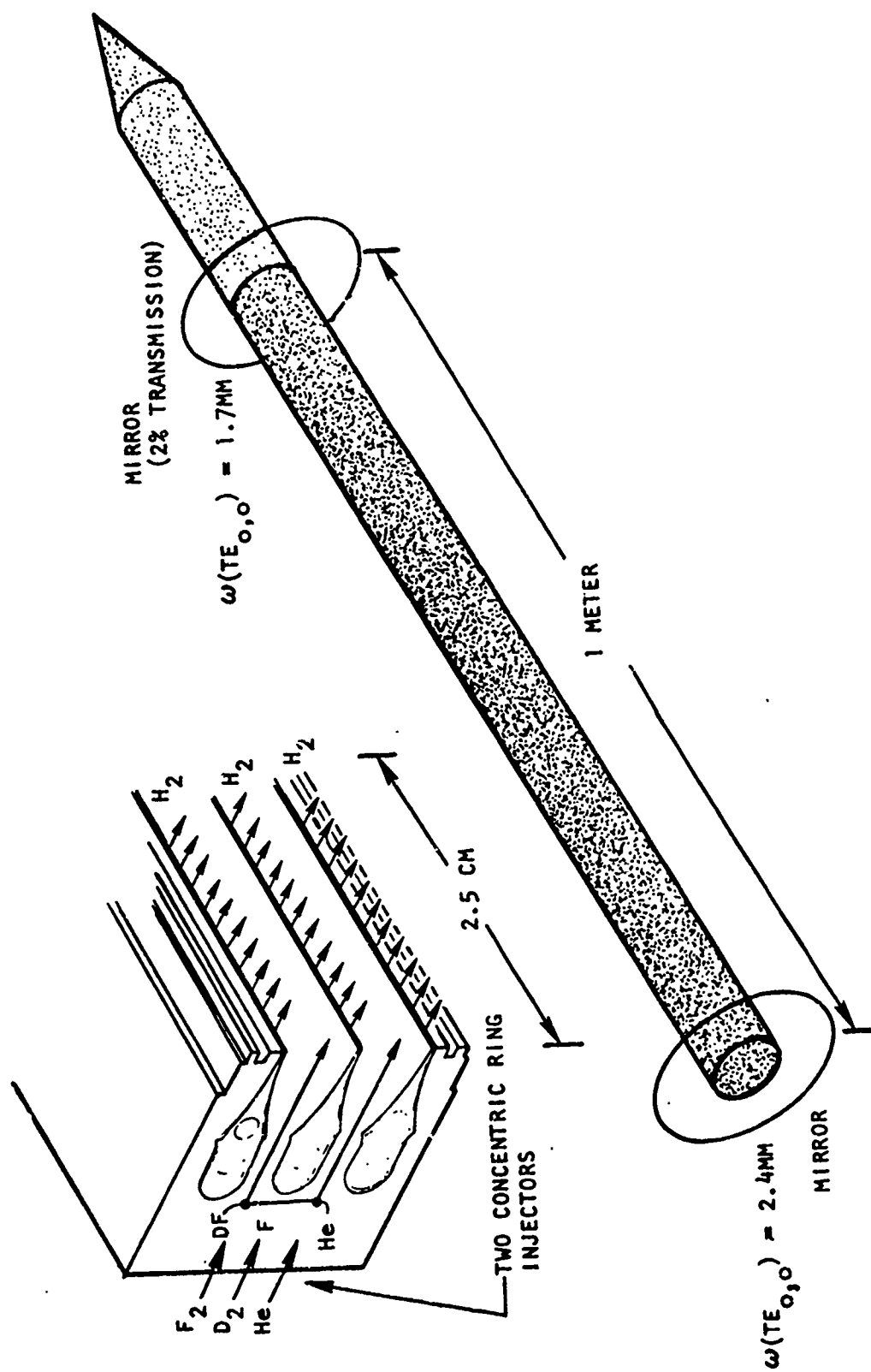
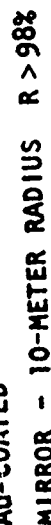


Figure 144. Spatial Relationship of Laser Beam to Nozzle Geometry

Several resonator configurations were utilized before the most practical arrangement was found. In all configurations, the mirrors were mounted in precision angular orientation devices. One mirror mount was, in turn, mounted on a precision x-y translation stage. The mirror mounts were separated 1 meter on an invar framework. All spherical mirrors utilized had a radius of 10 meters.

The first resonator configuration was utilized as shown in Fig. 145. In this concept, an attempt was made to obtain a high Q (low loss) configuration by utilizing AR-coated windows. The AR coating was specified, to the supplier, to give transmission greater than 99.5 at 2.7μ . A slight cant of 5 degrees was provided to eliminate potential parasitic oscillations. This configuration results in a much smaller dead space than is obtained with windows mounted at the Brewster angle, thus minimizing the possibility of collecting much ground-state HF in this dead space. Also, this configuration permits the use of high-reflectance mirrors (closed cavity) with performance monitored using output from a window reflection. This configuration worked reasonably well for operation with H_2 as the cavity fuel. Later experiments with other cavity fuels indicated poor performance, so the transmission of the windows was determined experimentally. The results are shown in Fig. 146, where it can be seen that the actual transmission losses were quite large, amounting to almost 40-percent round trip loss on some transitions.

These large window losses rendered operation on lower gain conditions impossible; therefore, another set of window fittings was designed and the windows changed to CaF_2 at the Brewster angle. The fittings are shown in the photograph in Fig. 148. The windows are mounted with the standard, accepted (though somewhat sloppy in appearance) method for holding vacuum without stressing the windows. The angle of the fitting was designed for CaF_2 windows. A wedge adapter was designed so that Al_2O_3 windows also could be used. The row of holes readily visible in the left-hand fitting provide an He sweep to purge the fittings so that ground-state HF cannot accumulate in the "dead" space. Figure 149 shows a laser emission spectrum taken with the first configuration, and Fig. 150 shows the laser emission spectrum taken with the Brewster angle windows. Comparison of the two figures shows that several additional transitions achieve threshold in the higher Q resonator.



285

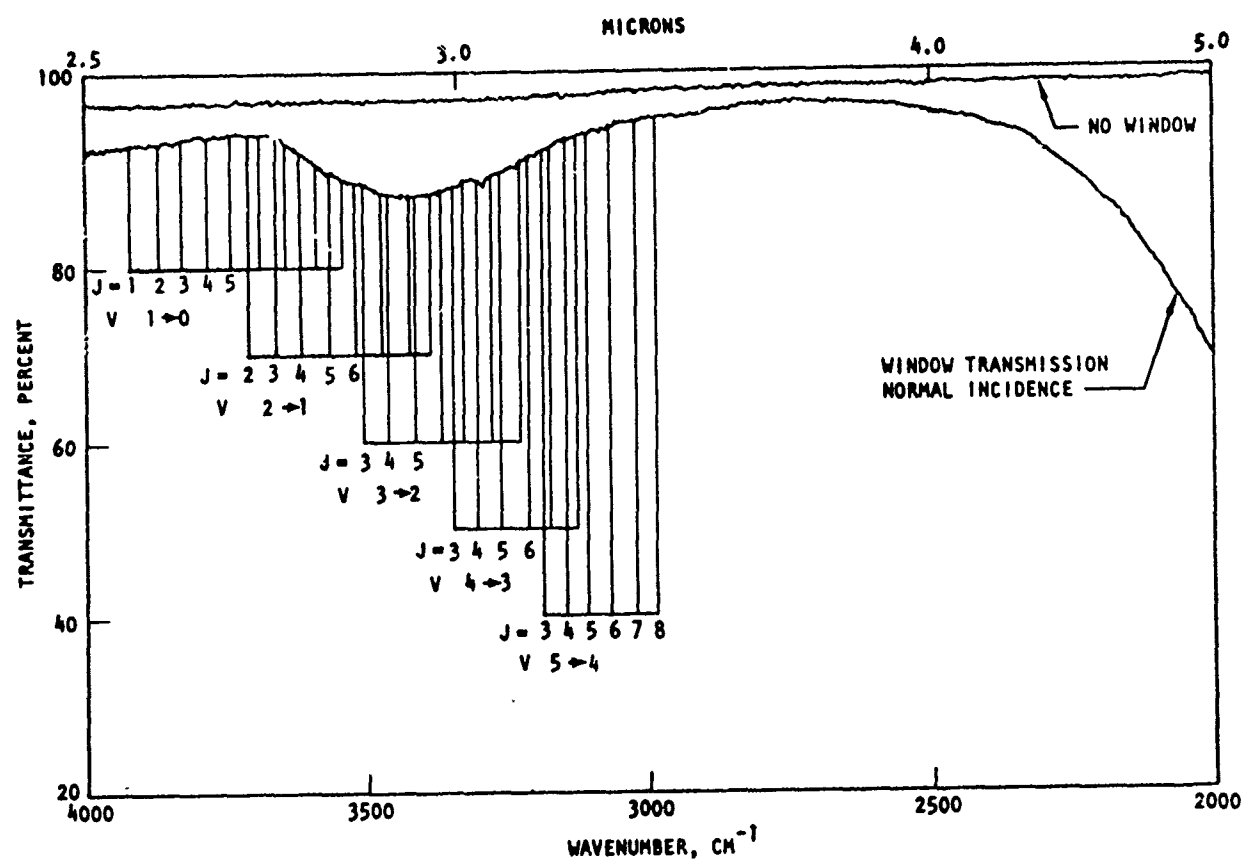


Figure 146. Measured Transmission of AR-Coated, 0-Degree Al_2O_3 Window

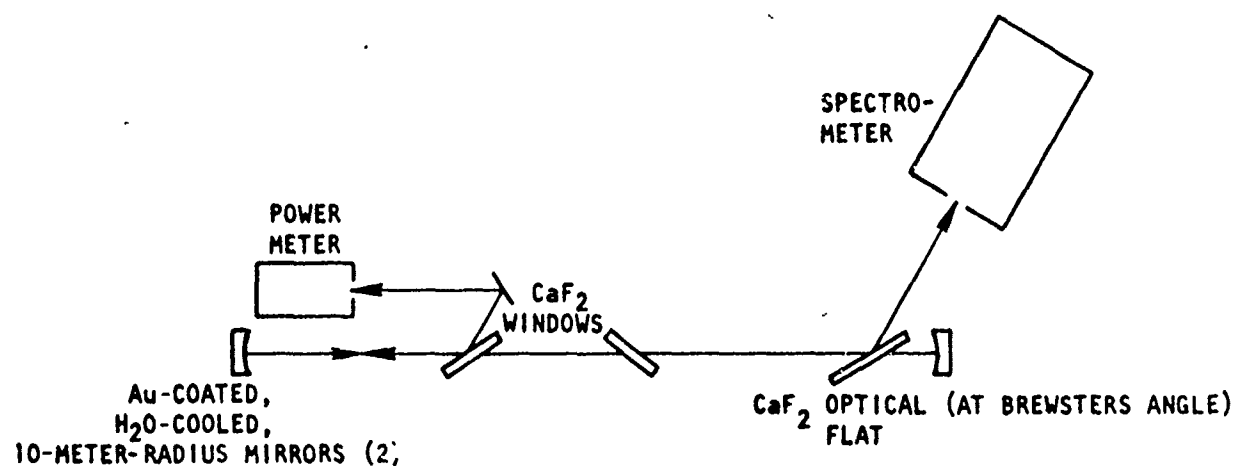


Figure 147. High Q Cavity/Resonator Configuration

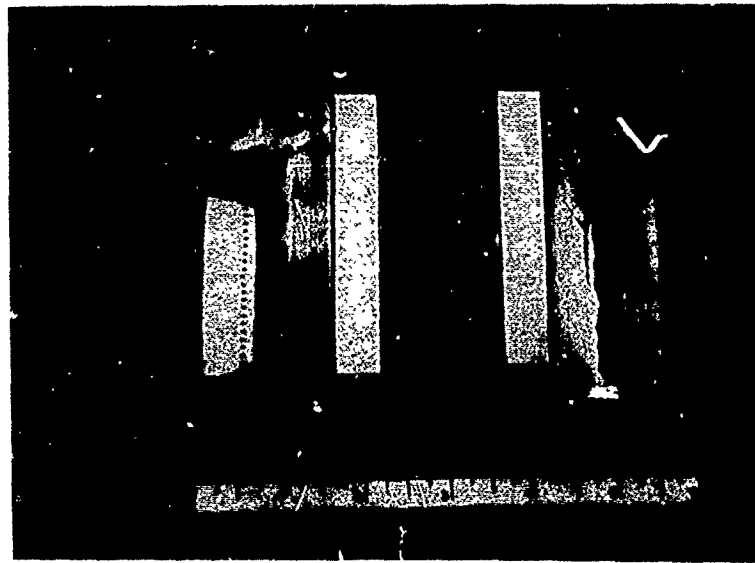


Figure 148. Brewster Angle Fittings With Windows Mounted

Alignment of this system proved to be difficult to achieve and maintain. To solve this problem, a resonator with outcoupling was then used with outcoupling provided by a small hole in one of the mirrors, as shown in Fig. 151. The hole permits ready alignment of the resonator with an He-Ne laser beam. This configuration solved all the alignment problems, but the hole coupling introduces larger losses in low-order modes, requiring that the system be aligned so that the hole is somewhat displaced from the axis of the resonator, which is an unsatisfactory situation.

The hole outcoupling arrangement did provide a useful arrangement so, to maintain all the alignment advantages of the hole coupler but to eliminate the rather large losses, a third resonator configuration was set up. This is shown in Fig. 152. Performance is monitored with the light transmitted by the 2-percent Al_2O_3 dielectric coated flat. This resonator proved to be an excellent configuration and, once installed and checked out, was used exclusively. Its only general drawback is that it is only useful in a wavelength region in the immediate vicinity of 2.7μ . For operation at other wavelengths, e.g., DF, another dielectric-coated flat "tuned" to 3.8μ would be required.

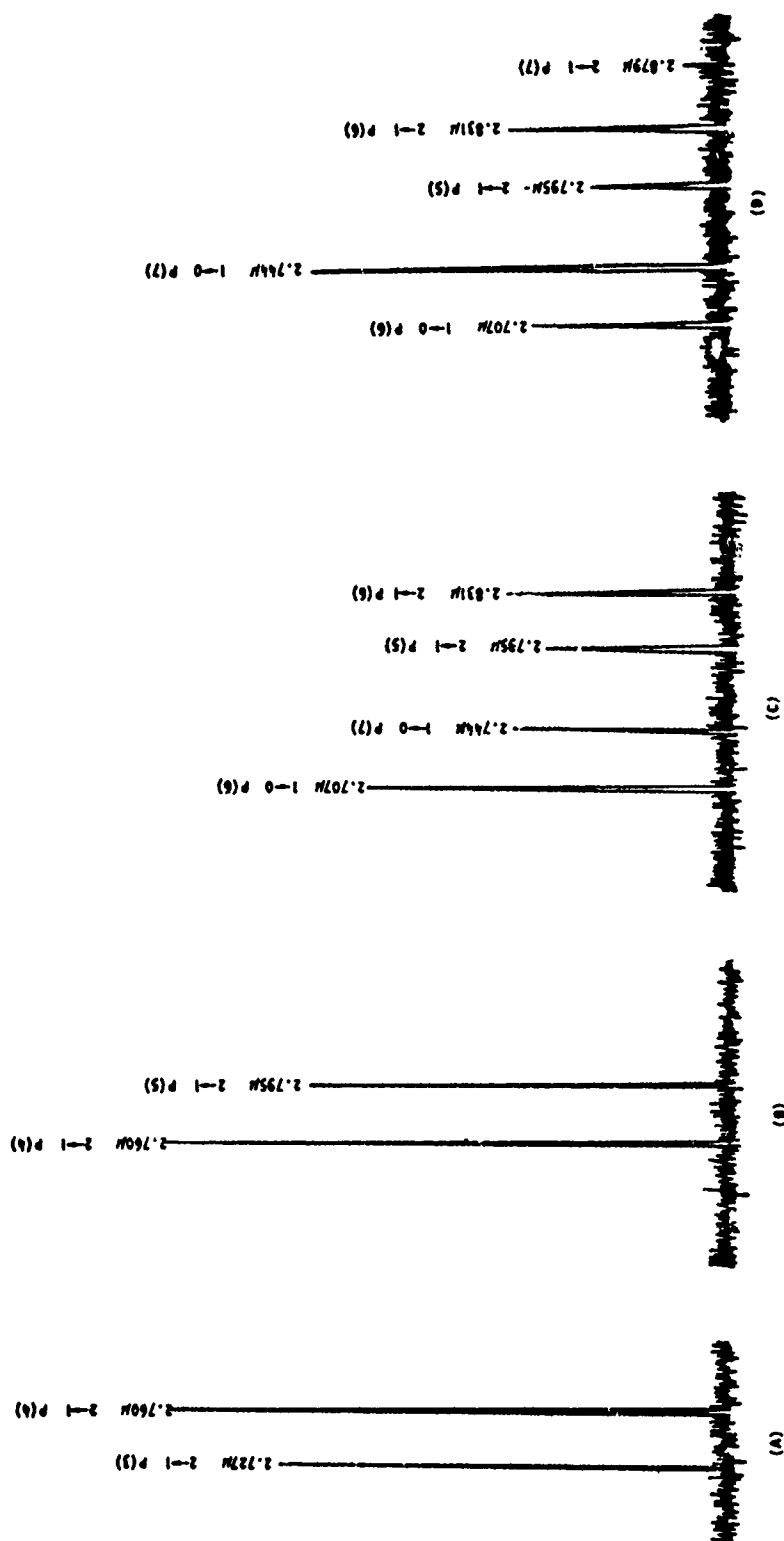


Figure 149. Laser Emission Spectra at 0.25 Inch Downstream With Increasing Precombustor Temperature A Through D

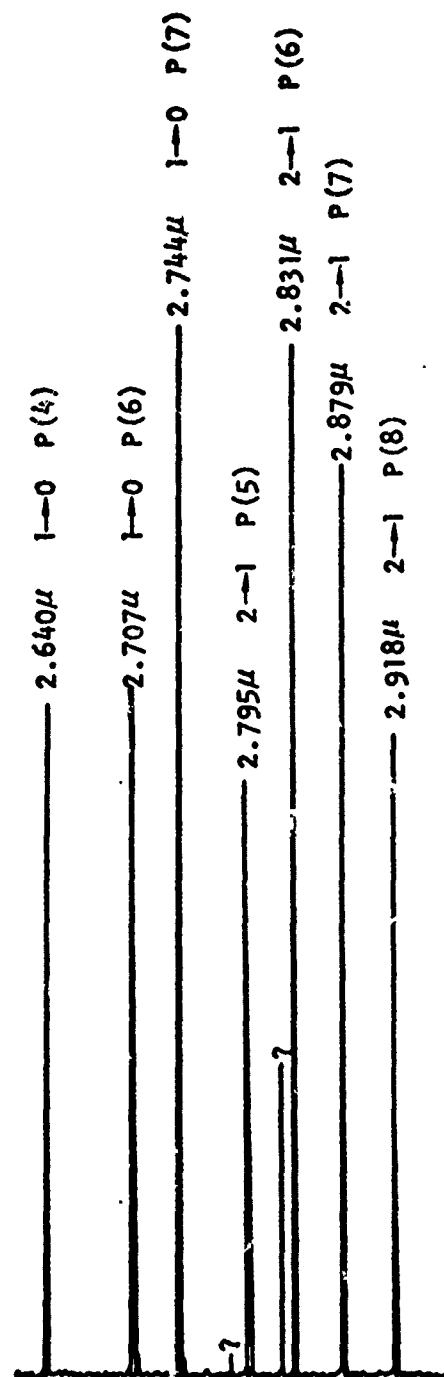


Figure 150. Laser Emission Spectrum 0.25 inch Downstream

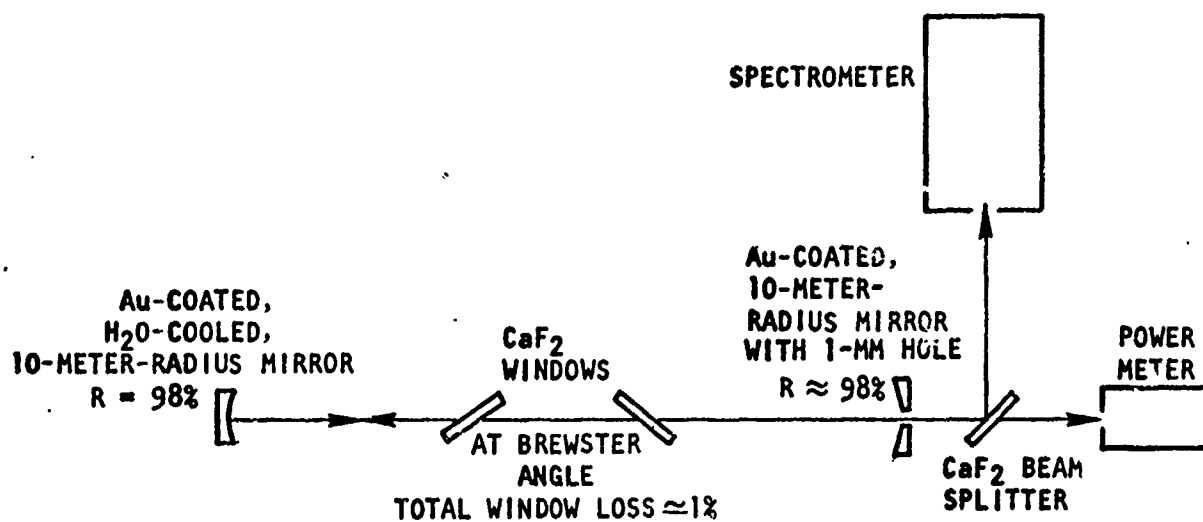


Figure 151. High Q Cavity With Hole Outcoupler Configuration

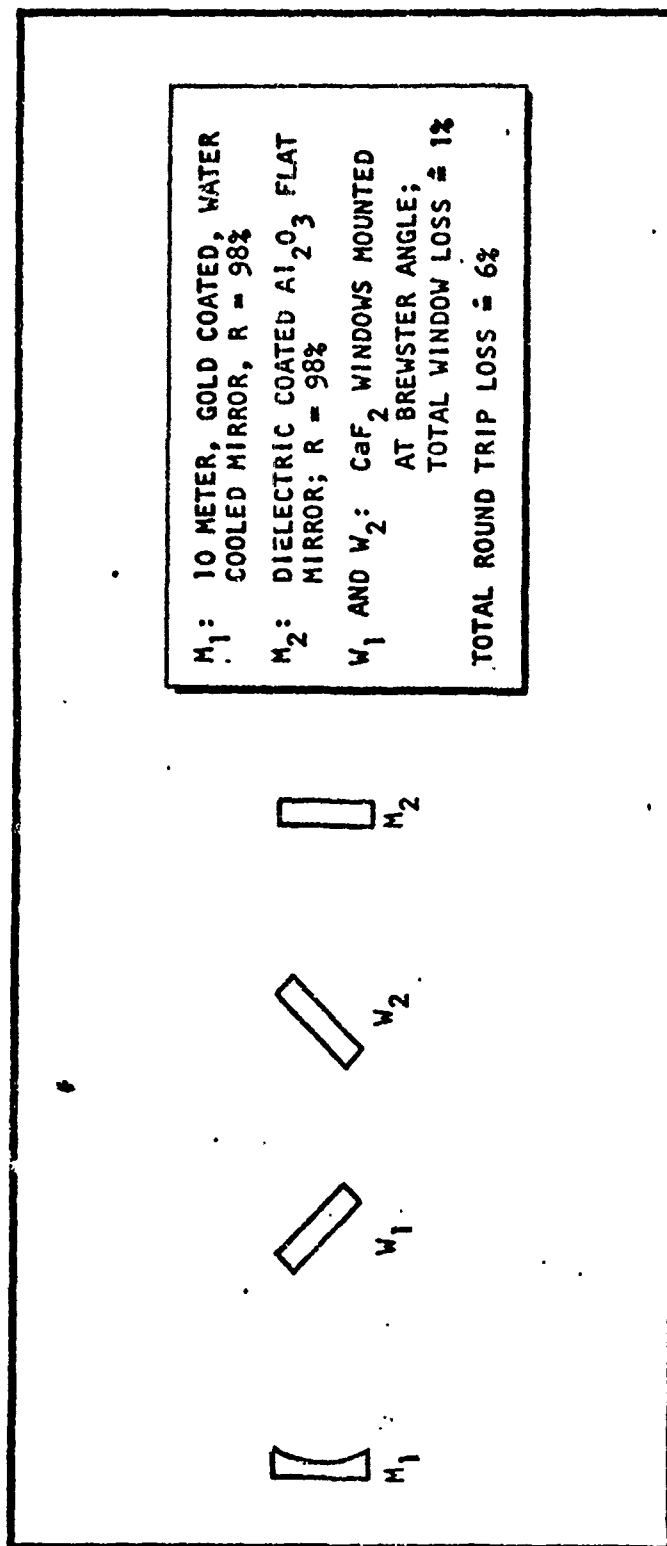


Figure 152. Low-Loss Optical Resonator Configuration

With this configuration, low-order transverse modes were easily obtained. Examples are shown in Fig. 153. These burn patterns were obtained by exposing "slick" cardboard to the outcoupled beam about 30 centimeters from the 2-percent partial transmitter. The mode pattern was most affected by tuning this mirror, and low-order mode patterns were readily obtained.

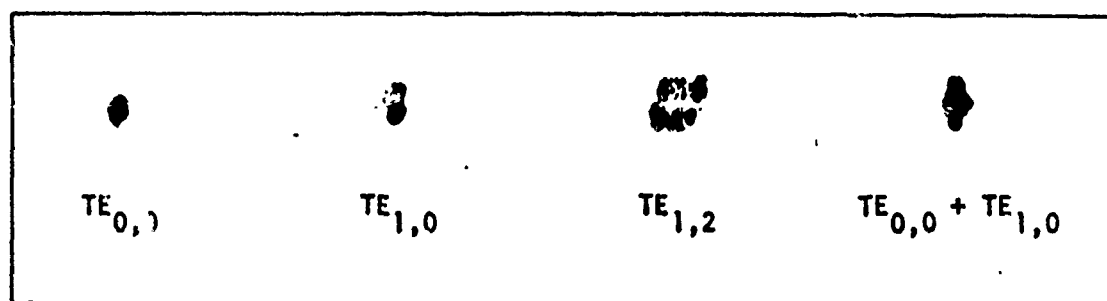


Figure 153. Burn Pattern Display of Mode Structure

Diagnostic Equipment

For the small-scale laser studies, four diagnostic experiments were utilized: (1) outcoupled power in one mode volume, (2) power scans across the flowfield at various downstream locations, (3) high-resolution laser emission spectra, and (4) rapid scan laser emission spectra. These are shown collectively in Fig. 154 and are discussed separately below.

Beam Power. The experimental arrangement for monitoring beam power is shown in Fig. 155. A CaF_2 beam splitter located in the outcoupled beam reflects about 6 percent of the outcoupled power into a disk calorimeter-type power meter that can be calibrated electrically. To calibrate the beam splitter, a power reading is taken with the power meter at the calibration position indicated in Fig. 155 and then another reading is taken in its normal position. The ratio of these readings determines the reflectivity of the beam splitter directly. The power meter is visually monitored in real time and its output is also recorded on a strip chart recorder for data analysis.

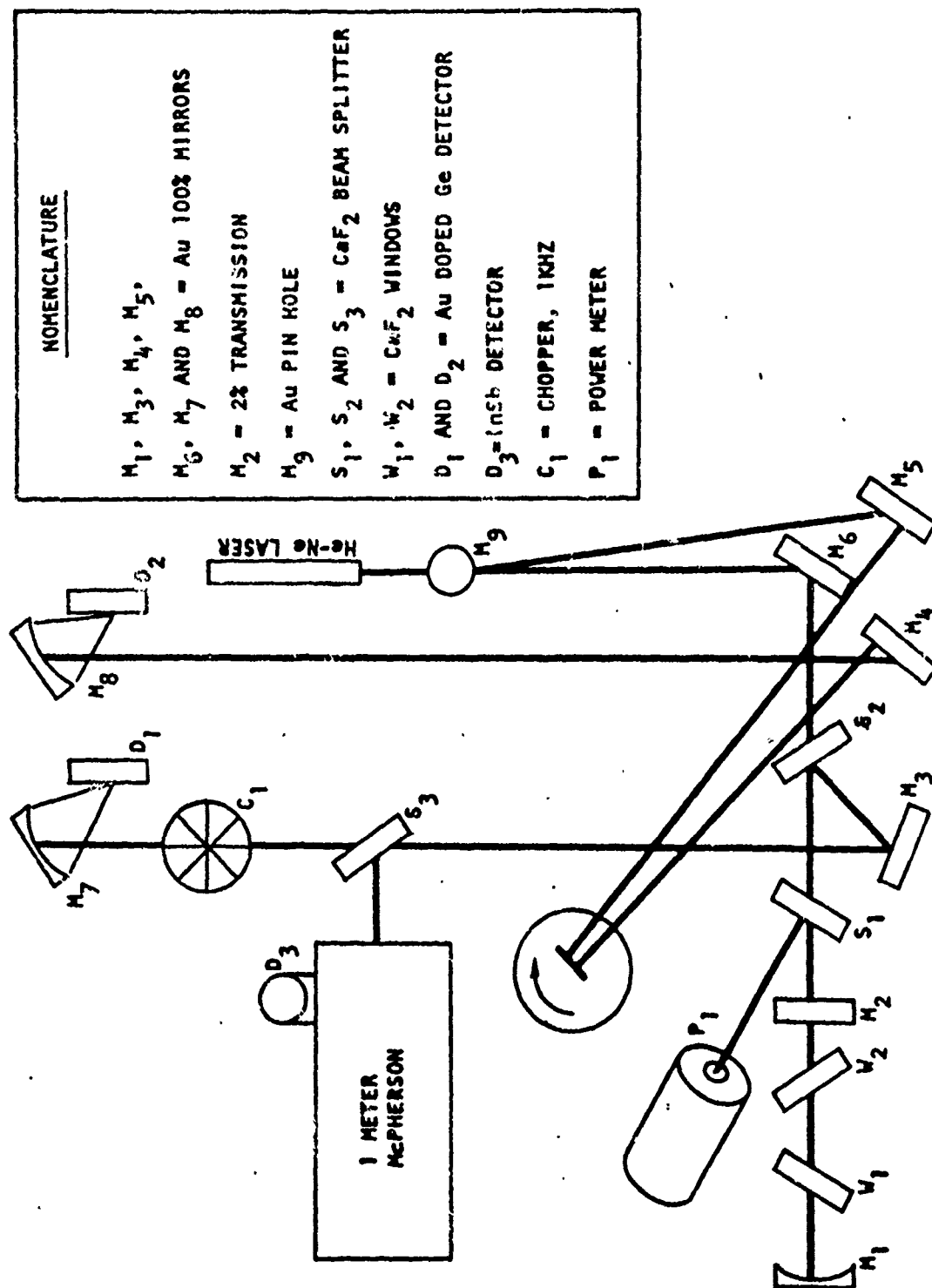


Figure 154. HF Laser Beam Diagnostics

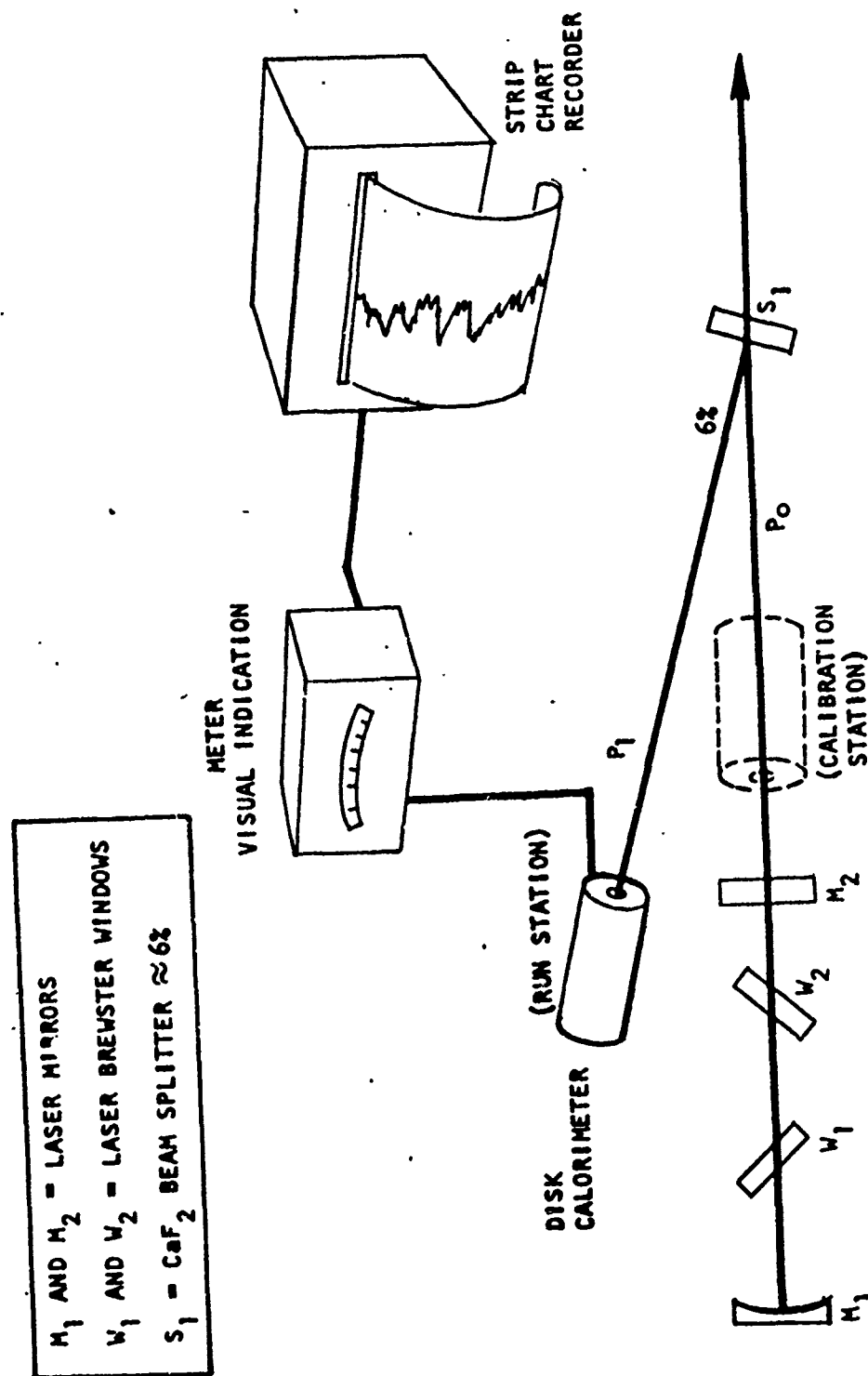


Figure 155. Power Measurement

Power Scans. Having established the power in the mode volume, a detailed power scan of the medium is obtained by moving the laser hardware relative to the optical axis determined by the optical resonator and the optical diagnostic "train." This is shown schematically in Fig. 156. There are two drive motors on the system. One drives the laser hardware vertically with the vacuum maintained with a piston moving in an O-ring seal. The other drive motor moves the device transversely so that the optical axis moves through the medium relative to the nozzles as shown in Fig. 157. During moving of the medium, part of the outcoupled beam is split with a CaF_2 flat and passed through a chopper and into a fast-response, gold-doped germanium (77 K) detector. The signal is recorded on an x-y recorder that is coupled to the motion via a voltage developed by a linear potentiometer. The result is a curve of out-coupled power in one mode volume versus position in the medium, for example, as shown in Fig. 158.

Laser Emission Spectra. High-resolution laser emission spectra are obtained with a spectrometer, which is shown in Fig. 159, comprising a 1-meter Czerny-Turner grating (blazed at 2.5μ) monochrometer, an InSb photo voltaic (77 K) detector, a d-c amplifier, and a strip chart recorder. A 6-percent CaF_2 beam splitter provides beam sampling. This light is split again (6 percent) prior to the entry slits of the monochrometer. The monochrometer has been modified to increase the scanning speed. However, it still takes about 30 seconds to scan the usual HF laser emission spectrum. To obtain a good spectrum, this requires that the medium be stationary for this period of time.

Rapid-Scan Laser Emission Spectroscopy. A special 12-meter rapid-scan spectrometer has been set up to provide essentially real-time laser emission spectra. This is shown in Fig. 160. A portion of the outcoupled beam illuminates a rotating grating which is blazed at 2.6μ . The grating and a mirror make up a "roof" reflector and the reflected, dispersed light is detected, after traveling 12 meters (folded path), with a fast-response gold-doped germanium (77 K) detector. The detector output is displayed on an oscilloscope. With a standard set of conditions, the scope sweep is about 500 microseconds/centimeter with a total sweep time of about 0.5 millisecond required to scan the HF laser emission spectra. A hard copy is obtained

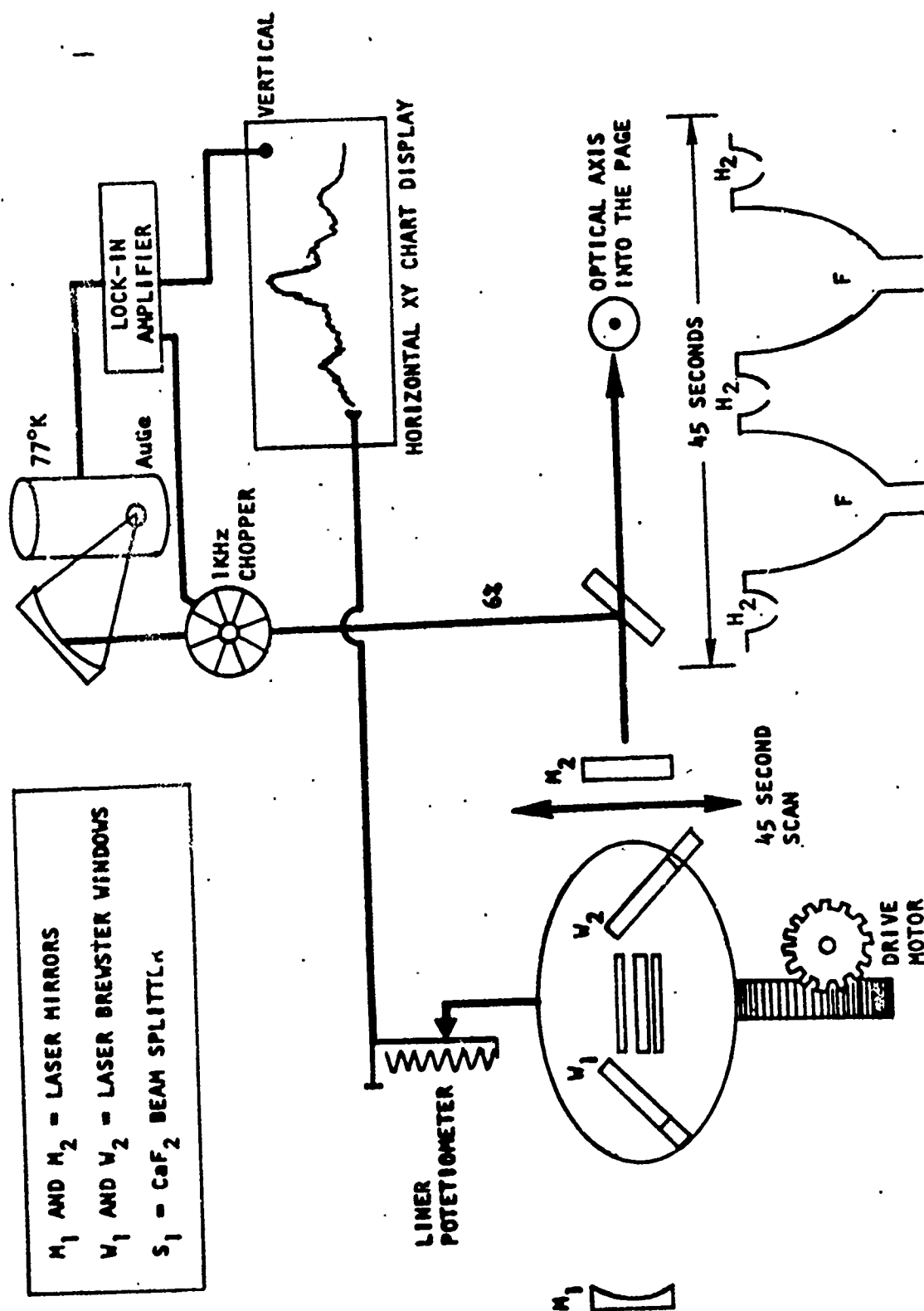


Figure 156. Power Scan Schematic

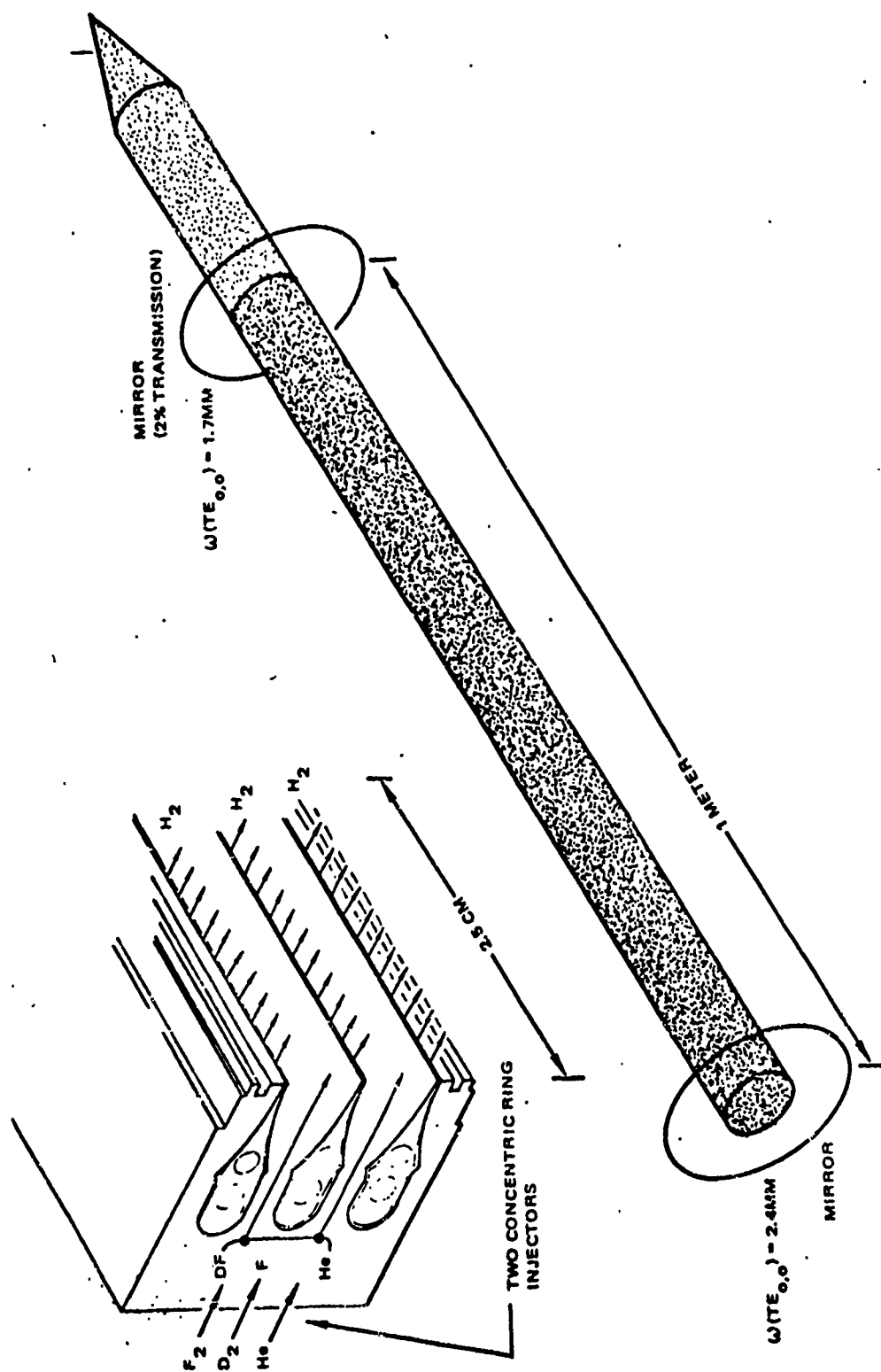


Figure 157. Spatial Relationship of Laser Beam to Nozzle Geometry

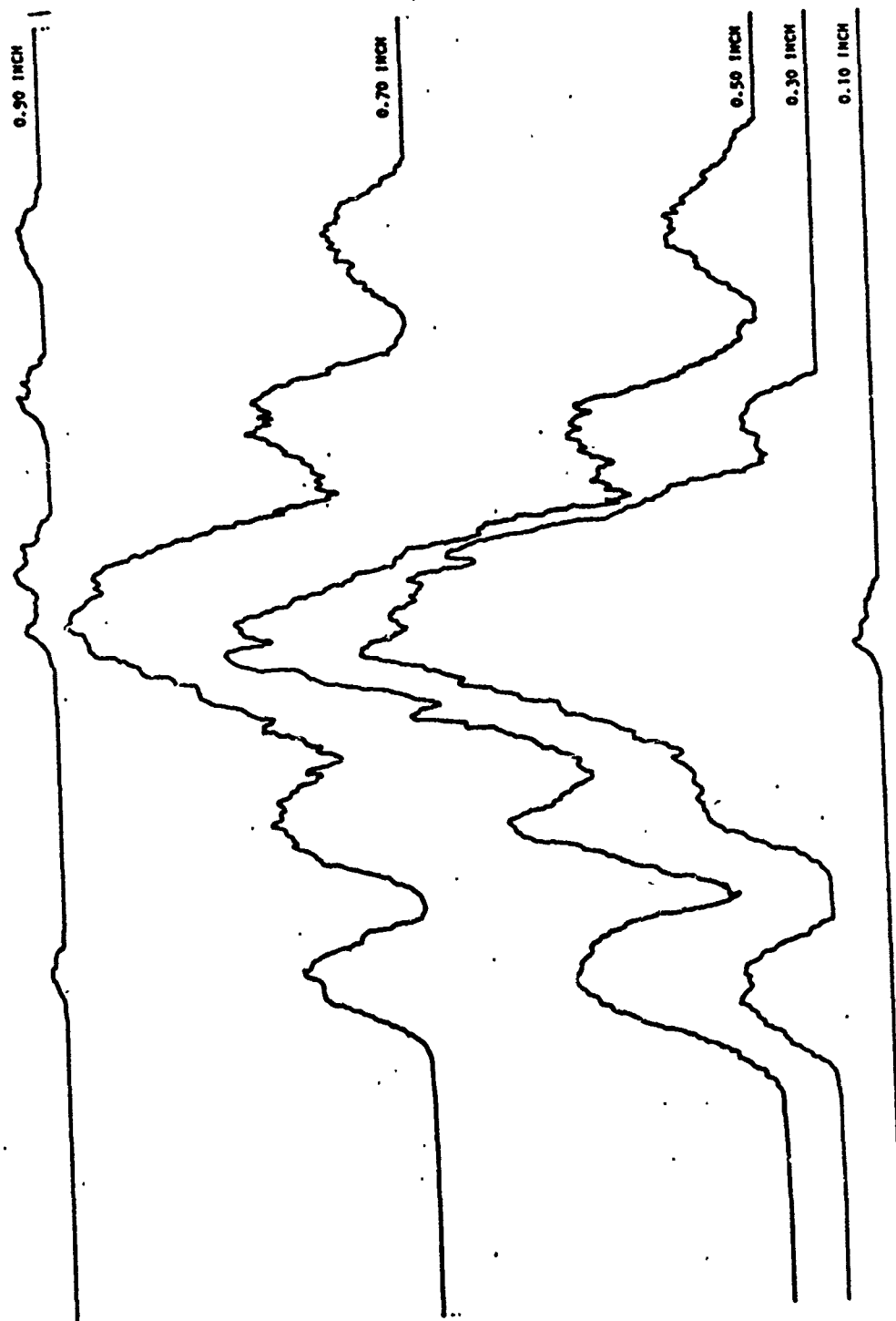


Figure 158. Power Scan Data for F + HCl

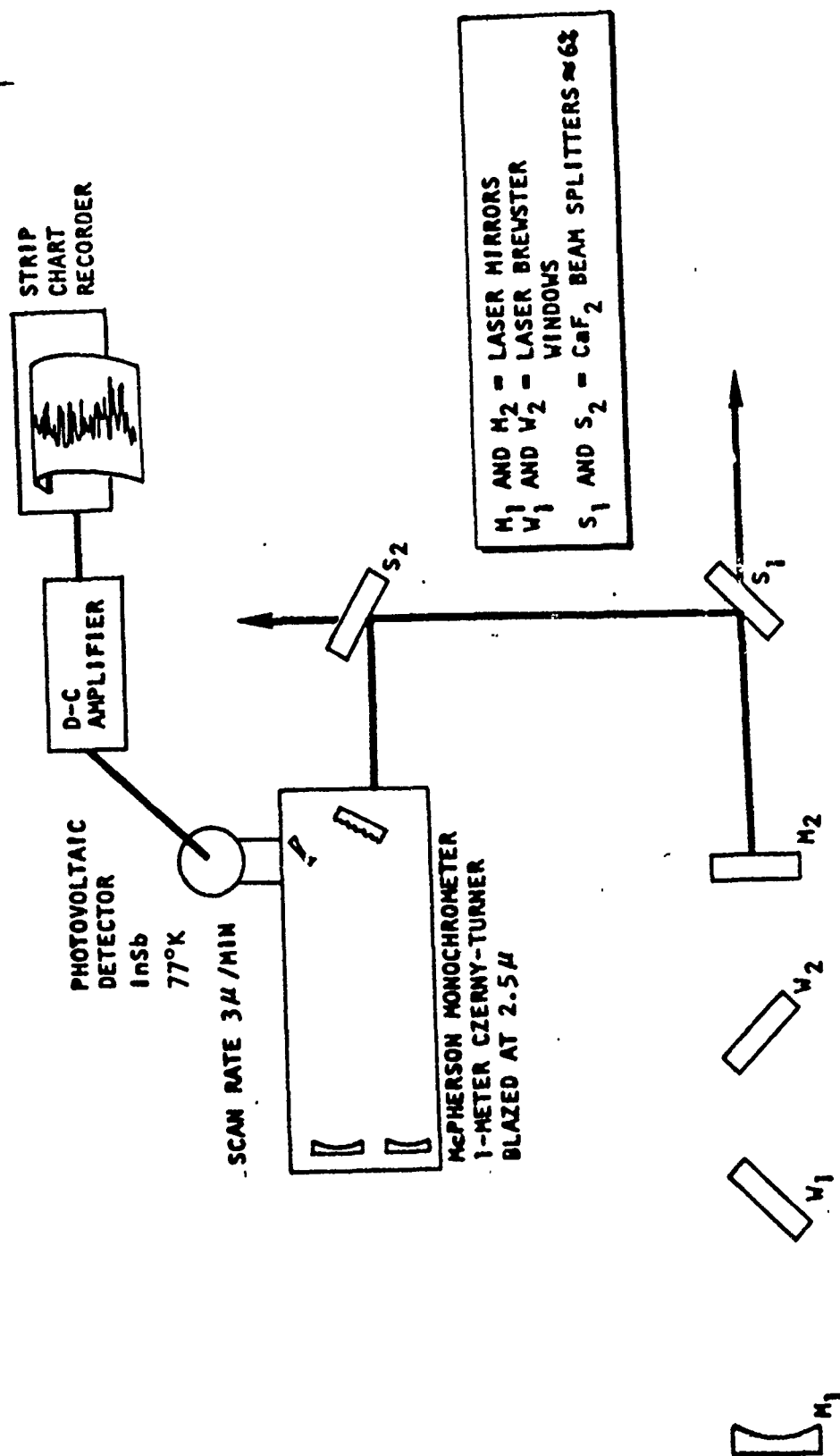


Figure 159. High-Resolution Spectroscopy

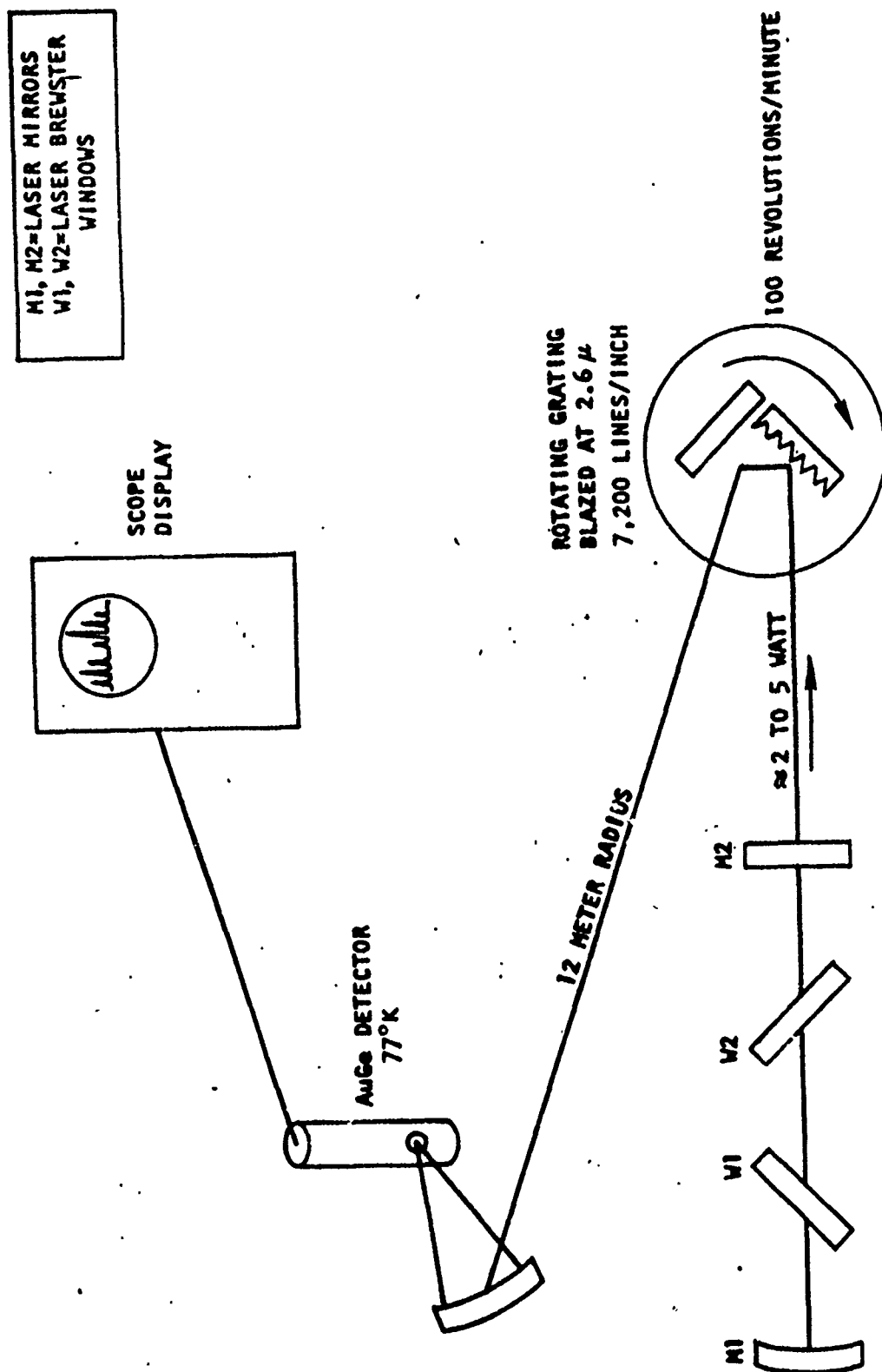
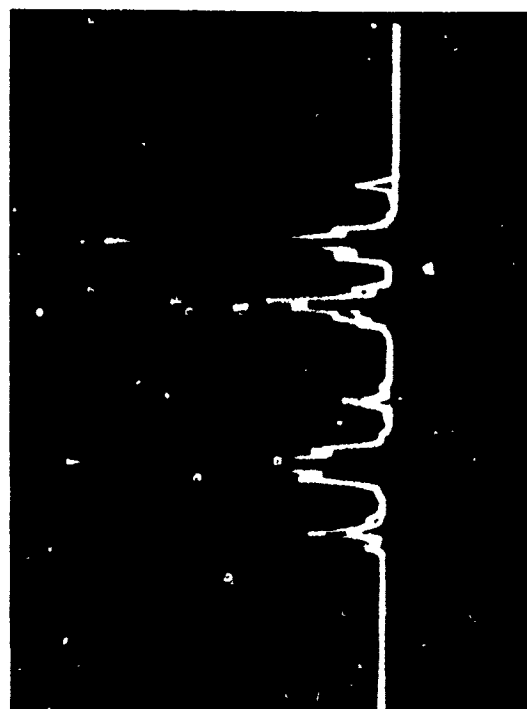
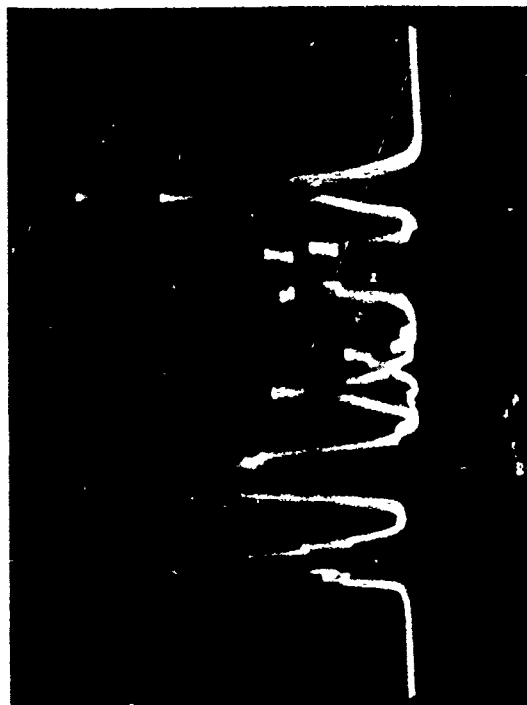


Figure 1f0. Time-Resolved Emission Spectroscopy (12-Meter, Rapid-Scan Spectrometer)

when desired, with a polaroid oscilloscope camera. Two typical photographs are shown in Fig. 161. In Fig. 161a, the scope triggered twice during the exposure and it can be seen that there are fluctuations in the output intensities of the laser emission line. Figure 161b shows another photograph with two sweeps. In this photograph, it can be seen that during this run there were large fluctuations on the 2-1 P(3) and 1-0 P(6) lines. Both of these photographs were obtained from lasing derived from the $F + H_2$ baseline pumping reaction.



(A)

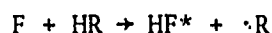


(B)

Figure 161. Typical Oscilloscope Display of Rapid-Scan Spectra

CAVITY FUEL EVALUATION

To evaluate alternate cavity fuels, the small-scale hardware described above was utilized with a direct replacement of the H_2 cavity fuel flow with the cavity fuel to be evaluated. The cavity fuels selected for evaluation are shown in Table XXVI. In all cases, the fuels are storable as liquids at ambient temperature in pressurized vessels. The selection was based on this and the desire to evaluate several classes of compounds. Thus, the list includes hydrogen halides, freons, simple hydrocarbons, and an ether. Included in the list is cyclopropane to compare with the linear compound normal propane. The energetics of all the compounds, HR, in the reaction:



is sufficient to obtain vibrational excitation up to, and including, $v = 3$, and this compares favorably with the baseline fuel H_2 . For HBr, there is sufficient energy to activate $v = 4$.

TABLE XXVI. CAVITY FUELS EVALUATED

Cavity Fuel	Molecular Weight	Vapor Pressure (25 C), psia
HCl	36.46	650
HBr	80.92	350
HCF_2Cl	86.47	141
HCF_3	70.02	655
$n-C_4H_{10}$	58.12	36
$n-C_3H_8$	44.09	126
Cyclo- C_3H_6	42.07	90
CH_3OCH_3	46.07	80

As shown in Table XXVI, the weight of all the alternate cavity fuels is substantially greater than that of H_2 , so it was anticipated that mixing of the cavity fuel with the F atom-containing stream would be sufficiently reduced to affect

performance. Thus, results comparing the alternate cavity fuels would be more accurate than the comparison with H_2 . As described later, a normalization of data was utilized to aid in comparison results with H_2 .

Preliminary Tests

Two series of tests was run to evaluate cavity fuels. In the first series, several of the cavity fuels were given preliminary evaluation by measuring outcoupled power with the optical resonator axis 1/4-inch downstream of the nozzle exit plane. Downstream power scans, as shown in Fig. 162, show that this was where optimum results could be obtained. In these tests, the hole outcoupled resonator shown in Fig. 151 was utilized. The results obtained from these tests are shown in Table XXVII. For these tests, the plenum pressure for the cavities fuel nozzle was maintained at design, which results in substantially lower molar flowrates. For example, the molar flowrate of propane is about 20 percent that of H_2 , and that of butane is 85 percent that of propane. To partially account for these effects, the results in Table XXVII denoted as relative energy have been normalized to molar flowrate. In these tests, the mode volume of the resonator was maintained in low order. An additional comparison of propane and butane with H_2 was made in which the resonator was permitted to operate in higher order modes where additional gain media volume contributed to the outcoupled power. These results are shown in Table XXVIII. Again, when normalized to molar flowrate, the performance of propane and butane, which is quite low in absolute power, is quite comparable to H_2 .

The precombustor operating conditions for the comparison runs were maintained constant so that differences in precombustor conditions would not reflect on the data. These conditions were as shown in Table XXIX. Under these operating conditions, the theoretical temperature is reduced by heat loss to give a nozzle entrance temperature of 1460 K, which yields an α (discounting recombination in the nozzle) of 0.99.

It was visually observed during runs with both propane and butane that the reaction region, as denoted by light emission, above the center cavity fuel nozzle,

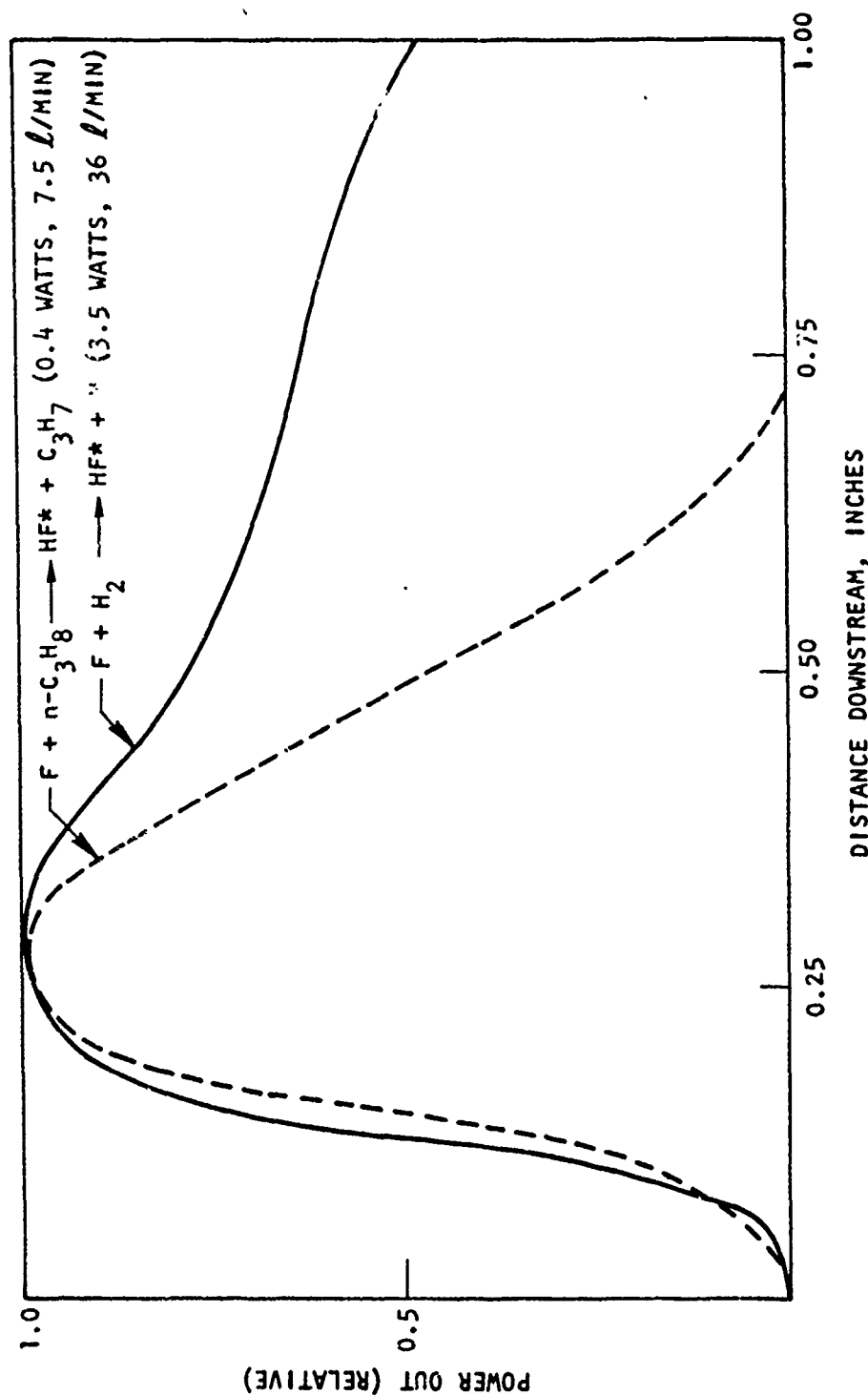


Figure 162. Power Out Versus Downstream Position (In Line With Center Cavity Fuel Nozzle)

TABLE XXVII. SUMMARY OF PRELIMINARY TEST RESULTS OF F + HR

HR	Relative Energy ⁽¹⁾	Power Out, watts
H ₂ (baseline)	1.0	2.5
HCl	0.4	0.3
HBr	4.8	2.0
HCF ₃	NL*	
HCF ₂ Cl	NL	NL
n - C ₃ H ₈	0.26 (2.2) ⁽²⁾	0.15
c - C ₃ H ₆	0.10 ⁽³⁾	
n - C ₄ H ₁₀	0.20 (1.7) ⁽²⁾	
CH ₃ OCH ₃	NL	NL

*NL = no lasing

(1) Ratio of power out in one mode volume divided by molar flowrate of HR to power out in one mode volume divided by molar flowrate of H₂

(2) Values in parenthesis are derived from the reduced cavity fuel pressure reduced molar flowrate experiments.

(3) This value obtained from later screening studies is an approximate comparison because the optical resonator used when c-C₃H₆ provided sufficient gain to lase was different than that used in obtaining the other results.

TABLE XXVIII. CAVITY FUEL COMPARISON

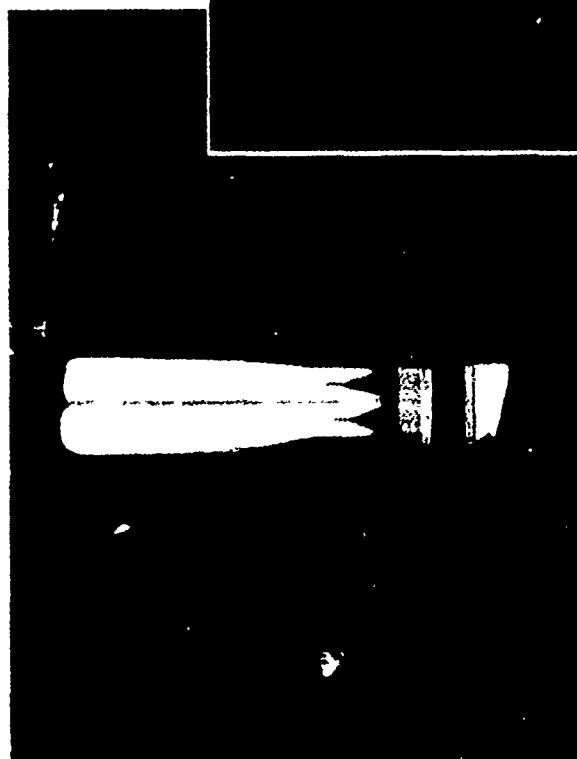
Cavity Fuel	Power Out, watts	Power Out*/ Molar Fuel Flow
H ₂	4.95	1.00
C ₃ H ₈	0.45	0.53
C ₄ H ₁₀	0.36	0.41

*Normalized to baseline (H₂) of unity

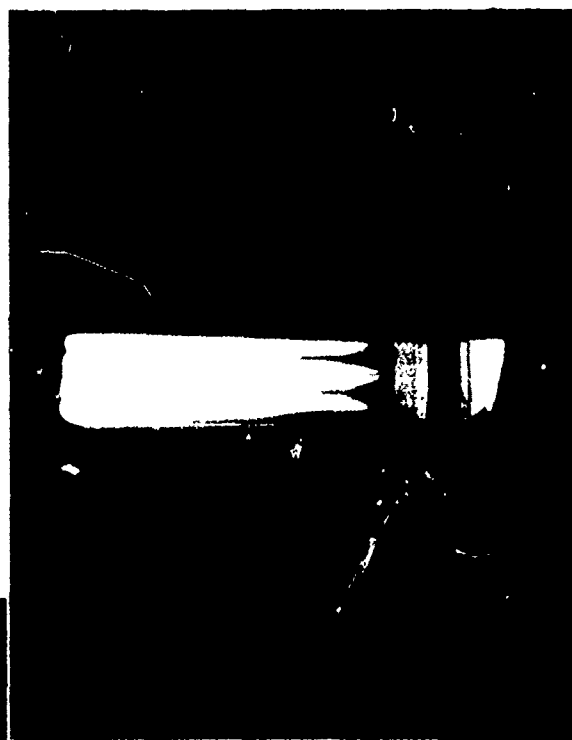
diverged downstream when the cavity fuel driving pressure was near the design pressure for matching flows. A downstream (from the center cavity fuel nozzle) power scan for propane displayed in Fig. 162 shows peak power about 0.30 inch downstream, reducing to zero about 0.50 to 0.75 inch downstream, whereas with H₂ (also shown in Fig. 162) the gain region extended beyond 1 inch. Because the more rapid drop-off with propane may have been a reflection of the apparent divergence in the reaction zones, the driving pressure of the cavity fuel nozzles, with propane, was reduced until visually there was no longer a divergence. A comparison of the "on-design" and reduced driving pressure flowfields is shown in Fig. 163. Concurrent with this reduced driving pressure is a reduction in flow of the cavity fuel. Despite this reduction in flow, at 0.25-inch downstream, the outcoupled power (in one mode volume) increased (an explanation of this is given later). A similar experiment with butane gave the same result. These results are summarized in Table XXIX. In Table XXIX, the reduced power entry is obtained by normalizing the power outcoupled to the molar flowrate and to the baseline (F + H₂) case as unity. (This presents a comparison to F + H₂ which is somewhat misleading in that the flowrate of H₂ can be decreased by two with less than a factor of two decrease in power.) A downstream power scan under these operating conditions shows that the gain region for propane is extended by about 50 percent.

Evaluation Tests.

Following the preliminary runs, tests were conducted to obtain a better intercomparison of the alternate cavity fuels. Power scan data were taken in some detail



DRIVING PRESSURE ON DESIGN



DRIVING PRESSURE REDUCED

Figure 163. Flow Fields With $n\text{-C}_7\text{H}_{16}$ Cavity Fuel

Table XXIX. RESULTS OF F + HR \rightarrow HF + \cdot R TESTS

HR	Powerout, watts (One Mode Volume)	Flowrate, ℓ/min	Reduced Power	HR/F	Lasing Lines Observed
H ₂	4.95	39	1	2.06	1 \rightarrow 0 P(4), P(5), P(6), P(7) 2 \rightarrow 1 P(4), P(5), P(6)
C ₃ H ₈	0.40	7.5	0.41	0.42	
C ₃ H ₈	0.75	0.60	2.2	0.3	1 \rightarrow 0 P(5), P(6), P(7) 2 \rightarrow 1 P(5), P(6)
C ₄ H ₁₀	0.30	6.9	0.32	0.35	
C ₄ H ₁₀	0.65	0.63	1.7	0.3	1 \rightarrow 0 P(5), P(6), P(7) 2 \rightarrow 1 P(5), P(6)

• Combustor Parameters: F₂, 31.7 ℓ/min ; D₂, 21.2 ℓ/min ; He, 126 ℓ/min , T_{theo} = 2500 K,
P_C = 15.1 psia

• Cavity Pressure: 3.9 torr

and, concurrently, laser emission spectra were observed. Theoretically, the performance of several of the alternate cavity fuels is potentially better than that of H_2 in a CW HF chemical laser. Based on a premixed model, the rapid pumping obtained from $F + C_3H_8$ provides higher gain than the $F + H_2$ reaction, as shown in the Kinetic Analysis section earlier in this report; yet, in terms of actual out-coupled power, H_2 gave the best results in the preliminary tests. The power scan data provide a basis for understanding this apparent discrepancy, which will be discussed later.

Power Scans. Power scans are made by moving the active medium relative to the axis of the optical resonator and monitoring the outcoupled power as described earlier. The general procedure for an alternate cavity fuel scan is to first run $F + H_2$ to ensure that the laser is operating in a normal fashion. This includes reactant flowrates, cavity pressure, power out, and laser emission spectroscopy. After the "baseline" checkout, the alternate cavity fuel is utilized in place of H_2 , with all other reactant flows, F_2 , D_2 , and He, maintained at the baseline flowrates. These flowrates vary somewhat but not significantly from run to run. Float level and metering pressures are recorded and actual flowrates are calculated during data reduction. After the run with an alternate fuel, the laser is again run with H_2 as a check on operating characteristics. Power Scans are run across the nozzles at several stations downstream of the nozzle exit plane.

The power scan data are compiled in Fig. 164 through 168. For comparison, Fig. 167 shows a scan for the baseline $F + H_2$. The vertical scales in these illustrations are quite different, so that "intensity" comparisons between them is invalid. However, within a given illustration, intensity comparisons are valid. Results of an aperturing experiment described below are shown in Fig. 168 as well as in Fig. 167. Figures 164 through 166 shows that the power scan data are quite similar for all of the high molecular weight cavity fuels. In all cases except $F + c-C_3H_6$, and $n-C_4H_{10}$, there are power maxima above each outboard cavity fuel nozzle, as well as the center nozzle, and a greater maxima between the outboard nozzle and the center nozzle. It is believed that these maxima between the nozzles are a result of the fact that the spatial resolution of the mode volume is less than the separation of the reaction regions occurring at the interface of the reactive

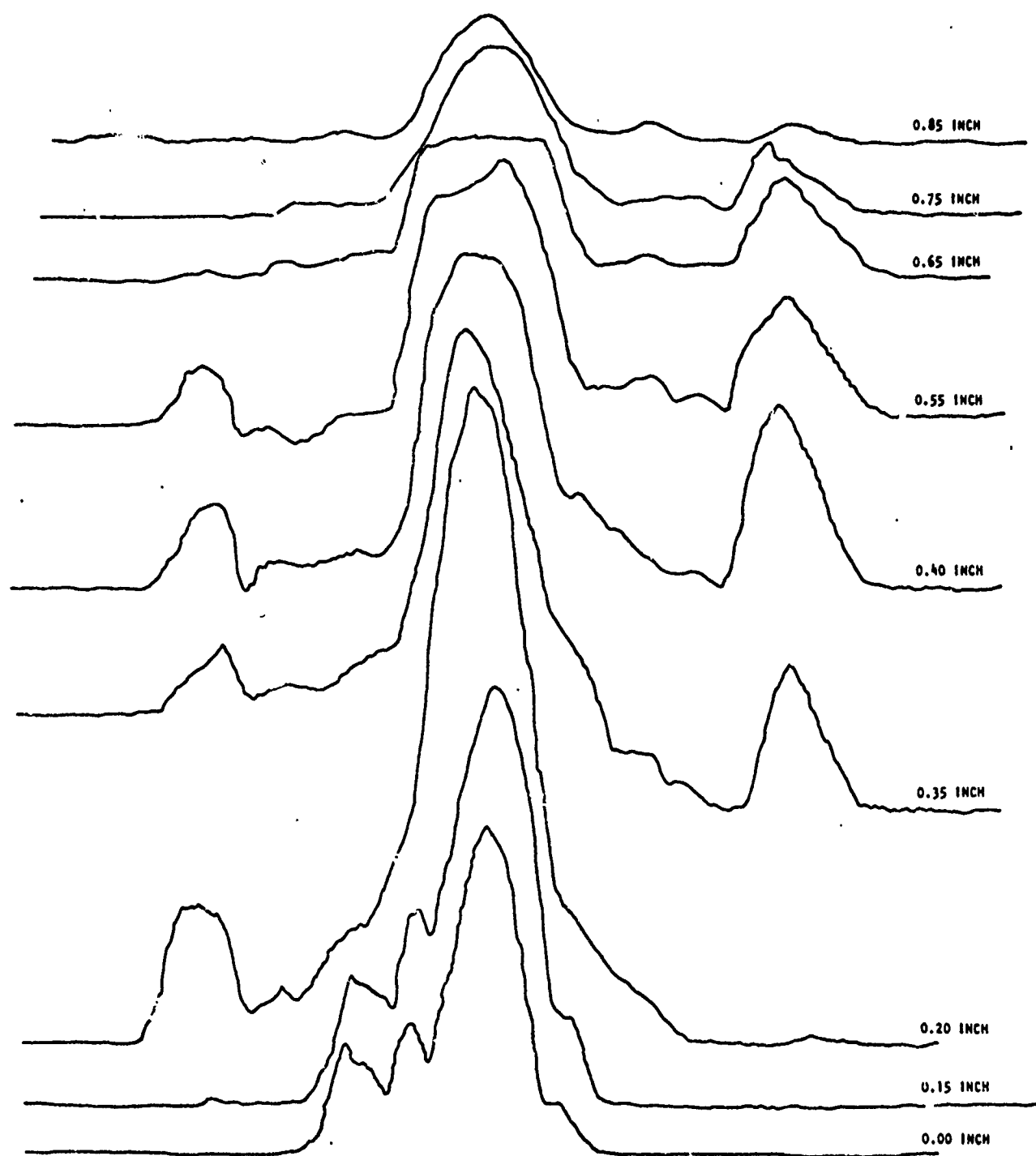


Fig. 164. Power Scan Data for F + n-Propane

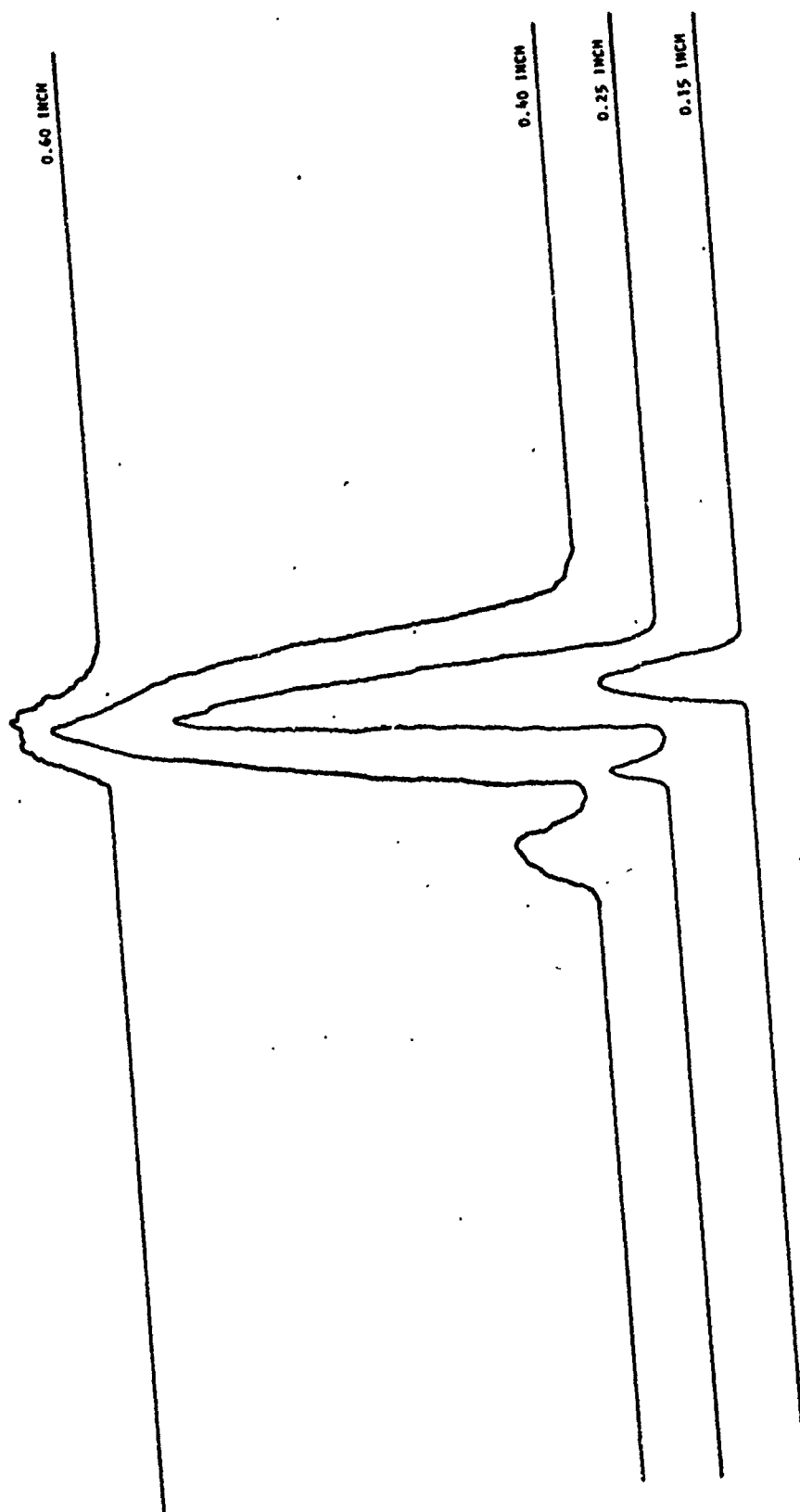


Fig. 165. Power Scan Data for F + c-Propane

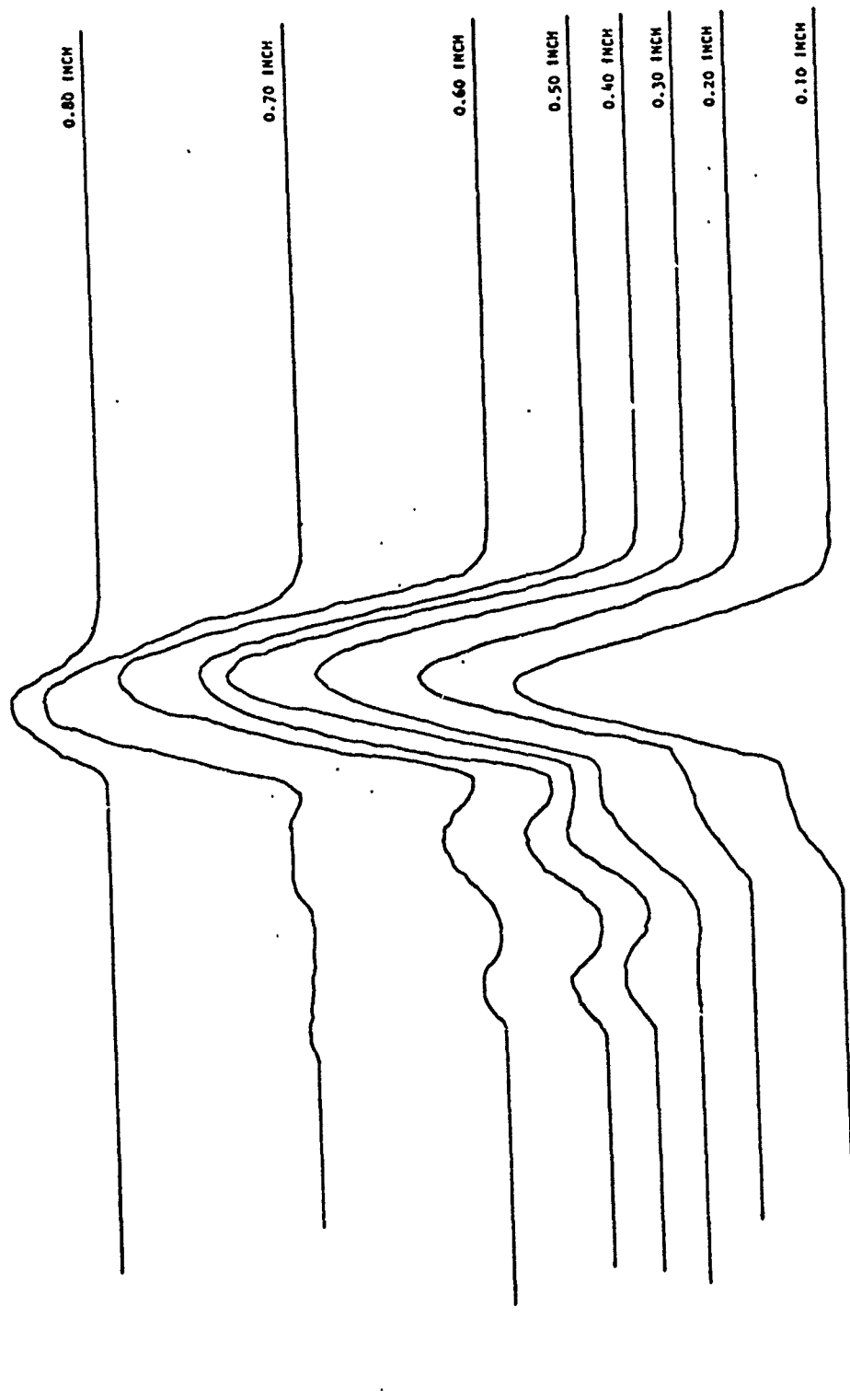


Fig. 166. Power Scan Data for F + n-Butane

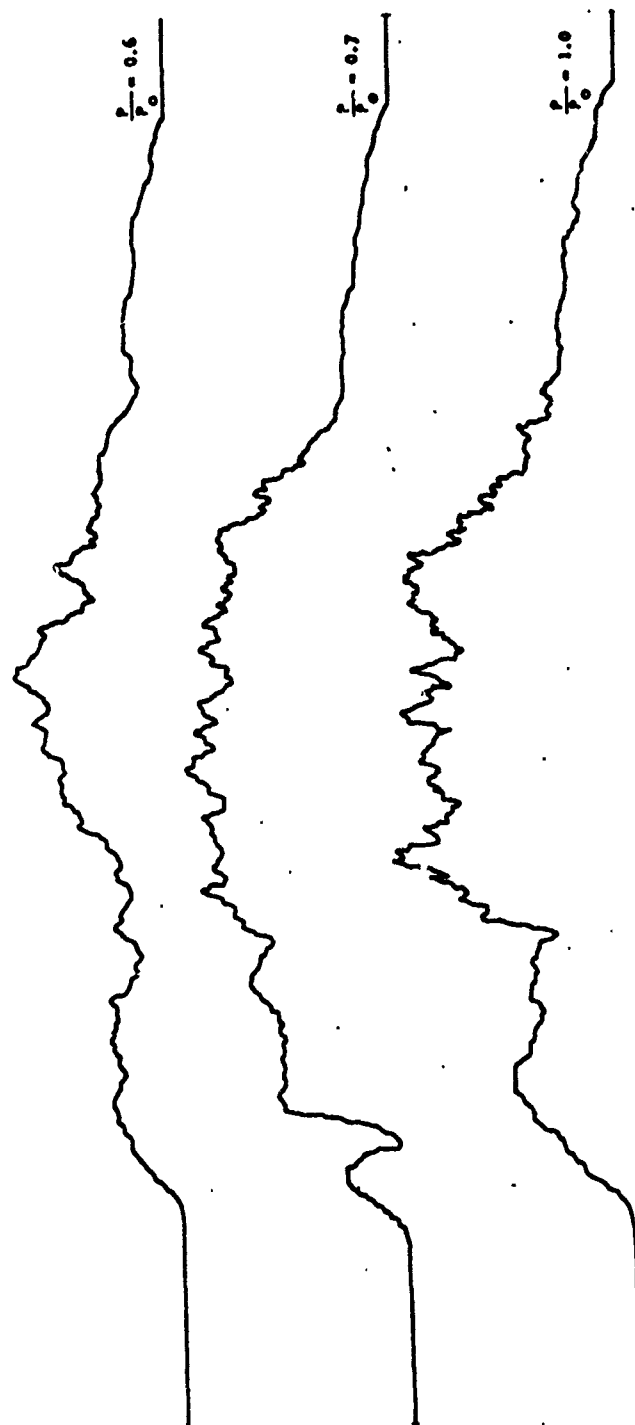


Fig. 167 Power Scan Data for $F + H_2$

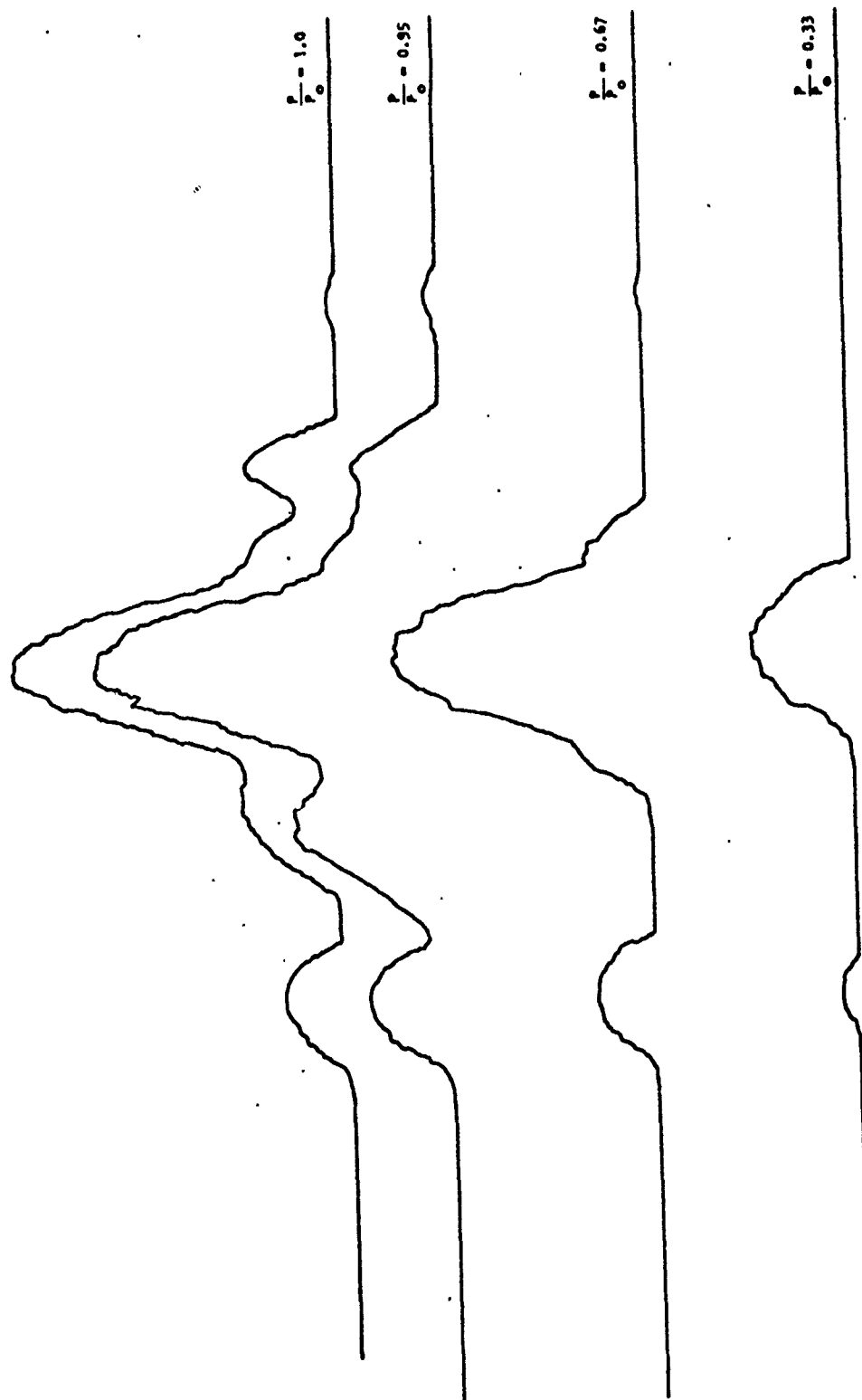


Fig. 168 Power Scan Data for F + n-Propane

streams, as will be discussed later. The scans also show that the outboard nozzles are apparently not identical (Fig. 164 is a good example). In general, the reaction zone downstream of the left-hand nozzle reaches threshold gain earlier than that downstream of the right-hand nozzle, but the zone downstream of the right-hand nozzle maintains gain above threshold longer, thus producing a downstream displacement of the gain region. The reason for this is probably related to a difference in expansion ratios of the two nozzles.

Aperture Experiment. The approximate relative sizes of the mode volume and the reaction region are shown in Fig. 169. With the mode volume centered downstream of an outboard nozzle (position 1), the gain is greater than threshold and output power is obtained as the mode volume is scanned through the medium. Another maxima is observed when the mode volume spans part of the outboard nozzle region and the center nozzle region (position 2). The largest maxima is observed with the mode volume centered above the center cavity fuel nozzle.

To test this hypothesis, a simple aperture experiment was run. In this experiment, an iris was mounted on the 10-meter, gold-coated, water-cooled mirror and the laser volume stepped down until the power outcoupled decreased. Figure 168 shows scans at about 0.25 inch downstream for power reduced by 95 percent, $2/3$ and $1/3$ with propane as the cavity fuel (so that the intracavity flux is relatively small). As the aperture is decreased, the spatial resolution is increased. These results indicate that the above argument is valid. One could say that the peaks observed at position 2 are real and that the aperturing causes them to quench out; however, in comparison with the outboard nozzle peak on the right-hand side of Fig. 168 the position 2 peaks appear much stronger, yet disappear more rapidly. If they were real they would be expected to remain longer as the aperture is decreased. Also, they would not move as indicated in the $P/P_0 = 2/3$ trace. With this understanding of why position 2 peaks occur, the scanning runs are made without aperturing so that lower gain regions may be observed. The $P/P_0 = 1/3$ trace shows that this type of aperturing does decrease gain within the reduced mode volume, thereby requiring greater gain to reach oscillation threshold.

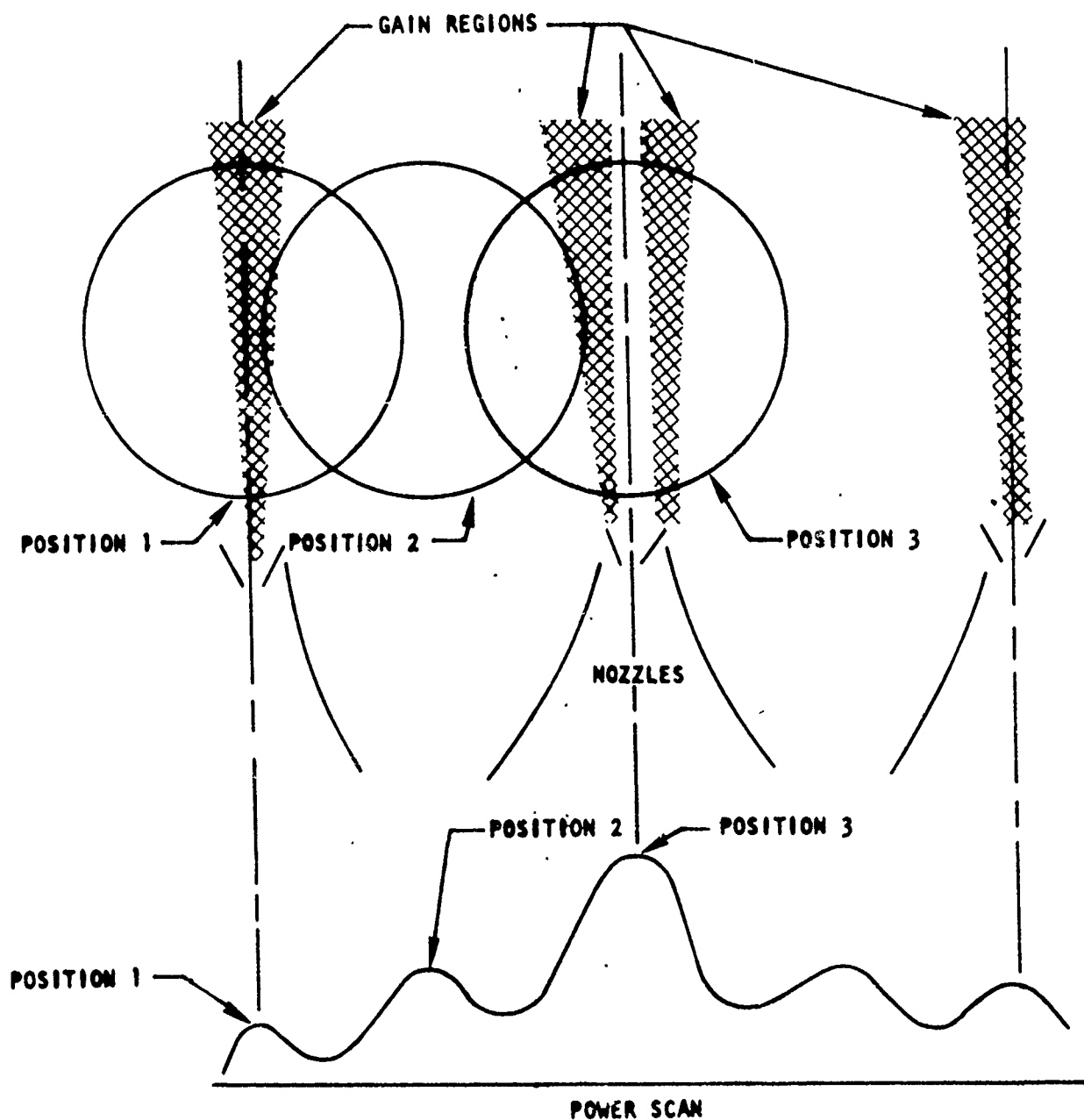


Figure 169. Relative Spatial Positions of Mode Diameter to Gain Regions Giving Maxima in Power Scans

The apparent increase in spatial resolution that is introduced by aperturing the beam below the natural stable resonator beam diameter is intuitive, but not immediately obvious. A schematic of the experiment is shown in Fig. 170. From this figure it is clear that the immediate effect of the aperture is to introduce large diffraction losses as the aperture diameter approaches the natural stable resonator mode diameter. Figure 171 shows the relationship of the natural mode diameter, depicted by a circle, and the gain region indicated by the shaded gaussian distribution. In this figure the center of the gain region is not located at the center of the natural mode volume.

The cross-hatched area shows the extent of the gain region that lies within the mode diameter. As the aperture is closed, introducing greater losses, the oscillation will cease even though part of the gain region is within the mode diameter. To obtain oscillation again, the mode diameter must be moved close to the center of the gain region. The increased losses introduced by the aperture, permitting oscillation to occur only when the center of the natural mode diameter is at the peak of the gain distribution, yields the apparent increased resolution.

Figure 167 shows the results of a partial aperturing experiment run with H_2 as the cavity fuel. The iris is within the optical resonator and the high intracavity flux caused the iris to smoke as the aperture approached the diameter of the natural mode. Because of this, the reduction of the aperture diameter was limited.

Laser Emission Spectra. Laser emission spectra were obtained as described above under Experimental Arrangement. Laser emission spectra have been taken during many runs. Figure 172a through 172d shows a series of laser emission spectra taken as a function of increasing precombustor temperature. As expected, the higher J value transitions reach threshold as the temperature is increased. These spectra were taken with a 5-degree-cant, AR-coated Al_2O_3 window, high-loss cavity/resonator configuration. The general family of lines observed while testing alternate cavity fuels was shown in Table XXIX. No lines other than those shown in this table have been observed for any of the alternate cavity fuels. In general, only some of the lines are observed. As the power outcoupled decreases, the number of lasing lines reduces.

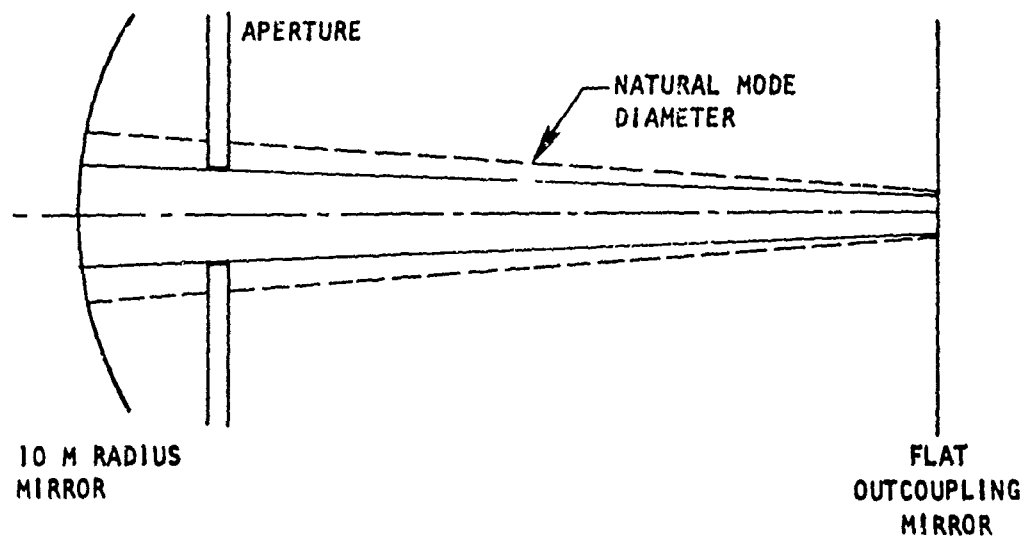


Figure 170. Aperture Experiment Schematic

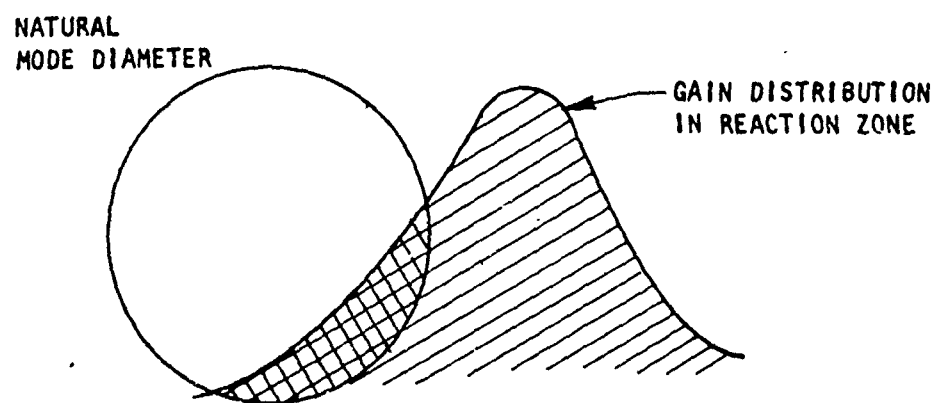


Figure 171. Mode Diameter--Gain Distribution Spatial Relationship Schematic for Aperture Experiment Argument

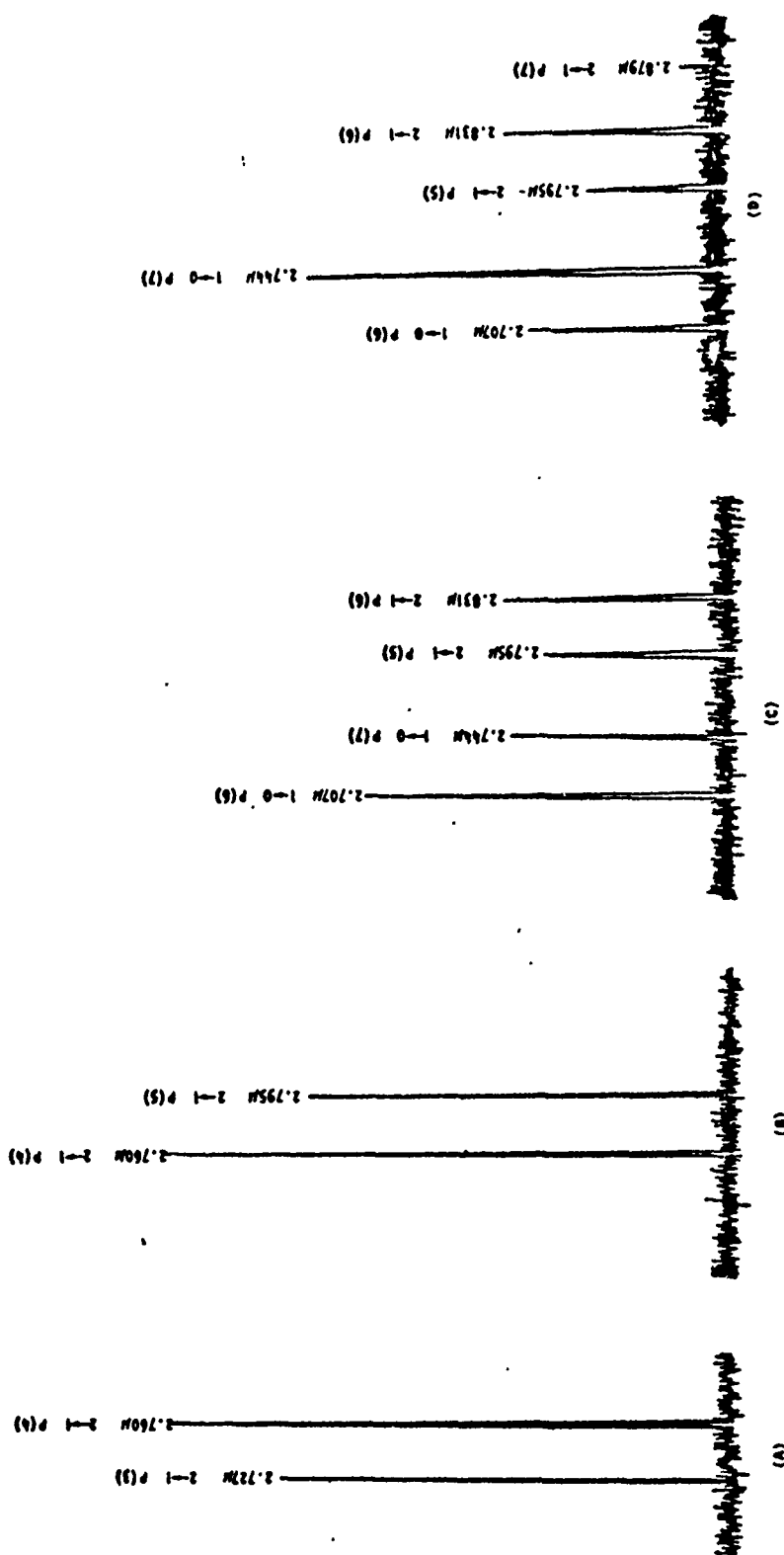


Figure 172. Laser Emission Spectra at 0.25 Inch Downstream With Increasing Precombustor Temperature A Through D

Figures 173 and 174 were taken using the CaF_2 Brewster angle windows and a hole outcoupler as shown in Fig. 175. With the appreciably lower loss cavity/resonator configuration, several additional laser transitions exceed oscillation threshold. The spectra shown in Fig. 173 were obtained 0.25 inch downstream, while the spectra shown in Fig. 174 were obtained 0.90 inch downstream. The lines in these figures marked with a "?" have not yet been positively identified.

The spectrum shown in Fig. 173 was obtained with the resonator structure open to the atmosphere. When the resonator is purged with dry nitrogen, the $1 \rightarrow 0$ P(5) line also lases.

Discussion

The results of the small-scale laser tests when coupled with mixing and deactivating characteristics of the alternate cavity fuels, provide a general picture of the place of alternate cavity fuel in supersonic, mixing chemical lasers. Most importantly, it is evident that the high molecular weight of the alternate cavity fuels inhibits the mixing of the cavity fuel into the F atom-containing stream. In all the alternate cavity fuel scan data, the power distribution is greatly peaked directly downstream of the cavity fuel nozzles. In comparison, the scan data using the baseline cavity fuel H_2 (Fig. 167) indicate a gain region reaction zone of greater extent. If the flow were laminar, the primary mixing mechanism would be diffusion which decreases with the square root of the molecular weight. This factor is 6 for the lightest alternate cavity fuel, so this effect could be quite significant. Whereas, with H_2 , the reaction zone is determined by the extent that H_2 penetrates the F atom stream, the reaction zone associated with an alternate cavity fuel is probably determined by the penetration of the F atoms into the cavity fuel stream. Consequently, the newly formed excited HF is surrounded by cavity fuel molecules. Therefore, performance in this configuration may be highly dependent upon the deactivation rate of HF by cavity fuel molecules given that the pumping rate is sufficiently fast that oscillation threshold gain is exceeded. Table XXX is a listing of room temperature rates for deactivating HF ($v=1$) and overall reaction rates. Most of these have been obtained experimentally.

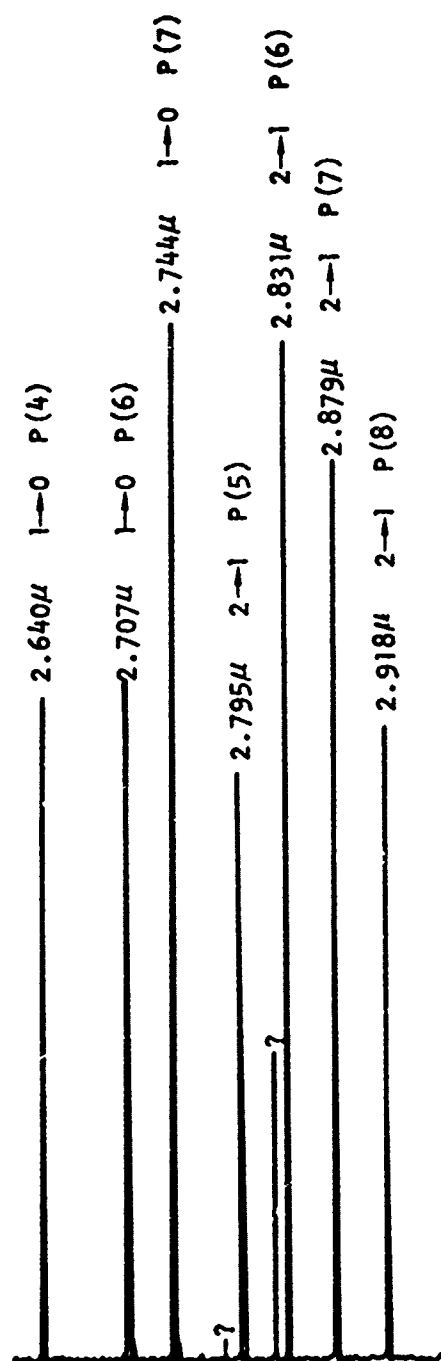


Figure 173. Laser Emission Spectrum 0.25 inch Downstream

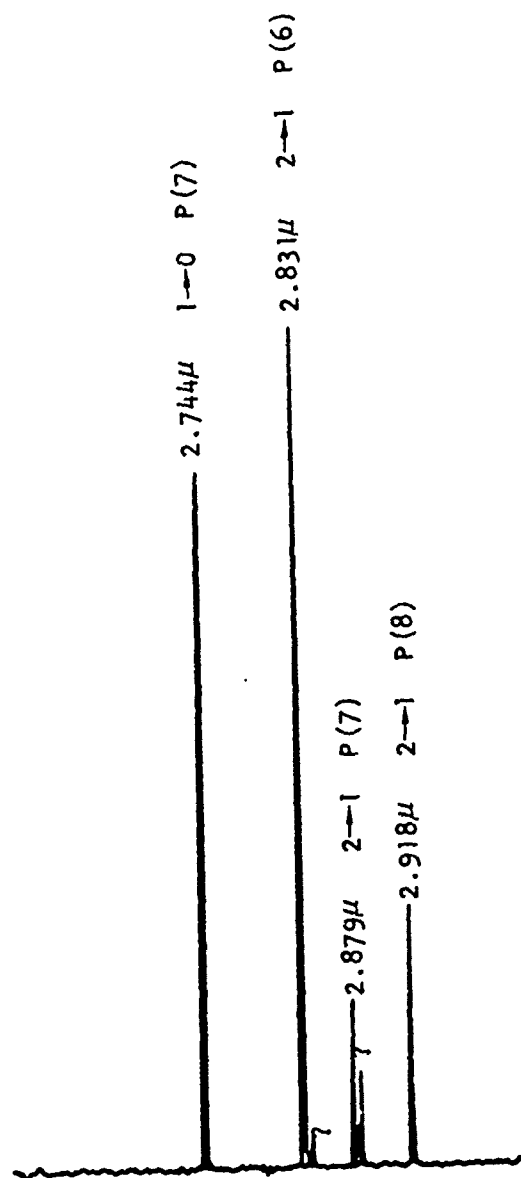


Figure 174. Laser Emission Spectra 0.90 inch Downstream

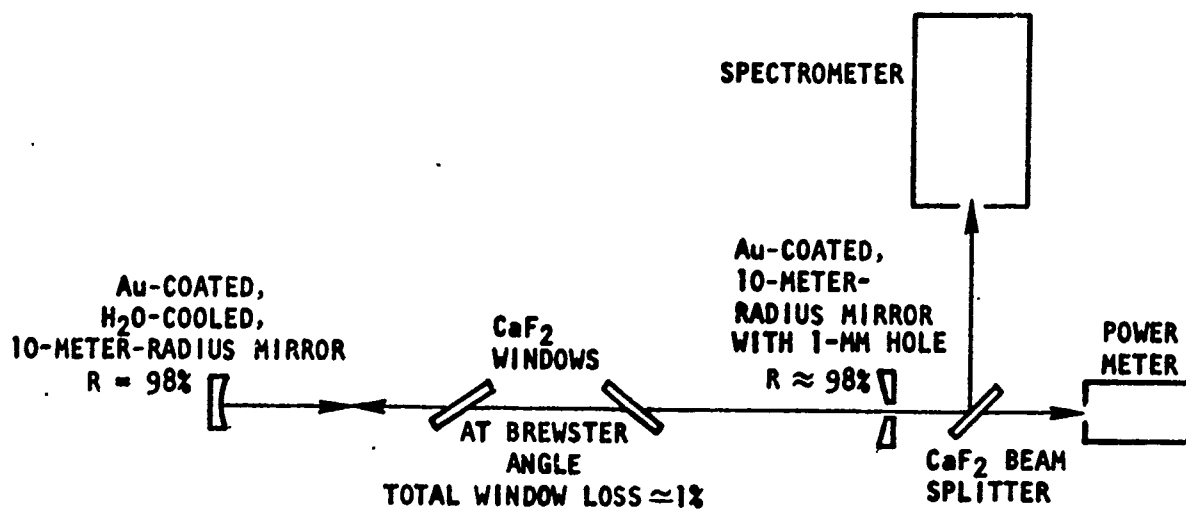


Figure 175. High Q Cavity With Hole Outcoupler Configuration

TABLE XXX. PUMPING, k_g , AND DEACTIVATION RATES
FOR SOME CAVITY FUELS

Fuel	k_g , cm ³ mole ⁻¹ sec ⁻¹	k_d , sec ⁻¹ torr ⁻¹	k_g/k_d , cm ³ mole ⁻¹ torr
n-C ₃ H ₈	3.3 x 10 ¹³	1.4 x 10 ⁶	2.36 x 10 ⁷
n-C ₄ H ₁₀	2.9	1.7 x 10 ⁶	1.71 x 10 ⁷
c-C ₃ H ₆	2.9	3.2 x 10 ⁶	0.90 x 10 ⁷
H ₂	1.0	2.4 x 10 ^{5*}	4.17 x 10 ⁷
HCl	0.9	7.0 x 10 ⁴	1.29 x 10 ⁸
HBr	2.3	7.0 x 10 ³	3.43 x 10 ⁹

*Does not include deactivation by H atom

Hydrocarbon Cavity Fuels. As shown in Table XXX, the deactivation rates of the hydrocarbon cavity fuels are relatively high. This, coupled with the power scan data that show that these cavity fuels apparently do not mix well as H₂, provides an explanation of why the performance indicated by the premixed model is not realized in the test device. Assuming that the concept of role reversal of the two streams (that for the high molecular weight cavity fuels the F atom must diffuse into the cavity fuel stream to form HF) is at least qualitatively correct, then, as mentioned above, the excited HF is in a high local density of rather rapid deactivators decreasing the gain and power available from the active medium. This also explains the behavior noted in the preliminary runs with propane and butane where the power outcoupled increased when the cavity fuel flowrates were decreased. In effect, the decrease in flowrate decreased the local concentration of deactivators with no loss in pumping, thus increasing the gain and power available to lase. Further decrease in flowrate would eventually reduce the pumping rate and thus reduce gain and available power.

If the hydrocarbon cavity fuels are assumed to mix at the same rate, which is probably a reasonable assumption because the disparity in molecular weights is small, under these poor mixing conditions, the relative performance would be

determined by the ratio of the pumping reaction to the deactivating rate, k_g/k_d . This ratio is also given in Table XXX. Based upon this ratio, the relative performance of these fuels should be that n-propane is better than n-butane, which, in turn, should be better than cyclopropane. This is the order indicated by the data (Table XXVII).

The reasons for the lack of lasing found with CF_3H , CF_2ClH , and CH_3OCH_3 have not been completely established. In the case of CF_3H the overall reaction rate for $F + CF_3H \rightarrow HF + CF_3$ is very slow compared to $F + H_2 \rightarrow HF + H$, as reported later in this document. This could be the primary reason for not observing lasing. Because of the structural similarity of CF_2ClH to CF_3H , a slow reaction rate would also be expected and, consequently, would also explain the lack of observed lasing. The abundance of methyl protons on CH_3OCH_3 suggest that the overall reaction rate would be high. In this case, the lack of lasing may be a consequence of an even higher deactivation rate of CH_3OCH_3 compared to n-propane. The presence of a basic site at the O atom in this molecule might promote "sticky" deactivating collisions.

Hydrogen Halides. Power scan data obtained with HCl as the cavity fuel (Fig. 158) gives results that are about the same as for the hydrocarbon fuels that provide gain. Again, the high molecular weight leads to a reduced reaction zone. Based upon the k_g/k_d ratio, HCl would perform better than the hydrocarbons in the test device. As shown in Table XXVII, more power was outcoupled in one mode volume using HCl as the cavity fuel than that obtained with propane.

Preliminary data obtained with HBr as the cavity fuel gave very good results (Table XXVII) in the first experiments. This is consistent with the k_g/k_d ratio of HBr from Table XXX. However, in subsequent tests, the performance with HBr was considerably less than that observed initially. Suspecting contamination of the HBr, a cold trap was put into the HBr line and a cursory run was made. The performance was considerably improved, but still far below the original results. Inspection of the cold trap revealed that considerable material had been trapped, much of it appearing to be H_2O . (Later in this report, where the measurements of the overall reaction rate of $F + HBr$ are described, this also is discussed.) Additional tests were conducted on this compound and are reported and discussed later.

Chemical Analyses. Because of the apparent contamination of the HBr and the quite deleterious effects contaminants could have, chemical analyses were performed on the other cavity fuel reactants. The results of chemical analyses, which were performed by an outside laboratory, of the hydrocarbon alternate cavity fuel candidates are shown in Table XXXI. In all reactants, except cyclopropane, the purity is greater than 99.5 mole percent. The impurities present, in amounts less than 0.5 mole percent, are not species which would have any greater HF* deactivating characteristics than the stipulated reactant, so they would not affect the results. This is also true for cyclopropane, which contains 4.34 mole percent of propylene, which is not expected to deactivate HF* more rapidly than cyclopropane.

TABLE XXXI. RESULTS OF CHEMICAL ANALYSES OF HYDROCARBON CAVITY FUELS*

Fuel	Composition	
	Constituents	Mole Percent
n-C ₃ H ₈	n-C ₃ H ₈	99.893
	C ₂ H ₆	0.034
	C ₃ H ₆	0.073
c-C ₃ H ₆	c-C ₃ H ₆	95.660
	C ₃ H ₆	4.340
n-C ₄ H ₁₀	n-C ₄ H ₁₀	99.542
	i-C ₄ H ₁₀	0.422
	n-C ₃ H ₈	0.036
i-C ₄ H ₁₀	i-C ₄ H ₁₀	99.781
	n-C ₄ H ₁₀	0.091
	n-C ₃ H ₈	0.128
CF ₃ H	CF ₃ H	99.980
	CF ₂ Cl ₂	0.020
CF ₂ ClH	CF ₂ ClH	100.00
CH ₃ OCH ₃	CH ₃ OCH ₃	99.940
	CH ₃ OC ₂ H ₅	0.060

* Performed by West Coast Technical Service Inc., Cerritos, Calif.

PRECOMBUSTOR FUEL EVALUATION

As noted above, the original scope of work for this part of Phase II was to evaluate, through simulation experiments, various precombustor reactant systems deemed acceptable from Phase I thermochemical and kinetic analysis. Most of the reactant systems studied in Phase I contained hydrogen (or deuterium replacement for hydrogen) because the high deactivation rate of H_2 or D_2 was unknown early in the program. However, DF was found by other investigations to have an appreciable deleterious effect on HF performance prior to the initiation of this phase.

Measurements of DF deactivation of excited HF was shown to have a deactivation rate about 50 percent faster than HF V-T deactivation of HF ($v = 1$). This rate is much faster (more than 2 orders of magnitude) than that found for CF_4 , N_2 , and SF_6 . To observe the effect of CF_4 , N_2 , SF_6 , etc., on laser performance, large concentrations of simulants (on the order of 100 times that of DF) would be required to match the relative effects of the DF. Consequently, the approach was modified to find a precombustor fuel other than D_2 to eliminate the formation of DF in the combustor. Fluorocarbon fuels were selected for this effort inasmuch as no DF is formed.

$C_3F_6/F_2/He$ and $C_4F_8/F_2/He$ reactant combinations were experimentally evaluated in combustor tests. Preliminary evaluations were performed in workhorse hardware. Based on the results of these preliminary tests, C_4F_8 was selected for further evaluation because of superior burning characteristics (as noted by higher combustion efficiency and less evidence of sooting in the exhaust stream). Checkout tests with the $C_4F_8/F_2/He$ combination utilizing the lasing hardware were successfully completed. It was found that combustion of the reactants could not be sustained in the presence of diluent injected with the fuel. As a result, a secondary injector was fabricated and evaluated to permit sustained operation. This injector was designed and fabricated for use in follow-up lasing experiments.

Following the characterization of the new precombustor assembly and reactant combination, baseline tests were conducted to ascertain the performance of the CWLL chemical laser using $D_2/F_2/He$ and $C_4F_8/F_2/He$ reactant systems. Laser power,

outcoupled in one mode volume, was measured as a function of position in the active medium, and laser emission spectra were recorded. Hydrogen was used as the cavity fuel.

Effort in this phase principally focused on characterization of the newly developed $C_4F_8/F_2/He$ combination. Following this effort, tests were conducted to evaluate NF_3 as a replacement oxidizer and N_2 as a replacement for helium diluent.

DF-Free Combustor Tests

Selection of Alternate Precombustor Fuels. Several alternate precombustor fuels were considered to evaluate a DF-free precombustor, as listed below:



Of these, both CS_2 and C_6F_6 are liquids at room temperature. These were eliminated from further consideration because available hardware and facilities did not permit liquid system evaluation with minimum effort. $(CN)_2$ was also eliminated for evaluation in this program. This fuel, while having great promise for providing high laser performance, is hazardous to handle due to its severe fire and explosive characteristics. Of the four remaining gaseous fluorocarbons, C_2F_4 and C_2F_6 were eliminated from further consideration. C_2F_4 can be explosive and requires an inhibitor (about 1 percent of $C_{10}H_{16}$) for safe handling. If some of this stabilizer were carried with the C_2F_4 vapor, it would form HF, which is to be avoided. C_2F_6 requires cryogenic storage and was suspected to be a less efficient laser performer due to the reactant's low heat of combustion. As a result, C_3F_6 and/or C_4F_8 were chosen for evaluation as gas reactants. Handling, storage, and delivery features presented no known serious problem with existing facilities and combustor hardware. These materials are nontoxic, noncryogenic, nonexplosive, require no inhibitor, and can be stored as liquid. Vapor pressure at only slightly elevated temperatures would permit evaluation of the reactant as a gas.

Facility Description. Test activities to evaluate DF-free combustors were conducted at TARE stand in the Propulsion Research Area (PRA) of Rocketdynamics Santa Susana Research Laboratories. TARE stand was activated to provide a versatile facility capable of testing baseline H_2 and F_2 reactants, fluorocarbon fuels and F_2 , and fluorocarbons with NF_3 . This last combination is nonhypergolic, and an ignition sequence utilizing F_2 was also provided. Figure 176 presents the stand schematic; within this system is a water heater unit which provides the desired run pressure at elevated temperatures when C_4F_8 is used. (C_4F_8 has insufficient vapor pressure at ambient temperatures.) Also included is an accumulator to provide adequate fuel supply for a 5-second run duration. C_3F_8 flow capability is provided by simply teeing this system into the main fuel storage system line. The combustor was mounted horizontally (Fig. 177). Propellant and diluent supply pressure were set by motorized loaders/regulators in conjunction with electrically operated tank vent and control valves. Purge pressures were set with hand loaders. Firing sequencing was controlled through an electronic sequencer from the blockhouse.

Pressures were measured with bonded strain-gage transducers (Taber Teledyne). Chamber pressure was measured at two positions in the chamber in all tests. Liquid water coolant flowrates were measured by means of turbine flowmeters. The gaseous propellant flowrate was measured by sonic venturi meters. Temperature was measured using iron-constantan thermocouples. Transducer calibrations were employed to obtain appropriate factors for test data reduction.

Pressure transducers were calibrated end to end by mounting them on stand manifolds in which pressures are read with high-precision Heise-Bourdon tube gages. The latter is calibrated periodically on a Ruska deadweight testers. All pressure transducers had a four-time calibration at the start of the test program with the length of pickup line from pressure tap to transducer minimized. The turbine flowmeters were calibrated prior to the initial test and the sonic venturi meters were calibrated by the manufacturer to determine the discharge coefficient (C_D).

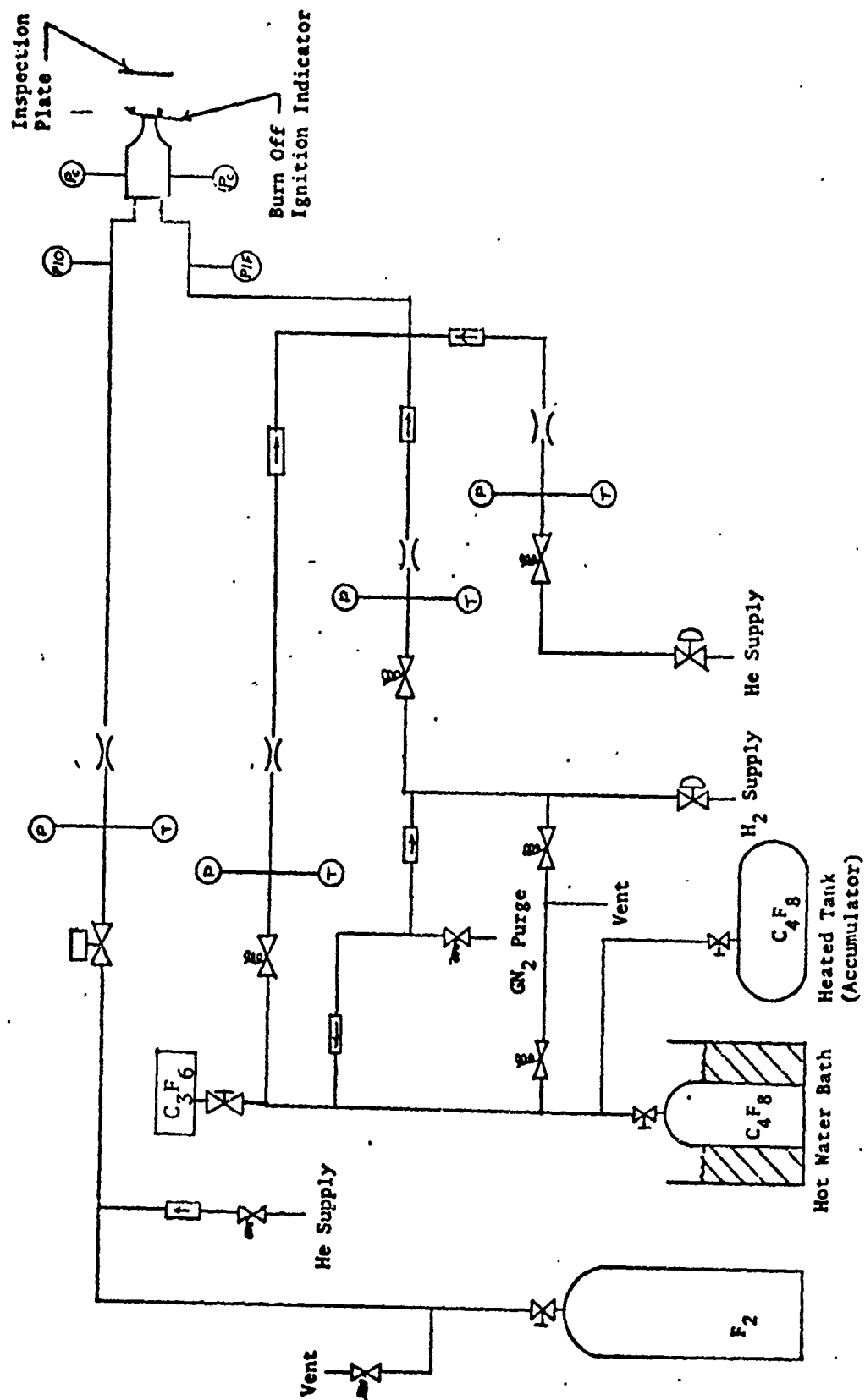


Figure 176. Facility Flow Schematic, TARE Stand



4LC34-12/10/73-S1A

Figure 177. TARE Facility (PRA)

Thermocouples were used on the basis of the standard NBS millivolt/temperature tables and thermocouple recorders were electrically calibrated. The following auxiliary recording systems were employed:

1. An 8-channel, Brush, Mark 200 recorder was employed in conjunction with a Beckman unit, primarily to establish time intervals for computer data reduction and, additionally, for "quick-look" information on the most important parameters. This is a direct-inking system, with display on high-gloss, graduated paper moving at 20 mm/sec.
2. Direct-inking graphic recorders (DIGR's), either Dynalog rotary chart or Esterline-Angus strip chart, were used to set prerun propellant supply pressures, for recording of propellant manifold pressures, to provide quick-look information, and as secondary backup to the Beckman and oscillograph recorders.
3. An Esterline-Angus, 20-channel event recorder was used for direct-inking recording of main propellant valve signal and travel; as well as for chart drive and camera actuations.

Combustor Hardware. The basic combustor hardware associated with the small-scale laser test device was described in "Experimental Apparatus." For the combustor testing of alternate fuels to develop a DF-free combustor, additional combustor hardware was utilized as described below.

Workhorse Hardware. Four workhorse components were available to support this test program: (1) a copper, single-element triplet injector; (2) a copper, uncooled combustor; (3) a stainless-steel, uncooled combustor; and (4) a water-cooled, copper nozzle.

The copper, single-element triplet injector (Fig. 178) was utilized in early experiments to provide optimum mixing of the gas/gas reactants when used in conjunction with the uncooled stainless-steel combustor (Fig. 179). Heat loss data with this configuration are unavailable; however, assumed heat losses at given flow conditions were determined from available heat flux data on similar hardware where empirical data were available.

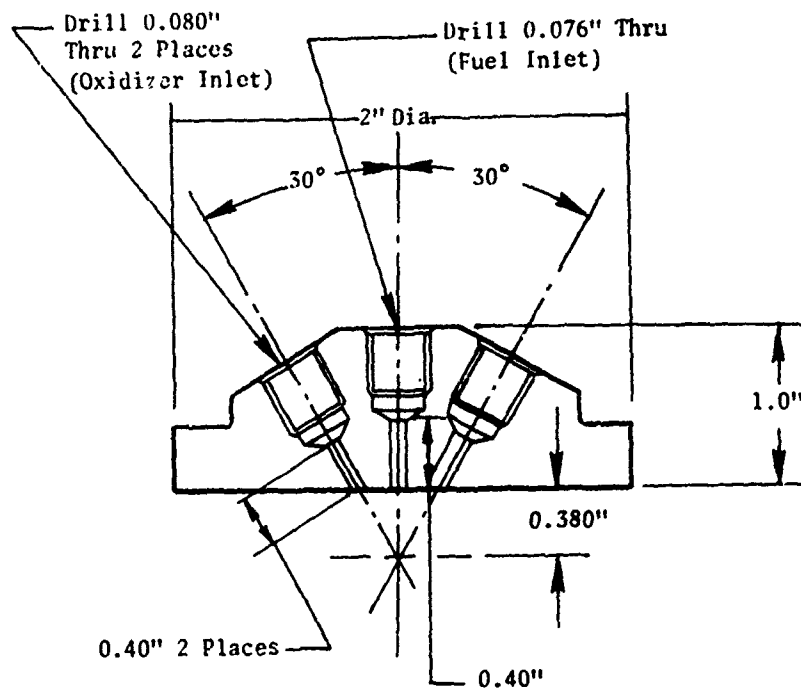


Figure 178. Experimental Copper Injector

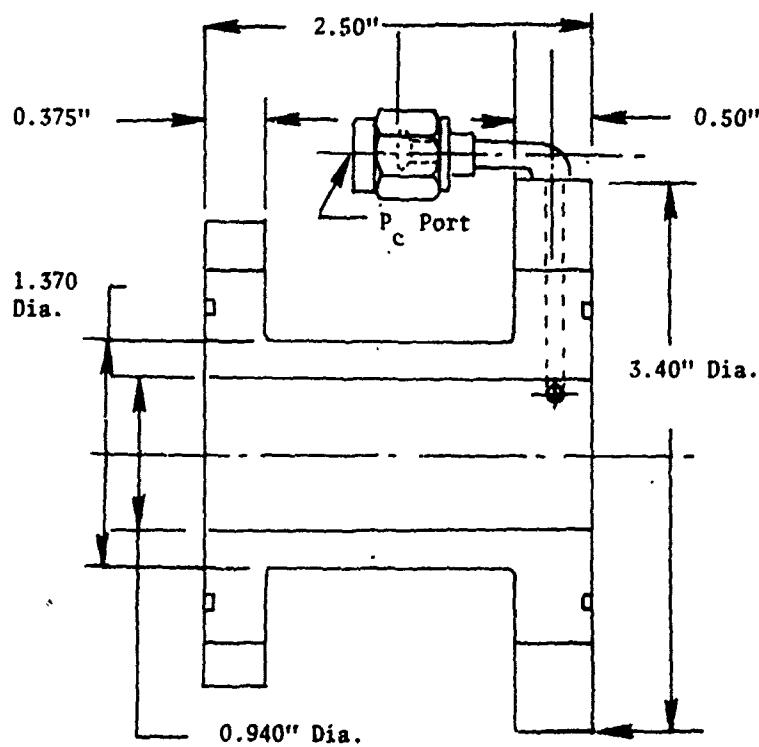


Figure 179. Precombustor Assembly, Uncooled
Material: 304L CRES

An uncooled, copper combustor assembly (Fig. 180 and 181) was also utilized in this program with an upstream configuration identical to the regenerative/dump-cooled combustor. With this component, the concentric element injector could be evaluated prior to receipt of the sophisticated regenerative/dump-cooled combustor.

The last additional workhorse component utilized in this program was a water-cooled, three-element nozzle (Fig. 182). The flow characteristic of this nozzle is matched to the Baseline 30 nozzle array and was utilized in many of the original tests.

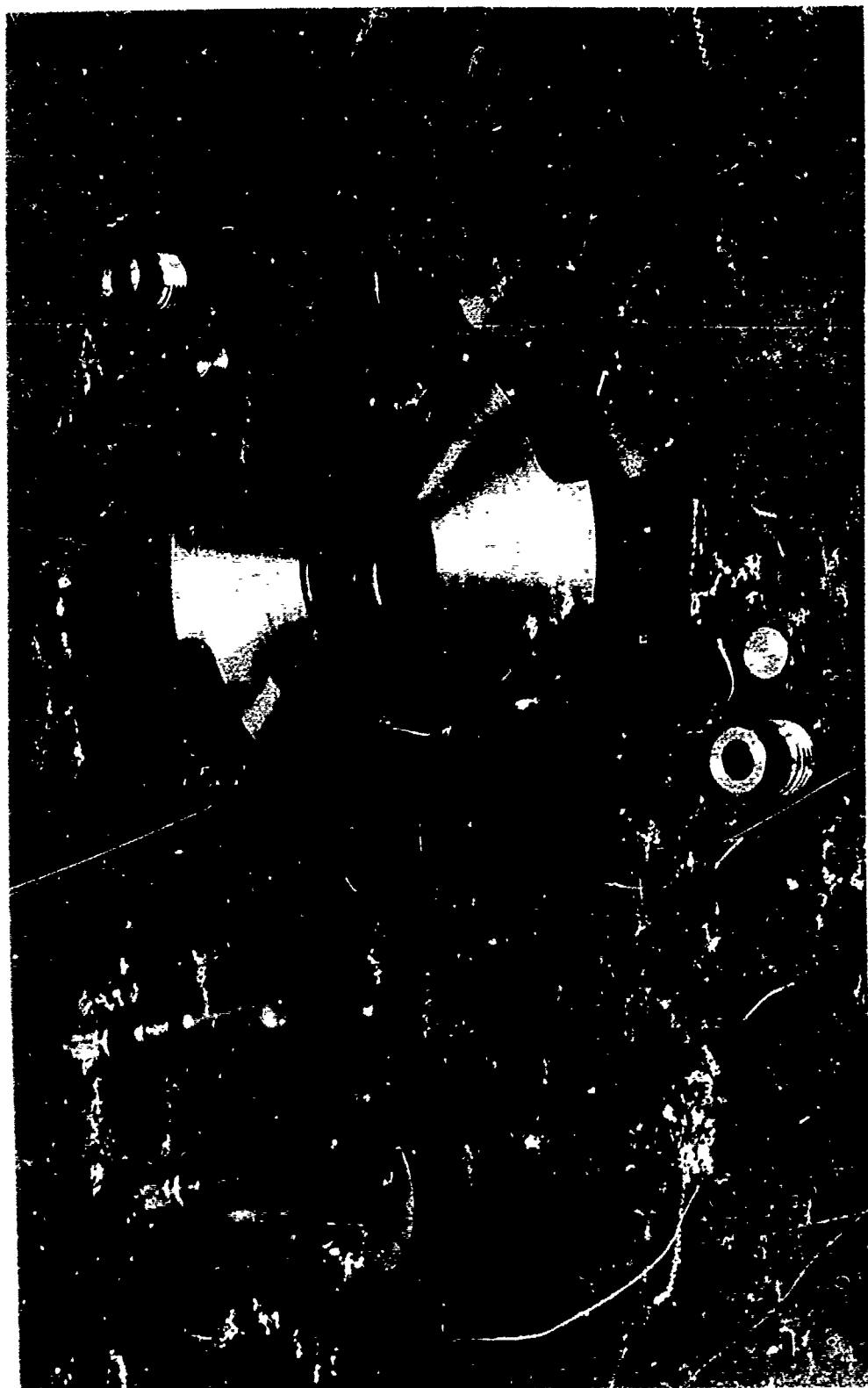
Secondary Injector. During the course of the test program, the need for staged diluent injection became apparent. Instabilities and quenching occurred upon introduction of the helium stream. To provide for adequate operation, a staging injector (Fig. 183) was fabricated for use. This component is installed between the combustor and nozzle array. Approximately 1 inch of mixing length is provided downstream of the second and last row of elements. The element configuration is designed to place one-fourth of the total flow into the center of each quadrant of the combustor cross section. Cooling is provided by regenerative flow of the diluent and some heat extraction by the H₂O coolant of the adjacent components. As a result, very little additional heat loss is introduced into the assembly by incorporation of this component.

Data Reduction Technique/Description. For laser operation, composition of the products of combustion in the fluorine nozzle are required, and can be determined only if the driving pressure and nozzle inlet temperature are known. In addition, the unburned/undissociated reactants are required. To provide this information, the following procedure was employed:

1. Flowrates, heat losses, and chamber pressure are directly measured and are provided for each test.
2. c^* is determined by the relation^①

$$c^* = \frac{P_c A_t}{\dot{w}_t}$$

^①See nomenclature listing for symbol definitions



5AJ43-8/14/72-C2D*

Figure 181. Copper Combustor

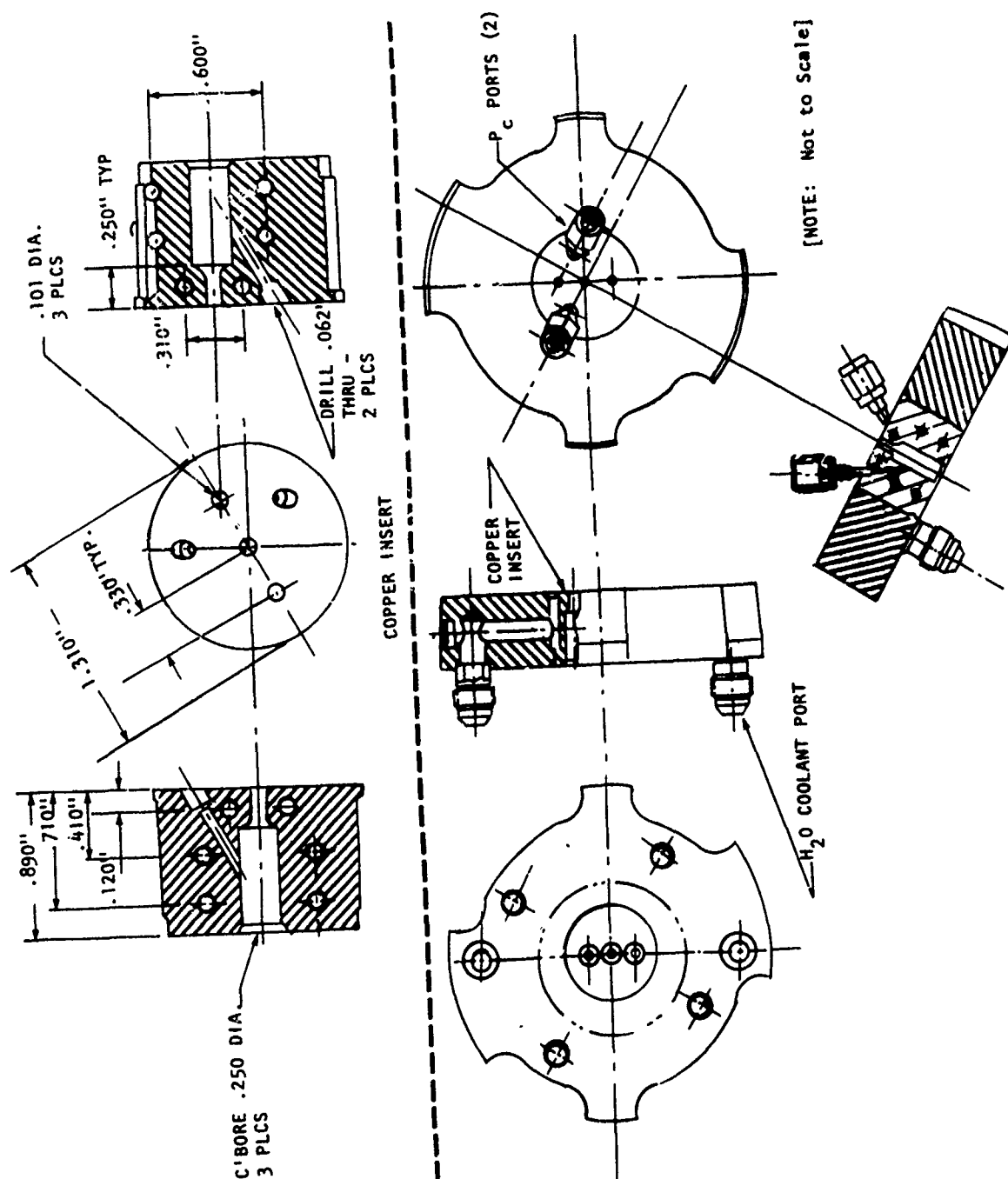


Figure 182. H₂O Cooled Copper Workhorse Nozzle

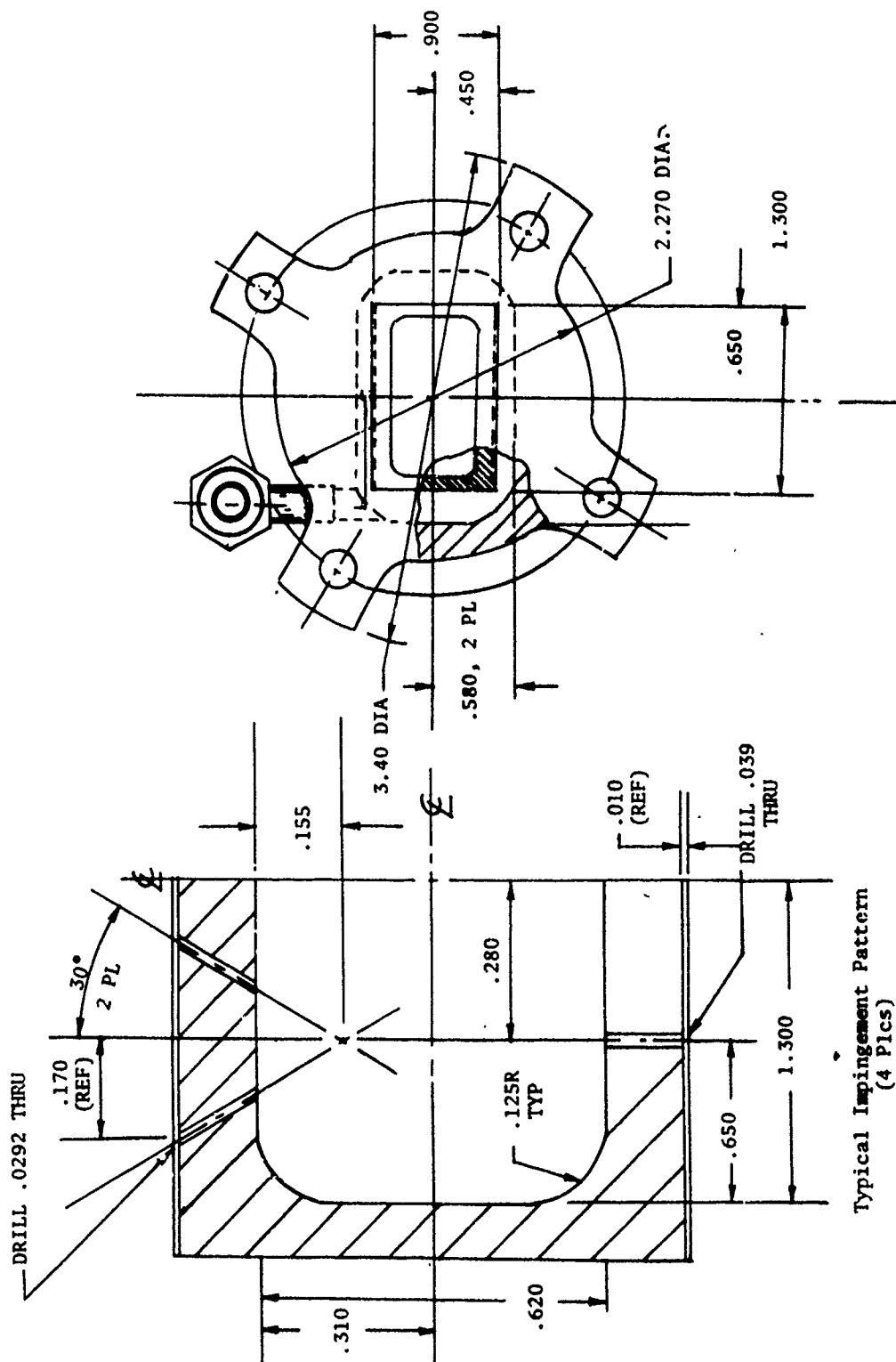


Figure 183. Secondary (Staging) Diluent Injector, CWLL

where:

- P_c = a measured value averaged between two Taber 0- to 100-psia transducer outputs
- A_t = the cold-flow area based on cold GN_2 blowdowns with constant applied boundary layer
- \dot{w}_t = the total flow of the system summed by three flow-control devices, one on each gas-flow line
- c^*_{theo} = either the frozen or full shifting theoretical c^* value from Rocketdyne's η -element program which has been utilized in nearly all of Rocketdyne's rocket engine test programs

The theoretical c^* value is generated with and without heat loss corrections. Efficiency quantities are then determined as a measure of the injector mixing/reactant burning to completion efficiency.

3. Combustor efficiency is defined as:

$$\eta_{c^*_{uncorr}} \equiv \frac{c^*_{act}}{c^*_{theo}} \text{ (no heat loss correction)}$$

and

$$\eta_{c^*_{corr}} \equiv \frac{c^*_{act}}{c^*_{theo}} \text{ (with heat loss correction)}$$

and c^*_{theo} is generated for full-shifting composition unless otherwise noted

- 4. The nozzle stagnation temperature, T_o^F , is determined by the η -element shifting program, having been calculated based on an energy balance of heats of combustion, heat losses, pressures, reactants, dissociation, and recombination.
- 5. The products are determined by the same energy balance program, from which β , MW, γ , C_p , α and $F_{2_{avail}}$ are determined.

$C_3F_6/F_2/He$ Reactant Combination Evaluation. Combustion tests were initiated to assess ignition, performance, and heat transfer characteristics of C_3F_6 when used in combination with fluorine (F_2) and helium (He). The combustor assembly employed in these tests consisted of a two-element (concentric) injector (Fig. 135 and 136), an uncooled copper chamber, and a water-cooled workhorse nozzle.

Conventional strain-gage pressure transducers were used for all pressure measurements. Temperatures were determined with either iron-constantan or chromel-alumel thermocouples. Gas flows were metered through conventional sonic nozzles, while the nozzle coolant flowrate was measured with a conventional turbine-type meter.

Initial checkout tests were conducted using a short ignition lead of gaseous hydrogen to initial combustion. Results indicated that the F_2/C_3F_6 reaction could be initiated and sustained at the mixture ratio evaluated and subsequent data tests were conducted without auxiliary hydrogen. Four tests of approximately 3 seconds duration were conducted (tests 4 through 7, Table XXXII). Run duration was minimized to preclude overheating the uncooled chamber. For these four initial tests (No. 4 through 7), the flow-control orifice was located approximately 18 inches upstream of the fuel main valve. To reach steady operation, up to 3 seconds of run time is required. (The data slice quoted was immediately prior to shutdown.) As such, the fuel flowrate quoted for these tests could be lower than the actual flowrate achieved. The nominal corrected c^* efficiency quoted for these tests is nominally 75 percent. Posttest examination of the combustor interior disclosed substantial carbon buildup of a sooty consistency.

Because of these preliminary test results, two additional tests (No. 8 and 9) of approximately 5 seconds duration were conducted to verify the operation of the combustor and performance characteristics of the C_3F_6 . Before testing, the C_3F_6 flow system was modified to incorporate a larger diameter supply line and a reduced distance between the sonic nozzle and main valve. These modifications were designed to more fully ensure a constant flow of C_3F_6 to the combustor which appeared erratic due to the high pressure, uncontrolled gas present between the flow-control orifice and main valve. Modifications reduced the volume to one-sixth the original volume so that flow control was reached in approximately 0.5 second.

To verify combustor operation, test No. 8 was conducted using H_2 instead of C_3F_6 . The resulting calculated corrected c^* efficiency value of 91.0 percent indicated somewhat lower performance than data obtained from previous testing (see $H_2/F_2/He$ Baseline tests) using the same type of injector and the same nozzle. However,

TABLE XXXII. $C_3F_6/F_2/He$ TEST DATA

Test No.	\dot{W}_{F_2} , gm/sec	$\dot{W}_{C_3F_6}$, gm/sec	\dot{W}_{He} , gm/sec	\dot{W}_{tot} , gm/sec	He , percent	P_c , psia	$C_{p,act}$, ft/sec	$C_{p,theo}$, ft/sec	$\eta_{c,uncorr}$, percent	$\eta_{c,corr}$, percent	T_F , °K	Q_c , cal/sec	Q_h , cal/sec	Q_t , cal/sec	B_c , MW	γ	C_p , Btu/gm-mole	α	$F_{2,avail}$, gm/sec	Comments
1																				
2	2.68	0.88	0.93	3.05	20.7	20														
3																				
4	5.38	1.54	1.81	3.48	8.78	20.6	2465	3944	62.5	73.6	876	~728	~292	~1020	4.1	14.5	6.51	0.07	1.9	Heat Transfer Data Assumed - Not recorded due to facility malfunction
5	5.14	1.61	1.63	3.19	8.38	19.5	2518	3943	63.8	74.1	924	~728	~292	~1020	4.0	15.1	6.67	0.12	1.8	
6	4.77	1.67	1.33	2.86	7.77	17.1	26.6	2665	67.7	78.9	978	~728	~292	~1020	3.6	16.3	6.87	0.20	1.6	
7	4.50	1.81	1.05	2.49	7.36	14.3	26.2	2751	69.8	81.7	1057	~728	~292	~1020	3.2	17.9	7.14	0.37	1.4	
8	4.40	0.12 (He_2)	1.05	39.6	5.56	18.9	31.5	4375	73.5	91.0	1464	799	512	1311	4.7	11.3	5.65	0.98	1.0	Heat Transfer Data Assumed - Not recorded due to facility malfunction
9	4.33	1.80	1.05	2.40	7.18	14.6	29.0	3121	78.2	91.5	1066	728	292	1020	3.4	17.7	7.13	0.38	1.3	
10	6.51	2.85	0	2.28	5.36	0	29.8	2458	70.5	85.1	1415	~728	~292	~1020	0.34	9	9.47	0.84	2.0	
11	5.24	2.69	0	1.95	7.83	0	27.0	2662	68.8	85.8	1642	~728	~292	~1020	0.36	11.25	9.95	0.97	1.9	
12	5.13	2.58	0.65	1.99	8.36	7.8	31.4	2900	71.0	84.8	1350	~728	~292	~1020	1.9	22.8	7.90	0.83	2.0	Heat Transfer Data Assumed - Not recorded due to facility malfunction
13	4.57	1.99	1.1	2.30	7.66	14.4	29.8	3005	74.4	86.4	1112	~728	~292	~1020	3.4	17.7	7.14	0.45	1.4	
14	4.50	0.12 (He_2)	1.1	38.8	5.72	19.2	32.5	4387	75.1	96.6	1306	~799	~512	~1311	4.5	11.3	5.89	0.94	1.0	

the uncooled copper chamber heat loss was determined by a temperature measurement placed into the cutout segment of this assembly (Fig. 180). A heat flux value was calculated by the isolation pad temperature rise. Extrapolating this presumed average heat flux over the entire mass permitted the determination of the total heat loss. Heat loss calculations made for this test compare favorably with measurement made in the $H_2/F_2/He$ checkout series; however, the corrected η_{c*} value for this "baseline" test is approximately 8 percent lower than previously determined and may be due to the rather short-duration test measurement of isolation pad temperature rise.

Test No. 9, using C_3F_6 as the fuel, resulted in a calculated corrected c^* efficiency of 91.5 percent. A comparison of the chamber pressure traces, as shown in Fig. 184, shows that the combination of $F_2/H_2/He$ of test No. 8 produced a very stable P_c trace, while the $F_2/C_3F_6/He$ combination in test No. 9 exhibited oscillations (24 Hz). These results suggest that the combustor itself is performing nominally, while the combination of F_2/C_3F_6 results in instability. Substantial carbon buildup was once again noted.

From these checkout tests, it was concluded that: (1) a reaction between F_2 and C_3F_6 could be initiated and sustained but combustion was unstable and appreciable amounts of soot were formed, and (2) additional testing over a wider operating range should be conducted to confirm the preceding observations.

For tests No. 10 through 14, a new unlike-impinging triplet, copper injector (Fig. 185) was designed for optimum mixing at a single nominal test condition. In addition, a simple matching chamber was also designed for use with the new injector (see Workhorse Hardware description).

Five tests of approximately 5 seconds each were conducted. The initial two tests were conducted with F_2/C_3F_6 and no helium dilution. The next two tests were with $F_2/C_3F_6/He$, in which the latter was at a specific operating condition closer to where the injector was optimized. Finally, the last test was conducted with $F_2/H_2/He$ as a reference base for performance comparison and for verification of performance consistency with previous test results.

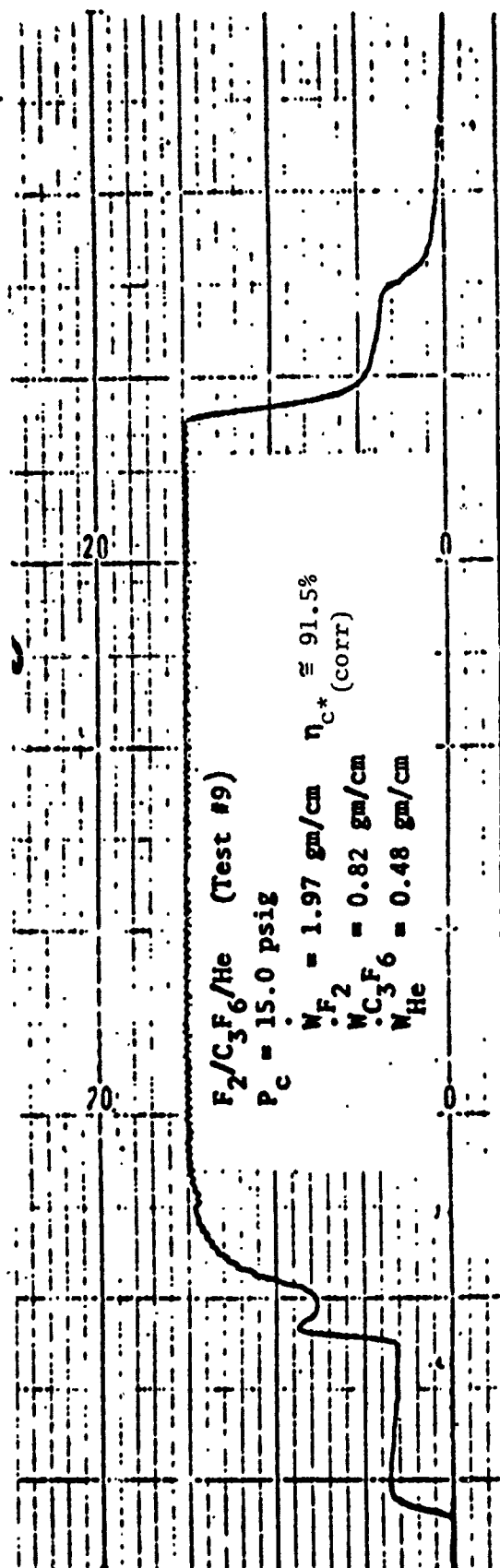
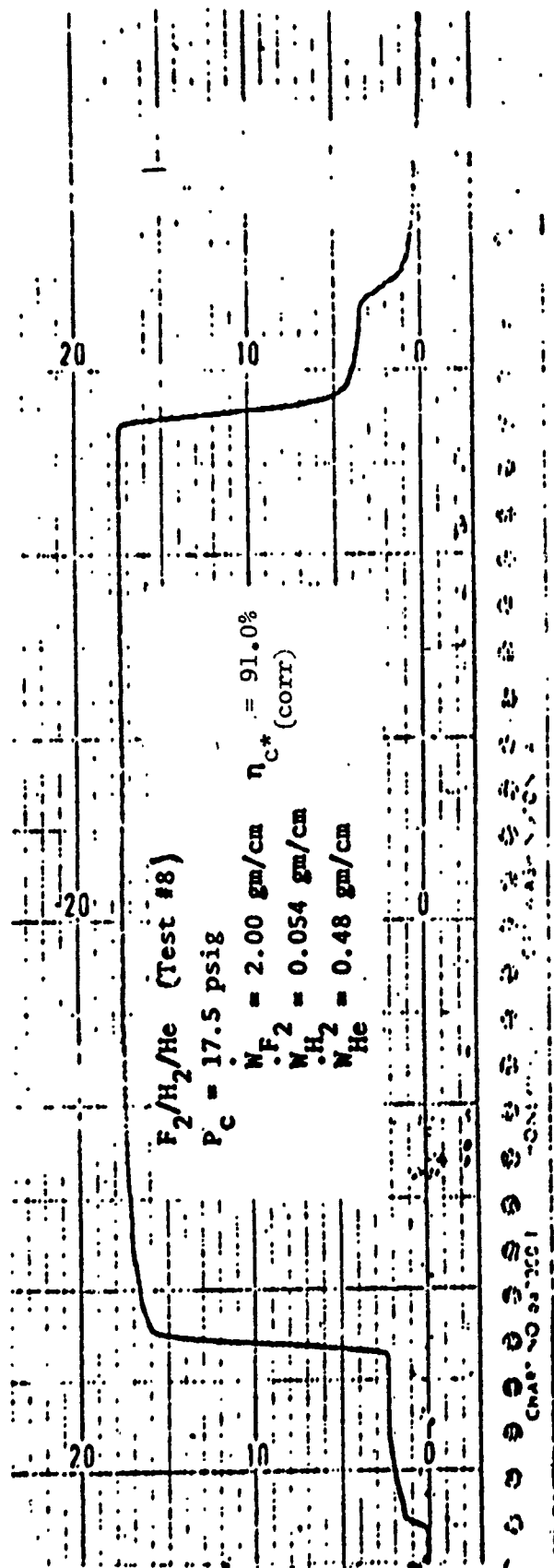


Figure 184. Comparative Chamber Pressure Traces for $F_2/H_2/He$ and $F_2/C_3F_6/He$ Tests With CWLL Combustor

Oxid. Dia. = .076"
 Fuel Dia. = .080"

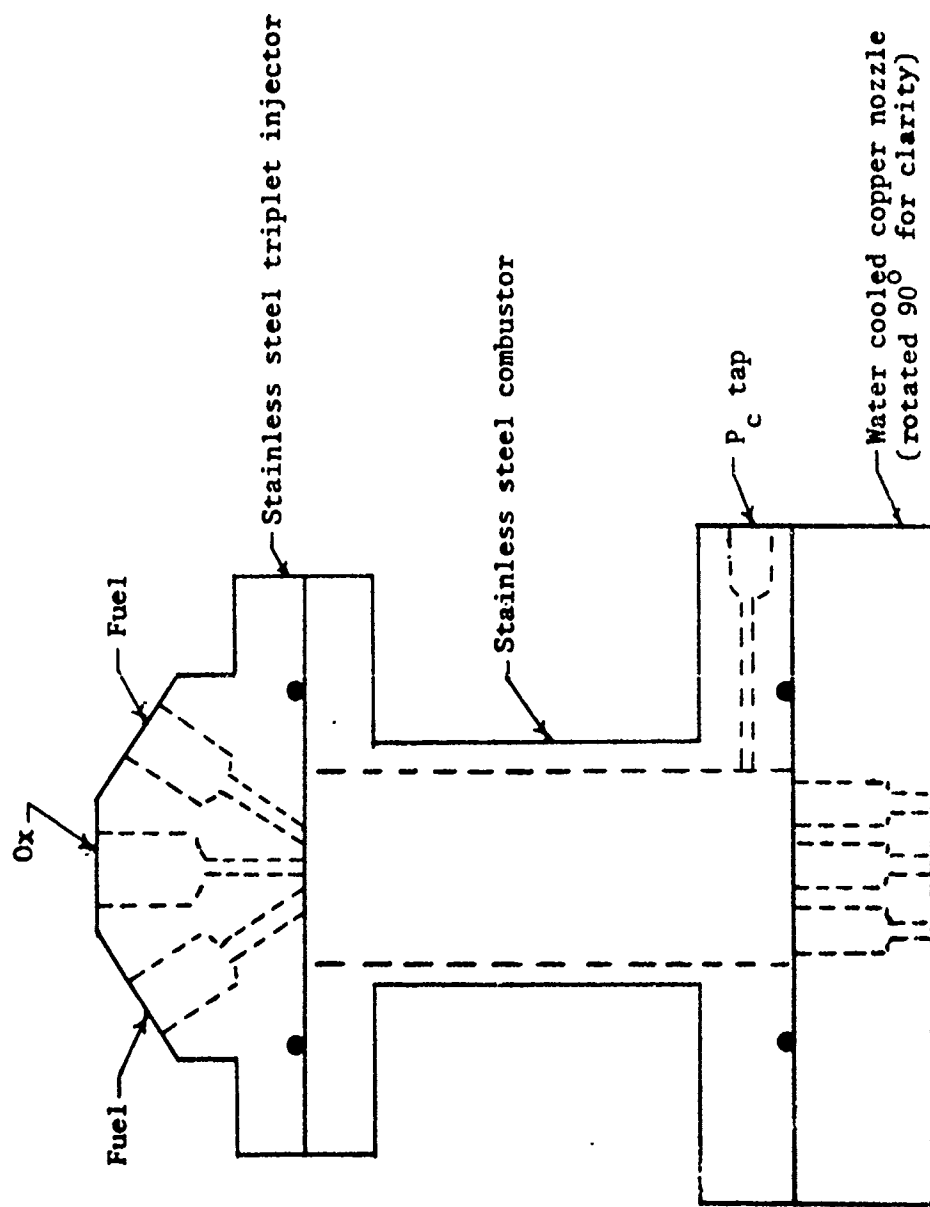


Figure 185. Schematic of Injector, Combustor, and Nozzle Used in Tests 10 Through 14 (C_3F_6)

The results of the five tests are outlined in Table XXXII. Test conditions for the $C_3F_6/F_2/He$ tests were well above the nominal stoichiometric condition for F_2/C_3F_6 . The calculated corrected c^* efficiencies for these tests were nominally 85 percent.

The results of tests 12 and 13, which were without helium dilution, indicated the same order c^* efficiency (and similar temperature degradation) as for neat operation. It should be noted that test 13 was the operating condition for which the injector mixing characteristics were more closely optimized. The level of performance (~ 86 percent) for these tests appears to be approximately nominal for this reactant combination.

Finally, the last test was conducted with $F_2/H_2/He$ (no C_3F_6) to establish a performance reference with the preceding four tests and with those previously conducted with equivalent combustor configurations. The indicated c^* efficiency of ~ 97 percent appears consistent with those conducted with the original concentric orifice CWLL configuration.

The chamber pressure traces for the five tests were compared. Tests using $F_2/C_3F_6/He$ with 7.8 percent or less helium dilution did not exhibit any oscillations. When the helium dilution was increased to 14.4 percent by weight, oscillations (24 Hz) as shown in Fig. 186 occurred. Test 14 using $F_2/H_2/He$ with 19.2-percent helium dilution did not exhibit oscillations.

Posttest examination of the combustor interior disclosed a substantial carbon deposit on the injector face and chamber walls. This buildup was also present in the previous series of tests and is indicative of reduced $F_2/C_3F_6/He$ combustion efficiency since, under the normally F_2 -rich operating conditions, little free carbon should be present.

The results of these supplementary experiments clearly indicate the performance characteristic for F_2/C_3F_6 and $F_2/C_3F_6/He$ is reduced by ~ 10 percent in comparison with those observed with $F_2/H_2/He$. There is some speculation that C_3F_6 may be decomposing ($2 C_3F_6 \rightarrow 3 CF_4 + 3C$) and that subsequent carbon reaction with F_2 results in reduced performance.

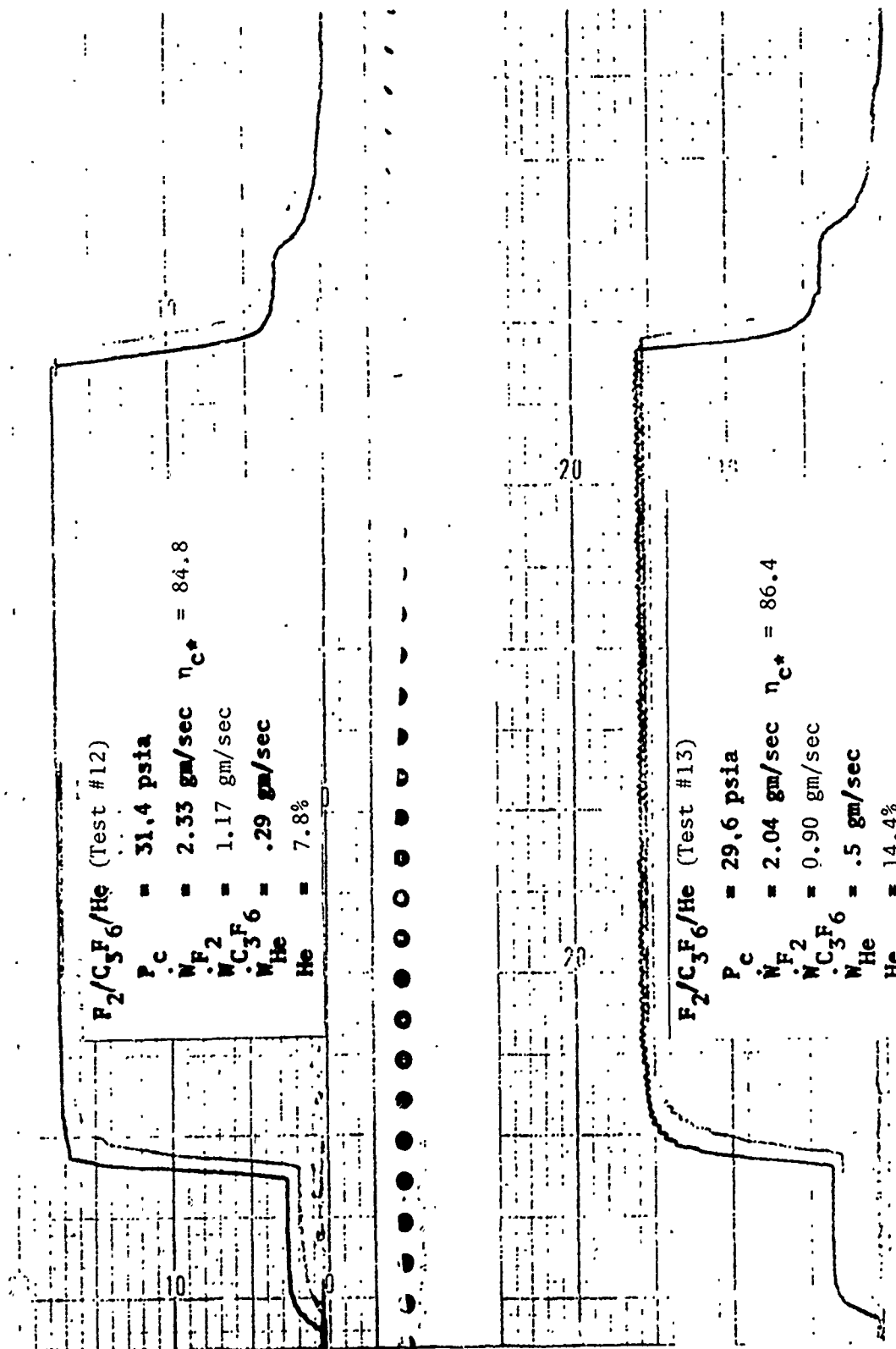


Figure 186. Comparative Chamber Pressure Traces for $F_2/C_3F_6/He$ Tests With 5.9 and 11.6 Percent Helium Solution

These results show that hypergolic combustion between F_2 and an unsaturated fluorocarbon can be obtained. However, the reduced combustion efficiency of C_3F_6 , the excessive soot level and the instability with helium dilution, suggests a need to seek a different fluorocarbon fuel that will provide improved overall characteristics.

$C_4F_8/F_2/He$ Reactant Combination Evaluation. A review of fluorocarbons available for test evaluation at this time indicated that C_4F_8 could be utilized in the combustor test activity. C_4F_8 has similar theoretical thermochemical performance as C_3F_6 when reacted with F_2 and diluted with helium. However, burner test results at AFRPL-EAFB indicated that the fluorocarbon C_4F_8 might burn "cleaner" than the C_3F_6 fluorocarbon and, as a result, might also achieve higher combustion efficiencies in the CWLL subscale hardware. Therefore, effort to provide a DF-free combustor was revised from burning $C_3F_8/F_2/He$ to $C_4F_8/F_2/He$.

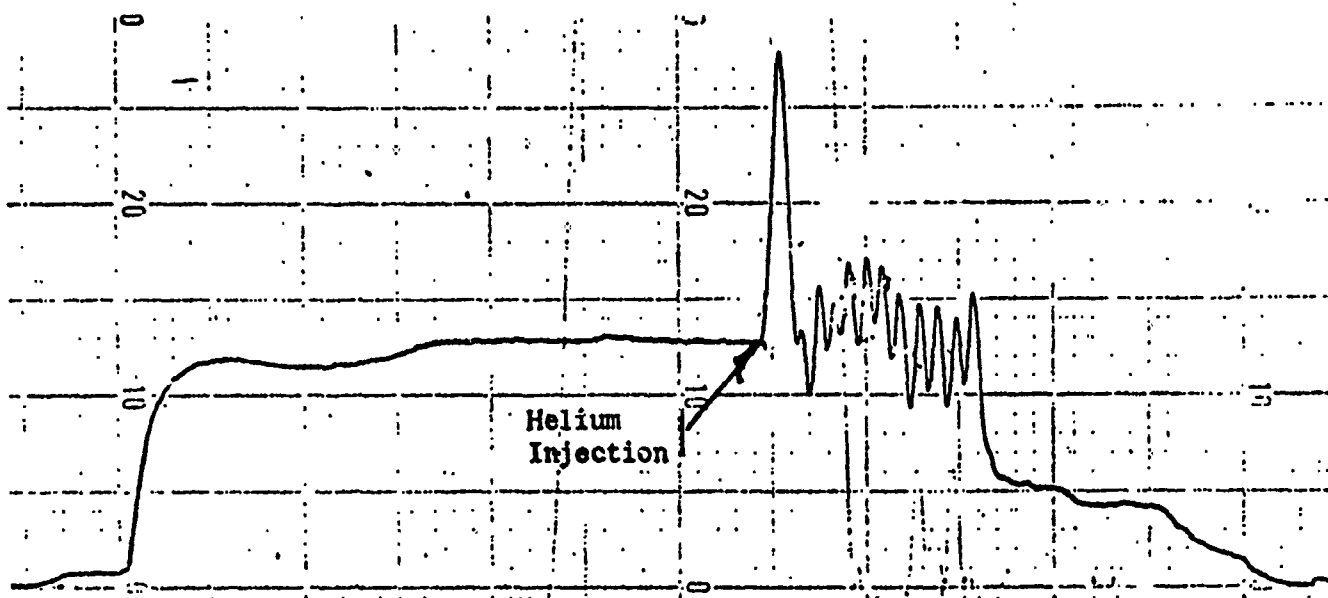
Test activity was then initiated employing the F_2/C_4F_8 propellant combination. Tests 1 through 11 (Table XXXIII) were conducted to verify test procedures and adequacy of the data acquisition system. Tests 12 through 25 were conducted to evaluate the operation of C_4F_8 and F_2 . These 25 tests were conducted utilizing the copper triplet injector, the stainless-steel uncooled combustor, and the water-cooled nozzle assembly used in previous experiments.

Inspections of the combustor hardware were made following tests No. 15, 20, 23, and 25. Carbon depositions were noted, in varying degrees; however, all inspections indicated less buildup than noted in the C_3F_6/F_2 experiments. Following test No. 25, a hardware problem was detected. A pinhole leak in the upstream portion of the nozzle assembly was noted and small quantities of water had been leaking into the combustor. As a result, performance data acquired and reported in Table XXXIII are apparently invalid and the cause of high c^*_{corr} is apparent. However, some qualitative data were obtained. Initial tests conducted with helium and C_4F_8/F_2 in this series indicated marginal combustion (Fig. 187) when the helium was injected into the primary combustion zone. In test No. 14, combustion was erratically maintained, while in test No. 23, combustion ceased when the helium diluent was introduced (Fig. 187). In addition, less carbon is formed by the C_4F_8/F_2 reaction than in the C_3F_6/F_2 reaction.

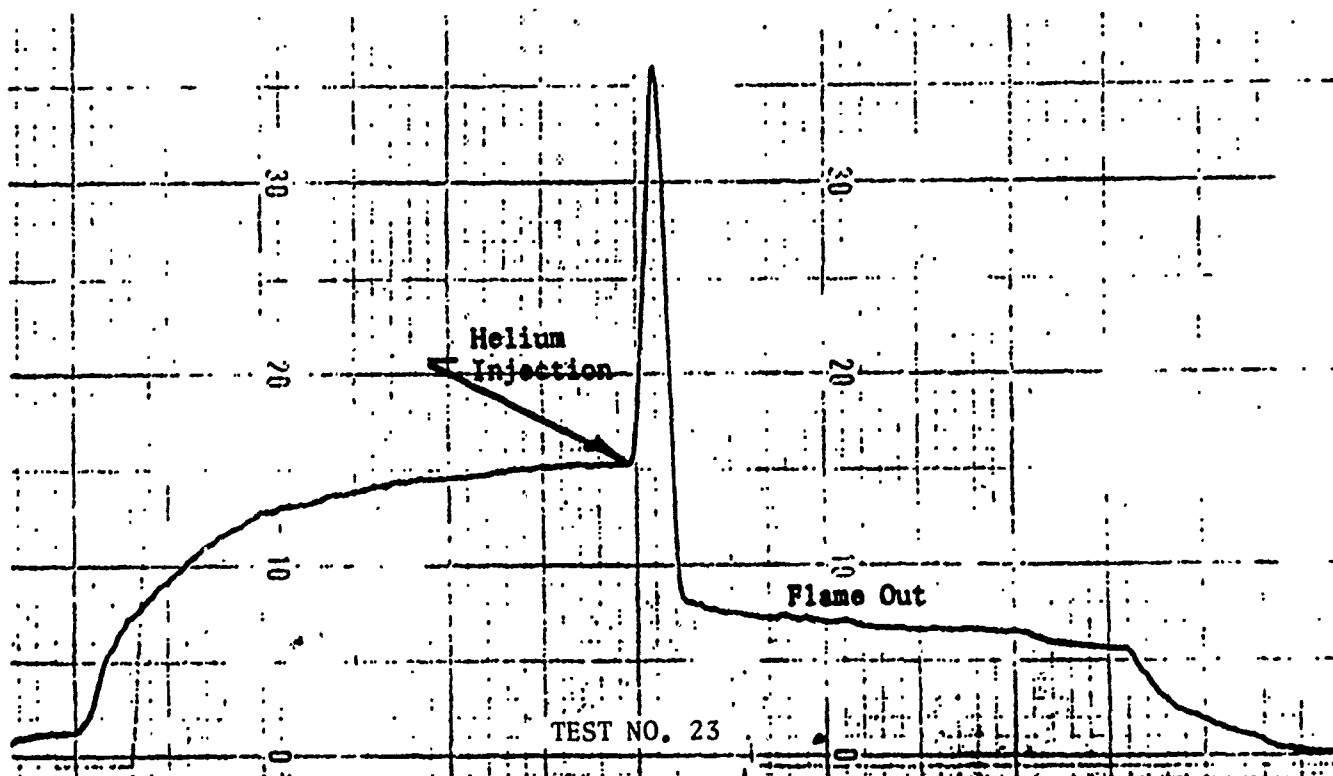
TABLE XXXIII. C_4F_8/F_2 INITIAL TEST SERIES*

Test No.	\dot{V}_{F_2} g/sec	$\dot{V}_{C_4F_8}$ g/sec	\dot{V}_{He} g/sec	Mixture Ratio	\dot{V}_{tot} g/sec	P_c psia	C_{act} ft/sec	C_{theo} ft/sec	$\eta_{c,uncorr}$ percent	$\eta_{c,corr}$ percent	T_c^f K	\dot{Q}_c cal/sec	\dot{Q}_w cal/sec	\dot{Q}_r cal/sec	E_c	MD	γ	C_p Btu/lb-mole	α	$f_{2,He(1)}$	Comments
1-11																					
12	1.84	0.210	0	2.27	2.65	26.0	3136	3381	181.6	123.1	1365	-728	-254	-1022	0	40.4	1.23	10.78	0.54	1.22	Unstable combustion with addition of 52 percent helium
13	1.81	0.840	0	2.15	2.65	27.5	3635	3496	184.0	134.0	1404	-748	-254	-1022	0	40.0	1.23	10.75	0.60	1.72	
14	1.81	0.830	0	2.18	2.87	27.0	3582	3470	181.2	127.0	1356	-546	-232	-838	0	38.1	1.24	10.3	0.70	1.18	
15	1.78	0.790	0	2.25	2.57	22.0	2538	3396	88.3	106.5	1408	0	0	0	0	38.3	0.65	10.3	0.65	1.180	
16																					
17	3.08	0.710	0	4.25	3.73	30.0	2817	2791	100.9	114.0	1193	-546	-232	-838	0	40.6	1.24	10.3	0.19	2.48	Primary combustion quenched with addition of 33.6 percent helium
18	3.00	0.720	0	4.11	3.73	34.5	2864	2811	101.9	114.8	1208	0	0	0	0	40.4	0.21	10.3	0.21	2.45	
19	2.97	0.760	0	3.91	3.73	30.8	2892	2861	101.8	114.5	1230	0	0	0	0	40.0	0.24	10.2	0.24	2.39	
20	2.89	0.810	0	3.56	3.70	30.3	2849	2896	99.0	111.1	1264	0	0	0	0	39.4	0.30	10.2	0.30	2.27	
21	2.44	0.860	0	5.00	4.30	29.9	3174	3070	103.4	117.6	1348	0	0	0	0	38.4	0.46	10.1	0.46	1.79	
22	2.42	0.860	0	4.97	4.28	30.3	3236	3079	105.1	119.7	1352	0	0	0	0	38.4	0.47	10.1	0.47	1.757	
23	2.40	0.870	0	3.76	3.61	29.0	3106	3095	100.4	111.4	1358	0	0	0	0	38.2	0.49	10.1	0.49	1.735	
24	4.50	0.99	0	5.49	5.44	41.8	2667	2775	96.1	104.3	1240	0	0	0	0	39.2	1.25	10.0	0.22	3.748	
25	4.42	0.99	0	5.46	5.41	42.7	2764	2785	99.2	107.8	1246	0	0	0	0	39.2	1.25	10.0	0.23	3.648	

*A pinhole water leak into the combustor section was noted upon disassembly of the hardware following test No. 25 which furnished the data presented in this table and created the high efficiency time quoted.



TEST NO. 14



TEST NO. 23

Figure 187. Chamber Pressure Traces for Helium Injection Tests - C_4F_8/F_2

To alleviate the quenching problem noted by helium addition to the primary reaction zone, a secondary injector (Fig. 183) was fabricated from Nickel 200 material. This injector was fabricated to be used in conjunction with the CWLL laser experimental hardware for use not only in combustor experimental work but small-scale DF-free laser experiments. This component was designed to provide regenerative cooling of the diluent and ample downstream length for mixing.

Subsequent combustor experiments (Tables XXXIV and XXXV) were conducted utilizing the secondary injector in conjunction with the two-element concentric injector, the water/regenerative-cooled combustor, and the Baseline 30 water-cooled nozzle array. No flameouts or oscillations were detected and staging was considered successful. Tests No. 26 through 29 were conducted with the new hardware configurations and with swirlers placed into the concentric element to enhance mixing. This configuration is shown in Fig. 188.

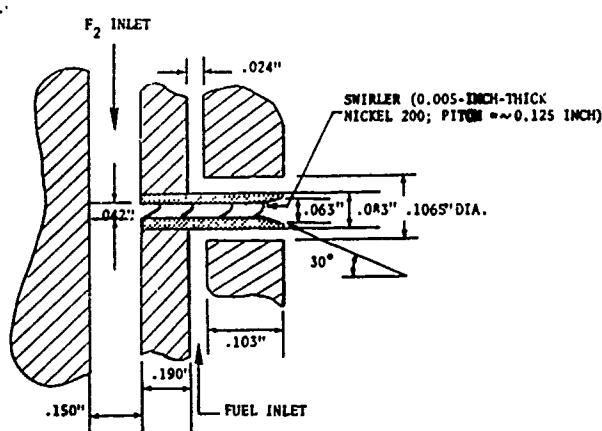


Figure 188. Swirler Schematic

For these tests, corrected c^* values were 95 to 97 percent, with and without diluent flow through the secondary injector. However, difficulty existed in retaining the swirler configuration.

Subsequent tests were conducted without swirlers. Maintaining the swirler configuration for extended run times was found to be possible only by a major hardware modification. As such, the swirlers were removed and additional data

TABLE XXXIV. C_4F_8/F_2 TEST DATA

Test No.	\dot{V}_{F_2} g/sec	$\dot{V}_{C_4F_8}$ g/sec	\dot{V}_{He} g/sec	MR	\dot{V}_{tot} g/sec	He, percent	P_c psi	\dot{Q}_{act} ft/sec	\dot{Q}_{theo} ft/sec	ϵ_{uncorr} percent	ϵ_{corr} percent	T_F °K	$\tau_{1/2}$ ca sec	\dot{Q}_{He} cal/sec	\dot{Q}_{F_2} cal/sec	T_c °C	MR	γ	C_p Btu/lbm-°F	β	$f_{2,app}$ g/sec	Comments
26	2.70	0.94	1.26	2.87	4.90	25.7	47.8	3417	4194	81.5	96.6	852	2.0	335	1405	6.0	12.7	1.45	6.35	0.01	1.98	Secondary injector - swirlers installed
27	2.67	1.04	1.27	2.7	4.98	25.5	51.0	3587	4273	83.9	97.0	936	1.25	302	1411	6.4	12.8	1.45	6.42	0.04	1.88	Secondary injector - swirlers installed with He
28	2.89	1.31	0	2.21	4.20	0	30.6	2552	3446	74.0	95.0	1391	1.25	688	1714	0	40.4	1.22	10.83	0.59	1.89	Secondary injector - swirlers installed without He
29	2.82	1.38	0	2.04	4.20	0	31.5	2627	3612	72.7	95.6	1444	1.25	692	1743	0	40.7	1.22	10.83	0.66	1.77	Secondary injector - swirlers installed without He
30	2.67	1.27	1.47	2.10	5.41	27.2	50.0	3237	4466	72.5	81.4	1036	1.2	358	1574	8.2	12.2	1.45	6.40	0.11	1.71	Removed swirlers - with He
31	2.63	1.33	0.77	1.96	4.73	16.3	42.5	3147	4238	74.3	88.7	1136	1.25	737	2042	4.5	17.5	1.37	7.34	0.22	1.42	Removed swirlers - with He
32	2.61	1.03	0	2.53	3.64	0	27.8	2875	3192	83.3	103.3	1313	1.25	444	1401	0	41.1	1.22	11.84	0.41	1.83	Jet baseline test with secondary injector
33	2.54	1.08	0	2.39	3.66	0	28.1	2689	3385	81.9	103.8	1325	1.25	597	1542	0	41.5	1.22	10.99	0.42	1.76	
34	3.11	1.28	0	2.45	4.39	0	31.4	2505	3267	76.8	95.4	1340	1.25	792	1780	0	41.0	1.22	10.87	0.45	2.14	
35	3.03	1.23	0	2.46	4.26	0	28.8	2348	3235	73.2	95.5	1346	1.25	620	1572	0	40.2	1.23	10.67	0.47	2.10	Test operation checkout
36	4.10	1.31	0	3.13	5.41	0	38.7	2506	3003	83.4	98.4	1276	1.25	791	1779	0	41.1	1.23	10.66	0.29	3.18	
37	3.99	1.14	0	2.98	5.33	0	38.0	2497	3042	82.1	96.2	1318	1.25	621	1569	0	39.9	1.24	10.44	0.36	2.97	
38	2.08	1.047	0.5	44.3	2.63	15.0	24.3	3240	5274	81.4	81.1	1040	1.25	604	1416	4.0	11.6	1.55	5.60	0.75	1.19	h_2/F_2 baseline checkout
39	2.06	0.071	0.5	25.0	2.63	19.0	27.4	3648	6387	57.1	46.2	1888	1.25	857	1752	6.6	1.3	1.51	5.31	1.00	0.72	
40	2.02	0.089	0.5	22.7	2.61	19.2	30.4	4427	8260	53.6	40	>3000	1.25	1412	2878	0	0	0	0	0	0	

Comments - He used when at the high-temperature condition

TABLE XXXV. C₄F₈/F₂ TEST DATA

Test No.	W _{F₂} gr/sec	W _{C₄F₈} gr/sec	W _{He} gr/sec	W _{tot} gr/sec	He, percent	P _c , psia	C _{act} , ft/sec	C _{theo} , ft/sec	%uncorr., percent	%corr., percent	T _o , K	Q _o , cal/sec	Q _g , cal/sec	Q _t , cal/sec	g _c	MW	Y	C _p , Btu/gm-mole	α	T _{avail} , gm/sec	Comments	
41	1.62	1.66	±0.65	0.98	--	30.9	--	--	--	--	--	639	510	1149	--	--	--	--	--	--	{ He leakage into chamber	
42	1.57	1.68	±0.65	0.93	--	30.1	--	--	--	--	--	606	510	1116	--	--	--	--	--	--		
43	1.31	0.83	0.62	1.58	22.1	30.6	3886	4708	82.6	97.2	1181	590	491	1081	8.6	14.0	1.41	6.81	0.41	0.68	{ Facility Problems--Helium leakage into chamber and two-phase flow of C ₄ F ₈	
44	1.31	0.82	0.50	1.59	2.63	28.0	3723	4662	79.9	97.2	1204	639	491	1230	6.9	15.7	1.39	7.10	0.45	0.62		
45	2.29	1.69	±0.65	1.35	--	36.5	--	--	--	--	--	917	491	1408	--	--	--	--	--	--		
46	2.26	1.66	±0.65	1.36	--	36.5	--	--	--	--	--	950	491	1441	--	--	--	--	--	--		
47	1.08	>1.05	0.54	<1.02	--	26.3	--	--	--	--	--	762	465	1227	--	--	--	--	--	--		
48	1.07	>1.11	0.54	<1.04	--	28.8	--	--	--	--	--	762	465	1227	--	--	--	--	--	--		
49	1.36	0.87 (C ₃ F ₆)	0.59	1.56	2.82	21.0	29.3	3646	4820	75.6	88.1	587	480	1067	8.0	14.5	1.41	6.87	0.59	0.70	{ Two-phase flow of C ₄ F ₈	
50	1.34	1.19 (C ₃ F ₆)	0.60	1.13	3.13	19.2	34.9	3909	5470	71.5	84.1	1772	667	480	1147	13.0	15.9	1.37	7.40	1.00		0.44
51	2.13	0.057 (He)	0.47	37.3	2.65	17.7	29.7	3920	6043	64.9	80.0	1568	762	480	1242	4.2	11.7	1.53	5.71	0.94		1.05
52	2.12	0.073 (He)	0.47	29.1	2.67	17.6	40.5	5321	6156	70.3	86.2	2408	861	454	1315	6.0	11.6	1.49	6.06	1.00		0.75
53	1.99	0.061 (He)	0.50	32.7	2.55	19.6	34.9	4786	6602	72.5	89.8	1754	905	454	1359	5.6	11.1	1.53	5.76	1.00		0.84
54	1.97	0.072 (He)	0.54	27.4	2.58	20.9	40.9	6011	7380	81.5	88.8	2302	968	454	1422	8.4	10.8	1.50	5.98	1.00		0.61
55																					{ Two-phase flow of C ₄ F ₈	
56																						
57	1.08	1.16	0.46	0.94	2.70	17.0	33.8	4381	5626	77.9	94.4	815	446	1261	21.2	18.1	1.32	8.12	1.00	0.21	{ Two-phase flow of C ₄ F ₈	
58	1.08	1.00	0.46	1.08	2.73	18.2	31.2	4313	5424	79.5	102.3	881	416	1297	13.7	16.8	1.35	7.60	0.96	0.32		

acquired indicated adequate performance could be attained without their use. $C_3F_6/F_2/He$ was reevaluated in tests No. 49 and 50, and equivalent performance data were obtained to that previously reported.

At this time, another hardware difficulty was noted. Cooling of the injector face is accomplished by the diluent flowing through the coolant passages of the regenerative/water-cooled combustor, exiting into the coaxial injector face, separated from the fuel manifold by a metal seal. Warpage of the combustor face from numerous test cycles had produced a leak path for helium injection into the fuel flow system. Refacing of this warped surface permitted acquisition of satisfactory data in tests No. 49 through 58.

Tests No. 57 and 58 indicated the ability to adequately react $C_4F_8/F_2/He$ to achieve the desired laser operating conditions for DF-free laser experiments utilizing the CWLL hardware.

Discussion of Results. Information acquired in DF-free combustor experiments conducted in support of this contract effort can be summarized as follows:

1. Temperatures for dissociating fluorine at proper diluent ratios for chemical lasers can be obtained by combusting C_4F_8 with F_2 and He added to obtain a DF-free fluorine stream.
2. The C_4F_8 reaction with F_2 produces less soot and reacts more closely to completion than C_3F_6 with F_2 with the injectors used in this effort.
3. Instabilities and quenching of the primary reaction can be expected in many instances when C_4F_8/F_2 and C_3F_6/F_2 are reacted in the presence of helium, at least in small-scale hardware.
4. Diluent addition into a secondary zone can be adequately mixed into the primary gas stream and virtually unaffected the primary reaction, thus eliminating the above effect.
5. Fluorocarbon fuels, C_4F_8 and C_3F_6 , are hypergolic with fluorine.

The ability to produce the necessary laser operating conditions was demonstrated as shown in Table XXXVI for the last two $C_4F_8/F_2/He$ tests where the operating conditions most closely approximate the desired lasing operating condition.

Furthermore, the DF-free combustor can be operated at conditions "matching" the baseline $D_2/F_2/He$ operating conditions based on the available heat transfer data from the combustor experiments. The predicted matched conditions for $H_2/F_2/He$ and $C_4F_8/F_2/He$ are shown in Table XXXVII where matching is based on a nozzle entrance temperature of 1550 K, $a = 12$, a nozzle exit pressure of 10 torr and a nominal production of 0.285 gm/sec of available fluorine. Also shown (case II) is a low diluent condition where $a = 4$ and all other constants are fixed for $C_4F_8/F_2/He$. This case is presented to note the approximate operating condition where the high molecular weight fluorine stream was optimized for outcoupled power in subsequent experiments.

Secondary injection of the diluent flow was found to be satisfactory in combustor experiments. Quenching and chugging were eliminated and no performance degradation could be noted. The ability to properly mix the diluent into the primary stream was not evaluated in this task; however, subsequent lasing experiments did confirm a proper injection scheme.

A plot of experimental results in this phase is presented in Fig. 189. Corrected combustion efficiency versus mixture ratio for the baseline $H_2/F_2/He$, $C_3F_6/F_2/He$, and $C_4F_8/F_2/He$ reactant combinations is shown along with the nominal operating regime for chemical laser operation. Numerous experiments were conducted at high mixture ratios to obtain the desired temperature level when conducting "neat" experiments and to assist in evaluating the injector performance when operating with and without diluent effects.

Though error limits are not shown, there are several potential sources of error which should be noted. For example, for all test conditions, a constant throat dimension was assumed. Boundary layer growth and nozzle dimensional changes due to heat loading affect the throat dimension utilized in the efficiency calculations.

TABLE XXXVI. OPERATING CHART - C_4F_8/F_2

Test No.	Reactant Combination	Mixture Ratio	Percent He	$T_{o\min}^F$ (K) (Nozzle Entrance Temperature)	α	β	$(F_2)_{avail}$ gm/sec	MW
57	$C_4F_8/F_2/He$	0.94	17	2100	1.00	21.2	0.21	18.1
58	$C_4F_8/F_2/He$	1.08	18.2	1675	0.96	13.7	0.32	16.8

TABLE XXXVII. CHEMICAL LASER COMPARISON OPERATING CHART

$\beta = 12$									
Case I	$T_{othroat}^F$	Percent Diluent	α	MW	C_p	γ	F_{2avail}	MR	P_c
H_2/F_2	913	31.6	0.985	8.79	5.40	1.58	0.285	30.3	13.9
C_4F_8/F_2	1002	20.9	0.976	14.72	6.94	1.40	0.285	1.26	18
$\beta = 4$									
Case II									
C_4F_8/F_2	526	10.07	0.976	22.17	7.51	1.36	0.285	1.40	8
FIXED PARAMETERS: $T_o^F = 1550K$ (Nozzle entrance temperature),									
$(F_2)_{avail} = 0.285$, $P_{cav} = 10$ torr									

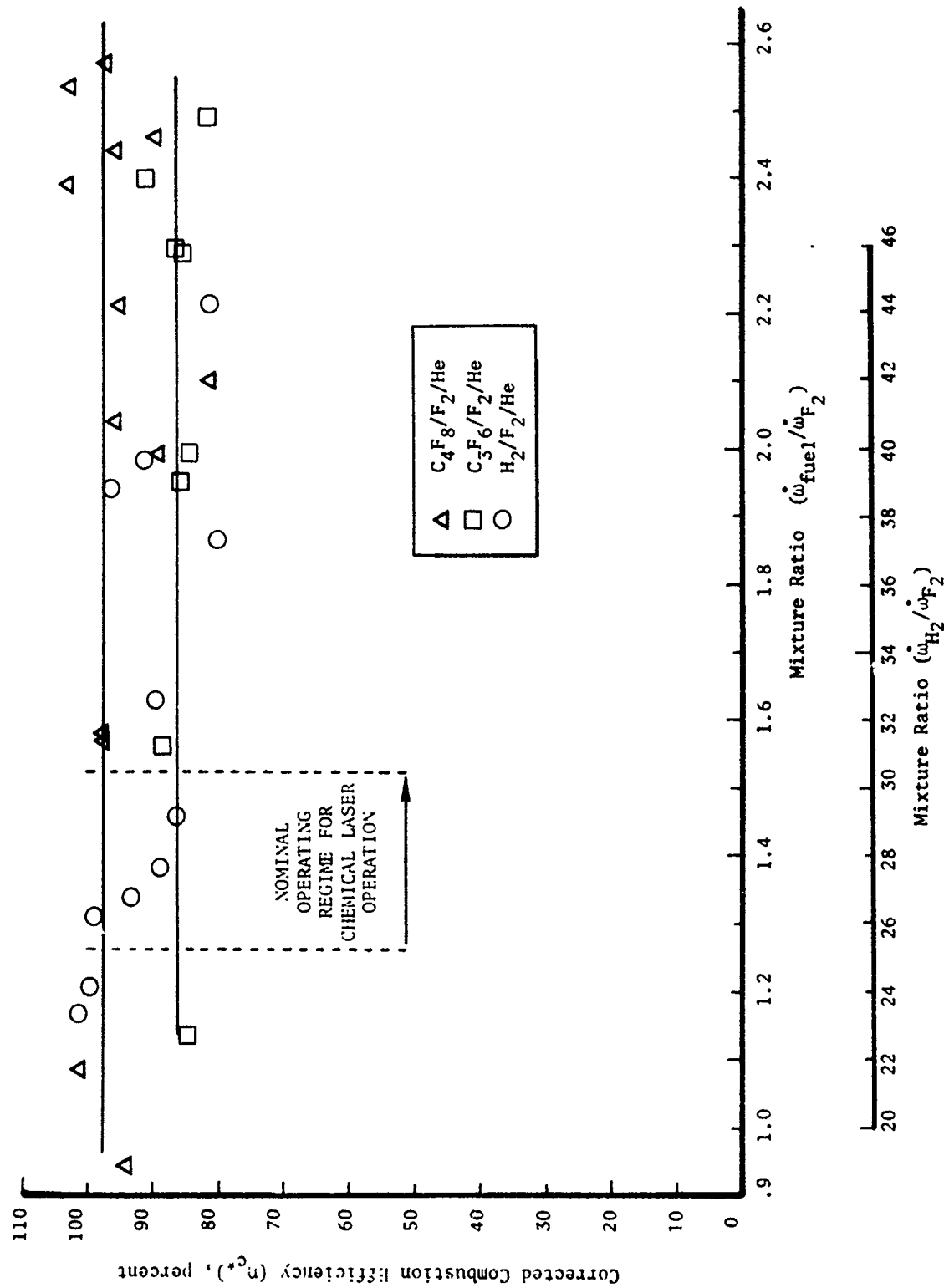


Figure 189. DF-Free Combustor Experimental Results (η_{c^*} vs Mixture Ratio)

Corrections for the numerous test conditions would be impractical. In addition, good heat loss data were not obtained because heat sink hardware was used on many tests and many tests were of short duration.

Physical constants for C_3F_6 and C_4F_8 are not well defined. When it is necessary to deal with substances not adequately described by the perfect gas law, such as C_3F_6 and C_4F_8 , and for which tables or charts are not available, use of plotted correction factors to apply to the perfect gas law are required. For this task, reduced properties of pressure and temperature were assumed for the given test conditions; and assuming the general shape of the vapor dome and assuming the constant temperature lines on the p-v plane are similar to all other substances, a compressibility factor can be determined. This method is approximate, but necessary until detailed data become available on C_3F_6 and C_4F_8 .

Small-Scale Lasing Tests

With the development of the DF-free precombustor which required the use of secondary diluent injection, and with NF_3 becoming available, so that both an advanced fuel and an advanced oxidizer could be evaluated directly, the small-scale laser test plan for evaluating precombustor reactants was revised in several ways. These revisions led to a series of lasing tests which were conducted to:

1. Evaluate the effect of secondary diluent injection
2. Evaluate $\text{C}_4\text{F}_8/\text{F}_2/\text{He}$
3. Evaluate the replacement of He with N_2
4. Evaluate the replacement of F_2 with NF_3
5. Evaluate the simulation of NF_3 with F_2 and N_2

A somewhat different philosophy insofar as resonator alignment is concerned was followed in these tests. Whereas in the prior, cavity fuel evaluation tests, the resonator was tuned to low-order modes to permit some spatial resolution, in these precombustor reactant tests, the resonator was permitted to operate in higher-order modes so that a larger portion of the active medium would participate in the generation of power. This procedure provides a better comparison of the effects of different precombustor reaction products.

$\text{D}_2/\text{F}_2/\text{He}$ Laser Tests/Effect of Secondary Diluent Injector. Lasing tests with increased (higher order) mode sizes were run with the baseline $\text{D}_2/\text{F}_2/\text{He}$ precombustor to obtain comparative data and to evaluate the secondary diluent injection mode of operation. Two optical resonator mirror configurations were employed. The first configuration was that (shown in Fig. 152) used in previous tests. With this configuration and the increased mode size, significantly larger powers were outcoupled. The maximum outcoupled power was about 23 watts with the resonator axis 0.22 inch ($C_x = 0.22$ inch) downstream of the nozzle exit plane. Another mirror also specified by the vendor to be a 2-percent dielectric tuned transmitting mirror, was employed in some tests (run after some C_4F_8 tests, see later discussion) in which about 10 watts was outcoupled under what should have been identical conditions. This apparent discrepancy will be discussed later.

This $D_2/F_2/He$ baseline flow conditions and test data are presented in Table XXXVIII. Table XXXIX shows the laser emission spectral content at $C_x = 0.22$ inch with a dry N_2 resonator purge. Figure 190 shows horizontal power scans recorded at $C_x = 0.22$ inch, 0.42 inch, and 0.65 inch. The location of the H_2 nozzles are indicated in the figure. By and large, the curves are similar to those recorded earlier (Fig. 167) except that there is some "peaking" directly downstream of the middle H_2 nozzle. (The two figures, Fig. 190 and 191, showing scan data are somewhat qualitative. A physical rearrangement of the optical train used for these scans produced vignetting so that on the right-hand half of the sweep of these scans, the recorded intensity was artificially attenuated. This was not discovered until after the experimental effort was completed. The curves shown in these four figures were generated by reflecting the left-hand portion of the sweep to generate the right-hand portion. Based on the data shown earlier, this is reasonable and all that is lost is the fact noted earlier that the two outboard H_2 nozzles are apparently not identical.)

The mode volumes, as determined by plexiglas burn patterns, are shown in Fig. 192 for these tests. Operating conditions (i.e., T_O^F , β , MR, P_C) could be varied somewhat from those at which maximum power was obtained with little loss in power.

To test the effect of secondary diluent injection, a series of runs was made proportioning the diluent between the secondary diluent injector and the primary injectors. A full 0- to 100-percent range was achieved with no change in performance.

It is of interest to estimate the specific power potentially achievable based on the above results. To do this, a few assumptions must be made: (1) the total round trip loss in the resonator is estimated at 6 percent so that with the 2-percent outcoupling, the medium is delivering three times the measured, outcoupled power; (2) based on the nozzle scan data, one and one-half mode volumes across the nozzle (on the average) could deliver the outcoupled power measured; and (3) from the downstream scans, at least one mode volume located 0.3 inch downstream would deliver 20 watts, a second located 0.9 inch downstream would deliver 10 watts, a third located 1.5 inches downstream would deliver 5 watts. Thus, a somewhat conservative estimate of "integrated" power outcoupled is $1.5 (20 + 10 + 5) = 52.5$

TABLE XXXVIII. FLOW CONDITIONS* SUMMARY SHEET, BASELINE 30-1X NOZZLE

Test	[D ₂]	[C ₄ F ₈]	[F ₂]	[NF ₃]	[He]	[N ₂]	MR (o/f)	% Dil P _c psia	\dot{w}_t (gm/ sec)	γ	T _o (K)	[D ₂]	[F]	[F ₂]	[DF]	[CF ₄]	Power watts	Fuel Burned %				
D ₂ /F ₂ /He Baseline Test	[.0157]	-	[.0205]	-	[.0590]	-	12.32	21.90	11.6	12.3	1.08	1.50	11.0	1648	[.005]	.006	.002	.020	-	23	.60	68.1
C ₄ F ₈ /F ₂ /He Baseline	-	[.0022]	[.0182]	-	[.0337]	-	1.54	10.59	7.9	3.6	1.27	1.32	22.0	1224	-	.012	.003	-	.009	10	.64	100.0
D ₂ /F ₂ /N ₂	[.0074]	-	[.0096]	-	-	[.0141]	12.12	40.11	5.8	6.6	0.79	1.35	24.3	1900	-	[.002]	.003	.010	-	17	.61	67.4
C ₄ F ₈ /F ₂ /N ₂	-	.0026	.0185	-	-	.0198	1.36	31.22	10.8	2.4	1.78	1.21	41.9	1316	-	.008	.004	-	.010	7	.50	90.9
C ₄ F ₈ /F ₂ /He/N ₂ (N ₂ Simulation)	-	[.0031]	[.0179]	-	[.0345]	[.0111]	1.61	7.92	12.2	8.1	1.08	1.27	26.77	1256	-	.008	.002	-	.012	5	.70	87.8
C ₄ F ₈ /NF ₃ /He	-	[.0031]	-	[.0131]	[.0332]	-	1.51	9.02	12.2	6.1	1.08	1.28	25.60	1188	-	.008	.003	-	.012	10	.55	93.9
C ₄ F ₈ /NF ₃ /He	-	[.0033]	-	[.0159]	[.0342]	-	1.71	7.12	13.1	4.0	1.16	1.27	28.22	1183	-	.010	.006	-	.013	7	.45	97.3

*For all tests, the laser cavity pressure was 3.8 to 3.9 torr

TABLE XXXIX. SPECTRAL CONTENT SUMMARY SHEET

	1 → 0								2 → 1					
	P3	P4	P5	P6	P7	P8	P9		P4	P5	P6	P7	P8	P9
D ₂ /F ₂ /He Baseline	-	-	W	S	S	8	VW		-	M	S	S	S	VW
F ₂ /D ₂ /N ₂	-	-	VW	S	S	M/S	.		-	S	S	S	W	-
C ₄ F ₈ /F ₂ /He Baseline	-	-	VW	S	S	-	-		M	S	S	M	M	-
C ₄ F ₈ /F ₂ /N ₂	-	VW	S	S	S	-	-		S	S	S	VW	-	-
C ₄ F ₈ /F ₂ /N ₂ /He (NF ₃ Simulation)	-	-	-	M	S	-	-		-	VS	M	S	VVW	-
C ₄ F ₈ /NF ₃ /He	-	-	M	S	S	-	-		S	S	S	VW	-	-
C ₄ F ₈ /NF ₃ /He	-	-	-	S	S	-	-		M	S	S	-	-	-

VVW--very, very weak

VW --very weak

W --weak

M --moderate

S --strong

VS --very strong

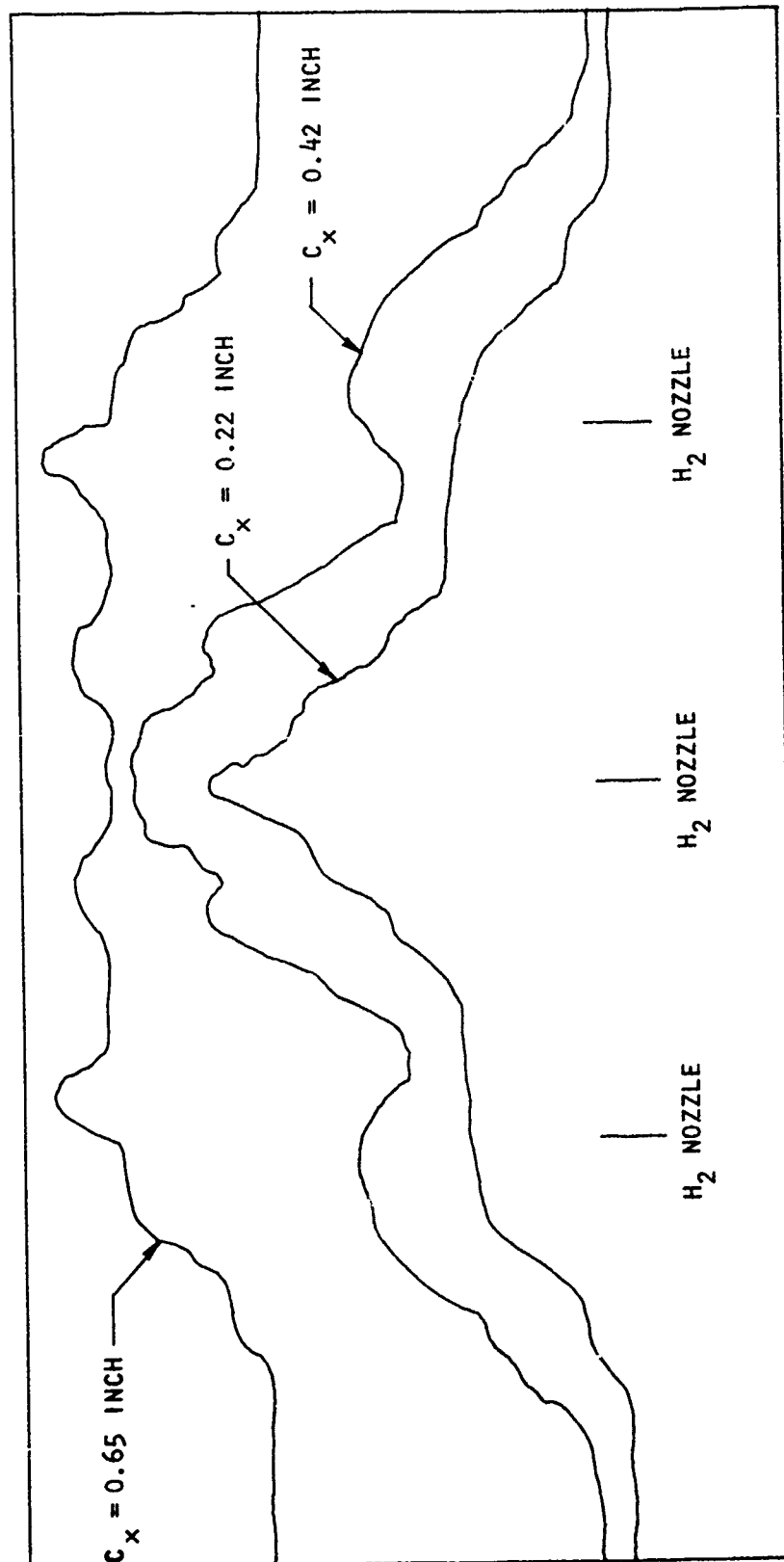


Figure 190. $D_2/F_2/He$ Baseline Tests

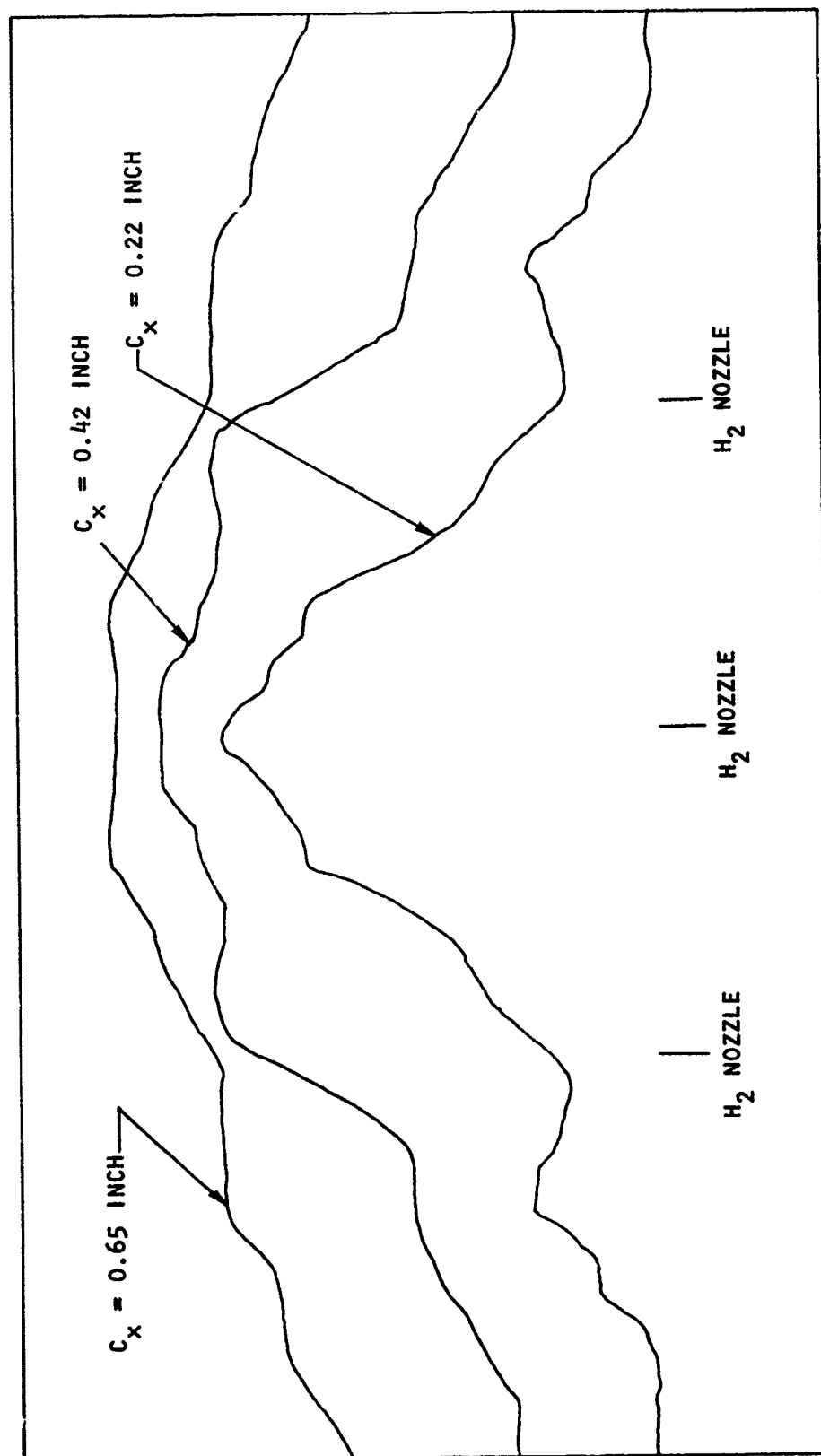


Figure 191. $C_4F_8/F_2/He$ Baseline Test

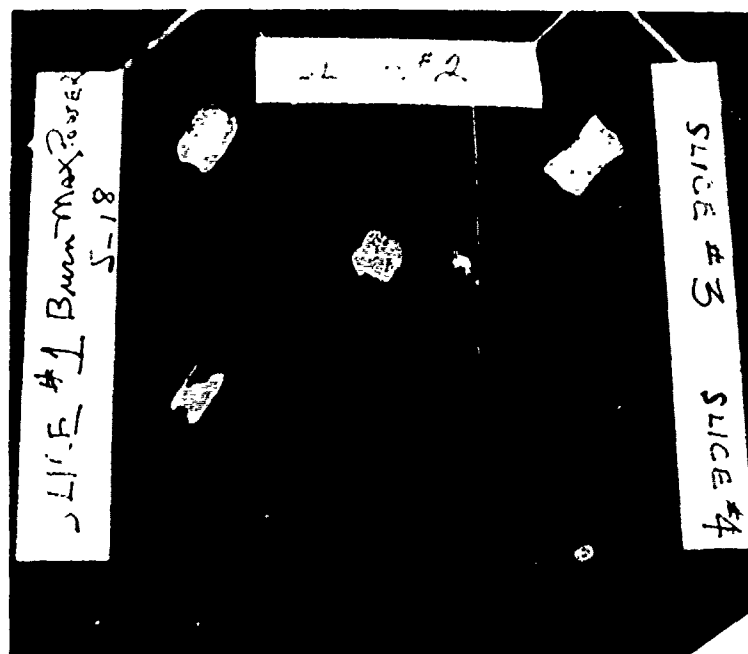


Figure 192. Burn Patterns, $D_2/F_2/He$ Baseline Test

Slice No. 1	$C_x = 0.22$ inch	$P_{outcoupled} = 23$ watts
Slice No. 2	$C_x = 0.42$ inch	$P_{outcoupled} = 18$ watts
Slice No. 3	$C_x = 0.65$ inch	$P_{outcoupled} = 18$ watts
Slice No. 4	$C_x = 0.85$ inch	$P_{outcoupled} = 13$ watts

watts. Total power delivered is then 157.5 watts (this would correspond to what would be measured in a closed cavity measurement) for a total flow of 1.1 gm/sec. The specific energy available is thus greater than 66 kJ/lb.

The intracavity flux density is about 850 watts for the peak power point, which is somewhat low compared to a very high power device, but sufficiently high so that at least partial saturation is achieved. With increased flux, some increase in specific power could be anticipated. All in all, the projected specific power for this baseline test appears quite consistent with good chemical laser performance.

C₄F₈/F₂/He Laser Tests. For the laser tests utilizing C₄F₈ in place of D₂, the same resonator configuration was used as in the baseline tests described above. Tests were made with both 2-percent mirrors. However, in these tests, the out-coupled power did not depend on the mirror used. The reason for this is unknown (and will be discussed later).

Typical flow conditions for these tests are shown in Table XXXVIII and spectral content in Table XXXIX. The maximum outcoupled power was 10 watts at $C_x = 0.22$ inch with 9 watts at 0.42 inch, and 9 watts at 0.65 inch. Fewer spectral lines were observed with relative intensities peaking at lower J values than for the baseline case. The latter is consistent with the nozzle entrance temperature as shown in Table XXXIX.

Across-the-nozzle scans are shown in Fig. 191. There is a significant difference in the fluid dynamic operating conditions, compared to the baseline case, as shown by these scans. The location of the H₂ cavity fuel nozzles are as shown in the figure so that it can be seen that in this test the flowfield exhibited considerable divergence. Laser power was outcoupled over a range exceeding the nozzle separation that increased with downstream location. This circumstance was generally noted in tests where the fluorine flowfield γ is less than in the baseline case. This is to be expected because with the fixed area ratio of the nozzle, which was designed for $\gamma = 1.5$, the flow for a $\gamma = 1.25$, for example, will be underexpanded by a factor of 2 for the same pressure difference.

The optimum diluent ratio was substantially less than for the baseline case. The high heat loss characteristics of the precombustor required high theoretical temperatures. Reducing the mixture ratio to achieve higher temperatures (and thus higher α) reduces the fluorine available with resulting decrease in laser performance. Higher performance is believed achievable with larger (scaled up) hardware where heat loss would be a smaller percentage. Lower chamber pressure was utilized to reduce overexpansion, as noted above.

An important feature of these results is the lengthened lasing zone with power outcoupled almost independent of downstream position up to $C_x = 0.65$ inch (the maximum downstream position where data were taken). This is consistent with a lower nozzle entrance temperature which would result in a reduced temperature after expansion, compared with the baseline case and the fact that the boundary layer growth will be substantially less than that in the baseline case. Considering the warm boundary layer as the "match" which initiates the F atom-cavity fuel reaction, the C_4F_8 flow generates a smaller, cooler "match," so that the pumping reaction will be slower and the downstream lasing length will increase.

The generally slower reaction rates resulting in the longer lasing zone would also result in less gain. Again, the data are consistent. As noted above, fewer lasing lines reached threshold (lower gain) and, furthermore, the line intensity peaked at lower J value (lower temperature). Another factor in the longer lasing zone may be the lack of DF with the concomitant reduction of deactivation effects.

With this background, a qualitative performance comparison can be made. An estimate of power available can be made in a similar fashion to that for the $D_2/F_2/He$ baseline data. Assume 1.5 mode volumes across the nozzle and from the nearly constant outcoupled power as a function of downstream position, 3 mode volumes at 9 watts downstream, plus at least one more with half this power. This gives an integrated outcoupled power of 47 watts which gives a power available greater than 142 watts (equivalent closed cavity power). For the total flow of 1.27 gm/sec,

this yields a projected specific energy available greater than 50 kJ/lb. In view of the fact that the lasing zone may be considerably longer than assumed and that the nozzle configuration, specifically designed for the baseline flow, is far from optimum for the $C_4F_8/F_2/He$ flow, the results are quite encouraging and strongly suggests that with optimum nozzles, laser performance with the DF-free combination may not only match but could exceed that of the baseline case on power available and even on specific power.

N_2 Diluent Evaluation. Two experiments were run to obtain a preliminary evaluation of the use of N_2 in place of He for diluent. In this experiment, N_2 was simply substituted for the He and some adjustments made in flow conditions to account, at least in part, for different properties of N_2 as a diluent to replace He. Prior to these experiments, it had been anticipated that performance would be substantially reduced so power outcoupled was measured only at $C_x = 0.22$ inch. (Because of the expected lower performance power scan, data were not taken and the program ended before the taking of additional data could be considered.) Flow conditions are shown in Table XXVIII and spectral data are shown in Table XXXIX. The resonator configuration used for the $D_2/F_2/N_2$ experiment was the same as for the $D_2/F_2/He$ experiment, and that for the $C_4F_8/F_2/N_2$ the same as for $C_4F_8/F_2/He$. Surprisingly, the actual power outcoupled for both the baseline reactant $H_2/F_2/He \rightarrow N_2$ and the DF-free $C_4F_8/F_2/He \rightarrow N_2$ cases was only reduced about 28 percent. In the baseline case (H_2/F_2), the total mass flow was also reduced about the same amount, so that specific power was reduced even less. Also, the spectral content was quite similar in both cases though fewer lines lased with N_2 diluent and intensity peaked at somewhat lower J values. For the C_4F_8/F_2 case, where the power outcoupled was reduced, total flowrate was greater so that specific power would be reduced further.

Based on these results, it is concluded that the assumption that replacing He with N_2 will necessarily reduce performance is incorrect. With nozzles designed specifically for N_2 diluent, increased performance over what was found in these experiments would be expected, in which case operation with N_2 diluents would provide comparable performance to He dilution on power available and, possibly, on specific power as well.

NF₃ Evaluation. NF₃ as a replacement oxidizer for F₂ was evaluated with C₄F₈ as the fuel with He diluent. This gives an all-advanced reactant (not counting the diluent) precombustor. The resonator utilized was the same as in the C₄F₈/F₂/He experiments. Flow conditions are given in Table XXXVIII and spectral data in Table XXXIX. Two flow conditions were run with NF₃ and C₄F₈. In the first, the power outcoupled at C_x = 0.22 inch is the same as the C₄F₈/F₂/He baseline case. In the second case, with diluent reduced, outcoupled power was reduced. These results indicate that NF₃ can be substituted for F₂ in conjunction with C₄F₈ and He with no loss in performance.

Another experiment was run in an attempt to simulate NF₃ by using F₂ and N₂. To truly simulate NF₃ with no hardware change would require thermal conditioning of the reactants prior to injection into the combustor. This was beyond the scope of this effort so simulation was approximated by adding diluent to account for the higher energy release in the reaction of F₂ with C₄F₈ compared to NF₃ with C₄F₈. Thus, β for the simulation experiment is larger than for the actual case. Power outcoupled at C_x = 0.22 inch was reduced in comparison to the actual (non-simulation) runs. This simulation run indicates both the problems associated with simulation of NF₃ and suggests that because the power reduction was not prohibitive, with proper reactant preconditioners, NF₃ can be simulated with F₂ and N₂ to provide reasonably reliable data. With the relatively high current cost of NF₃ compared to F₂, such simulation would be highly cost effective in testing large devices.

Additional Advanced Reactant Laser Tests

The very last set of small-scale laser tests was designed to evaluate an advanced fuel precombustor and an advanced cavity fuel together. Because of mixing difficulties attendant to the use of high molecular weight cavity fuels, it was decided to use another nozzle which had been developed under company funds. This nozzle, described earlier in this report, was designed to occupy essentially the same volume as the Baseline 30-1X nozzle, with the cavity fuel nozzle enlarged by a factor of 2 to increase the molar flow. This necessitated a reduction of the F₂ nozzles. The same fluid dynamic flow philosophy for nozzle contouring was incorporated into the design.

Baseline Tests. Three checkout baseline tests were conducted utilizing $D_2/F_2/He$ and this high molecular weight nozzle.

The baseline $D_2/F_2/He$ operating point with the standard Baseline 30-1X nozzle array used in previous experiments (Table XI) had a nominal combustor reactant flow of 0.0362 mole. To provide the desired nozzle exit pressure for the high molecular weight nozzle, 0.0261 mole of combustor reactants are required, resulting in a 28-percent reduction in available energy. Total heat loss for this new baseline system has very little difference from the higher flow system and, as a result, significantly lower nozzle entrance temperatures are acquired. To compensate for this difference, a $\beta \approx 4 T_O^F = 1212$ K was determined to be optimum for this system. Outcoupled power of 15 watts was measured at this maximum power operating condition, with the resonator used in the previous tests, at $C_x = 0.22$ inch. This compares well with the Baseline 30-1X nozzle where 23 watts was outcoupled for 1.52 times as much total flow.

An experiment with N_2 showed some performance reduction. However, when compared to the second $D_2/F_2/He$ run data to which the N_2 run data more closely compares, the reduction is much the same, as noted in the Baseline 30-1X tests with N_2 .

HBr Evaluation Experiments. To obtain additional data on HBr as a cavity fuel, two additional tests were run. In the first test, HBr was re-evaluated following baseline evaluation of the $D_2/F_2/He$ combustor system with the new nozzle as described above. A substantially greater diluent ratio was required for this operation. Combustor reactant flows were varied to lower the exit pressure and increase the temperature by lowering of the overall mixture ratio. A peak outcoupled power measurement of 1 watt was obtained when the baseline operating point was varied to the condition shown in Table XL. The HBr utilized in this experiment was a new supply received from Matheson Gas Products with a certification of compliance to the quoted specification of minimum purity of 99.8 percent. A heated, dry GN_2 purge was applied to the HBr supply system prior to HBr flow initiation.

TABLE XL. FLOW CONDITIONS, HIGH MOLECULAR WEIGHT NOZZLE

Remarks	Reactants					MR, o/f	Percent Diluent, Mass	P _c , psia	ḡ, gm/sec	Y	T _o , K	Products					Power, watts	α	Percent Fuel Burned, mole percent		
	[D ₂]	[C ₄ F ₈]	[F ₂]	[NF ₃]	[He]							[C ₄ F ₈]	[D ₂]	[F]	[F ₂]	[DF]				[CF ₄]	
D ₂ /F ₂ /He Baseline	0.0078	----	0.0147	----	0.0300	17.74	16.91	9.55	4.36	1.50	12.49	1212	----	0.0087	0.0026	0.0156	----	15	0.63	100	
D ₂ /F ₂ /He Baseline	0.0098	----	0.0163	----	0.0542	15.64	24.79	11.7	8.38	1.53	10.11	1504	----	0.0126	0.0002	0.0196	----	12-13	0.97	100	
D ₂ /F ₂ /N ₂ Baseline	0.0098	----	0.0155	----	0.0117	14.85	34.28	11.7	2.07	0.954	1.35	22.40	2298	----	0.0113	0	0.0196	----	10	1.0	100
D ₂ /F ₂ /He (Compare He to N ₂)	0.0080	----	0.0133	----	0.0695	15.60	34.10	11.9	13.22	0.815	1.56	8.66	1177	----	0.0067	0.0019	0.0161	----	7	0.64	100
D ₂ /F ₂ /He NBR Cavity Fuel	0.0063	----	0.0102	----	0.0745	15.25	41.86	12.85	19.10	0.712	1.57	7.78	945	----	0.0011	0.0034	0.0126	----	1	0.14	100
C ₄ F ₈ /F ₂ / N ₂ NBR Eval- uation	----	0.0011	0.0093	----	----	1.56	34.80	6.5	2.31	0.885	1.23	38.34	1207	----	0.0057	0.0019	----	0.0040	1.35	0.59	100
C ₄ F ₈ /F ₂ / N ₂ NBR Eval- uation	----	0.0013	0.0105	----	----	1.60	32.10	7.2	1.99	0.960	1.23	37.78	1268	----	0.0077	0.0017	----	0.0050	0.75	0.70	100
D ₂ /F ₂ /He Split Diluent 50/50	0.0078	----	0.0147	----	0.0137	17.74	8.53	8.15	2.00	0.665	1.47	15.35	1337	----	0.0115	0.0011	0.0156	----	9	0.84	100

A demonstration test utilizing HBr cavity fuel was also run in combination with a DF-free precombustor reactant system. With the constraint of a higher heat loss percentage with the high molecular weight nozzle, a DF-free combustor experiment in combination with HBr could be evaluated only using $C_4F_8/F_2/N_2$ combustor reactants and the high molecular weight nozzle. (The higher heat loss pre-empted the use of C_4F_8 with NF_3 .) These test data are tabulated in TABLE XL at two operating conditions, and 1.35 watts of outcoupled power was recorded at the maximum power point. As occurred in all N_2 diluent tests, a low diluent ratio was required. The C_4F_8/F_2 mixture ratio was nominal, and the necessary low chamber pressure was obtained to provide the maximum power.

As a consequence of these experiments, a definite conclusion on the viability of HBr as an alternate to H_2 as a cavity fuel based on all of the results of experiments with HBr on this program is impossible. The very early data showing promise were not corroborated in later experiments. Results of other workers (Ref. 47), however, does indicate that HBr gives reasonable performance compared to H_2 . It is not clear at this point whether the later data in this program showing poorer results with HBr are due to the hardware utilized, and the original data are suspect, or a continuing problem with water contamination even though attempts were made to eliminate this possibility.

Split Diluent Evaluation. Because of the mixing problem associated with HBr, splitting the diluent between the combustor and the cavity fuel flow was considered as a means to improve mixing. As a baseline experiment, a test was run with an approximate 50/50 diluent split using the baseline $D_2/F_2/He$ precombustor with H_2 cavity fuel. The high molecular weight nozzle was appropriate for this because the larger cavity fuel nozzle throat dimension accommodates the increased flow. Test results are shown in Table XL for this experiment. The outcoupled power of 9 watts at $C_x = 0.22$ inch indicate no improvement but, rather, performance reduction for this one experiment. The program ended before this could be explored further with the baseline case or for the HBr case.

Hydrocarbon Simulation Experiments. At the very end of the program, a series of experiments was attempted to evaluate hydrocarbon precombustor fuels through simulation by using the DF-free reactant combination, C_4F_8/NF_3 , and seeding the C_4F_8 with D_2 to generate DF in amounts equivalent to those that would be generated with hydrocarbon fuels.

The baseline test case (no DF) did not achieve the required temperature for fluorine dissociation due to the high heat loss compared with the decreased energy from NF_3 as noted earlier. Tests of this nature, which would have to be conducted with the Baseline 30-1X nozzle, could not be carried out because of time limitations.

Summary and Conclusions (Phase II)

It was the overall objective of this effort to find and evaluate advanced reactants for the HF/DF chemical laser. Many advanced fuels for the chemical HF/DF laser were tested in a small-scale CW HF chemical laser pursuant to the overall objective of the program. Because fluid dynamics plays an important role in determining laser performance, because the fluid properties of the various reactants (and their reaction products) are substantially different from one reactant to another, and because virtually all testing could be done with only one set of hardware, designed specifically for the baseline reaction set $D_2/F_2/He$ with H_2 cavity fuel, it was recognized from the outset that direct, quantitative results and comparisons would not always be possible. Nonetheless, several reactant types and several specific reactants were identified and evaluated in quantitative or semi-quantitative fashion so that several conclusions can be made. Also, as befitting an exploratory-type program, surprises and additional questions emerged which suggest areas where further work would be beneficial.

Advanced Cavity Fuels. There are three basic technical issues regarding alternate cavity fuels: (1) pumping rates, (2) degradation in mixing, and (3) deactivation rates. The results show that there are many cavity fuels that react with F-atoms sufficiently fast to produce sufficient gain for lasing. These include the hydrogen halides and simple aliphatic hydrocarbons. There is evidence that other simple

hydrocarbons, i.e., the freons, do not react sufficiently fast to produce gain. One example of a cyclic-compound suggests that such compounds may provide less gain than their aliphatic equivalent. Relative performance can be predicted on the basis of the rate of pumping compared to the rate at which the same H atom donor deactivates HF. Mixing characteristics play an important role in this effort as the results indicate that with poor mixing, the higher the deactivation rate, the poorer the performance. Another class of compounds such as dimethyl-ether may not produce sufficient gain in poor mixing circumstances because of high deactivation rates.

A specific candidate alternate fuel, HBr, which is thought to hold promise, gave varied results. It yielded the best results of the cavity fuels evaluated, but its performance relative to H_2 is still in question.

Some alternate, storable, cavity fuels, in general, can be expected to provide good performance if advanced nozzle concepts that sufficiently reduce the mixing problems can be devised. An important issue in ultimate performance achievable by simple hydrocarbons is the question of how many H atoms can be utilized per molecule.

Advanced Precombustor Reactants. The demonstration of lasing with the combinations $C_4F_8/F_2/He$ and $C_4F_8/NF_3/He$ shows that there are alternate oxidizer/fuel combinations more readily stored than F_2 and H_2 that will generate F-atoms via combustion sufficient to produce lasing. Semi-quantitative assessment of $C_4F_8/F_2/He$ suggests good performance potential. Substitution of N_2 for He appears quite feasible based on data obtained in this program, despite initial concern that performance would be severely reduced.

To fully realize the potential of advanced precombustor reactants and the potential of N_2 as a diluent, additional studies are needed and specifically designed hardware may be required. The question of the quantitative effect of DF as a deactivator did not get answered. Further work should be done in this area.

Other Issues. Evidence was obtained regarding the importance of the boundary layer on initiating the pumping reaction and the effect this can have on the length of the lasing zone. This should be studied further.

An issue that may have great importance in the ultimate application of advanced reactants is that of the effect on optimum outcoupling optics of substantial changes in deactivation characteristics and achievable small signal gains. This issue was raised when apparently identical, though based on results obtained, clearly different outcoupling optics gave substantially different results. A tentative explanation that this was caused by the interaction of the outcoupling optics with gain media possibly having different characteristics needs further work for clarification.

PHASE III: KINETIC MEASUREMENTS - GLOBAL PUMPING RATES

Experiments were conducted under this phase of the program to measure the global (overall) rates of selected pumping reactions. The six reactions investigated were the reactions of F-atoms with H_2 , HBr, CF_3H , CH_4 , C_3H_8 , and HI, respectively, to form HF. The rates of these hydrogen abstraction reactions were measured in a fast-flow EPR reactor.

The global rate constant for hydrogen abstraction from a fuel molecule determines if the given pumping reaction is fast enough to compete with the deactivation processes. The use of an EPR spectrometer coupled with a fast-flow reactor appears to be the best means for measuring the rates of fast atom-molecule reactions. As a diagnostic tool the EPR technique provides:

1. A direct, definitive identification of atomic species including different electronic and, if the paramagnetic component is diatomic, vibrational states
2. A determination of the absolute concentration from line shapes (first moments), if necessary
3. An extremely high sensitivity of about 10^{10} spins/gauss
4. A method that involves no interference from singlet state components
5. A measurement that does not perturb the reaction system

Moreover, the experimental conditions closely resemble laser experiments so that transfer of information is optimum.

The theoretical background concerning the apparatus and experiments is discussed first. This is followed by a description of the fast-flow EPR system and presentation and analysis of the rate data obtained. A computer program has been

written that solves numerically a set of equations which describe the fast-flow reactor EPR system with rigor. The program was used to obtain values for the global rate constants from the fast-flow reactor data.

THEORETICAL ANALYSIS

The method of determination of chemical reaction rates by the use of a fast-flow reactor will be described. Equations that define the rate of a chemical reaction in a flow system are presented and discussed, along with some elements of fluid mechanics needed for a description of the velocity and pressure gradients in the flow tube. This is followed by an explanation of how the EPR spectrometer is used to measure the progress of the reaction. Finally, computer programs for the rigorous analysis of reaction rate data are described.

Determination of Reaction Rates

Kinetic studies in fast-flow reactors are almost always analyzed assuming that gradients in both pressure and axial velocity are negligible and that the species concentration profiles are flat in the radial direction. For the hypothetical reaction,



occurring in a fast-flow reactor in which reactant B is present in excess,

$$-\frac{d[A]}{dt} = k[A][B] \quad (\text{III-2})$$

and

$$[B] = [B]_0 - [A]_0 + [A] \quad (\text{III-3})$$

Letting $dt = dx/v$, substituting Eq. III-3 in III-2, and integrating the result (assuming v is not a function of x), yields the equation:

$$k \approx - \frac{v}{\Delta x ([B]_0 - [A]_0)} \ln \frac{[A] [B]_0}{[A]_0 [B]} \quad (\text{III-4})$$

A nomenclature list is given at the end of this report.

Values of k are determined by measurements of $[A]$ as a function of distance down the flow tube, Δx . When k is large it is necessary to increase v and/or decrease the initial reactant concentrations, $[A]_0$ and $[B]_0$, to obtain reasonably sized variations in Δx for large changes in $[A]$.

Because of the very fast rates of the reactions studied in the experiments reported here, the fast-flow reactor was designed to maximize v while operating with a reactant (F-atom) concentration large enough to be detectable by EPR techniques. Constraints on the velocity were imposed: (1) by the necessity to operate at a pressure of no more than a few torr to avoid pressure broadening of the EPR lines for F, (2) by the 25-mm OD maximum tube size that could be accommodated by the EPR cavity, and (3) by the distance between the downstream sonic choke point and the region of the reactor over which kinetic measurements were to be made.

The necessity of operating the fast-flow reactor at low pressures and high flow velocities resulted in moderate variations of pressure and velocity with axial distance through the reactor. In addition, laminar flow in the reactor coupled with high reaction rates will result in radial concentration gradients in spite of the increased diffusional rates at low pressures. All of these conditions tend to undermine the assumptions used in deriving Eq. III-4 and, hence, reduce the confidence in values of k determined through its use. Therefore, more rigorous methods of obtaining rate constants from fast-flow reactor data have been applied to the present study. These will be described in a later section.

The relationships between pressure, Reynolds Number, friction factor, and velocity as a function of distance are important to the apparatus design and the analysis of the experimental data. These relationships are discussed in the next section.

Discussion of Fluid Mechanics

For a fast-flow tube being operated at a pressure of a few torr to reduce the reaction rate, the Reynold's Number (Dvp/μ) is usually less than 100, indicating that the flow is laminar. The friction factor, f , for laminar pipe flow is given by the expression:

$$f = 16/Re \quad (\text{III-5})$$

The effect of wall drag on compressible gas flow conditions in a tube can be obtained from Shapiro (Ref. 25). An equation relating Mach Number, M , to the friction factor, tube diameter and length, and L_{\max} from the point of measurement to the point where $M = 1$ (the sonic choke point) is:

$$4f \frac{L_{\max}}{D} = \frac{1-M^2}{\gamma M^2} + \frac{\gamma+1}{2\gamma} \ln \frac{(\gamma+1) M^2}{2 \left(1 + \frac{\gamma-1}{2} M^2\right)} \quad (\text{III-6})$$

for isentropic flow. This equation has been found to fit experimental v , p data rather well. The axial velocity as a function of distance to the sonic choke point, L_{\max} , computed for the fast-flow reactor for a typical mass flowrate using Eq. III-6, is shown in Fig. 193 together with the measured velocities at three points along the tube. The near exact agreement between the computed curve and the three data points is due to a minor adjustment (5 percent) in the gas viscosity. Once this adjustment has been determined, Eq. III-5 and III-6 can be used to relate v and p to the distance x for use in numerical solutions of the appropriate rate equations for a more accurate determination of k . Differences in v versus L_{\max} predicted by Eq. III-6 and the following expression:

$$4f \frac{L_{\max}}{D} = \frac{1 - \gamma M^2}{\gamma M^2} + \ln (\gamma M^2) \quad (\text{III-7})$$

for isothermal flow, are insignificant in the low Mach Number region of interest in this study.

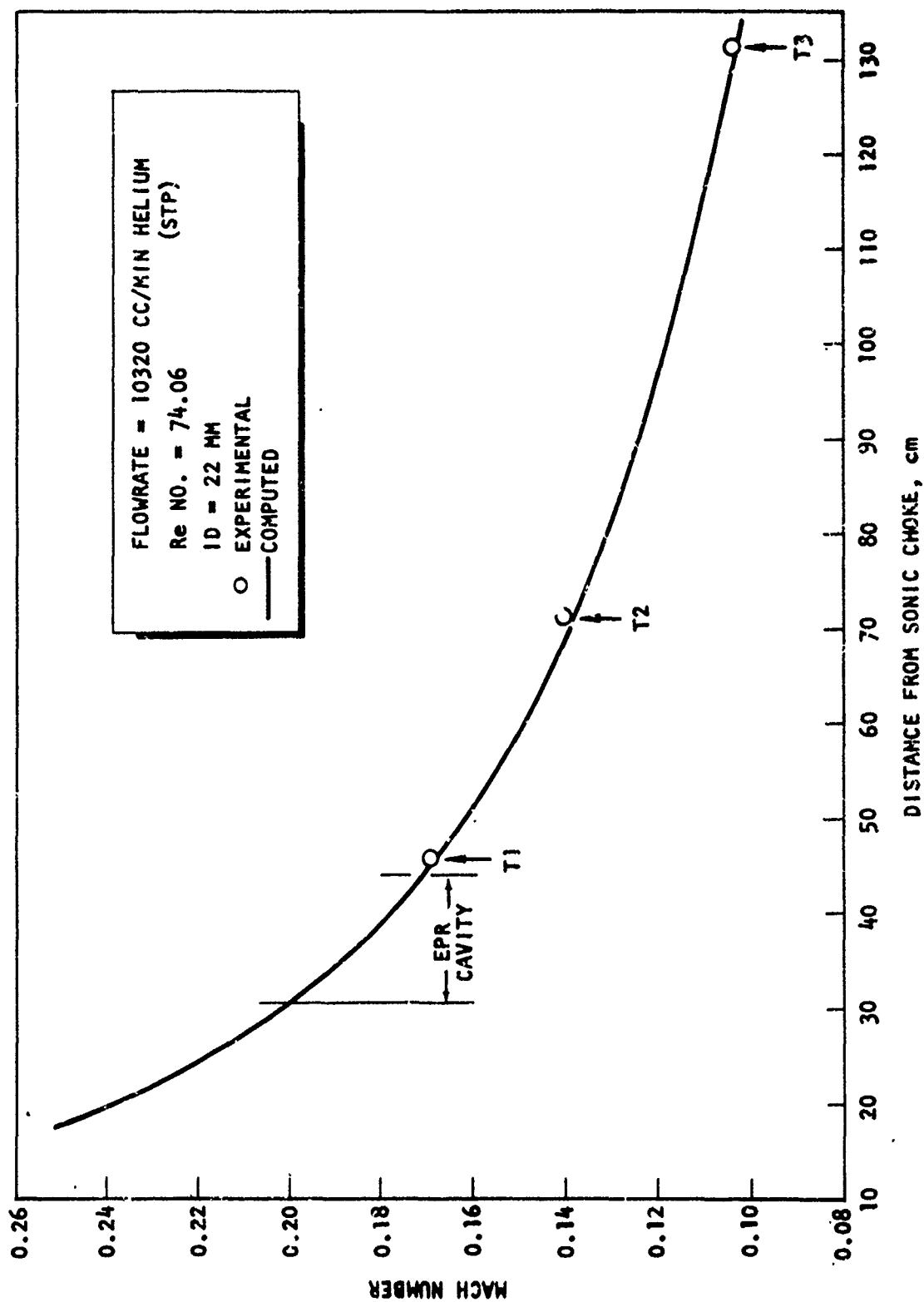


Figure 193. Fast Flow Reactor - Mach Number Versus Distance

According to Eq. III-4, it is desirable to use a high gas velocity when measuring a large rate constant since this serves to increase the distance, Δx , needed to produce a specified change in reactant concentration. There are constraints, however, on the gas velocity that can be used. From Fig. 193 it is clear that, for a total flowrate of 10,320 cc/min stp, the axial velocity gradients become very steep in a 22-mm ID tube at a Mach Number of 0.2. Small errors in Δx or in the pressure measurements could lead to large errors in k . An increase in flow tube diameter would lead to a lower velocity gradient, but the EPR cavity can accommodate only a 25-mm OD tube. An increase in total pressure in the fast flow tube would increase the Reynolds number, decrease f and, hence, also reduce the axial velocity gradient. Increased pressure, however, would broaden the EPR lines for F and result in a reduction in the sensitivity of F concentration measurements.

Another constraint on the velocity used in a fast-flow reactor is a consequence of the laminar flow condition. Laminar flow in a round tube produces a parabolic velocity profile given by the equation:

$$\frac{v}{v_0} = 1 - \frac{r^2}{r_0^2} \quad (\text{III-8})$$

where v_0 is the velocity at the center of a tube of radius r_0 and v is the velocity at a distance r from the center. The average velocity of the gas is equal to $v_0/2$.

A rigorous description of the fast-flow reactor will be developed after the theoretical considerations involved in the measurement of F -atom concentrations in the EPR spectrometer are discussed.

EPR Measurements

The EPR spectrometer measures the average of the reactant concentration over a finite length of the flow tube. Exactly how this average is taken over the length of flow tube monitored by the EPR cavity is determined by the coupling of the

cavity signal distribution function, $s(x)$, and a function relating the change of reactant concentration to the axial distance along the flow tube, $g[A]$. The EPR response, $S(x)$, resulting from this coupling is given by the expression:

$$S(x) \propto \int_{x_0 - \ell}^{x_0 + \ell} g[A] s(x) dx \quad (\text{III-9})$$

which links $S(x)$ to a distance x taken between any axial point within the EPR cavity (from $x_0 - \ell$ to $x_0 + \ell$) to the point in the flow tube where the reaction was initiated. The function $g[A]$ can be determined from the rate equations written for the fast-flow reactor.

For the simple case of a first-order reaction and a velocity which is independent of x , the rate constant can be determined from the slope of a plot of the natural log of the EPR signal of the monitored reactant versus the relative distance of the point at which the reaction was initiated. This can be shown as follows:

The cavity signal distribution function fitted to the experimental data is:

$$s(x) = \cos^2 \left[\frac{\pi}{2\ell} (x_0 - x) \right] + B \sin^2 \left[\frac{\pi}{\ell} (x_0 - x) \right] \quad (\text{III-10})$$

and the reactant concentration function for a first-order reaction is:

$$g[A] = C_0 e^{-k'x/v} \quad (\text{III-11})$$

Substituting Eq. III-10 and III-11 into Eq. III-9 yields the following expression for the EPR response:

$$S(x) \propto \int_{x_0 - \ell}^{x_0 + \ell} C_0 e^{-k'x/v} \left\{ \cos^2 \left[\frac{\pi}{2\ell} (x_0 - x) \right] + B \sin^2 \left[\frac{\pi}{\ell} (x_0 - x) \right] \right\} dx \quad (\text{III-12})$$

Letting $x - x_0 = y$, so that $dx = dy$ and the limits $x_0 + l$ and $x_0 - l$ become l and $-l$, the following expression results:

$$S(x) \propto C_0 e^{\frac{-k'}{v} x_0} \int_{-l}^l e^{\frac{-k'y}{v}} \left(\cos^2 \frac{\pi y}{2l} + B \sin^2 \frac{\pi y}{l} \right) dy \quad (\text{III-13})$$

The term $e^{-k'x_0/v}$ has been removed from the integral sign since it is not a function of y but is fixed for a particular measurement. As the distance x_0 is varied by moving the injector probe in the fast-flow reactor, the integral will remain constant. Thus, the slope of a plot of $\ln S(x)$ versus x_0 will yield k'/v . When v varies with x , $e^{-k'x_0/v}$ cannot be removed from the integral and the evaluation of k' requires knowledge of the signal distribution function and a numerical integration of Eq. III-9. This integration was carried out to obtain the global rate constants reported from this study. The determination of the signal distribution function is described in the experimental section.

Rigorous Description of Fast-Flow Reactor

It is apparent from Fig. III-1 that the assumption of constant velocity employed in the derivation of Equation III-4 is not valid and a more rigorous mathematical approach must be employed if accurate rate constants are to be obtained from the experimental results. In addition, axial and radial concentration gradients must be considered as well as the EPR cavity signal distribution function.

The general equation and boundary conditions which rigorously describe the concentration of the i th species in the fast-flow reactor are:

$$\partial_i \left(\frac{\partial^2 C_i}{\partial x^2} + \frac{\partial^2 C_i}{\partial r^2} + \frac{1}{r} \cdot \frac{\partial C_i}{\partial r} \right) - v_0 \left(1 - \frac{r^2}{r_0^2} \right) \frac{\partial C_i}{\partial x} - k C_i C_j = 0 \quad (\text{III-14})$$

$$\left. \begin{aligned} \mathcal{D}_i \left(\frac{\partial C_i}{\partial r} \right) &= -k_w C_i \text{ at } r = r_0 \text{ (at the wall)} \\ \frac{\partial C_i}{\partial r} &= 0 \text{ at } r = 0 \end{aligned} \right\} \quad \text{Boundary Conditions} \quad \begin{matrix} \text{(III-15)} \\ \text{(III-16)} \end{matrix}$$

Other equations are required to describe the change in velocity and pressure with axial distance x before Eq. III-14 can be solved. These remaining expressions are the continuity equation:

$$\frac{\partial(\rho A v)}{\partial x} = 0 \quad \text{(III-17)}$$

and the Poiseuille flow equation:

$$p_2^2 - p_1^2 = \frac{16 \mu R T N L}{\pi r_0^4} \quad \text{(III-18)}$$

where L is the distance between points 1 and 2, N is the total molar flowrate, and R is the gas constant.

Computer programs have been developed to solve the rigorous Eq. III-14 through III-18 for the fast-flow reactor. These computer programs additionally take into account the EPR cavity signal distribution function to determine the point along the cavity axis where the reactant concentration matches the concentration measured by the EPR spectrometer. A brief description of the numerical procedures used in these computer programs is given in Appendix C.

The numerical solution of the complete set of equations describing the chemical reaction in the fast-flow reactor can be substantially simplified if the axial diffusion term, $\mathcal{D}(\partial^2 C_1 / \partial x^2)$, in Eq. III-14 can be neglected. Ordinarily, axial diffusion is quite small when compared with the bulk flow in the axial direction. However, at low pressures where \mathcal{D} is large and near the tube wall where the velocity is small, the axial diffusion may not be negligible. To check out the

possible importance of axial diffusion, numerical solutions were obtained (Appendix III-A) for Eq. III-14 with and without the axial diffusion term and a comparison of species mole fraction profiles was made for one typical case involving the reaction $H_2 + F \rightarrow HF + H$. Computed radial profiles for the mole fraction of H and F at a distance of 25 cm from the mixing point are presented in Table XLI. The few percent discrepancy in mole fraction values obtained from the solutions with and without axial diffusion (the first two sets of columns) is, in part, attributable to a difference in the reactant molar flux rates at the mixing point. Both solutions were obtained using the same initial values of species volumetric flowrates, Avf_i , in the axial direction, whereas the solutions should have been obtained using identical initial values of the species volumetric flux rate; for the nonaxial diffusion case, this flux is Avf_i , while, for the axial diffusion case, it is $A(vf_i - \partial f_i / \partial x)$. The solution of the nonaxial diffusion case was determined using appropriately altered species feed rates (based on the solution of the axial diffusion case to determine $\partial f_i / \partial x$ at the mixing point). Radial profiles from this latter solution, presented in the third set of columns in Table XLI, are in better agreement with those given for the problem with axial diffusion. From the results presented in Table XLI, it would appear that for these fast-flow experiments the axial diffusion term in Eq. III-14 can be neglected.

EXPERIMENTAL

Apparatus

The fast-flow apparatus used to determine the reaction rate of F-atoms with various gases consists of a quartz flow tube in which the reaction takes place, an EPR spectrometer to monitor the concentration of the reactants, an injector system to introduce one of the reactants into the flow tube, a microwave discharge, a flow control system, and two vacuum pumps. A schematic of the apparatus is shown in Fig. 194. (Design considerations for the flow tube were presented in the Theoretical Analysis discussion.) The apparatus is similar in design to that employed by Westenberg and deHaas (Ref. 26).

TABLE XII. EFFECT OF AXIAL DIFFUSION ON RADIAL MOLE FRACTION GRADIENTS FOR THE
REACTION $F + H_2$ ($\Delta X = 25$ cm)

$\Delta r(\text{cm})$	No Axial Diffusion*		With Axial Diffusion		No Axial Diffusion (Feed Rate Adjusted)**	
	$f_H \times 10^4$	$f_F \times 10^5$	$f_H \times 10^4$	$f_F \times 10^5$	$f_H \times 10^4$	$f_F \times 10^5$
0	3.714	1.90178	3.699898	1.943657	3.70203	1.92288
0.1	3.7148	1.88719	3.700743	1.928807	3.70287	1.90815
0.2	3.71733	1.84342	3.703278	1.884255	3.7054	1.86395
0.3	3.72132	1.7744	3.707320	1.814004	3.70943	1.79425
0.4	3.72652	1.68585	3.712592	1.723878	3.71468	1.70482
0.5	3.73259	1.58487	3.718734	1.621126	3.72051	1.60284
0.6	3.73909	1.47931	3.725307	1.513760	3.72738	1.49622
0.7	3.74557	1.37712	3.731828	1.409992	3.73393	1.39301
0.8	3.75153	1.286	3.737754	1.317832	3.73995	1.30096
0.9	3.75644	1.21309	3.742543	1.244878	3.74491	1.22732
1.0	3.75975	1.16521	3.745663	1.197976	3.74825	1.17894
1.1	3.76085	1.14924	3.746704	1.182342	3.74936	1.16282

* Molar feed rate is equal to molar flux rate used for the axial diffusion case.

** Feed rate was adjusted so that molar flux rate equaled that used for the axial diffusion case.

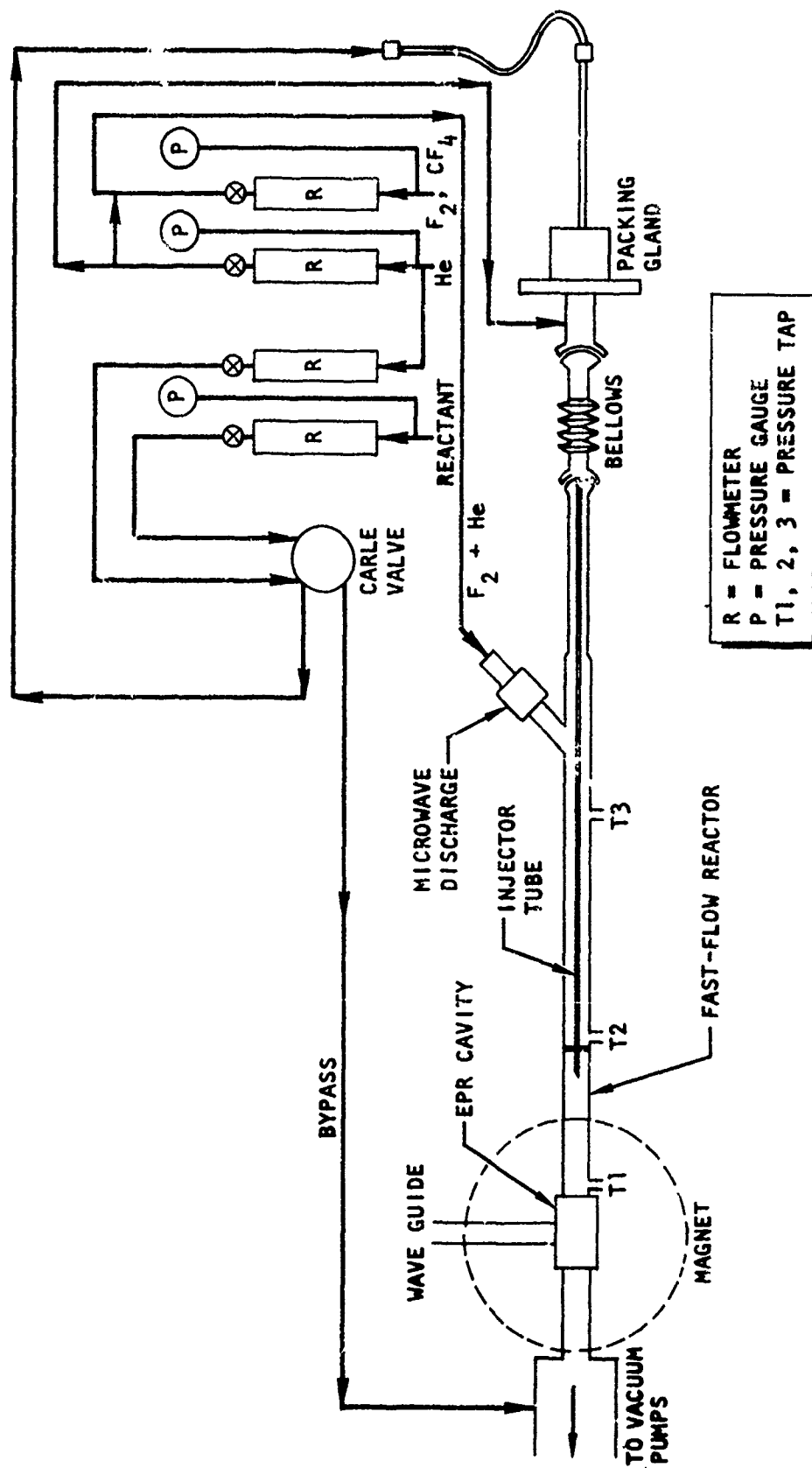


Figure 194. Schematic of Fast-Flow-EPR System

The portion of the fast-flow reactor where measurements are taken was constructed of 22-mm ID quartz tubing that had been washed in an HF solution. Pressure taps were placed at three points along the length of the flow tube: directly in front of the EPR cavity, and at distances of 25.5 and 85.5 cm upstream from this tap. Under experimental conditions, the flow will produce a sonic choke at the point where the 22-mm ID quartz tube enters a 4-inch-diameter vacuum line. The flowrate and pressure at any point upstream from the sonic choke can be computed from a known feed rate to the tube or from a measurement of the pressure at any of the three locations down the flow tube. Pressure measurements were made to the nearest 0.001 torr with an MKS Baratron pressure meter. The reference vacuum for the Baratron was maintained with a Varian vac-ion pump.

Fluorine atoms for the kinetic study were produced by passing a mixture of helium and either F_2 or CF_4 through a microwave discharge formed in an alumina tube. The F-atom stream enters the main flow tube through a side arm located about 100 cm upstream from the center of the EPR cavity. A mixture of the second reactant with helium is passed through an injector tube and enters the flow tube via a number of small holes at the tip of the 4-mm OD injector tube. The holes at the injector tip are set so as to direct the reactant flow radially into the flow tube, i.e., perpendicular to the flow of helium/F-atom stream, for rapid mixing. Three legs affixed to the injector serve to position the injector tube tip at the center of the flow tube. The injector tube enters the flow tube through a pressure tight packing gland which permits axial movement of the injector. By manual positioning of the injector tip along the flow tube, the distance (and, hence, reaction time) from the initiation of the chemical reaction to the EPR cavity can be varied.

All of the gases used were metered with Browne flowmeters. With the exception of F_2 , all flowmeters were calibrated with the gas itself. For F_2 , the calibration was determined using O_2 and the flowrate was corrected for density and viscosity differences between O_2 and F_2 . Before entering the flowmeter, the gas was passed through a bed of NaF to remove HF. In spite of this precaution, the glass flowmeter would undergo a slow chemical attack and require frequent

cleaning and recalibration. After the response of the EPR spectrometer to the F line at 5211 gauss was established, the F-atom concentration could be easily measured by the peak-to-peak amplitude of the strong EPR line, and the flowmeter was used less frequently.

A Carle valve located on the gas flow control panel can be positioned to send either helium or the reactant into either the injectortube or a "bypass" line which enters the fast flow system downstream of the EPR cavity. The valve provides a convenient way of stopping the chemical reaction periodically during an experiment to check the F concentration without altering the flowrate of the other reactant. The helium flow substituted for the reactant when the Carle valve is switched, serves to maintain a constant pressure in the flow tube.

The mass flowrates employed in this study were easily handled by a Roots blower and a Kinney KDH-130 high vacuum pump connected in series. The pressure within the 4-inch OD vacuum line was typically less than 0.01 torr at about 20 cm downstream of the choke point.

The EPR detection system was a standard Varian E-9 EPR spectrometer, equipped with a 9-inch magnet and a wide access TE_{01N} cavity. The cavity is able to accommodate a tube of 25-mm OD. The best cavity Q-factor was obtained when the microwave frequency was about 8.846 GHz. This corresponds to a value of $N = 2$ for the EPR cavity. The magnetic field range that could be studied was 0 to 9.6 KG. At 5 KG, the resolution over the sample volume was about 0.25 G.

EPR Spectra of Fluorine Atoms

The EPR spectrum of fluorine in the $2P_{3/2}$ ground state exhibits an extremely large hyperfine interaction. As a result, the usual high field approximation for calculation of the EPR spectrum is not valid, and it is not possible to separate the wave functions which describe the electron spin and orbital angular momentum from the nuclear spin. Experimental and theoretical analyses (Ref. 27, 28, and

29) show that the ground state exhibits six intense lines and two weak lines. The weak lines are due to forbidden transitions. Of the six intense lines, two have about 30 percent greater intensity than the other four. One of the two more intense lines occurs near the spectrum of oxygen atoms while the line that occurs at the higher field is away from any common interference. The higher-field line was therefore chosen for use in the kinetic measurements of fluorine. This line corresponds to the transition $F = 2, m_f = 0$ to $F = 2, m_f = -1$, and occurs at a magnetic field of 5211 gauss at the frequency used in these experiments, 8.846 GHz. The location of any of the F lines can be calculated for any frequency from the relationships given by Valence et al. (Ref. 29).

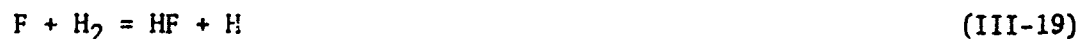
The particular line chosen is less sensitive to pressure broadening than any of the other F lines. When kinetic measurements were made, the small variation in line width over the small variation in pressure which was incurred in each run was found to be insignificant. In these experiments, sensitivity is considerably more important than resolution. As a result, the fluorine line was overmodulated under conditions of slight rf power saturation so that the maximum signal-to-noise ratio could be obtained. Since the line width increases rapidly with modulation amplitude at the point where the maximum signal intensity is obtained, it was advisable to sacrifice about 10 percent of the maximum signal to decrease the line width by nearly a factor of 2. This permits examination of the line shape to see whether any gross effect occurs. When the flow tube was operated at 2.2 torr, the modulation amplitude and incident microwave power were 2.0 gauss and 30 mW; at 1.15 torr the values were 1.6 gauss and 25 mW.

Titration and Calibration of the EPR Spectrometer for Atomic Fluorine Flow

Gas titration experiments in the fast flow reactor were conducted by withdrawing the injector tube until the tip was even with the feed line through which F entered the flow tube. This position allowed the maximum reaction time for the gases before reaching the EPR cavity. The F_2 or CF_4 volumetric flowrate to the microwave discharge would be adjusted to some arbitrary value and the peak-to-peak

height of the EPR signal of F measured. As the EPR spectrometer monitored the F concentration, metered amounts of the titrating gas, H₂ or HBr, were fed into the fast-flow reactor via the injector tube. The reaction was fast enough so that it could be considered essentially completed when the gases passed through the zone monitored by the EPR spectrometer.

The results of a typical titration of F by H₂ are plotted in Fig. 195. The measured concentration of F-atoms decreased linearly with H₂ flowrate except very near the end point of the titration. If any appreciable amount of F₂ did not dissociate, the F₂-H₂ chain reaction



could occur, resulting in consumption of H₂ without a decrease in F-atom concentration. If the rate of reaction III-20 is sufficiently fast and 20 percent of the F₂ did not dissociate, the broken linear titration curve in Fig. 195, which has a sharp break at 2 cc/min of H₂, would have been obtained. If reactions III-19 and III-20 have rate constants of 1×10^{13} and 2×10^{12} (mole/cc)⁻¹ sec⁻¹, respectively, it can be calculated that the smooth broken curve would have been obtained if 20 percent of F₂ were not dissociated.

The experimental curve in Fig. 195 intersects the y axis at 1.00 indicating that essentially complete dissociation of F₂ occurred in the microwave discharge. With CF₄, however, on the order of only 10 to 20 percent was dissociated (to F + CF₃) under these conditions. Extrapolation of the linear portion of the experimental curve to the x axis gives the flowrate of F + F₂ (in this case, 16 cc/min) and from this, the pressure, and the total flowrate, the F-atom concentration can be calculated. Extrapolation of the linear portion of the curve to the y axis gives the fraction F₂ undissociated from the intercept, I, as follows:

$$\text{Fraction Undissociated} = \frac{2(I - 1)}{1 + 2(I - 1)} \quad (III-22)$$

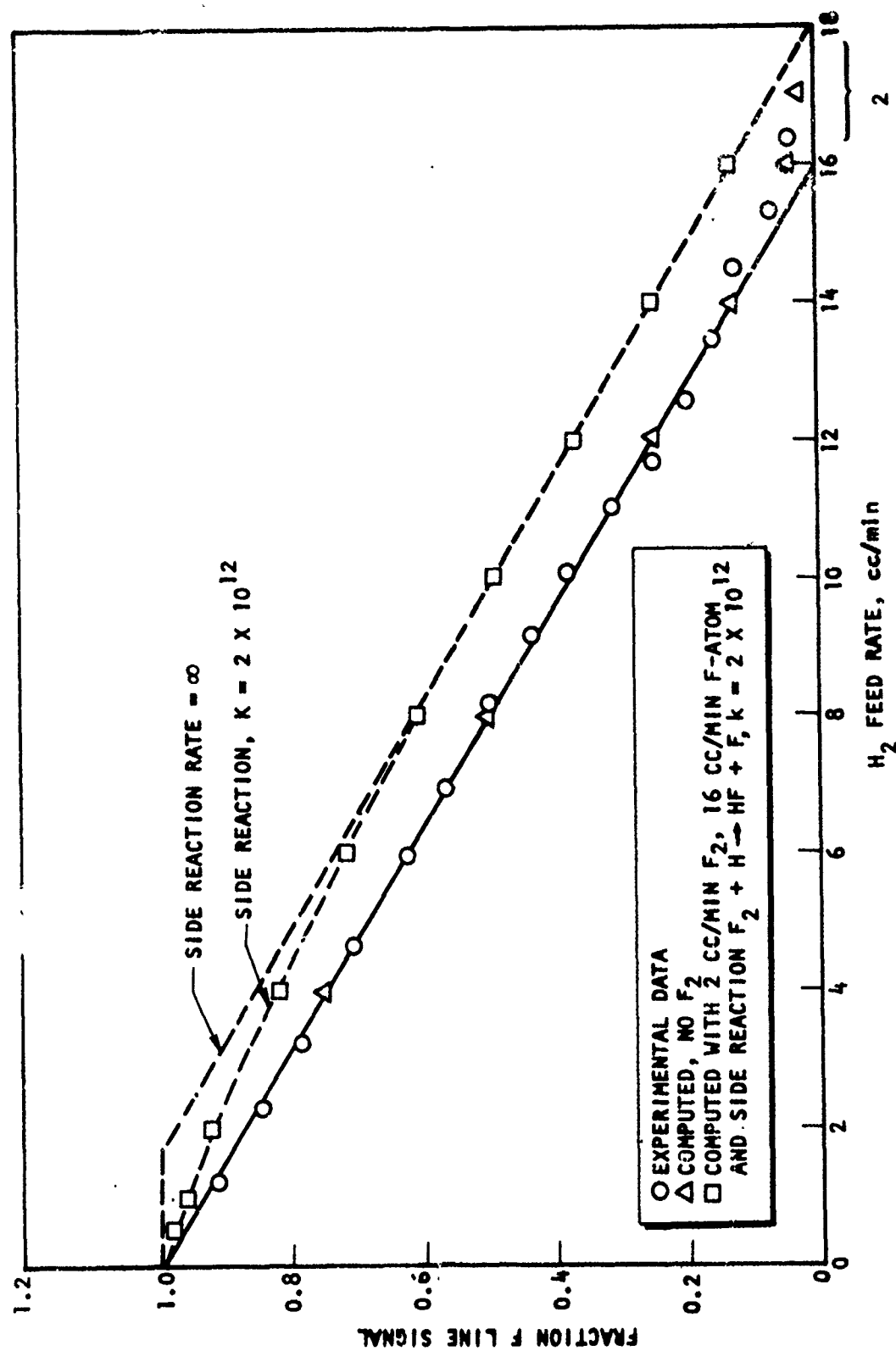


Figure 195. Titration Experiment, $F + H_2 \rightarrow HF + H$

Since the EPR line width and, therefore, the peak-to-peak amplitude, is a function of the pressure, the standardization and calibration of the EPR signal had to be repeated for each total pressure at which the fast-flow reactor was operated. During each kinetic experiment, the pressure distribution in the reactor was constant to within ± 1 percent so that the EPR signal intensity did not deviate by more than ± 2 percent from the calibration factor. Other errors, such as resetting the EPR power, crystal bias, and modulation amplitude also contribute at least that much error.

Wall Reactions

Several experiments were conducted to determine the amount of wall recombination of atomic fluorine occurring in the fast-flow reactor. Experiments were performed using both F_2 and CF_4 as sources of F. During these experiments, the flow through the injector tube was turned off. One measurement of F concentration was taken with the injector tube drawn back so that the F would contact only the inside wall of the 22-mm ID quartz flow tube; another F measurement was taken with the injector tube pushed in up to the EPR cavity. Any change in the atomic fluorine EPR line after insertion of the injector tube would be attributed to the additional wall area in contact with F (the fractional increase in wall surface was given by the ratio of the diameters of the injector tube and the flow tube, or $4/22$). When F_2 was used as a source of F, no change in concentration was detected upon injector insertion. Use of CF_4 as a source of F produced a small but reproducible change in F concentration. The CF_3 appears to have an effect on the rate of wall recombination.

At a later date, when the fast-flow apparatus was disassembled for repair, re-washing the flow tube with a dilute HF solution revealed a thin film of Teflon-like material that had been deposited on the flow tube. This film was undoubtedly produced by the species resulting when CF_4 passed through the microwave discharge and the film formation could account for the small disappearance of F by wall reaction when CF_4 was used.

Cavity Signal Distribution Function

The EPR measures the number of unpaired electrons over a finite distance along the cavity axis. As shown in the theoretical section, the distribution of the signal density within this sampling zone is needed to determine kinetic rate parameters in a fast-flow system.

Axial dependence of the signal density was measured by placing a sample of diphenyl picryl hydrazyl (DPPH), smaller than 0.5 mm in its longest dimension, in a capillary and recording the intensity of the DPPH transition line as a function of the position of the capillary tube. The capillary was moved along the cavity axis by attaching it to the movable jaw of a vernier caliper. Signal amplitudes were repeatable to within ± 0.5 mm. A least-squares regression was carried out on the data so that it fit a function of the form of Eq. III-10 where x is the position along the axis of the cavity and x_0 is the position of maximum sensitivity on that axis. B and l may be considered as empirical parameters for the purpose of this discussion. Of these, only l has any real significance since l represents one-half of the effective length of the cavity. Values of l were systematically varied and best values of B were determined. The set of values of B and l which gave the minimum least-squares deviation from the experimental values was selected. The best values were -0.192 for B and 3.60 cm for l .

It was assumed that the signal density at a given radius from the axis is proportional to the signal density along the axis. This assumption is probably valid over most of the volume of the flow tube within the cavity, but near the values of x close to $+3.6$ or -3.6 cm, the signal density is probably smaller than would be predicted from Eq. III-10.

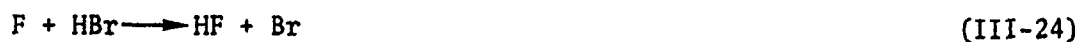
Experimental Procedure

The experimental procedure consisted first of establishing the desired flow conditions (pressure, velocity, reactant concentration) in the fast-flow reactor, turning on the microwave discharge, and tuning and setting the EPR spectrometer

to monitor the appropriate transition of F. With the Carle valve positioned so that the gas to be reacted with F enters downstream of the EPR cavity, the EPR spectrometer was used to monitor the F concentration so that the F₂ or CF₄ feed rate could be adjusted to the desired level. To simplify the data analysis, the ratio of fuel to F was usually kept at, or above, 5 to 1. When the reactant concentrations were properly set, the Carle valve was switched to initiate the chemical reaction at the tip of the injector tube. The injector tube was then positioned at various distances from the EPR cavity, and at each position the F concentration was determined from the peak-to-peak amplitude of the 5211 gauss EPR line. After several concentration-distance measurements, the Carle valve would be switched and the initial F concentration would be measured to ascertain whether any drift in F concentration had occurred. The data recorded during a typical experiment included the initial reactant flowrates, the pressure at the EPR cavity, and the injector position and F concentration. The ratio of (a) the EPR signal measured with reacting gas to (b) the EPR signal measured in the absence of reacting gas, determined as a function of the injector distance, was used to ascertain the reaction rate constant.

RESULTS AND DISCUSSION

Reaction rate data were obtained with the fast-flow EPR system for the following reactions:



The computer program written for the case in which axial diffusion was disregarded was used to generate several curves (each representing a different reaction

rate constant) on a plot of $\ln ([F]/[F]_0)$ versus ΔX . The best value of k was chosen by matching the slopes of the computed curves to the experimental data. Diffusion coefficients for reactants in helium were estimated using various procedures outlined by Reed and Sherwood (Ref. 30) or Sherwood and Pigford (Ref. 31) whenever they could not be obtained from the literature. The diffusion coefficients used in solving Eq. III-14 through III-18 for the chemical reactions (Eq. III-23 through III-27) are given in Table XLII.

TABLE XLII. DIFFUSION COEFFICIENTS OF REACTANT IN HELIUM

Reactant	D at 1 atm cm ² /sec	Source
F	1.45	Estimated (Ref. 31)
H ₂	1.62	Experiment
HBr	0.652	Estimated (Ref. 30)
CF ₃ H	0.612	Estimated (Ref. 30)
CH ₄	0.675	Experiment
C ₃ H ₈	0.485	Estimated (Ref. 30)

Reaction of F with H₂

The experimental results obtained for the F + H₂ system are summarized in Table XLIII. A plot of a typical experiment is shown in Fig. 196. The reaction rate constants listed in the column labeled Eq. III-4 were determined using Eq. III-4, i.e., plotting $\ln ([F]/[F]_0)$ versus Δx with the assumption that the quantity $\ln ([H_2]_0/[H_2])$ was zero and that the concentration of F measured in the EPR cavity corresponded to the actual F concentration at a point in the cavity that was independent of the axial position of the injector tube tip (this was shown to be true for a first-order reaction with a constant average axial velocity, Eq. III-13).

The second column under the rate constant heading in Table XLIII lists the rate constants obtained using the numerical solution to Eq. III-14 through III-18. This solution takes into account radial diffusion and the radial velocity gradient

TABLE XLIII. RATE DATA FOR $F + H_2 \rightarrow HF + H$ AT 298 K

Fluorine Source	Pressure, torr	Initial F-Atom Concentration $\times 10^{-13}$, atoms per cc	(H_2/F)	Velocity*, cm/sec	Rate Constant $\times 10^{-13}$ (mole/cc) $^{-1}$ sec $^{-1}$	
					** Eq. III-4	*** Eq. III-14 through III-18
F ₂	2.15	6.94	5.0	17,160	0.88	0.85
F ₂	2.14	4.15	5.0	17,130	0.93	0.95
CF ₄	2.2	1.4	5.0	16,670	0.95	1.1
↓	2.16	3.54	5.0	16,920	1.06	1.1
	2.17	2.90	5.9	16,600	1.07	1.04
	1.16	3.13	3.7	11,200	1.09	1.0
	1.15	4.01	5.25	11,200	0.906	0.95
	1.14	2.72	4.79	11,270	1.06	1.0

*Velocity at the pressure tap closest to the EPR cavity

**Radial gradients ignored

***Radial gradients considered, axial diffusion ignored (negligible)

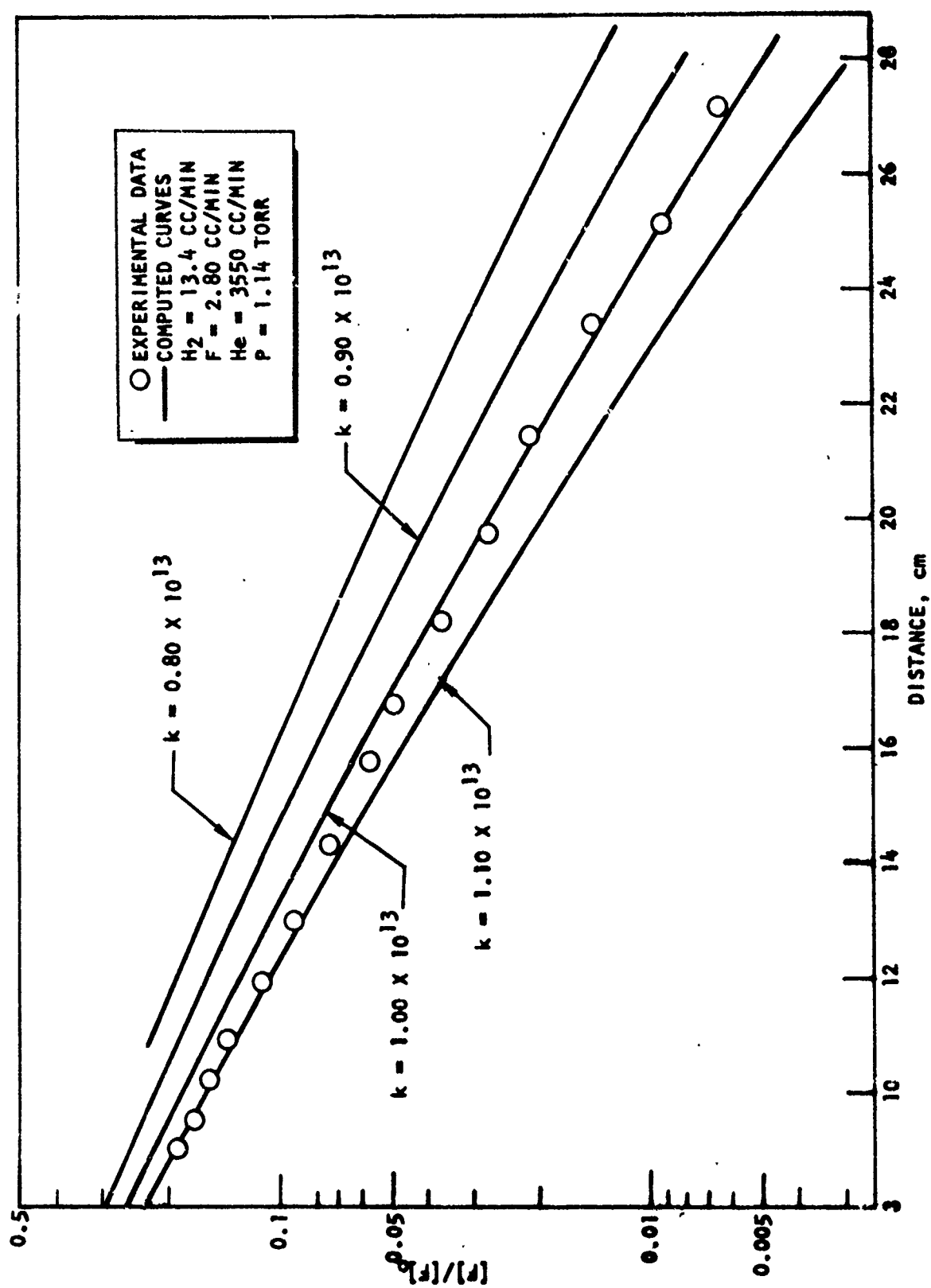


Figure 196. Determination of Reaction Rate Constant ($F + H_2$)

but ignores the axial diffusion term in Eq. III-14. A comparison between the reaction rate constants acquired via Eq. III-4 and the more sophisticated analysis embodied in the application of Eq. III-14 through III-18 reveals only minor differences of at most 10 or 15 percent. The near agreement of the values is attributed to the large diffusion coefficients of H_2 and F which tend to flatten the radial concentration profiles that might otherwise result from the parabolic radial velocity distribution. An examination of the computer printout also revealed that the point in the EPR cavity at which the F concentration was, in effect, being measured, was nearly independent of the distance between the cavity and the initial mixing point.

The average rate constant for the eight $F + H_2$ experiments is 1.0×10^{13} cc/mole/sec. This compares favorably with several previous measurements of this rate constant (see Table III of Ref. 32 for a summary). The first rate measurement was reported by Fettis, Knox, and Trotman-Dickenson in 1960 (Ref. 33). Their reported rate constant at 300 K was 5×10^{12} (later revised to 1.1×10^{14} , Ref. 34). Homann, et al. (Ref. 35) and Dodonov, et al. (Ref. 36) used flow systems and mass spectrometric analysis to measure the rate of this reaction. Homann, et al., determined a rate constant at 300 K of 1.0×10^{13} in agreement with the rates obtained on this program. They used flowrates of only 1700 cm/sec, but worked at very low reactant concentration to spread the reaction zone sufficiently. Dodonov, et al., also measured the rate of this reaction using a mass spectrometer technique. They obtained a rate constant at 300 K of 2×10^{13} and state that the mass spectrometer was sensitive to about 10^{10} to 10^{11} particles per cm^3 . Their flow velocity was only 580 cm/sec and the F-atom concentration was 0.001 torr. Dodonov, et al., apparently followed the H_2 concentration as a function of distance. From their data, the half-distance for H_2 disappearance was only 6 mm (a factor of 10 less than the reaction distance achieved in our studies), suggesting that the method was not accurate. From their method of calculating the rate constant, Dodonov, et al., must have used pseudo first-order conditions with F-atoms in excess.

The use of mass spectrometric analysis in a fast-flow reactor has the serious disadvantage that the sample must be taken either from the boundary layer or

from a point where the flow is diverted, giving an uncertainty in the calculated residence time. The fast-flow EPR systems have the advantage that reactants continue to flow at high velocity through the measurement cavity.

More than one-half of the HF formed in the $F + H_2$ reaction is in the second vibrational level. The following distributions of vibrational energy have been reported:

	<u>HF(3),%</u>	<u>HF(2),%</u>	<u>HF(1),%</u>	<u>HF(0),%</u>
Jonathan, et al. (Ref. 37)	28	55	17	0
Chang and Sesser (Ref. 38)	28	55	17	--
Berry (Ref. 39)	32	50	15	3

Reaction of F with HBr

The data and results determined for the reaction of F with HBr are summarized in Table XLIV. Rate constants determined using Eq. III-4 and the simplified computer program for Eq. III-14 through III-18 are appropriately labeled and listed under the Rate Constant heading. In contradistinction to the $F + H_2$ reaction, there is a noticeable increase in the value of the rate constant for $F + HBr$ determined using the numerical solution of Eq. III-14 through III-18 over that found via Eq. III-4. The increases range from 10 to nearly 50 percent. This is undoubtedly caused by the lower diffusion coefficient of HBr which, in turn, results in larger radial concentration gradients. As with the $F + H_2$ reaction, the point within the EPR cavity at which, in effect, the measurement of F concentration is made, varied negligibly as the position of the initial mixing point was changed.

Initial studies of the $F + HBr$ reaction revealed that at longer reaction times (large Δx) the F concentration declined much faster than would be expected for a simple chemical reaction. As shown in Fig. 197, the data could have been correlated by two different lines suggesting that more than one reaction was occurring. The rate constants given in Table XLIV were determined using the slope

TABLE XLIV. RATE DATA FOR $F + HBr \rightarrow HF + Br$ AT 298 K

Fluorine Source	Pressure, torr	Initial F Atom Concentration $\times 10^{-13}$ atoms per cc	(HBr/F)	Velocity*, cm/sec	Rate Constant $\times 10^{-13}$ (mole/cc) $^{-1}$ sec $^{-1}$	
					Eq. III-4	Eq. III-14 through III-18
F ₂	2.22	8.65	5.0	16,550	1.65	2.4
F ₂	2.20	5.12	4.88	16,700	1.70	2.1
CF ₄	2.22	3.26	5.52	16,320	2.05	2.6
	2.21	3.01	5.10	16,800	1.99	2.3
	2.18	2.22	4.92	16,900	2.12	2.5
	2.20	2.16	10.3	16,920	2.01	2.2
	1.15	2.52	5.62	11,320	3.02	3.4
	1.15	1.25	6.0	11,420	2.74	3.3
F ₂	2.19	1.46	7.10***	16,700	2.62	3.1
F ₂	2.21	2.48	5.86***	16,800	2.02**	2.4**

* Velocity at the pressure tap closest to the EPR cavity.

** Air leak during experiment probably affected result.

*** Purified HBr.

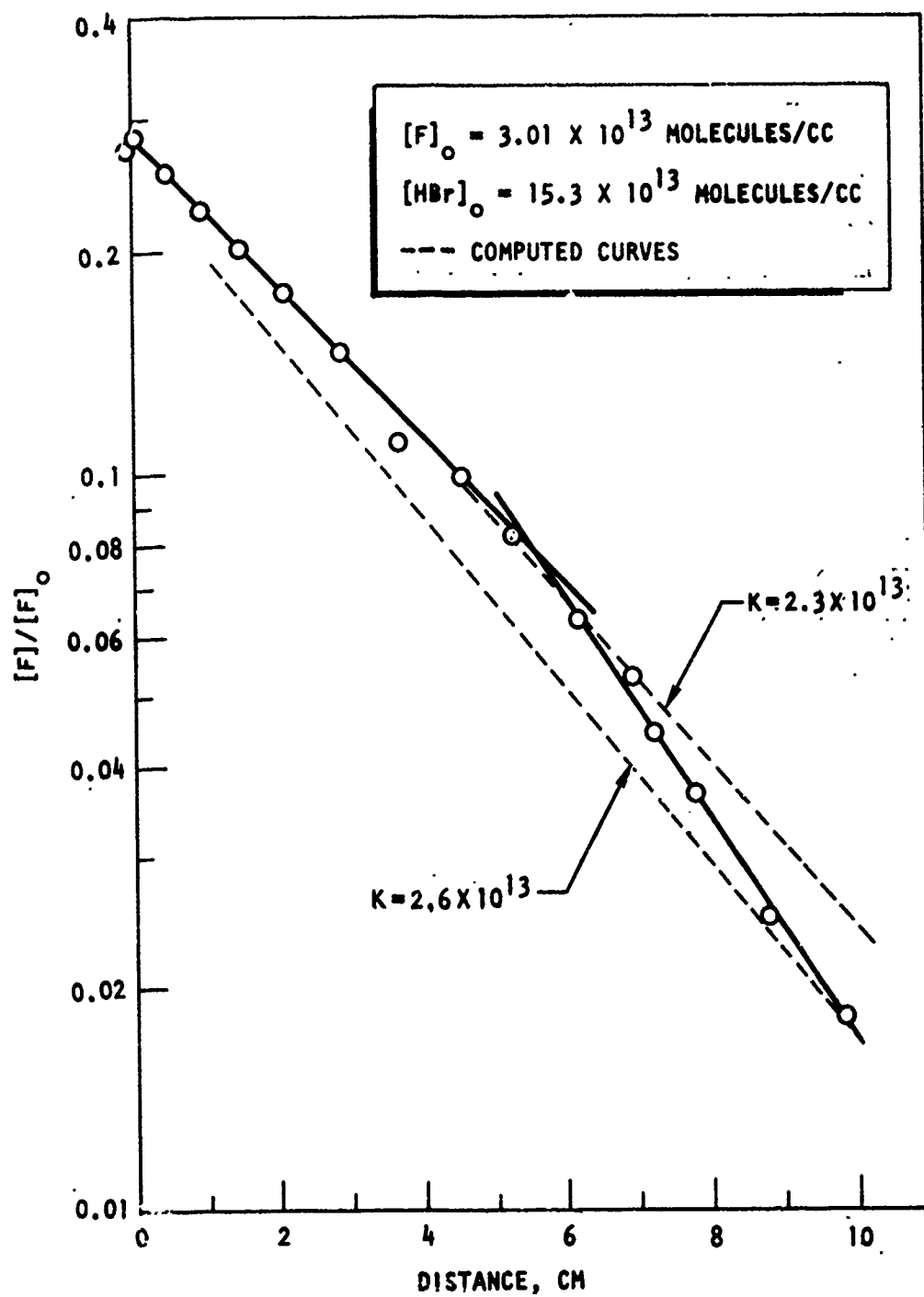


Figure 197. Experimental Data, $F + HBr \rightarrow HF + Br$

representative of the data points taken at lower Δx . At the time these data were taken, the HBr supply was suspected of being contaminated with water (which would aid the decomposition of HBr in the presence of metal). After the first two experiments listed in Table XLIV were conducted, the HBr cylinder was routinely chilled in solid CO_2 and then vented to remove any H_2 that might have accumulated from HBr decomposition between experiments.

The existence of side reactions that could account for the type of experimental data correlation shown in Fig. 197 was checked out by using a sample of HBr purified by redistillation from several cold traps in a titration experiment with F. The F was found to disappear in a one-to-one relationship to the amount of HBr fed to the fast-flow reactor; there was no evidence of side reactions involving F. The same batch of purified HBr was used to conduct the last two experiments listed in Table XLIV. Data taken near the end of the second of these two experiments did not correlate well with previous data. An air leak into the fast-flow system, found after the experiments were concluded, could have been responsible.

The average of the 10 experimental values given in Table XLIV is 2.6×10^{13} (mole/cc) $^{-1}$ cm $^{-1}$. However, three of the rate constants are substantially higher than the rest, two determined at a lower pressure than the others, and one determined using purified HBr. It is difficult to choose which group of values is nearer the true rate constant but based on the fact that one of the three higher values was obtained using purified HBr, it appears reasonable to favor the higher value of 3.1×10^{13} (mole/cc) $^{-1}$ sec $^{-1}$. However, because the cause of the discrepancy is not known, a rate constant of 2.4 to 3.1×10^{13} will be reported.

Jonathan, et al. (Ref. 37) studied the F + HBr reaction by an infrared chemiluminescent technique and determined that the vibrational energy is distributed in the product HF as follows: HF(4), 20%; HF(3), 27%; HF(2) 29%; HF(1), 18% and HF(0), 6%. They also estimated from their results that the global rate constant for the F + HBr reaction is 0.87 times that for the F + CH_4 reaction. The rate measured in this study (next section) for the F + CH_4 reaction was 3.2×10^{13} . Applying the factor of 0.87 would give a value of 2.7×10^{13} for the expected rate of the F + HBr reaction in good agreement with the rates listed in Table XLIV.

Reaction of F with CF₃H and CH₄

Phase II small-scale laser tests indicated CF₃H was one of several reactants studied that did not produce lasing. The reaction rate of CF₃H with F was investigated in the fast-flow-EPR system to provide a verification of the suspected low pumping rate. For comparison with the rate of hydrogen extraction from CF₃H, a single experiment was performed on the reaction F + CH₄.

The results of the reaction rate study of CF₃H are listed in Table XLV. Rate constants determined using Eq. III-14 through III-18 are considered to be the best values for the reaction F + CF₃H. The average is 1.0×10^{11} .

It is curious that for this reaction, the rate constant determined using the more exact method of data analysis is less than the values measured using Eq. III-4 while, for most of the other reactions studies, the opposite is true.

TABLE XLV. RATE DATA FOR F + CF₃H → H + CF₃ AT 298 K

Fluorine Source	Pressure, torr	(CF ₃ H/F)	Velocity,* cm/sec	Rate Constant x 10 ⁻¹¹ (mole/cc) ⁻¹ sec ⁻¹	
				Eq III-4	Eq III-14 through III-18
F ₂	1.17	10.5	11,400	1.41	0.9
F ₂	1.16	>40	11,420	1.16	0.9
F ₂	0.74	>40	8,540	1.21	1.1

*Average velocity measured at the pressure tap closest to the EPR cavity.

The rate of the reaction F + CH₄ was investigated for comparison with the reaction of F with CF₃H. The numerical solution of Eq. III-14 through III-18 yielded a value of 3.2×10^{13} (mole/cc)⁻¹sec⁻¹. Using Eq. III-4, the reaction rate was estimated to be 2.6×10^{13} (mole/cc)⁻¹sec⁻¹. The reaction F + CH₄ is about 350 times faster than the F + CF₃H reaction. About a factor of 10 of this difference

might be expected from steric considerations. If the other factor of 35 results from a difference in activation energy, the activation energy of the $F + CF_3H$ reaction would have to be larger by about 2.1 kcal/mole.

Two studies (Ref. 37 and 38) have established that the energy distribution in the $F + CH_4$ reactions is HF(3), 14%; HF(2), 64%; and HF(1), 22%, assuming no HF(0) is formed. Johnathan, et al. (Ref. 37) reported that the $F + CH_4$ global rate is faster by a factor of 1.35 than that of the $F + H_2$ reaction. In this study, the reaction with CH_4 was found to be faster than the reaction with H_2 by a factor of 3. A rate constant of $3 \times 10^{14} \exp(-1150/RT)$ has been reported for $F + CH_4$ (Ref. 40). At 298 K, this gives a rate constant of 4.3×10^{13} , only slightly larger than the value of 3.2×10^{13} reported here. However, this literature value is reported per H atom in CH_4 making the reported rate more than 5 times faster than the rate measured in the EPR reactor. Thus, the rates reported in the literature for the $F + CH_4$ reaction vary by an order-of-magnitude but bracket the rate measured in this study.

Reaction of F with C_3H_8

The rate of the reaction $F + C_3H_8$ was investigated using instrument grade propane. The fluorine atoms were produced from molecular fluorine by microwave discharge.

A summary of the experimental conditions and the value of the global rate constants calculated using Eq. III-4 and the simplified numerical solution to Eq. III-14 through III-18 are given in Table XLVI. The first three experiments listed in Table XLVI were conducted at too high a concentration of C_3H_8 . As a result, the reactions were too fast to be measured with accuracy, i.e., the concentration of F dropped quite rapidly with small changes in the injector probe position. Two of these experiments could not be reasonably fitted with a single rate constant and, hence, no value is given for them in Table XLVI. The value of $5 \times 10^{13} (\text{mole/cc})^{-1}\text{sec}^{-1}$, obtained in the fourth and fifth experiments listed in Table XLVI is considered to be the best value of the rate constant for the

Table XLVI. RATE DATA $F_2 + F + C_3H_8 \rightarrow C_3H_7$ at 298 K

Fluorine Source	Pressure, torr	F, atoms/cc	$(C_3H_8)/(F)$	Velocity, * cm/sec	Rate Constant $(\text{mole/cc})^{-1} \text{sec}^{-1} \times 10^{-13}$	
					Eq. III-4	Eq. III-14 through III-18
F ₂	2.21	0.82×10^{13}	26.5	16,220	2.6 to 4.2	-
F ₂	2.21	3.22×10^{13}	4.41	16,720	3.64	4.7
F ₂	1.88	2.41×10^{13}	7.25	14,600	3.1 to 5.5	-
F ₂	2.21	1.07×10^{13}	5.9	16,550	4.5	5
F ₂	2.51	1.01×10^{13}	4.67	17,600	4.7	5

* Average velocity at the pressure tap closest to the EPR cavity.

reaction $F + C_3H_8 \rightarrow HF + C_3H_7$ obtained from these fast-flow experiments. This rate constant can be compared with the values 2.2×10^{13} to 5.2×10^{13} (mole/cc) $^{-1}$ sec $^{-1}$ for the abstraction of a primary hydrogen and 0.82×10^{13} to 2.0×10^{13} (mole/cc) $^{-1}$ sec $^{-1}$ for the abstraction of the secondary hydrogen obtained by Fettis, Knox, and Trotman-Dickenson (Ref. 33 and 34).

Side reactions between F and the C_3H_7 radical are possible and undoubtedly occur. The importance of these reactions is minimized by keeping the initial C_3H_8/F ratio high (as in these experiments) so that the ratio C_3H_8/C_3H_7 will always be large.

Reaction of F with HI

During the course of determining the rate constant for the reaction $F + HI \rightarrow HF + I$, it was found that the 5220 G fluorine line was overlapped by a strong iodine line. Because of this problem, another F line at 5311 G was calibrated using the 5220 G line. While not as strong a line, the 5311 G line at 8.860 GHz proved to be satisfactory for the rate measurement. About a five-fold excess of HI was employed so that the reaction would again approximate a first-order process.

Figure 198 contains the experimental data plotted as the log of the fraction of remaining F versus distance from the point of reactant mixing to the EPR cavity. Plotted on the same figure are the theoretical lines computed for three different values of the rate constant. The experimental data yielded a curve which changes in slope with Δx in a way that is not predicted by the theoretical lines. The difference may be caused by mixing effects at the injector tip or perhaps by some side reaction with F. The best value for the rate constant of the F + HI reaction is about 1.7×10^{13} (mole/cc) $^{-1}$ sec $^{-1}$.

Jonathan et al. (Ref. 37) determined the following product distribution for the very exothermic F + HI reaction: HF(6), 14%; HF(5), 22%; HF(4), 17%; HF(3), 14%; HF(2), 13%; HF(1), 11% and HF(0), 9%. They estimated that the global rate constant for the F + HI reactions is larger by 20 percent than that for the F + CH_4 reaction. In this study, the HI global rate was found to be smaller than the CH_4 rate by about a factor of 2.

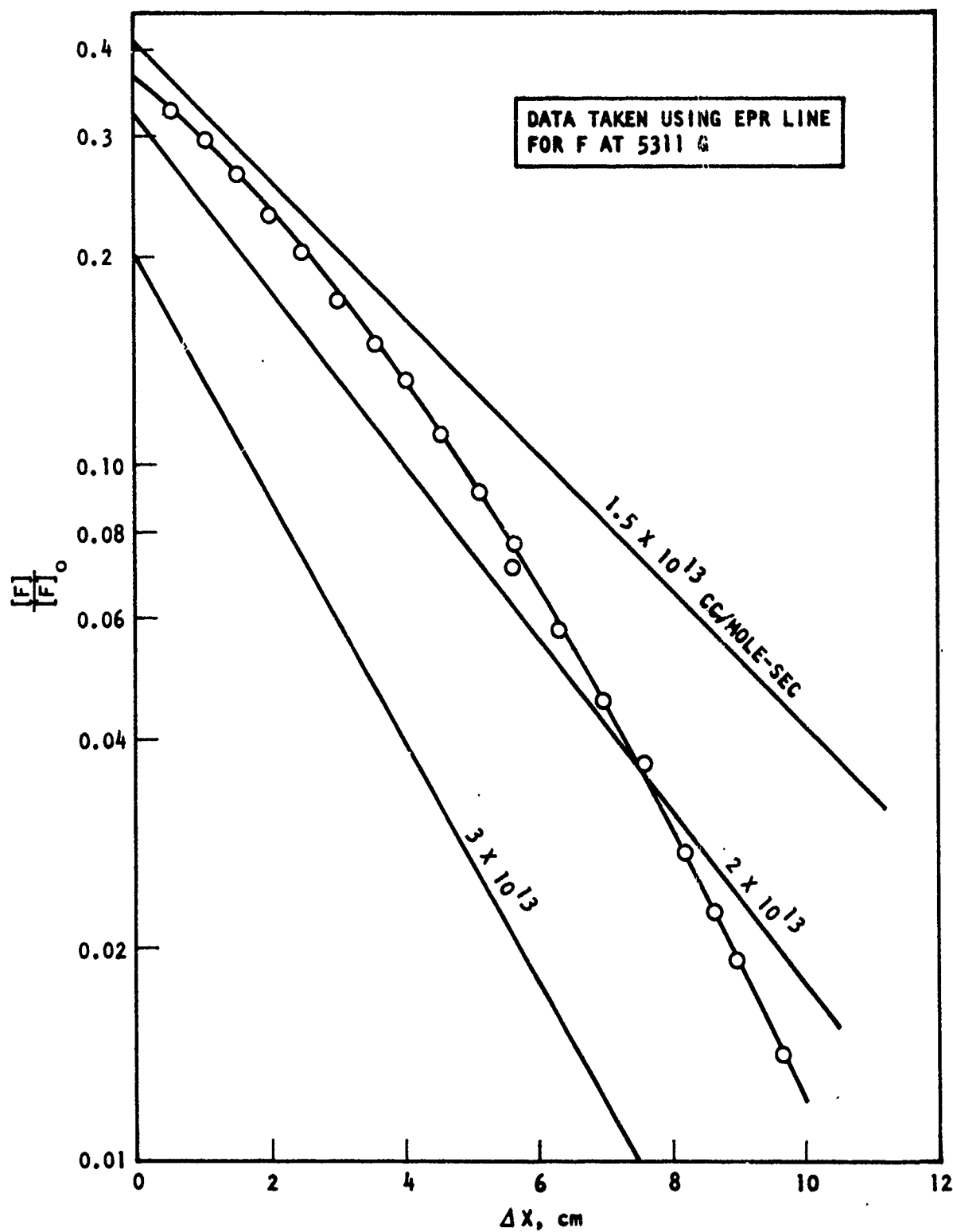


Figure 198. . Experimental Data, $F + HI \rightarrow HF + I$

Summary of Measured Rate Constants

The global rate constants measured in this study in the EPR fast-flow reactor at room temperature are summarized in Table XLVII.

TABLE XLVII. SUMMARY OF MEASURED GLOBAL RATE CONSTANTS (298 K)

Reaction	Global Rate Constant, (mole/cc) ⁻¹ sec ⁻¹	ΔH, 298 K, Kcal/mole
F + H ₂ = HF + H	1.0 x 10 ¹³	-31.9
F + HBr = HF + Br	2.4-3.1 x 10 ¹³	-48.6
F + CF ₃ H = HF + CF ₃	1.0 x 10 ¹¹	
F + CH ₄ = HF + CH ₃	3.2 x 10 ¹³	-31.3
F + C ₃ H ₈ = HF + C ₃ H ₇	5 x 10 ¹³	
F + HI = HF + I	1.7 x 10 ¹³	-64.8

NOMENCLATURE

A	= area, in. ² or cm ²
a_e	= nozzle exit flow speed of sound, cm/sec
A_j	= coefficient for $i-1$ step
A_k	= matrix of coefficients
$[A]$	= concentration of A
$[A]_0$	= initial concentration of A
B	= empirical constant in the cavity signal distribution function
$[B]$	= concentration of B
B_j	= coefficient for i th step
C_j	= coefficient for $i + 1$ step
C_i	= concentration of specie i (moles/vol)
C^*_{act}, C^*_{nom}	= measured characteristic velocity, $P_c A_t / \dot{w}_{total}$, ft/sec
C^*_{theo}	= theoretical characteristic velocity, ft/sec
D	= diameter, in. or cm
\mathcal{D}_i	= diffusion coefficient
EPR	= electron paramagnetic resonance
f	= friction factor
F	= quantum number, the magnitude of the resultant angular momentum vector
f_{ij}^k	= mole fraction of species k at point i, j
f_k	= mole fraction of species k
g	= throat gap, cm
$g[A]$	= reactant concentration as a function of axial distance along the flow tube
He, percent	= mass percent of helium flow, $\dot{w}_{He} / \dot{w}_{total}$
ΔH_{del}	= enthalph change in heating one mole diluent
ΔH_{fuel}	= heat of combustion half-reaction, B-12, per mole F-atom combusted
ΔH_c	= overall heat of combustion per mole F combusted
ΔH_{ox}	= enthalpy change when oxidizer dissociates to form one mole F atom
i, j, k	= used as subscripts or superscripts to denote species or location in axial and radial direction
k, k'	= kinetic rate constant
K_p	= equilibrium constant in pressure units

k_w	= reaction rate constant for wall reactions
l	= 1/2 of the effective length of the ERP cavity
L	= length, in. or cm
L_{max}	= distance from the sonic choke point, in. or cm
m	= number of increments in the radial direction
m_f	= sum of the spin orbital angular momentum and the nuclear angular momentum
M	= Mach number, the ratio of the gas velocity to the velocity of sound
MR	= mixture ratio, $\dot{w}_{oxid}/\dot{w}_{fuel}$
M_e	= nozzle exit flow Mach number
MW	= molecular weight, gm/mole
N	= number of nozzles (in Phase 2)
n_{fuel}^{prod}	= total moles products formed when one mole of F atoms is combusted with fuel
n_{fuel}	= fuel stoichiometric factor in Eq. I-18
n_{ox}^c	= oxidizer stoichiometric factor in Eq. I-18
n_{prod}^c	= total moles products formed in overall combustion reaction (Eq. I-18) per mole F combusted
N	= total molar flowrate
p	= pressure, lb/in. ²
p_i	= partial pressure of species i
$p_{t,o}$	= total pressure, lb/in. ²
p_L	= cavity pressure, torr
Q	= measured heat loss = $(C_p \Delta T \dot{w})_{coolant}$, calories/sec
r	= radius, in. or cm
r_o	= tube radius, in. or cm
R	= gas constant, Btu/lb-K
R_c	= $\frac{\text{moles } F_2}{\text{moles } D_2}$ in combustor
R_L	= $\frac{\text{moles } H_2}{\text{moles of } F_2 \text{ available for lasing}}$ in cavity
R_ψ	= $\frac{\psi_c}{\psi_L}$
R_1	= moles F combusted per mole F atom burned

R_2	= moles diluent in products per mole F atom formed
Re	= Reynolds number ($Dv\rho/\mu$)
$s(x)$	= EPR signal distribution function
$S(X)$	= EPR signal
t	= time, sec
T	= temperature, K
T_0	= total temperature, K
v	= velocity, cm/sec
v_0	= velocity at the center of the fast-flow reactor, cm/sec
\dot{w}_x	= flowrate of component x, lb/sec or gm/sec
x, x	= axial distance, cm or in.
x_0	= distance from the injector probe tip to the center of the EPR cavity, cm or in.
y_E	= nozzle exit half width, cm
y_{NS}	= nozzle separation thickness, cm

GREEK LETTERS

α	= $\frac{\text{moles F}}{\text{moles F} + 2 \text{ moles F}_2}$ in combustor
γ	= ratio of specific heat at constant pressure to specific heat at constant volume
μ	= viscosity
ρ	= density, lb/ft ³
ψ_c	= $\frac{\text{moles DF} + \text{moles He}}{\text{moles of F}_2 \text{ available for lasing}}$ in combustor
ψ_L	= $\frac{\text{moles DF} + \text{moles He}}{\text{moles of F}_2 \text{ available for lasing}}$ in cavity

REFERENCES

1. J. A. Shirley, R. N. Sileo, R. R. Stephens, and T. A. Cool: AIAA Paper, No. 71-27, New York, New York, January 25-27, 1971.
2. O. D. Krogh and G. C. Pimentel: J. Chem. Phys. 56, 969 (1972).
3. S. M. King, D. Taylor, M. A. Kwok, and S. W. Mayer: The Aerospace Corp. (preprint), March 1971.
4. M. C. Lin and W. H. Green; J. Chem. Phys. 53, 3383 (1970).
5. Pearson, et al.: 3rd Conference on Chemical and Molecular Lasers, 1, 2, 3, May 1972 paper WB7, St. Louis, Missouri.
6. Axworthy, A. E., J. Q. Weber, E. C. Curtis, and C. Selph: Paper WSS/CI 74-13, presented at the 1974 Spring Meeting of the Western States Section of the Combustion Institute, Pullman, Washington, 7 May 1974.
7. Decorpo, J. J., R. P. Steiger, J. L. Franklin, and J. L. Margave: J. Chem. Phys., 53, 936 (1970).
8. Fletcher, E. A. and L. L. Ambs: Comb. and Flame, 12, 115 (1968).
9. JANNAF Thermochemical Tables, Dow Chemical Co., Midland, Michigan.
10. Lowery, J. J., J. L. Jack, and L. E. Wilson: AFWL-TR-73-273, p. 260-266.
11. Kaufman, F., N. J. Gerri, and D. A. Pascale: J. Chem. Phys., 24, 32 (1956).
12. Benson, S. W. and J. G. Buss: J. Chem. Phys., 27, 1382 (1957).
13. Wilkins, R. C., SAMSO-TR-68-371, Thermodynamics of SF₆ and Its Decomposition and Oxidation Products, Aerospace Corporation, Los Angeles, California, July 1968.
14. Bott, J. F. and N. Cohen: J. Chem. Phys., 59, 4539 (1973).
15. Ahl, J. L. and T. A. Cool: J. Chem. Phys., 58, 5540 (1975).
16. Hinchey, J. J.: J. Chem. Phys., 59, 233 (1973).
17. R-9171, Advanced Fuels for Chemical Lasers, Interim Report, FO4611-72-C-0094, Rocketdyne Division of Rockwell International, Canoga Park, California, 26 January 1973.

18. Lucht, R. A. and T. A. Cool: J. Chem. Phys., 60, 1026 (1974)
19. Hancock, J. K. and W. H. Green: J. Chem. Phys. 59, 6350 (1973).
20. Hinchey, J. J.: J. Chem. Phys. 59, 233 (1973)
21. Ahl, J. L. and T. A. Cool: J. Chem. Phys. 58, 5540 (1973).
22. Osgood, R. M., P. J. Sackett, and A. Javan: J. Chem. Phys. 60, 1464 (1974).
23. Fettis, G. C., J. H. Knox, and A. F. Trotman-Dickenson: J. Chem. Soc. 1960, p. 1064.
24. R-9171, Interim Report, Advanced Fuels for Chemical Lasers, Rocketdyne Division, Rockwell International, Contract F04611-72-C-0094, January 1973.
25. Shapiro, A. H., The Dynamics and Thermodynamics of Compressible Fluid Flow, Vol. I, Ronald Press Co., p. 167, New York, N. Y.
26. Westenburg, A. A. and N. DeHaas, J. Chem. Phys., 50, 707, 1959.
27. Radford, H. E., V. W. Heghes, and V. Beltran-Lopez, Phys. Rev. 123, 153, 1961.
28. Carrington, A., D. H. Levy, and T. A. Miller, J. Chem. Phys., 45, 4093, 1966.
29. Valence, W., B. Birang, and D. I. MacLean, Dept. of Chemistry, Boston College, ONR Contract No. N00014-69-A-0453, Task No. NR-92-53614-25-69 (473), October 1971.
30. Reed, R. C. and Sherwood, T. K., The Properties of Gases and Liquids, Second Edition, Chapter 11, McGraw-Hill, New York, N. Y., 1966.
31. Sherwood, T. K. and R. L. Pigford, Absorption and Extraction, p. 11, McGraw-Hill, New York, N. Y., 1952.
32. Cohen, N., Aerospace Report No. TR-0073(3430)-9, November 1972.
33. Fettis, G. C., J. H. Knox, and A. F. Trotman-Dickenson, J. Chem. Soc., 1064, 1960.
34. Fettis, G. C. and H. H. Knox, Progress in Reaction Kinetics, Vol. 2, Pergamon Press, p. 3, New York, N. Y., 1964.
35. Homann, K. H., et al., Ber. Der Buns. fur physick Chemie, 74, 595, 1970.
36. Dodonov, A. F., et al., reported at the International Symposium on Lasers, Moscow, U.S.S.R., 1969.
37. Jonathan, N., C. M. Melliar-Smith, S. Okuda, D. H. Slater, and D. Timlin, Mol. Phys. 22, 561, 1971.

38. Chang, H. W. and D. W. Setser, J. Chem. Phys., 58, 2298, 1973.
39. Berry, M. J., J. Chem. Phys., 59, 6229, 1973.
40. Wagner, H. G. and J. Wolfrum, Angew. Chem. Int. Ed., 10, 604, 1971.
41. Hancock, J. K. and W. H. Green, J. Chem. Phys., 57, 4515 (1972).
42. Ibid, 56, 2474 (1972).
43. Green, W. H. and J. F. Hancock, IEEE J. Quantum Elec., 9, 50 (1973).
44. Anlaub, K. G., et al., J. Chem. Phys., 58, 5354 (1973).
45. Airey, J. R. and S. F. Fried, Chem. Phys. Lett., 8, 23 (1971).
46. Hosack, G. A., Curtis, E. C., Hyde, J. C. and R. J. Burick, Aero-dynamic Reactive Flow Studies of the HF Laser, Technical Report AFWL-TR-73-100, September 1973.
- 47.

APPENDIX A

ROCKETDYNE THERMOCHEMICAL COMPUTER CODE

A series of thermochemical programs has been developed at Rocketdyne for solving propulsion problems. The basic thermochemical computer program calculates the equilibrium composition at a given pressure and either an assigned temperature or enthalpy. The heart of this program is an efficient method of solving for equilibrium conditions by minimization of the free energy of all possible products. The program is completely general in terms of handling any combination of elements (up to 15 in any given calculation), up to 180 chemical products, and a large variety of multiple-case options. Thermodynamic data for over 600 products (based primarily on the JANNAF data) are available to the program, and this file is continually kept up to date. The program computes combustion parameters such as heat capacity, gamma, molecular weight, density, viscosity, thermal conductivity, and temperature. Options in the basic program include computation of ion concentrations and nonequilibrium control over composition. The sample cases shown in the following printouts consumed only 1 second of computer time, each with a billing cost of \$1.20 per second.

When CRT plots of composition or other gas properties as a function of temperature are desired, the performance program punches the appropriate cards. These cards are read by another program that generates the CRT plots.

The Thermochemical Computer Code is programmed for the IBM System 370, Model 165 computers. The program input requires reactant mixture ratios and temperature. All of the required thermochemical data are stored on the data tape. The code can also be used as a subroutine in other programs.

REFILLANT	RELATIVE MASS IN MIXT OF MIXT	MASS FRACTION	P = MR =	60 PSIA 0.294
F2	1.0000			
OXIDIZER	486.4000	0.2101		
BENZENE	1.0000			
OXIDIZER	39.9380	0.0172		
AIR	1.0000			
EIFL	1788.7400	0.7727		
PRESSURE (PSIA)	60.000			
TEMPERATURE (DEG K)	1509.5			
U (CAL/GM)	622.0			
S (CAL/GM-DEG K)	1.030			
CP, SM. (CAL/GM-DEG K)	0.450			
CP, EQ. (CAL/GM-DEG K)	0.290			
GAMMA, SHIFTING	1.237			
GAMMA, FROZEN	1.293			
VISCOSITY, CENTIPOISE	0.0554			
VISCOSITY (LR/M-FT)	0.1345			
K (RTU/M-FT-DEG F)	0.0540			
PRANDTL NUMBER	0.7252			
MAFF, (GMS/GM-MOLE)	30.177			
WISS, (GMS/LITER)	0.9947			
VELOCITY (FT/SEC)	0.0			
MACH NO, SHIFTING	0.0			
MACH NO, FROZEN	0.0			

COMPOSITION - MOLE PERCENT

F	10.65589
HE	3.99887
F2O	0.00100
CF4	3.98787
NO	0.10453
N2F	1.64499
N2	0.00007
NE3	0.00027
N2	62.95207
FN	0.00019
F2	16.07425
F2	0.54492

CONDILLANT RELATIVE MASS IN MIXT OF MIXT P= 60 PSIA
MR= 0.434

F2 1.0000 484.4000 0.2799
PEN7F1E 1.0000 39.8380 0.0229
FUEL 1.0000 1211.7300 0.6972

PRESSURE (PSIA) 60.000
TEMPERATURE (DEG K) 1744.6
H (CAL/GM) 784.3

S (CAL/GM-DEG K) 1.988
CP,CH. (CAL/GM-DEG K) 0.404
CP,CP. (CAL/GM-DEG K) 0.205
GAMMA, SHIFTING 1.239
GAMMA, FROZEN 1.201

VISCOSITY,CENTIPoise 0.0623
VISCOSITY (LR/HR-FT) 0.1507
K (BTU/HR-FT-DEG F) 0.0610
PRANDTL NUMBER 0.7285
M,FFF. (GMS/GM-MOLE) 29.896
DENSITY (GMS/LITER) 0.8420

VELOCITY (FT/SEC) 0.0
MACH NO, SHIFTING 0.0
MACH NO, FROZEN 0.0

COMPOSITION - MOLE PERCENT

N 0.00166
F 17.07037
HF 5.26363
F2O 0.00611
CO2 0.00050
C6H4 5.16701
NO 0.28203
NOF 0.43065
NO2 0.00124
N2 54.71428
FO 0.00060
O2 14.76038
F2 0.20275

P = 60 PSIA
MR = 39.458

MASS
FRACTION

RELATIVE MASS
IN MIXT OF MIXT

0.2788
0.6965
0.0247

1.0000 485.0000
1.0000 1211.7000
1.0000 43.0000

PROPELLANT

F2 OXIDIZER
AIR
OXIDIZER
BENZENE
FUEL

PRESSURE (PSIA) 60.000
TEMPERATURE (DEG K) 1870.4
H (CAL/GM) 800.2
S (CAL/GM-DEG K) 2.003
CP,SH. (CAL/GM-DEG K) 0.604
CP,FR. (CAL/GM-DEG K) 0.297
GAMMA, SHIFTING 1.184
GAMMA, FROZEN 1.287
VISCOSITY,CENTIPOISE 0.0645
VISCOSITY (LB/MR-FT) 0.1561
K (BTU/MR-FT-DEG F) 0.0637
PRANDTL NUMBER 0.7286
M,EFF. (GMS/GM-MOLE) 30.019
DENSITY (GMS/LITER) 0.7986
VELOCITY (FT/SEC) 0.0
MACH NO, SHIFTING 0.0
MACH NO, FROZEN 0.0

COMPOSITION - MOLE PERCENT

O 0.00434
F 16.33371
HF 5.69915
F2CO 0.57689
CO2 0.01564
CF4 5.10662
NO 0.39537
NOF 0.23910
NO2 0.00139
N2 56.93459
FO 0.00057
O2 14.59385
F2 0.09872

APPENDIX B

LASER KINETICS COMPUTER CODE - VIREL

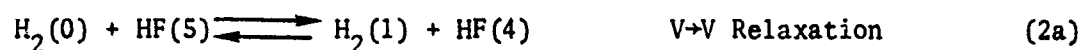
Rocketdyne started work on a computer code (VIREL) in 1966 for analyses of the gas dynamic laser. The computer code at this point is quite general and can consider any gas laser in the one-dimensional or premixed approximation including optics in the plane-parallel wave approximation. Provision was made for communication with a gas-mixing code to permit integration of the rate processes in a chemical, gas transfer, and gas dynamic laser. Particular attention was given to the output and informative plots can be made of all the results of interest. A brief description of the code and the theoretical bases follows.

The initial conditions (i.e., concentration of all constituents and the flowfield) are required as data in addition to the rate processes and rate constants. These rate processes are then integrated over the region of interest giving the concentration of constituents, including the amount of radiation, and the flowfield as a function of distance or time.

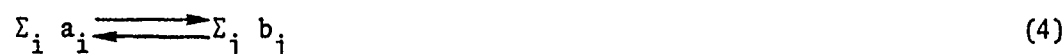
The constituents may be atoms, molecules, or even photons or electrons. Their concentrations are expressed in terms of mole fractions. The number of photons is, of course, arbitrary. Internal energy levels are accounted for as species and the concentration of all species of a given component is forced to add up to the concentration of that component.

Rate processes given as data name the reaction or relaxation process between the individual components and species. Examples are:





Here, H, F₂, F, and H₂ are components and HF(5), HF(4), HF(6), H₂(0), and H₂(1) are species. From chemical kinetics, a rate process (i.e., a reaction between the species) can be written as:



and the rate expression can be written as:

$$\frac{\partial}{\partial t} = k_f \Pi_i a_i - k_r \Pi_j b_j \quad (5)$$

The general process (4) may be shown to be a combination of the simple processes given in reactions 1 through 3. Even the three- to two-body process (1b) is a relatively rare event at pressures below 0.1 atmosphere. The computer code also permits optical or electrical pumping, photo-dissociation, spontaneous emission, and one-body processes.

Stimulated emission is treated by the Einstein equation:

$$\dot{n} = w S(\nu) (B_{21} n_2 - B_{12} n_1) \quad (6)$$

where w is the optical flux density, $S(\nu)$, a line shape function, and B_{21} and B_{12} the rate constants, and n_2 and n_1 , the concentration of the upper and lower levels. The optical flux density is normally expressed as data in a linearly interpolatable table, but may be computed in a self-consistent fashion. When zero optical flux is specified, the low level gain is computed. When a number of uniform optical fluxes are specified, the saturation level and available power may be deduced.

The line shape function is treated by the Voigt model, which reduces the Doppler broadening at low pressures and pressure broadening at higher pressures.* The B coefficient is required as data. The species to which n_2 and n_1 correspond are specified as data and the concentration of each rotational level is computed using the rigid rotor approximation.

The flowfield may be constant pressure, constant or specified area, or constant volume. The ideal gas law with varying specific heat and molecular weight is assumed. The change in flowfield due to heat of reaction, heat addition, and area ratio changes is computed using the influence equations (Ref. 1) for flowing systems which reduces to the ideal gas law for constant-volume systems. The ability to treat heat and mass addition permits using the code to treat boundary layer flow and gas mixing in a relatively straightforward fashion.

The integration formula currently used is an optimized second-order Runge-Kutta predictor corrector method. The method appears to be the most efficient method for a chemical laser and requires as few as 30 steps to integrate the reaction over the length having positive gain. Integration control criteria are required as data and the step size is adjusted to meet but not exceed the accuracy criteria.

The results of a computation may be given in as much or as little detail as required. The contribution of the various processes is listed at selected stations as required. Program outputs are concentrations of the species and components reaction rates, gain and amount of simulated emission, and the flowfield.

APPENDIX B REFERENCE

1. Shapiro, A. H., The Dynamics and Thermodynamics of Compressible Fluid Flow, Vol. I, Ronald Press Co., New York, New York.

*Doppler half-widths are approximately 0.01 cm^{-1} and pressure widths are approximately 0.1 cm^{-1} at standard temperature and pressure so that, at 76-torr pressure, broadening is negligible, although the Voigt method is used until pressure broadening is only 1 percent of Doppler broadening. On the other extreme, the Voigt model is used until the Doppler width is 1/10 of the pressure width.

APPENDIX C

NUMERICAL SOLUTION OF FAST FLOW REACTOR EQUATIONS

WITHOUT AXIAL DIFFUSION

A numerical solution to Eq. III-14 without the axial diffusion term, subjected to the boundary conditions specified by Eq. III-15 and III-16, was obtained by the usual discretization process using the Crank-Nicolson method (Ref. 1).^{*} This involves dividing the field into a number of increments (i and j) in the axial and radial direction and replacing each derivative by a difference approximation. In terms of mole fraction, the difference approximations are given as:

$$f^k(x, r) = f^k(i\Delta x, j\Delta r) = f_{ij}^k, \text{ then}$$

$$\frac{\partial^2 f^k}{\partial r^2} = (f_{i,j+1}^k - 2f_{i,j}^k + f_{i,j-1}^k + f_{i+1,j+1}^k - 2f_{i+1,j}^k + f_{i+1,j-1}^k) / 2\Delta r^2 \quad (1)$$

$$\frac{\partial f^k}{\partial r} = (f_{i,j+1}^k - f_{i,j-1}^k + f_{i+1,j+1}^k - f_{i+1,j-1}^k) / 4\Delta r \quad (2)$$

$$\frac{\partial f^k}{\partial x} = (f_{i+1,j}^k - f_{ij}^k) / \Delta x \quad (3)$$

A bound on the error resulting from the use of these approximations is proportional to $\Delta x^2 + \Delta r^2$ (Ref. 1, p. 193).

This second-order accuracy is maintained for the boundary conditions by using the following approximations in the program

$$\left. \frac{\partial f^k}{\partial r} \right|_{r=r_0} = (f_{i+1,m-1}^k - 4f_{i+1,m}^k + 3f_{i+1,m+1}^k) / 2\Delta r \quad (4)$$

^{*}See References at end of this Appendix.

$$\left. \frac{\partial f_k}{\partial r} \right|_{r=0} = (-3 f_{i+1,j}^k + 4 f_{i+1,j+1}^k - f_{i+1,j+2}^k) / 2\Delta r \quad (5)$$

Employing the above discretization transforms the system of partial differential equations into a system of $m + 1$ linear algebraic equations applicable at any arbitrary axial distance $(i + 1)\Delta x$ from the point where the reaction is initiated. The $m + 1$ algebraic equations are arranged so that all mole fractions of the k th species at position $(i + 1)\Delta x$, $f_{i+1,j-1}^k$, $f_{i+1,j}^k$, and $f_{i+1,j+1}^k$, are on the left side of the equations and are equated to G_j^k which is comprised of the terms involving mole fractions of the k th species at position $i\Delta x$ plus the average of the reaction rate terms at $i(\Delta x)$ and $(i + 1)\Delta x$, i.e.,

$$B_1 f_{i+1,1}^k + C_1 f_{i+1,2}^k + t_{1,3} f_{i+1,3}^k = G_1^k \quad j = 1 \quad (6)$$

$$A_j f_{i+1,j-1}^k + B_j f_{i+1,j}^k + C_j f_{i+1,j+1}^k = G_j^k \quad 2 \leq j \leq m \quad (7)$$

$$t_{m+1,m+1} f_{i+1,m-1}^k + A_{m+1} f_{i+1,m}^k + B_{m+1} f_{i+1,m+1}^k = G_{m+1}^k \quad j = m + 1 \quad (8)$$

Writing the equations for the k th species in matrix form

$$\begin{bmatrix} B_1 & C_1 & t_{1,3} & 0 & 0 & \dots \\ A_2 & B_2 & C_2 & 0 & 0 & \dots \\ 0 & A_3 & B_3 & C_3 & 0 & \dots \\ \vdots & & & & & \end{bmatrix} \begin{bmatrix} f_{i+1,1}^k \\ f_{i+1,2}^k \\ f_{i+1,3}^k \\ \vdots \\ \vdots \end{bmatrix} = \begin{bmatrix} G_1^k \\ G_2^k \\ G_3^k \\ \vdots \\ \vdots \end{bmatrix} \quad (9)$$

and using some predicted value for the $f_{i+1,j}^k$ that appear in the reaction rate term included in G_j^k , the computer program then solves for new values of $f_{i+1,j}^k$ which are compared with the predicted values. If the predicted and new values of $f_{i+1,j}^k$ do not agree within the required amount, the new value of $f_{i+1,j}^k$ becomes the predicted value and the cycle is repeated. This iterative procedure is

continued until successively computed $f_{i+1,j}^k$ agree within specified limits. The matrices solved at each iteration, one for each reactant species, are coupled via the reaction rate terms. Convergence to within 0.01 percent is usually attained in 4 or 5 iterations. The program then proceeds to the next axial increment and again iteratively solves the matrix equation (Eq. 9).

When the axial increments stepped off have passed through the region of the flow tube monitored by the EPR, the solution is completed. All monitored species mole fractions at increments included in the sensing zone of the EPR cavity are multiplied by a suitable cavity signal distribution function, summed, and then averaged over the sensing zone to determine the mole fraction sensed by the EPR and the point x in the flow tube where the average mole fraction equals that measured by the EPR.

WITH AXIAL DIFFUSION

When axial diffusion is not ignored, it is necessary to add another boundary condition to Eq. III-14. Assuming a flow tube of infinite length, the boundary condition at infinity is that the f^k be uniformly bounded. This implies that

$$\frac{\partial f^k}{\partial x} = \frac{\partial f^k}{\partial r} = 0 \quad \text{at } x = \infty \quad (\text{Ref. 3}) \quad (10)$$

At the initial plane, one may specify an initial flux, i.e.

$$\int (vf^k - \mathcal{Q}_k \frac{\partial f^k}{\partial x}) dA = F^k \quad (11)$$

The problem becomes well defined on a closed region, $0 \leq x \leq L$, if L is chosen large enough so that chemical equilibrium has essentially been reached at L . If it is further assumed that f is constant at $r = 0$, then the problem is to solve Eq. III-14 subject to Eq. III-15 and III-16 as well as

$$f^k(0,r) = \bar{f}^k \quad 0 \leq r \leq r_0 \quad (12)$$

$$\left. \frac{\partial f^k}{\partial x} \right|_L = 0 \quad 0 \leq r \leq r_0 \quad (13)$$

where f_k is defined in the expression

$$\bar{f}^k \int \nu dA \left. \frac{\partial f^k}{\partial x} \right|_{x=0} dA = F^k \quad (14)$$

When axial diffusion is ignored, Eq. 12 and 14 reduce to the usual conditions that the initial profile of the k^{th} species be proportional to the feed rate of the k^{th} species.

A computer program has been written which solves Eq. III-14 subject to Eq. III-15, III-16, 12, 13, and 14. Equation 14 is not programmed in explicitly. Rather, \bar{f}^k is set equal to a prescribed input value. Iteration on \bar{f}^k to satisfy Eq. 14 is then performed.

Equation III-14 and the boundary conditions were discretized by an approximation using centered differences:

$$\frac{\partial^2 f^k}{\partial x^2} = (f_{i+1,j}^k - 2f_{ij}^k + f_{i-1,j}^k) / \Delta x^2 \quad (15)$$

$$\frac{\partial^2 f^k}{\partial r^2} = (f_{i,j+1}^k - 2f_{ij}^k + f_{i,j-1}^k) / \Delta r^2 \quad (16)$$

$$\frac{\partial f^k}{\partial r} = (f_{i,j+1}^k - f_{i,j-1}^k) / 2\Delta r \quad (17)$$

$$\frac{\partial f^k}{\partial x} = (f_{i+1,j}^k - f_{i-1,j}^k) / 2\Delta x \quad (18)$$

This results in an error in the differential equation of $O(h^2)$ for $h = \Delta x = \Delta r$ (Ref. 1). For $\Delta x \neq \Delta r$, the simple transformation $r' = r \frac{\Delta x}{\Delta r}$ leads to the same result.

This second-order accuracy is maintained for the boundary conditions by using the following approximations in the program:

$$\left. \frac{\partial f^k}{\partial x} \right|_{x=L} = \frac{f_{N-2,j}^k - 4f_{N-1,j}^k + 3f_{N,j}^k}{2\Delta x} \quad (19)$$

$$\left. \frac{\partial f^k}{\partial r} \right|_{r=r_w} = \frac{f_{i,M-2}^k - 4f_{i,M-1}^k + 3f_{i,M}^k}{2\Delta r} \quad (20)$$

$$\left. \frac{\partial f^k}{\partial r} \right|_{r=0} = \frac{-3f_{i,1}^k + 4f_{i,2}^k - f_{i,3}^k}{2\Delta r} \quad (21)$$

Employing the above discretization transforms the system of differential equations into a system of linear algebraic equations:

The resulting system of linear algebraic equations for species k is coupled to the system for other reactant species through the source terms.

Specifically, the equation is

$$A^k \vec{f}^k = \vec{R}^k \quad (22)$$

Where \vec{f}^k is the vector $(f_{1,1}^k, f_{1,2}^k, \dots, f_{1,M}^k \dots f_{N,M}^k)^t$, \vec{R}^k is the vector representing (except for the boundary equations) the kinetic coupling, and A^k is the matrix of coefficients given by the discretization of Eq. III-14, III-15, III-16, 12, and 13. This matrix is very sparse and banded. Solution of Eq. 22 for each reactant species k is carried out using an elimination algorithm especially designed to take into the account the special nature of A^k .

Great care has to be exercised since, even though the discretization used is appropriate for elliptic equations like Eq. III-14, the presence of a large axial convection term tends to make the system behave as an initial value problem (e.g., Ref. 3). This being the case, the whole matrix solution portion was coded in double precision.

The right side of Eq. 22, \vec{R}^k , will, in general, be a function of $\vec{f}^1, \dots, \vec{f}^K$, where K equals the number of species. That portion that is a function of \vec{f}^k is linearized and brought over to the left side and combined with A^k . The remainder is left on the right side. In solving the k^{th} system, the computer program iterates successively using at each stage the most current estimate of $\vec{f}^{k'}$, $k' \neq k$. Typically, convergence is reached in four to five steps.

APPENDIX C REFERENCES

1. Forsyth, G. E. and W. R. Wasow, Finite Difference Methods for Partial Differential Equations, p. 143; Theorem 20.8, p. 193, John Wiley & Sons, Inc., New York, N. Y., 1960.
2. Tychonov, A. and A. Samarski, Partial Differential Equations of Mathematical Physics, P. 265-267, Holden-Day, Inc., San Francisco, 1970.
3. Strang, G. and G. J. Fix, An Analysis of the Finite Element Method, p. 120, Prentice Hall, Inc., Englewood Cliff, N. J., 1973.

APPENDIX D

DISTRIBUTION LIST

<u>Addresses</u>	<u>Copies</u>
Aero-Chem Research Library P. O. Box 12 Princeton, New Jersey 08540	1
Aerospace Corporation Attn: Dr. G. P. Millburn P. O. Box 95085 Los Angeles, California 90045	1
AFRPL/Technical Library	1
AFRPL/DOZ	1
Edwards, California 93523	
Kirtland AFB, New Mexico 87117	
AFWL/ALD	2
AFWL/LR	1
AFWL/PG	1
Air University Library For SE70-325a Maxwell AFB, Alabama 36112	1
AVCO/Everett Res. Laboratory Attn: Dr. George Sutton	1
Dr. Jack Daugherty	1
2385 Revere Beach Parkway Everett, Massachusetts 02149	
Dr. Don Bell 6151 W. Century Blvd., Suite 500 Los Angeles, California 90045	1
Bell Aerospace Company P. O. Box One Buffalo, New York 14240 Attn: Dr. W. C. Solomon	1
Boeing Company P. O. Box 3999 Seattle, Washington 98124 Attn: Dr. E. K. Bjornerud (2-1414, MS 8C-88)	1

<u>Addresses</u>	<u>Copies</u>
Defense Advanced Research Projects Agency 1400 Wilson Boulevard Arlington, Virginia 22209 Attn: Director, Laser Division	1
Hughes Aircraft Company Attn: Dr. Mastrup, Bldg. 6 Mail Sta. C-129 Culver City, California 90230	1
Hercules, Incorporated Industrial Systems Dept. Wilmington, Delaware 19899 Attn: Mr. J. E. Greer, Director Systems Group	1
Martin-Marietta Corporation Denver Division Attn: Mr. S. G. Chapin P. O. Box 179 Denver, Colorado 80201	1
Navy Laser Liaison Office AFWL (HELP-LO) Kirtland AFB, New Mexico 87117 Attn: Dr. John L. Walsh	1
Naval Research Laboratory Washington, D.C. 20390 Attn: Dr. W. R. Cooy (Code 6503-LTPO) Dr. W. H. Gandy (Code 6506) Dr. A. I. Schindler (Code 6330) Dr. H. Shenker (Code 6530) Mr. D. J. McLaughlin (Code 6507)	1 1 1 1 1
TRW Systems Group One Space Park, Bldg R-1, Rm. 2044 Redondo Beach, California 90278 Attn: Mr. Norman Campbell	1
U. S. Army Missile Command/R&D Division Redstone Arsenal, Alabama 35809 Attn: Dr. J. P. Hallowes, Jr. Mr. Walter Jennings Dr. Tom Barr	1 1 1

<u>Addresses</u>	<u>Copies</u>
United Aircraft Res. Laboratories 400 Main Street East Hartford, Connecticut 06108 Attn: Mr. G. H. McLafferty Mr. Albert Angelbeck	3 1
U. S. Naval Ordnance Laboratory Chemical Engineering Division Attn: Barry Pallay, Bldg. 308 White Oak, Silver Spring, Maryland 20910	1
McDonell Douglas Corporation Library P. O. Box 516 St. Louis, Missouri	1 1